RADAR EQUATIONS for Modern Radar

DVD INCLUDED

David K. Barton

Radar Equations for Modern Radar

DISCLAIMER OF WARRANTY

The technical descriptions, procedures, and computer programs in this book have been developed with the greatest of care and they have been useful to the author in a broad range of applications; however, they are provided as is, without warranty of any kind. Artech House and the author and editors of the book titled *Radar Equations for Modern Radar* make no warranties, expressed or implied, that the equations, programs, and procedures in this book or its associated software are free of error, or are consistent with any particular standard of merchantability, or will meet your requirements for any particular application. They should not be relied upon for solving a problem whose incorrect solution could result in injury to a person or loss of property. Any use of the programs or procedures in such a manner is at the user's own risk. The editors, author, and publisher disclaim all liability for direct, incidental, or consequent damages resulting from use of the programs or procedures in this book or the associated software.

For a complete listing of titles in the
Artech House Radar Series,
turn to the back of this book.

Radar Equations for Modern Radar

David K. Barton

ARTECH
HOUSE
BOSTON | LONDON
artechhouse.com

Library of Congress Cataloging-in-Publication Data
A catalog record for this book is available from the U.S. Library of Congress.

British Library Cataloguing in Publication Data
A catalogue record for this book is available from the British Library.

Cover design by Vicki Kane

ISBN 13: 978-1-60807-521-8

685 Canton Street
Norwood, MA 02062

10 9 8 7 6 5 4 3 2 1

Contents

Preface

The starting point for analysis of radar performance is the *radar range equation*, which gives the maximum range at which a specified signal-to-noise ratio, required for successful detection of a target, can be obtained. The physical principles behind what is usually called simply the *radar equation* have been known since the work performed during World War II and reported in the unclassified post-war paper by Norton and Omberg.[1] Subsequent books on radar systems, starting with Ridenour's *Radar System Engineering* in 1947, have included chapters in which the equation is derived and expressed in different ways, with terms characterizing the radar, the target, the detection requirements, and the environment in which the radar operates. The complexity of environmental effects leads most of these discussions to presentation of an equation giving the range in an environment where thermal noise is the only source of interference competing with the target echo, and where the path between the radar and the target is characterized by a range-dependent atmospheric attenuation factor.

The most thorough discussion of the radar equation appeared in Blake's *Radar Range-Performance Analysis*, based on work by that author at the Naval Research Laboratory between 1940 and 1972, and published in 1980. That book is of lasting value and remains in print after more than thirty years. The reader is urged to obtain and read it.

The objective of this new volume is to extend Blake's classic work to ensure applicability of radar equations to design and analysis of modern radars, to identi-

[1] See the list of references at the end of Chapter 1.

fy what information on the radar and its environment is needed to predict detection range, and to provide equations and data to improve the accuracy of range calculations. The chapter outline follows generally that of Blake's book so that the reader can better appreciate his contributions while identifying extensions that are useful in application to modern radars. Special attention is directed to propagation effects, methods of range calculation in environments that include clutter and jamming in addition to thermal noise, and to establishing the many loss factors that reduce radar performance.

There are two conflicting approaches to deriving a radar equation. Following the Naval Research Laboratory work of World War II and Blake's elegant extensions, we adopt here the first approach. In addition to the standard geometrical relationships for a wave spreading as it moves through space, it uses the concept of the *matched filter*, in which the ratio of input signal energy to noise spectral density, during the *observation time* on the target, is used to calculate the *maximum possible* output signal-to-noise (power) ratio SNR that would be obtained in an ideal (lossless) system. The input signal *energy* is proportional to the average power of the transmission, regardless of its waveform. A succession of loss factors is applied to find the output SNR for the practical radar being considered, as a function of the target range. The detection range is then the range at which that SNR meets the requirement for a stated probability of detection, given a required false-alarm probability. That requirement is identified as the *detectability factor*, and it depends on details of the practical signal processing method used in the radar.

Following the first approach, the efficiency of the radar can be compared to that of an "ideal" system in terms of the total of losses that have been introduced the practical implementation. Inspection of the loss budget may suggest improvements in design or modeling, but performance beyond that of the ideal system is clearly ruled out.

The alternative approach calculates the output SNR of a single pulse at the receiver output as a *power* ratio, dependent on such parameters as receiver bandwidth, peak power of the transmission, and many other factors in design of the practical radar. In most cases that SNR is inadequate for reliable detection, and a succession of *processing gains* is applied to bring it to the required level at some calculated detection range. That evaluation, if correctly performed, would give the same range as the first approach.

The hazard in the second approach is that no theoretical limit to performance is established as a check on how much processing gain is theoretically available. The receiver bandwidth and processing gains in a modern radar, using complex pulse-compression waveforms, mixtures of coherent and noncoherent integration, and digital processing, are difficult to define. Too many cases have occurred in which the calculated performance exceeds that available from a matched-filter system, as cascaded gains are applied incorrectly to the analysis.

Blake's work was motivated by the requirement that Naval Research Laboratory perform accurate evaluations of competing contractor proposals for new naval radar designs. It provided a means of comparing systems when detailed information was omitted or described in a way that protected "proprietary technology." The *Blake Chart*, discussed here in Chapter 1, became the gold standard for clarifying issues of radar range performance. Open publications of the work allowed radar professionals to obtain reproducible results on a wide variety of radar system designs.

What is surprising is that subsequently published radar texts fail to take advantage of this work. Blake contributed the chapter on the radar equation to the 1970 and 1990 editions of Skolnik's *Radar Handbook*, but to this day other texts continue to use radar equations in which a "receiver bandwidth B" appears in the denominator of the equation to give receiver "noise power" that is proportional to that bandwidth. The radar novice might conclude that as $B \rightarrow 0$ the SNR $\rightarrow \infty$, although disabling the receiver does not improve its detection performance. Transmission of a pulse-compression waveform having B = 100 MHz yields a *noise bandwidth* B_n = 100 MHz for the matched pulse-compression filter, according to the accepted definition of that term given in Chapter 6 of this book. A large "pulse-compression gain" must be included somewhere in the equation if that bandwidth is used in the denominator. Similar confusion applies when digital Doppler filtering is used with a coherent pulse train, or when multiple pulses are integrated after envelope detection.

Experience shows that a radar range equation containing receiver bandwidth B has a high probability of causing serious errors, which can be avoided using Blake's approach.

Another source of error is using *noise figure* F and a standard temperature T_0 = 290K in the denominator of the radar equation. When the product $N = kT_0FB$ is used for noise power, the result is pessimistic for radars that look into a cold sky. An alternative form appearing in a least one recent text substitutes the expression $N = kT_0(F - 1)B$, which predicts that $N \rightarrow 0$ as $F \rightarrow 1$. This leads to optimistic results for any radar operating in an environment with temperature above –273° Celsius. Blake addresses this problem in a way that achieves accurate results for any environment, as discussed here in Chapter 6.

Blake's inclusion of the *pattern-propagation factors* F_t and F_r in the radar equation addresses a host of problems that complicate range calculation. Omission of that factor from presentation of the equation, even when propagation effects are discussed elsewhere in a text, invites error.

Given that Blake uses the approach in his papers and textbook that avoids these errors, what justifies a new book on the subject?

First, equations for detection in environments in which clutter and jamming add to thermal noise are discussed only briefly by Blake. More detailed treatment is needed, especially in the case of clutter, which cannot be modeled by a Gaussi-

an probability density function and a uniform spectral density. This subject is covered here in Chapters 3 and 9.

Second, use of diversity (in time, frequency, space, or polarization) is an important method of minimizing the energy required for detection probabilities greater than 50%. This subject is explored in detail in Chapter 4. That chapter presents methods not discussed by Blake or the collaborator in his text by which the detectability factor can be calculated on personal computers for different radar and target models that provide measures of diversity to reduce the detectability factor.

Third, new radar technology such as active phased arrays presents problems in analysis that were not anticipated in Blake's work. For example, the multifunction array radar (MFAR) must often economize on scan time by minimizing overlap in beam positions. The optimization of beam spacing during scanning of a volume requires a compromise between scan time and total energy expended to achieve the required detection probability. This subject is explored in Chapter 5.

Fourth, much of Blake's material involves a mixture of metric and "U.S. customary units" such as nautical miles and kilofeet. We have found that consistent use of metric units in radar performance analysis avoids introducing errors in conversions to and from other systems. When presenting results to U.S. Navy or Air Force personnel or others unaccustomed to using metric units, a simple conversion after completion of the analysis provides the modified data with minimal opportunity for error.

Lastly, this writer hopes that Blake's legacy to the profession will not be compromised by calling attention to an inconsistency in use of his *bandwidth correction factor* C_b as a factor multiplying the detectability factor in the denominator of the radar equation (see Section 1.3). That factor, as defined and plotted by Blake, is unity for an optimum product of bandwidth and pulsewidth $B_n\tau \approx 1.2$, and hence is applicable only to multiply the *visibility factor* of a cathode-ray-tube display. If it is applied to multiply the detectability factor for electronic detection, the result is optimistic by ≈ 2 dB, an error which is inconsistent with the accuracy desired and available from the rest of Blake's approach.

What accuracy should be expected of range calculations using the radar equation? Blake discusses this issue at the end of his chapter on pulse-radar detection-range computation without arriving at numerical estimates. Marcum, in his classic work on detection theory,[2] warned of pitfalls in range calculation:

> The number of pitfalls that may be encountered in the use of the [radar] equation are almost without limit, and many of these difficulties have been recognized in the past

He goes on to mention three of the most troublesome as evaluation of the target cross section, the minimum discernible signal power, and the statistical nature of detection range as a function of detection probability. To his list we must add

[2] See reference [4] of Chapter 4.

the uncertainty in target location relative to points of maximum radar system response in four-dimensional radar space, and the presence of other than thermal noise in the environment.

Even in cases where only thermal noise is present, the accuracy can seldom be better than about three decibels in required and achieved energy ratio (equivalent to about 20% in free-space range). In a clutter environment, reduced accuracy is inevitable, and the resulting error in range, even for 3-dB error in signal-to-clutter ratio, may exceed 20%.

It remains useful to perform calculations to precisions of a fraction of one decibel. This permits alternative designs to be compared with greater precision, and loss budgets to be evaluated as a guide to improved designs. With careful modeling, it is unnecessary to add several decibels of error to that caused by uncertainties in the environment or the performance of radar operating and maintenance personnel. When radar performance in field tests fails to measure up to specifications and predictions, it is common to attribute the difference to a "field service loss" or "operator loss" of several decibels, when in fact the performance was never designed into the radar system.

This book is intended to provide methods by which the errors in predicting radar range performance can be minimized, even though they cannot be avoided completely.

The author would like to express his thanks to Dr. Paul Hamilton for his review of the manuscript during its generation, and to many colleagues, especially Harold Ward and William Shrader, whose advice over many years has been essential to understanding the factors that affect radar detection range. Lamont Blake was one of those colleagues, and his insights will continue to guide the future efforts of the radar community.

CHAPTER 1

Development of the Radar Equation

The radar range equation was developed during World War II to permit analysis of radar system performance and to guide radar developers in choosing among the limited design options available in that era. The earliest literature on the subject was subject to military security restrictions but was published after the end of the war and has been widely distributed.

The basic approach to predicting radar detection range has remained consistent with the early work, summarized in the first published paper on the radar equation: the 1947 paper by Norton and Omberg of the U.S. Naval Research Laboratory [1, 2]. We will refer to that equation as the *original radar equation*. In this chapter we review the steps by which the radar equation was developed, and discuss its evolution to forms that can be applied to analysis and design of modern radar systems. To avoid confusion from varied symbols used by different authors, we replace those used in the referenced works with a consistent system of symbols, defined as they occur and listed in Appendix A at the end of this book. This permits direct comparison of the equations and their limitations and applicability to current problems.

1.1 RADAR EQUATION FUNDAMENTALS

The objective of the radar equation is to calculate the maximum range R_m at which the desired detection performance can be achieved for a specified set of radar, target, and environmental parameters. The radar equation discussed in this chapter is limited to an environment in which thermal noise is the only source of interference against which a target echo signal must successfully compete to be detected. Equations for other environments are developed in Chapter 3.

The radar range equation is derived in three steps:

1. Express the *maximum* signal-to-noise ratio that is *available* with given parameters, as a function of range;
2. Express the *minimum* signal-to-noise ratio that is *required* to meet detection requirements;
3. Combine these expressions to solve for the *maximum* range at which the requirement is met for the specified radar.

1.1.1 Maximum Available Signal-to-Noise Ratio

It was determined in classified work by North during World War II [3], subsequently reprinted in *Proceedings of the IEEE*, that the maximum possible signal-to-noise power ratio $(S/N)_{\max}$ is obtained when the receiving system uses the *matched filter* for the transmitted waveform. This maximum ratio is equal to the energy ratio E/N_0 of the waveform,[1] where E is the energy of the echo signal and N_0 is the spectral density of competing thermal noise. The expression to be developed in step 1 gives E/N_0 for the specified system parameters. In [1], E/N_0 is defined as the available energy ratio of a single pulse, referred to the output port of the receiving antenna. That reference point is used throughout this book.

The energy density E_p of the outgoing pulse, measured at an arbitrary range R from an isotropic transmitting antenna, is

$$E_p = \frac{E_t}{4\pi R^2} \quad \left(\text{J/m}^2\right) \tag{1.1}$$

where E_t (joules) is the energy of the transmitted pulse and $4\pi R^2$ is the area of a sphere of radius R centered on the radar. For an assumed rectangular pulse of width τ (s) and peak power P_t (W), $E_t = P_t\tau$ (J). For a transmitting antenna with gain G_t, the energy density on the axis of the beam is increased by that gain:

$$E_p = \frac{E_t G_t}{4\pi R^2} = \frac{P_t \tau G_t}{4\pi R^2} \quad \left(\text{J/m}^2\right) \tag{1.2}$$

After reflection from a target having a radar cross section σ (m^2), the energy density E_a of the echo incident on the radar receiving antenna is

$$E_a = \frac{E_p \sigma}{4\pi R^2} = \frac{P_t \tau \sigma}{\left(4\pi R^2\right)^2} \quad \left(\text{J/m}^2\right) \tag{1.3}$$

Equation (1.3) follows from the definition of radar cross section [4].

---

[1] Note that *energy ratio* in this book is E/N_0, not $\Re = 2E/N_0$ used in some texts.

The radar receiving antenna with effective aperture A_r captures energy E given by

$$E = E_a A_r = \frac{P_t \tau G_t A_r \sigma}{\left(4\pi R^2\right)^2} \quad \text{(J)} \tag{1.4}$$

Using the expression for receiving antenna gain

$$G_r = \frac{4\pi A_r}{\lambda^2} \tag{1.5}$$

where λ is wavelength, we obtain the desired equation for the maximum available signal energy at the output port of a pulsed radar receiving antenna:

$$E = \frac{P_t \tau G_t G_r \lambda^2 \sigma}{\left(4\pi\right)^3 R^4} \quad \text{(J)} \tag{1.6}$$

So far we have considered an ideal case in which the transmitter delivers its output directly to the antenna, and where there are no losses along the transmitter-target-receiver path that reduce the received signal energy. To allow for such radio-frequency (RF) losses, a factor L_1 can be included in the denominator, yielding

$$E = \frac{P_t \tau G_t G_r \lambda^2 \sigma}{\left(4\pi\right)^3 R^4 L_1} \quad \text{(J)} \tag{1.7}$$

The derivation of (1.7) follows the procedure presented in today's radar texts, but differs from many of these in expressing the *energy* of the transmitted and received pulses rather than *power*.

To find the available energy ratio, the noise spectral density N_0 (W/Hz), referred to a receiver connected directly to the antenna output port, is expressed as

$$N_0 = kT_s \quad \text{(W/Hz or J)} \tag{1.8}$$

where

k = 1.38×10^{-23} J/K is Boltzmann's constant;
T_s = system noise temperature in kelvins (K) (see Chapter 6).

Combining (1.7) and (1.8), we obtain the maximum available signal-to-noise power ratio:

$$\left(\frac{S}{N}\right)_{\max} = \frac{E}{N_0} = \frac{P_t \tau G_t G_r \lambda^2 \sigma}{(4\pi)^3 R^4 k T_s L_1} \tag{1.9}$$

1.1.2 Minimum Required Signal-to-Noise Ratio

The second expression used in derivation of the radar equation gives the energy ratio required to obtain the specified detection performance. It is assumed in [1] that detection is performed by a human operator observing a cathode-ray-tube display that presents *n* successive echo pulses:

$$V(n) = \frac{E_{\min}}{N_0} \tag{1.10}$$

where $E_{\min}$ is the minimum energy of each received pulse that renders the *n*-pulse group visible on the display under optimum viewing conditions. This is consistent with the current definition [4]:

> **visibility factor (pulsed radar)** The ratio of single-pulse signal energy to noise power per unit bandwidth that provides stated probabilities of detection and false alarm on a display, measured in the intermediate-frequency portion of the receiver under conditions of optimum bandwidth and viewing environment.

The minimum required energy is thus

$$E_{\min} = N_0 V(n) = k T_s V(n) \quad (\mathrm{J}) \tag{1.11}$$

The number of pulses *n* is given by the product of the pulse repetition frequency f_r and the observation time t_o, which is the lesser of the dwell time of the radar beam on the target or the time constant of the display and human observer:

$$n = f_r t_o \tag{1.12}$$

Thus the required energy ratio can be reduced by integration of successive pulses obtained with broad beams or slow scanning of the radar across the target position.

Experimental values for $V(n)$ with an optimum A-scope[2] were reported in [5]. These and similar results for the PPI displays[3] are presented in [6–12]. For radar systems in which electronic detection replaces visual detection, the visibility factor is replaced by a *detectability factor* $D(n)$, defined [4]:

---

[2] The A-scope displays receiver output voltage vs. range.

[3] The PPI displays receiver voltage as intensity on a polar plot of range vs. azimuth angle.

In pulsed radar, the ratio of single-pulse signal energy to noise power per unit bandwidth that provides stated probability of detection for a given false alarm, probability, measured in the intermediate-frequency amplifier bandwidth and using an intermediate-frequency filter matched to the single pulse and followed by optimum video integration.

Subscripts are sometimes added to V and D to denote the target model and the detection probability to which they apply (e.g., $V_{0(50)}$, denoting the energy ratio required for 50% probability of detection on a steady (Case 0) target [6–12]). In general, V exceeds D as a result of the lower efficiency of the visual detection process, as discussed in Section 4.6.

1.1.3 Maximum Detection Range for Pulsed Radar

Setting the available E/N_0 in (1.9) equal to the required value V or D, the equation for maximum range of a pulsed radar is obtained:

For visual detection:
$$R_m = \left[\frac{P_t \tau G_t G_r \lambda^2 \sigma}{(4\pi)^3 k T_s V(n) L_1} \right]^{1/4} \quad (\text{m}) \tag{1.13}$$

For electronic detection:
$$R_m = \left[\frac{P_t \tau G_t G_r \lambda^2 \sigma}{(4\pi)^3 k T_s D(n) L_1} \right]^{1/4} \quad (\text{m}) \tag{1.14}$$

These equations are only the starting point for prediction of radar detection range. They give the range along the axis of a common transmitting-receiving antenna beam at which the received energy ratio is adequate under free-space conditions, when using an optimum filter (for visual detection) or a matched filter (for electronic detection).

1.2 The Original Radar Equation

The range equation derived by Norton and Omberg [1] is expressed by (1.13), with the following understandings:

- *Noise Spectral Density*. The noise power spectral density calculated as

$$N_0 = kTF_n \quad (\text{W/Hz}) \tag{1.15}$$

  for a system at a "room temperature" T = 300K with receiver noise figure F_n.

- *Visibility Factor*. The visibility factor is derived for a pulse "barely visible" on an A-scope display [5], and is defined to include the effects of

nonoptimum bandwidth rather than using separate values of an ideal visibility factor, as defined in [4], and a bandwidth correction factor, introduced in [6–12].

- *Propagation Effects*. The authors in [1] discuss the effects of tropospheric absorption and refraction and reflections from the surface underlying the radar-target path, but these are not included as terms in the original radar equation.
- *RF Losses.* Transmitting and receiving line losses L_t and L_r are included in a final equation in [1] based on (1.13). That form of the equation, complicated by several numerical conversion constants, is no longer useful.

A numerical conversion factor is introduced in [1] to present the resulting range in miles. Other numerical factors are introduced by substitution for the constants 4π, k, and T, and by inclusion of approximations for visibility factor and target cross section, such that the final expression is encumbered by a numerical constant that obscures the basic relationships used in derivation. This was done to combine as many factors as possible into a single numerical value in an era when calculations were made by slide rule or electromechanical calculators. That is no longer necessary or desirable. In order to expose the relationships and permit comparison of different forms of the radar equation, we retain in subsequent discussion the terms used in derivation, without conversion factors or introduction of numerical values.

In spite of these limitations, the original radar equation, formulated during World War II, remains relevant today in that it uses the signal-to-noise energy ratio to capture the fundamental relationships between detection range for a free-space path and parameters of the radar and target. The insight of the originators of this equation, in relying on North's matched-filter relationship and using energy ratios as the criterion for successful detection, deserves the recognition accorded by Blake and overlooked in much of the current literature.

1.3 BLAKE'S RADAR EQUATION FOR PULSED RADAR

Lamont V. Blake at the Naval Research Laboratory [6–13] builds on the World War II work, while introducing more precise definitions of terms in the radar equation. His basic radar range equation for pulsed radar takes the form [12, p. 19, Eq. (1.34)]:

$$R_m = \left[\frac{P_t \tau G_t G_r \lambda^2 \sigma F_t^2 F_r^2}{(4\pi)^3 k T_s D(n) C_b L} \right]^{1/4} \text{(m)} \tag{1.16}$$

The numerator of (1.16) has dimension J-m^4, when the terms are expressed in fundamental units. The new terms added to (1.14) are:

F_t = pattern-propagation factor for the transmitting path;
F_r = pattern-propagation factor for the receiving path (see Chapter 8).

The denominator of (1.16) has dimension J, where the new terms are:

T_s = system input temperature in kelvins (see Chapter 6);
$D(n)$ = detectability factor (defined in Section 1.1.2; see Chapter 4);
C_b = bandwidth correction factor (see Section 10.2.3);
L = L_1L_2 = system loss factor.

The system loss L is expressed by the product of two components: L_1, the RF loss in (1.7) that reduces the available energy ratio, and L_2, the signal processing loss that increases the required energy ratio relative to $D(n)$.

1.3.1 Significance of Terms in Blake's Equation

The terms in Blake's radar equation are defined to provide accurate results for pulsed radars with or without intrapulse modulation, using noncoherent integration, and operating in the natural environment. Attention should be paid to following factors.

- *Transmitter Energy.* The use of pulse energy $P_t\tau$ allows (1.16) to be applied directly to radars using pulse compression waveforms for which the time-bandwidth product $\tau B >> 1$, where B is the width of the transmitted pulse spectrum. This contrasts with equations in which P_t is used without τ in the numerator, and a competing noise power N_0B appears in the denominator. Such equations are inapplicable to transmissions with intrapulse modulation.

- *Pattern-Propagation Factors.* Blake introduces directly into the radar equation the factors F_t and F_r that account for the elevation pattern of the antenna and the effects of surface reflections, both functions of elevation angle and essentially invariant with range. The pattern-propagation factor is defined [14, p. 35] as

  > the ratio of the amplitude of the electric field at a given point under specified conditions to the amplitude of the electric field under free-space conditions with the beam of the transmitter directed toward the point in question.

- As used in (1.16), this factor is understood to exclude the effects of the azimuth antenna pattern and attenuation of the medium, both of which Blake includes as components of L. The F factors include the antenna gains at the target elevation relative to those on the axes at which G_t and G_r are defined, the contribution of surface reflections to the radiated and received fields, and modification of the fields by diffraction on low-elevation paths. For array antennas, they include also the reduced gain from off-broadside operation, calculation of which is discussed in Chapter 10.

- *Noise Temperature*. Blake introduces the system noise temperature T_s to express the effects of both internal and external noise sources, replacing the product TF_n in (1.15). This change is especially important when the receiver noise figure is small and the antenna beam points into the cold sky. It should be noted that T_s is referred to the output terminal of the receiving antenna, and includes the effects of thermal noise output from the antenna and receiving line loss L_r between the antenna and the receiver, as well as that from the receiver itself.

- *Use of Energy Ratios.* Blake continues the use of energy ratios for the available and required signals, as in the original radar equation.

- *Detectability Factor*. The detection process can be either electronic or visual, but any departure from the ideal process that is assumed in deriving the detectability factor requires inclusion of an appropriate component in the loss factor L_2.

- *Bandwidth Factor*. The factor C_b, is given by [12, Eq. (8.14a)] as

$$C_b = \frac{B_n\tau}{4.8}\left(1+\frac{1.2}{B_n\tau}\right)^2 \tag{1.17}$$

  where B_n is the noise bandwidth of the receiver. This factor is equal to unity for an "optimum" receiver noise bandwidth $B_n = 1.2/\tau$. Its origin and use are discussed in Section 10.3.3, and the error arising from use of C_b in radars with electronic detection is discussed in Section 1.5.4.

- *Loss Factor*. The system loss factor L, appearing in (1.16), is the product of the following factors:

L_t, transmission line loss in the path connecting the transmitter output to the antenna terminal at which G_t is measured;

L_α, atmospheric absorption loss for the two-way path;

L_p, beamshape loss[4] for a scanning radar [13];

L_x, miscellaneous signal processing loss that represents the product of other receiving and signal processing losses not specifically included in T_s, C_b, L_p, or L_α.

Of these losses, L_t and L_α contribute to the RF loss L_1 that decreases available on-axis energy ratio, while L_p and L_x contribute to the loss L_2 that increases required energy ratio. The treatment of loss factors and the fact that some are functions of the required detection probability are discussed in detail in Chapters 4 and 10.

[4] Blake refers to this as "antenna pattern loss," but beamshape loss is the original and currently accepted term. This loss is discussed in detail in Chapter 5.

1.3.2 Methods of Solving for Range

Because of the complicated range-dependence of the terms F_t, F_r, and L_α, there is no closed-form solution for R_m using (1.16). Blake discusses iterative and graphical methods for solution [12, pp. 379–388]. One simple method is embedded in the "Pulse-Radar Range-Calculation Worksheet," commonly known as the *Blake chart*, shown in Figure 1.1. This chart is used to solve the equation by addition and subtraction of decibel values, easily performed with pocket calculators.

The antenna height above the surrounding surface and the target elevation angle are entered in the Blake chart for record, because the result is only valid for those specific conditions. The user then enters five parameters in part (1), using them to calculate the system noise temperature T_s. The terms listed as coming from figures and tables are discussed in Chapter 6, where the applicable figures are presented along with equations to replace conversion tables. Remaining range factors are entered in part (2) of the chart, converted to decibel form in part (3), and summed to find the decibel value $40\log R_{0(\text{nmi})}$. The free-space range R_0 in nautical miles is found as the antilogarithm. The pattern-propagation factor F is calculated separately (see Chapter 8), and multiplies R_0 to obtain an initial range estimate R'. That estimate is input to a two-stage iteration to correct for atmospheric attenuation. Additional iteration steps may be required when the attenuation coefficient of the atmosphere at the target is large, as in some millimeter-wave radar cases or in microwave radar when precipitation is present.

A complication in the Blake chart is the use of mixed units for entry of range factors. These include the radar frequency $f_{\text{MHz}} = (c/\lambda)/10^6$ rather than λ that appears in the radar equation. The resulting range-equation constant collects the several conversion factors, constants, and their dimensions as:

$$
\begin{aligned}
&10\log\left[\frac{\left(10^3\ \text{W/kW}\right)\left(10^{-6}\ \text{s/}\mu\text{s}\right)\left(3\times10^8\ \text{m/s}\right)^2 \Big/ \left(10^6\ \text{Hz/MHz}\right)^2}{\left(4\pi\right)^3\left(1.38\times10^{-23}\ \text{W}\cdot\text{s/K}\right)\left(185,200\ \text{m/100 nmi}\right)^4}\right] \\
&\quad = 10\log\left[1.292^4\left(\text{K}\cdot\text{nmi}^4/\text{W}\cdot\text{s}^3\cdot\text{m}^2\right)\right] \\
&\quad = 4.45\ \text{dB}\left[\text{ref}\left(\text{K}\cdot\text{nmi}^4/\text{W}\cdot\text{s}^3\cdot\text{m}^2\right)\right]
\end{aligned}
$$

Note that a median radar cross section σ_{50} and a corresponding visibility factor $V_{0(50)}$ are entered into the Blake chart, to arrive at the range R_{50} for a probability of detection P_d = 50%. The radar cross section normally specified is its average value, which for a fluctuating target characterized as Swerling Case 1 (see Section 4.3.3) is 1.5 dB greater than the median.

PULSE-RADAR RANGE-CALCULATION WORK SHEET

1. Compute system input noise temperature, T_{NI}, following outline in section (1) below.
2. Enter range factors known in other than decibel form in section (2) below, for reference.
3. Enter logarithmic and decibel values in section (3) below, positive values in plus column, negative in minus. (Example: If $V_{o(50)(db)}$ as given by Fig. A1 or A2 is negative, then - $V_{o(50)(db)}$ is positive, goes in plus column.) To convert range factors to decibel values, use Table A2. For $C_{B(db)}$ use Fig. A3.

Radar antenna height: h = ft. Target elevation angle: θ = °. (See Fig. A12).

(1) COMPUTATION OF T_{NI}: $T_{NI} = T_a + T_{r(I)} + L_r T_e$	(2) RANGE FACTORS	(3) DECIBEL VALUES	PLUS (+)	MINUS (-)
	$P_{t(kw)}$	10 log $P_{t(kw)}$ -	.	.
	$\tau_{\mu sec}$	10 log $\tau_{\mu sec}$	.	.
(a) For general range computation, use Figure A5 for T_a.	G_t	$G_{t(db)}$	.	.
	G_r	$G_{r(db)}$	.	.
	$\sigma_{50(sq.m.)}$	10 log σ_{50}	.	.
(b) To find L_r, given $L_{r(db)}$, use first and second columns of Table A2.	f_{Mc}	- 20 log f_{Mc}	.	.
	T_{NI}, °K	- 10 log T_{NI}	.	.
	$V_{o(50)}$	- $V_{o(50)(db)}$	.	.
(c) Also in Table A2, opposite $L_{r(db)}$ in first column, read $T_{r(I)}$ in third column. Note: If thermal temperature (T_t) of transmission line is appreciably different from 290°K, multiply Table A2 values of $T_{r(I)}$ by $T_t/290$.	C_B	- $C_{B(db)}$		.
	L_t	- $L_{t(db)}$		.
	L_p	- $L_{p(db)}$		.
	L_x	- $L_{x(db)}$		.
	Range-equation constant (40 log 1.292)		4 . 45	
	4. Obtain column totals →		.	.
	5. Enter smaller total below larger →		.	.
	6. Subtract to obtain net decibels →		+ .	- .

(d) Opposite $\overline{NF}_{db}$ in first column, read T_e in third col.

T_t		T_a	
L_r		$T_{r(I)}$	
$\overline{NF}_{db}$		$L_r T_e$	
T_e		T_{NI}	

7. In Table A3, find range ratio corresponding to this net decibel value, taking its sign (±) into account. Multiply this ratio by 100. This is R_o →

8. Multiply R_o by the pattern-propagation factor.

F = See Eqs. 27 - 44, and Figs. 8 - 12.

$R_o \times F = R'$ →

9. On the appropriate curve of Figures A6 - A11, determine the atmospheric-absorption loss factor, $L_{a(db)}$, corresponding to R'. This is $L_{a(db)(1)}$ →

10. In Table A3, find the range-decrease factor corresponding to $L_{a(db)(1)}$, δ_1 →

11. Multiply R' by δ_1. This is a first approximation of the range, R_1 →

12. If R_1 differs appreciably from R', on the appropriate curve of Figures A6 - A11 find the new value of $L_{a(db)}$ corresponding to R_1. This is $L_{a(db)(2)}$ →

13. In Table A3, find the range-increase factor corresponding to the difference between $L_{a(db)(1)}$ and $L_{a(db)(2)}$. This is δ_2. →

14. Multiply R_1 by δ_2. This is the radar range in nautical miles, R_{50} →

Note: If the difference between $L_{a(db)(1)}$ and $L_{a(db)(2)}$ is less than 0.1 db, R_1 may be taken as the final range value, and steps 12 - 14 may be omitted. If $L_{a(db)(1)}$ is less than 0.1 db, R' may be taken as the final range value, and steps 9 - 14 may be omitted. (For radar frequencies up to 10,000 megacycles, correction of the atmospheric attenuation beyond the $L_{a(db)(2)}$ value would amount to less than 0.1 db.)

Figure 1.1 Blake's Pulse-Radar Range-Calculation Worksheet [8]. The referenced figures are reproduced in Chapters 4, 6 and 7, and the referenced tables for conversions between decibels and ratios are now replaced by digital calculation.

Plots of $V_{0(50)}$ and corresponding $D_{0(50)}$ for electronic detection are presented in [6–8], but calculations for values of P_d other than 50% are often needed. Blake's subsequent presentations in [9–12] provide plots of D for different values of P_d and for several target models. These plots require use of the average (rather than the median) value of σ in (1.16) and in the Blake chart.

1.3.3 Advantages of the Blake Chart

A major advantage of the Blake chart is that it records the input values on which the range calculation is based, along with several intermediate results. In the absence of this discipline, essential data may be left unrecorded and unavailable for later reference. When engineering calculators or digital computer methods are used to replace Blake's conversion tables and manual intermediate steps, the process is rapid and accurate. The exact form of the chart has undergone successive modifications from Blake's original in [6] to its final form in [12], but the basic approach remains. A modification of the chart that maintains entries in fundamental units is described in Section 1.4.2.

The Blake chart formalizes the iteration that solves for the effects of range-dependent attenuation. It has been widely accepted as a standard range-calculation method, although parameters would preferably be entered in fundamental units. Procedures for conversions between decibels and ratios no longer require recourse to associated tables because they are performed readily on pocket calculators or computers. Preservation of the basic format of the chart remains an important element in providing traceability of results. There are all too many opportunities for error when the entire process is reduced to entry of parameters into a computer program and reading an output representing detection range, without recording and inspection of inputs and intermediate results.

1.3.4 Blake's Coherent Radar Equation

Blake extends (1.16) to coherent radars [12, p. 20, Eq. (1.35)]:

$$\text{Coherent radar:} \quad R_m = \left[\frac{P_{av} t_f \tau G_t G_r \lambda^2 \sigma F_t^2 F_r^2}{(4\pi)^3 k T_s D(1) C_b L} \right]^{1/4} \text{(m)} \tag{1.18}$$

Here the energy $P_{av}t_f$ of the observed waveform replaces the single-pulse transmitted energy $P_t\tau = P_{av}t_r$, where P_{av} is average power, t_f is the coherent processing interval (CPI), and t_r is the pulse repetition interval (PRI). The required energy ratio $D(1)$ for detection is the value for the single output of the coherent integrator. The result is a general radar equation (similar to that of Hall, discussed in Section

1.4.1), applicable to continuous-wave (CW) and pulsed Doppler radars as well as to noncoherent pulsed radars.

The application of the Blake chart to coherent radar requires merely the replacement of P_t with average power P_{av} in kW, and τ with t_f in μs. If those units are inconvenient for CW radars, they may be replaced by watts and milliseconds without changing the range-equation constant.

Equation (1.18) is based on the assumption that detection is performed using the output of a Doppler filter without subsequent noncoherent integration. This limitation can be avoided, and the equation applied to radars using noncoherent integration of n' filter outputs, by replacing $D(1)$ with $D(n')$. The increase in available energy, relative to (1.16), is expressed by the ratio $P_{av}t_f / P_t\tau > 1$ in the numerator, and the decrease in required single-sample energy relative to (1.18) through the ratio $D(n')/D(1) < 1$ in the denominator. The coherent and noncoherent gains from all n pulses are thereby included in the range calculation.

Blake's radar equation, promulgated also through the first two editions of Skolnik's *Radar Handbook* [15, 16], yields an accurate prediction of the maximum detection range for a target at any elevation angle, using realistic models of radars with any types of waveform and processing under actual environmental conditions. The steps required to modify his equations for modern radar problems are relatively minor, and are discussed in Section 1.6.

1.3.5 Blake's Bistatic Range Equation

Blake extends his basic radar equation to bistatic systems [12, Eq. (1.38)]:

$$\text{Bistatic radar:} \qquad \left(R_t R_r\right)_m^{1/2} = \left[\frac{P_t \tau G_t G_r \lambda^2 \sigma_b F_t^2 F_r^2}{(4\pi)^3 k T_s D(n) C_b L}\right]^{1/4} \quad \text{(m)} \tag{1.19}$$

where R_t and R_r are the transmitter-to-target and target-to-receiver paths, respectively. The quantity $(R_t R_r)^{1/2}$ is the geometric mean of the two paths in the bistatic system. The comments of Section 1.3.1 apply equally to this equation.

The Blake chart can also be used with bistatic radar, yielding the geometric mean range. Separate calculations of the pattern-propagation factors F_t and F_r are needed to arrive at the two-way factor $F = (F_t F_r)^{1/2}$ in line 8 of the chart. The iteration procedures for attenuation in lines 9–14 are carried out using the sums of one-way attenuations over the two paths, considering their elevation angles (which should be recorded separately at the top of the chart along with the two antenna heights).

Blake's equations and chart are intended primarily for use in cases where targets are detected within the unambiguous range of the radar waveform. The results will be correct for detections beyond the unambiguous range, but errors may

arise from eclipsing by the transmission (see Section 1.6.1 and 10.1.2) or loss of integration caused by use of varying PRIs.

1.4 OTHER FORMS OF THE RADAR EQUATION

1.4.1 Hall's Radar Equations

Hall presents in [17] a radar equation for pulsed radar, preceding Blake's work, and clarifying many of the issues in previous literature:

$$\text{Pulsed radar:} \quad R_m = \left[\frac{P_t \tau G^2 \lambda^2 \sigma F^4}{(4\pi)^3 k T_0 F_n \times 1.2\, D_x(n) L_t L_\alpha} \right]^{1/4} \quad \text{(m)} \qquad (1.20)$$

This is equivalent to (1.14) with the following substitutions:

- The gain G^2 for a common transmitting/receiving antenna replaces $G_t G_r$;
- F^4 is included in the numerator as the two-way pattern-propagation factor;
- System temperature $T_0 F_n$ is used for a receiver connected directly to the output terminal of an antenna in an environment at standard temperature T_0 = 290K;
- The product $1.2 D_x(n) L_t L_\alpha$, replaces DL, where $D_x(n)$ is the *effective detectability factor* given by the product of the following five terms:

$D(n)$	=	basic (theoretical) detectability factor for noncoherent integration of n pulses;
L_m	=	loss for nonoptimum bandwidth;
L_p	=	beamshape loss;
L_c	=	collapsing loss;
L_o	=	operator and degradation factor.

The factor D_x is used in the equation for modern radars (see Section 1.6). The factor 1.2 that multiplies D_x in (1.20) represents the matching loss for an optimum receiver bandwidth $B_n = 1.2/\tau$, assuming an unmodulated pulse. Additional loss related to nonoptimum IF bandwidth is captured in the loss L_m.

A subsequent presentation by Hall of a general radar equation is applicable to monostatic and bistatic radars systems that use any waveform [18, Eq. (8)]:

$$\text{General case:} \quad \left(R_t R_r\right)_m^{1/2} = \left[\frac{P_{av} t_o G_t G_r \lambda^2 \sigma F_t^2 F_r^2}{(4\pi)^3 k T_s D_x(1) L_{\alpha t} L_{\alpha r}}\right]^{1/4} \text{ (m)} \qquad (1.21)$$

This expression combines Blake's (1.18) and (1.19), with the following substitutions:

- The coherent integration time t_f is assumed equal to the observation time t_o;
- The product of detectability factor and loss $D(1)L$ is replaced by $D_x(1)L_{\alpha t}L_{\alpha r}$.
- The product of one-way atmospheric attenuations $L_{\alpha t}$ and $L_{\alpha r}$ for the transmitting and receiving paths is used in the denominator.

Accurate results are available from Blake's widely promulgated method, so Hall's expressions have received little attention. They are included here to illustrate appropriate use of the energy ratio in radar equations.

1.4.2 Barton's Radar Equations

The initial radar equation used in the 1964 *Radar System Analysis* [19] used peak transmitter power and noise power in the receiver bandwidth rather than energies. This lapse was corrected in the 1988 *Modern Radar System Analysis* [20] where radar equations are based on Blake's and Hall's work, the latter having introduced the *effective* detectability factor $D_x(n)$ in place of the basic factor $D(n)$ and its associated losses. Barton's equation for pulsed radar is [20, Eq. (1.2.25)]:

$$\text{Pulsed radar:} \quad R_m = \left[\frac{P_t \tau G_t G_r \lambda^2 \sigma F^4}{(4\pi)^3 k T_s D_x(n) L_t L_\alpha}\right]^{1/4} \text{ (m)} \qquad (1.22)$$

The RF loss L_1 that reduces available energy ratio are stated as separate terms L_t and L_α. The loss L_2 that increases the required energy ratio is included in D_x, and is defined to avoid error caused by use Blake's factor C_b in connection with electronic detection. Alternate forms of the equation are given for two types of coherent radar:

- Coherent integration over entire observation time [20, Eq. (1.2.26)], where energy $P_{av}t_o$ in the observation time replaces single-pulse energy $P_t\tau$, and single-sample $D_x(1)$ replaces $D_x(n)$;
- Coherent integration over CPI, followed by noncoherent integration over t_o [20, Eq. (1.2.27)], where energy $P_{av}t_f$ in the CPI replaces single-pulse energy $P_t\tau$, and $D_x(n)$ is replaced by $D_x(n')$, where $n' = t_o/t_f$.

The second alternate form is used as the basis for a modified Blake chart, an example of which is shown in Figure 1.2.

PULSE-RADAR RANGE-CALCULATION WORKSHEET

The calculation is made for the parameters recorded in the two top lines of the chart.
1. Compute the system input noise temperature T_s following the outline in Part A.
2. Enter the range factors in basic units in Part B.
3. Convert these factors to decibel form and enter in Part C.

Detection probability P_d			**0.**	False-alarm probability P_{fa}		**10^-**	Target case:	.	Hits n		.
				Radar antenna height h_r (m)		.	Target elevation angle $\Theta°$				.
A. Computation of T_s: $T_s = T_a + T_r + L_r T_e$				**B. Range Factors**			**C. Decibel Values**		Plus		Minus
				P_t or P_{av} (W)		.	10 log P (dBW)		.		.
	Compute T_a			τ or t_f (s)		.	10 log τ (dBs)		.		.
	For $T_{tg} = T_{ta} = 290$K, $T_g = 36$:			G_t		.	G_t(dB)		.		.
	$T_a = (0.876T_a' - 254)(1/L_a) + 290$			G_r		.	G_r(dB)		.		.
	L_α(dB)	.	L_α: .	σ (m^2)		.	10 log σ (dBm^2)		.		.
			T_a' (K) .	λ (m)		.	20 log λ (dBm^2)		.		.
(a)			T_a (K) .	T_s (K)		.	−10 log T_s (dBK)				.
	Compute $T_r = T_{tr}(L_r - 1)$			D		.	$-D$(dB)		.		.
	L_r(dB)	.	L_r : .	M		.	$-M$(dB)				.
(b)	T_{tr}	.	T_r (K) .	L_p		.	$-L_p$(dB)				.
	Compute $T_e = T_0(F_n - 1)$			L_x		.	$-L_x$(dB)				.
	F_n(dB)	.	F_n: .	L_t		.	$-L_t$(dB)				.
	T_e (K)	.	L_r: .	Range-equation constant 3.65×10^7 K/J					**+75.62**		
(c)			$L_r T_e$ (K) .	**4. Obtain** column totals					.		.
(d)	**Add (a) + (b) + (c) = T_s** (K)		.	**5. Enter** the smaller total below the larger					.		.
6.	**Subtract** to obtain net decibels $X = 40 \log R_{0(km)}$ (dBm^4)								.		

7.	**Calculate** $R_{0(km)}$ = antilog (X/40)	$R_{0(km)}$	.
8.	**Calculate** the pattern-propagation factor $F = (F_t F_r)^{1/2}$	F	.
9.	**Multiply** R_0 by the pattern-propagation factor to obtain $R' = R_0 \times F$	R'	.
10.	**Determine** the atmospheric attenuation, loss L_α(dB), corresponding to R'. This is $L_\alpha(\text{dB})_{(1)}$.	$L_\alpha(\text{dB})_{(1)}$	.
11.	**Find** the range factor δ_1 = antilog ($-L_\alpha(\text{dB})_{(1)}$/40).	δ_1	.
12.	**Multiply** R' by δ_1. This is a first approximation of range, R_1.	R_1	.
13.	If R_1 differs appreciably from R', **find** a new value of L_α(dB) corresponding to R_1. This is $L_\alpha(\text{dB})_{(2)}$.	$L_\alpha(\text{dB})_{(2)}$	.
14.	**Find** the range increase factor δ_2 corresponding to the difference between $L_\alpha(\text{dB})_{(1)}$ and $L_\alpha(\text{dB})_{(2)}$.	δ_2	.
15.	**Multiply** R_1 by δ_2 to obtain the maximum radar detection range R_m in km	R_m(km)	.

Figure 1.2 Modified Blake chart [20, p. 21].

The user entries in this version of the Blake chart are in basic units, avoiding the multiple conversion factors of the original chart. The range-equation constant now includes only the factors $(4\pi)^3$, k, and a factor converting range in m to km:

$$\text{Constant} = \left[(4\pi)^3 \cdot 1.38\times10^{-23}\,(\text{J/K})(1000\text{m/km})^4 \right]^{-1}$$
$$= 3.65\times10^7\left(\text{K}\cdot\text{km}^4/\text{J}\cdot\text{m}^4\right) = 75.6\ \text{dB}\left[\text{ref}\left(\text{K}\cdot\text{km}^4/\text{J}\cdot\text{m}^4\right)\right]$$

The procedures for entry, intermediate calculations, conversion to and from decibels, and iteration to account for atmospheric attenuation are the same as in the original Blake chart. Blake's C_b is replaced by the matching factor M, defined in Section 10.2.3.

The 2005 *Radar System Analysis and Modeling* gives the most general form of the radar equation as [21, Eq. (1.20)]:

$$\text{General case:} \qquad R_m^4 = \frac{P_{av} t_f G_t G_r \lambda^2 \sigma F_p^2 F_t^2 F_r^2}{(4\pi)^3 kT_s D_x(n') L_t L_\alpha} \ \text{(m)} \qquad (1.23)$$

This is the form used for the modified Blake chart of Figure 1.2, but with an added factor F_p^2 to account for possible polarization mismatch between transmitting and receiving antennas. That factor, normally set to unity, is included to emphasize the need to consider that the polarization of the receiving antenna may not match that applicable to the echo as calculated using the transmitted polarization and the normally specified target cross section σ in the radar equation. For example, when right-hand circular polarization is used both for transmission and reception, the usually specified σ gives the echo of the left-hand circular polarization component to which the receiving antenna is insensitive (see Section 10.1.1).

1.5 AVOIDING PITFALLS IN RANGE CALCULATION

It is appropriate here to comment on the different forms of the radar equation presented above and elsewhere in the literature, and to point out sources of error involved in their use.

1.5.1 System Noise Temperature T_s

The product kTF_n in the original equation (1.9) was intended to represent the noise spectral density N_0 at the receiver input. Blake carefully defines his corresponding product kT_s and its several components to improve the accuracy of noise calcula-

tions [12, p. 152]. His approach is especially important in modern systems where the noise figure is low and the antenna is directed toward the cold sky. His expressions are discussed in Chapter 6, with examples showing significant errors in results of the radar equation when the temperature of the environment that surrounds the radar is simply assumed to be $T_0 = 290$K.

Blake's formulation should be adopted as a permanent substitute for less meticulous expressions for thermal noise in any radar equation. This practice has been followed in the first two editions of Skolnik's *Radar Handbook* [15, 16] and in Barton [20–22]. Other presentations of the radar equation mistakenly rely on a simplified relationship $N_0 = kT_0F_n$, which is adequate only for radars in which F_n >10 dB. For modern radars it fails to model accurately the noise spectral density, with resulting errors in the order of 1–2 dB in calculation of the minimum required signal energy.

1.5.2 Use of Signal-to-Noise Energy Ratio

Both the original equation and those of Blake and Hall are properly based on ratios of input signal energy to noise spectral density, rather than of input power to noise power in some ill-defined (and generally unmeasureable) bandwidth. This allows the use of North's fundamental matched-filter relationship for the maximum available signal-to-noise ratio [3]:

$$\left(\frac{S}{N}\right)_{\max} = \frac{E}{N_0} \tag{1.24}$$

where E is signal energy and N_0 the noise spectral density at the filter input. This gives the upper limit to potential radar performance, and can be applied to a radar using any waveform by applying a matching factor for cases in which the actual receiver and processor fall below the performance of the matched filter. The required input energy ratio is increased by this matching factor.

Radar equations using transmitter power P_t in the numerator and receiver bandwidth B_n or some "effective receiver bandwidth" in the denominator almost inevitably lead to errors, and are inapplicable when pulse compression or frequency-modulated CW signals are transmitted. Even with unmodulated pulses, when $B_n < 1/\tau$, the small value of B_n in the denominator of the equation leads to an erroneously large R_m, approaching infinity for $B_n \rightarrow 0$ (which corresponds to an inoperative receiver). With $B_n >> 1/\tau$, the resulting R_m may be too small because smaller video (or display) bandwidth reduces the noise relative to that passed by the receiver.

Surveying the radar literature, many authors place the noise power for receiver bandwidth B_n in the denominator of the radar equation. In cases where the pulse

energy does appear in the numerator, the derivation is often based on the assumption that an unmodulated pulse with $B_n\tau = 1$ is used.

1.5.3 Use of Average Power

Radar equations that include average rather than peak transmitter power, such as (1.18), (1.21), or (1.23), are to be preferred because they emphasize the dependence of radar detection range in the thermal noise environment on average power, rather than on peak power or other waveform parameters. Those parameters are of practical importance for reasons other than establishing detection range. Use of peak power is not necessarily erroneous, as long as the contributions and losses from approximately matched filtering and integration, both coherent and noncoherent, are properly expressed for the waveform and processing actually used by the radar. Such expressions become increasingly difficult in modern radars, where system bandwidth is not a measureable parameter.

1.5.4 Bandwidth Correction and Matching Factors

An error arises when C_b expressed by (1.17) is applied in the equation for radars using electronic detection. The value $C_b = 1.0$ for $B_n\tau = 1.2$ falsely implies that such an "optimum filter" is a matched filter. The original radar equation was derived for radars with detection performed visually on a cathode-ray-tube display. The value of V, as determined experimentally, includes losses of 2–3 dB inherent in the display/observer process even when the "optimum bandwidth" is used [19, p. 171]. The detectability factor D used in (1.14) or (1.16) is defined for systems in which a matched filter is used, and hence requires use of a *matching factor* M, differing from C_b, to express any filter mismatch effects. This issue is discussed further in Sections 4.6 and 10.3.

1.5.5 Detectability Factors for Arbitrary Targets

Exact equations for detectability factors of commonly used target models are given in the literature and in Chapter 4. An expression for the single-pulse, steady target (Case 0) value denoted by $D_0(1)$, as derived by Rice [23], is readily solved using mathematical programs that run rapidly on personal computers. Marcum [24] extends the theory to $D_0(n)$ for radars using noncoherent integration of multiple pulses. Swerling [25] gives expressions for detectability factors applicable to target models denoted by Cases 1–4 with amplitude statistics corresponding to chi-square distributions with two or four degrees of freedom and with slow or fast fluctuations of amplitude, denoted in this book by $D_1(n)...D_4(n)$. These exact expressions are supplemented in [21] by a generalized model leading to a factor $D_e(n, n_e)$ for targets whose statistics follow the chi-square distribution with $2n_e$

degrees of freedom. The generalized model covers Cases 0–4 and also targets for which the number of independent target samples is $1 \leq n_e \leq n$, including noninteger values commonly encountered.

Chapter 4 presents both exact and approximate methods of calculating detectability factors for all these models. Errors of several decibels can result from use of an inappropriate target model, as is likely for targets described by Swerling models when the radar system takes advantage of diversity in time, frequency, space, or polarization.

1.5.6 Pattern-Propagation Factor

Inclusion of pattern-propagation factors F_t and F_r, or their geometric mean F, in the numerator of the radar equation is essential for accurate range calculation in any case where the target is not on the elevation beam axis and the elevation mainlobe is not clear of the surface underlying the radar-target path. Most texts contain some reference to the need for these factors, often discussing them separately from the radar equation, rather than embedding the factors in the equation. The treatment of this factor for phased array radars observing off-broadside targets requires special attention (see Section 10.2.1).

1.5.7 Loss Factors

The beamshape loss L_p is listed as one component of the loss factor L included in (1.16) and (1.18). This assumes that the target is not on the axis of the radar beam during the entire integration time of the echo pulses (e.g., when the radar scans across the target position). It is shown in Chapter 5 that L_p is a function of the required detection probability P_d unless several pulses, distributed across the mainlobe of the antenna pattern, are integrated as the beam scans.

Another issue that requires careful consideration is the relationship between beamshape loss and the antenna pattern embedded in the pattern-propagation factor F. Blake's method applies L_p to the effect of azimuth scan of a conventional 2-D search radar, while allowing F^4 to describe the effect of the target position in the elevation pattern. For two-dimensional scan, $F = 1$ can be used along with a loss L_p^2 for regions where there are no surface-reflection effects and where the average performance over an elevation sector is to be evaluated. This issue will be discussed in Chapter 8.

In phased array radars, the gain at the beam axis varies with off-broadside scan angle. The gains G_t and G_r are normally defined on the beam axis at broadside, and the off-broadside scanning factor is included in the pattern-propagation F, which is then a function of both elevation and azimuth. Alternatively, an average scan loss over the sector may be defined (see Section 10.2.1) to account for the gain variation over the scan. As with beamshape loss, the scan sector loss in-

creases the energy ratio required at broadside by an amount that depends on the specified P_d, unless the energy transmitted in each beam dwell is adjusted as a function of scan angle to compensate for the reduced gain of the off-broadside beams (see Section 10.2.1).

The miscellaneous loss L_x in the equations is intended to include a number of loss factors, discussed in detail in Chapter 10. Several of these loss factors are also functions of the required P_d, and hence must be varied along with the detectability factor D if accurate range results are to be obtained.

1.5.8 Summary of Pitfalls in Range Calculation

Common errors in using the radar equation include the following:

- Use of T_0 = 290K rather than the actual system noise temperature T_s.
- Use of signal-to-noise power ratio in an ill-defined bandwidth B, instead of energy ratio. *Any radar equation that includes a receiver bandwidth B will cause confusion, at best, and at worst will cause serious errors in the range calculation.*
- Use of peak power without including the corresponding processing factors and losses.
- Use of the bandwidth correction factor C_b with other than the visibility factor V that includes the losses from visual detection.
- Use of a visibility factor or detectability factor that fails to account for statistics of the actual target and radar diversity.
- Failure to include the appropriate pattern-propagation factor.
- Failure to account for all the actual losses.

1.6 RADAR EQUATION FOR MODERN RADAR SYSTEMS

1.6.1 Factors Requiring Modifications to the Range Equation

Developments in radar technology and countermeasures to radar have imposed new problems in applying the radar range equation. Most of these problems can be solved by including an appropriate *range-dependent response factor* F_{rdr} in the numerator of the radar equation. The factor F_{rdr} includes several components as described below. The factors become especially important with low-observable targets, whose reduced cross sections may prevent detection beyond the range at which eclipsing and STC take effect.

1.6.1.1 Eclipsing

Eclipsing of the received signal occurs with two classes of waveform: (1) low-PRF radars using solid-state transmitters with duty cycles in excess of ≈ 1%; and (2) medium- and high-PRF radars.[5]

- Solid-State Transmitters. Solid-state RF power amplifiers cannot provide high peak powers in exchange for low duty cycle[6], as is the case for power tubes. Hence, the design of solid-state transmitters tends toward higher duty cycles, typically D_u = 5% to 20%, in order to obtain the required average power while staying within the low peak rating of the devices. For low-PRF radar the pulse repetition interval t_r must be long enough to avoid range ambiguity, and higher D_u requires longer pulses than commonly used in tube transmitters. For example, an unambiguous range of 450 km requires $t_r \geq 3$ ms. For D_u = 20% the resulting transmitted pulsewidth $\tau \geq 600$ μs. Echoes from targets at range $R < R_{\min} = \tau c/2 \approx 90$ km, are eclipsed: the early portions of the echo overlap the transmission, causing loss in signal-to-noise ratio. Echoes from $R > R_u - R_{\min}$, where $R_u = c/2f_r$, also suffer eclipsing of the far end of the echo. The radar equation for such cases includes a range-dependent *eclipsing factor* F_{ecl} as a component of F_{rdr}.

  Some solid-state radars use dual-pulse groups in which each long pulse is accompanied by a shorter pulse, offset in frequency from the long pulse, to cover the short-range region eclipsed by the long pulse. In this case, only the average power of the longer pulse contributes to the detection of long-range targets, and the radar equation should reflect this. Eclipsing at the far end of the unambiguous range region is not avoided by using the short-range pulses.

  The eclipsing factor for a radar that cannot detect a low-observable target beyond $R_{\min}$ may prevent detection within that range.

- MPRF and HPRF waveforms have long been used in airborne radars, and appear also in some types of surface-based radar. Implicit in these waveforms is the requirement to detect targets with $R > R_u$. Calculation of maximum detection range then requires introduction of the eclipsing factor in the radar equation. The factor at a particular PRF is a deterministic function of range. When multiple PRFs are used in each beam position (either within the beam dwell or from scan to scan) the factor is usually represented statistically (see Section 10.2.1).

---

[5] The desired targets for low-PRF waveforms are within the unambiguous range; for high-PRF waveforms they are within the unambiguous velocity; for medium-PRF waveforms they are beyond both unambiguous range and velocity.

[6] Duty cycle (or duty factor) is the ratio of the pulse duration to the pulse repetition interval.

1.6.1.2 Sensitivity Time Control (STC)

Many low-PRF radars use STC to avoid saturation of the receiver or processor on large targets or clutter at medium and short range, and to suppress undesired detections of small moving objects such as birds and vehicle traffic at those ranges. STC is applied to reduce receive sensitivity at delays within some STC range R_{stc}, which is chosen to establish a threshold target cross section σ_{min} above which targets are to be detected. Attenuation is applied at RF prior to the receiver, or in the early stages of the receiver, to restrict the amplitude level of expected echo inputs. The effect of the range-dependent *STC factor* F_{stc} is illustrated below in Figure 1.5. A radar with STC loses the ability to detect, even at short range, a low-observable target whose cross section is less than σ_{min}.

1.6.1.3 Beam Dwell Factor

Radars may in some cases move the beam so rapidly that the receiving beam axis does not remain near the angle at which the transmitted pulse illuminates a long-range target, and from which the echo arrives after a delay $t_d < t_r$.

- If continuous scan occurs at a rate ω such that the angular change $\Delta\theta = \omega t_r$ between pulses is significant but less than the beamwidth in the scanned coordinate, a beam-dwell factor is introduced that depends on range. If $\Delta\theta$ is greater than the beamwidth, the echo signal is lost.
- Radars with electronic scan usually scan in steps such that the beam dwells at the position used for transmission until the echo from the most distant expected target has arrived. In some cases, the receiving beam may return to the angle of a target that was illuminated by a prior pulse whose echo is sought, but that mode of operation is unusual, and the time available for the return dwell among other radar functions is limited.

In either case, the scanning radar discriminates against signals arriving with delay exceeding the dwell time of the beam in the direction of transmission, and a *beam dwell factor* F_{bd} is included as a component of F_{rdr} in the radar equation to describe this effect.

1.6.1.4 Frequency Agility or Diversity

Pulse-to-pulse change in frequency (agility) or group-to-group change (diversity) is used to evade jamming and to average the observed target RCS (e.g., for reduction in fluctuation loss). In either technique the receiver frequency is changed to that of the immediately preceding transmitted pulse. The beneficial effect on RCS averaging is included in the target model used to calculate the detectability factor $D_e(n, n_e)$. Discrimination against echo signals arriving after the frequency change

requires inclusion of a *frequency diversity factor* F_{fd} as a component of F_{rdr} in the radar equation.

1.6.1.5 Lens Factor

The *lens loss* introduced by Weil [26] is caused by the change in tropospheric refraction with elevation angle. Although discussed by Blake [12, pp. 188–192], it is sometimes overlooked omitted because it does not appear as a specific term in the radar equation. To avoid this, the two-way *lens factor* F_{lens2} is included here as a component of F_{rdr}. It must not be lumped with the atmospheric attenuation L_α in the denominator of the equation because it is not a dissipative loss that increases the system noise temperature.

1.6.2 Equations Applicable to Modern Radars

Modern Radar System Analysis Software, Version 3.0 [22] is a comprehensive set of worksheets (to be referred to as *MRSAS3*, and loosely termed a *program*), that runs under the Mathcad© program to calculate radar detection range and measurement accuracy. This version of program was developed during a period in which changes in radar technology and increased concern over reduction of target cross section exposed limitations in earlier forms of the radar equation, as discussed in Section 1.6.1. The program was designed to provide a more thorough analysis of radar performance, in which (1.23) was modified by addition of the range-dependent response factor F_{rdr} for voltage response of the system, whose square modifies the *available* energy as a function of range:

$$E = \frac{P_{av} t_f G_t G_r \lambda^2 \sigma F_p^2 F_t^2 F_r^2 F_{rdr}^2}{(4\pi)^3 R^4 L_t L_\alpha} \quad \text{(J)} \tag{1.25}$$

where

F_{rdr} = $F_{ecl}F_{stc}F_{bd}F_{fd}F_{lens2}$ = product of radar response factors varying with range;
F_{ecl} = eclipsing factor;
F_{stc} = sensitivity-time-control factor;
F_{bd} = beam-dwell factor;
F_{fd} = frequency-diversity factor;
F_{lens2} = two-way lens factor.

These five factors are discussed in detail in Chapters 7 and 10, and for the present the following brief descriptions will suffice.

- *Eclipsing Factor*. Eclipsing has long been recognized as an important factor in high- and medium-PRF airborne radar, where the duty cycle exceeds that

commonly found in low-PRF systems. With the advent of high-duty-cycle, solid-state radar transmitters in surface-based radar, eclipsing becomes a more general problem. The resulting factor F_{ecl} is discussed in Section 10.1.2.

- *STC Factor*. STC applies a variable voltage gain $F_{\text{stc}} \le 1$ at RF prior to the receiver or in the early stages of the receiver (see Section 10.1.2). It is assumed here that significant competing noise is introduced in receiver stages subsequent to the STC, so that the output signal-to-noise ratio varies as the square of F_{stc}, compared to its value with constant gain.
- *Beam-Dwell Factor*. The beam-dwell factor F_{bd} is normally unity, but decreases when beam motion reduces the antenna gain on the target between the time the signal is transmitted and when the echo is received (see Section 10.1.2).
- *Frequency Diversity Factor*. The frequency diversity factor F_{fd} is unity as long as the receiver remains tuned to the frequency of the echo arriving at the radar. It is included here to ensure that echoes from ambiguous ranges are excluded, as dictated by use of frequency diversity or agility.
- *Lens Factor*. Weil showed that this factor reduces the available energy for targets near the horizon at long range, where the beam is spread in elevation by tropospheric refraction (see Section 7.4). Because it is not a dissipative loss that increases the antenna temperature, as does the atmospheric absorption loss L_α, it is best expressed as a factor separate from absorption.

The resulting radar equation [22, Eq. (7.67)] is rewritten here to include the new range-dependent response factor:

$$\text{Modern radar:} \qquad R_m^4 = \frac{P_{av} t_f G_t G_r \lambda^2 \sigma F_p^2 F_t^2 F_r^2 F_{\text{rdr}}^2}{(4\pi)^3 k T_s D_x(n') L_t L_\alpha} \quad \text{(m)} \tag{1.26}$$

1.6.3 Method of Calculating Detection Range

A simple iteration procedure is used in the Blake chart to solve for detection range in the presence of range-dependent atmospheric attenuation. The introduction of the additional range-dependent response factors and the possible change in signal processing mode with range require a more robust method. This is based on the fundamental approach described in Section 1.1: the available and required energy ratios are found as functions of range, and the maximum range is found for which the two ratios are equal. The process can be graphical [21, Section 1.6], or implemented by computer [22]. Graphs generated as intermediate results in [22] illustrate that procedure and the effects of range-dependent terms on both available and required energy ratios.

1.6.3.1 Example Radar Range Calculation

Table 1.1 lists the parameters of a noncoherent 2-D low-altitude surveillance radar to be used as an example. The available and required energy ratios E/N_0 and D_x for P_d = 50% are shown in Figure 1.3, for a 1.0-m^2 target flying inbound at a constant 1° elevation, using *Modern Radar System Analysis Software* [22]. The program makes calculations at 100 equal inward steps in range, from a user-selected maximum (150 km in this case). To find R_m, values of E/N_0 and D_x (in decibels) are inspected until their difference is positive. Interpolation is applied to find the exact

Table 1.1 Example 2-D Radar

Radar frequency f_0	3.0 GHz	Wavelength λ	0.10m
Peak power P_t	100 kW	Average power P_{av}	110.8W
Pulsewidth $\tau = \tau_n$	1.0 μs	Pulse repetition frequency f_r	1108 Hz
Transmitter line loss L_t	1.0 dB	Antenna gain G	40.0 dB
Azimuth beamwidth θ_a,	1.3°	Elevation beamwidth θ_e	2.0°
Azimuth scan sector A_m	360°	Frame time t_s	6.0
Pulses per dwell n	24	System temperature T_s	987K
Detection probability P_d	0.50	False-alarm probability P_{fa}	10^{-6}
Basic detectability factor D	2.7 dB	Matching factor M	0.8 dB
Beamshape loss L_p	1.2 dB	Miscellaneous loss L_x	3.3 dB
Detectability factor D_x	8.0 dB	Attenuation L_α (at R_m)	1.8 dB
Pattern-propagation factor F	1.0	Range-dependent factor F_{rdr}	0 dB
Target RCS σ	1.0 m^2	Range in thermal noise R_m	132 km

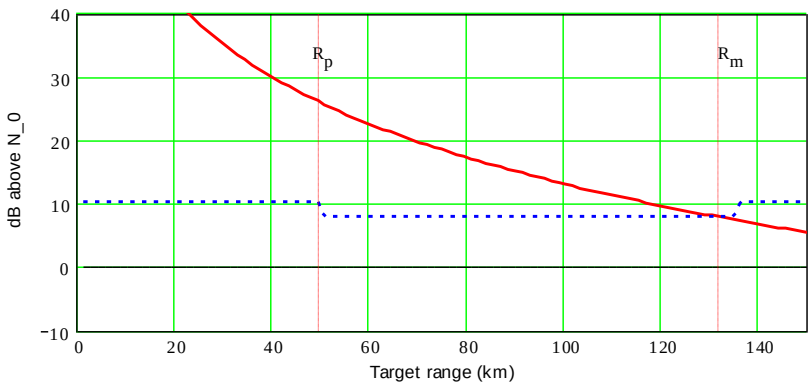

Figure 1.3 Energy ratios versus range for example radar: signal energy (solid line), required energy (dashed line). MTI processing increases L_x for $R < R_p$ = 50 km.

range (R_m = 132 km, in this case) for which $E/N_0 = D_x$. The example radar is modeled as using MTI processing out to a range R_p = 50 km, but the increase in D_x caused by MTI loss within that range does not affect R_m as long as $R_p < R_p. < R_u$. (where in this case R_u = 135 km).

1.6.3.2 Example for Solid-State Radar

A possible solid-state version of the example radar is modeled, having the same average power and unambiguous range but a duty cycle of 20%, giving a pulse width τ = 180 μs. Eclipsing occurs for R < 27 km, and for 108 km < R < 162 km, giving the effect as shown by the available energy ratio plotted in Figure 1.4. Detection now occurs at R_m = 114 km, where almost full pulse compression gain becomes available as the incoming target emerges from the eclipsed region. Eclipsing at short range has no effect on R_m in this case.

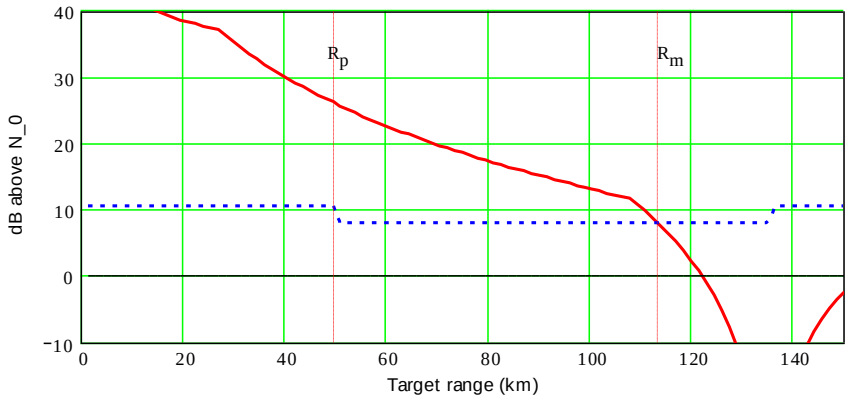

Figure 1.4 Energy ratios versus range for solid-state radar with D_u = 20%.

1.6.3.3 Example for Radar with STC

Figure 1.5 shows the result of applying STC within the first half of the unambiguous range of the example radar. The upper curve shows the desired effect for a target cross section $\sigma = 1\text{m}^2$, where the available energy is maintained well above the requirement for all $R < R_m$. The solid curve is plotted for a smaller target ($\sigma = 0.032\text{m}^2 = -15$ dBsm), showing that such a target fails to reach the requirement for P_d = 50% at any range. This performance would be desirable in an air traffic control radar, for example, where the desired targets have $\sigma \geq 1\text{m}^2$ and

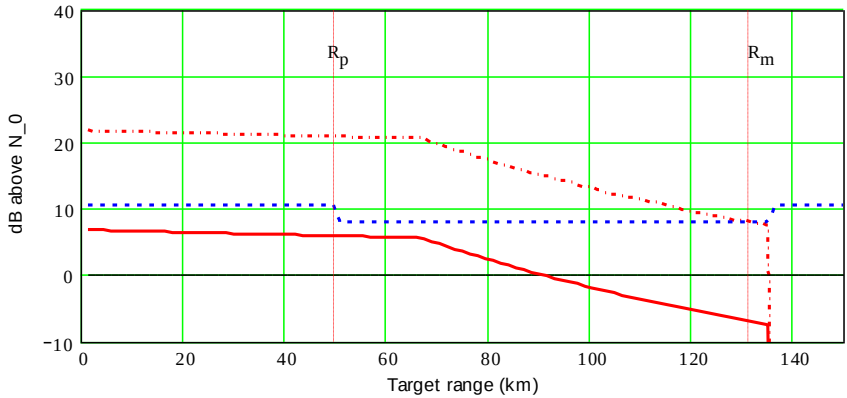

Figure 1.5 Energy ratios versus range for example radar with STC.

where almost all birds would be rejected. It would be unacceptable in a modern air defense radar.

1.6.4 Vertical Coverage Charts

The result of a Blake chart or other solution to the radar range equation gives one point in the vertical-plane coverage of a surveillance radar, for which the pattern-propagation factor $F(\theta_t)$ is valid, where θ_t is the specific target elevation used in calculation. Because the range R' in the Blake chart is directly proportional to F, a simple method of constructing the plot is to calculate $F(\theta)$ as a function of varying elevation angle θ, and express the detection range envelope as $R'(\theta)$. This would be adequate if there were no significant change in the atmospheric attenuation over the elevation beamwidth, but otherwise the iterative procedure for calculation of attenuation would have to be repeated at several elevation angles over the sector to be plotted. The procedure used in [22] calculates the available energy ratio using F, L_α, and L_{rdr} as functions of range for each plotted elevation, using small enough steps to produce smooth coverage curves. Calculation of the required energy ratio D_x as a function of range, caused by factors such as beamshape, MTI losses, and STC, also provides results not readily obtained in using the Blake chart. Coverage for the example radar is shown in Figure 1.6.

The chart shown in Figure 1.6 was calculated for the radar of Table 1.1 operating over a land surface with rms height deviation σ_h = 3m, generating only one significant reflection lobe that lies below 0.1° elevation. This lobe would extend beyond the unambiguous range R_u = 135 km, except that the increased D_x in that region exceeds the available energy ratio, truncating the coverage to R_u. The same increased D_x, caused by use of MTI processing for $R < R_p$ = 50 km, causes a slight lump in the curves at the top of the beam, where they pass through that range. At

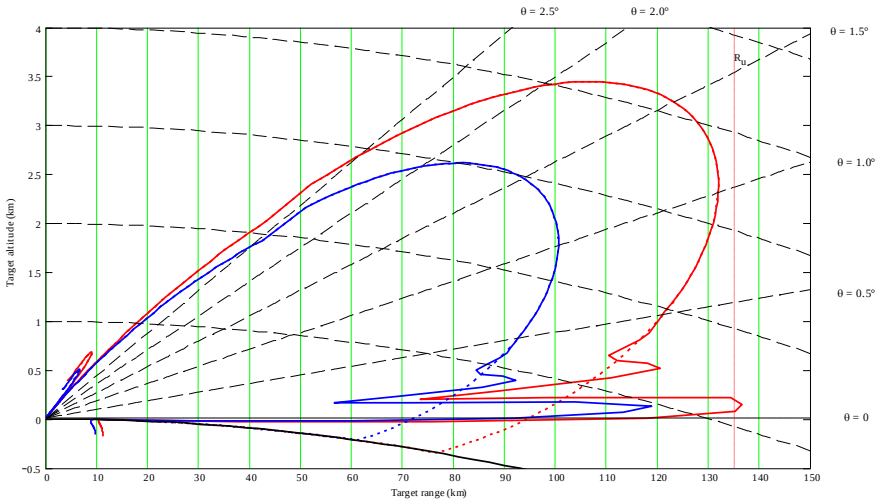

Figure 1.6 Vertical coverage chart for example radar, for P_d = 90% (inner curve) and P_d = 50% (outer curve).

the center of the beam, θ = 1°, the curve for P_d = 50% agrees with the detection range shown in Figure 1.3.

Range calculations at a single elevation are useful for many purposes, but they fail to convey the information shown in the vertical coverage chart. That chart provides, in visually interpretable form, data necessary for evaluation of surveillance radar performance. On the other hand, plots such as those shown in Figure 1.3–1.5 are necessary to interpret the factors that control the detection range at a given elevation. Both presentations, and other intermediate results, are needed to avoid errors that are commonly encountered in estimating radar range.

1.6.5 Required Probability of Detection

The detectability factor D used in the radar equation depends on the required probability of detection. That probability is often assumed to be P_d = 0.5–0.9, based on an arbitrary specification. The requirement actually depends on the operating mode of the system that accepts the radar output. A single alarm is seldom sufficient to alert the system to target presence, since reaction to such an alarm would be triggered by each random false alarm from noise or interference. Confirmation by a second detection and initiation of a track file is usually required, implying single-scan $P_d \geq 0.5$ (often ≥ 0.8) for reliable track acquisition and maintenance. Figure 1.7 shows the number of scans required to obtain a given cumulative probability of track acquisition, as a function of single-scan P_d.

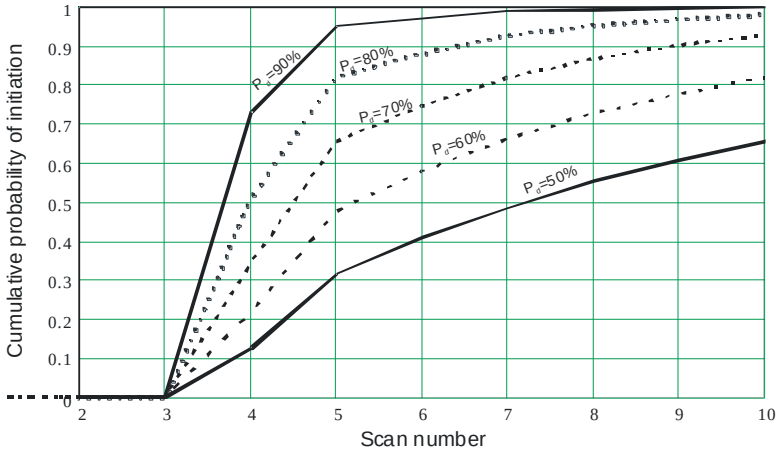

Figure 1.7 Cumulative probability of track acquisition versus scan number for single-scan detection probabilities from 50% to 90%, for a typical track-while-scan system. The track initiation requirement is detection on at least 3 out of 5 successive scans. (From [21].)

The probability of track retention for a given number of scans is shown in Figure 1.8, for different values of single-scan P_d. It is apparent from these two figures that $P_d \geq 0.8$ is a requirement if the radar is to support reliable track-while-scan.

Many modern radars, including multifunction array radars and conventional search radars that are associated with phased-array tracking radars, can allocate

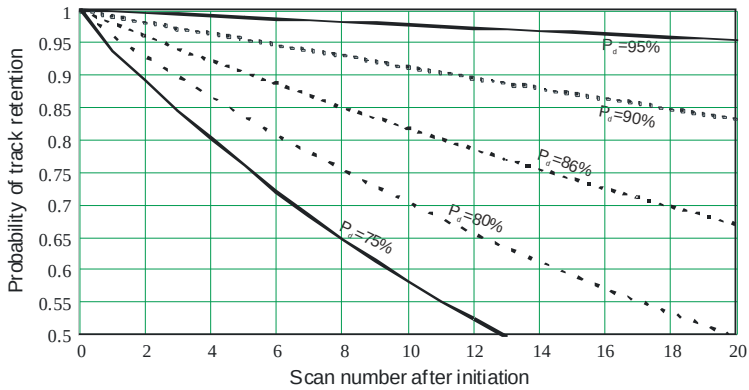

Figure 1.8 Probability of track retention versus number of scans for different single-scan detection probabilities, applicable to a typical track-while-scan system in which track is dropped after two successive missed detections. (From [21].)

their resources in such a way as to initiate and maintain tracks when P_d in the search mode is much lower than 0.8. Ability to schedule an immediate validation dwell after initial detection, possibly with an increase in transmitted energy relative to that used in the routine search function, permits target presence to be confirmed and tracking to be initiated with high probability, with small increases in time and energy requirements. The result is that the maximum tracking range is that at which the cumulative probability of detection P_c, rather than P_d, reaches an acceptable value. Values of $P_d \approx 0.3$ or less can then be used in the radar equation, significantly extending radar range [27].

1.7 SUMMARY OF RADAR EQUATION DEVELOPMENT

This chapter traces the evolution of the radar equation from its origin during World War II through its application to modern radars. The contributions of Lamont Blake are emphasized, and his method of expressing the equations is suggested as an accurate starting point for current and future analyses of radar performance. Modifications to Blake's equations are presented that adapt them to more complex characteristics and modes of modern radar systems, but his fundamental approach remains the foundation of reliable estimates of radar detection range. To quote Marcum [24, p. 1] in discussing the original radar equation,

> The number of pitfalls that may be encountered in the use of the above equation are almost without limit, and many of these difficulties have been recognized in the past.

New difficulties have been recognized since Marcum published his study. Modern computational techniques overcome many of these limitations and provide results with high precision, but they often mask other problems while encouraging reliance on procedures that induce errors far greater than the displayed precision. Avoiding such errors was central to Blake's careful analysis of the problem. That is also the aim of the subsequent developments discussed in [20–22], in this chapter, and throughout the remainder this book.

References

[1] Norton, K. A. and A. C. Omberg, "The Maximum Range of a Radar Set," *Proc. IRE*, Vol. 35, No. 1, January 1947, pp. 4–24. Reprinted in [2].

[2] Barton, D. K., (ed.), *The Radar Equation*, Dedham, MA: Artech House, 1974.

[3] North, D. O., "An Analysis of the Factors Which Determine Signal/Noise Discrimination in Pulsed Carrier Systems," *RCA Laboratories Technical Report PTR-6C*, June 25, 1943. Reprinted: *Proc. IEEE*, Vol. 51, No. 67, July 1963, pp. 1015–1027.

[4] IEEE Standard 100, *The Authoritative Dictionary of IEEE Standards Terms, 7th ed*., New York: IEEE Press, 2000.

[5] Haeff, A. W., "Minimum Detectable Radar Signal and Its Dependence Upon Parameters of Radar Systems," *Proc. IRE*, Vol. 34, No. 11, November 1946, pp. 857–861.

[6] Blake, L. V., "Interim Report on Basic Pulse-Radar Maximum Range Calculations," *Naval Research Laboratory Report 1106*, November 1960.

[7] Blake, L. V., "Recent Advancements in Basic Radar Range Calculation," *IRE Trans. on Military Electronics*, Vol. MIL-5, No. 2, April 1961, pp. 154–164. Reprinted in [2].

[8] Blake, L. V., "A Guide to Basic Pulse-Radar Maximum-Range Calculation, Part 1–Equations, Definitions, and Aids to Calculation," *Naval Research Laboratory Report 5868*, December 28, 1962.

[9] Blake, L. V., "A Guide to Basic Pulse-Radar Maximum-Range Calculation, Part 1–Equations, Definitions, and Aids to Calculation," *Naval Research Laboratory Report 6930*, December 23, 1969. Summarized in [2].

[10] Blake, L. V., "A Guide to Basic Pulse-Radar Maximum-Range Calculation, Part 2–Derivation of Equations, Bases of Graphs, and Additional Explanations," *Naval Research Laboratory Report 7010*, December 31, 1969.

[11] Blake, L. V., "Prediction of Radar Range," Chapter 2 in [15, 16].

[12] Blake, L. V., *Radar Range-Performance Analysis*, Lexington, MA: D. C. Heath, 1980; Dedham, MA: Artech House, 1986.

[13] Blake, L. V., "The Effective Number of Pulses per Beamwidth for a Scanning Radar," *Proc IRE*, Vol. 41, No. 6, June 1953, pp. 770–774, with addendum: December 1953, p. 1785. Reprinted in [2].

[14] Kerr, D. E., (ed.), *Propagation of Short Radio Waves*, Vol. 13 in MIT Radiation Laboratory Series, New York: McGraw-Hill, 1951. Reprinted (CD ROM edition): Norwood, MA: Artech House, 1999.

[15] Skolnik, M. I., (ed.), *Radar Handbook*, New York: McGraw-Hill, 1970.

[16] Skolnik, M. I., (ed.), *Radar Handbook*, 2nd ed., New York: McGraw-Hill, 1990.

[17] Hall, W. M., "Prediction of Pulse Radar Performance," *Proc. IRE*, Vol. 44, No. 2, February 1956, pp. 224–231. Reprinted in [2].

[18] Hall, W. M., "General Radar Equation," *Space/Aeronautics R and D Handbook*, 1962-63. Reprinted in [2].

[19] Barton, D. K., *Radar System Analysis*, Englewood Cliffs, NJ: Prentice-Hall, 1964; Dedham, MA: Artech House 1976.

[20] Barton, D.. K., *Modern Radar System Analysis*, Norwood, MA: Artech House, 1988.

[21] Barton, D. K., *Radar System Analysis and Modeling*, Norwood, MA: Artech House, 2005.

[22] Barton, D. K., *Modern Radar System Analysis Software and User's Manual, Version 3.0*, Norwood, MA: Artech House, 2007.

[23] Rice, S. O., "Mathematical Analysis of Random Noise," *Bell Sys. Tech. J.*, Vol. 23, No. 3, July 1944, pp. 282–332 and Vol. 24, No. 1, January 1945, pp. 461–556. Reprinted: *Selected Papers on Noise and Stochastic Processes*, (N. Wax, ed.), New York: Dover Publ., 1954.

[24] Marcum, J. I., "A Statistical Theory of Target Detection by Pulsed Radar, *RAND Corp. Research Memo RM-754*, December 1, 1947. Reprinted: *IRE Trans. on Information Theory*, Vol.

IT-6, No. 2, April 1960, pp. 59–144; excerpted: *Detection and Estimation*, (S. S. Haykin, ed.), Stroudsburg, PA: Halstad Press, 1976, pp. 57–121.

[25] Swerling, P., "Probability of Detection for Fluctuating Targets," *RAND Corp. Research Memo RM-1217*, March 17, 1954. Reprinted: *IRE Trans. on Information Theory*, Vol. IT-6, No. 2, April 1960, pp. 269–308; *Detection and Estimation*, (S. S. Haykin, ed.), Stroudsburg, PA: Halstad Press, 1976, 122–158.

[26] Weil, T. A., "Atmospheric Lens Effect, Another Loss for the Radar Range Equation," *IEEE Trans. on Aerospace and Electronic Systems*, Vol. AES-9, No. 1, January 1973, pp. 51–54. Reprinted in [2].

[27] Barton, D. K., "Maximizing Firm-Track Range on Low-Observable Targets," *IEEE International Conf. Radar-2000*, Washington, DC, May 8–12, 2000, pp. 24–29.

CHAPTER 2

The Search Radar Equation

The radar equations presented in Chapter 1 give the detection range of an existing or proposed radar for which the major parameters are known. They can be used to test different sets of parameters and to compare the results of competing radar designs for a given task, determining which best meets requirements such as the range at which a specified detection performance is available given the available beam dwell time and investment in equipment and input power.

The *search radar equation* is a modification of the basic equation that allows one to avoid the process of generating many alternative designs and testing them to see which can meet a specified objective. It provides an estimate of the minimum radar size, as measured by the product of average transmitter power P_{av} and receiving antenna aperture area A, that can search a given volume of three-dimensional space with a specified level of detection performance. Alternatively, it can define the volume that can be searched by a radar of specified size while providing a specified level of detection performance. Neither the wavelength nor the waveform need be known to obtain these estimates, and hence it is unnecessary to postulate details such as the signal processing methods or the resolution properties of the radar until a later stage in the synthesis or analysis of the radar design.

The search radar equation originated in a 1948 study by Edward Barlow and his associates at Sperry Gyroscope Company that was presented in a classified report [1]. That report has apparently never been declassified, but the derivation of the equation was presented in [2] and it has subsequently seen wide use. For example, it provides the basis for the definition of a class of radars whose siting was limited by the (now defunct) U.S.-Russian ABM Treaty to locations on the periphery of the using country, looking outward. It serves as a reference for quick evaluation and comparison of proposed radar designs and systems on which available data are limited.

2.1 DERIVATION OF THE SEARCH RADAR EQUATION

The search radar equation is derived from an idealized model of the search process. An angular sector is to be searched in a specified period of time by a transmitting beam that may either scan the sector or illuminate it continuously, while one or more receiving beams recover and integrate the energy of resulting target echoes. Free-space propagation is assumed. A combined search loss factor is included to account for departures from the idealized model of the radar and environment. Steps in derivations of the equations are as follows.

Search Sector. The first step in derivation of the search radar equation is to establish an idealized model of the *search sector*, specified as a solid angle ψ_s steradians, within which the radar resources of time and energy are to be confined. The solid angle ψ_s is normally specified in terms of the width A_m of the azimuth sector and the upper and lower limits θ_m and θ_0 of the elevation sector:

$$\psi_s = A_m \left(\sin\theta_m - \sin\theta_0 \right) \quad (\text{steradians}) \tag{2.1}$$

where A_m is in radians. Note that the elevation angle θ_m is positive for a surface-based radar, for which normally $\theta_0 \geq 0$. For a radar elevated above the surface, either or both angles can be negative, the only requirement being that $\theta_m > \theta_0$.

Transmitting Beam Sector. The transmitting beam is modeled as rectangular in shape with uniform gain over a beam sector $\psi_{bt} \leq \psi_s$ given by

$$\psi_{bt} = \theta_{at} \left(\sin\theta_{t\max} - \sin\theta_{t\min} \right) \approx \theta_{at}\theta_{et} \quad \text{steradian} \tag{2.2}$$

where

θ_{at} = azimuth width of transmitting beam (rad);
$\theta_{t\max}$ = elevation of upper edge of transmitting beam (rad);
$\theta_{t\min}$ = elevation of lower edge of transmitting beam (rad);
θ_{et} = $\theta_{t\max} - \theta_{t\min}$ = elevation width of transmitting beam (rad).

The transmitting beamwidths are either matched to the search sector or made small enough that the radar can scan the sector ψ_s with no overlap between adjacent beams or excursion beyond the sector. The latter case is normally assumed, justifying the small-angle approximation in (2.2). The solid angle ψ_b of the beam is related to the gain G_t of the idealized transmitting antenna by a simple expression, based on the assumption that the transmitted energy is confined to and uniformly distributed within the rectangular-shaped beam:

$$\psi_{bt} = \theta_{at}\theta_{et} = \frac{4\pi}{G_t} \quad (\text{steradians}) \tag{2.3}$$

where 4π is the solid angle of a sphere surrounding the radar, over which an isotropic antenna would spread the radiated power. Equation (2.3) states the fact that the gain G_t of an antenna varies inversely with the solid angle of its beam. We consider later the limitation on the gain that can be produced by a practical antenna, requiring replacement of the factor 4π by $4\pi/L_n \approx 10.75$ from [3, p. 334].

Search Frame Time. Targets in the search sector are to be detected with specified probability within a *search frame time* t_s. This allows expression of the observation (or dwell) time t_o in each transmitting beam position as

$$t_o = \frac{t_s}{n_{bt}} = \frac{t_s \psi_{bt}}{\psi_s} = \frac{4\pi t_s}{G_t \psi_s} \quad (\text{sec}) \tag{2.4}$$

where $n_{bt} = \psi_s/\psi_{bt}$ is the number of transmitting beam positions in the search sector.[1]

Coherent Integration. The idealized radar performs coherent integration of the echo energy received in the period t_o, during which the transmitted energy is

$$E_t = P_{av} t_o = \frac{4\pi P_{av} t_s}{G_t \psi_s} \quad (\text{J}) \tag{2.5}$$

Further Assumptions. The following assumptions also apply to the idealized search radar and process:

- The gain of the ideal receiving antenna is given by (1.5), with the receiving aperture equal to the physical area[2] of the receiving antenna, $A_r = A$:

$$G_r = \frac{4\pi A}{\lambda^2} \tag{2.6}$$

- The target cross section is a constant σ, located on the axes of the nearest transmitting and receiving beams, at broadside to the antenna array if one is used. The basic steady-target detectability factor $D_0(1)$ for this case is as given by Rice [4] (see Section 4.2).
- Free-space paths give pattern-propagation factors $F_t = F_r = 1$.
- The system noise temperature $T_s = T_0 = 290$K.

---

[1] For electronically scanned array antennas, broadening of the beam at angles off broadside reduces the number of beams required to scan a given sector.

[2] We use here the physical aperture A rather than the effective receiving aperture A_r appearing in some discussions, to base the equation on a truly ideal reference.

- All losses relative to the ideal are lumped into a *search loss factor* L_s.

Search Radar Range. With these assumptions, the maximum detection range from (1.18) becomes

$$R_m = \left[\frac{P_{av} t_s A \sigma}{4\pi \psi_s k T_0 D_0 (1) L_s} \right]^{1/4} \quad (\mathrm{m}) \tag{2.7}$$

The three-dimensional search volume is defined by the angular sector ψ_s and the maximum range R_m. The transmitting antenna gain and number of beams transmitted into the search sector cancel out of the equation, leaving the energy density per unit solid angle $P_{av}t_s/\psi_s$ (in J/steradian) as the transmitter illumination density in the search sector. As long as the echo energy is collected efficiently by the receiving aperture A, it makes no difference whether the energy appears in short periods $t_o << t_s$ from a transmitting antenna with high G_t, or any longer period with lower G_t, approaching the limiting case of continuous low-gain illumination of the full sector for t_s seconds by a nonscanning transmission: $\psi_{bt} = \psi_s$, $n_{bt} = 1$. If the transmitting beam scans the sector, the receiving beam must follow it to receive all the echo energy incident on the receiving aperture from the illumination of each beam position. If the transmitting beam illuminates a solid angle ψ_{bt} greater than that of a single receiving beam (i.e., the transmitting aperture is smaller than A), then multiple receiving beams must be formed in parallel to collect the echo energy returned to the receiving antenna. Receiving aperture efficiency $\eta_a < 1.0$ for requires that the corresponding loss factor $L_\eta = 1/\eta_a$ be included in the system loss factor. If coherent integration is not performed over the observation time t_o, a corresponding noncoherent integration loss must be included in L_s.

Power-Aperture Required for Search. Inversion of (2.7) to solve for the *power-aperture product* $P_{av}A$ required to meet a search specification gives

$$P_{av} A = \frac{4\pi \psi_s R_m^4 k T_0 D_0 (1) L_s}{t_s \sigma} \quad (\mathrm{W \cdot m^2}) \tag{2.8}$$

The task assigned to the search radar determines five of the terms in (2.8):

$$\psi_s,\ R_m,\ D_0,\ t_s, \text{ and } \sigma.$$

The factors 4π, k and T_0 are constants. Only P_{av} and A on the left side and L_s on the right side are controlled by decisions of the radar designer. The challenge in applying the search radar equation is to define the appropriate search sector ψ_s and estimate the losses that enter into L_s. These steps are critical to use of the equation,

since the idealized assumptions made in its derivation require that ψ_s be carefully defined and that many losses, usually totaling ≈ 20 dB or more, be identified and quantified.

2.2 SEARCH SECTORS FOR 2-D AIR SURVEILLANCE

Air surveillance radars are described as two-dimensional (2-D) when their output data are range and azimuth, and three-dimensional (3-D) when range, azimuth, and elevation data are provided. Both types search within the three-dimensional space used in the search radar equation.

2.2.1 Elevation Coverage in 2-D Surveillance

The 2-D air surveillance radar coverage pattern in elevation can seldom be defined simply in terms of the maximum and minimum elevation angles θ_m and θ_0 used in (2.1). Requirements typically follow one of the curves plotted in Figure 2.1.

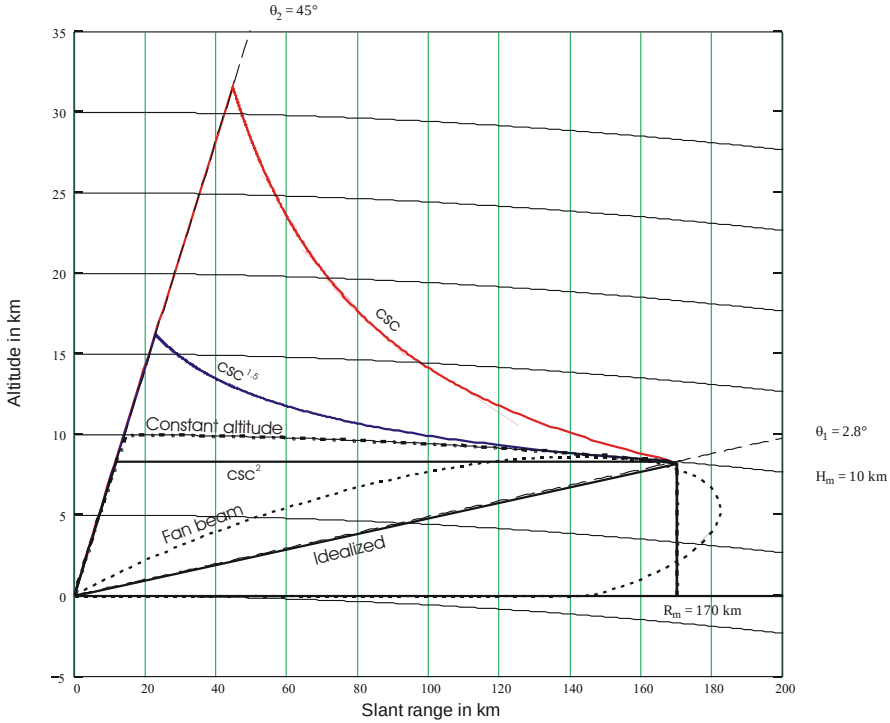

Figure 2.1 Typical vertical coverage requirement options for 2-D air surveillance radar.

Air surveillance coverage is customarily specified in terms of the maximum altitude H_m of intended targets and required detection range R_m, over the full 360° azimuth sector. The elevation coverage of the idealized beam, which is rectangular in angle space, is shown by solid lines as a right triangle. Its lower side extends horizontally (at zero elevation) from the radar to range R_m; the right side extends vertically from that point to an altitude H_m above the curved Earth; and the hypotenuse is a straight line returning from that point to the radar. The elevation beamwidth θ_1 (2.8° in the example shown) is expressed as

$$\theta_1 = \arcsin\left(\frac{H_m}{R_m} - \frac{R_m}{2k_e a_e}\right) \text{ (rad)} \tag{2.9}$$

where

H_m = maximum target altitude (m);
k_e = ≈ 4/3 = Earth's radius factor;
a_e = 6,378,000m = Earth's radius.

The minimum and maximum elevations for use in (2.1) are $\theta_0 = 0$ and $\theta_m = \theta_1$. The maximum-altitude target is detected the at range R_m, but at shorter ranges it lies above the idealized beam. This is far from ideal in the practical sense. One of the five other patterns shown will typically be used in practice, with appropriate entries in the search radar equation as described below.

2.2.2 Fan-Beam Pattern for 2-D Surveillance

In fan-beam 2-D radar the elevation beam patterns for transmitting and receiving are matched to the required elevation search sector. A possible fan beam contour, shown in Figure 2.1 as a dashed curve, approximates the idealized triangle, but its half-power beamwidth has been adjusted to $\theta_e \approx 1.5\theta_1$ to include the point R_m, H_m. This moves the upper shoulder of its pattern above the hypotenuse of the triangle and extends the beam peak beyond R_m. Targets at altitude H_m still lie above the beam at $R < 0.9R_m$, so detection at maximum altitude is only possible in a narrow range interval near R_m. Even this small departure of the fan beam from the idealized coverage triangle requires the following adjustments of entries in the search radar equation.

- An elevation beamshape loss $L_{pe} = \theta_e/\theta_1 \approx 1.5 = 1.76$ dB is included as a component of L_s to account for the increase in beamwidth of the 2-D radar antenna. This results from inability to synthesize the square-ended beam corresponding to the idealized triangular pattern shown in Figure 2.1, thus violating the assumption that the transmitted energy is uniform from 0 to θ_1, as used in defining ψ_s. This loss is reduced if the aperture height h is large enough to permit the full-range coverage pattern to be synthesized by com-

bining two or more narrow elevation beams to approximate a square-ended beam (see Section 10.1.4).

- The elevation beamshape loss included in L_s is squared, to account also for the reduction in effective receiving aperture area $A_r = A/L_{pe}$. The two-way loss L_{pe}^2 in the search radar equation replaces the beamshape loss L_p = 1.24 dB used in the conventional radar equation to give the reduction in average two-way gain for targets distributed over the elevation beamwidth (see Section 5.2).
- The search solid angle ψ_s for fan-beam 2-D radar is calculated using $\theta_m = \theta_1$ and $\theta_0 = 0$ in (2.1).

2.2.3 Cosecant-Squared Pattern for 2-D Surveillance

Another curve in Figure 2.1 shows a *cosecant-squared* elevation beam pattern. Here the mainlobe extends from zero elevation to θ_1 at range $\geq R_m$, but coverage continues along a horizontal line from that point to an upper elevation limit θ_2. Above θ_2 is a *cone of silence* in which coverage is lost. The idealized antenna gain as a function of elevation angle is

$$\begin{aligned} G(\theta) &= G_m, && 0 \leq \theta \leq \theta_1 \\ &= G_m \frac{\csc^2 \theta}{\csc^2 \theta_1}, && \theta_1 < \theta \leq \theta_2 \\ &= 0, && \theta_2 < \theta \end{aligned} \tag{2.10}$$

where G_m is the gain required to achieve detection at R_m.

The search sector specified in the search radar equation can be adjusted for an idealized $\csc^2$ pattern by using an equivalent value of upper elevation given by [5, p. 315, Eq. (7.4)]:

$$\theta_m = L_{\csc}\theta_1 = \left[2 - \frac{\sin\theta_1}{\sin\theta_2}\right]\theta_1 \ \text{(rad)} \tag{2.11}$$

where $L_{\csc}$ is the pattern loss in gain for the $\csc^2$ coverage compared to the fan beam with half-power width θ_1. This loss approaches a maximum of 3 dB for $\theta_2 >> \theta_1$. Use of the equivalent upper elevation angle in calculating ψ_s accounts for the transmitted energy density over the search sector, but a second application of $L_{\csc}$ is needed to reflect the reduction in effective receiving aperture. Thus, entries in the search radar equation must be adjusted for the $\csc^2$ pattern as follows:

- The required search solid angle ψ_s is increased by L_{csc}, relative to the fan-beam radar, to allow for diversion of transmitted energy into the upper shoulder of the pattern.
- The L_{csc} in effective receiving aperture is included in L_s.
- The elevation beamshape loss L_{pe} remains as listed in Section 2.2.2.

2.2.4 Coverage to Constant Altitude

Even with its extension above θ_1, the csc^2 pattern does not quite meet the required altitude coverage to altitude H_m at ranges within R_m, because θ_1 from (2.9) has been reduced by the Earth's curvature relative to the angle that would apply over a flat Earth. A slight adjustment to (2.10) can preserve coverage to that labeled "constant altitude" in Figure 2.1. The resulting losses in on-axis gain for the csc^2 and constant altitude patterns are shown in Figure 2.2, along with data for two other types of enhanced upper coverage, discussed below. The pattern loss due to the use of csc^2 or other patterns with elevation coverage extended at ranges within R_m will be denoted here by L_{csc} regardless of the exponent of the csc function used or the adjustment for coverage to constant target altitude. All the plots in Figure 2.2 are calculated for a maximum elevation coverage angle $\theta_2 = 45°$, but there is negligible change as that angle varies from 30° to 60°. The factor L_{csc} appears both as an increase in ψ_s (for transmitting) and in L_s (for receiving).

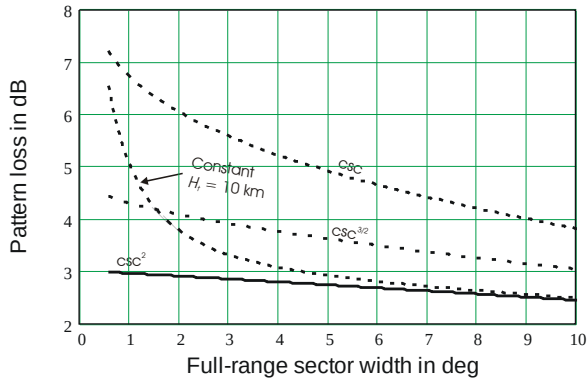

Figure 2.2 Pattern loss L_{csc} for csc^2 and other patterns with extended upper coverage, as a function of full-range elevation sector width θ_1.

2.2.5 Enhanced Upper Coverage for 2-D Surveillance Radar

When sensitivity time control (STC) is used in a 2-D surveillance radar with a csc^2 or constant-altitude pattern, the detection range is reduced on targets at ranges

where STC is applied. To avoid this, an antenna pattern with enhanced upper coverage is used [6]. Two such curves are shown in Figure 2.1, corresponding to gains varying as $\csc^{3/2}\theta$ and $\csc\theta$. Figure 2.2 includes plots of loss $L_{\csc}$ for these two cases. For the $\csc\theta$ pattern the equivalent upper elevation is given by

$$\theta_m = L_{\csc}\theta_1 = \left[1+\ln\left(\frac{\sin\theta_2}{\sin\theta_1}\right)\right]\theta_1 \ \ (\text{rad}) \tag{2.12}$$

As with $\csc^2$ coverage, both ψ_s and L_s are increased in the search radar equation to account for the extended coverage, and the elevation beamshape loss L_{pe} is also applied.

2.2.6 Reflector Antenna Design for 2-D Surveillance Radar

Reflector antennas for $\csc^2$ or other enhanced upper coverage are designed in either of two ways: (1) reflector area is added at the top or bottom of the parabolic surface, deviating from the parabola to divert that energy into the upper coverage region and illuminated by a broadened horn pattern; or (2) multiple feed horns are stacked one above the other, fed from a power divider whose coupling is adjusted to provide the desired pattern shape. Option (1) increases the physical aperture A but reduces the effective area A_r relative to a simple paraboloid, increasing the loss by the factor $L_{\csc}$ relative to the fan beam (and by a greater factor relative to the increased area A). Option (2) uses the aperture height required for the mainlobe of width $\approx \theta_1$, but reduces its effective area by $L_{\csc}$. In both cases there is an increase in receiving aperture loss included in L_s, in addition to that caused by illumination tapers applied for sidelobe reduction in both coordinates and by spillover and feed blockage.

2.2.7 Array Antennas for 2-D Surveillance Radar

There are also two design approaches available for electrically fixed array antennas with $\csc^2$ or other enhanced upper coverage: (1) rows of radiators are added at the top or bottom of the array, for which the amplitudes and phases are adjusted to form the desired upper coverage; or (2) the number of element rows is chosen for an elevation beamwidth $\approx \theta_1$, and multiple feed lines are coupled to each row with complex weights that generate the radiated field contributions required for the upper coverage. The two methods are equivalent to those discussed for reflectors, and the same loss considerations apply. Active arrays are seldom used in 2-D radars, but if this is done the first option may be required to avoid distortion caused by saturation of power amplifiers with variation in the amplitude of excitation.

2.2.8 Example of Required Power-Aperture Product for 2-D Radar

The search radar equation can be applied to estimate the power-aperture products required for each coverage curve of Figure 2.1. Typical parameters common to all coverage options are shown in Table 2.1. To compare results for a specific choice of radar band, the wavelength has been assumed as 0.23m (L-band), and the aperture dimensions calculated based on a beamwidth constant $K_\theta = \theta_a w/\lambda = 1.1$. The upper coverage is assumed to be obtained by manipulation of the illumination over the aperture height $h = 5.2$m needed to obtain $\theta_e = 1.5\theta_1$.

Table 2.1 Parameters Common to Example 2-D Search Radar

Target cross section σ	m^2	1.0	Frame time t_s	s	6
System noise temperature T_s	K	500	Detectability factor $D_0(1)$	dB	12
Search loss L_s (excluding L_{pe}, L_{csc})	dB	20	Maximum range R_m	km	170
Azimuth sector A_m	deg	360	Minimum elevation θ_0	deg	0
Maximum full-range elevation θ_1	deg	2.8	Maximum target altitude H_m	km	10
Wavelength λ	m	0.23	Azimuth beamwidth θ_a	deg	1.5
Aperture width w	m	9.7	Aperture height h	m	5.2
Aperture area A	m^2	50			

Table 2.2 shows the results of applying (2.8) to the parameters shown in Table 2.1. The required power-aperture product increases as more power is diverted into the upper coverage. The increased requirement shown in the last two columns is attributable to the enhanced upper coverage made necessary by the application of STC to avoid receiver saturation from clutter and false alarms from small moving targets at short range.

Table 2.2 Results from Search Radar Equation

Requirement	*Unit*	*Elevation pattern*				
		Fan	*csc*^{2}	*Const. H*	*csc*$^{1.5}$	*csc*
Maximum elevation θ_2	deg	2.8	45	45	45	45
Elevation beamshape loss L_{pe}	dB	1.76	1.76	1.76	1.76	1.76
Pattern loss L_{csc}	dB	0.0	2.86	3.42	3.98	5.65
Effective elevation sector θ_m	deg	4.2	5.4	6.2	7.0	10.3
Solid angle of sector ψ_s	sterad	0.31	0.59	0.67	0.77	1.13
Power-aperture product	$kW \cdot m^2$	7.66	28.6	37.1	47.9	103.3
Average power P_{av}	W	153	570	740	956	2,063

2.3 THREE-DIMENSIONAL AIR SURVEILLANCE

This section considers air surveillance conducted by radars that scan mechanically in azimuth, with elevation coverage provided by stacked beams that operate in parallel to cover the elevation sector or a single beam that scans the sector. Electronic scan in both coordinates, using a mechanically fixed array, is discussed in Section 2.4.

2.3.1 Stacked-Beam 3-D Surveillance Radars

The stacked-beam 3-D radar uses a single transmitting pattern similar to that of the 2-D radar. Multiple, narrow receiving beams are stacked one above the other, within the transmitted beamwidth, to cover the elevation sector. The equivalent upper elevation angle θ_m used in the search radar equation is given in Sections 2.2.1–2.2.5. The gains of the receiving beams are selected independently, giving flexibility in apportioning of transmitting and receiving gains over the elevation sector. To obtain the equivalent of the $\csc^2$ 2-D coverage, for example, one of the following approaches may be used:

- Receiving beams use the gain of the full aperture, allowing the transmitting pattern to follow a $\csc^4$ pattern that minimizes the loss $L_{\csc}$.
- Receiving beamwidths vary with elevation so that both transmitting and receiving gains follow the $\csc^2$ envelope, with losses as given in Section 2.2.3.
- The transmitting pattern is $\csc^2$, while receiving beams following the $\csc^{1.5}$ or csc envelope to overcome the STC effect discussed in Section 2.2.5, while providing consistent height accuracy in the upper coverage.

The first method is seldom used because it requires the largest number of receiving channels. The second uses fewer channels but the broad beamwidths at high elevations increase losses and compromise the accuracy of height measurement.

The elevation beamshape loss L_{pe} applies to the transmitting antenna of a stacked-beam 3-D radar when the full-range coverage sector is provided by a single beam (i.e., when the aperture height $h \approx K_\theta \lambda/\theta_1$). The loss is reduced when two or more beams are combined to approach a square-ended beam. For the stacked receiving beams $L_{pe} \approx L_p = 1.24$ dB, and $L_{\csc}$ is based on the receiving gain profile applied to the upper coverage.

2.3.2 Scanning-Beam 3-D Surveillance Radars

The scanning-beam 3-D radar has achieved wide use since development of the electronically scanned array (ESA). The basic problem is to cover all elevation beams in succession during the time of antenna scan through the azimuth beam-

width (the *azimuth dwell time* t_{oa}). Electronic scanning is combined with variation in elevation beamwidth, transmitted energy, and pulse repetition interval as a function of beam elevation, in order to cover the elevation sector within that time. As a result, the full aperture A is brought to bear only on lower elevation portions of the search sector. The equivalent upper elevation calculated in Sections 2.2.1–2.2.5 accounts for the additional energy transmitted into the upper coverage, and the loss L_{csc} approximately measures of the effect of the coverage extension on effective receiving aperture. The azimuth spacing between elevation scans often leads to increased beamshape losses relative to other types of surveillance radar (see Sections 2.4.2 and Chapter 5).

The elevation beamshape loss L_{pe} applies to the transmitting antenna of a scanning-beam 3-D radar when the full-range coverage sector is provided by a single beam, but is reduced when two or more beams are combined to form a square-ended beam. The loss L_{pe} is the *net beamshape loss* L_{pn} for the scanned receiving beams (see Sections 5.3.5, 5.4.6, and 5.5.6), and L_{csc} is based on the receiving gain profile applied to the upper coverage.

2.3.3 Search Losses in 3-D Surveillance Radar

The class of 3-D surveillance radars discussed above rotate mechanically to cover the azimuth sector. The net azimuth beamshape loss L_{pn} is that calculated for the search radar equation but with a smaller number of samples per beamwidth for scanning-beam types, because of the need to cover many elevation beam positions during the azimuth dwell time. This increases the azimuth beamshape loss, especially for high values of P_d (see Chapter 5). In elevation, the specified P_d is required at range R_m on targets averaged over elevations $0 \le \theta \le \theta_1$, considering the pattern-propagation factor within the elevation mainlobe. To avoid too deep a drop in P_d near the horizon, the axis of the lowest beam is normally placed below $\theta_1/2$. In stacked-beam systems this may require a half-power transmitting beamwidth greater than θ_1, as discussed in Section 2.2.2. Other search loss components are as discussed in Section 2.6.

2.4 SURVEILLANCE WITH MULTIFUNCTION ARRAY RADAR

The multifunction array radar (MFAR) can perform search as well as tracking and fire control functions, using one or more planar array faces. Each face may be served by an individual transmitter, or a common transmitter may be switched among faces. Allocation of radar resources in transmitted energy and time is varied under software control according to the defense strategy or in response to the threat and environmental conditions. In place of a fixed search volume, as described in Section 2.2, the MFAR search coverage is commonly divided into sev-

eral sectors, $i = 1, 2, \ldots m$, with different values of R_{mi}, angle limits, and frame times t_{si}, and each sector is allocated some fraction of the resources. To establish requirements for the search fraction of the power-aperture product, the search radar equation is applied separately to each sector, and often to more than one threat condition. For example, there may be a "normal" condition under which a major fraction of the resources is assigned to the search function, and one or more "battle management" conditions requiring diversion of search resources to fire control.

2.4.1 Example of MFAR Search Sectors

A typical search allocation for the normal condition (clear air, low engagement rate) is ≈ 50% of the total resources. An example of vertical coverage sectors for a long-range surface-to-air missile (SAM) system for use against aircraft is shown in Figure 2.3. The requirements on each of $m = 3$ sectors are listed in Table 2.3. Within each sector, the narrow MFAR beam performs a raster scan with beams spaced by approximately θ_3, the half-power beamwidth ($\theta_3 = 1.4°$ at broadside).

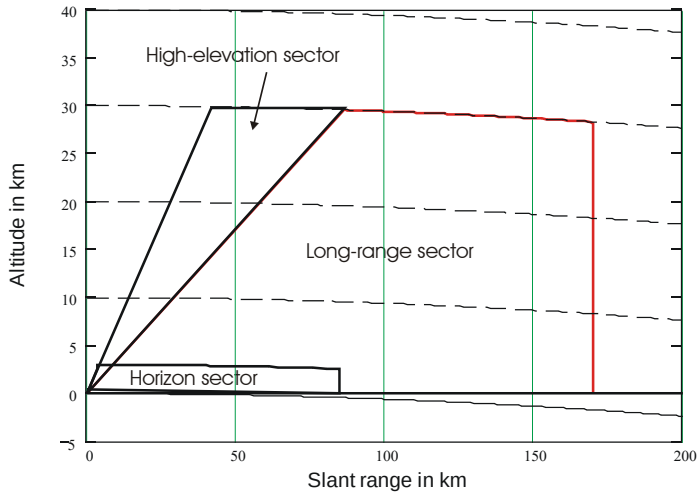

Figure 2.3 Example of vertical coverage sectors for MFAR air defense radar.

The example assumes that a single array face is used, with azimuth sectors that are within the scan capability of typical array designs. The long-range and horizon sectors use a $\csc^2$ envelope, slightly modified to preserve coverage up to the maximum target altitude of the sector. The high-elevation sector is specified to provide coverage to the maximum target altitude at elevations above the long-range sector, without overlapping that coverage. The horizon search sector overlaps the long-range sector, and uses a high revisit rate to guard against low-

Table 2.3 Example of MFAR Search Sectors

Requirement	*Unit*	*Sector*		
		Long-Range	*High-Elevation*	*Horizon*
Maximum range R_{mi}	km	170	89	85
Maximum target altitude H_{mi}	km	30	30	3
Maximum range R_{hi} at H_{mi}	km	85	42	4
Maximum elevation θ_{2i}	deg	20	45	45
Minimum elevation θ_{0i}	deg	0	20	0
Azimuth sector A_{mi}	deg	90	120	120
Effective elevation sector θ_m	deg	14.6	10.2	3.7
Solid angle of sector ψ_{si}	steradian	0.26	0.37	0.13
Frame time t_{si}	s	10	5	1
Dwells per s		38	108	196
Pulses per dwell n		3	3	3
Average dwell time nt_{ri}	ms	4.2	2.5	0.31
Sector time fraction T_{Fi}		0.159	0.266	0.060
Total search time fraction T_F		0.485		

altitude threats that might be masked by terrain until they pop up at relatively short range. Its angular extent is minimized to avoid an excessive time allocation. Each dwell is assumed to use three pulses, providing frequency diversity or alternatively supporting moving-target indication (MTI).

2.4.2 Advantages and Disadvantages of MFAR Search

An advantage of the MFAR search mode is that tracks can be initiated using validation and multiple track-initiation dwells immediately following the first detection, even when that detection results from a low signal-to-noise ratio with resulting low single-scan P_d. The range of track initiation is that for which the *cumulative probability of detection* P_c, rather than single-scan P_d, reaches the desired level [7]. This rapid-validation approach is a form of *sequential detection* [8].

Disadvantages in MFAR search are scan loss and the need to share radar resources among the search sectors, including validation dwells and other radar functions. A further disadvantage is that the frequency band must be chosen to accommodate both search and tracking functions, and in general is too high for optimum search and too low for optimum tracking. The sharing of resources is best expressed by applying (2.7) separately to each search sector, using only the fraction of average power allocated to that sector. Similarly, (2.8) will yield the

required product of receiving aperture and the average power that must be allocated to the sector.

MFAR design normally holds the peak power constant, but permits adjustment of transmitted energy per beam through changes in pulsewidth. The same aperture is used for all sectors, but its effective value can be varied by defocusing, to reduce the allocated search time at the expense of increased energy per beam.

MFAR beam broadening and pattern losses L_θ and L_{csc} are calculated in the same way as for a scanning-beam 3-D radar. For the coverage shown in Figure 2.3 it can be assumed that $L_{pe} = L_p = 1.24$ dB for the long-range and high-altitude sectors, because the detection envelope of the narrow scanning beam can be closely matched to the required coverage. For the low-altitude sector, $L_{pe} \approx 1.5 = 1.76$ dB because the beamwidth is approximately equal to the sector width.

2.4.3 Example of Search Radar Equation for MFAR

As an example of using the search radar equation, assume that the terms common to the three regions shown in Figure 2.3 are as follows:

Target cross section $\sigma = 1.0$ m^2;
Detectability factor $D_0(1) = 15$ dB;
Search loss $L_s = 20$ dB;
Array aperture $A = 1.6$ m^2.

The system temperature, search loss, and other parameters vary as shown in Table 2.4. Other values in the table are obtained from (2.8) and Table 2.3. The example array aperture assumes an X-band radar with broadside beamwidth of 1.4°, a broadening factor given by the secant of the off-broadside angle, and use of a focused beam throughout the coverage.

Note that the average powers given by application of (2.8) are averaged over the entire operating time of the radar. The power averaged over a single sector is given by P_{avi}/T_{Fi} for sector i, and that averaged over the search time fraction is $P_{av}/T_F = 11.5$ kW. A transmitter rated for ≈ 10 kW average power would be adequate, provided that individual dwells up to 25.3 kW for ≈ 2 ms could be supported for the horizon sector.

In this example, the fact that the high-elevation sector consumes the largest time fraction while using the least average power suggests that it would be appropriate to defocus the beamwidths in that sector. Table 2.5 shows the result of increasing both beamwidths by a factor of two. The time allocated for search is reduced, average power in the three search sectors is more uniform, but over the reduced search time fraction it averages twice that for the original allocations. Use of the search radar equation, however, makes this type of trade-off a simple exercise.

Table 2.4 Example of MFAR Power Calculation

Requirement	*Unit*	*Sector*		
		Long-Range	*High-Elevation*	*Horizon*
Maximum range R_{mi}	km	170	89	85
Solid angle of sector ψ_{si}	steradian	0.34	0.21	0.09
Frame time t_{si}	s	10	5	1
Sector time fraction T_{Fi}		0.159	0.266	0.060
System temperature T_{si}	K	350	300	400
Search loss L_{si} (excluding L_{ps}, L_{csc})	dB	20	18	22
Elevation beamshape loss L_{pe}	dB	1.24	1.24	1.76
Pattern loss L_{csc}	dB	1.19	0.0	1.57
Product $P_{avi}A$	W-m^2	5,500	252	1,650
Average power P_{avi}	kW	3.44	0.16	1.03
Average power P_{avi}/T_{Fi}	W	16.5	1.0	25.3
Total search average power P_{av}	W	4.6		
Total search time fraction T_F		0.40		
Average power during search	W	11.5		

Table 2.5 MFAR Power Calculation with Defocusing in High-Elevation Sector

Requirement	*Unit*	*Sector*		
		Long-Range	*High-Elevation*	*Horizon*
Sector time fraction T_{Fi}		0.159	0.038	0.060
Average power P_{avi}	kW	3.44	5.11	1.03
Average power P_{avi}/T_{Fi}	kW	16.5	16.6	25.3
Total search average power P_{av}	kW	5.1		
Total search time fraction T_F		0.287		
Average power during search	kW	17.8		

2.5 THE SEARCH FENCE

The search fence is a narrow coverage region, usually in elevation, through which a target must pass to enter a defended area. Warning of a target entering the defended area is obtained using minimum resources, and subsequent tracking is assigned either to the tracking mode of the radar that provides the fence or to a separate radar. An example of the search fence is the scan of a narrow elevation sector for detection of ballistic targets as they rise above the launch site or the radar horizon. An early application of the technique was in location of hostile mortar or

artillery sites, near the end of World War II. It has subsequently been applied in the Ballistic Missile Early Warning System (BMEWS) designed to alert the United States to attack by intercontinental missiles.

2.5.1 Search Sector for the Fence

The geometry of a ballistic missile search fence is shown in Figure 2.4. Most search fence applications require coverage of a limited azimuth sector A_m, typically 60°–180°. rather than the 360° coverage used in air surveillance. The minimum elevation is typically near zero, to minimize the delay between target launch and detection, although it may be set at 1°–2° to reduce atmospheric attenuation in missile defense or surface clutter in hostile battery location.

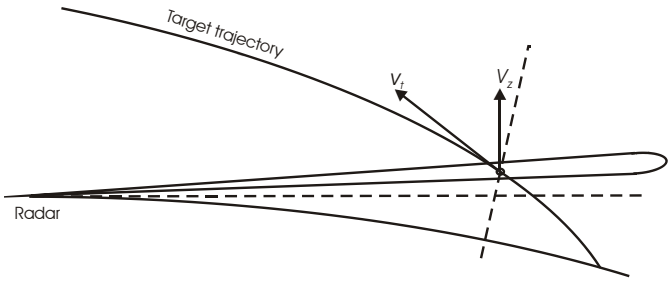

Figure 2.4 Ballistic missile search fence.

The available search frame time is determined by the maximum vertical velocity v_z of the expected targets, the number of scans n_{sc} required for reliable detection, and the elevation sector width:

$$t_s = \frac{\Delta\theta}{n_{sc}\omega_e} = \frac{R_m \Delta\theta}{n_{sc} v_z} \quad (\text{s}) \tag{2.13}$$

where

t_s = frame time (s);
$\Delta\theta$ = $\theta_m - \theta_0$ = elevation width of fence (rad);
ω_e = maximum target elevation rate (rad/s);
v_z = maximum vertical component of target velocity (m/s) with respect to the plane tangent to the surface at the radar site;
R_m = maximum range (m) at which targets can enter the fence.

The required number of scans is usually set to $n_{sc} \geq 2$, with a high probability of detection on each scan, since there will not be another opportunity for detection after the target rises above the fence.

Substituting (2.13) into (2.8), we obtain the search-fence equation:

$$P_{av}A = \frac{4\pi A_m R_m^3 n_{sc} v_z k T_s D_0(1) L_s}{\sigma} \quad \left(\mathrm{W \cdot m^2}\right) \tag{2.14}$$

Note that the power-aperture product depends on the cube, rather than the fourth power of range, because targets at longer range have smaller elevation rates, allowing larger frame times.

2.5.2 Example ICBM Fence

For example, assume an ICBM search fence for the conditions shown in Table 2.6. The target for this case is an ICBM launched from a site 2,600 km from the radar, which is deployed halfway between the defended area and the launch site.

Table 2.6 ICBM Search Fence

Azimuth sector A_m	deg	90	Maximum range R_m	km	2,000
Number of scans n_{sc}		2	Elevation beamwidth θ_e	deg	2.0
System noise temperature T_s	K	400	Detectability factor $D_0(1)$	dB	15
Search loss L_s	dB	15	Target cross section σ	m^2	1
Target vertical velocity v_z	km/s	3.9			

At the end of its boost phase, the ICBM is 600 km downrange with 250 km altitude and a velocity v_t = 7 km/s directed 16° above the horizontal at that point, 2,000 km from the radar. The tangent plane at the radar is tilted by some 18° from the horizontal at the target. The elevation angle of the velocity vector from the radar plane is 34°, and the vertical velocity component is 3.9 km/s, resulting in an elevation rate ω_e = 0.11°/s. Assuming the two scans must be obtained during the passage of the target through the scan sector, the time per scan is t_s = 9s. The required power-aperture product from (2.14) is

$$P_{av}A = 47 \times 10^6 \quad \left(\mathrm{W \cdot m^2}\right)$$

If the early warning radar operates at 450 MHz (λ = 0.67m) with a circular reflector antenna, its diameter D_a = 23m, and its area A = 412m^2. The resulting average power requirement is P_{av} = 114 kW. If subsequent tracking tasks are assigned to the same radar, the required power is increased.

2.6 SEARCH LOSSES

The apparent simplicity of the search radar equation is the result of the many assumptions imposed on the idealized system. This approach leads, however, to the requirement that the system loss factor L_s accommodate many nonideal factors that characterize actual radar systems and environmental conditions.

In Chapter 1, separate factors are included in the range equation for reductions in available energy ratio at the antenna output and increases in required energy ratio for the specified detection performance. The search loss factor L_s includes both sets of factors, along with others that are unique to the search radar equation. The losses, including reciprocals of the range-dependent factors F_{rdr}^2, are summarized here.

2.6.1 Reduction in Available Energy Ratio

Components of L_s that reduce the available energy ratio are as follows:

- *Elevation Beamshape Loss* L_{pe}. This loss results from obtaining the coverage to range R_m up to elevation angle θ_1 using a fan beam rather than the idealized square-ended triangular beam (see Section 2.2.2).
- *Pattern Loss* L_{csc}. The loss results from extending elevation coverage above θ_1 at ranges $R < R_m$. (see Section 2.2.3).
- *Antenna Dissipative Loss* L_a. This loss adjusts the idealized antenna gains used in (2.3) and (2.6), which are actually the *directivities* D_t and D_r of the antennas, to the actual power gains G_t. and G_r (see Section 10.1.5).
- *Pattern Constant* L_n. This loss adjusts the gain-beamwidth relationship of the idealized transmitting beam assumed in deriving (2.3) to correspond to the value achievable in actual antennas. L_n = 1.16–1.28 (0.64–1.07 dB) applies to rectangular and elliptical apertures with illumination varying from uniform to low-sidelobe tapers. Reflector and lens antennas typically have an additional loss of 0.6–1.0 dB from spillover and (in reflectors) from blockage (see Section 10.1.5).
- *Receiving Aperture Efficiency* η_a. The ideal gain G_r appearing in (2.6) applies to a uniformly illuminated aperture under ideal conditions, but must be reduced for factors that result from tapered illumination, blockage of the path into space, spillover in space-fed antennas, and tolerances in construction that cause departures from a radiated plane wave (see Section 10.1.5).
- *Receiving Noise Loss* L_{rec}. The temperature T_0 = 290K is used to establish the noise spectral density in (2.7). The loss that accounts for the actual system noise temperature T_s (see Chapter 6) is defined as

$L_{\text{rec}} = T_s / T_0$, where T_s is averaged over the search sector.

- *Transmission Line Loss* L_t (see Section 10.1.1).
- *Atmospheric Attenuation* L_α. For use in the search radar equation this loss (see Chapter 7) is calculated by averaging the attenuation over the two-way path to the limits of the search sector.[3]
- *Polarization Loss* L_{pol}. This loss is the reciprocal of the polarization factor F_p^2 introduced in (1.23) to describe the reduced received energy resulting from mismatch of the received polarization to that of the echo from a target cross section σ when illuminated by the transmitting antenna (see Section 10.1.1).
- *Range-Dependent Response Loss* L_{rdr}. This loss is the reciprocal of the range-dependent response factor F_{rdr} (see Sections 1.6.2 and 10.1.2).

2.6.2 Increase in Required Energy Ratio

The product $kT_0D_0(1)$ in (2.8) represents the minimum required energy ratio for detection on a steady target using a single coherently integrated sample of the received signal, for an idealized receiving system in a room-temperature environment. Factors in the radar that increase the required energy ratio and must be included in L_s are listed below.

- *Integration Loss* L_i (see Section 4.4.3).
- *Fluctuation Loss* L_f (see Section 4.4.5).
- *Matching Factor M* (see Section 10.2.3).
- *Beamshape Loss* L_{pe} (see Section 2.2.2 and Chapter 5).
- *Miscellaneous Signal Processing Loss* L_x (see Sections 1.3.1 and 10.2.5).
- *Scan Sector Loss* L_{sector} (see Section 10.2.1).
- *Scan Distribution Loss* L_d (see Section 10.1.4).

2.6.3 Summary of Losses

The losses listed in Section 2.6.1 include ten factors (some of them consisting of contributions from several components), that reduce the available energy ratio. Those can be grouped into a single value L_1, as used previously in (1.7) to represent the RF loss in energy ratio at the antenna output, as listed in the first part of Table 2.7. Four components of L_{rdr} are listed separately. A further seven losses

[3] Strictly speaking, the fraction of energy $1/L_\alpha$ after attenuation is averaged over the elevation sector, and the attenuation calculated as the reciprocal of that average.

Table 2.7 Search Loss for Typical Air Surveillance Radar Systems

Loss Component	*Symbol*	*Loss in dB*	
		2-D System	*3-D AESA*
Elevation beamshape loss	L_{pe}	1.8	1.8
Pattern ($\csc^2$) loss	$L_{\csc}$	2.2	2.2
Antenna dissipative	$L_{at} + L_{ar}$	0.8	0.8
Pattern constant	L_n	1.4	0.4
Antenna efficiency	L_η	1.8	0.9
Receiving noise	L_{rec}	2.7	-0.1
Transmission line	L_t	0.8	0.2
Atmospheric attenuation	L_α	1.5	1.5
Polarization	L_{pol}	0.0	0.0
Lens	L_{lens}	1.0	1.0
STC	L_{stc}	0.0	0.0
Frequency diversity	L_{fd}	0.0	0.0
Eclipsing	L_{ecl}	0.0	0.0
Subtotal L_1	L_1	14.00	8.70
Integration	L_i	2.0	1.0
Fluctuation	L_f	1.5	1.5
Matching factor	M	1.0	1.0
Azimuth beamshape	L_{p0}	1.3	1.3
Miscellaneous	L_x	4.0	3.0
Scan sector	L_{sector}	0.0	1.5
Scan distribution	L_d	0.0	0.0
Subtotal L_2	L_2	9.8	9.3
Total L_s	L_s	23.80	18.00

that increase the required energy ratio, listed in Section 2.6.2, can be grouped into a value L_2, also listed in the table.

Estimates of loss are shown for two typical systems: a mechanically scanning 2-D radar with the constant-altitude coverage shown in Figure 2.1, and an active electronically scanned array (AESA) that covers the same elevation coverage in an azimuth sector ±45° from broadside. No attempt has been made to detail the time budget for the AESA, and the loss estimates are approximate for both systems, but the total losses are realistic for both systems, relative to the results predicted for a given product of average power P_{av} and physical receiving aperture A.

The total search loss is normally in the order of 20 dB, reducing the detection range to about one-third of that available in a "perfect" radar with the same product of average power and physical aperture. The mechanically scanned system estimates shown in Table 2.7 total almost 24 dB, while the AESA system total is 18 dB, in spite of the minimal RF losses within the radar. More accurate evaluations are possible only when the radar parameters are defined in much greater detail than is usual in early phases of a radar development or procurement. When considering using the search radar equation in a particular application, however, it is possible to use results from a number of radars that have been developed for similar applications, and to estimate the minimum L_{smin} that can be expected. Substituting L_{smin} in the search radar equation provides a starting point for estimating the minimum size of the radar that will be required. When that process leads to a specific radar design, the applicable loss components may then be determined to refine the calculation.

References

[1] Barlow, E., "Radar System Analysis," *Sperry Gyroscope Company Report No. 5223-1109*, June 1948.

[2] Barton, D. K., *Radar System Analysis*, Englewood Cliffs, NJ: Prentice-Hall, 1964; Dedham, MA: Artech House, 1976.

[3] Barton, D. K. and H. R. Ward, *Handbook of Radar Measurement*, Englewood Cliffs, NJ: Prentice-Hall, 1969; Dedham, MA: Artech House, 1984.

[4] Rice, S. O., "Mathematical Analysis of Random Noise," *Bell Sys. Tech. J.*, Vol. 23, No. 3, July 1944, pp. 282–332 and Vol. 24, No. 1, January 1945, pp. 461–556. Reprinted: *Selected Papers on Noise and Stochastic Processes*, (N. Wax, ed.), New York: Dover Publ. 1954.

[5] D. K. Barton, *Radar System Analysis and Modeling*, Norwood, MA: Artech House, 2005.

[6] Shrader, W. W., "Antenna Considerations for Surveillance Radar Systems," *Proc. 7th IRE East Coast Conf. on Aero. and Navig. Electronics*, Baltimore, MD, October 1960.

[7] Barton, D. K., "Maximizing Firm-Track Range on Low-Observable Targets," *IEEE Int. Conf. Radar-2000*, Washington, DC, May 8–12, 2000, pp. 24–29.

[8] IEEE Standard 100, *The Authoritative Dictionary of IEEE Standards Terms, 7th ed*., New York: IEEE Press, 2000.

CHAPTER 3

RADAR EQUATIONS FOR CLUTTER AND JAMMING

3.1 SIGNAL-TO-INTERFERENCE RATIO

IEEE definitions [1] are used in this book.

> *Clutter*: Unwanted echoes, typically from the ground, sea, rain or other precipitation, chaff, birds, insects, meteors, and aurora.
>
> *Jamming*: A form of electronic countermeasures (ECM) in which interfering signals are transmitted at frequencies in the receiving band of a radar for the purpose of obscuring the radar signal (as in noise jamming) or causing confusion in interpreting the radar signal (as in repeater jamming).
>
> *Target*: Broadly, any discrete object that scatters energy back to the radar. Specifically, an object of radar search or tracking.

The typical sources of clutter listed in the definition apply to radars whose targets are manmade objects such as aircraft, missiles, land vehicles, or vessels operating in the natural environment that contributes the clutter. In this chapter we adhere to that definition. Radars used in navigation, mapping, meteorology, or geophysical research are intended to detect or image the natural environment as the target, and hence will regard the manmade objects as clutter. Radar equations applicable to those applications differ from those discussed here.

In this book, the *signal* is the echo from a target, while *interference* is the sum of unwanted inputs to the receiver, including thermal noise, clutter, and jamming. To be consistent with the description of target signals and thermal noise in Chapter 1, interference is described by the energy I_0 that passes the processor within a resolution cell that may also contain the target:

$$I_0 = N_0 + C_0 + J_0 \ = N_0\left(1 + \frac{C_0}{N_0} + \frac{J_0}{N_0}\right) \ (\text{W/Hz}) \tag{3.1}$$

where N_0 is the spectral density of thermal noise, C_0 the energy of the clutter, and J_0 that of the jamming, all referred to the output port of the receiving antenna. The *resolution cell* in which interference is measured is defined as [1]:

> The one-dimensional or multidimensional region related to the ability of a radar to resolve multiple targets. *Note*: The dimensions that involve resolution can include range, angle, and radial velocity (Doppler frequency). The three-dimensional spatial resolution cell is, for example:
>
> $$\theta_a \times \theta_e \times (c\tau/2)$$
>
> where θ_a = azimuth beamwidth, θ_e = elevation beamwidth, τ = pulsewidth, c = velocity of electromagnetic waves.

Interference whose spectrum is spread across the bandwidth of the processor (e.g., thermal noise or broadband jamming) is described by the spectral density within that bandwidth, replacing N_0 in (1.8) and in subsequent radar equations.

Clutter enters the receiver with the RF spectrum of the transmitted signal, and with a Doppler shift that is usually different from that of the target. Its effect on the processed output, and on the required threshold setting that determines detection probability, must be evaluated differently from that of broadband interference. When signal processing is used to suppress clutter (e.g., Doppler-based processing), an *effective input spectral density* C_{0e} expresses the effect of the suppressed interference, referred back to the input where signal energy is measured:

$$I_{0e} = N_0 + C_{0e} + J_{0e} = N_0\left(1 + \frac{C_{0e}}{N_0} + \frac{J_{0e}}{N_0}\right) \quad (\text{W/Hz}) \tag{3.2}$$

The procedure for calculation and use of effective interference spectral density I_{0e} is to evaluate the noise density N_0 and the energy ratios C_{0e}/N_0 and J_{0e}/N_0, insert these in (3.2), and then replace the noise spectral density N_0 in the denominator of the radar equation with I_{0e}. Derivation of such an equation requires the same basic steps that were used in Chapter 1 for the noise environment:

- Express the maximum signal-to-interference ratio E/I_{0e} that is available with given parameters, as a function of target range R;
- Express the minimum signal-to-interference ratio D_x that is required to meet detection requirements;
- Combine these expressions to solve for the maximum target range R_m at which the requirement is met for the specified radar in the environment.

The interference that competes with a target at range R may enter the radar simultaneously with the target signal and at the same frequency, or may be superimposed on the signal as a result of ambiguous response of the receiver/processor in time delay (range) or frequency. In general, the equations for interference spectral density are complicated functions of target range, radar waveform, and envi-

ronmental conditions. Closed-form solutions for detection range can be obtained only for special cases. Solutions using graphical techniques or root-finding algorithms are used for the more general case.

3.2 CLUTTER EFFECT ON DETECTION RANGE

Clutter may arise from a *surface area* on the Earth (land or sea), from a *volume* in the atmosphere (precipitation, chaff, insects, or aurora), or from *discrete objects* on or above the surface (prominent surface features, birds, or meteors). The general method of range calculation for all types of clutter is discussed here, and applied in following sections to each individual type.

3.2.1 Range-Ambiguous Clutter

Energy from clutter in the spatial resolution cell at a range R_c equal to the target range R is one source of interference that competes with the signal entering the receiver. However, calculation of input clutter energy, even for low PRF waveforms intended to avoid range ambiguity, must also consider all cells at ranges given by

$$R_{ci} = R + iR_u \quad (\text{m}) \tag{3.3}$$

where

R_u = $ct_r/2 = c/2f_r$ is the unambiguous range;
i = ambiguity index, $i_{\min} \le i \le i_{\max}$;
$i_{\min}$ = smallest (or largest negative) integer that gives $R_{ci} > 0$;
$i_{\max}$ = largest positive integer for which a cell at R_{ci} contains clutter;
c = velocity of light;
t_r = pulse repetition interval (PRI);
f_r = pulse repetition rate (PRF).

The clutter energy C_i from ambiguous area i is found by replacing in (1.25) the target terms $\sigma F_p^2 F_t^2 F_r^2 F_{rdr}^2 / L_\alpha$ with the corresponding clutter terms to obtain

$$C_i = \frac{P_{av} t_f G_t G_r \lambda^2 \sigma_{ci} F_{pc}^2 F_{ci}^4 F_{\text{rdrc}i}^2}{(4\pi)^3 R_{ci}^4 L_t L_{\alpha ci}} \quad (\text{J}) \tag{3.4}$$

where

σ_{ci} = clutter cross section (see Sections 3.2–3.6);
F_{pc} = polarization factor for clutter (see Section 10.1.1);
F_{ci} = pattern-propagation factor for clutter (see Chapters 8 and 9);
$F_{\text{rdrc}i}$ = range-dependent response factor for clutter (see Section 1.6.2);
$L_{\alpha ci}$ = atmospheric attenuation for clutter (see Sections 7.2 and 7.3).

The total clutter input energy C_0 is the sum of C_i over all ambiguities containing clutter:

$$C_0 = \sum_i C_i = \frac{P_{av} t_f G_t G_r \lambda^2 F_{pc}^2}{(4\pi)^3 L_t} \sum_i \frac{\sigma_{ci} F_{ci}^4 F_{rdrci}^2}{R_{ci}^4 L_{\alpha ci}} \quad \text{(J)} \tag{3.5}$$

3.2.2 Types of Radar Waveforms

Radar waveforms are defined [1] as belonging to one of four types, for each of which a different clutter analysis is necessary.

- Low-PRF (LPRF) Waveform:

  A pulsed-radar waveform whose pulse-repetition frequency is such that targets of interest are unambiguously resolved with respect to range.

  While targets of interest lie within the unambiguous range, clutter may originate beyond that range ($i > 0$). The energy received from each ambiguity is multiplied by the factor $(R/R_{ci})^4 = R^4/(R + iR_u)^4$, relative to clutter at target range R, and may contribute to interference even for $i > 0$, especially if it is not reduced by the clutter improvement factor applicable to clutter at range R.

- Medium-PRF (MPRF) Waveform:

  A pulsed-radar waveform whose pulse-repetition frequency is such that targets of interest are ambiguous with respect to both range and Doppler shift.

  For this waveform, clutter at $R_c < R$ (for which $i < 0$), as well as at $R_c \geq R$, contributes to interference. The contributions from short-range ambiguities exceed that from $R_c = R$ by a large factor when $(R + i_{\min} R_u) << R$.

- High-PRF (HPRF) Waveform:

  A pulsed-radar waveform whose pulse-repetition frequency is such that targets of interest are ambiguous with respect to range.

  The HPRF, chosen to avoid Doppler ambiguities, exceeds the MPRF, introducing more range ambiguities and increasing the input interference, especially from clutter at range $R_{ci} << R$.

- Continuous-Wave (CW) Waveform:

  The CW radar is defined as a radar that transmits a continuous-wave signal that may be phase-modulated. The spatial resolution cell for an unmodulated CW waveform is bounded by the antenna beam and extends to a maximum range $t_o c/2$, where t_o is the dwell time of the antenna beam. The input clutter energy in any given environment is greater than that of an HPRF waveform, although use of separate transmitting and receiving antennas may reduce clutter from very short ranges. CW waveforms with periodic phase modulation

having repetition interval t_r produce range ambiguities at intervals R_u identical to those of pulsed radars with PRI = t_r.

3.2.3 Clutter Detectability Factor

The detectability factor D_x used in the radar equations of Chapter 1 is the required ratio of the signal energy to the spectral density of white Gaussian noise. Clutter differs from noise in two ways: (1) it is not random from pulse to pulse, and hence its spectrum consists of discrete lines within the signal bandwidth; and (2) its amplitude distribution may spread beyond that of the Rayleigh distribution that characterizes the sum of in-phase and quadrature Gaussian noise components. Hence, a different *clutter detectability factor* D_{xc} must be used.

3.2.3.1 Clutter Spectrum and Correlation Time

The spectra of different types of clutter (see Chapter 9) are characterized by the mean radial velocity relative to the radar and the spread of each spectral line. Velocity parameters are used in preference to the mean and spread of Doppler frequency because they characterize the clutter independently of the radar frequency.

Spread is measured by the standard deviation σ_v in velocity that results from random motion of the clutter scatterers, antenna beam scanning, and projection of the mean radial velocity on the antenna pattern. The spread affects the number n_c of independent clutter samples available for integration, which can be expressed as a function of the correlation time t_c of the clutter at the radar input and the observation (dwell) time of the radar beam [2, p. 117]:

$$n_c = 1 + \frac{t_o}{t_c} = 1 + \frac{2\sqrt{2\pi}\sigma_v t_o}{\lambda} \le n \tag{3.6}$$

where n is the number of noise samples integrated. When clutter appears in more than one range ambiguity, different values σ_{vi} and t_{ci} are found for each range R_i.

3.2.3.2 Clutter Correlation Loss

In the absence of Doppler processing, the clutter detectability factor depends on n_c, rather than the number n of target pulses integrated. The increase in required energy ratio is described by the *clutter correlation loss* L_{cc}:

$$L_{cc} = \frac{D_0(n_c)}{D_0(n)} \ge 1 \tag{3.7}$$

Note that this loss does not reduce the effect of clutter, but rather increases it to reflect the increase in signal-to-clutter ratio required for target detection, as compared to white Gaussian noise.

Doppler-based signal processing increases the number of independent samples in (3.6), which depends on the spectrum of the clutter at the processor *output*, thus reducing L_{cc} relative to that applicable to the input clutter. Methods of calculating n_c and L_{cc} for systems using Doppler processing are given in Chapter 9. The loss $L_{cc\,i}$ is applied to increase in the effective spectral density for each ambiguity.

3.2.3.3 Clutter Distribution Loss

The second source of increased clutter detectability factor is the broader amplitude distribution of some clutter. The detectability factors calculated for noise are based on a detection threshold that is high enough to meet the specified false-alarm probability on the exponentially distributed noise power, adjusted for integration. The probability density function (pdf) of volume clutter is approximately exponential, as is surface clutter when viewed at high grazing angles. But the pdf spreads as the grazing angle decreases, and can be modeled as a Weibull distribution having a spread parameter $a_w \geq 1$. The spread varies from $a_w = 1$ for the exponential distribution to $a_w \to 5$ for extreme cases.

This factor increases the clutter detectability factor D_{xc} by a *clutter distribution loss* L_{cd}. This loss applies to a two-parameter constant-false-alarm-rate (CFAR) processor that controls the threshold using estimates of both the mean and spread of input clutter. It is defined as the ratio of the threshold y_b required to obtain a specified false-alarm probability P_{fa} with the actual clutter distribution to that required for the exponential distribution (see Section 4.2.2). For clutter with a Weibull distribution:

$$L_{cd} = \frac{y_b\left(P_{fa}, a_w\right)}{y_b\left(P_{fa}, 1\right)} = \frac{P_w^{-1}\left(1-P_{fa}, a_w\right)}{P_\gamma^{-1}\left(1-P_{fa}\right)} \tag{3.8}$$

where $P_w^{-1}(p,a_w)$ is the inverse function of the integral of the Weibull distribution for probability p with spread parameter a_w and $P_\gamma^{-1}(p)$ is the inverse function for the incomplete gamma function. The width of the pdf varies over range ambiguities, and separate values of $L_{cd\,i}$ are applied as factors to find the effective spectral density at each range R_i.

Given the large loss that results when Weibull clutter with $a_w >> 1$ is input to a two-parameter CFAR processor, many radars supplement the CFAR process with a clutter map that suppresses clutter peaks (and targets) in the resolution cells where they are observed over several scans. Since these peaks are relatively sparse, even in regions of strong clutter, the loss is confined to individual map cells and the average loss in detection probability caused by target suppression is

relatively small. The peaks can be considered *discrete clutter*, effects of which are described in Section 3.5, rather than by the clutter distribution loss of (3.8).

3.2.3.4 Clutter Detectability Factor

The clutter detectability factor, denoted here by D_{xc}, is defined [1] as:

> The predetection signal-to-clutter ratio that provides stated probability of detection for a given false alarm probability in an automatic detection circuit. *Note*: In MTI systems, it is the ratio after cancellation or Doppler filtering.

The losses L_{cc} from Section 3.2.3.2 and L_{cd} from Section 3.2.3.3 give corrections that are applied to the detectability factor D_x to account for the difference between clutter and noise statistics:

$$D_{xc} = D_x L_{cc} L_{cd} \tag{3.9}$$

3.2.4 Effective Spectral Density of Clutter

To form the effective input spectral density I_{0e} in (3.2), the input clutter component C_{0i} is adjusted for use with a common detectability factor D_x. The adjustment required for clutter in ambiguity i is

$$C_{0e\,i} = C_i \frac{D_{xc\,i}}{D_x I_{m\,i}} = C_i \frac{L_{cc\,i} L_{cd\,i}}{I_{m\,i}} \quad \text{(W/Hz)} \tag{3.10}$$

where I_m is the MTI improvement factor, defined [1] as:

> The signal-to-clutter power ratio at the output of the clutter filter divided by the signal-to-clutter power ratio at the input of the clutter filter, average uniformly over all target velocities of interest. *Synonym*: clutter improvement factor.

The synonym in the definition covers CW and pulsed Doppler as well as MTI radars, and will be used here. The improvement factor for different processing methods is discussed in Section 9.6. It may vary over the individual ambiguous regions, but an average value $\overline{I_m}$ can be used to express the effective output spectral density of clutter as

$$C_{0e} = \sum_i \frac{C_i L_{cc\,i} L_{cd\,i}}{I_{m\,i}} = \frac{C_0 \overline{L_{cc} L_{cd}}}{\overline{I_m}} \tag{3.11}$$

where C_i is given by (3.4). The terms with overbars are weighted averages over the clutter region.

Adjustment of effective clutter spectral densities for clutter losses, before summation is carried out, and averaging of the improvement factor as in (3.11),

permits C_{0e} to be added directly to N_0 in (3.2), and the sum is used with a common value of D_x in the radar equation to solve for detection range.

3.2.5 Detection Range with Clutter

The effective clutter energy given by (3.11) is added to the noise spectral density N_0 to obtain the effective interference energy I_{0e} in the environment of clutter and noise. This allows the detection range R_{mc} in clutter to be expressed as:

$$R_{mc} = \left[\frac{P_{av} t_f G_t G_r \lambda^2 \sigma F_p^2 F_t^2 F_r^2 F_{rdr}^2}{(4\pi)^3 I_{0e} D_x(n') L_t L_\alpha} \right]^{1/4} \quad (\mathrm{m}) \tag{3.12}$$

where $n' = t_o/t_f$ is the number of intervals t_f over which noncoherent integration is performed during the observation time t_o. Since many terms on the right-hand side of this equation are range-dependent, R_{mc} must generally be found graphically or by root-finding. Exceptions to this general rule, where this equation may be written in closed form for surface and to volume clutter, are given in Sections 3.3.5 and 3.4.6.

The graphical procedure is to plot separately the signal energy E from (1.25) and required energy $I_{0e}D_x(n') = (N_0 + C_{0e})D_x(n')$ as functions of target range R. The detection requirement is met at ranges for which $E \geq I_{0e} + D_x(n')$ and the longest such range is R_{mc}. The root-finding procedure is to express E and $I_{0e}D_x(n')$ as separate functions of R, and create a computer program to find the largest R at which the two expressions are equal:

$$R_{mc} = \mathrm{root}_R \left[E(R) = I_{0e}(R)\, D_x(n') \right] \tag{3.13}$$

where $\mathrm{root}_x[\cdot]$ is the value of x at which the equality within the brackets is met.

3.3 DETECTION IN SURFACE CLUTTER

Surface clutter is backscatter from land or sea surfaces illuminated by the radar beam. Two geometrical models of surface clutter are described below: a simple, flat-Earth model, and a spherical-Earth model that is detailed further in Chapter 8.

3.3.1 Clutter from a Flat Surface

The geometry of surface clutter observed by a the mainlobe of a radar antenna at altitude h_r above a flat surface is shown in Figure 3.1. The clutter cell lies within

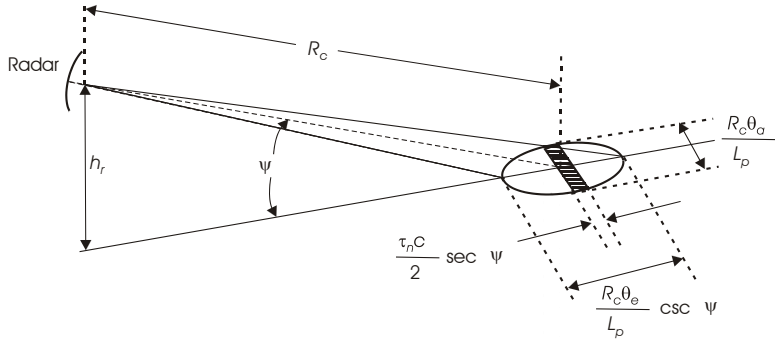

Figure 3.1 Surface clutter geometry.

the elliptical beam footprint defined by the beamwidths θ_e in elevation and θ_a in azimuth, reduced in each case by the beamshape loss L_p to account for the reduced two-way antenna gain of off-axis scatterers.[1] Sidelobe clutter is normally much smaller and insignificant, but is discussed in Section 3.6.

The width of the cell is set by the range R_c and the azimuth beamwidth θ_a. The depth (range dimension) is usually set by the range resolution Δ_r:[2]

$$\Delta_r = \frac{\tau_n c}{2} \quad (\text{m}) \tag{3.14}$$

where τ_n is the width of the processed pulse and c is the velocity of light. As stated by Blake [3, p. 297], τ_n is the *equivalent pulsewidth* after processing. This is not the 3-dB width τ_3 conventionally used, but rather a pulsewidth defined in [4, p. 342] in a way similar to the noise bandwidth of a network:

$$\tau_n \equiv \frac{1}{a_m^2} \int_{-\infty}^{\infty} \left| a(t)^2 \right| dt \quad (\text{s}) \tag{3.15}$$

where $a(t)$ is the pulse waveform voltage at the processor output and a_m is its peak value. The ratio τ_n/τ_3 varies from unity for a rectangular output pulse to approximately 1.06 = 0.24 dB for the outputs of matched filters for rectangular pulses and for most pulse compression waveforms.

---

[1] The beamshape loss used in equations for clutter is L_p = 1.33, as obtained for dense sampling by integration over the two-way beam pattern (5.1), and denoted by L_{p0} (see Section 5.2.3). The additional subscript $_0$ is used there to distinguish the dense-sampling value from the varying L_p applicable to targets for the general case that may include sparse sampling, as discussed in Chapter 5. The subscript $_0$ is omitted from equations in this chapter for compactness.

[2] The resolution cell depth for CW radar is discussed in Section 3.3.6.

Projected onto the surface, the depth of the beam footprint is increased by the cosecant of the grazing angle ψ:

$$\psi = \sin^{-1}\left(\frac{h_r}{R_c} - \frac{R_c}{2k_e a_e}\right) \approx \frac{h_r}{R_c} \quad (\text{rad}) \tag{3.16}$$

where R_c is the range to the clutter that competes with the target echo, $k_e a_e$ is the effective Earth radius, and the approximation assumes that a flat-Earth model is adequate ($R_c^2/2k_e a_e << h_r$).

The beam footprint usually extends beyond the range resolution cell, but as ψ increases, and especially for narrowband waveforms, the range resolution cell may extend beyond the footprint. This leads to two alternative expressions for the surface area included in the resolution cell.

3.3.1.1 Pulsewidth-Limited Cell

This cell depth is limited by the pulsewidth when

$$\Delta_{ri} = \frac{\tau_n c}{2} \le \frac{R_{ci}\theta_e}{L_p}\cot\psi \quad (\text{m}) \tag{3.17}$$

The area contributing to the surface clutter for this case is[3]

$$A_{ci} = \frac{R_{ci}\theta_a}{L_p}\frac{\tau_n c}{2}\sec\psi \quad (\text{m}^2) \tag{3.18}$$

The need to modify the half-power beamwidth in (3.18) by the factor L_p, now called beamshape loss, is recognized in early work on clutter [5, p. 483. Eq. (93)], but that factor is used inconsistently in subsequent work, perhaps because error from its omission is considered unimportant in comparison with other uncertainties in clutter modeling. Blake's simple formulation [3, p. 26, Eq. (1.43)] omits this factor, but his more detailed discussion of clutter [3, p. 296, Eq. (7.7)] presents an expression that invokes integration over the beam pattern.[4] Other literature uses a "two-way half-power beamwidth" defined as $\theta_a/\sqrt{2}$, which is 0.26 dB less than the correct value.

[3] The beamwidth in (3.18) is assumed small enough that the small-angle approximation applies. Otherwise, θ_a should be replaced by $2\tan(\theta_a/2)$; the error in approximation is < 0.01 dB for $\theta_a < 10°$.

[4] That equation contains a typographical error in using the one-way voltage pattern $f(\theta,\phi)$ rather than the two-way power pattern $f(\theta,\phi)^4$.

3.3.1.2 Beamwidth-Limited Cell

When the condition specified by (3.17) is not met, the surface clutter area is

$$A_{ci} = \frac{R_{ci}\theta_a}{L_p}\frac{R_{ci}\theta_e}{L_p}\csc\psi = \frac{R_{ci}^2\theta_a\theta_e}{L_p^2}\csc\psi \ \left(\mathrm{m}^2\right) \tag{3.19}$$

For this beamwidth-limited case, the factor $1/L_p^2$ is the same as the integral in the weather-radar equation [6, p. 590, Eq. (5)], and in Blake's detailed discussion previously cited. The factor $\pi/4 = -1.05$ dB, appearing in Blake [3, p. 296, (7.4)] and elsewhere, is inaccurate for actual antenna patterns, to which $1/L_p^2 = -2.48$ dB applies.

3.3.1.3 Unequal Transmitting and Receiving Beamwidths

The azimuth beamwidth used in calculating clutter area is the one-way, half-power beamwidth θ_a when the transmitting and receiving beam patterns are identical. When they differ, an effective beamwidth may be substituted, calculated as

$$\theta_{a\mathrm{eff}} = \frac{\sqrt{2}\theta_{at}\theta_{ar}}{\sqrt{\theta_{at}^2 + \theta_{ar}^2}} \tag{3.20}$$

It can be seen that $\theta_{a\mathrm{eff}} = \theta_{at} = \theta_{ar}$ when the two are equal, approaching $\sqrt{2}\theta_{a2}$ when $\theta_{a1} >> \theta_{a2}$. For the latter case, the angular width of the clutter cell becomes $\sqrt{2}\theta_{a2}/L_p = 1.06\theta_{a2}$. These relationships apply also to elevation beamwidth in (3.19) and in expressions derived in Section 3.4.1 for volume clutter.

3.3.1.4 Effect of Range Ambiguities

As discussed in Section 3.2, clutter energy originates not only from the resolution cell at the target range R but also in range ambiguities at intervals R_u within and beyond R. The range R_{ci} from the ith ambiguity is then used in (3.18) and (3.19) to find an area A_{ci} for each ambiguous clutter region, and (3.5) applied to find the total clutter energy. Multiple ambiguities may also occur for MPRF and HPRF in the beamwidth-limited case.

3.3.2 Surface Clutter from the Spherical Earth

The surface of the spherical Earth at range R lies below the plane tangent at the radar site by

$$\delta_h = k_e a_e \sqrt{1+\left(\frac{R\cos\theta}{k_e a_e}\right)^2} - 1 \approx \frac{R^2}{2k_e a_e} \quad \text{(m)} \tag{3.21}$$

where θ is the elevation angle, $k_e \approx 4/3$ is the effective Earth's radius constant for atmospheric refraction, and $a_e = 6.38 \times 10^6$m is the actual radius. The flat-Earth approximation is generally adequate at ranges such that $\delta_h < \sigma_h$, the local rough-surface height deviation:

$$R \le \sqrt{2k_e a_e \sigma_h} = 4{,}124\sqrt{\sigma_h} \ \ (\text{m}) \tag{3.22}$$

For moderate sea surfaces and flatland ($\sigma_h < 1$m), expressions for grazing angle over a spherical Earth from Chapter 8 are used at ranges $R > 4$ km, in place of (3.16), and for the pattern-propagation factor in (3.4) and (3.5).

3.3.3 Surface Clutter Cross Section

The radar cross section σ_{ci} of surface clutter in each area that competes with a target at range R_c is

$$\sigma_{ci} = \sigma_i^0 A_{ci} \ \ (\text{m}^2) \tag{3.23}$$

where σ^0 is the surface *clutter reflectivity*, defined in [1] as the "backscatter coefficient of clutter," which in turn is defined as:

> A normalized measure of radar return from a distributed scatterer. For area targets, such as ground or sea clutter, it is defined as the average *monostatic* radar cross section per unit surface area.

The superscript ^{0} originated at the MIT Radiation Laboratory [5, p. 483], probably to suggest that σ^0 is a dimensionless quantity expressing radar cross section in m^2 per m^2 of area A_c.

In some literature, σ^0 has been defined or assumed to include the pattern-propagation factor F_c. The two separate terms for reflectivity σ^0 and pattern-propagation factor F_c are used here to distinguish properties of the surface area A_{ci} (included in σ^0) from those of the radar-to-surface path (included in F_c). Folding the latter into σ^0 obscures the physical principles that underlie the effects of grazing angle and radar frequency on clutter echoes that reach the radar. Identical radars observing the same clutter cell with the same grazing angle will receive different echo powers depending on the contour of intervening terrain, and this cannot properly be attributed to σ^0 for that cell.

Data on σ^0 and F_c for different surfaces are given in Chapter 9, including discussion of the *constant-*γ model for surface clutter, [2, p. 108]:

$$\sigma^0 = \gamma \sin \psi \tag{3.24}$$

In this model, which we will use here and which agrees closely with measured data, a *reflectivity factor* γ describes the surface as observed at a given wavelength. The variation in backscattered power for different viewing geometries is captured in the grazing angle ψ and the clutter pattern-propagation factor F_c.

The factor $F_c \approx 1$ for clutter in the *near region*,[5] within which the grazing angle exceeds a critical value given by

$$\psi_c = \sin^{-1} \frac{\lambda}{4\pi\sigma_h} \approx \frac{\lambda}{4\pi\sigma_h} \quad (\text{rad}) \tag{3.25}$$

where λ is the radar wavelength and σ_h is the standard deviation of clutter height with respect to its average. For $\psi < \psi_c$ the factor F_c varies inversely with range, the transition occurring at a range R_1 given by

$$R_1 = \frac{h_r}{\sin \psi_c} \approx \frac{4\pi\sigma_h h_r}{\lambda} \quad (\text{m}) \tag{3.26}$$

where h_r is the altitude of the antenna phase center above the average clutter surface. For shipboard or airborne radar, h_r is the height of the ship superstructure or the altitude of the aircraft that carries the radar antenna. For land-based radar, it is the sum of antenna height above the ground and the altitude of that ground above the surface clutter viewed by the beam. A land-based radar site is usually selected on high ground that can be assumed to be $2\sigma_h$ above the mean surface. The approximation in (3.26) is adequate when the Earth's curvature permits use of the flat-Earth model within range R_1.

In the following discussions of surface clutter, examples are presented to illustrate the nature of the clutter problem for surface-based radars. The parameters of the pulsed and CW radars used in these examples, and the surface environment that characterizes the clutter, are shown in Table 3.1.

[5] The near region for clutter is not to be confused with near-field of the antenna, which is the region inside the far-field defined in Section 3.4.6. The different regions for clutter modeling are discussed further in Section 9.1.2.

Table 3.1 Example Radar and Surface Clutter Environment

Average power P_{av}	100W	Coherent processing interval t_f	0.01s
Wavelength λ	0.03m	Transmitter line loss L_t	0 dB
Antenna gain G	42.7 dB	Beamwidth constant K_θ	1.2
Aperture width, height w, h	1.5m	Antenna beamwidths θ_a, θ_e	1.4°
Phase-center height h_r	12m	Pattern constant L_n	1.17
Pattern-propagation factor F	1.0	Range-dependent factor $F_{\text{rdr}}^2 = F_{lens}^2$	0.984
System temperature	1,000K	Samples integrated n'	1.0
Detectability factor $D_x(1)$	100	Target RCS σ	1.0 m^2
Attenuation L_α (at R_m)	1.76 dB	Range in thermal noise R_m	93.2 km
Clutter reflectivity γ	0.063	Clutter polarization factor F_{cp}^2	1.0
Surface roughness σ_h	1.0m		

3.3.4 Input Energy of Surface Clutter

3.3.4.1 Input Surface Clutter Energy in Pulsed Radar

For pulsed radar, the surface clutter energy at the output of the antenna from each ambiguous area A_{ci} is found from (3.4) using σ_{ci} from (3.23). These contributions are summed as in (3.5) to yield the total input clutter energy:

$$\begin{aligned} C_0 &= \frac{P_{av} t_f G_t G_r \lambda^2 F_{pc}^2 \theta_a (\tau_n c/2) \gamma}{(4\pi)^3 L_t L_p} \sum_i \frac{F_{ci}^4 F_{rdrc\,i}^2 \sin\psi_i}{R_{ci}^3 L_{\alpha c\,i}} \quad \text{(J)} \\ &\approx \frac{P_{av} t_f G_t G_r \lambda^2 F_{pc}^2 \theta_a (\tau_n c/2) \gamma}{(4\pi)^3 L_t L_p} \sum_i \frac{F_{ci}^4 F_{rdrc\,i}^2}{R_{ci}^3 L_{\alpha c\,i}} \left(\frac{h_r}{R_{ci}} - \frac{R_{ci}}{2 k_e a_e} \right) \quad \text{(J)} \end{aligned} \tag{3.27}$$

The problem in applying this expression to a calculation of detection range R_{mc} is that the range dependence of the clutter pattern-propagation factor F_{ci} and the grazing angle ψ_i preclude writing of a closed-form expression for R_{mc}, even when the target pattern-propagation factor is constant.

For example, Figure 3.2 shows a plot of signal and clutter energy levels for an LPRF radar with a pulsewidth $\tau_n = 1$ μs. The radar achieves detection in noise at $R_m = 93.2$ km, but as the target, as it flies along the beam axis near zero elevation angle. Reflection lobing and possible diffraction loss is omitted from the calculation. As the target comes within the clutter horizon at 15 km the clutter rises, reducing the ratio of signal to interference below the required $D_x = 20$ dB. Within 1-km range, the clutter falls below the elevation beam, restoring the necessary detection margin. However, the range interval within which detection is impaired can-

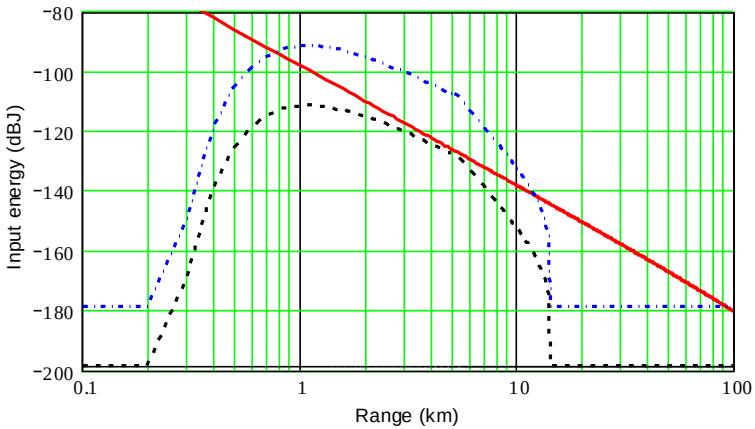

Figure 3.2 Input energy levels for the example radar using LPRF waveform: target signal E on beam axis (heavy sold line), interference I_{0e} (dashed line), detection threshold 20 dB above interference (dash-dot line), and noise (light solid line at $N_0 = -198.6$ dBJ).

not be found from any simple equation, and reading from the graph or an equivalent root-finding algorithm is necessary. The required improvement factor to avoid impairment, $I_m \approx 18$ dB, can be determined from the graph at $R = 5$ km.

3.3.4.2 Input Surface Clutter Energy in CW Radar

Although unmodulated continuous-wave (CW) radar is less widely used than in the past, equations developed in this section also serve as starting point for simplified clutter calculations in HPRF pulsed Doppler radar. Surface clutter in HPRF radar and in phase-modulated CW radar can be described by the expressions given in Section 3.3.4.1 for pulsed radar, with τ_n representing the width of the range resolution cell resulting from a modulated waveform. When several such ambiguities contain clutter, the expressions developed here, modified as in Section 3.3.4.3, provide an alternative method that is often more convenient.

Surface clutter in unmodulated CW radars is beamwidth-limited, according to (3.19). At low grazing angles the reflectivity, pattern-propagation factor, and improvement factor vary with range within the beam footprint in a way similar to those in different ambiguities of pulsed radars. The following expression for clutter energy density as a function of range replaces C_i in (3.5), as noted by Blake [3, pp. 298–300]:

$$dC = \frac{P_{av} t_f G_t G_r \lambda^2 F_{pc}^2}{(4\pi)^3 L_t} \left[\frac{F_c^4}{R_c^4} \right] d\sigma_c \quad \text{(J)} \tag{3.28}$$

where $d\sigma_c$ is the RCS density in m^2 per m of range, which varies with R_c, along with the term F_c^4 in brackets. In the CW radar case, the range-dependent response factor F_{rdr} and attenuation $L_{\alpha c}$ are taken as unity and omitted from (3.28), since STC cannot be used, the transmission does not eclipse the signal, and short-range clutter is dominant. The clutter RCS density is found from (3.19) with $\csc\psi \approx 1$:

$$d\sigma_c = \frac{R_c \theta_a \gamma \sin\psi}{L_p} dR_c \quad (m^2) \tag{3.29}$$

$$dC = \frac{P_{av} t_f G_t G_r \lambda^2 F_{pc}^2 \theta_a \gamma}{(4\pi)^3 L_t L_p} \left[\frac{F_c^4 \sin\psi}{R_c^3} \right] dR_c \quad (J) \tag{3.30}$$

Figure 3.3 shows the variation in the term dC for a typical CW radar characterized by: P_{av} = 100W, t_f = 0.01s, beamwidths $\theta_a = \theta_e$ = 1.7°, height h_r = 12m above a land surface for which σ_h = 1m and γ = –12 dB. The solid line applies to a horizontally directed beam. Ranges shown by vertical dotted lines are R_1, the limit of the near region, and R_a, the range at which the two-way antenna gain for a horizontal beam is 1/*e* at the surface:

$$R_a = \sqrt{8 \ln 2} \frac{h_r}{\theta_e} \tag{3.31}$$

In the example, R_a = 1,177m. The major contribution to clutter input comes from a region $0.5 < R_c/R_a < 2$, and contributions for $R_c/R_1 > 1$ are negligible.

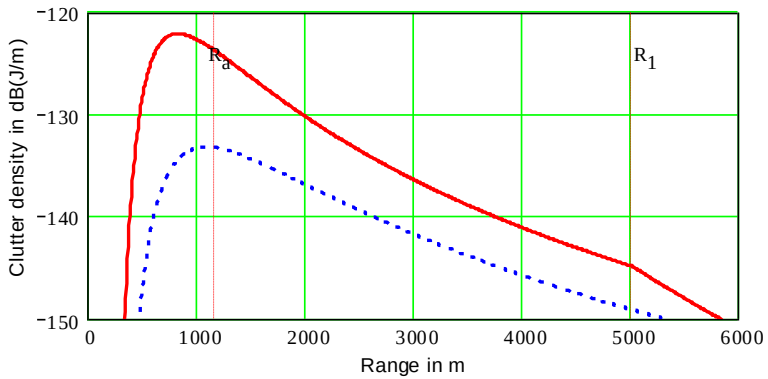

Figure 3.3 Surface clutter input energy levels with the constant-γ model of surface clutter for the example CW radar: horizontal beam (sold line), and beam elevation to $\theta_e/3$ (dashed line).

For a low-sited radar, where the flat-Earth approximation is valid over most of the near region $R_c < R_1$, the clutter pattern-propagation factor is

$$F_c^4 = f_c^4 = \exp\left[-\left(\frac{R_a}{R_c} + \frac{R_a\theta_b}{h_r}\right)^2\right] \tag{3.32}$$

where θ_b is the upward tilt of the beam axis. The summation for input clutter energy C_0 in (3.27) is replaced by integration:

$$C_0 = \int_{h_r}^{R_1} dC = \frac{P_{av}t_f G_t G_r \lambda^2 F_{pc}^2 \theta_a \gamma h_r}{(4\pi)^3 L_t L_p} \int_{h_r}^{R_1} \frac{f_c^4}{R_c^4} dR_c \quad \text{(J)} \tag{3.33}$$

Only terms within the integral are functions of clutter range R_c. The rapid reduction in f_c as $R_c \to 0$ makes the result insensitive to the lower limit of the integration, but for convenience it is taken here as the height h_r above the surface on which the antenna is mounted.

For $\theta_b = 0$ (horizontal beam), the integral in (3.33) reduces to $\sqrt{\pi}/4R_a^3$, yielding:

$$C_0 = \frac{P_{av}t_f G_t G_r \lambda^2 F_p^2 \theta_a \theta_e^3 \gamma}{(4\pi)^3 L_t L_p h_r^2} \frac{\sqrt{2\pi}}{128\sqrt{(\ln 2)^3}} = \frac{P_{av}t_f G_t G_r \lambda^2 F_p^2 \theta_a \theta_e^3 \gamma}{77{,}950 L_t h_r^2} \tag{3.34}$$

This can be simplified for equal transmitting and receiving gains given by

$$G = \frac{4\pi}{\theta_a \theta_e L_n} \approx \frac{10.75}{\theta_a \theta_e} \tag{3.35}$$

where $L_n \approx 1.17$ is the pattern constant from Section 2.6.1. The result is a very simple expression for CW radar clutter energy:

$$C_0 = \frac{P_{av}t_f \lambda^2 \theta_e \gamma}{256 L_p L_n^2 \sqrt{2\pi(\ln 2)^3} h_r^2 \theta_a} = \frac{P_{av}t_f \lambda^2 \theta_e \gamma}{675 h_r^2 \theta_a} \tag{3.36}$$

For example, with parameters as in Table 3.1, $C_0 = 5.8 \times 10^{-10}$ J, or 106.3 dB above the noise level for noise temperature T_s = 1,000K. Such large clutter-to-noise ratios define the challenge in design of surface-based CW radars for air de-

fense applications. Equation (3.36) shows that the clutter input, for a beam directed at the horizon, can be reduced only by increasing the height h_r of the antenna above the surface, decreasing the ratio of elevation to azimuth beamwidth or transmitting less energy (which also reduces signal energy).

Clutter input can be reduced by tilting the antenna axis upwards. The integral in (3.33) for arbitrary beam-axis elevation θ_b reduces to

$$\frac{1}{2R_a}\left\{\left(\frac{\sqrt{\pi}\theta_b^2}{h_r^2}+\frac{\sqrt{\pi}}{2R_a^2}\right)\left[1-\text{erf}\left(\frac{R_a\theta_b}{h_r}\right)\right]-\frac{\theta_b}{R_a h_r}\exp\left(-\frac{R_a^2\theta_b^2}{h_r^2}\right)\right\} \qquad (3.37)$$

where erf(·) is the error function. The result for $\theta_b = \theta_e/3$, shown by the dashed line in Figure 3.3, reduces the integrated clutter energy by 9.3 dB. The ratio of clutter energy for an elevated beam to that for a horizontal beam, given for clutter by (3.36), may be expressed by including a *beam elevation factor* F_b^4, plotted in Figure 3.4 for both the Gaussian beam and the beam pattern of an aperture with cosine taper. Also shown is the factor F^4 for targets at elevation $\theta_t = 0$. The clutter is slightly larger for the Gaussian beam with small elevation because the mainlobe pattern decays more slowly, but the more realistic cosine illumination generates sidelobes that govern the factor for axis elevations above one beamwidth. The improvement in signal-to-clutter ratio for elevated beams is the difference between the clutter and target factors (e.g., 6.6 dB for $\theta_b = 0.33\theta_e$).

The beam elevation factor in Figure 3.4 for the cosine taper was calculated by numerical integration. It shows that the clutter energy expressions developed for the Gaussian beam are adequate for beams elevated less than about one beamwidth.

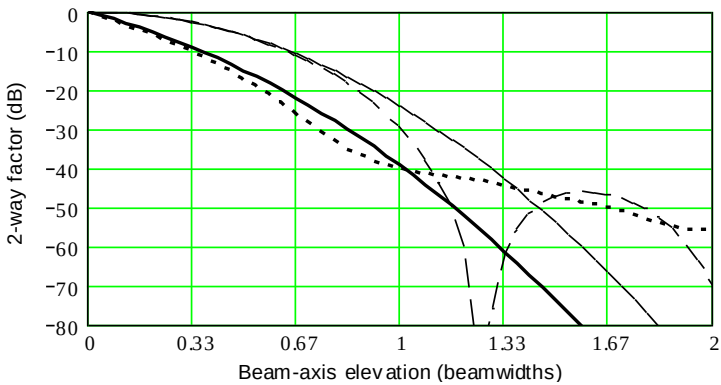

Figure 3.4 Beam elevation factor F_b^4 for surface clutter (heavy lines) and F^4 for targets at the horizon (light lines), with Gaussian beam (solid lines), and beam from cosine-illuminated aperture (dashed lines).

3.3.4.3 Input Surface Clutter Energy in Pulsed Doppler Radar

In pulsed Doppler radar, a range gate matched to the pulse width τ and centered at range R_c from the transmitted pulse passes clutter energy given by integration of the clutter density over ambiguous ranges $(R_c + iR_u) \pm \tau c/4$. Figure 3.5 shows the clutter energy in each of nine 1-μs gates between successive pulses at t_r = 10 μs, including the first four range ambiguities and using the clutter density shown in Figure 3.3. The rectangular gate, sampling over ±75m from its center, passes clutter energy given by

$$C_0 \text{ (dBJ)} = \text{density dB(J/m)} + 10\log(150\text{m}) = \text{density dB(J/m)} + 21.8 \text{ dB(m)}$$

at each ambiguous range. The clutter energy varies by 6 dB over the nine gates (the potential tenth gate is totally eclipsed by the transmitted pulse). The average over the gates is 10 dB below the level for the CW radar, as expected for a duty cycle $D_u = \tau/t_r = 0.1$. For gates 1 and 2 the beam does not reach the surface until the second range ambiguity, giving lower clutter than in gates 3–9.

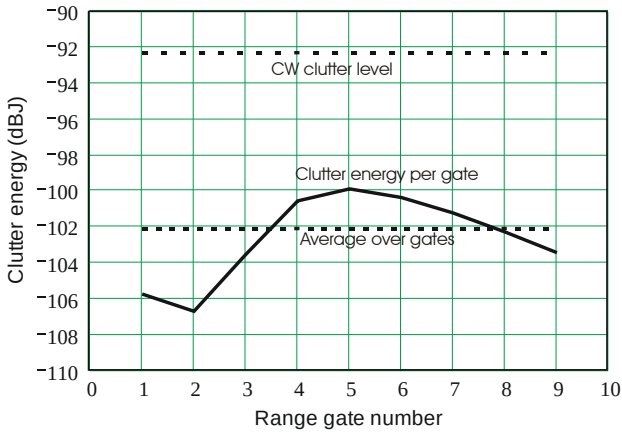

Figure 3.5 Surface clutter input energy levels in HPRF PD radar with D_u = 10% and a horizontal beam, under the same conditions as for the CW radar of Figure 3.3.

3.3.5 Detection Range of Surface-Based CW and HPRF Radars

3.3.5.1 CW Radar Detection Range

For an unmodulated CW radar the clutter energy is independent of target range, and for the horizontal beam the signal-to-clutter ratio at the processor output is given by

$$\frac{E}{C_{0e}} = \frac{39.2 h_r^2 \sigma F^4 \overline{I_m}}{R^4 \gamma \theta_a \theta_e^3 L_\alpha} \tag{3.38}$$

where $\overline{I_m}$ is the weighted average improvement factor over the ranges at which clutter appears, according to (3.11). It is assumed that the clutter residue in the Doppler filters has the same statistical properties as noise.

These expressions lead to simple expressions for maximum detection range for two special cases:

$$R_{mc} = \left(\frac{39.2 h_r^2 \sigma F^4 F_{rdr}^2 \overline{I_m}}{\gamma \theta_a \theta_e^3 D_x L_\alpha (R_{mc})} \right)^{1/4} \text{(m), for } \frac{C_{0e}}{N_0} >> 1,\ \theta_b = 0 \tag{3.39}$$

$$R_{mc} = \left[\frac{19.6 h_r^2 \sigma F^4 F_{rdr}^2 \overline{I_{m\text{req}}}}{\gamma \theta_a \theta_e^3 D_x L_\alpha (R_{mc})} \right]^{1/4} \approx \frac{R_m}{\sqrt[4]{2}} \ \text{(m), for } \frac{C_{0e}}{N_0} = 1 \tag{3.40}$$

where R_m is given by (1.26) and the approximation ignores reduced L_α at R_{mc}.[6] The value of $L_\alpha(R_{mc})$ within the brackets can be approximated, based on the range in thermal noise, or the result of the two-step iteration used in the Blake chart.

The average improvement factor required for the use of (3.40), for the example radar, is found using (3.36) and $N_0 = kT_s$:

$$\begin{aligned} \overline{I_{m\text{req}}} &= \frac{P_{av} t_f \lambda^2 \theta_e \gamma}{675 k T_s h_r^2 \theta_a} \\ &= \frac{100 \times 0.01 \times 0.03^2 \times 0.024 \times 0.063}{675 \times 1.38 \times 10^{-23} \times 1{,}000 \times 12^2 \times 0.024} \\ &= 4.23 \times 10^{10} = 106.3 \text{ dB} \end{aligned} \tag{3.41}$$

The detection ranges available for improvement factors that are above, equal to, or below that found from (3.41) are shown in Table 3.2, which also shows an example of performance with an elevated beam.

---

[6] These and subsequent expressions for detection range in clutter R_{mc} require application of an iteration process similar to that used in the Blake chart to solve for the attenuation $L_\alpha(R_{mc})$ and lens factor F_{lens}. Use of the attenuation and lens factor for the thermal-noise range R_m gives slightly pessimistic results, which are generally adequate given uncertainties in clutter characteristics. The accurate method is used in the Mathcad worksheets included on the accompanying DVD.

Table 3.2 Example Detection Ranges

I_m (dB)	θ_b (deg)	F^4 (dB)	I_{0e}/N_0 (dB)	R_{mc} (km)
>> 106.3	0	0	0	93.2
112.3	0	0	1.0	88.1
106.3	0	0	3.0	78.4
100.3	0.46	–2.7	1.7	72.5
100.3	0	0	7.0	62.4

3.3.5.2 Surface-Based PD Radar

Calculations for pulsed Doppler (PD) radars may be carried out using summation of power from range ambiguities as in (3.11) and (3.12), but when several ambiguities are occupied by clutter it may be easier to apply the CW radar equations with a correction for the effects of duty cycle and pulse compression. The clutter, when averaged over all ranges in the pulse repetition interval (PRI), is given by (3.28)–(3.36) with the duty cycle $D_u = \tau/t_r$ included as a factor in the numerators. Note that D_u is also applied to convert peak power P_t to in average power P_{av}, so the clutter energy varies with D_u^2 for a given peak power. The pulse compression ratio τ/τ_n appears also in the denominator when a phase-modulated pulse is used.

The clutter density as a function of range is as given in Figure 3.2, and is integrated over aliased responses as in Figure 3.4. The duty factor and the pulse compression ratio are included in the numerator of (3.36), leading to:

$$\overline{C_0} = \frac{P_{av} t_f \lambda^2 \theta_e \gamma D_u \tau_n}{675 h_r^2 \theta_a \tau} = \frac{P_{av} t_f \lambda^2 \theta_e \gamma \tau_n}{675 h_r^2 \theta_a t_r}, \quad \text{(pulsed Doppler, } \theta_b = 0) \tag{3.42}$$

where t_r is the PRI. The same factors and the ratio $C_{0e} / \overline{C_{0e}}$ of clutter in the target gate to that averaged over the PRI appear in the range equations (3.39) and (3.40), to give

$$R_{mc} = \left(\frac{39.2 h_r^2 \sigma F^4 F_{rdr}^2 t_r I_m \overline{C_0}}{\gamma \theta_a \theta_e^2 D_x L_\alpha (R_{mc}) \tau_n C_0} \right)^{1/4} \text{(m)}, \text{ for } \frac{C_0}{I_m N_0} >> 1, \ \theta_b = 0 \tag{3.43}$$

$$R_{mc} = \left(\frac{19.6 h_r^2 \sigma F^4 F_{rdr}^2 t_r I_m \overline{C_0}}{\gamma \theta_a \theta_e^2 D_x L_\alpha (R_{mc}) D_u \tau_n C_0} \right)^{1/4} \text{(m)} \approx \frac{R_m}{\sqrt[4]{2}} \ \text{(m)}, \text{ for } \frac{C_0}{I_m N_0} = 1 \tag{3.44}$$

As in the CW radar case, the value of $L_\alpha(R_{mc})$ within the brackets can be an approximation based on the range in thermal noise, or the result of the two-step iteration used in the Blake chart.

The pulsed Doppler radar has lower input clutter than a CW radar using the same antenna parameters and average power. The available improvement factor, however, is reduced by the aliasing of the clutter residue spectrum at intervals of the PRF, which adds multiple aliased components to the output of the target Doppler filter [2, pp. 248–252]. The resulting clutter performance is not necessarily better than the CW radar. The major advantages of the PD radar are that a common antenna is used for transmitting and receiving, and target range may be measured by combining observations at different PRFs.

3.3.6 Summary of Detection in Surface Clutter

The steps in solving for detection range in an environment of surface clutter and thermal noise can be summarized as requiring calculation of the surface clutter reflectivity γ, using data from Chapter 9, and the following quantities that are functions of range R_c:

- Ambiguous ranges R_{ci} at which clutter competes with the target at range R, from (3.3), the corresponding areas A_{ci}, from (3.18) or (3.19), and grazing angles ψ_i from (3.16) or equivalent spherical-Earth equations.
- Clutter pattern-propagation factor F_{ci}, and atmospheric attenuation $L_{\alpha ci}$ for each area, using data from Chapter 8.
- Clutter cross section from (3.23), and the resulting clutter input energy from (3.5) for clutter ranges R_{ci}.
- Clutter correlation loss L_{cci}, based on number of independent clutter samples available for integration from (3.7), using data on clutter velocity spread σ_{vi} for each ambiguity from Chapter 9, and accounting for Doppler improvement factor when such processing is used.
- Clutter distribution loss L_{cdi} from (3.8), based on Weibull spread parameter $1 \le a_{wi} \le 5$ from data in Chapter 9, modified as necessary for clutter-map processing.
- Effective clutter spectral density C_{0e} from (3.11), based on summation of effective clutter energies from all ambiguities, or from (3.33) for CW radar.
- Total interference spectral density I_{0e} from (3.2).
- Detection range R_{mc} from (3.12) for the general case, from (3.39) or (3.39) for CW radar, from (3.43) or (3.44) for pulsed Doppler, or from a graphical or root-finding method.

3.4 DETECTION IN VOLUME CLUTTER

Volume clutter arises from precipitation or chaff within the radar resolution cell. The inclusion of energy from volume clutter follows the procedures given in Sections 3.1 and 3.2 and applied to surface clutter in Section 3.3. The effective spectral density C_{0e} for volume clutter is added to that of surface clutter when both are present at the detection range.

3.4.1 Geometry of Volume Clutter

The geometry of volume clutter is shown in Figure 3.6. The resolution cell is defined by the antenna beamwidths, reduced by beamshape loss, and the range resolution cell Δ_r by (3.14) or for CW radar by the integration of (3.33).

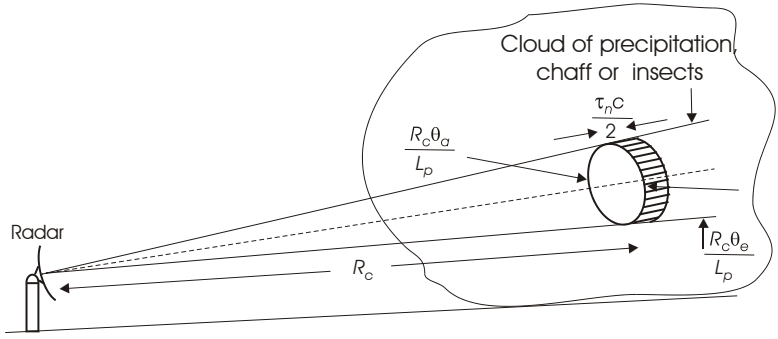

Figure 3.6 Volume clutter geometry.

At ranges where the cloud fills the radar beam, the volume V_c of the clutter in the resolution cell at range ambiguity i is

$$V_{ci} = \frac{R_{ci}\theta_a}{L_p}\frac{R_{ci}\theta_e}{L_p}\frac{\tau_n c}{2} \quad \left(\mathrm{m}^3\right) \tag{3.45}$$

where the lower and upper limits of the ambiguity index i are as defined in (3.3), depending on the location and radial dimension of the cloud. The horizontal cross-range dimension of the cloud is usually assumed to extend beyond the azimuth beamwidth, but in elevation it extends between the minimum altitude h_{cmin} (often the Earth's surface) and a maximum altitude h_{cmax} that depends on the origin of the scattering particles. When the elevation beam extends beyond those limits, the term $R_{ci}\theta_e/L_p$ of (3.45) is replaced by an effective cloud thickness:

$$\Delta h_i = R_{ci}\Delta\theta = R_{ci}\int_{\theta_{c\min}(R_{ci})}^{\theta_{c\max}(R_{ci})} f^4(\theta-\theta_b)d\theta \quad (\mathrm{m}) \tag{3.46}$$

where θ is the elevation angle and θ_b is the elevation of the beam axis. The upper and lower elevation limits of the clutter are functions of the altitude limits $h_{c\max}$ and $h_{c\min}$, and range R_{ci} of the clutter:

$$\begin{aligned}\theta_{c\max}(R_{ci}) &= \frac{h_{c\max}}{R_{ci}} - \frac{R_{ci}}{2k_e a_e} \quad (\mathrm{rad})\\ \theta_{c\min}(R_{ci}) &= \frac{h_{c\min}}{R_{ci}} - \frac{R_{ci}}{2k_e a_e} \quad (\mathrm{rad})\end{aligned} \tag{3.47}$$

As the limits expand beyond the elevation beamwidth, $\Delta\theta \to \theta_e/L_p$.

For a beam-axis elevation $\theta_b < \theta_e/2$ above horizontal, the beamwidth θ_e in (3.45) is replaced by the fraction $\theta_b + \theta_e/2$ of the beam lying above the surface. The fraction of the beam directed at the surface may contribute to the volume clutter energy through an increase in the pattern-propagation factor for the volume clutter, as will be discussed in Section 3.4.3.

As with surface clutter, range ambiguities defined by (3.3) may contain volume clutter. The resolution cell volumes are proportional to R_{ci}^2, both within and beyond the target range R. As noted in Chapter 5, the meteorological radar equation [6, p. 74, Eq. (4.13)] contains the constant term $\pi/(8\ln 2) = 1/L_{p0}^2 = 0.565$, consistent with (3.45), where L_{p0}^2 is the two-dimensional beamshape loss for dense sampling (see Chapter 5). Literature in which this constant is given as $\pi/4$ overestimates the volume by 1.4 dB because it substitutes the solid angle of a cylindrical beam with constant gain over an elliptical region for the beamshape loss that describes the off-axis reduction in antenna gain in both coordinates.

3.4.2 Volume Clutter Cross Section

The radar cross section of volume clutter in a resolution cell at range R_{ci} is

$$\sigma_{ci} = V_{ci}\eta_v \quad (\mathrm{m}^2) \tag{3.48}$$

where V_{ci} is the volume in m^3 of the clutter cell at range R_{ci} and η_v is the volume reflectivity of the scatterers making up the cloud, with dimension $\mathrm{m}^2/\mathrm{m}^3$. The volume reflectivity is a function of radar frequency as well as the physical properties of the scatterers, as described in Chapter 9. In the case of precipitation, insects, and chaff corridors, the cloud often extends over many resolution cells in all di-

mensions. Self-defense chaff bursts initially are smaller, gradually expanding to larger volumes with decreased reflectivity per unit volume.

3.4.3 Volume Clutter Energy

The volume clutter energy is given by (3.4) and (3.5), and the effective value for multiple range ambiguities by (3.11). Thus we can write

$$\begin{aligned} C_0 &= \sum_i C_i = \frac{P_{av} t_f G_t G_r \lambda^2 F_{pc}^2}{(4\pi)^3 L_t} \sum_i \frac{\sigma_{ci} F_{ci}^4 F_{rdrci}^2}{R_{ci}^4 L_{\alpha ci}} \quad \text{(J)} \\ &= \frac{P_{av} t_f G_t G_r \lambda^2 F_{pc}^2 \theta_e \theta_a (\tau_n c/2)}{(4\pi)^3 L_t L_p^2} \sum_i \frac{\eta_v F_{ci}^4 F_{rdrci}^2}{R_{ci}^2 L_{\alpha ci}} \end{aligned} \tag{3.49}$$

$$C_{0e} = \sum_i \frac{C_i L_{cci}}{I_{mi}} = \frac{C_0 \overline{L_{cci}}}{\overline{I_m}} \tag{3.50}$$

where the terms with overbars are weighted averages over the cutter region.

The pattern-propagation factor F_{ci}^4 for volume clutter varies less than for surface clutter. Where the beam is elevated above the horizon, only the pattern variation over the vertical dimension of the cell affects F_c, and this is included as L_p in one term of (3.45). When the surface is illuminated with significant gain, a strong lobing structure appears with elevation lobe widths $\lambda/2h_r$. The pattern-propagation factor F_{ci}^4, when averaged over the vertical extent of the clutter, then increases the clutter energy by a factor $\overline{F_{ci}^4} \le 6 = 7.8$ dB, which is the average value of $[2\sin(2\theta h_r/\lambda)]^4$ over elevations $0 < 2\theta h_r/\lambda < 2\pi$. Significant errors in estimates of detection range result when factors of this magnitude are ignored in applying the radar equation.

Volume and surface clutter differ also because a polarization factor $F_{pc} << 1$ may be obtained for precipitation through use of circular polarization (see Section 10.1.1), and elevated clouds may extend far beyond the surface-clutter horizon, producing clutter in multiple ambiguities even when the intended targets are within the unambiguous range. Surface clutter may have similar range extent when propagation ducts are present, but the problem is more common with high-altitude volume clutter.

3.4.4 Volume Clutter Detectability Factor

The effect of wind shear on volume clutter causes the mean and spread of velocity to increase with range. Clutter correlation loss L_{cc}, described by (3.6) and (3.7), applies to volume clutter, but is smaller than for surface clutter because of the larger velocity spread σ_v of volume clutter (see Chapter 9). The increasing spread reduces L_{cc}, even in the absence of MTI processing, causing the effective clutter spectral density to increase less rapidly with increasing range than would be predicted solely from the increasing volume in the resolution cell. The pdf of volume clutter is approximately Rayleigh, at least over range extents used in cell-averaging CFAR, giving $L_{cd} \approx 1$ in (3.8). The clutter detectability factor D_{xc} for volume clutter, given by (3.9), thus exceeds D_x for noise only by the clutter correlation loss L_{cc}.

3.4.5 Detection Range in Volume Clutter and Noise

After evaluating clutter volumes, reflectivities, and propagation factors as functions of the target range R, the effective clutter density can be found from (3.11), added to the noise density as in (3.2), and inserted as the interference spectral density I_{0e}, replacing noise density N_0 in (1.26), and used in (3.12) to find the maximum detection range in an environment of volume clutter and noise. As with surface clutter, many terms on the right-hand side of this equation are range-dependent, and R_{mc} must generally be found graphically or by root-finding.

A special case in which an equation for detection range of a LPRF radar may be written in closed form applies when the following conditions apply:

- No range-ambiguous clutter: $R_c = R$, $L_{\alpha c} = L_\alpha$, and $F_{rdrc} = F_{rdr}$;
- No surface-reflection lobing: $F_c = F = 1$;
- Clutter loss $L_{cd} = 1$, and constant L_{cc} with varying range;
- Improvement factor I_m constant with range;
- Clutter energy dominates the interference at the processor output: $C_{0e} >> N_0$, $I_{0e} = C_{0e}$.

Equations (3.45), (3.48), and (3.11) may then be combined to give

$$I_{0e} = C_{0e} = \frac{P_{av} t_f G_t G_r \lambda^2 \eta_v \theta_a \theta_e \left(\tau_n c/2\right) F_{pc}^2 F_{rdr}^2 L_{cc}}{\left(4\pi\right)^3 R^2 L_t L_\alpha L_p^2 I_m} \ \left(\text{W/Hz}\right),\ C_{0e} >> N_0 \qquad (3.51)$$

From this and (1.26) we may write, for LPRF radar (no range ambiguity):

$$\frac{E}{I_{0e}} = \frac{\sigma F_p^2 F_{rdr}^2 L_p^2 I_m}{R_{mc}^2 \eta_v \theta_a \theta_e \left(\tau_n c/2\right) F_{pc}^2 L_{cc}} = D_x\left(n'\right),\ C_{0e} >> N_0 \tag{3.52}$$

$$R_{mc}^2 = \frac{\sigma F_p^2 F_{rdr}^2 L_p^2 I_m}{\eta_v \theta_a \theta_e \left(\tau_n c/2\right) F_{pc}^2 L_{cc} D_x\left(n'\right)} \quad \left(\mathrm{m}^2\right),\ C_{0e} >> N_0 \tag{3.53}$$

Note that the beamshape loss L_p^2 appears in the numerator, while the corresponding loss for the target is included within D_x in the denominator. In this derivation the polarization factors F_p and F_{pc} are retained because they are not range-dependent. The antenna polarizations are sometimes chosen for rejection of precipitation: $F_p >> F_{pc}$. However, the other assumptions constrain the solution to a limited number of situations.

A typical example to which this expression applies is shown in Figure 3.7, where the X-band radar described in Table 3.1 uses an LPRF waveform, looks through a cloud of 1-mm/h rain without MTI but with circular polarization for clutter rejection: $F_{pc}^2 = 0.01$, $F_p^2 = 0.5$. The curve for signal energy lies below that shown in Figure 3.2 because of the reduced polarization factor F_p^2 for the target and increase attenuation in rain. The range scale is logarithmic to illustrate the linear dependence of target and clutter energy on R^{-4} and R^{-2}, respectively. The closed-form (3.53) is applicable because the clutter spectral density at R_{mc} is some 35 dB above noise at R_{mc}.

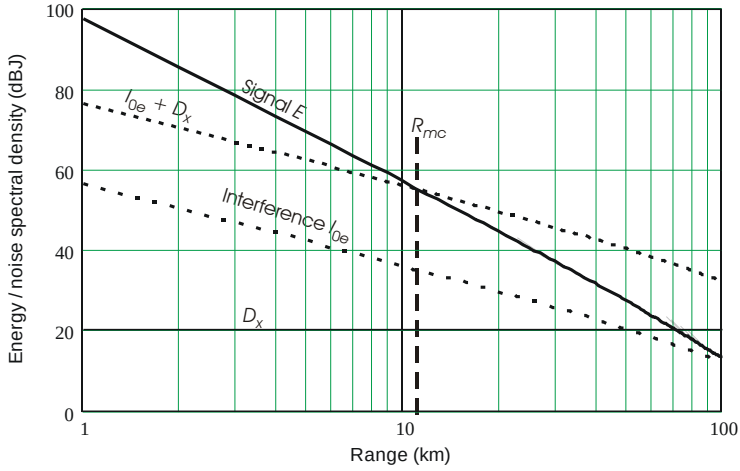

Figure 3.7 Typical target and volume clutter energy as a function of range, for LPRF radar with target on the beam axis, no MTI processing. The volume clutter fills the beam at all ranges.

In this example, no MTI improvement has been shown. It would obviously be advantageous to include MTI processing, which could provide about 15-dB clutter reduction (see Section 9.6.1), providing target detection near 50 km.

3.4.6 Volume Clutter in CW and PD Radars

Volume clutter in CW radars that use phase modulation to obtain range resolution τ_n is described by the expressions given in previous section for pulse radar. The cross-range dimension of the resolution cell in azimuth is determined by the beamwidth, and in elevation either by the beamwidth or the cloud thickness, as in (3.46).

In unmodulated CW radar, the range dimension of the clutter is the length of the path that lies within the cloud. Blake [3, p. 300, Eq. (7.18)] presents an expression using a triple integral (in range, azimuth, and elevation) to give the clutter energy for pulsed radar where η_v remains constant over a hemisphere, but the elevation limits of the cloud are, in general, range-dependent.

3.4.6.1 Volume Clutter Energy for CW Radar

Useful insight into CW radar performance in volume clutter may be gained under the assumption that the cloud extends beyond the radar beam in both angle coordinates, for which case the surface-clutter expressions (3.29)–(3.33) can be modified for volume clutter to yield

$$d\sigma_c = \frac{R_c^2 \theta_a \theta_e \eta_v}{L_p^2}\, dR_c \tag{3.54}$$

$$dC = \frac{P_{av} t_f G_t G_r \lambda^2 \theta_a \theta_e \eta_v F_{pc}^2}{(4\pi)^3 L_t L_p^2} \left[\frac{F_c^4}{R_c^2 L_{\alpha c}}\right] dR_c = K_{cv} \left[\frac{F_c^4}{R_c^2 L_{\alpha c}}\right] dR_c \quad \text{(J)} \tag{3.55}$$

$$C_{0e} = \int_{R_{c\min}}^{R_{c\max}} dC = K_{cv} \int_{R_{c\min}}^{R_{c\max}} \frac{F_c^4}{I_m R_c^2 L_{\alpha c}}\, dR_c \quad \text{(W/Hz)} \tag{3.56}$$

Consider again the X-band radar described in Table 3.1, operating in the rainfall rate of 1 mm/h assumed for Figure 3.7, but with a CW waveform and circular polarization. The clutter density resulting from (3.55) is shown in Figure 3.8. The peak density occurs at range R_{ff}, and most of the clutter energy comes from the volume within $\approx 6R_{ff}$ in front of the antenna.

The clutter reflectivity η_v is usually assumed constant within the cloud, and is included in K_{cv}, but may be moved within the integral of (3.56) if it varies in some

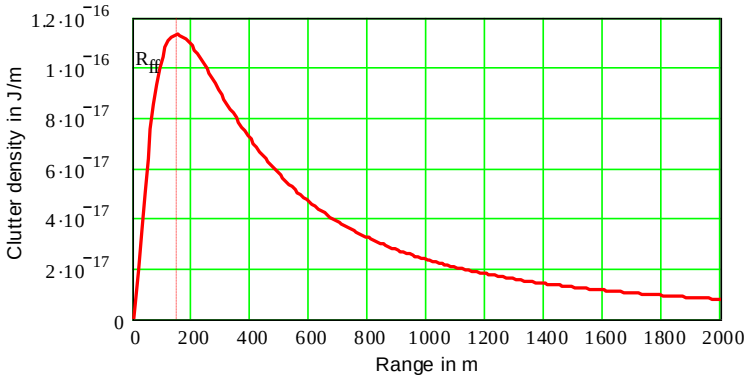

Figure 3.8 Volume clutter density as a function of range for CW radar enveloped in 1-mm/h rain, plotted for beamwidths $\theta_a = \theta_e = 1.4°$, $\lambda = 0.03$m, $R_{ff} = 150$m.

known way with range. Atmospheric attenuation is included within the integral because it may become significant for large R_{cmin}. As with the surface-clutter analysis, the factors F_{rdr} and L_{cc} are assumed unity for CW radar and omitted from the equations.

The range limits of the integral depend on the location and extent of the cloud. The minimum range R_{cmin} approaches zero when the cloud envelopes the radar, but the antenna beam is not fully formed within the *far-field range* of the antenna, given by

$$R_{ff} = \frac{2wh}{\lambda} = \frac{2\lambda K_\theta^2}{\theta_a \theta_e} \tag{3.57}$$

Here w and h are the width and height of the aperture and $K_\theta \approx 1.2$ is the beamwidth constant. Antennas separated horizontally by w or vertically by h are required in most CW radars to avoid direct coupling between the transmitter and receiver. Hence the two beams begin to overlap at $\approx R_{ff}/2$, and the gain product $G_t G_r$ is realized only beyond R_{ff}.

To account for the reduction in the antenna gain product at short range, the volume clutter pattern-propagation factor can be expressed as

$$F_c = \frac{R_c}{R_c + R_{ff}} \tag{3.58}$$

Redefining the terms $L_{\alpha c}$ and F_{rdr} to be weighted averages over the limits of integration, they may be placed outside the integral, which becomes

$$\int_{R_{c\min}}^{R_{c\max}} \frac{R_c^2}{\left(R_c + R_{ff}\right)^4} dR_c = \frac{R_{ff}^2 + 3R_{ff}R_{c\min} + 3R_{c\min}^2}{3\left(R_{ff} + R_{c\min}\right)^3} - \frac{R_{ff}^2 + 3R_{ff}R_{c\max} + 3R_{c\max}^2}{3\left(R_{ff} + R_{c\max}\right)^3}$$

$$\approx \frac{R_{ff}^2 + 3R_{ff}R_{c\min} + 3R_{c\min}^2}{3\left(R_{ff} + R_{c\min}\right)^3} \quad \text{for } R_{c\min} << R_{c\max} \tag{3.59}$$

$$\approx 1/3R_{ff} \qquad \text{for } R_{c\min} << R_{ff} < R_{c\max}$$

The final approximation in (3.59) applies where the clutter cloud envelopes the radar. The atmospheric attenuation $L_{\alpha c} \approx 1$, and input clutter energy is then

$$C_0 = \frac{P_{av} t_f G_t G_r \lambda^2 \theta_a \theta_e \eta_v F_{pc}^2}{(4\pi)^3 L_t L_p^2} \frac{1}{3R_{ff}}$$

$$= \frac{P_{av} t_f \lambda \eta_v F_{pc}^2}{24\pi L_t L_p^2 K_\theta^2 L_n^2} = \frac{P_{av} t_f \lambda \eta_v F_{pc}^2}{264 L_t} \quad \text{(J)} \tag{3.60}$$

The effective clutter energy is $C_{0e} = C_0 / \overline{I_m}$, where $\overline{I_m}$ is the weighted average improvement factor over the clutter region. The clutter energy is independent of antenna parameters other than the polarization factor.

3.4.6.2 Detection Range for CW Radar in Volume Clutter

Combining (1.26) and (3.58), the signal-to-clutter energy ratio can be written for the general case as

$$\frac{E(R)}{C_{0e}} = \frac{\sigma F_p F^4 F_{\text{rdr}}^2 L_p^2 L_{\alpha c} I_m}{R^4 \theta_a \theta_e \eta_v F_{pc}^2 L_\alpha(R)} \left[\frac{R_{ff}^2 + 3R_{ff}R_{c\min} + 3R_{c\min}^2}{3\left(R_{ff} + R_{c\min}\right)^3} - \frac{R_{ff}^2 + 3R_{ff}R_{c\max} + 3R_{c\max}^2}{3\left(R_{ff} + R_{c\max}\right)^3} \right]^{-1} \tag{3.61}$$

Note that the terms within the brackets are independent of target range *R*.

As with surface clutter, there are two special cases for which closed-form expressions can be written. Where clutter residue is dominant, $C_{0e} >> N_0$, we solve for the range R_{mc} at which $E/C_{0e} = D_x$ to obtain

$$R_{mc}^4 = \frac{\sigma F_p^2 F^4 F_{\rm rdr}^2 L_p^2 L_{\alpha c} I_m}{\theta_a \theta_e \eta_v D_x F_{pc}^2 L_\alpha(R_{mc})} \left[\frac{R_{ff}^2 + 3R_{ff} R_{c\min} + 3R_{c\min}^2}{3\left(R_{ff} + R_{c\min}\right)^3} - \frac{R_{ff}^2 + 3R_{ff} R_{c\max} + 3R_{c\max}^2}{3\left(R_{ff} + R_{c\max}\right)^3} \right]^{-1}$$

$$\approx \frac{\sigma F_p^2 F^4 F_{rdr}^2 L_p^2 L_{\alpha c} I_m}{\theta_a \theta_e \eta_v D_x F_{pc}^2 L_\alpha(R_{mc})} \frac{3\left(R_{ff} + R_{c\min}\right)^3}{R_{ff}^2 + 3R_{ff} R_{c\min} + 3R_{c\min}^2} \quad \text{for } R_{c\min} << R_{c\max}$$

$$\approx \frac{3R_{ff} \sigma F_p^2 F^4 F_{rdr}^2 L_p^2 I_m}{\theta_a \theta_e \eta_v D_x F_{pc}^2 L_\alpha(R_{mc})} \quad \text{for } R_{c\min} << R_{ff} < R_{c\max} \tag{3.62}$$

(See the footnote under (3.40) regarding evaluation of $L_\alpha(R_{mc})$ in these expressions.)

The final approximation in (3.62), for clutter enveloping the antenna, can be expressed directly in terms of the radar parameters by substituting (3.57) to obtain

$$R_{mc}^4 = \frac{6\lambda\sigma F_p^2 F^4 F_{\rm rdr}^2 L_p^2 K_0^2 I_m}{\theta_a^2 \theta_e^2 \eta_v D_x F_{pc}^2 L_\alpha(R_{mc})} = \frac{15.3\lambda\sigma F_p^2 F^4 F_{\rm rdr}^2 I_m}{\theta_a^2 \theta_e^2 \eta_v D_x F_{pc}^2 L_\alpha(R_{mc})}, \quad C_{0e} >> N_0 \tag{3.63}$$

If I_m= 50 dB in our example radar, this gives R_{mc} = 27.3 km. The variation of detection range with the inverse squares of the two beamwidths results from the combination of changing clutter volume and far-field range, the latter affecting the response to nearby clutter.

The closed-form solution for the second case is based on the assumption that $C_{0e} = N_0$:

$$R_{mc0} = \frac{R_m}{\sqrt[4]{2}} = \left[\frac{7.6\lambda\sigma F_p^2 F^4 F_{\rm rdr}^2 I_m}{\theta_a^2 \theta_e^2 \eta_v D_x F_{pc}^2 L_\alpha(R_{mc})} \right]^{1/4}, \quad C_{0e} = N_0 \tag{3.64}$$

The improvement factor required for this case is $I_m = C_0/N_0$, which from (3.60) is

$$I_{m\rm req} = \frac{P_{av} t_f \lambda \eta_v F_{pc}^2}{264 k T_s L_t} \tag{3.65}$$

For our example, this gives $I_{m\rm req}$ = 69.2 dB, R_{cm0} = 65.4 km.

3.4.6.3 Example of CW Radar in Rain

For a surface-based X-band CW radar with parameters listed in Table 3.1, with circular polarization in 1-mm/h rainfall rate, the received clutter energy given by (3.60) is $C_0 = 9 \times 10^{-14}$ J. An improvement factor $I_m = 60$ dB would reduce the effective clutter spectral density to $C_0 = 9 \times 10^{-20}$ W/Hz, compared to thermal noise with density $N_0 = 1.4 \times 10^{-20}$ W/Hz. The resulting $C_{0e}/N_0 = 8.2$ dB is high enough to permit (3.63) to be used to find an approximate range:

$$R_{mc}^4 \approx \frac{15.3\lambda\sigma F_p^2 F^4 F_{\text{rdr}}^2 I_m}{\theta_a^2 \theta_e^2 \eta_v D_x F_{pc}^2 L_\alpha(R_{mc})} = 5.6\times10^{18} \text{ (m)}; \quad R_{mc} \approx 49 \text{ km}$$

The accurate range is slightly less, because 8.2 dB is not quite high enough to allow noise to be neglected. The result is independent of the beam elevation, because the clutter arises within a few hundred meters from the antenna. The results given above are based on $I_m = 60$ dB, $F_{pc}^2 = 0.01$, and $F_p^2 = 0.5$, for circularly polarized antennas having the same sense (e.g., right-hand polarization for both transmitting and receiving). Much larger I_m values are generally available in CW radar designed for use against aircraft targets: values in excess of 100 dB were shown necessary in Section 3.3.5 for rejection of surface clutter. That level of Doppler performance would preserve the thermal-noise detection performance when operating in rain, even without the use of circular polarization.

3.4.6.4 Volume Clutter Energy for PD Radar

Volume clutter energy for pulsed Doppler radar may be found using (3.49), but when several range ambiguities are occupied by clutter it may be easier to apply the CW radar equations with a correction for the effects of duty cycle and pulse compression. The clutter, when averaged over all range gates in the pulse repetition interval (PRI), is given by adding duty cycle D_u as a factor in the numerator of K_{cv} in (3.28) and (3.56)–(3.58). The pulse compression ratio τ/τ_n is applied to the denominator of K_{cv} when a modulated pulse is used. The factor of 2 in the numerator of (3.57) is omitted in calculating the far-field range of PD radar antennas, because the transmitting and receiving beams are formed by the common antenna at a range $R_{ff} = wh/\lambda$ and the beams coincide at all ranges. The resulting expression for average PD volume clutter energy, when the cloud envelopes the radar, becomes:

$$\overline{C_{0e}} = \int_{R_{c\min}}^{R_{c\max}} dC = \frac{P_{av} t_f G_t G_r \lambda^2 \theta_a \theta_e \eta_v F_{pc}^2 D_u}{(4\pi)^3 L_t L_p^2 I_m (\tau/\tau_n)} \int_{R_{c\min}}^{R_{c\max}} \frac{F_c^4}{R_c^2 L_{\alpha c}} dR_c \quad \text{(W/Hz)}$$

$$\approx \frac{P_{av} t_f G_t G_r \lambda \theta_a^2 \theta_e^2 \eta_v F_{pc}^2 \tau_n}{3(4\pi)^3 L_t L_p^2 K_\theta^2 I_m t_r} \quad \text{for } R_{c\min} < R_{ff} = \frac{wh}{\lambda} \tag{3.66}$$

This average clutter energy is added to the noise spectral density to obtain I_{0e} for use in calculating an average detection range from (3.12).

The clutter density as a function of range is shown in Figure 3.7 with adjustment for duty cycle, pulse compression, and aliasing at the unambiguous range R_u. The clutter competing with the target varies about that average, as shown in Figure 3.9. The maximum value lies in the first gate that includes the range R_{ff} where the beam is fully formed. Clutter in that gate is ≈ 65 dB above noise level, requiring an improvement factor I_m > 75 dB to avoid reduction in target detectability.

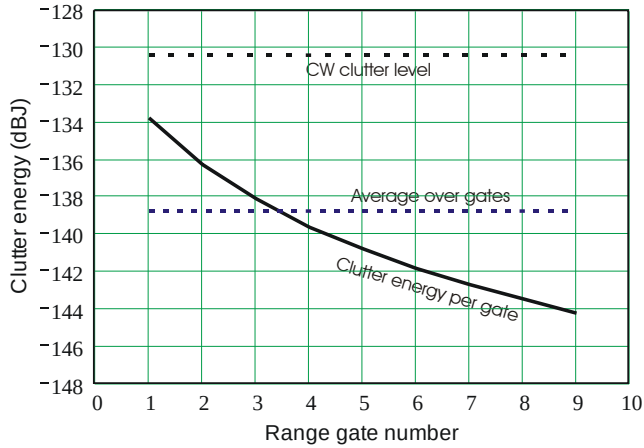

Figure 3.9 Volume clutter input energy levels in HPRF PD radar with D_u = 10%, under the same conditions as for the CW radar of Figure 3.8.

3.4.7 Summary of Detection in Volume Clutter

The steps in solving for detection range in an environment containing volume clutter and thermal noise can be summarized as requiring the calculation of the following factors:

- Ambiguous ranges R_{ci} at which clutter competes with the target at range R, from (3.3), and the corresponding volumes V_{ci} from (3.45).
- Volume clutter reflectivity η_{vi} for each area, using data from Chapter 9.
- Volume pattern-propagation factor F_{ci}, integrated over the resolution cell, and atmospheric attenuation $L_{\alpha ci}$ for each volume, using data from Chapter 8.
- Clutter cross sections from (3.48) and the resulting clutter input density from (3.5) for clutter ranges R_{ci}.
- Clutter correlation loss L_{cci}, based on number of independent clutter samples available for integration from (3.6), using data on clutter velocity spread σ_{vi} for each ambiguity, from Chapter 9, and accounting for Doppler improvement factor I_{mi} when such processing is used.
- Effective clutter spectral density C_{0e} from (3.11), with $C_{cd} = 1$, based on summation of effective clutter energies from any ambiguities, from (3.56) for CW radar or from (3.66) for PD radar.
- Effective interference spectral density I_{0e} from (3.2).
- Detection range R_{mc} from (3.12).

When both surface and volume clutter are present at the same range, the calculation of Doppler improvement I_{mi} must consider the differing velocities of the two clutter components. The effective clutter spectral density components C_{0e} from the two clutter sources are added to that of noise to find detection range.

3.5 EFFECTS OF DISCRETE CLUTTER

Two types of discrete clutter cause problems in radar that differ from the surface and volume clutter discussed in the previous sections:

- Echoes from moving objects such as birds or land vehicles;
- Large echoes from fixed objects on the surface, primarily manmade structures.

Radial velocities of moving objects may lie in the response band of Doppler processors and be passed to the output as targets, overloading the traffic capacity of human operators or track-while-scan channels. Echoes from large fixed objects may exceed the cancellation capability of the signal processor, producing visible clutter or alarms that impede detection and tracking of desired targets. The discrete nature of these echoes prevents their rejection by cell-averaging CFAR detectors, and other means of rejection may raise the threshold to levels that sup-

press target detection in several resolution cells including and surrounding that containing the strong clutter.

Models of both types of discrete clutter are discussed in Chapter 9, along with processing methods for its rejection. The effect of discrete clutter is not measured by a reduction in maximum detection range R_m on the desired targets. Instead, if not adequately suppressed in the signal processor, the false-alarm probability is increased, placing a burden on subsequent data processing. Adequate clutter suppression is inevitably accompanied by decreased target detection probability in some fraction of the coverage area, caused by increased loss of the signal in the suppression process.

3.5.1 Effect of False Alarms

In a track-while-scan or multifunction radar system, the data processor assigns a tracking channel to attempt track initiation at the location of an alarm that is not correlated with an existing track file. This channel is occupied for several scans after the alarm. For reliable track initiation, the number of tracking channels n_{ch} in the data processing system must be increased beyond the number n_{tr} of actual targets present:

$$n_{ch} \geq n_{tr} + n_{tin} n_r n_{az} P_{fa} + n_{tic} n_p \approx n_{tr} + \frac{n_{tin} A_m R_m^2}{2A_c} P_{fa} + n_{tic} n_p \tag{3.67}$$

where

n_{tin} = number of track initiation scans following a noise alarm;
n_r = number of range cells within R_m;
n_{az} = number of azimuth cells in the scan sector A_m;
P_{fa} = false-alarm probability for noise;
n_{tic} = number of track initiation scans following a clutter alarm;
n_p = number of unsuppressed clutter points;
A_c = area of the resolution cell given by (3.18);
$A_m R_m^2/2$ = surface area covered by scanning an azimuth sector to range R_m.

The first term on the right-hand side of (3.67) is the number of target tracks expected, the second is the average number of tracking channels consumed in attempts to validate and acquire track on noise alarms, and the third is the average number of channels consumed by similar attempts on discrete clutter. When tracking at out to an instrumented range $R_{\text{inst}} > R_m$ is desired on targets having large RCS, the range R_{inst} replaces R_m in (3.67).

3.5.2 Required Noise False-Alarm Probability

To avoid excessive burden on the data processor, P_{fa} is normally set so that the second term in (3.67) is a small fraction of the first. For example, if the maximum

number of targets expected is n_{tr} = 100, P_{fa} is set to make the second term < 10 channels. Noise alarms are uncorrelated and widely scattered in the search sector, so the number of track initiation attempts following a noise alarm can be limited to n_{tin} = 2. Thus, in our example, about five noise alarms are allowable per scan: $n_r n_{az} P_{fa} \leq 5$. In a typical search radar scanning 360°, n_r = 2,000 and n_{az} = 200, giving $n_r n_{az} = 4 \times 10^5$ resolution cells in the search sector, and requiring $P_{fa} \leq 5/n_r n_{az} = 1.25 \times 10^{-5}$. Use of higher resolution in search requires reduction in P_{fa}, increasing the required signal-to-noise ratio.

3.5.3 Requirements for Rejection of Discrete Clutter

The third term in (3.67) must be controlled by design of the signal processor. Since clutter alarms are correlated from scan to scan, attempted track initiation or recognition of a fixed echo typically requires n_{tic} = 5 scans after a clutter alarm. Accordingly, $n_p \leq 2$ clutter alarms per scan are permitted, if the track processor load for discrete clutter is to be less that 10 channels.

An important point in design of track-while-scan and multifunction radar systems is that every detectable target within the surveillance coverage must either be assigned a track file or placed in a clutter map. Otherwise there will be repeated alarms requiring attempts at track initiation. Bird statistics are such that most detections result from upward fluctuations of echoes whose average is too low to provide reliable tracking or mapping. Only discrimination using differences between target and bird RCS, altitude, or true velocity can avoid random false alarms from loading the data processor. Shrader [7, p. 2.87] describes a sensitivity-velocity control (SVC) system that combines measurements of RCS and true (unambiguous) radial velocity to perform this discrimination, using PRF diversity over several CPIs. He suggests that it is most applicable to radars operating below 1.4 GHz. For radar frequencies in the UHF or lower bands, most birds lie in the Rayleigh region where RCS varies as f_0^4, reducing the number of detectable objects. Operation in these low bands also discriminates against low-altitude objects, but these may include targets as well as birds and land vehicles.

Data from Table 9.3 show that metropolitan areas have fixed clutter sources exceeding +40 dBsm with densities up to ≈ 0.2 per km^2. The maximum range having such density is typically R_{cmax} = 20 km. The area within 20 km over a 360° scan is some 1,250 km^2, and so 250 clutter points exceeding +40 dBsm may be expected. Virtually all of these must be prevented from sending alarms to the data processor.

Suppression of fixed discrete clutter cannot be provided by cell-averaging CFAR threshold control, since the cells containing the clutter are scattered over the search area. Suppression must be provided by some combination of velocity discrimination and clutter mapping in the signal processor, as described in Section 9.6.5. Table 9.3 is based on data gathered prior to deployment of wind turbines

(Section 9.4.4), which combine large RCS, fixed locations, and large Doppler shifts. Clutter mapping appears to offer a solution to this type of fixed clutter.

3.5.4 Summary of Discrete Clutter Effects

The is no equation that describes the effect of discrete clutter on radar detection range. Discrete clutter controls the design of the signal processor, and the resulting processor losses are included in calculating the effective detectability factor D_x. High-resolution clutter maps offer a means of suppressing strong fixed clutter points at the expense of suppressing some fraction of target detections. To the extent discrete clutter passes the signal processor, the subsequent data processor must be designed to handle tracking loads greater than the number of targets actually present in the surveillance area, to avoid saturation that would result in failure to respond to actual target detections.

3.6 SIDELOBE CLUTTER

The ratio of mainlobe-to-sidelobe antenna gain is normally high enough that sidelobe clutter at the receiver input is negligible, relative to the mainlobe clutter discussed in previous sections. There are two cases, however, in which sidelobe clutter may become important:

- When the improvement factor for mainlobe clutter is much larger than that available for sidelobe clutter, due to relative motion of the radar and clutter;
- When the ratio of two-way mainlobe to sidelobe gain is insufficient to place the total sidelobe clutter power below that of the mainlobe.

Equations applicable to these situations are discussed here for both surface and volume clutter.

3.6.1 Surface Clutter in Sidelobes

The surface area contributing to clutter in the azimuth sidelobes is much larger than that given by (3.18), because the sidelobe sector (including backlobes) extends over $\pm(\pi - \theta_a) \approx \pm\pi$ radians from the beam axis. The clutter area A_c is a ring of radius $R_c \cos\psi$ centered on the surface immediately below the radar. The area is larger by a factor $\approx 2\pi L_p/\theta_a$ than that within the mainlobe:

$$A_{cs} = 2\pi R_c \frac{\tau_n c}{2} = \pi R_c \tau_n c \quad (\text{m}^2) \tag{3.68}$$

The two-way pattern-propagation factor F_{cs}^4 applicable to clutter within this area is reduced by the ratio $(G/G_s)^2$ relative to F_c^4 for mainlobe clutter, where G_s is the power gain of the azimuth sidelobes, averaged over the 2π radian ring. The far-sidelobe gain for a typical antenna is $G_s \approx -10$ dB relative to an isotropic antenna. A typical result, for a fan-beam surveillance radar antenna with mainlobe gain $G = +30$ dB and $\theta_a = 2°$, is:

$$A_{cs}/A_c = 360/\theta_a = 180 = +22.6 \text{ dB};$$
$$F_{cs}^4/F_c^4 = 10^{-8} = -80 \text{ dB};$$
$$\sigma_{cs}F_{cs}^4/\sigma_c F_c^4 = 1.8 \times 10^{-6} = -57.4 \text{ dB}.$$

This would justify neglecting the sidelobe clutter for the typical antenna in cases where the mainlobe improvement factor $I_m < 57$ dB. For land-based radars, the spectral spreading of the sidelobe and mainlobe clutter would be equal, and both would be reduced by Doppler processing.

3.6.1.1 Sidelobe Clutter in Moving Pulsed Doppler Radars

Radars using pulsed Doppler processing often achieve mainlobe clutter improvement factors $I_m > 60$ dB, using rejection notch widths that encompass the velocity spread of mainlobe clutter. When the velocity of the radar over the surface approaches or exceeds the notch width, however, I_m drops rapidly toward 0 dB, and sidelobe clutter may dominate the interference. This is the situation in shipboard radars using low-PRF pulsed Doppler waveforms (e.g., the *moving target detector,* MTD), and in airborne radars using pulsed Doppler waveforms at any PRF.

In the case of airborne MPRF and HPRF radars, the sidelobe-clutter problem is exacerbated by the presence of multiple range ambiguities, some at ranges much less than that of the target. Spectra of clutter in such radars appears as shown in Figure 3.10. For the MPRF radar, clutter occupies the entire velocity space, and detection of targets outside the mainlobe region is possible only if the sidelobe clutter spectral density is below the energy of the target by the required detectability factor D_x. With the HPRF waveform, although the clutter level is higher (because of the larger number of range ambiguities and their shorter range), a clear Doppler region exists in which detection above the noise level is possible.

3.6.1.2 Sidelobe Clutter in Low-Gain Antennas

Radar systems can be designed in which a broad-beam transmitting antenna illuminates a large area on the surface, within which the gain of narrow receiving beams and integration over long periods compensates for loss of transmitting gain. In the limit, the transmitting antenna pattern may be uniform in azimuth, and sidelobe clutter in the receiving beam is reduced only by the one-way sidelobe ratio G/G_s. In this case, the calculation of the ratio of sidelobe to mainlobe clutter,

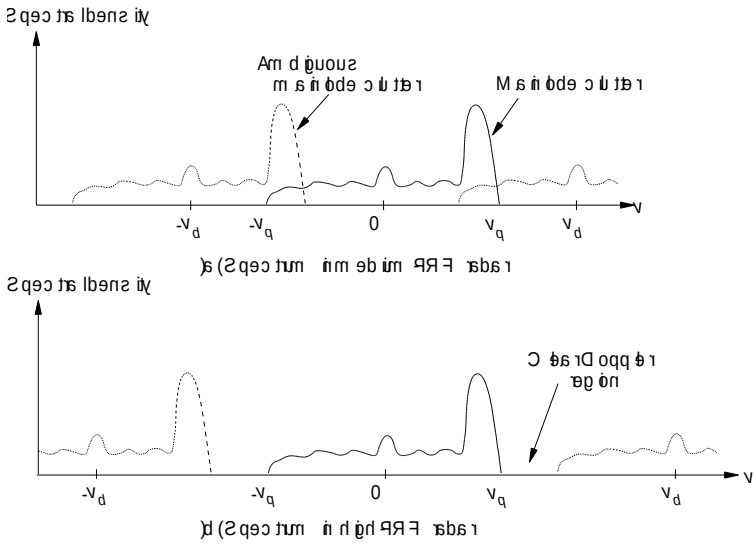

Figure 3.10 Surface clutter spectra in airborne pulsed Doppler radars: (a) medium PRF, (b) high PRF. (From [2]).

for the typical receiving antenna used in the example of the previous section, would have the following values:

$$A_{cs}/A_c = 360/\theta_a = 180 = +22.6 \text{ dB};$$
$$F_{cs}^4/F_c^4 = 10^{-4} = -40 \text{ dB};$$
$$\sigma_{cs}F_{cs}^4/\sigma_c F_c^4 = 0.018 = -17.4 \text{ dB}.$$

If the radar were moving with respect to the surface, the clutter improvement factor for the sidelobe clutter might well be insufficient to keep that clutter below the mainlobe clutter at the processor output, and application of (3.4) and (3.5) would require that $\sigma_{ci}F_{ci}^4$ include both the mainlobe and sidelobe clutter areas, with different improvement factors applied to these two components in (3.10)

3.6.2 Volume Clutter in Sidelobes

The volume contributing to clutter in the antenna sidelobes is much larger than that given by (3.45), since the sidelobe sector (including backlobes) extends over the entire hemisphere of 2π steradians about the beam axis (or 4π steradians for airborne radars). Precipitation clutter in the upper elevation sidelobes of surface-based radars is limited in range by the upper altitude limit h_{cmax} of the cloud, below which the volume V_c is:

$$V_{cs} = A_{cs} h_{c\max} = 2\pi R_c h_{c\max} \frac{\tau_n c}{2} = \pi R_c h_{c\max} \tau_n c \quad \left(\mathrm{m}^3\right) \tag{3.69}$$

where it is assumed that the cloud extends over all azimuths from the radar to range R_c.

The ratio of sidelobe clutter volume to that of the mainlobe is

$$\frac{V_{cs}}{V_c} = \frac{\pi L_p^2}{\theta_a} \frac{h_{c\max}}{R_c \theta_e} \tag{3.70}$$

For example, for a pencil-beam antenna with $\theta_a = \theta_e = 2° = 0.035$ rad, if we assume $h_{c\max} = 3$ km and $R_c = 30$ km, the volume ratio is

$$V_{cs}/V_c = \pi h_{c\max} L_{p0}^2 / R_c \theta_a \theta_e = 620 = +27.9 \text{ dB}.$$

The mainlobe gain of this antenna is $G = 6{,}700 = +38.3$ dB, and for an rms sidelobe level $G_s \approx -10$ dB relative to an isotropic antenna, we find:

$$F_{cs}^4/F_c^4 = 10^{-8} = -96.5 \text{ dB};$$
$$\sigma_{cs} F_{cs}^4/\sigma_c F_c^4 = 1.15 \times 10^{-6} = -59.4 \text{ dB}.$$

This justifies neglecting the sidelobe clutter for typical pencil-beam antennas, except in cases where the mainlobe clutter is subject to an improvement factor that is more than 59 dB greater than available for the sidelobe clutter. The velocity spectrum of precipitation clutter in sidelobes, with wind speed v_w, would extend over $\pm v_w$ and would not be expected to permit I_m as great as for mainlobe clutter.

With a transmitting beam that has uniform gain in azimuth, the pattern-propagation factor ratio becomes −48.3 dB, and a system with $I_m > 17$ dB would have to consider sidelobe volume clutter if its velocity spread placed it outside the clutter notch.

Chaff clutter would not normally extend over the entire sidelobe region, but if it did the procedure would be the same as for precipitation.

3.7 DETECTION IN NOISE JAMMING

3.7.1 Objective and Methods of Noise Jamming

Noise jamming is intended to mask the target, preventing its detection. Its effect is evaluated by including in the radar equation the effective jamming spectral density J_{0e} as a component of the interference I_{0e}.

3.7.1.1 Support Jamming

Noise jamming is primarily a *support jamming* technique [8, p. 11], in which the jammer is carried by a vehicle separated from the target to be protected. The jamming vehicle can be located at a range R_j from the victim radar beyond that of the target: $R_j > R$ (stand-off jammer, SOJ); near the target: $R_j \approx R$ (escort support jammer, ESJ); or within the target range: $R_j < R$ (stand-in jammer). The jammer is usually separated in angle from the target to lie in the sidelobes of a radar beam that illuminates the target. Jammer power is generally such that the radar is unable to measure the range of the jamming vehicle. Accurate angle data on the jammer are available, however, and these may be combined with data from other radar sites to locate the jammer by triangulation.

The support jammer is normally assigned to protect targets from several search or fire control radars, and hence must cover more than one radar frequency, often in different radar bands. To ensure this protection, *barrage noise jamming* that covers the tunable bandwidths of all victim radars is commonly used. When the available jammer power is insufficient for this mode of operation, the jammer may be controlled by an intercept receiver that measures the radar waveforms actually in use and assigns *spot jamming* that covers the bandwidth B of each radar signal. This mode requires periodic *look-through* periods [8, pp. 133–135] in which the jamming is discontinued long enough to intercept new or retuned radar threats. The so-called *smart jammer* also uses angle data from the intercept receiver system to direct high-gain jamming beams at each victim, reducing the power requirement while ensuring penetration of the radar sidelobes.

3.7.1.2 Self-Screening Jammer (SSJ)

Noise is not normally effective for self-screening, because it ensures detection of a target of interest along the *jamming strobe* produced by the large increase in noise as the mainlobe of the radar scans past the jammer. Even without range data from an individual radar, strobe angles can be used by the defense system to engage jamming vehicles within range of a weapon (e.g., using home-on-jam missiles).

An SSJ approach using noise is *cover-pulse jamming* [8, p. 145; 9, p. 227]. The noise power is increased gradually, at a time within the victim radar PRI that precedes arrival of the radar pulse at the target, to a level that increases the radar CFAR threshold (or AGC level) to suppress the target echo. The level is decreased again after arrival of the pulse. When properly implemented, the radar operator (or automatic detection circuitry) may be unable recognize that jamming has occurred, precluding generation of a jam strobe that provides angle data on the jamming vehicle. The jammer must be able to intercept the radar signal, measure the PRI, and respond at a time and with a noise burst of duration adequate to cover any variation in PRI from that previously intercepted. Thus the technique requires knowledge of the victim radar PRI, and is applicable when radars depend for de-

tection on integration of multiple pulses during a dwell, or when single-pulse dwells at almost equal intervals occur during scanning or multiple-target tracking.

3.7.2 Radar Equations for Noise Jamming

The radar equation can be used to determine the range at which a target can be detected in a given jamming environment, or the jammer power required to defeat detection at a given range.

3.7.2.1 Description of Jammer

The noise jammer is characterized by the following parameters:

P_j = transmitter power in W;
G_j = jammer antenna gain;
Q_j = jamming noise quality factor;
F_j = jammer-to-radar pattern-propagation factor;
F_{pj} = jammer-to-radar polarization factor;
B_j = noise bandwidth in Hz;
L_{tj} = jammer transmission line loss;
R_j = jammer range from radar in m;
$L_{\alpha j}$ = jammer-to-radar (one-way) atmospheric attenuation;
$L_{\text{lens}\,j}$ = jammer-to-radar (one-way) lens loss.

The *effective radiated power* (ERP) of the jammer is given by

$$\text{ERP} = P_j G_j / L_{tj} \tag{3.71}$$

ERP is a rough measure of jammer capability, but the other parameters listed must be known for a quantitative evaluation the effectiveness. An effective radiated noise power ERNP that accounts for the quality and polarization factors can be defined:

$$\text{ERNP} = \frac{Q_j P_j G_j F_{pj}^2}{L_{tj}} \tag{3.72}$$

The jamming noise quality factor Q_j describes the ability of the jammer emission to affect target detection. Ideally the noise jammer waveform is white Gaussian noise covering the radar signal bandwidth B, and $J_{0e} = J_0$. Transmission of true Gaussian noise requires that the peak power rating of the final amplifier exceed P_j by 7–10 dB [8, pp. 129–133]. To economize on size and weight, the amplifier is normally operated in the saturated mode, and frequency modulation over $B_j > B$ is used to approximate the effect of Gaussian noise in the victim receiver. The effec-

tive noise density is then given by $Q_j J_0$, where typical values of Q_j are in the range 0.3–0.6 (–5 to –2 dB).

The jammer-to-radar pattern-propagation factor F_j is the ratio of the jamming field amplitude produced at the radar antenna to the amplitude that would be produced if the radar were on the axis of the jammer antenna beam in the absence of reflection or obstruction by the jamming platform or its surroundings. The product $G_j F_j^2$ thus represents the jammer antenna power gain in the direction of the radar. Except in the smart jammer with directional response along the measured angle of intercepted signals, the beamwidth of the jammer antenna must be broad enough to cover all the assigned victim radars, and the antenna must have a clear path in the direction to the radar. Gains of 3–5 dB are typical, implying broad beams for which F_j falls off slowly with off-axis angle.

The jamming received by the radar antenna depends on the product $G_j F_j^2 G_r F_r^2$ of the effective jammer and radar antenna gains along the jammer-to-radar path, where the radar receiving pattern-propagation factor F_r, introduced in (1.16), describes departure from the on-axis, free-space receiving antenna gain. The effect of sidelobe cancellation (SLC) or adaptive array nulling in the radar is to reduce the receiving voltage gain pattern that enters into F_r. Ideally this will decrease F_r to place the jamming at or below the level of thermal noise. Practical SLC implementation limits the reduction to 15–20 dB relative to the basic sidelobe level of the antenna.

The polarization factor F_{pj} is the ratio of received jamming voltage to that of an antenna to which the jammer is matched. Among several radars in a band, more than one receiving polarization may be used. To avoid encountering a radar that is insensitive to the polarization of the jammer, the jammer antenna polarization is typically circular, or linear at ±45° from the vertical. The resulting polarization factor is $F_{pj}^2 = 0.5 = -3$ dB for any linearly or circularly polarized radar antenna. If the known types of victim radar antennas include circular polarization (e.g., for rain rejection), using the ±45° linearly polarized jammer antenna option would avoid possible orthogonal polarization.

The jamming bandwidth B_j is determined by the assigned mission. For barrage jamming, it is typically 5%–10% of the center frequency of the assigned radar band, while for spot jamming it is slightly greater than the bandwidth B of the intercepted signal, to allow for errors in measurement.

The one-way atmospheric attenuation and lens factor for the jammer are calculated by methods described in Chapter 7, using one-half the decibel values calculated for the two-way radar-target path at the same range.

3.7.2.2 Jamming Contribution to Interference

The jamming power density at the radar antenna terminal is:

$$J_0 = \frac{P_j G_j G_r \lambda^2 F_{pj}^2 F_j^2 F_r^2 F_{\text{lens}\,j}^2}{(4\pi)^2 R_j^2 B_j L_{tj} L_{\alpha j}} \tag{3.73}$$

The jamming noise quality expresses the effectiveness of the jamming waveform in interfering with radar detection, relative to white Gaussian noise. The effective jamming power density is

$$J_{0e} = Q_j J_0 = \frac{Q_j P_j G_j G_r \lambda^2 F_{pj}^2 F_j^2 F_r^2 F_{\text{lens}\,j}^2}{(4\pi)^2 R_j^2 B_j L_{tj} L_{\alpha j}} \tag{3.74}$$

This density is added to other interference terms in (3.2) to evaluate the radar detection range using any of the radar equations developed for the thermal noise environment. However, if only thermal and jamming noise are present at the receiver input within the range interval in which detection is obtained, it is convenient to express the jamming as an *equivalent temperature* T_j [3, p. 29], given by

$$T_j = \frac{J_{0e}}{k} = \frac{Q_j P_j G_j G_r \lambda^2 F_{pj}^2 F_j^2 F_r^2 F_{\text{lens}\,j}^2}{(4\pi)^2 R_j^2 k B_j L_{tj} L_{\alpha j}} \quad \text{(K)} \tag{3.75}$$

In the presence of one or more jammers, 1, 2, … *i*, the system input noise T_s in the radar equation is replaced by

$$T_s' = T_s + \sum_i T_{ji} \quad \text{(K)} \tag{3.76}$$

The maximum detection range with the jamming present is denoted by R_{mj}, replacing R_m while T_s' replaces T_s in (1.26):

$$R_{mj}^4 = \frac{P_{av} t_f G_t G_r \lambda^2 \sigma F_p^2 F_t^2 F_r^2 F_{\text{lens}}^2}{(4\pi)^3 k T_s' D_x(n') L_t L_\alpha(R_{mj})} \quad \text{(m)} \tag{3.77}$$

This is called the *burnthrough range* against the noise jammer.

3.7.3 Examples of Noise Jamming

3.7.3.1 Barrage Jamming

Consider the barrage jammer parameters listed in Table 3.3, operating at R_j = 150 km against the example radar of Table 3.1, several of which may lie in the operat-

ing area and be assigned as victims for the jammer. The targets to be protected by the jamming have 1-m^2 RCS, and in the absence of jamming are detectable with P_d = 50% at R_m = 93 km from the radar, where the single-sample SNR = $D_x \approx 20$ dB. It is desired to find the number of jammers required mask these targets at R_{mj} = 40 km from the radar. The pattern-propagation factor F_j = –25 dB shown in the table results from jamming through major radar antenna sidelobes, with some allowance for radars that are not on the axis of the jammer antenna mainlobe. No sidelobe cancellation is assumed.

Table 3.3 Example Barrage Jammer

Radar frequency band	X-band	Radar tunable bandwidth	500 MHz
Transmitter power P_j	1 kW	Jammer antenna gain G_j	10 dB
Jammer transmission loss L_{tj}	1.0 dB	Jammer ERP	8 kW
Noise quality factor Q_j	–2 dB	Jammer polarization factor F_{pj}^2	–3 dB
Jammer ERNP	2.5 kW	Pattern-propagation factor F_j^2	–25 dB
Noise bandwidth in MHz, B_j	500 MHz	Jammer range R_j	100 km
Atmospheric loss $L_{\alpha j}$	0.8 dB	Lens factor $F_{\text{lens}j}^2$	–0.1 dB
Screening range R_{mj}	40 km		

The first step is to determine from (1.26) the noise temperature required to reduce the detection range from R_m = 93 km to R_{mj} = 40 km:

$$\begin{aligned} T_j = T_s' - T_s &= T_s \left[\left(\frac{R_m}{R_{mj}} \right)^4 \frac{L_\alpha(R_m)}{L_\alpha(R_{mj})} \frac{F_{\text{lens}}^2(R_{mj})}{F_{\text{lens}}^2(R_m)} - 1 \right] \\ &= 1{,}000\text{K} \left[\left(\frac{93}{40} \right)^4 \frac{1.53}{1.23} \frac{0.98}{0.96} - 1 \right] = 3.5 \times 10^4 \text{K} \end{aligned} \tag{3.78}$$

where T_j/T_s is given by the fourth power of the range ratio, multiplied by the ratio of atmospheric and lens losses for the radar at R_m to those losses at R_{mj}. The input noise temperature T_s = 1,000K in this example must be increased by a factor of 37 = 15.5 dB to obtain the range reduction factor of 93/30. The required jamming temperature can be compared to the temperature for a single barrage jammer of Table 3.3, given by (3.75):

$$T_{j1} = \frac{Q_j P_j G_j G_r \lambda^2 F_{pj}^2 F_j^2 F_{\text{lens}j}^2}{(4\pi)^2 R_j^2 k B_j L_j L_{\alpha j}}$$

$$= \frac{0.63 \times 1{,}000 \times 10 \times 1.86 \times 10^4 \times 0.03^2 \times 0.5 \times 0.0032 \times 0.98}{(4\pi)^2 \times (100 \times 10^3)^2 (1.38 \times 10^{-23})(500 \times 10^6) \times 1.26 \times 1.2} = 10^4 \text{ K}$$

Four jammers are required to provide adequate masking. If the jammers are carried by aircraft orbiting on a racetrack course at R_j = 100 km with selectable antennas on either side of each aircraft, five aircraft and jammers would be required, four to maintain the screen while a fifth performs a 180° turn to maintain its orbit. The high power and number of jammers shows the problem in barrage jamming of multiple radars.

3.7.3.2 Spot Jamming

Spot jamming based on signal intercepts from periodic look-through is an option, because the victim radars used as in the example in the preceding section require multiple-pulse integration for detection. The jammer parameters of Table 3.3 would apply, except that emission would be concentrated in several narrow bands (e.g., 10 MHz each) identified by the intercepts. If there were five such bands, the total bandwidth would be B_j = 50 MHz instead of 500 MHz, increasing the jamming density by a factor of 10:

$$T_{j1} = 10^5 \text{K}$$

The screening for a single 1-kW jammer would be effective to range $R_{mj} \approx 31$ km, or P_j = 370W would suffice, assuming that the jammer antenna could cover continuously the azimuth sector occupied by the radars.

Spot jamming becomes difficult if each radar uses frequency diversity to force the jammer to cover many spot frequencies in the band. Pulse-to-pulse frequency agility forces a return to barrage jamming, but precludes implementation of MTI by the radars. This suggests the advantage of combining passive ECM (chaff) with active jamming, to force the radar to use bursts of coherent pulses subject to interception and spot jamming.

3.7.3.3 Self-Screening Noise Jamming

Relatively low powers provide self-screening on the axis of the radar mainlobe (F_j = 1). The effect of the 1-kW jammer in Section 3.7.3.1 can be produced with 3W jammer power in the mainlobe. A special range equation gives the burnthrough range for this case:

$$R_{bt}^2 = \frac{P_{av} t_f G_t \sigma F_p^2 F_t^2 B_j L_j}{4\pi Q_j P_j G_j F_{pj}^2 D_x(n') L_t} \tag{3.79}$$

where n' is the number of coherent outputs integrated following envelope detection, and $B_j \geq B$. This equation is derived from (1.26) by replacing T_s by T_j from (3.75) and setting $R_{bt} = R_{mj} = R_j$.

Using the example jammer from Table 3.4 for self-screening, the burnthrough range of the example radar is

$$R_{bt} = \left[\frac{100 \times 0.01 \times 1.86 \times 10^4 \times 1.0 \times 1.0 \times 1.0 \times 500 \times 10^6 \times 1.26}{4\pi \times 0.63 \times 1,000 \times 10 \times 0.5 \times 6.3 \times 1.0} \right]^{1/2} = 1,720 \text{ m}$$

A smaller jammer with P_j = 10W and G_j = 3.2 = 5 dB still achieves a burnthrough range of 31 km, adequate for most operations against the example radar. These ranges are obtained with barrage noise covering 500 MHz.

The preceding calculations apply also to a self-screening noise jammer using the cover-pulse technique. The noise power P_j is the level after the jammer has reached its full output. In a typical case, the duty cycle of such a jammer would be ≈ 10% for each radar being jammed, and the average power would be correspondingly lower. This type of jammer adjusts its output power based on the level of received pulses in order to minimize the chances that a jam strobe would be generated. If implemented using a digital RF memory (DRFM), the noise bandwidth would also be restricted to spot jamming centered on the radar frequency, making it possible to use very low power levels that would further reduce the probability of jam-strobe generation.

3.8 DECEPTIVE JAMMING

In deceptive jamming (also called deceptive ECM or DECM), the emissions are designed to appear as radar echoes at locations where no target actually exists. The purpose is to introduce confusion into the radar system and the network that uses the radar data, and possibly to saturate the data processor to impede or prevent reliable tracking of actual targets. There are two types of deceptive jammers [9, p. 86]:

> Transponder jammers generate noncoherent returns that emulate the temporal characteristics of the actual radar return. Repeaters generate coherent returns that attempt to emulate the amplitude, frequency, and temporal characteristics of the actual radar return.

The repeater jammer has become the preferred method for creating synthetic targets that are realistic enough to pass from the radar processor into the data stream.

This type of jammer includes an intercept receiver, a memory to store features of the radar waveform, and a modulated transmitter in which the radar waveform is regenerated with time delays and Doppler shifts that correspond to false target positions and velocities.

Deceptive jammers are used extensively against tracking radars that are elements of a fire-control system. Their use in this application is designed to prevent the fire control radar from locking on the target, or to break lock if the radar has already locked on. A number of sophisticated techniques are available for this purpose, the success of which generally requires the transmission of the selected jamming waveform at high very jamming-to-signal ratios. The evaluation of the effectiveness of this type of jamming does not generally lend itself to analysis, and testing using the actual radar and jamming equipment (or hardware simulators) is usually required.

The current technology for waveform storage is the digital RF memory (DRFM). The operation of this device is described in [9, Chapter 5], and will not be repeated here. The state of the art has advanced steadily, providing the ability to store and regenerate most radar signals with adequate accuracy and with controllable time delays and Doppler shifts. The accompanying intercept receiver is also implemented digitally [10].

A significant challenge to repeater jamming is the presence of multiple radar signals that overlap in time and have large time-bandwidth products. This causes cross-products to appear in the jammer output when overlapping signals are processed through nonlinear circuits in the repeater.

3.8.1 Range Equations for Deceptive Jamming

Deceptive jammers operate by responding to individual pulses received from the radar, with time delay, Doppler shift, or modulations that prevent proper operation of the radar or interpretation of its data. The applicable range equations are based on single-pulse peak power level rather than energy levels over a CPI.

3.8.1.1 Transponder Equations

A transponder is used to generate false targets in a radar that uses noncoherent integration (as opposed to a pulsed Doppler process). The transponder response is triggered by an incoming pulse from the radar, but is generated by an RF source that does not maintain phase coherence with the received pulse. The transponder is characterized by the following parameters:

G_j = jammer antenna gain;
F_{pj} = jammer-to-radar polarization factor;
F_j = jammer-to-radar pattern-propagation factor;
$F_{\text{lens}\,j}$ = jammer-to-radar (one-way) lens factor.

$S_{\min j}$ = transponder sensitivity in W;[7]
P_j = peak response power in W;
L_j = transmission or reception line loss;
$L_{\alpha j}$ = jammer-to-radar (one-way) atmospheric attenuation;

It is assumed here that the antenna gain and patterns and the line losses are identical for transmitting and receiving, and that the response pulsewidth is the same as that of the radar transmission.

For a radar with ERP = $P_t G_t / L_t$, the range R_{rt} at which a transponder response is triggered is found as

$$R_{rt} = \left(\frac{P_t G_t G_j \lambda^2 F_{pj}^2 F_t^2 F_j^2 F_{\text{lens}\,j}^2}{(4\pi)^2 S_{\min j} L_t L_j L_{\alpha j}} \right)^{1/2} \tag{3.80}$$

The corresponding range at which the radar detects the response is

$$R_{mt} = \left(\frac{P_j G_j G_r \lambda^2 F_{pj}^2 F_r^2 F_j^2 F_{\text{lens}\,j}^2}{(4\pi)^2 S_{\min r} L_j L_{\alpha j}} \right)^{1/2} \tag{3.81}$$

where $S_{\min r}$ is the minimum single-pulse signal power at the radar for given detection probability P_d. A probability P_d = 90% should be used for reliable transponder jamming. In terms of the radar parameters used in Chapter 1:

$$S_{\min r} = \frac{kT_s D_0(n) M L_p L_x}{\tau} = \frac{kT_s D_x}{\tau} \frac{L_i}{nL_f} \tag{3.82}$$

where $D_0(n)$ is the steady-signal, single-pulse SNR required for P_d, assuming n-pulse noncoherent integration with loss L_i, and L_f, M, L_p, and L_x are the loss factors used to determine D_x in (1.26).

As an example, consider the radar described in Table 3.1, transmitting 1-μs pulses, and transponder characteristic listed in Table 3.4. The pattern-propagation factor F_j^2 = –30 dB is chosen to allow response in the radar's sidelobe region. The sensitivity is typical of a receiver using a low-noise RF amplifier followed by a square-law detector and video amplifier [8, p. 429].

---

[7] The usual transponder specification gives the *tangential sensitivity*, corresponding to a signal-to-noise ratio of +4 dB at the input of a square-law detector [8, p. 427]. For reliable triggering, $S_{\min j}$ should be several decibels above that level. Receiver sensitivity is commonly specified in dBm (decibels with respect to 1 mW).

Table 3.4 Example Transponder Jammer

Radar frequency band	X-band	Transmitter peak power P_j	50W
Antenna gain G_j	10 dB	Transmit or receive loss L_j	1.0 dB
Polarization factor F_{pj}^2	–3 dB	Pattern-propagation factor F_j^2	–30 dB
Atmospheric loss $L_{\alpha j}$	0.9 dB	Lens factor $F_{\text{lens}\,j}^2$	–0.1 dB
Sensitivity $S_{\min j}$	–70 dBm		

Application of (3.80)–(3.82) with parameters from Tables 3.1 and 3.4 gives the following results:

Range for triggering response: R_{rt} = 366 km
Radar receiver sensitivity: $S_{\min r}$ = –100.6 dBm
Range for detection of response: R_{mt} = 311 km

3.8.1.2 Repeater Equations

The repeater differs from the transponder in that it accepts the signal received with antenna gain G_j, amplifies it with electronic gain G_e, and retransmits it with antenna gain G_j, and usually with duty cycle $D_u < 0.5$ to avoid self-oscillation. Design of the repeater is based on responding with a power representing a target with radar cross section σ_e, viewed by the radar mainlobe at range R_j.

Radar cross section may be considered in terms of an equivalent sphere of radius r having projected area πr^2. Scattering from the sphere is isotropic, so the RCS may be regarded as the product of the projected area and an isotropic gain $G = 1$:

$$\sigma = AG = \pi r^2 \tag{3.83}$$

An idealized repeater passes the incoming radar pulse received in aperture area $A_e = G_r\lambda^2/4\pi$ directly to the transmitting antenna with gain G_j, producing an equivalent RCS given by

$$\sigma_e = A_e G_t = \frac{G_r G_t \lambda^2}{4\pi} \tag{3.84}$$

From this, the idealized repeater gain G_{rep} required for a specified σ_e is

$$G_{\text{rep}} = G_r G_t = \frac{4\pi\sigma_e}{\lambda^2} \tag{3.85}$$

In practice, repeater antennas are too small to provide this gain, and the repeater gain is increased by electronic amplification G_e placed between G_r and G_t,

which must also overcome RF losses L_{jr} and L_{jt} within the repeater, in the pattern-propagation factors F_{jr} and F_{jt} of the receiving and transmitting paths, and in their polarization factors F_{pjr} and F_{pjt}. Assuming equal gains and losses for receiving and transmitting, and use of gating with duty cycle D_u to isolate the receiver from the transmitter, the required electronic gain G_e, as derived in [8, p. 424], is

$$G_e = \frac{4\pi\sigma_e L}{\lambda^2 G_j^2 D_u^2} = \frac{4\pi\sigma_e L_j^2}{\lambda^2 G_j^2 D_u^2 F_{pj}^4 F_j^4} \tag{3.86}$$

The second form of (3.86) replaces L from [8] with the two-way RF loss within the repeater and the two-way polarization and pattern-propagation factors. The factor F_j^4 is included on the assumption that a repeater located off the axis of the radar beam, and possibly in the radar sidelobes, is intended to reproduce the signal power that would result from an on-axis target with RCS equal to σ_e.

An escort repeater located in a region of –30 dB sidelobes, with the same parameters as were used for the transponder example, Table 3.4, requires a very large electronic gain:

$$G_e = \frac{4\pi \times 10 \times 1.58}{0.03^2 \times 10^2 \times 0.5^2 \times 0.001^2} = 8.86 \times 10^9 = +99.4 \text{ dB}$$

A stand-off repeater would require even greater gain to account for the ratio $(R_j/R)^4$. Gains of this sort would apply, for example, to escort or stand-off DRFM jammers. The signal power received from the example radar at R_j = 100 km is –58.4 dBm, and the RF receiver gain brings this to a level high enough to drive the DRFM. The DRFM is followed by A/D conversion and sufficient RF transmitter gain to raise the analog signal to the required output power of 12.6W = +41 dBm. Introduction of time gating and delay between intercept and transmission of the signal prevents self-oscillation.

For a self-protection repeater (F_j = 1) the required electronic gain is +39.5 dB (input signal –25.8 dBm, output power +13.7 dBm). Additional gain would be required to overcome the duty-cycle loss inherent in a self-protection jammer, since it cannot isolate the output from the input with gating and time delay, and must operate as a straight-through repeater.

Note that these range equations do not describe limits to radar detection range, but rather jammer requirements that allow the radar to trigger and receive the deceptive emission. The effect on the radar depends on factors other than range equations.

3.9 SUMMARY OF DETECTION IN JAMMING

3.9.1 Range with Noise Jamming

Noise jamming is used for masking of targets, and is usually generated by a support jammer. The steps in calculating detection range are as follows.

- The jamming noise density J_0 is calculated from (3.73).
- The jamming density J_0 is converted to an effective value by applying the jamming quality factor Q_j, according to (3.74)
- The equivalent jamming temperature T_j is found by dividing J_{0e} by Boltzmann's constant, according to (3.75).
- If more than one jammer is present, their noise temperatures are summed and added to the system temperature to find the total input noise temperature T_s', according to (3.76).
- The maximum detection range is found by substitution of T_s' for T_s in (1.26).

When noise is used for self-screening, these steps are replaced by calculations of a burnthrough range from (3.79).

3.9.2 Deceptive Jammer Equations

The jammer sensitivity, gain, and output power required for deceptive jamming are given by (3.80)–(3.86). Radar detection range on targets is affected only if the deceptive jamming distracts the operator or automatic circuitry from otherwise detectable signals.

3.10 DETECTION IN COMBINED INTERFERENCE

The range equations given for special cases in preceding sections apply to combinations of jamming and thermal noise. When clutter is present as well, at the ranges where target detection is required, it is necessary to calculate the effective spectral densities of the several interference components and add these to find, at each range, effective total interference level I_{0e} from (3.2). That level then replaces $N_0 = kT_s$ in (1.26) or similar equations for maximum detection range. The definitions of effective interference spectral density take into account the properties of the signal processor, so there is no need to make further adjustment for "processing gain" or other factors sometimes appearing in the literature.

The constraints imposed by multiple, simultaneous interference components on the choice of waveform and processing method must not be ignored, however.

Measures that improve the performance with one type of interference often increase vulnerability to others. A notable example is the combination of active jamming with chaff or natural clutter. Use of frequency agility to overcome spot jamming is precluded by presence of any type of clutter at the required detection range (or its ambiguities), since Doppler processing for clutter rejection requires waveforms that maintain coherence over the coherent processing interval (CPI). Responsive jammers can measure the signal properties on pulses early in each CPI and achieve masking by responding to subsequent pulses.

Another constraint is imposed by presence of clutter at ranges both within and beyond the unambiguous range of the waveform. While there is a theoretical potential for cancellation of multiple-time-around clutter with staggered PRI waveforms, uniform-PRI waveforms are required in practice. Coherent processing must start only after clutter from the longest ranges has entered the receiver. If blind speeds exist within the spectrum of potential targets, PRI diversity from one pulse group to the next is necessary to fill those gaps, increasing the required dwell time. This imposes a burden especially on scanning-beam radars that perform search scans within tightly constrained time budgets.

Waveform and processor requirements for different environments are discussed in Chapter 9.

References

[1] IEEE Standard 100, *The Authoritative Dictionary of IEEE Standards Terms*, 7th ed., New York: IEEE Press, 2000.

[2] Barton, D. K., *Radar System Analysis and Modeling*, Norwood, MA: Artech House, 2005.

[3] Blake, L. V., *Radar Range-Performance Analysis*, Lexington, MA: D. C. Heath, 1980; Dedham, MA: Artech House, 1986.

[4] Barton, D. K. and H. R. Ward, *Handbook of Radar Measurement*, Englewood Cliffs, NJ: Prentice-Hall, 1968; Dedham, MA: Artech House, 1984.

[5] Goldstein, H., "Sea Echo," Section 6.6, and "Meteorological Echoes," Chapter 7, in *Propagation of Short Radio Waves*, Vol. 13 in MIT Radiation Laboratory Series, New York: McGraw-Hill, 1951. Reprinted (CD ROM edition), Artech House, 1999.

[6] Doviak, R. J. and D. S. Zrnic, *Doppler Radar and Weather Observations*, 2nd ed., New York: Academic Press, 1993.

[7] Shrader, W. W. and V. Gregers-Hansen, "MTI Radar," Chap. 2 in *Radar Handbook*, 3rd ed., (M. I. Skolnik, ed.), New York: McGraw-Hill, 2008.

[8] Schleher, D. C., *Introduction to Electronic Warfare*, Dedham, MA: Artech House, 1986.

[9] Schleher, D. C., *Electronic Warfare in the Information Age*, Norwood, MA: Artech House, 1999.

CHAPTER 4

Detection Theory

The first step in derivation of the radar equation in Chapter 1 was to express through (1.9) the ratio E/N_0 of signal-to-noise energy *available* at target range R. The second step expressed the ratio *required* for each of n pulses to achieve target detection. For an idealized radar we call this value, denoted by $D(n)$, the *basic detectability factor*: the signal-to-noise ratio derived from the theory of target detection before application of losses encountered in practical radar systems. The maximum range R_m is that at which $E/N_0 = D(n)$. This chapter summarizes methods of calculating $D(n)$ for different radar waveforms and target models. Chapters 5, 9, and 10 discuss the losses that increase the requirement for input energy ratio from $D(n)$ to $D_x(n)$, the *effective detectability factor* that must be used in a complete radar equation such as (1.22).

4.1 BACKGROUND

Blake [1] summarizes the refinement of the radar range equation at the Naval Research Laboratory in years following WWII. He defines the *visibility factor* V_0 as the single-pulse signal-to-noise energy ratio E/N_0 required to obtain a specified probability of detection P_d when n pulses are integrated on a cathode-ray-tube display for visual detection by a human operator. He generalizes this to the detectability factor $D(n)$ for radars in which integration and detection is performed electronically or digitally. This factor appears in (1.16) and other simplified forms of the radar equation. It represents a theoretical value for each of n pulses received with equal power, passed through a matched filter along with white Gaussian noise, envelope detected, integrated noncoherently with equal weights, and applied to the detection threshold.

Because the idealized radar receiver is matched to the signal spectrum, the signal-to-noise power ratio S/N delivered to the envelope detector equals the energy ratio E/N_0 at the radar input. The detectability factor $D(n)$ is expressed by theoretical equations that are based on S/N at the input to the envelope detector.

Exact equations have been developed giving the detection probability for several statistical target models. These equations are complex, requiring numerical integration or reference to special tabulated functions. As a result, much of the literature on radar detection is devoted to development of approximations that permit quick calculation of P_d for given signal-to-noise power ratio S/N, and vice versa, avoiding the theoretical equations required for exact solutions. Many pages (and an entire book) of graphs have been published showing P_d as a function of S/N, for different target models and with specific values of P_{fa} and n. The graphs provide insight into the effects on detection of different radar and target characteristics, but numerical values with adequate accuracy for use in the radar equation are best found by solving the underlying equations, either exactly or approximately.

Personal computers and mathematical programs such as Mathcad® and MATLAB® can provide rapid and accurate solutions of the exact detection equations. Built-in Bessel, gamma, and other functions simplify use of these equations, and the root-finding ability of the mathematical platforms provides results when there is no closed-form expression for $D(n)$ as a function of P_d. Where repetitive calculation of multiple values is required, reasonably accurate approximations are available to minimize computation time. The procedures outlined in this chapter, available as a Mathcad program in the accompanying DVD, are described here to permit implementation in any programming language. Approximations of varying complexity and accuracy are also given.

4.2 STEADY-TARGET DETECTABILITY FACTOR

The basic detectability factor for a steady (nonfluctuating) target (Case 0) is denoted by $D_0(n)$. It is the theoretical value derived by Rice [3] for a single pulse, and by Marcum [4, 5] for n noncoherently integrated pulses. Exact expressions are given by DiFranco and Rubin [6], whose comprehensive work provides the basis for much of this chapter.

The input parameters required for calculation of D_0 are:

- Detection probability P_d;
- False-alarm probability P_{fa};
- Number n of envelope-detected pulses integrated.

In coherent radar applications, n is replaced by $n' = t_o/t_f$, the number of *samples* from prior coherent integration, where t_o is the observation (integration) time and t_f is the coherent integration time.

Notations used here are translated from those in the referenced literature (e.g., number of pulses N and signal-to-noise energy ratio $\mathcal{R}_p/2$ in [6] are replaced by n and s). The factor $D_0(n)$ is denoted by $D_0(P_d, P_{fa}, n)$ and the detection probability P_d by $P_d(s, n, P_{fa})$ in some equations, to emphasize the dependence on all three input parameters. A simple s replaces the signal-to-noise power ratio S/N, for compactness.

4.2.1 Exact Steady-Target Detection Probability

The steady target is seldom found in practice, but it serves as a useful reference, generally giving the lower limit of $D(n)$. An exact expression for detection probability, assuming a square-law detector,[1] is [6, p. 348, Eq. (10.4-27)]:

$$P_{d0}\left(s, n, y_b\right) = 1 - \int_0^{y_b} \left(\frac{y}{ns}\right)^{\frac{n-1}{2}} \exp\left(-y - ns\right) I_{n-1}\left(\sqrt{4nsy}\right) dy \tag{4.1}$$

where

s	=	S/N = signal-to-noise power ratio at the input of the envelope detector;
n	=	number of pulses integrated;
y_b	=	threshold voltage normalized to rms noise at detector output;
y	=	sum of detector output voltages for n pulses;
$I_n(x)$	=	modified Bessel function of the first kind of order n.

4.2.2 Threshold Level

To apply (4.1) we must first establish the threshold level y_b that is the upper limit of the integral. Exact and approximate solutions for this threshold, which is common to all target models, are given here, before we return to calculations of detection probability.

The probability of false alarm for a system that integrates n pulses is given by [6, p. 347, Eq. (10.4-18)]:

---

[1] The relative performance of square-law and linear detectors is discussed by Marcum [5, pp. 35, 99], showing that the difference is < 0.1 dB, favoring the linear detector for $2 \le n < 70$ and the square-law for $n > 70$, with equal performance for $n = 1$ and $n = 70$. We will consider here only the square-law detector.

$$P_{fa} = \frac{1}{(n-1)!}\int_{y_b}^{\infty} y^{n-1}e^{-y}dy = 1 - \frac{1}{(n-1)!}\int_{0}^{y_b} y^{n-1}e^{-y}dy \tag{4.2}$$

The last term in (4.2) is the *incomplete gamma function* [7, p. 260, Eq. (6.5.1)]:

$$P_{\gamma}(x,n) = \frac{1}{\Gamma(n)}\int_{0}^{x} e^{-t}t^{n-1}dt = 1 - P_{fa} \tag{4.3}$$

We use the symbol P_{γ} to avoid confusion with other symbols, and to emphasize that the incomplete gamma function expresses a probability. The function $\Gamma(n)$ in (4.3) replaces $(n-1)!$ in (4.2) to extend the expression to noninteger values of n. The false-alarm probability can be expressed in terms of the incomplete gamma function:

$$P_{fa} = 1 - P_{\gamma}(n, y_b) \tag{4.4}$$

Note that $P_{\gamma}(x,n)$ differs from Pearson's incomplete gamma function $I(x,n)$ used in [6, p. 347, Eq. (10.4-19)]:

$$\begin{aligned} I(x,n) &= P_{\gamma}\left(x\sqrt{n+1}, n+1\right) \\ P_{\gamma}(x,n) &= I\left(\frac{x}{\sqrt{n-1}}, n-1\right) \end{aligned} \tag{4.5}$$

Care is needed to ensure that tabulated incomplete gamma functions or those built into computer programs[2] are defined consistently with (4.3). This and similar functions in other mathematical programs permit rapid evaluations without numerical integration.

The solution of (4.4) for threshold level requires either a root-finding algorithm or implementation of the inverse function $P_{\gamma}^{-1}(p,n)$:

$$y_b\left(P_{fa}, n\right) = \text{root}_{y_b}\left[P_{fa} = 1 - P_{\gamma}\left(y_{b,n}\right)\right] = P_{\gamma}^{-1}\left(1 - P_{fa}, n\right) \tag{4.6}$$

[2] Mathcad has a built-in function $P_{\gamma}(x,n)$, denoted by *pgamma*(x,n) and its inverse function $P_{\gamma}^{-1}(p,n)$, denoted by *qgamma*(p,n), using algorithms derived from [7, p. 263]. Another function $\Gamma(n,x)$ built into Mathcad is the integral in (4.3) without the factorial term $(n-1)!$ or $\Gamma(n)$.

where the notation $\text{root}_{y_b}\left[\, p = f\left(y_b\right)\right]$ denotes the value of y_b that yields equality in the bracketed expression.

If root-finding or the inverse of the incomplete gamma function is not available, or is computationally burdensome, an excellent approximation to the inverse of (4.3) has been developed [8, 9]. In this method, applicable to either square-law or linear envelope detectors, the threshold is expressed as a function of the mean and standard deviation of the detected noise voltage:

$$y_b = m_x + k_t \sigma_x = n m_1 + k_t \sqrt{n}\sigma_1 \tag{4.7}$$

where

m_x = mean of integrated output voltage;
m_1 = single-pulse mean voltage (= 1 for square-law detector);
σ_x = standard deviation of integrated output voltage;
σ_1 = single-pulse standard deviation (= 1 for square-law detector);
k_t = threshold constant.

For the square-law detector, the k_t for $n = 1$ is simply $k_{t1} = -\ln(P_{fa}) - 1$, while for $n \to \infty$ it is $k_{t\infty} = \Phi^{-1}(P_{fa})$, where $\Phi(\cdot)$ is the integral of the normal distribution and $\Phi^{-1}(\cdot)$ is the inverse function:

$$\begin{aligned} \Phi\left(E\right) &= \frac{1}{\sqrt{2\pi}} \int_E^{\infty} \exp\left(-\frac{v^2}{2}\right) dv = P \\ \Phi^{-1}\left(P\right) &= E \end{aligned} \tag{4.8}$$

These normal probability functions have been tabulated and are built into many calculators and mathematical programs, making numerical integration unnecessary. Interpolation for k_{tn} over $1 \le n \le \infty$ gives

$$k_{t\,n}\left(P_{fa}\right) = k_{t\infty}\left(P_{fa}\right) + \frac{k_{t1}\left(P_{fa}\right) - k_{t\infty}\left(P_{fa}\right)}{\left[1.1\left(n-1\right)+1\right]^{0.51}} \tag{4.9}$$

from which $y_b(P_{fa},n)$ is found using (4.7):

$$y_b\left(P_{fa,n}\right) \approx n + \sqrt{n}\left\{\Phi^{-1}\left(P_{fa}\right) - \frac{\Phi^{-1}\left(P_{fa}\right) + \ln P_{fa} + 1}{\left[1.1\left(n-1\right)+1\right]^{0.51}}\right\} \tag{4.10}$$

Neither integration nor root-finding is needed, assuming that the inverse normal distribution function $\Phi^{-1}(P_{fa})$ is available from analytic approximations [7, p. 933, Eq. (26.2.23)]. Equation (4.10) is accurate within ±0.15 dB for $n \le 100$ and $P_f \le 0.1$. The method provides accurate inversion of the incomplete gamma function when that is not available as a built-in function:

$$p = P_\gamma(y,n) \quad \leftrightarrow \quad y = P_\gamma^{-1}(p,n)$$
$$P_\gamma^{-1}(p,n) \approx n + \sqrt{n}\left\{\Phi^{-1}(p) - \frac{\Phi^{-1}(p) + \ln p + 1}{\left[1.1(n-1)+1\right]^{0.51}}\right\} \tag{4.11}$$

This inversion, valid for $p < 0.95$, will prove useful in calculations for the Swerling and other chi-square target models in Section 4.3.

4.2.3 Exact Steady-Target Detectability Factor

The radar equation does not include P_d, requiring instead the detectability factor $D(n)$ that supports the specified P_d. Since (4.1) for P_d cannot be inverted to obtain a closed-form expression for $D(n)$, the detectability factor is found by solving for $D_0(n) = s$:

$$D_0(n) = s = \text{root}_s\left[P_{d0}(s,n,Y_b) = 1 - \int_0^{y_b}\left(\frac{y}{ns}\right)^{\frac{n-1}{2}} \exp(-y-ns)\, I_{n-1}\left(\sqrt{4nsy}\right) dy\right] \tag{4.12}$$

If root-finding is not available or is too computationally burdensome, approximate methods described in Section 4.2.6 can be used.

4.2.4 Exact Single-Pulse, Steady-Target Detectability Factor

The detection probability for a single pulse on a steady target is obtained by integrating the Rician distribution [3] of signal-plus-noise voltage to find P_d as the fraction of the distribution lying above the threshold:

$$P_d = \int_{E_t}^{\infty} \frac{E_n}{N} \exp\left(-\frac{E_s^2 + E_n^2}{N}\right) I_0\left(\frac{E_n E_s}{N}\right) dE_n \tag{4.13}$$

where

E_n = instantaneous noise voltage;
N = average noise power;
E_s = peak signal voltage;
E_t = threshold voltage;
I_0 = modified Bessel function of the first kind.

The signal-to-noise power ratio is

$$s = \frac{S}{N} = \frac{E_s^2}{2N} \tag{4.14}$$

The threshold voltage is found from the false-alarm probability by setting $E_s = 0$ in (4.13):

$$\begin{aligned} P_{fa} &= \int_{E_t}^{\infty} \frac{E_n}{N} \exp\left(-\frac{E_n^2}{2N}\right) dE_n = \exp\left(-\frac{E_t^2}{2N}\right) \\ E_t &= \sqrt{2N \ln\left(1/P_{fa}\right)} \end{aligned} \tag{4.15}$$

Figure 4.1 is a plot of P_d as a function of S/N, obtained from (4.1) with thresholds corresponding to different values of P_{fa}. For a given P_{fa}, the value of $D_0(1)$ can be read from Figure 4.1 to within ≈0.1 dB for any required P_d, or vice versa. Exact values can be calculated using the root of (4.13):

$$D_0(1) = \text{root}_{E_s^2/2N}\left[P_d = \int_{E_t}^{\infty} \frac{E_n}{N} \exp\left(-\frac{E_s^2 + E_n^2}{N}\right) I_0\left(\frac{E_n E_s}{N}\right) dE_n\right] \tag{4.16}$$

4.2.5 Approximations for Single-Pulse, Steady-Target Detectability Factor

To avoid integration and root-finding, closed-form approximations for P_d and D_0 can be derived using North's approximation [10]:

$$P_d = \Phi\left[\frac{E_t}{\sqrt{N}} - \sqrt{2s+1}\right] = \Phi\left[\sqrt{2\ln\left(1/P_{fa}\right)} - \sqrt{2s+1}\right] \tag{4.17}$$

$$D_0(1) = \frac{1}{2}\left[\frac{E_t}{\sqrt{N}} - \Phi^{-1}\left(P_d\right)\right]^2 - \frac{1}{2} = \left[\sqrt{\ln\frac{1}{P_{fa}}} - \frac{1}{\sqrt{2}}\Phi^{-1}\left(P_d\right)\right]^2 - \frac{1}{2} \tag{4.18}$$

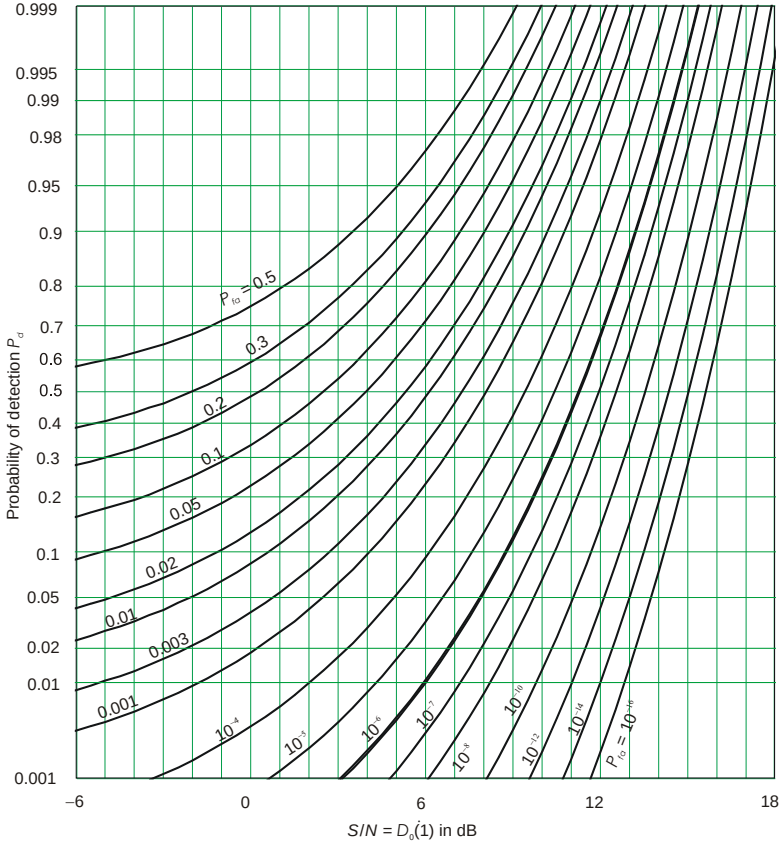

Figure 4.1 Single-pulse, steady-target detectability factor $D_0(1)$.

The accuracies of these approximations are excellent except at low P_d, as shown in Figure 4.2. Errors are within 0.1 dB for values used in most practical applications of the radar equation.

Another approach to approximation of $D_0(1)$ is to start with the simple, exact calculation for the Case 1 target (Section 4.3.4) and subtract the fluctuation loss (see Section 4.4.5) that applies to that target, as approximated by (4.54).

4.2.6 Approximations for *n*-Pulse, Steady-Target Detectability Factor

An approximate method of calculating the *n*-pulse detectability factor for the steady target is given by Shnidman [11]. He defines a parameter η:

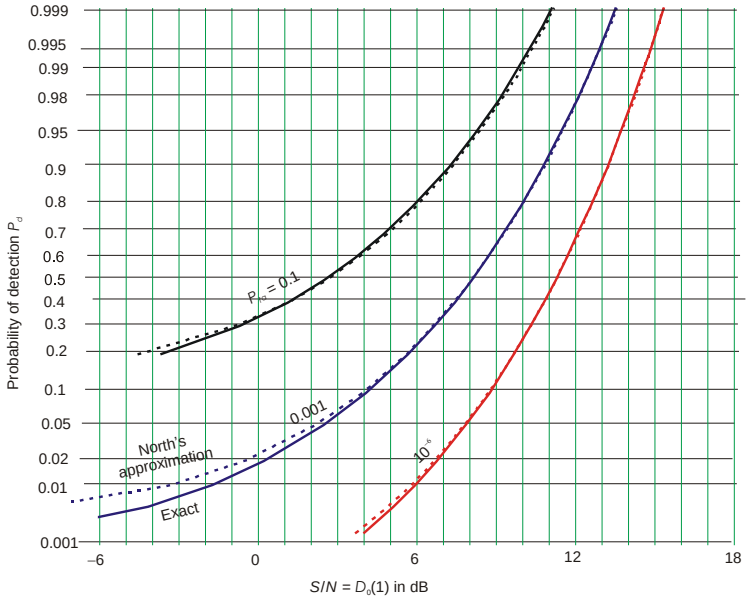

Figure 4.2 Comparison of North's approximation with exact values for $D_0(1)$.

$$\eta\left(P_d, P_{fa}\right) = \sqrt{-0.8\ln\left[4P_{fa}\left(1-P_{fa}\right)\right]} - \text{sign}\left(0.5-P_d\right)\sqrt{-0.8\ln\left[4P_d\left(1-P_d\right)\right]} \quad (4.19)$$

where the function sign(x) = 1 for $x \geq 0$ and –1 for $x < 0$. From (4.19) the detectability factor is found as

$$D_{0s}(n) = \frac{\eta^2}{n} + \frac{2\eta}{n}\sqrt{\frac{n}{2} - \frac{1}{4}} \quad (4.20)$$

The added subscript $_s$ denotes the Shnidman approximation. Only square roots and logarithms are required in this procedure. Figure 4.3 shows P_d versus detectability factor for three pairs of (P_{fa}, n). The approximation is accurate within 0.1 dB for values normally encountered.

Another approximate method of approximating $D_0(n)$ is to start with the simple, exact calculation for the Case 1 target (Section 4.3.3), add the integration loss as approximated by (4.51), and subtract the fluctuation loss (see Section 4.4.5) that applies to that target, as approximated by (4.54).

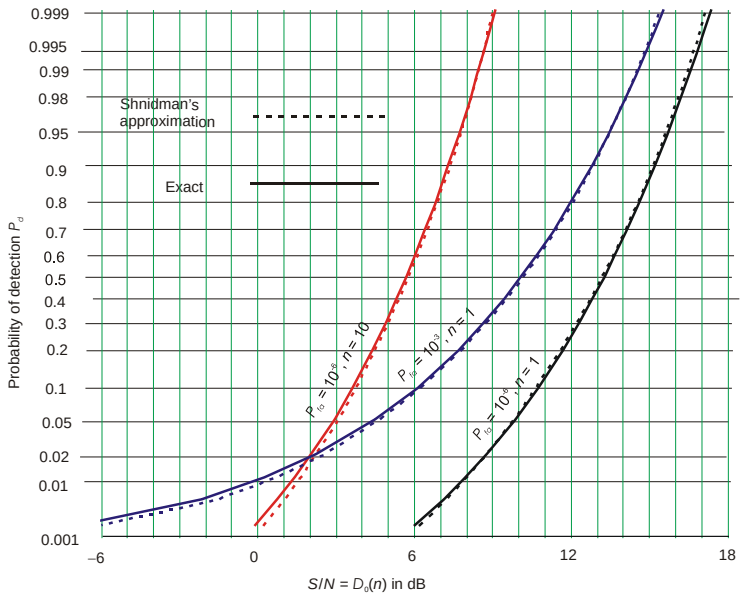

Figure 4.3 Comparison of Shnidman's approximation with exact values for $D_0(n)$.

4.3 DETECTABILITY FACTORS FOR FLUCTUATING TARGETS

4.3.1 Generalized Chi-Square Target Fluctuation Model

Virtually all actual radar targets have cross sections that vary with time, frequency, aspect angle, and polarization. The statistics of most fluctuating targets are described by the chi-square distribution. The chi-square distribution with m degrees of freedom (dof) is the distribution of the sum of m independent, normally distributed components. A target echo received and processed through an envelope detector, without preceding coherent integration, has a chi-square distribution with $m = 2n_e$ dof, where n_e is the number of independent pulses or signal samples, each contributing a vector signal component with normally distributed in-phase and quadrature components.

Four commonly used models for targets fluctuating in time were introduced by Swerling [12]. These models have voltage statistics corresponding to chi-square distributions with different degrees of freedom, representing samples of the Gaussian in-phase and quadrature components of the vector voltage for a target with either slow or fast fluctuation. Table 4.1 describes the Swerling model statistics in terms of the number of dof, the number n_e of independent target samples,

and the fluctuation rate, defined in terms of the relationship of the target correlation time t_c to the pulse repetition interval t_r at which n pulses are received over an integration time $t_o = nt_r$.

Table 4.1 Parameters of Swerling Target Models

Case	*dof*	n_e	*Fluctuation Rate*
1	2	1	Slow: $t_c >> nt_r$
2	$2n$	n	Fast: $t_c < t_r$
3	4	2	Slow: $t_c >> nt_r$
4	$4n$	$2n$	Fast: $t_c < t_r$

The models must be interpreted as applying not to the targets themselves, but to the *echo signals* of the target as observed by a radar system whose location, relative to the target, may change with time, and whose radiated waveform may also change as a result of frequency or polarization diversity. The radar system designer can change the fluctuation statistics of a given target to avoid prolonged fades by exploiting diversity, usually in frequency, where multiple channels operating in parallel or in sequence are available.

The four Swerling cases are described by Table 4.1, but the general chi-square distribution is more broadly applicable. Methods of estimating n_e for radars with diversity are described in Section 4.5. Integer values other than $n_e = 1$, 2, n, or $2n$ are commonly observed, as well as noninteger values, and these are accommodated in the general expressions developed in [13], given in Section 4.3.2.

4.3.2 Detection of Signals with Chi-Square Statistics

The probability that a chi-square distributed quantity with m dof lies below χ^2 is given by [7, p. 262, Eq. (6.5.5]:

$$P_\chi\left(\chi^2, m\right) = \frac{1}{2^{m/2}\Gamma\left(m/2\right)} \int_0^{\chi^2} t^{(m/2)-1} e^{-t/2} dt, \quad 0 \le \chi^2 \le \infty \tag{4.21}$$

Barton presents in [2, 13] an approximate method of finding P_d and $D(n)$ for all Swerling cases and for signal models with arbitrary dof and n_e. The integral of the chi-square distribution[3] $P_\chi(\chi^2, m)$ and its inverse function $P_\chi^{-1}(p, m)$ are used in [2, 13], but are replaced here by the corresponding incomplete gamma function P_γ and its inverse for comparison with equations for the Swerling models given in [6]. The relationship between the functions is:

[3] The symbols K_m and K_m^{-1} in [2, 13] are replaced here by P_χ and P_χ^{-1}.

$$P_\chi\left(\chi^2, m\right) = 1 - P_\gamma\left(\chi^2/2, m/2\right)$$
$$P_\chi^{-1}\left(p, m\right) = 2P_\gamma^{-1}\left(1-p, m/2\right) \tag{4.22}$$

The detection probability and basic detectability factor for the chi-square fluctuating target are [2, p. 68, Eq. (2.64)]:

$$\begin{aligned} P_d\left(s, P_{fa}, n, n_e\right) &= P_\chi\left[\frac{P_\chi^{-1}\left(P_{fa}, 2n\right) - 2\left(n - n_e\right)}{\left(n/n_e\right)s + 1}, 2n_e\right] \\ &= 1 - P_\gamma\left[\frac{P_\gamma^{-1}\left(1 - P_{fa}, n\right) - \left(n - n_e\right)}{\left(n/n_e\right)s + 1}, n_e\right] \end{aligned} \tag{4.23}$$

$$\begin{aligned} D\left(P_d, P_{fa}, n, n_e\right) &= \left[\frac{P_\chi^{-1}\left(P_{fa}, 2n\right) - 2\left(n - n_e\right)}{P_\chi^{-1}\left(P_d, 2n_e\right)} - 1\right]\frac{n_e}{n} \\ &= \left[\frac{P_\gamma^{-1}\left(1 - P_{fa}, n\right) - \left(n - n_e\right)}{P_\gamma^{-1}\left(1 - P_d, n_e\right)} - 1\right]\frac{n_e}{n} \end{aligned} \tag{4.24}$$

The notation $D(P_d, P_{fa}, n, n_e)$ can be simplified to $D(n, n_e)$. Both P_χ and P_γ and their inverse functions are included as built-in functions in platforms such as Mathcad. Approximation errors in D from (4.24) are shown in Sections 4.3.3–4.3.5, with errors less than 0.2 dB for most radar and target parameters.

The notation $D(n, n_e)$, with the appropriate value of n_e, replaces $D(n)$ as the basic detectability factor in the radar equation, covering all target statistics discussed above, as well as fractional values of m discussed by Weinstock [14]. While the steady target can be approximated by the chi-square distribution with $n_e \geq 50$, better accuracy is obtained using Shnidman's approximation (Section 4.2.5).

4.3.3 Swerling Case 1

This section discusses Case 1, known as the Rayleigh target (the Rayleigh distribution is the chi-square with two degrees of freedom). It is of primary importance in radar, because it is the distribution inherent in any target echo that results from multiple (e.g., more than about four) scattering sources of comparable magnitude. The central limit theorem states that the distribution of the sum of m independent-

ly varying quantities tends toward the Gaussian distribution as m increases, regardless of their individual distributions. Hence the vector echo voltage from multiple scatterers ($m > 4$) consists of Gaussian in-phase and quadrature components, and the magnitude of the vector has a Rayleigh distribution. Very few targets encountered in actual radar operation depart significantly from this distribution, except through the exploitation of diversity in the radar transmission (see Section 4.5).

The target echo from a Rayleigh-distributed (Swerling Case 1) target has signal-plus-noise voltage and power distributions like those of noise alone, but the mean power is the sum of the mean signal and mean noise powers:

$$dP_v = \frac{v}{\bar{S}+N}\exp\left(-\frac{v^2}{2\left(\bar{S}+N\right)}\right)dv$$
$$dP_p = \frac{1}{\bar{S}+N}\exp\left(-\frac{p}{\bar{S}+N}\right)dp \tag{4.25}$$

where

v = instantaneous signal-plus-noise voltage;
$\bar{S}$ = average signal power;
N = average noise power;
dP_v = probability that instantaneous signal-plus-noise voltage lies between v and $v + dv$;
p = instantaneous signal-plus-noise power;
dP_p = probability that instantaneous signal-plus-noise power lies between p and $p + dp$.

4.3.3.1 Exact Equations for Single-Pulse, Case 1

The detection probability for a single Case 1 echo pulse is

$$P_d = \int_{y_b}^{\infty} dP_v = \exp\left(-\frac{y_b^2}{2\left(\bar{S}+N\right)}\right) = \exp\left(\frac{\ln P_{fa}}{1+\bar{S}/N}\right) \tag{4.26}$$

where y_b is the single-pulse threshold voltage from (4.15).

Equation (4.26) is readily inverted to find the basic single-pulse detectability factor $D_{11} = D_1(1)$:

$$D_{11} = \frac{\ln P_{fa}}{\ln P_d} - 1 \tag{4.27}$$

Because the exact equations are so simple, approximations are nor needed for single-pulse, Case 1 detection calculations.

4.3.3.2 Exact Expressions for *n*-Pulses, Case 1

The exact expression for P_d with *n*-pulse integration of a Case 1 target is [6, p. 390, Eq. (11.2-38)]:

$$P_{d1} = 1 - P_\gamma\left(y_b, n-1\right) + \left(1 + \frac{1}{ns}\right)^{n-1} \exp\left(-\frac{y_b}{1+ns}\right) P_\gamma\left[\frac{y_b}{1+1/ns}, n-1\right], \quad n > 1 \tag{4.28}$$

where $P_\gamma(x,n)$ is the incomplete gamma function (4.3), y_b is the threshold given by (4.6), and $s = \bar{S}/N$ is the average signal-to-noise ratio.

The exact detectability factor for the Case 1 target with $n > 1$ can be found only by root-finding from (4.28):

$$D_1(n) = \text{root}_s\left\{P_{d1} = 1 - P_\gamma\left(y_b, n-1\right) + \left(1 + \frac{1}{ns}\right)^{n-1} \exp\left(-\frac{y_b}{1+ns}\right) P_\gamma\left[\frac{y_b}{1+1/ns}, n-1\right]\right\} \tag{4.29}$$

4.3.3.3 Approximations for *n*-Pulse Case 1 Detectability Factor

An approximation for the detection probability is [6, p. 390, Eq. (11.2-39)]:

$$P_d \approx \left(1 + \frac{1}{sn}\right)^{n-1} \exp\left(-\frac{y_b}{1+ns}\right) \tag{4.30}$$

This expression is found by assuming that the incomplete gamma functions in (4.28) are near unity for $P_{fa} << 1$. It is exact for $n = 1$, and the error in P_d is < 0.005 for $P_{fa} < 0.05$ and negligible for $P_{fa} < 0.01$ or $s > 10$. However, this approximation cannot be inverted to yield the detectability factor, requiring a further approximation.

The detectability factor is obtained from [6, p. 392, Eq. (11.2-43)], which is derived by first taking the natural logarithm of both sides, and then assuming that $\ln(1 + 1/ns) \approx 1/ns$ and $1 + ns \approx ns$ in (4.30), to obtain

$$D_1(n) \approx \frac{n-1-y_b}{n \ln P_d} \tag{4.31}$$

Using Gregers-Hansen's approximation of y_b, this becomes:

$$D_1(n) \approx \frac{1}{n \ln(1/P_d)} \left\{ \sqrt{n} \left[\Phi^{-1}(P_{fa}) - \frac{\Phi^{-1}(P_{fa}) + \ln P_{fa} + 1}{(1.1n - 0.1)^{0.51}} \right] + 1 \right\} \tag{4.32}$$

The accuracy of this approximation is shown in Figure 4.4, which shows agreement within ≈0.5 dB for $P_d \geq 0.3$, $P_{fa} \leq 10^{-3}$, and increasing accuracy for $n > 10$. Curves are not shown for $n = 1$, where exact solutions are readily computed from (4.27). Note that the approximations are very accurate for high detection probabilities and large n, where the exact expressions may not lie within the range at which built-in functions can be used.

Detection performance on the Case 1 target is described by the universal equations (4.23) and (4.24), expressed in terms of the incomplete gamma function P_γ and its inverse P_γ^{-1}, with the number of independent target samples $n_e = 1$:

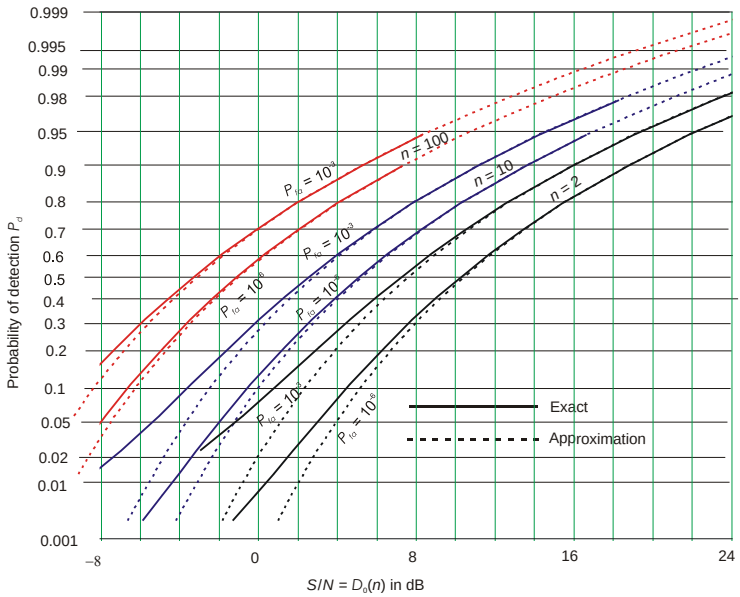

Figure 4.4 Comparison of DiFranco and Rubin Case 1 approximation with exact values, for $n = 2$, 10, 100 and $P_{fa} = 10^{-3}$ and 10^{-6}.

$$P_{d1}\left(s,P_{fa},n\right)=P_d\left(s,P_{fa},n,1\right)=1-P_\gamma\left[\frac{P_\gamma^{-1}\left(1-P_{fa},n\right)-\left(n-1\right)}{ns+1},1\right] \quad (4.33)$$

$$D_1\left(P_d,P_{fa},n\right)=D_\gamma\left(P_d,P_{fa},n,1\right)=\left[\frac{P_\gamma^{-1}\left(1-P_{fa},n\right)-\left(n-1\right)}{P_\gamma^{-1}\left(1-P_d,1\right)}-1\right]\frac{1}{n} \quad (4.34)$$

The accuracy of this approximation is far better than that given in (4.31) or (4.32), as shown in Figure 4.5. The universal equation also gives exact results for $n = 1$.

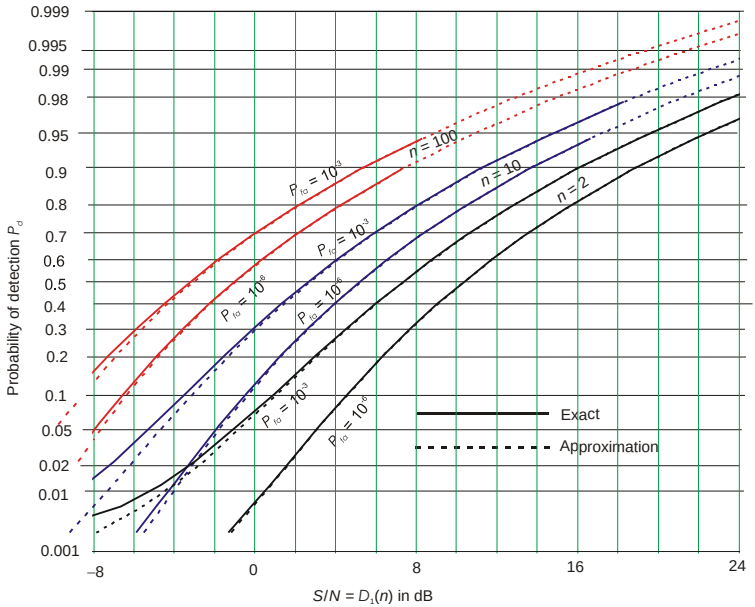

Figure 4.5 Comparison of universal equation (dashed curves) with exact values for Case 1 detectability factor.

4.3.4 Swerling Case 2

4.3.4.1 Exact Equations for Case 2

The exact expression for P_d with a Case 2 target [6, p. 404, Eq. (11.3-21)] is:

$$P_{d2} = 1 - \frac{1}{(n-1)!}\int_0^{y_b/(s+1)} y^{n-1}e^{y}\,dy = 1 - P_\gamma\left(\frac{y_b}{s+1}, n\right) = 1 - P_\gamma\left[\frac{P_\gamma^{-1}\left(1-P_{fa}, n\right)}{s+1}, n\right] \tag{4.35}$$

This exact result is also obtained from the universal equation (4.23) with $n_e = n$:

$$P_{d2}\left(s, P_{fa}, n\right) = P_d\left(s, P_{fa}, n, n\right) = 1 - P_\gamma\left[\frac{P_\gamma^{-1}\left(1-P_{fa}, n\right)}{s+1}, n\right] \tag{4.36}$$

The detectability factor $D_2(n)$ may be obtained as the root of (4.35) with respect to s, or through the inverse incomplete gamma function. We write, from (4.35)

$$D_2(n) = s = \frac{y_b\left(P_{fa}, n\right)}{P_\gamma^{-1}\left(1-P_d, n\right)} = \frac{P_\gamma^{-1}\left(1-P_{fa}, n\right)}{P_\gamma^{-1}\left(1-P_d, n\right)} - 1 \tag{4.37}$$

This exact expression is also found from the universal equation (4.24) by setting $n_e = n$.

4.3.4.2 Approximations for Case 2 Detection Probability and Detectability Factor

Where the inverse incomplete gamma function is not available, it may be approximated as derived by Gregers-Hansen, using (4.11). That approximation has difficulty with the denominator of (4.37), however, when $P_d > 0.95$, and hence should be used with caution. Approximations in [6, p. 407] exhibit larger errors, and are not recommended, given the ease with which the inverse incomplete gamma function can be evaluated. The steady-target D_0 approximations with $n > 20$ give D_2 with adequate accuracy for many purposes.

4.3.5 Swerling Case 3

In [6, p. 410, Eq. (11.4-21)] an expression is derived for the probability density function of signal plus noise for Case 3. From this, an approximate expression for Case 3 detection probability is obtained [6, p. 421, Eq. (11.4-24)]:

$$P_{d3} = \left(1 + \frac{2}{ns}\right)^{n-2}\left(1 + \frac{y_b}{1+(ns/2)} - \frac{n-2}{ns/2}\right)\exp\left(\frac{-y_b}{1+(ns/2)}\right) \tag{4.38}$$

This is stated to be exact for $n = 1$ or 2, and approximate for larger n. Inversion of (4.38) to obtain detectability factor $D_3(n)$ is possible only through root-finding methods.

Approximations are given in [6] for Case 3 with $n >> 1$, using a graphical method for inversion of the P_d equation to yield $D_3(n)$. More accurate approximations are found from the universal equations with $n_e = 2$:

$$P_{d3}\left(s, P_{fa}, n\right) = P_d\left(s, P_{fa}, n, 2\right) = 1 - P_\gamma\left[\frac{P_\gamma^{-1}\left(1-P_{fa}, n\right) - (n-2)}{(n/2)s + 1}, 2\right] \quad (4.39)$$

$$D_3\left(P_d P_{fa}, n\right) = D_e\left(P_d P_{fa}, n, 2\right) = \left[\frac{P_\gamma^{-1}\left(1-P_{fa}, n\right) - (n-2)}{P_\gamma^{-1}\left(1-P_d, 2\right)} - 1\right]\frac{2}{n} \quad (4.40)$$

The results are shown in Figure 4.6, in which the difference between the curves for (4.38) and (4.40) for $n = 10$ and 100 may result from inexactness in (4.38), since the two sets of curves are identical for $n = 2$.

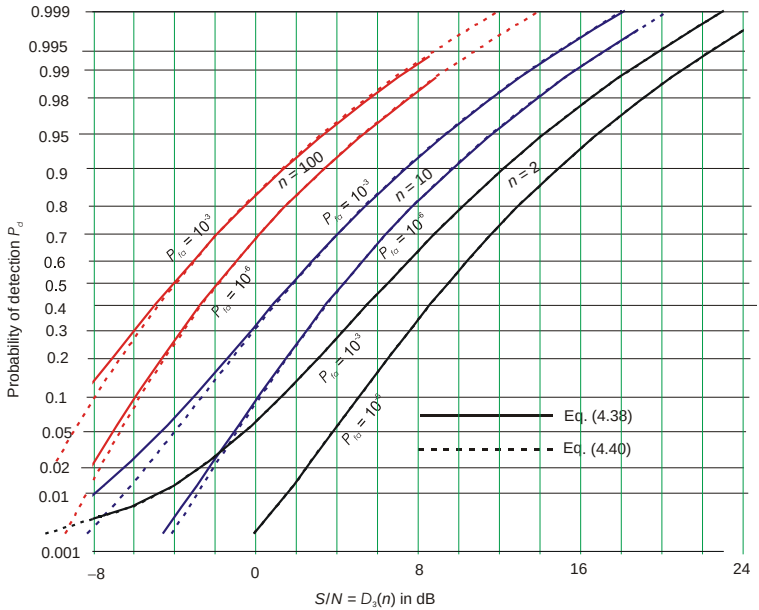

Figure 4.6 Comparison of Case 3 detectability factor from universal equation (4.40) with values from (4.38). The universal equation overlies the exact values for $n = 2$.

4.3.6 Swerling Case 4

The exact expression for Case 4 P_d is [6, p. 427, Eq. (11.5-19)]:

$$P_{d4} = 1 - \frac{n!}{\left[1+(s/2)\right]^n} \sum_{k=0}^{n} \left[\frac{(s/2)^k}{k!(n-k)!} P_\gamma \left(\frac{y_b}{1+(s/2)}, n+k \right) \right] \tag{4.41}$$

The root of (4.41) with respect to s yields $D_4(n)$.

The approximation for Case 4 detection probability [6, p. 438, Eq. (11.5-25c)] is inadequate, but approximations derived from the universal equations are:

$$P_{d4}(s, P_{fa}, n) = P_d(s, P_{fa}, n, 2n) = 1 - P_\gamma \left[\frac{P_\gamma^{-1}(1-P_{fa}, n) + n}{(1/2)s + 1}, 2n \right] \tag{4.42}$$

$$D_4(P_d P_{fa}, n) = D_e(P_d P_{fa}, n, 2n) = 2 \left[\frac{P_\gamma^{-1}(1-P_{fa}, n) + n}{P_\gamma^{-1}(1-P_d, 2n)} - 1 \right] \tag{4.43}$$

The accuracy of (4.43) is shown in Figure 4.7.

4.4 APPROXIMATE EQUATIONS BASED ON DETECTOR LOSS

In [15] a method was developed approximate the detectability factor using functions commonly available on pocket calculators without numerical integration or root-finding. The only special functions used in this method are $\Phi(E)$, the integral of the normal distribution and its inverse $\Phi^{-1}(P)$, given by (4.8) and available through analytic approximations in [7]. The method is of continuing value because it associates the integration loss with the signal-to-noise ratio at the input to the envelope detector, whose nonlinearity destroys information that would be available if coherent detection could be used.

4.4.1 Coherent Detection

Detection of an exactly known signal is discussed in [6, pp. 291–298]. A single pulse arriving with known frequency and phase is passed through a coherent detector, in which a reference sinusoid having that frequency and phase performs linear conversion of the input signal to a positive pulse at baseband. The resulting detector output signal-to-noise ratio s_o is exactly twice that of the input s, half the noise power being rejected by the detector. The threshold level is given exactly as

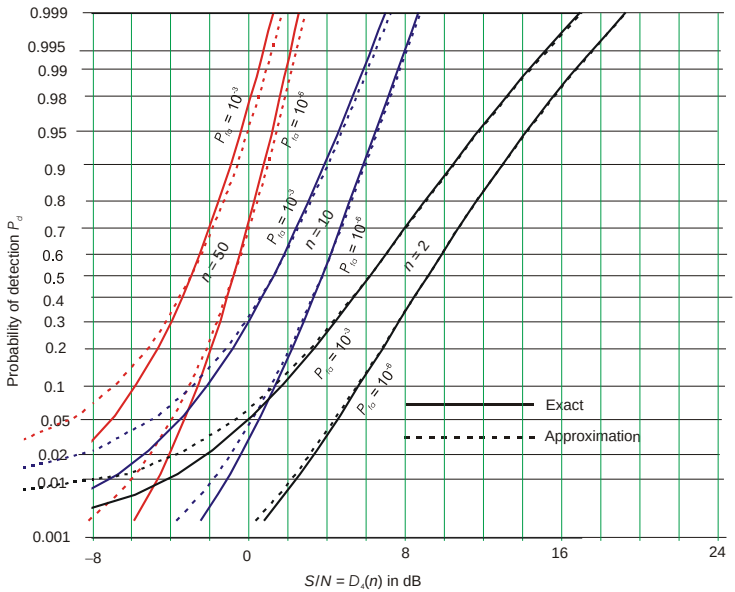

Figure 4.7 Comparison of Case 4 detectability factor from universal equation (4.42) with exact values from (4.41).

$$y_b = \Phi^{-1}\left(P_{fa}\right) \tag{4.44}$$

The detection probability is

$$P_d\left(s, P_{fa}\right) = \Phi\left[\Phi^{-1}\left(P_{fa}\right) - \sqrt{2s}\right] \tag{4.45}$$

Solving (4.45) for the single-pulse detectability factor for coherent detection of a steady target, we obtain

$$D_{c1}\left(P_d, P_{fa}\right) = s = \frac{1}{2}\left[\Phi^{-1}\left(P_{fa}\right) - \Phi^{-1}\left(P_d\right)\right]^2 \tag{4.46}$$

For example, the requirement for coherent detection is $D_{c1}(0.9, 10^{-6})$ = 12.60 dB, for a single pulse, compared with $D_0(1)$ = 13.18 dB for the envelope-detected pulse. Coherent integration of n pulses results in a requirement for each pulse given by

$$D_c\left(P_d, P_{fa}, n\right) = \frac{D_{c1}\left(P_d, P_{fa}\right)}{n} = \frac{1}{2n}\left[\Phi^{-1}\left(P_{fa}\right) - \Phi^{-1}\left(P_d\right)\right]^2 \tag{4.47}$$

Since the phase of a previously undetected signal is unpredictable, coherent detection cannot be implemented in practice. However, it provides a minimum reference requirement from which values applicable to noncoherent detection and integration can be calculated if the loss inherent in envelope detection is known.

4.4.2 Envelope Detection and Detector Loss

Detector loss, also called the "small-signal suppression effect," occurs when a signal, accompanied by noise, is passed through an envelope detector. The output signal-to-noise ratio s_o is reduced from 2*s*, as in the coherent detector, to

$$s_o = \frac{2s}{C_x} \approx \frac{2s^2}{s + 2.3} \tag{4.48}$$

The approximation $C_x = (s + 2.3)/s$ was determined empirically in [15]. Setting $s_o = 2D_{c1}$, as required to meet detection requirements, and solving for $s = D_0(n)$, the *n*-pulse, steady target detectability factor, we obtain

$$D_0\left(P_d, P_{fa}, n\right) \approx \frac{D_{c1}\left(P_d, P_{fa}\right)}{n}\left[\frac{1}{2} + \sqrt{\frac{1}{4} + \frac{2.3n}{D_{c1}\left(P_d, P_{fa}\right)}}\right] \tag{4.49}$$

The error is calculating the detectability factor from detector loss is shown in Figure 4.8, for $n = 1$, 10, and 100 and $P_{fa} = 10^{-3}$ and 10^{-6}. This procedure underestimates the requirement for very high P_d, overestimates it for very low P_d, and is within tenths of a decibel for $0.3 < P_d < 0.9$.

4.4.3 Integration Loss

The total signal energy required at the input of the envelope detector is $nD_0(n)$, and the ratio of that total to the single-pulse energy requirement is called *integration loss*, as defined by Marcum [4]:

$$L_i\left(n\right) \equiv \frac{nD_0\left(n\right)}{D_{01}} \tag{4.50}$$

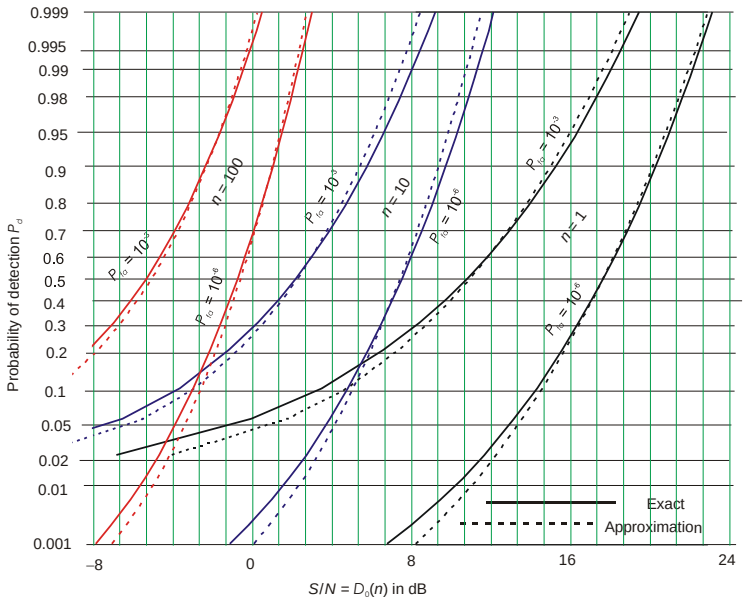

Figure 4.8 Comparison of detectability factor $D_0(n)$ derived from detector loss with exact values from (4.12).

where we abbreviate $D_0(1)$ as D_{01}. The integration loss can be expressed as a function of D_{01}, from (4.49), substituting $D_{c1} = D_{01}/C_x = D_{01}^2/(D_{01} + 2.3)$:

$$L_i(n) = \frac{1 + \sqrt{1 + 9.2n(D_{01} + 2.3)/D_{01}^2}}{1 + \sqrt{1 + 9.2(D_{01} + 2.3)/D_{01}^2}} \tag{4.51}$$

As shown in [15], integration loss is not a property of the integrator, but rather is an increase in *detector loss* due to the reduced input *S*/*N* made possible by the integration gain. Note that L_i depends on P_d and P_{fa} only to the extent that these probabilities affect D_{01}. A single family of curves for L_i, Figure 4.9, thus covers all combinations of detection requirements, rather than having an infinite number of curves for possible pairs of P_d and P_{fa}, some of which are presented in [4] and other literature.

It can be seen that the penalty for noncoherent integration of $n < 10$ pulses is small when the requirement is for $D_{01} > 10$ dB, but that it increases as $\sqrt{n}$ for larger n.

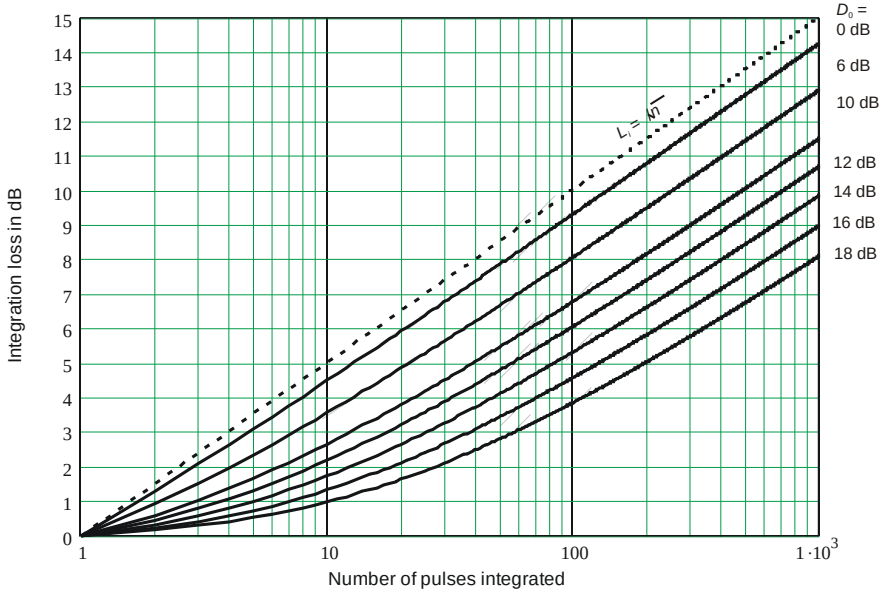

Figure 4.9 Integration loss versus number of pulses for different values of D_{01}.

4.4.4 Integration Gain

The fact that noncoherent integration carries a loss L_i does not mean that this type of integration is undesirable. It means that it is less effective than coherent integration of the same number of input pulses, but coherent integration is often impossible or even undesirable. As will be shown in Section 4.5.1, noncoherent integration of $2 \le n \le 10$ samples, obtained with diversity, may provide better performance for $P_d > 0.5$ than coherent integration, even when the latter can be implemented.

The gain in performance from noncoherent integration, compared with a single pulse, is

$$G_i(n) = \frac{n}{L_i(n)} \tag{4.52}$$

and this gain is always within the limits $\sqrt{n} \le G_i \le n$. For moderate values of n, it is $\approx n^{0.8}$ (e.g., $L_i(n) \approx 2$ dB for $n = 10$), when P_d and P_{fa} are such that $D_{01} \ge 12$ dB is required.

4.4.5 Fluctuation Loss

The detectability factor for a Case 1 fluctuating target may be found by multiplying the steady-target detectability factor $D_0(n)$ by a *fluctuation loss* L_{f1}, defined as

$$L_{f1}(n) \equiv \frac{D_1(n)}{D_0(n)} \tag{4.53}$$

where it is understood that the probabilities P_d and P_{fa} are the same for both targets. The loss is a strong function of P_d and a weak function of P_{fa} and n, as can be seen from Figure 4.10. The loss is ≈ 0 dB for $P_d \approx 0.35$, and turns negative (becomes a gain) for $P_d < 0.35$.

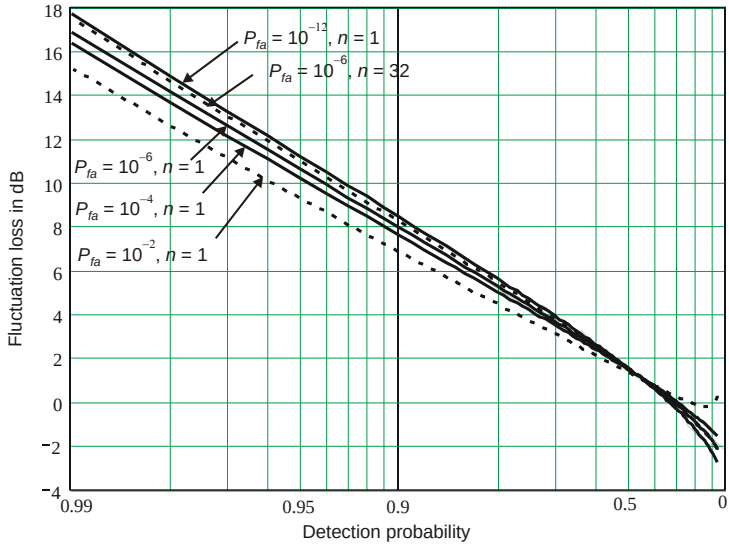

Figure 4.10 Case 1 fluctuation loss L_{f1} versus P_d for different P_{fa} and n.

An analytic approximation of the data in Figure 4.10 gives the fluctuation loss L'_{f1} in decibels as a function of n, P_d, and P_{fa}:

$$L'_{f1}(n) \approx \left[0.895\log\left(1-P_d\right)-2\left(1-P_d\right)^4\right]\left(1+0.03\log n\right)\left[1-0.02\left(6+\log P_{fa}\right)\right]-1 \tag{4.54}$$

4.4.6 Case 1 Detectability Factor

Using (4.18), (4.51), and (4.54), the Case 1 detectability factor is

$$D_1\left(P_d, P_{fa}, n\right) = \frac{1}{n} D_{01}\left(P_d, P_{fa}\right) L_i(n) L_{f1}\left(P_d, P_{fa}, n\right) \tag{4.55}$$

This formulation requires only the inverse integral of the normal distribution and the log function, along with multiplication and division. The accuracy of this process, using the North approximation for D_{01}, the detector loss approximation for L_i, and (4.54) for L_{f1},is shown in Figure 4.11.

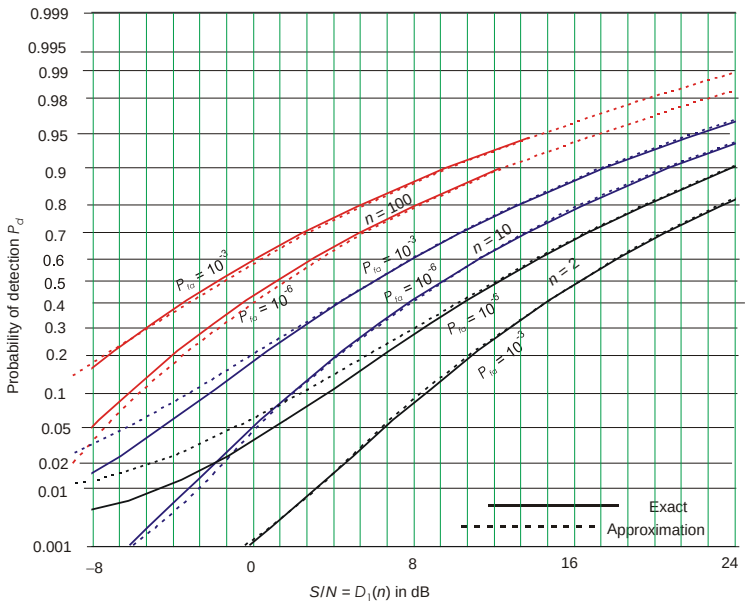

Figure 4.11 Case 1 detectability factor $D_1(n)$ versus P_d for different P_{fa} and n.

The calculation can also be done by reading and adding the decibels values of steady-target detectability factor D_{01} from Figure 4.1, integration loss L_i from Figure 4.9, and fluctuation loss L_{f1} from Figure 4.10, and subtracting $10\log n$:

$$D_1'(n) = D_{01}' + L_i'(n) + L_{f1}'(n) - 10\log n \tag{4.56}$$

where the primed symbols denote decibel values. There is no systematic error in such calculations, but each curve is readable only to about ±0.1 dB.

4.4.7 Detectability Factors for Other Fluctuating Targets

It was established in [15] that the decibel value of fluctuation loss varies inversely with the number n_e of independent target samples:

$$\begin{aligned} 10\log\left[L_f(n, n_e)\right] &\approx (1/n_e)10\log\left[L_{f1}(n)\right] \\ L_f'(n, n_e) &\approx (1/n_e)L_{f1}'(n) \end{aligned} \tag{4.57}$$

This approximation is very close to the exact results obtained by Kanter [16]. Thus, the detectability factor D' in decibels, for any chi-square target model, can be approximated as

$$D_e'(n, n_e) = D_{01}' + L_i'(n) + (1/n_e)L_{f1}'(n) - 10\log n \tag{4.58}$$

The value of n_e for the Swerling models is listed in Table 4.1, and for other chi-square models can be determined as shown in the following section.

4.5 DIVERSITY IN RADAR

4.5.1 Diversity Gain

The large fluctuation loss for $P_d > 0.5$ suggests that noncoherent integration of multiple independent target samples ($n_e > 1$) obtained by diversity can result in improved detection performance. As an example, assume that 16 pulses are received during a beam dwell time t_o on a Case 1 target: $t_o = 16t_r$. They might be integrated coherently to provide a single sample at the envelope detector with energy $E/N_0 = 16E_1/N_0$, where E_1 is the single-pulse energy. For a specified $P_d = 0.9$, $P_{fa} = 10^{-6}$, (4.27) yields

$$D_1(1) = 130.1 = 21.1 \text{ dB}$$

Alternatively, if the RF bandwidth of the transmitter, antenna, and the microwave components of the receiving system permit, the 16 pulses can be transmitted in

two 8-pulse groups at different frequencies, four 4-pulse groups at four frequencies, eight 2-pulse groups at eight frequencies, or 16 single pulses at different frequencies. Coherent integration could be performed on the pulses within a given frequency group, and noncoherent integration performed on the resulting outputs at different frequencies. Assuming that the frequencies differ by an the amount needed to decorrelate the echoes (see Section 4.5.2), the total energy required will follow the curves shown in Figure 4.12.

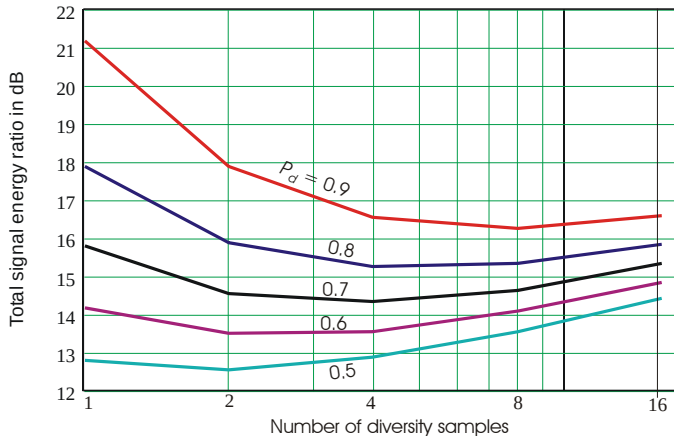

Figure 4.12 Total energy required versus number of diversity samples within 16 pulses for Rayleigh target at different detection probabilities, $P_{fa} = 10^{-6}$.

For $P_d = 0.9$, the best performance is obtained with $n_e = 8$, with a total energy requirement 4.9 dB less than a system without diversity; $n_e = 4$ is almost as good. The optimum n_e is reduced to four, and then to two, as P_d is reduced through 0.8 to 0.5.

4.5.2 Signal and Target Models with Diversity

The radar target usually consists of several scattering sources whose reflected fields add vectorially at the radar antenna. As long as the number of such sources exceeds about four, the statistics of each quadrature component in the combined field approach Gaussian, leading to the Case 1 target ($n_e = 1$, dof = 2) that has a Rayleigh distribution of voltage. There is no physical basis for a target having dof > 2, although a target containing one dominant scatterer is often modeled approximately as Case 3 (dof = 4). The Swerling models should, instead, be interpreted as representing the distribution of echo *signals* received and processed by a

radar in which *diversity* can provide independent samples in time, frequency, space, and possibly in polarization.

4.5.2.1 Time Diversity

As pulses are received over the integration time t_o, the in-phase and quadrature voltage components may change to produce $n_{et} > 1$ independent samples for integration [2, p. 86, Eq. (2.50)]:

$$n_{et} = 1 + \frac{t_o}{t_c} \le n \tag{4.59}$$

Here t_c is the *correlation time* of target echoes, given by [2, p. 86, Eq. (2.60)]

$$t_c = \frac{\lambda}{2\omega_a L_x} \tag{4.60}$$

where λ is the radar wavelength, ω_a is the rate of change of aspect angle, and L_x is the cross-range span of the target scatterers in the plane containing the line of sight. Note that the effective coherent integration time is limited to $t_f \le t_c$, since the signal phase is decorrelated over longer periods.

4.5.2.2 Frequency Diversity

Radars often use frequency diversity or agility to obtain additional independent echo samples [2, p. 87, Eq. (2.61)]:

$$n_{ef} = 1 + \frac{\Delta f}{f_c} \le n \tag{4.61}$$

Here Δf is the band over which the radar frequency is varied and f_c is the *correlation frequency* of the target [2, p. 87, Eq. (2.62)]:

$$f_c = \frac{c}{2L_r} \tag{4.62}$$

Here c is the velocity of light and L_r is the radial span of the target scatterers. The multiple frequencies may appear in subpulses within each pulse, or by variation between pulses. If m subpulses are used, the number of samples integrated increases to $n' = mt_o/t_f$. The carrier frequency must not change during the coherent integration time t_f.

4.5.2.3 Space Diversity

Monostatic radars view a target over a single path such that the aspect angle of the target changes slowly with time, as expressed by ω_a in (4.60). Multistatic radar uses multiple simultaneous paths and can take advantage of space diversity to obtain multiple independent samples on each pulse. When the angle θ of the bisector of transmitting and receiving paths, measured with respect to the target axis, varies by $\Delta\theta$, the number of independent signal samples is

$$n_{es} = 1 + \frac{\Delta\theta}{\theta_c} \tag{4.63}$$

where $\theta_c = \lambda/2L_x$ is the lobe width of the reflection pattern of the target, measured on a two-way path.

4.5.2.4 Polarization Diversity

Orthogonally polarized antenna channels are rare in radar, but if present they may increase the number independent echo signals by $n_{ep} = 2$. There are only two orthogonal polarizations (e.g., vertical and horizontal, right- and left-hand circular, or any pair of orthogonal elliptical polarizations).

4.5.2.5 Available Independent Samples

The number of independent signal samples integrated during the dwell time is

$$n_e = n_{et} n_{ef} n_{es} n_{ep} \le n \tag{4.64}$$

The Marcum/Swerling models for which detectability factors were derived above can represent the following target and radar descriptions:

Case 0: A single scatterer, a corner reflector with fixed aspect angle, or a spherical target, modeled by $n_e \to \infty$;

Case 1: Rayleigh target, $t_o << t_c$ with fixed-frequency radar, giving $n_e = 1$;

Case 2: Rayleigh target, $t_r \ge t_c$ or $\Delta f / f_c \ge n$, or a combination giving $n_e = n$;

Case 3: Rayleigh target, $t_o << t_c$ with dual-frequency or dual-polarization radar, giving $n_e = 2$;

Case 4: Case 2 with space or polarization diversity, giving $n_e = 2n$.

Thus the Swerling models describe not different *target types*, but rather the echo signals received from the multiple-scatterer target viewed by radars with different degrees of diversity. An aircraft or other complex target will be Case 1 for fixed-frequency radar unless t_o is at least a significant fraction of t_c. For aircraft viewed at microwave frequencies, $t_c > 0.1$s is normal, and for typical integration times $1 < n_e < 1.5$. In order for a target to approach Case 2, t_c must approach the pulse repetition interval t_r, implying (even for millimeter-wave radar) aspect angle rates exceeding those normally experienced. Thus, radar-target situations typically give $n_e \approx 1$, unless frequency diversity or agility, space diversity, or polarization diversity is used.

4.6 VISIBILITY FACTOR

Useful data on detection performance of human operators, viewing cathode-ray-tube displays, are very limited. During World War II, experiments were performed at the MIT Radiation Laboratory to determine the visibility factor for different types of display. One result is the PPI visibility factor $V_{0(50)}$, applicable to $P_d = 50\%$ on a steady target under optimum viewing conditions, shown in Figure 5.13. Blake [17, p. 2] notes that that this curve is applicable to intensity-modulated displays generally, and states that it is

> based on Figs. 8.2 and 9.2 of [18] or Figs 1 and 21 of [19], adjusted to 0.5 probability and extrapolated to single-pulse detection, with slight revision of slopes as ends of the curve.

It is impossible to determine the false-alarm probability for the process represented by Figure 5.13. A typical PPI displays about 10^5 radar resolution cells and presents data over a scan period of ≈ 10s. Hence, if a single false alarm per scan results from the process, $P_{fa} = 10^{-6}$ can be assumed. Comparing the single-pulse value $V_{0(50)} = 13.2$ dB with the steady-target detectability factor $D_0 = 11.2$ dB for $P_d = 50\%$, $P_{fa} = 10^{-6}$, it can be seen that the visual detection process incurs a loss of some 2 dB compared with electronic detection on a single output of a matched filter. The bandwidth correction factor C_b appearing in (1.16) is *in addition* to that 2-dB loss, so for $C_b = 0$ dB there is still a 2-dB reduction in performance relative to the matched filter with electronic detection.

When other than $P_d = 0.50$ and $P_{fa} = 10^{-6}$ on steady targets is required, the V_0 data offer no guidance as to the change in required energy ratio. An approximation can be made based on the data developed for electronic detection in previous sections of this chapter. Adjustments for nonoptimum viewing conditions and operator performance are discussed in [18], but, as Blake notes in [20, p. 370]:

> The concept of *operator* loss is also sometimes employed, to describe the increase in D_0 required by a typical operator compared to an ideal integrator. However, again the approach here has been to express D_0 directly … as the value applicable to an actual human operator.

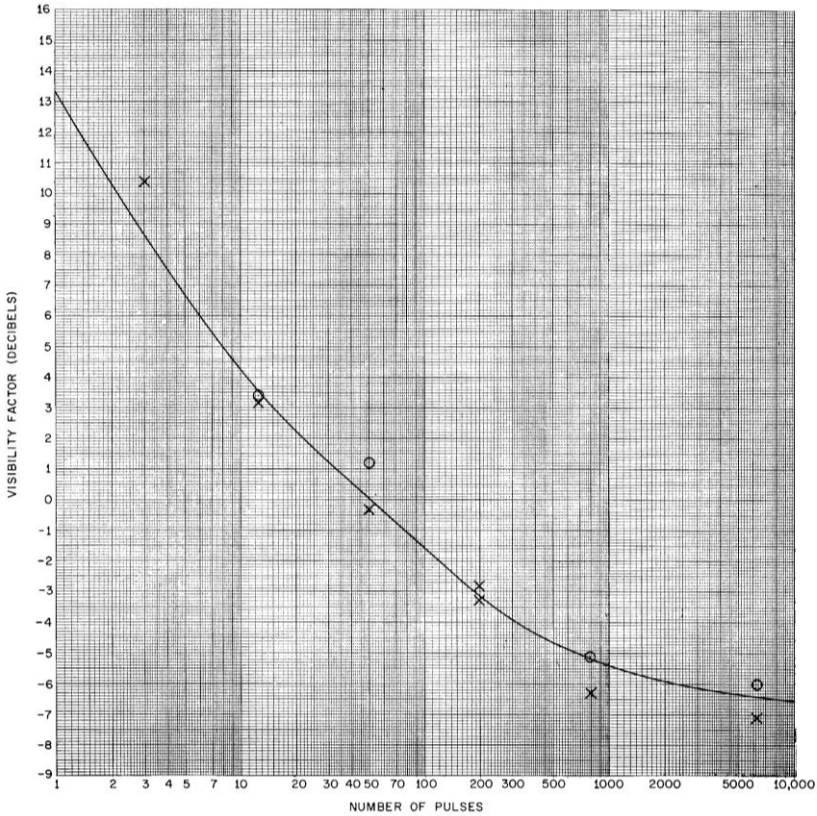

Figure 4.13 Visibility factor $V_{0(50)}$ for PPI display under optimum viewing conditions [17].

> The operator loss tends in practice to become an arbitrary factor to account for observe discrepancies between computer performance and observed radar performance; and while in some cases it may be a valid explanation, in others it may be misused to conceal ignorance to why a radar's actual performance is less than predicted by calculations. In any case, it is too vague a concept to employ in a range calculation aimed at evaluating the merit of a particular radar design or for other engineering purposes.

Omitted from that discussion is the difference between D_0 for electronic detection with a matched filter and V_0 for visual detection with a receiver noise bandwidth $B_n = 1.2/\tau$ and a video bandwidth restricted by resolution on the display. That issue requires that visual detection procedures include losses different from those used in electronic detection.

4.7 SUMMARY OF DETECTION THEORY

This chapter presented methods for calculating the basic detectability factor, based on detection theory, for target models including the steady target (Case 0), fluctuating targets described by Swerling Cases 1–4, and the more general class of target echoes having chi-square distributions with an arbitrary number of degrees of freedom.

- Exact expressions for P_d that are accurate to within 0.01 dB in the corresponding signal-to-noise ratios are available from [6] for Cases 0–5. Solutions to these expressions using root-finding methods are thus able to give the detectability factors to that accuracy.
- Approximations for calculating $D(n)$ that approach this accuracy for most cases of practical interest have also been presented, with plots that compare their results with the solutions for $D(n)$ obtained by root-finding from the exact equations.
- The value of $D(n)$ includes two factors that may or may not appear as separate terms: the integration loss $L_i(n)$ (see Section 4.4.3) and the fluctuation loss L_f (see Section 4.4.5). Both these losses increase $D(n)$ relative to a theoretical minimum value given by D_{01}/n that would apply to a steady signal integrated coherently. They must be included as components of system loss L_s when the search radar equation is used, but need not be evaluated individually for use in the normal radar equation.
- Any radar equation requires, once $D(n)$ has been found, that a series of practical losses be calculated for the practical radar under consideration. The Blake chart described in Section 1.3.2 has separate entries for a bandwidth correction factor C_b, a beamshape loss L_p, and a miscellaneous loss L_x. The chart as modified in Section 1.4.2 includes L_p and L_x, and substitutes a matching factor M for C_b.
- The beamshape loss L_p, is the subject of Chapter 5, and the matching factor M along with a number of components of L_x are discussed in Chapter 10. The effective detectability factor $D_x(n)$ used in radar equations (1.19)–(1.23) is calculated as the product of these losses and $D(n)$. Thus D_x includes the losses that increase the required signal-to-noise energy ratio.
- Losses that reduce the available energy ratio, including RF loss L_t, atmospheric loss L_α, other losses that depend on range, are included as separate factors in (1.26).

References

[1] Blake, L. V., "Recent Advancements in Basic Radar Range Calculation Technique," *IRE Trans. on Military Electronics*, Vol. MIL-5, No. 2, April 1961, pp. 154–164.

[2] Barton, D. K., *Radar System Analysis and Modeling*, Norwood, MA: Artech House, 2005.

[3] Rice, S. O., **"**Mathematical Analysis of Random Noise," *Bell System Tech. J.*, Vol. 23, No. 3, July 1944, pp. 282–332, and Vol. 24, No. 1, January 1945, pp. 461–556. Reprinted: *Selected Papers on Noise and Stochastic processes*, (N. Wax, ed.), New York: Dover Publ., 1954.

[4] Marcum, J. I., "A Statistical Theory of Target Detection by Pulsed Radar," *RAND Corp. Res. Memo. RM-754*, December 1, 1947. Reprinted: *IRE Trans. on Information Theory*, Vol. IT-6, No. 2, April. 1960, pp. 59–144. Reprinted: *Detection and Estimation*, (S. S. Haykin, ed.), Stroudsberg, PA: Halstad Press, 1976, pp. 57–121.

[5] Marcum, J. I., "A Statistical Theory of Target Detection by Pulsed Radar (Mathematical Appendix)," *RAND Corp. Res. Memo. RM-753*, July 1, 1948. Reprinted: *IRE Trans. on Information Theory*, Vol. IT-6, No. 2, April 1960, pp. 145–268.

[6] DiFranco, J. V. and W. L. Rubin, *Radar Detection*, Englewood Cliffs, NJ: Prentice-Hall, 1968; Artech House, 1980.

[7] Abramowitz, M. and I. A. Stegun, *Handbook of Mathematical Tables*, Natl. Bureau of Standards Applied Mathematics Series 55, Washington: U.S. Gov't. Printing Office, 1964.

[8] Gregers-Hansen, V., "Simple Expressions for Determining Radar Detection Thresholds," *IEEE Trans. on Aerospace and Electronics Systems*, Vol. AES-18, No. 4, July 1982, pp. 510–512. See corrections in [9].

[9] Urkowitz, H., "Corrections to and Comments on 'Simple Expressions for Determining Radar Detection Thresholds,'" *IEEE Trans. on Aerospace and Electronics Systems*, Vol. AES-21, No. 4, July 1985, pp. 583–558.

[10] North, D. O., "An Analysis of the Factors Which Determine Signal/Noise Discrimination in Pulsed Carrier Systems," *RCA Laboratories Technical Report PTR-6C*, June 25, 1943. Reprinted: *Proc. IEEE*, Vol. 51, No. 67, July 1963, pp. 1015–1027.

[11] Shnidman, D. A., "Determination of Required SNR Values," *IEEE Trans. on Aerospace and Electronic Systems*, Vol. AES-38, No. 3, July 2002, pp. 1059–1064.

[12] Swerling, P., "Probability of Detection for Fluctuating Targets," *RAND Corp Res. Memo RM-1217*, March 17, 1954. Reprinted: *IRE Trans. on Information Theory*, Vol. IT-6, No. 2, April 1960, pp. 269–308. Reprinted: *Detection and Estimation*, (S. S. Haykin, ed.), Stroudsberg, PA: Halstad Press, 1976, pp. 122–158.

[13] Barton, D. K., "Universal Equations for Radar Target Detection," *IEEE Trans. on Aerospace and Electronic Systems*, Vol. AES-41, No. 3, July 2005, pp. 1049–1052.

[14] Weinstock, W. W., "Radar Cross-Section Target Models," Chapter VI-5 in *Modern Radar*, (R. S. Berkowitz, ed.), New York: John Wiley, 1965.

[15] Barton, D. K., "Simple Procedures for Radar Detection Calculations," *IEEE Trans. on Aerospace and Electronic Systems*, Vol. AES-5, No. 5, September 1969, pp. 837–846. Reprinted: *Radars*, Vol. 2, *The Radar Equation*, (D. K. Barton, ed.), Dedham, MA: Artech House, 1974, pp. 113–122.

[16] Kanter, I., **"**Exact Detection Probability for Partially Correlated Rayleigh Targets," *IEEE Trans. on Aerospace and Electronic Systems*, Vol. AES-22, No. 2, March 1986, pp. 184–196.

[17] Blake, L. V., "A Guide to Basic Pulse-Radar Maximum-Range Calculations," *Naval Res. Lab. Report 5868*, December 28, 1962.

[18] Lawson, J. L., and G. E. Uhlenbeck, *Threshold Signals*, Vol. 24 in MIT Radiation Laboratory Series, New York: McGraw-Hill, 1950. Reprinted (CD ROM edition): Norwood, MA: Artech House, 1999.

[19] Ashby, R. M., V. Josephson, and S. G. Sydoriak, "Signal Threshold Studies," *Naval Res. Lab. Report 3007*, December 1946.

[20] Blake, L. V., *Radar Range-Performance Analysis*, Lexington, MA: D.C. Heath, 1980; Dedham, MA: Artech House, 1986.

CHAPTER 5

Beamshape Loss

The basic detectability factors derived in Chapter 4 could be used directly in the radar equation for an idealized radar design only if the signal were transmitted and received with constant two-way antenna gain G_tG_r during the time t_o required to collect n pulses or n' coherently integrated samples of the signal, and if matched filtering and ideal post-detection integration were used. For a given antenna, variation in gain is represented in the radar equation by the product $f_t f_r$ that is included in the pattern-propagation factor $F^2 = F_tF_r$ (see Chapter 8). When a radar scans in angle to detect a target, the gain varies either during t_o (for continuous scan) or from one scan or beam dwell to another (for electronic raster scan or step-scan).The effect of the resulting pattern modulation on the n pulses used in calculating D is expressed by the *beamshape loss* (or *beamshape factor*), denoted by L_p. This loss is discussed in this chapter for different target types and processing methods. It applies both to search radar and to tracking radar in its acquisition mode. In most cases the tracking radar after acquisition holds its beam close enough to the target to achieve the on-axis antenna gain, and no beamshape loss occurs in that mode of operation.

5.1 BACKGROUND

5.1.1 Definition of Beamshape Loss

Beamshape loss is defined [1] as:

> A loss factor included in the radar equation to account for the use of the peak antenna gain in the radar equation instead of the effective gain that results when the received train of pulses is modulated by the two-way pattern of a scanning antenna. *Synonym:* antenna-pattern loss.

Recall that the number of integrated pulses n for a scanning radar is conventionally calculated as the number received while the target is within the one-way, half-power beamwidth θ_3. The detection probability is conventionally calculated assuming integration of n pulses of equal level, and the inclusion of the loss component L_p in radar equation is intended to ensure that the on-axis signal power is high enough that the detection probability P_d can be calculated as though all n pulses had been received with the on-axis antenna gain. Figure 5.1 shows a sequence of pulses received from a Gaussian beam scanning in one dimension, where $n = 10$ and the on-axis power is $L_p = 1.33$ times the power in the rectangular reference beam. This peak level of the modulated train has been set to make the energy of the modulated train equal to that of the rectangular beam. To recover that energy in signal processing, the integrator weighting must match the two-way Gaussian pattern of the beam, with significant contributions in the case illustrated from about 16 pulses rather than only the 10 within the half-power beamwidth.

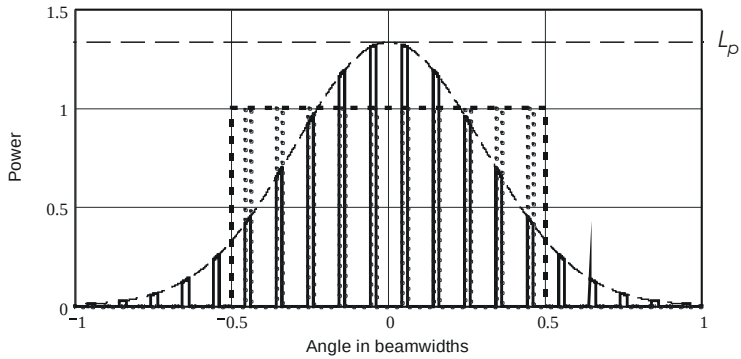

Figure 5.1 Pulse train modulated by Gaussian beam scanning in one dimension with $n = 10$ pulses. The energy of the entire modulated train with on-axis power $L_{p1} = 1.33$ is equal to that of 10 pulses of power 1.0 in the rectangular reference beam shown by the heavy dashed line.

5.1.2 Sampling in Angle Space

The scanning radar performs sampling the angle space. For one-dimensional (1-D) scanning, a sample is either an individual pulse of the continuously scanning pulse train or the n-pulse group of a step-scanned antenna.[1] Each line in the search raster for two-dimensional (2-D) scanning is sampled first in the coordinate of rapid scanning. With electronic step-scanning, the n pulses have the same amplitude, but that amplitude varies with the position of the target relative to the axis of the

[1] When step scans or raster scans are used, n is to be interpreted as the number of groups or scan lines per beamwidth.

beam and has a Gaussian distribution when targets are uniformly distributed in angle. The successive scan lines in 2-D scanning provide samples in the other coordinate, usually combined through the cumulative probability of detection, defined as the probability that detection occurs on at least one line of the scan rather than by integration (see Section 10.2.5).

The angular sampling interval Δ is defined here in units of the one-way, half-power beamwidth θ_3 in the angle coordinate of interest.[2] Radars normally obtain samples that are spaced by $\Delta \leq 0.71$, which can be described as *dense sampling*, and for which $n \geq 1.41$. The beamshape loss is then simply the ratio of the target echo energy that would have been received if the beam were rectangular, with widths equal to the half-power widths of the actual beam, to the energy received during the scan by the actual beam pattern. The center of the beam in 1-D scanning is assumed to pass directly across the target. When it does not, the pattern-propagation factor F is applied in the unscanned coordinate to account for the reduced signal.

Sampling intervals $\Delta > 0.71$ provide *sparse sampling* in angle space. The beamshape loss is no longer a simple ratio of average energy received in the scanning beam to that of a rectangular reference beam. Rather, it must be defined as the increase in on-axis power required to achieve an average probability of detection P_d equal to what would have been achieved for a target lying on the beam axis during all n pulses. The average P_d over angle space cannot be found by integrating n samples whose total energy is n times that of the average sample. This is because, in seeking to obtain $P_d > 0.4$, the reduced P_d for samples near the edge of the beam pattern reduces the average P_d more than it is increased by samples near the axis.

5.1.3 Literature on Beamshape Loss

5.1.3.1 Dense Sampling

Beamshape loss was introduced in Blake's 1953 paper [2]. He expresses the loss in terms of a reduction in the number of full-amplitude (on-axis) pulses that would provide the same total energy as obtained from the pulse train modulated by the pattern of the scanning beam. Blake considers an exponential beam than scans across the target, delivering pulses to a receiver using a square-law detector. The improvement from integration of the received pulse train is given in terms of integrals over the portion of the beam pattern that lies within a rectangular *integration window*, from which he derives the optimum window width and integration gain. He expresses the result in terms of an equivalent number of equal-amplitude puls-

[2] In electronic scanning from an array antenna, it will be assumed that the intervals Δ are constant in sine space, maintaining their values relative to the varying beamwidth at off-broadside angles.

es given by $0.473n$, assuming initially $n >> 1$ and uniform integrator weighting over the optimum angular interval $0.844\theta_3$. Because large n implies low single-pulse signal-to-noise ratio (snr), the integration gain is proportional to $\sqrt{n}$.

To retain detection probability when the target does not remain on the axis during the n pulses used for integration, the on-axis signal power must be increased by the factor $L_p = 1/\sqrt{0.473} = 1.45 = 1.6$ dB. For lower pulse densities, but excluding the sparse sampling case, Blake derives the available integration gain using summations rather than integrals, and concludes that the results agree closely with the high-density case.

In the addendum [3] to his paper, Blake notes that for a linear detector giving integration gain proportional to n, the optimum integration interval is $1.2\theta_3$ and the loss is $L_p = 1/0.67 = 1.5 = 1.7$ dB. He subsequently presents the range calculation [4] in the form now known as the Blake chart that includes an entry for L_p. He suggests the following values as a simple model for beamshape loss:

$L'_{p1} = 1.6$ dB for one-coordinate (1-D) scanning;
$L'_{p2} = 2L'_{p1} = 3.2$ dB for two-coordinate (2-D) scanning.

where the primed symbols denote values in decibels. We will consider in Sections 5.1.3 and 5.3–5.5 the relationship between this simple beamshape loss model and results of subsequent studies.

5.1.3.2 Sparse Sampling

Studies on beamshape loss by Hall and Barton [5,6] consider lower sample densities ($0.5 < n < 2$), such as might occur in radars using electronic scan, or in two-dimensional (2-D) scans where successive beam dwells and scan lines are spaced in the order of the beamwidth. The beamshape loss, expressed as the increase in on-axis signal power needed to maintain a given P_d for targets uniformly distributed in angle space with respect to sample points, is found to depend strongly on P_d, sample spacing, processing method, and the target fluctuation model.

Analytical approximations for beamshape loss with sparse sampling are given by Barton in [7, p. 137; 8, p. 494; 9, p. 87]. The procedures for generating these approximations are refined in this chapter to obtain more accurate models for different scan patterns and targets over the range of sampling densities and detection probabilities typically required in calculation of detection range.

5.2 BEAMSHAPE LOSS WITH DENSE SAMPLING

5.2.1 Simple Beamshape Loss Model

The loss in signal energy for matched weighting of the integrator is calculated by integrating the two-way power pattern of the beam as its axis moves over the scan path relative the target position. The loss for 1-D scanning, denoted by the subscript $_{p1}$, is:

$$L_{p1} = \left[\frac{1}{\theta_3} \int_{-\pi}^{\pi} f^4(\theta) d\theta \right]^{-1} \tag{5.1}$$

where $f(\theta)$ is the one-way voltage pattern of the beam in the scanned coordinate θ. For a 2-D scan in coordinates θ and ϕ, with an antenna having identical, separable illuminations, we denote the loss by a subscript $_{p2}$:

$$\begin{aligned} L_{p2} &= \left[\frac{1}{\theta_3 \phi_3} \int_{-\pi/2}^{\pi/2} \int_{-\pi}^{\pi} f^4(\theta) f^4(\phi) d\theta d\phi \right]^{-1} \\ &= \left[\frac{1}{\theta_3} \int_{-\pi}^{\pi} f^4(\theta) d\theta \right]^{-1} \left[\frac{1}{\phi_3} \int_{-\pi/2}^{\pi/2} f^4(\phi) d\phi \right]^{-1} = L_{p1}^2 \end{aligned} \tag{5.2}$$

5.2.2 Antenna Patterns

A common model for the radar antenna voltage pattern[3] is the Gaussian beam, which closely follows the pattern of most antennas out to about the −10 dB level, but has no sidelobes:

$$f_g(\theta) = \exp\left[-2(\ln 2) \frac{\theta^2}{\theta_3^2} \right] \tag{5.3}$$

At the other extreme, the uniformly illuminated rectangular antenna, for which the sidelobes are −13.6 dB relative to the on-axis gain, has a voltage pattern:

$$f_u(\theta) = \frac{\sin(\pi K_\theta \theta/\theta_3)}{\pi K_\theta \theta/\theta_3} = \frac{\sin(0.8859\pi\theta/\theta_3)}{0.8859\pi\theta/\theta_3} \tag{5.4}$$

[3] Beamwidths are assumed to be narrow enough to justify the small-angle approximation $\sin\theta \approx \theta$.

An intermediate example is the cosine-illuminated rectangular antenna, with first sidelobes −23 dB relative to the on-axis gain and a voltage pattern:

$$f_{\cos}(\theta) = \frac{\cos(\pi K_\theta \theta/\theta_3)}{1-(2K_\theta \theta/\theta_3)^2} = \frac{\cos(3.7353\theta/\theta_3)}{1-(2.3779\theta/\theta_3)^2} \tag{5.5}$$

where $K_\theta = 1.1889$ is the beamwidth constant for angle in radians. Another intermediate example, with nonseparable illuminations, is the uniformly illuminated circular antenna, for which the sidelobes are −17.6 dB relative to the on-axis gain:

$$f_{\text{cir}}(\theta) = \frac{2J_1(K_\theta \pi \theta/\theta_3)}{\pi K_\theta \theta/\theta_3} = \frac{2J_1(1.0290\pi\theta/\theta_3)}{1.0290\pi\theta/\theta_3} \tag{5.6}$$

where $J_1(\cdot)$ is the first-order Bessel function of the first kind. The 2-D beamshape loss in this case is calculated by integration of elemental rings having equal radius θ from the axis:

$$L_{p2\text{cir}} = 2\pi \int_0^\pi \theta f_{\text{cir}}^4(\theta)\, d\theta \tag{5.7}$$

When the transmitting and receiving beamwidths θ_t and θ_r differ, the effective beamwidth to be used in the preceding equations is

$$\theta_3 = \theta_{\text{eff}} = \frac{\sqrt{2}\theta_t\theta_r}{\sqrt{\theta_t^2 + \theta_r^2}} \tag{5.8}$$

5.2.3 Beamshape Loss for Different Patterns

The 1-D and 2-D beamshape losses for the Gaussian beam are given exactly by:

$$L_{p1} = \sqrt{\frac{8\ln 2}{\pi}} = 1.3288 \tag{5.9}$$

$$L_{p2} = \frac{8\ln 2}{\pi} = 1.7658 \tag{5.10}$$

Values of beamshape loss for other illuminations are shown in Table 5.1. It can be seen that calculations using the Gaussian pattern model adequately express the

beamshape loss in all these cases, and hence can be used for other radar antenna patterns. The value of L_{p2} is the same as derived in expressing volume resolution cell containing precipitation used in the weather radar equation [10, p. 74, Eq. (4.13)].

Nominal values with adequate accuracy for any radar beam pattern are shown in the last row of the table, expressed to two decimal places. The 1.24 dB loss for 1-D scan, to be used extensively as a reference, will be denoted here by L'_{p0}.

Table 5.1 Beamshape Loss for Commonly Used Pattern Models

Pattern Model	1-*D Scan*		2-*D Scan*	
	L_{p1} (power ratio)	L'_{p1} (dB)	L_{p1} (power ratio)	L'_{p2} (dB)
Gaussian	1.3280	1.234	1.7651	2.468
Uniform rectangular	1.3290	1.235	1.7697	2.479
Cosine rectangular	1.3317	1.244	1.7733	2.488
Uniform circular	1.3314	1.245	1.7742	2.549
Typical radar beam	1.33	1.24	1.77	2.48

The values shown in Table 5.1 are beamshape losses used in the normal radar equation for dense sampling ($\Delta < 0.71$). As will be shown below, the search radar equation and the normal equation with sparse sampling require loss values that vary with Δ, approaching the values of Table 5.1 only in special cases.

5.3 SPARSE SAMPLING IN 1-D SCAN

Radars that perform search with narrow beams must generally minimize the time allocated to searching a given angle space, which may lead to sparse sampling (beam dwells spaced by $\Delta > 0.71$). The beamshape loss then depends on the required detection probability P_d, the spacing, the integration procedure, and the target fluctuation model.

When using radar equations developed in Chapter 1 it is assumed that the scan pattern of the radar has been taken into account in calculating the radar parameters, and that the transmitted energy per beam *dwell* is constant (independent of the spacing of the dwells). If spacing less than the beamwidth is used, more energy is allocated to a given solid angle. On the other hand, when the search radar equation of Chapter 2 is used, the transmitted energy per *scan* is constant, because in the derivation of the equation the idealized rectangular beams were assumed to be contiguous with no overlap. This changes the reference used in calculation of beamshape loss, as explained in Section 5.3.5. Spacing of dwells closer than the beamwidth then reduces the available energy per dwell. Hence, the

beamshape loss required for use in the search radar equation differs from that used in the normal radar equation.

5.3.1 Method of Calculation for 1-D Scan

The number of samples n available for integration is the reciprocal of the beam spacing Δ in beamwidths. Sparse sampling, $\Delta > 0.71$, corresponds to $n < 1.41$. We will assume that the integrator weighting function is matched to the beam pattern, so that the output snr depends on the total signal energy received during the scan. A small integration loss, increasing for $n > 1$, appears separately in calculation of the basic detectability factor, Section 4.4.3. The procedure for selecting and averaging sample positions and amplitudes to calculate beamshape loss is as follows.

- *Beam Spacing*. The beam spacing Δ_k is expressed in units of the beamwidth θ_3, and is varied over $0.5 \le \Delta \le 1.5$ to overlap with the dense sampling case and extend to the maximum practical beam spacing. To generate smooth output plots, the spacing is varied in increments $\delta = 0.05$, giving $\Delta_k = k\delta$ for $k = 10, 11, \ldots, 30$.
- *Beam Angles*. Three beams are denoted by $m = 1, 2, 3$, and are centered at angles $\theta_b(k,m) = (m - 2)\Delta_k$, as shown in Figure 5.2.

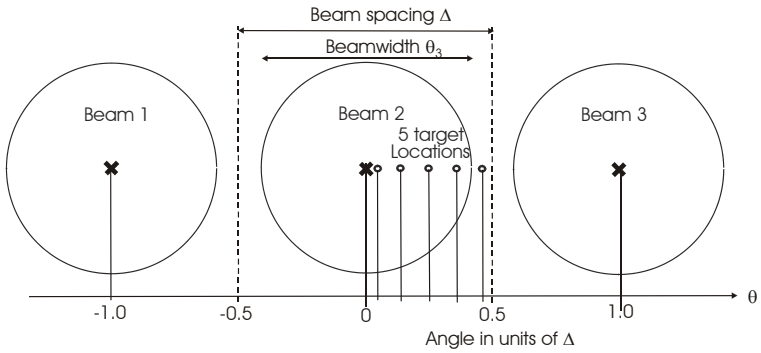

Figure 5.2 Beam and target locations for calculation of beamshape loss with 1-D scan.

- *Target Angles.* To represent targets distributed uniformly in angle θ, five targets are placed at angles $\theta_t(j,k)$ between the axis of beam 2 and a point halfway to the axis of beam 3, as shown in Figure 5.2. The target index varies over $j = 1, 2, \ldots, j_{\max}$, where $j_{\max} = 5$:

$$\theta_t(j,k) = (0.1j - 0.05)\Delta_k \tag{5.11}$$

- *Off-Axis Angles.* The angle between target position $\theta_t(j,k)$ and the axis $\theta_b(k,m)$ of beam m is calculated to obtain a three-dimensional matrix of off-axis angle for each signal sample:

$$\theta(j,k,m) = \theta_b(k,m) - \theta_t(j,k) \tag{5.12}$$

- *Sample SNR.* The snr for each sample is calculated using the beam pattern $f_{\cos}(\theta)$ of an aperture with cosine illumination from (5.5). That pattern closely represents that of many practical radars, in which the mainlobe is bounded by nulls, with a first sidelobe level of −23 dB. The result is a four-dimensional matrix:

$$s(i,j,k,m) = s_i f_c^4\left[\theta(j,k,m)\right] \tag{5.13}$$

where s_i is the on-axis snr. This snr is varied in decibel steps: $s_i' = 0, 1, \ldots, 35$ dB to cover the desired values of P_d. Different procedures are then used to calculate L_{p1}, depending on the target model and signal processing method.

5.3.2 Steady-Target Beamshape Loss for 1-D Scan

The steps in calculating beamshape loss for the steady target with two processing methods of combining the signals are listed in Table 5.2.

The subscript $_{\{0\}}$ denotes the steady target. The detectability factors in (5.17) and (5.23) are calculated for four values of detection probability to be used in subsequent plots of beamshape loss: $P_{du} = 0.1u$, where $u = 3, 5, 7, 9$. The reference detectability factor $D_{r\{0\}}$ given by (5.18) is obtained from (4.18), adjusted for coherent integration of the $n_k = 1/\Delta_k$ signal samples that would be received in the rectangular reference beam of Figure 5.1. Integration loss is a separate component of D_x in the radar equation. For $\Delta > 1$, a single sample with power $1/\Delta_k$ is assumed in calculating the reference $D_{r\{0\}}$.

5.3.2.1 Steady Target with Integration

The 1-D beamshape loss $L_{p1\{0\}}$ for a steady target with integration is shown in Figure 5.3. Curves for all values of P_d merge with the dense-sample value $L_{p0}' = 1.24$ dB for spacings $\Delta < 0.71$. For $\Delta > 0.71$ and $P_d \le 0.45$, the loss drops below L_{p0} because the increase in P_d near the axis more than compensates for the decrease near the edge of the beam. Increasing loss for $\Delta_k > 0.8$, $P_d > 0.45$ confirms the results of [5, 6]. Since spacings $\Delta \ge 1.5$ cause losses that are excessive for most radar applications, the data presented here are limited to $\Delta \le 1.5$.

Table 5.2 Steps in Calculating Beamshape Loss for 1-D Scan, Steady Target

Integration over entire scan		
(1) Sum signals from all m beams	$S_i(i,j,k)=\sum_m s(i,j,k,m)$	(5.14)
(2) Detection probability for integrated signal	$P_{di\{0\}}(i,j,k)=\Phi\left[\sqrt{2\ln(1/P_{fa})}-\sqrt{2S_i(i,j,k)+1}\right]$	(5.15)
(3) Average $P_{di\{0\}}$ over target positions	$\overline{P_{d\{0\}}}(i,k)=\frac{1}{j_{\max}}\sum_j P_{di\{0\}}(i,j,k)$	(5.16)
(4) Detectability factor with beamshape loss	$D_{p\{0\}}(k,u)=s_x, x \;=\; \text{root}_i\left[\overline{P_{d\{0\}}}(i,k)=P_{du}\right]$	(5.17)
(5) Reference detectability factor	$D_{r\{0\}}(k,u)=\frac{\Delta_k}{2}\left\{\left[\sqrt{2\ln(1/P_{fa})}-\Phi^{-1}(P_{du})\right]^2-1\right\}$	(5.18)
(6) Beamshape loss	$L_{p1\{0\}}(k,u)=D_{p\{0\}}(k,u)/D_{r\{0\}}(k,u)$	(5.19)
Cumulative detection over entire scan		
(1) Detection probability for single beam	$P_{d1\{0\}}(i,j,k,m)=\Phi\left[\sqrt{2\ln(1/P_{fa})}-\sqrt{2s(i,j,k,m)+1}\right]$	(5.20)
(2) Cumulative probability over all m beams	$P_{c\{0\}}(i,j,k)=1-\prod_m\left[1-P_{d1\{0\}}(i,j,k,m)\right]$	(5.21)
(3) Average $P_{c\{0\}}$ over all target positions	$\overline{P_{c\{0\}}}(i,k)=\frac{1}{j_{\max}}\sum_j P_{c\{0\}}(i,j,k)$	(5.22)
(4) Detectability factor with beamshape loss	$D_{p\{0\}}(k,u)=s_x, x \;=\; \text{root}_i\left[\overline{P_{c\{0\}}}(i,k)=P_{du}\right]$	(5.23)
Steps (5) and (6) are the same as for integration.		

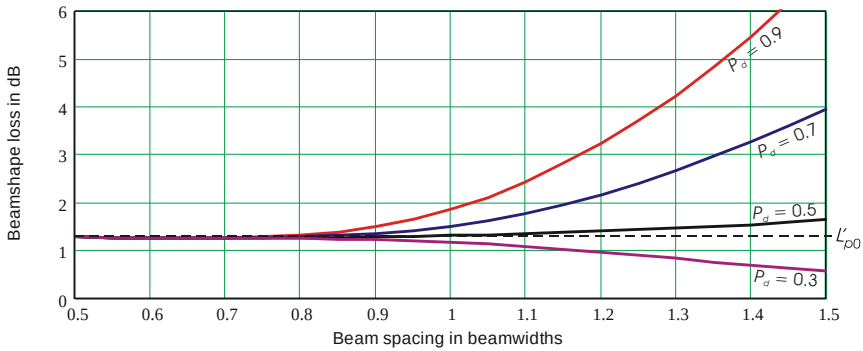

Figure 5.3 Beamshape loss L_{p1} versus sample spacing Δ for steady target with integration. A dashed line shows the dense-sample value L'_{p0} = 1.24 dB.

5.3.2.2 Steady Target with Cumulative Detection

The cumulative detection probability is the probability that detection will be achieved in at least one of several attempts during the scan. With respect to beamshape loss, detection is attempted separately in each beam position (dwell). The results are shown in Figure 5.4. The loss now includes the effect the lower efficiency of cumulative detection, as compared with integration (see Section 10.2.5). There is an optimum beam spacing near 0.75 beamwidths for high P_d, when cumulative detection over successive beam positions replaces integration. Thus it appears that integration of steady-target samples is worthwhile even when the number of samples per beamwidth drops to unity.

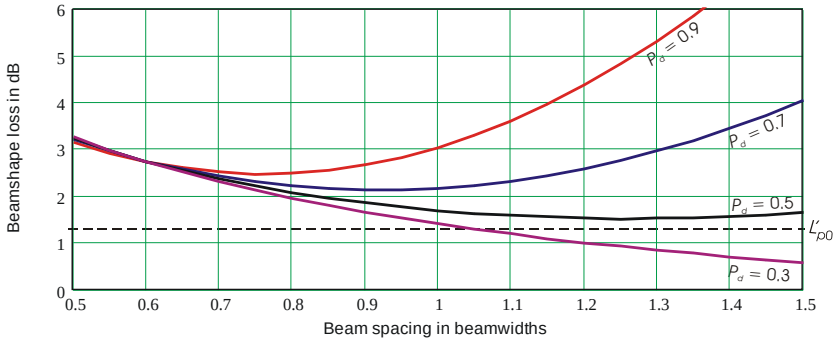

Figure 5.4 Beamshape loss L_{p1} versus sample spacing Δ for steady target with cumulative detection.

5.3.3 Case 1 Beamshape Loss for 1-D Scan

The steps in calculating beamshape loss for the Case 1 target with the two processing methods of combining the signals are listed in Table 5.3. For integration, the steps are parallel to those used with the steady target, but substituting the Case 1 terms $P_{d\{1\}}$ from (4.26) and $D_{r\{1\}}$ from (4.27) in steps (2) and (5). Because the samples of the Case 1 target are correlated over the scan, it is necessary to calculate the cumulative probability of detection by first calculating $P_{c\{0\}}$ for the steady target (see Table 5.2), and then finding $P_{c\{1\}}$ by integrating $P_{c\{0\}}$ over the exponential distribution that describes the Case 1 fluctuation from one scan to the next. Subsequent steps parallel those for the steady target.

Table 5.3 Steps in Calculating Beamshape Loss for Case 1

Integration over entire scan		
(1) Add signals from *m* beams	$S_i(i,j,k)=\sum_m s(i,j,k,m)$	(5.24)
(2) Detection probability for integrated signal	$P_{di\{1\}}(i,j,k)=\exp\left(\ln P_{fa}/\left[1+S_i(i,j,k)\right]\right)$	(5.25)
(3) Average over *j* target positions	$\overline{P_{di\{1\}}}(i,k)=\frac{1}{j_{\max}}\sum_j P_{di\{1\}}(i,j,k)$	(5.26)
(4) Detectability factor for signal on beam axis	$D_{p\{1\}}(k,u)=s_x$, where x = root$_i\left[\overline{P_{di\{1\}}}(i,k)=P_{du}\right]$	(5.27)
(5) Reference detectability factor	$D_{r1}(k,u)=\Delta_k\left[\left(\ln P_{fa}/\ln P_d\right)-1\right]$	(5.28)
(6) Beamshape loss	$L_{p1\{1\}}(k,u)=D_{p\{1\}}(k,u)/D_{r\{1\}}(k,u)$	(5.29)
Cumulative detection over entire scan		
(1) Steady-target detection probability in single beam	$P_{d\{0\}}(i,j,k,m)=\Phi\left[\sqrt{2\ln\left(1/P_{fa}\right)}-\sqrt{2s(i,j,k,m)+1}\right]$	(5.30)
(2) Steady-target cumulative probability over *m* beams	$P_{c\{0\}}(i,j,k)=1-\prod_m\left[1-P_{d\{0\}}(i,j,k,m)\right]$	(5.31)
(3) Case 1 cumulative probability over *m* beams	$P_{c\{1\}}(i,j,k)=(1/s)\int_0^\infty \exp(-p/s)P_{c\{0\}}(p,j,k)\,dp$	(5.32)
(4) Average probability over *j* target positions	$\overline{P_{c\{1\}}}(i,k)=\frac{1}{j_{\max}}\sum_j P_{c\{1\}}(i,j,k)$	(5.33)
Steps (5–7) are the same as (4–6) for integration, with $P_{c\{1\}}$ replacing $P_{di\{1\}}$.		

5.3.3.1 Case 1 with Integration

The results for Case 1 with integration are shown in Figure 5.5. Compared with the steady target, the beamshape loss is less dependent on P_d, lying above

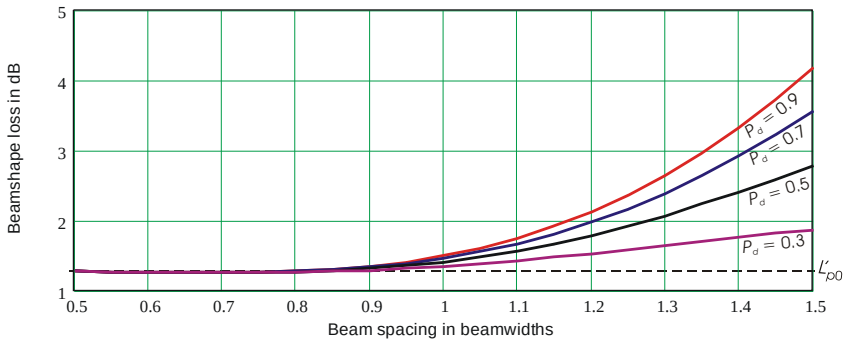

Figure 5.5 Beamshape loss L_{p1} versus sample spacing Δ_k for Case 1 with integration.

L_{p0} = 1.24 dB and below 4.2 dB for 0.5 < Δ < 1.5. This is because target fluctuation causes the values of detectability factor for Case 1 targets to change more rapidly with varying P_d, masking the variation in signal power caused by the beam pattern. The beamshape loss for Case 1 is less than for the steady target for P_d > 0.65, and greater below that probability.

5.3.3.2 Case 1 with Cumulative Detection

The results for Case 1 with cumulative detection are shown in Figure 5.6. The loss is greater than with integration for all sample spacings. The optimum beam spacing is near 0.95 beamwidths for high P_d. The loss shows less variation with P_d for Δ > 1 that was found with the steady-target.

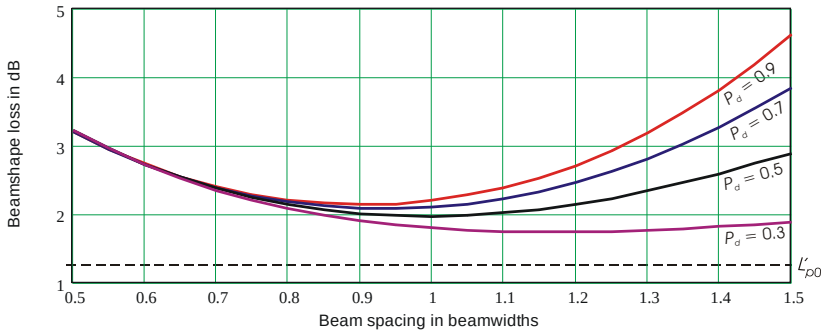

Figure 5.6 Beamshape loss $L_{p1}(k,u)$ versus sample spacing Δ_k for Case 1 with cumulative detection.

5.3.4 Case 2 Beamshape Loss for 1-D Scan

The Case 2 target provides independent target amplitudes for each sample. For integration, however, the number of such independent samples in the three beams, used in calculating the probability of detection $P_{d\{2\}}$ and reference detectability factor $D_{r\{2\}}$, depends on the weightings of samples in the matched integrator:

$$n_e(k) = \frac{1}{j_{\max}} \sum_j \left[m_{\max} - \frac{1}{\overline{f_g^4\left[\theta(j,k,m)\right]}} \sum_m \left\{ f_g^2\left[\theta(j,k,m)\right] - \overline{f_g^2\left[\theta(j,k,m)\right]} \right\}^2 \right] \tag{5.34}$$

where the terms $\overline{f_g^x\left[\theta(j,k,m)\right]}$ are averages over the three beams, m = 1, 2, 3. Figure 5.7 shows the number of samples as a function of spacing of the beams.

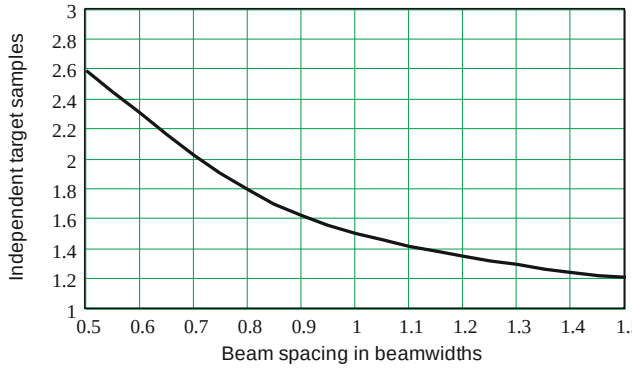

Figure 5.7 Number of independent target samples n_e as a function of beam spacing Δ_k.

The reference detectability factors for the three target models are shown in Figure 5.8, for a beam spacing $\Delta_k = 1$, at which $n_e(k) = 1.5$. The factor for Case 2 approaches that for Case 1 with large spacings, for which $n_e(k) \rightarrow 1$, and approaches that for the steady target with small spacings, $n_e(k) >> 1$.

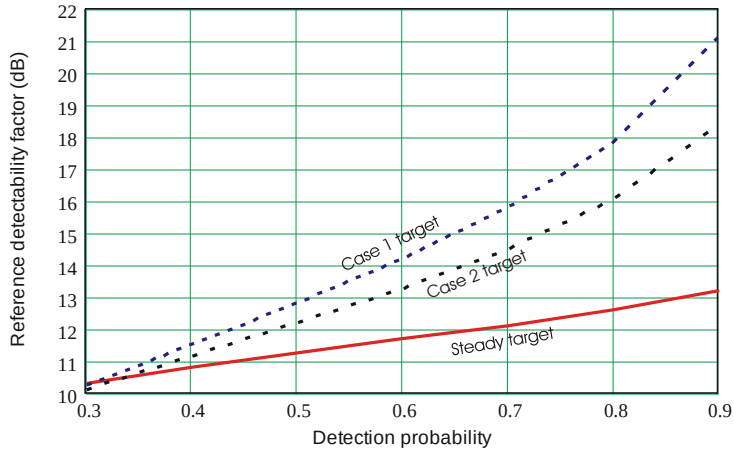

Figure 5.8 Reference detectability factors $D_{r\{0,1,2\}}$ for 1-D scan with $\Delta_k = 1$.

The steps in calculating beamshape loss for the Case 2 target with two processing methods of combining the signals are listed in Table 5.4. For integration, the steps parallel those used with the steady target, but with substitution of the Case 2 terms $P_{d\{2\}}$ from (4.36) in step (2) and $D_{r\{2\}}$ from (4.37), adjusted for Δ_k, in step (5).

Table 5.4 Method of Calculating Beamshape Loss for Case 2 Target

Integration over entire scan		
(1) Add signals from *m* beams	$S_i(i,j,k)=\sum_m s(i,j,k,m)$	(5.35)
(2) Detection probability for integrated signal with $n(k)$ target samples	$P_{d\{2\}}(i,j,k)=1-P_\gamma\left\{\frac{P_\gamma^{-1}(1-P_{fa},1)-\left[1-n_e(k)\right]}{\left[1/n_e(k)\right]S_i(i,j,k)+1},n_e(k)\right\}$	(5.36)
(3) Average $P_{d\{2\}}$ over target positions	$\overline{P_{d\{2\}}}(i,k)=\frac{1}{j_{\max}}\sum_j P_{d\{2\}}(i,j,k)$	(5.37)
(4) Detectability factor with beamshape loss	$D_{p\{2\}}(k,u)=s_x,\ \text{where}\ x\ =\ \text{root}_i\left[\overline{P_{d\{2\}}}(i,k)=P_{du}\right]$	(5.38)
(5) Reference detectability factor	$D_{r2}(k,u)=\Delta_k\left\{\frac{P_\gamma^{-1}(1-P_{fa},1)-\left[1-n_e(k)\right]}{P_\gamma^{-1}\left[1-P_{d_u},n_e(k)\right]}-1\right\}n_e(k)$	(5.39)
(6) Beamshape loss	$L_{p1\{2\}}(k,u)=D_{p\{2\}}(k,u)/D_{r\{2\}}(k,u)$	(5.40)
Cumulative detection over entire scan		
(1) Detection probability for single Rayleigh sample	$P_{d\{1\}}(i,j,k,m)=\exp\left\{\ln P_{fa}/\left[1+s(i,j,k,m)\right]\right\}$	(5.41)
(2) Cumulative probability over *m* beams	$P_{c\{2\}}(i,j,k)=1-\prod_m\left\{1-P_{d1\{1\}}\left[s(i,j,k,m)\right]\right\}$	(5.42)
(3) Average probability over target positions	$\overline{P_{c\{2\}}}(i,k)=\frac{1}{j_{\max}}\sum_j P_{c\{2\}}(i,j,k)$	(5.43)

Steps (4–6) are the same as for integration, with $P_{c\{2\}}$ replacing $P_{d\{2\}}$.

5.3.4.1 Case 2 with Integration

The loss for Case 2 with integration is not illustrated because it is practically indistinguishable from that of Case 1 (Figure 5.5). There is slightly greater spread of the curves as $\Delta \rightarrow 1.5$, but the differences from Case 1 are less than 0.2 dB.

5.3.4.2 Case 2 with Cumulative Detection

The results for Case 2 with cumulative detection are shown in Figure 5.9. The results for $\Delta > 1$ are between those for the steady target and Case 1. Because the reference detectability factor includes the diversity benefit of Case 2 with integration, relative to Case 1, the losses at $\Delta = 0.5$ are spread slightly about the value that applies to the steady target and Case 1, and the beamshape loss for $P_d > 0.3$ is higher than for Case 1. This does not imply that greater snr is necessary, however, because the reference value has been reduced by a greater amount than the increase in L_p.

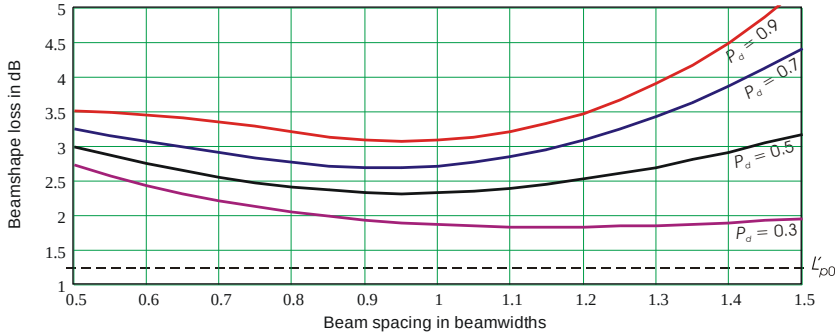

Figure 5.9 Beamshape loss $L_{p1}(k,u)$ versus sample spacing Δ_k for Case 2 target with cumulative detection.

5.3.5 Beamshape Loss Used in the Search Radar Equation for 1-D Scan

The search radar equation is based on uniform distribution of the energy transmitted during the frame time t_s among contiguous dwells of the idealized rectangular beam ($\Delta = 1$) covering the defined search sector. With continuous scan, the "dwell" can be considered the processing time leading to a detection decision, while in step-scan it is the dwell time of each step.

The energy per dwell must be reduced for actual beam spacings $\Delta < 1$, and increased for $\Delta > 1$, to keep the total energy during t_s constant. Application of the search radar equation to 1-D scan thus requires that the energy per dwell vary directly with the spacing Δ. When calculating beamshape loss as a function of Δ, it is convenient to include this variation of energy as contributing to a *net beamshape loss* L_{pn1} for use in the search radar equation. The result is

$$L_{pn1}(k,u) = \frac{L_{p1}(k,u)}{\Delta_k} \tag{5.44}$$

The procedure for calculating net beamshape loss L_{pn1} is the same as for L_{p1}, except that the sample snr given by (5.13) is replaced by:

$$s(i,j,k,m) = \Delta_k s_i f_c^4 \left[\theta(j,k,m)\right] \tag{5.45}$$

The net effect on beamshape loss of reapportionment of energy is shown in Figures 5.10 and 5.11 for steady and Case 1 targets with integration. The data

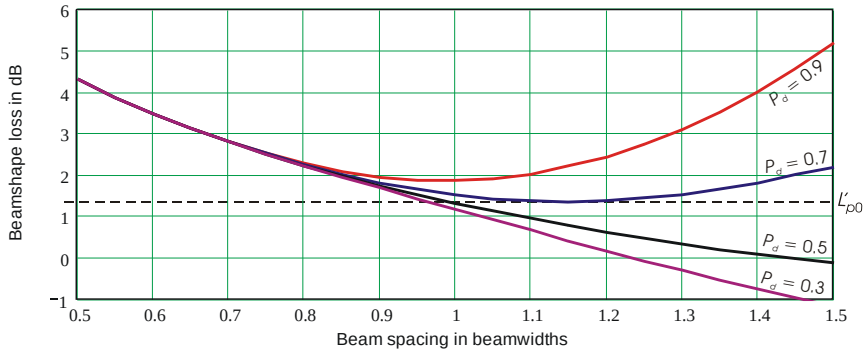

Figure 5.10 Net beamshape loss L_{pn1} versus sample spacing Δ_k for steady target with integration.

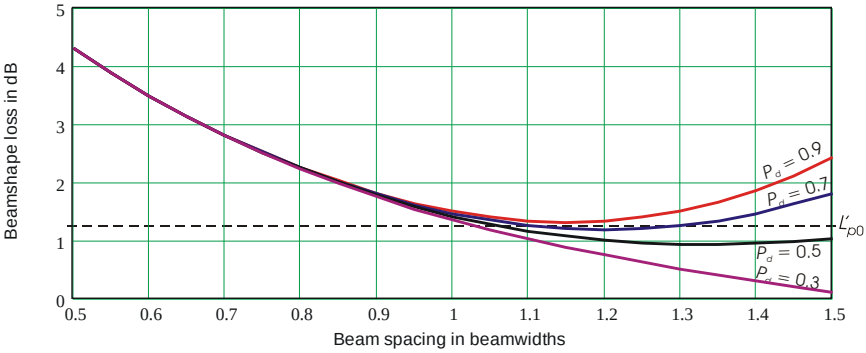

Figure 5.11 Net beamshape loss L_{pn1} versus sample spacing Δ_k for Case 1 with integration,

suggest that the optimum beam spacing with integration is $\Delta \approx 1.1$ for $P_d = 0.9$, increasing as P_d is reduced.

An electronically scanned search might perform a pseudorandom scan rather than a deterministic step-scan. In this case, integration over adjacent beams might be too difficult to perform, and the cumulative detection process would be used. The net beamshape loss with cumulative detection is shown in Figures 5.12 and 5.13 for steady and Case 1 targets. Optimum spacing for the steady target is the same as for integration of the signal, increasing to $\Delta_k = 1.2$ for Case 1. The losses for optimum spacing are $L_{pn1} = 3.1$ dB for the steady target and $L_{pn1} = 1.9$ dB for the fluctuating target.

Net beamshape loss curves for other fluctuating targets are not included here, since Case 1 is the predominant type for which radar systems must be designed, and Case 2 results lie between those for the steady target and Case 1.

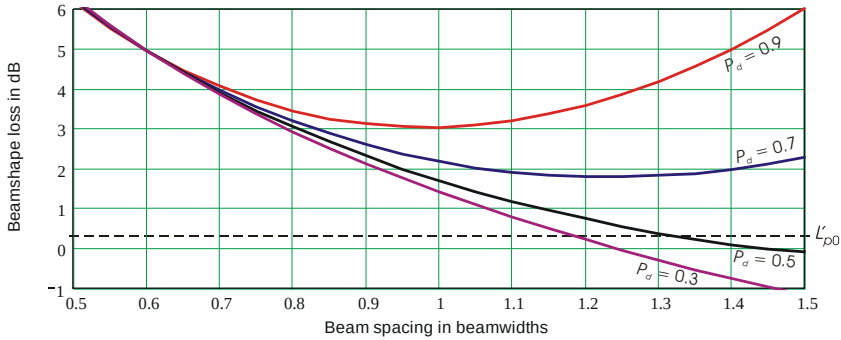

Figure 5.12 Net beamshape loss versus sample spacing Δ_k for steady target with cumulative detection.

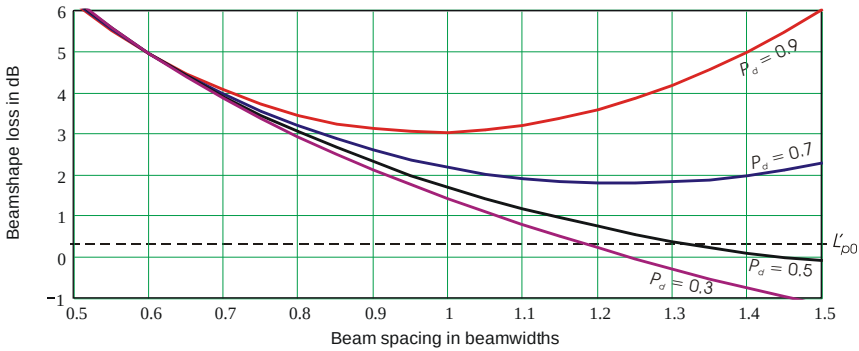

Figure 5.13 Net beamshape loss versus sample spacing Δ_k for Case 1 with mixed processing.

5.4 SPARSE SAMPLING IN 2-D RASTER SCAN

The 2-D raster scan uses a rectangular beam grid, as shown in Figure 5.14. The target locations used to find averages over angle space occupy one quadrant of the center beam. Analysis of beamshape loss is more complicated than for 1-D scan, but can be simplified by assuming the same beam spacing for the two coordinates, as is usually the case. Although the figure shows circular beams, the analysis is applicable to elliptical beams where the spacing is scaled to the beamwidth in each coordinate.

A second complication is that any of three processing methods may be used: integration or cumulative detection over the entire scan or integration across each line followed by cumulative detection over the three lines, which we will call *mixed processing*.

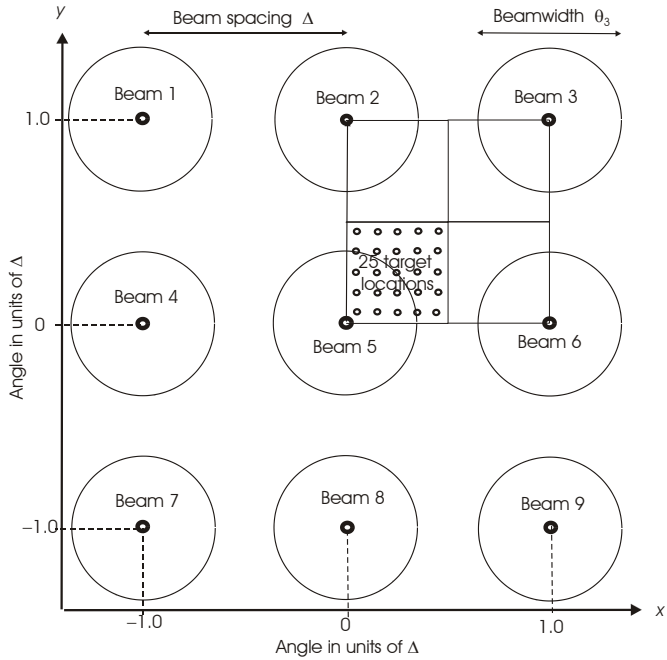

Figure 5.14 Beam grids and target sample positions for 2-D raster scan.

A third complication is that four target models must now be considered, rather than three:

- Steady target: Equal signal power for all samples in the scan;
- Case 1 target: Fluctuating power, correlated over the entire scan (Case 1);
- Case 2 target: Fluctuating power, decorrelated from dwell to dwell (Case 2);
- Diversity target: Fluctuating power, correlated over each line but decorrelated between successive lines of the scan. The decorrelation results from some form of diversity, and this target case will be denoted by the subscript $_D$.

Although procedures for analysis of all four models are presented, only results for the last three cases are given, as the steady target is seldom encountered. Chi-squared statistics for the fluctuating target will be treated, and other models can be analyzed using the procedure described for chi-squared targets. Analytic approximations for the steady-target beamshape loss in other cases are presented in Appendix 5A. The results for integration may be found as the square (twice the decibel value) of the losses shown in Figure 5.3 for 1-D scan.

5.4.1 Method of Calculation for 2-D Scan

The geometry for 2-D scan is similar to that in Section 5.3.1 for the 1-D scan, with the following changes:

- *Beam Spacing*. The beam spacing $0.5 \le \Delta_k \le 1.5$ beamwidths remains the same as for the 1-D scan, and is applied equally to both angle coordinates.
- *Beam Angles*. There are nine beams, denoted by subscripts $m = 1, 2, ..., 9$, with axes located at positions $\theta_m(k,m) = x_{k,m}, y_{k,m}$, as shown in Figure 5.14. The three scan lines are denoted by $a = 1, 2, 3$, each containing three beams $m_1(a) \le m \le m_2(a)$. For example, $m_1(1) = 1$ and $m_2(1) = 3$.
- *Target Angles*. There are 25 target positions $\theta_t(j,k) = x_{j,m}, y_{j,m}$, as shown in Figure 5.14, where $j = 1, 2, ..., 25$.

  The coordinate x is understood to be the coordinate of the more rapid scan line, over which integration is more easily performed. It may be either azimuth, elevation, or a coordinate in sine space. The orthogonal coordinate is y.
- *Off-Axis Angles*. The off-axis angle from the center of each beam to each target location is calculated as

$$\theta(j,k,m) = \sqrt{\left(x_{k,m} - x_{j,m}\right)^2 + \left(y_{k,m} - y_{j,m}\right)^2} \tag{5.46}$$

  before applying (5.13). Angles θ, x, and y are expressed in units of the beamwidth θ_3.
- *Sample SNR*. Calculation of the sample snr $s(i,j,k,m)$ is the same as for the 1-D scan, using (5.13).

5.4.2 Steady-Target Beamshape Loss for 2-D Scan

The steps for integration and cumulative detection over the entire scan remain as listed in Table 5.2, but with Δ_k^2 replacing Δ_k in the reference detectability factors of step (5), and the 2-D loss L_{p2} replacing L_{p1}. The upper limits for m and j are 9 and 25, respectively.

The steps in calculation for mixed processing are listed in Table 5.5. Data for the steady target are not plotted here because it has been found that a close approximation can be obtained by squaring the 1-D loss (doubling the decibel value) from Figures 5.3 and 5.4.

Table 5.5 Steps in Calculating Beamshape Loss for Steady Target with Mixed Processing

(1) Sum signals from each beam in lines a = 1, 2, 3	$S_i(i,j,k,a) = \sum_{m=m_1(a)}^{m_2(a)} s(i,j,k,m)$	(5.47)
(2) Detection probability for integrated signal in line a	$P_{di\{0\}}(i,j,k,a) = \Phi\left[\sqrt{2\ln(1/P_{fa})} - \sqrt{2S_i(i,j,k,a)+1}\right]$	(5.48)
(3) Cumulative probability over all lines	$P_{di\{0\}}(i,j,k) = 1 - \prod_{m=m_1(a)}^{m_2(a)} \left[1 - P_{di\{0\}}(i,j,k,a)\right]$	(5.49)
(4) Average $P_{di\{0\}}$ over target positions	$\overline{P_{di\{0\}}}(i,k) = \frac{1}{j_{\max}} \sum_j P_{di\{0\}}(i,j,k)$	(5.50)
(5) Detectability factor with beamshape loss	$D_{p\{0\}}(k,u) = s_x,\ x = \text{root}_i\left[\overline{P_{di\{0\}}}(i,k) = P_{du}\right]$	(5.51)
(6) Reference detectability factor	$D_{r\{0\}}(k,u) = \frac{\Delta_k}{2}\left\{\left[\sqrt{2\ln(1/P_{fa})} - \Phi^{-1}(P_{du})\right]^2 - 1\right\}$	(5.52)
(7) Beamshape loss	$L_{p2\{0\}}(k,u) = D_{p\{0\}}(k,u) / D_{r\{0\}}(k,u)$	(5.53)

5.4.3 Case 1 Beamshape Loss for 2-D Scan

The steps for integration and cumulative detection over the entire scan are as listed in Table 5.3 for 1-D scan, but with Δ_k^2 replacing Δ_k in the reference detectability factors of step (5). Limits for m and j are changed to 9 and 25, respectively.

5.4.3.1 Case 1 with Integration

The results for Case 1 with integration are shown in Figure 5.15. The beamshape loss lies above $2L'_{p0}$ = 2.48 dB and below 9.6 dB for 0.5 < Δ_k < 1.5. Compared

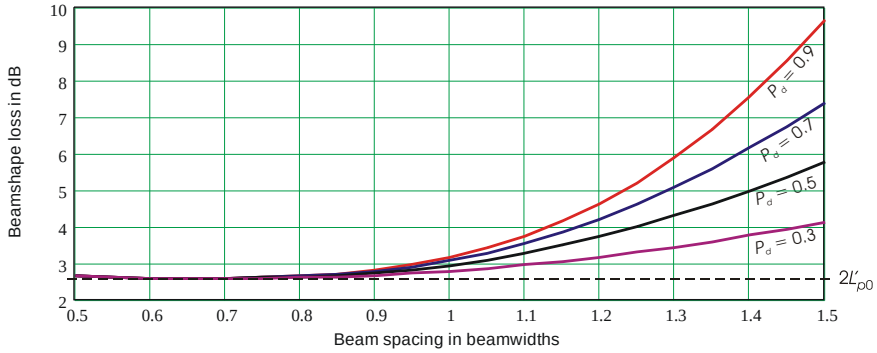

Figure 5.15 Beamshape loss L_{p2} versus sample spacing Δ_k for Case 1 with integration. A dashed line is shown for the dense-sample value L'_{p2} = 2.48 dB.

with the Case 1 loss for the 1-D scan, it is seen that the 2-D loss is almost exactly the square of the 1-D loss (twice the decibel value).

5.4.3.2 Case 1 with Cumulative Detection

The results for Case 1 with cumulative detection are shown in Figure 5.16. The lower efficiency of the cumulative detection process is included, increasing the loss for small sample spacings. As was the case with integration, the 2-D loss is approximately the square of the 1-D loss.

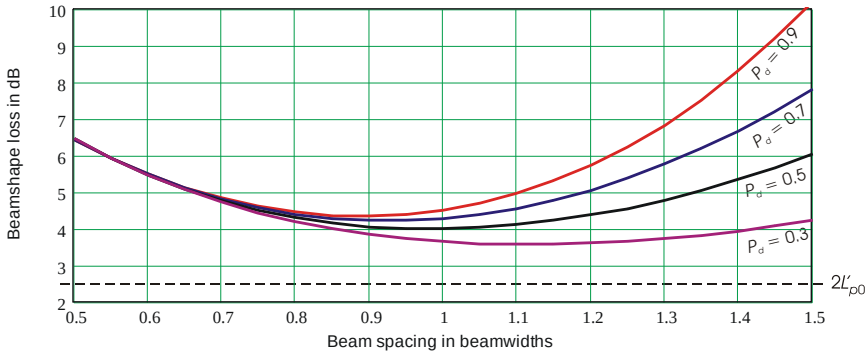

Figure 5.16 Beamshape loss L_{p2} versus sample spacing Δ_k for Case 1 with cumulative detection.

5.4.3.3 Case 1 with Mixed Processing

The steps in calculating beamshape loss for the Case 1 target with mixed processing are listed in Table 5.6. Step (1) performs integration over each line a = 1, 2, 3. Step (2) gives the corresponding steady-target detection probabilities, and step (3) forms the steady-target cumulative probability. Step (4) converts to the Case 1 cumulative probability P_m. Steps (5)–(8) parallel (3)–(6) of Table 5.3.

The Case 1 beamshape loss with mixed processing is shown in Figure 5.17. The cumulative detection loss is reduced by integration over each line, so the loss at $\Delta = 0.5$ drops to 4.5 dB, which is midway between the losses at that spacing for integration and cumulative detection over the entire scan. The loss for large spacings approaches that for cumulative detection over the entire scan.

Table 5.6 Steps in Calculating Beamshape Loss for Case 1 with Mixed Processing

(1) Add signals from beams in line *a* (5.47)	$S_i(i,j,k,a) = \sum_{m=m_1(a)}^{m_2(a)} s(i,j,k,m,a)$	
(2) Steady-target detection probability for integrated signal in line *a* (5.48)	$P_{di\{0\}}(i,j,k,a) = \Phi\left[\sqrt{2\ln(1/P_{fa})} - \sqrt{2S_i(i,,j,k,a)+1}\right]$	
(3) Steady-target cumulative probability over all lines (5.49)	$P_{c\{0\}}(i,j,k) = 1 - \prod_{m=m_1(a)}^{m_2(a)} \left[1 - P_{di\{0\}}(i,j,k,a)\right]$	
(4) Case 1 cumulative probability over all lines	$P_{c\{1\}}(i,j,k) = (1/s)\int_0^\infty \exp(-p/s) P_{c\{0\}}(p,j,k)\,dp$	(5.54)
(5) Average $P_{mi\{1\}}$ over all target positions	$\overline{P_{c\{1\}}}(i,k) = \frac{1}{j_{\max}} \sum_j P_{c\{1\}}(i,j,k)$	(5.55)
(6) Detectability factor with beamshape loss	$D_{p\{1\}}(k,u) = s_x, x \;=\; \text{root}_i\left[\overline{P_{c\{1\}}}(i,k) = P_{du}\right]$	(5.56)
(7) Reference detectability factor	$D_{r1}(k,u) = \Delta_k\left[(\ln P_{fa}/\ln P_d) - 1\right]$	(5.57)
(8) Beamshape loss	$L_{p2\{1\}}(k,u) = D_{p\{1\}}(k,u)/D_{r\{1\}}(k,u)$	(5.58)

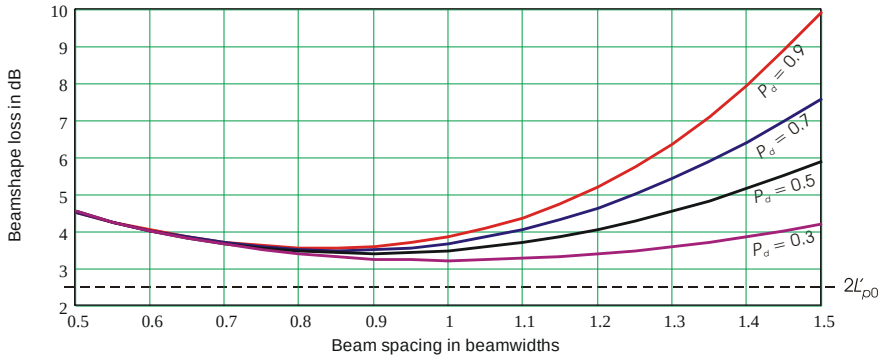

Figure 5.17 Beamshape loss L_{p2} versus sample spacing Δ_k for Case 1 with mixed processing.

5.4.4 Case 2 Beamshape Loss for 2-D Scan

The steps for integration and cumulative detection over the entire scan remain as listed in Table 5.4, but with Δ_k^2 replacing Δ_k in the reference detectability factors of step (5). The upper limits for *m* and *j* are 9 and 25, respectively. The number of independent target samples within the $m_{\max} = 9$ beams of the 2-D scan is given by

$$n_e(k) = \frac{1}{j_{\max}} \sum_j \left[m_{\max} - \frac{1}{\overline{f_c^4\left[\theta(j,k,m)\right]}} \sum_m \left\{ f_c^2\left[\theta(j,k,m)\right] - \overline{f_c^2\left[\theta(j,k,m)\right]} \right\}^2 \right] \tag{5.59}$$

Figure 5.18 shows the number of samples as a function of beam spacing. The reference detectability factors for all target models (including the diversity target discussed in Section 5.4.5) are shown in Figure 19. It can be seen that the diversity target detectability factor lies midway between the Case 1 and Case 2 targets.

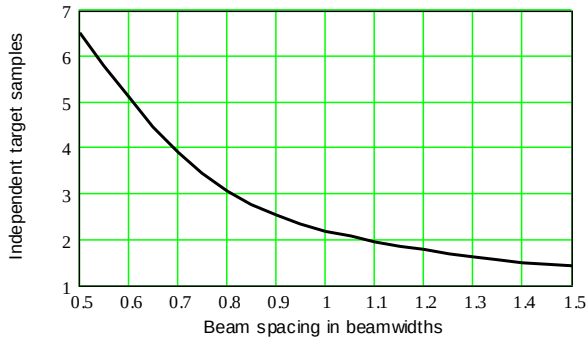

Figure 5.18 Number of independent target samples as a function of beam spacing, for 2-D scan.

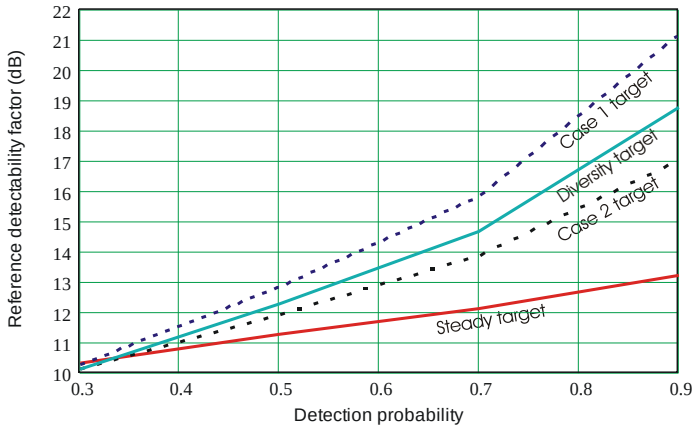

Figure 5.19 Reference detectability factors $D_{r\{0,1,2,D\}}(P_d)$ for 2-D scan with $\Delta_k = 1$.

5.4.4.1 Case 2 with Integration

The beamshape loss for the Case 2 target with integration is shown in Figure 5.20. As with the Case 1 target, the losses converge to the dense-sample value for $\Delta < 0.71$. For high P_d, they are slightly greater than for Case 1 as Δ increases.

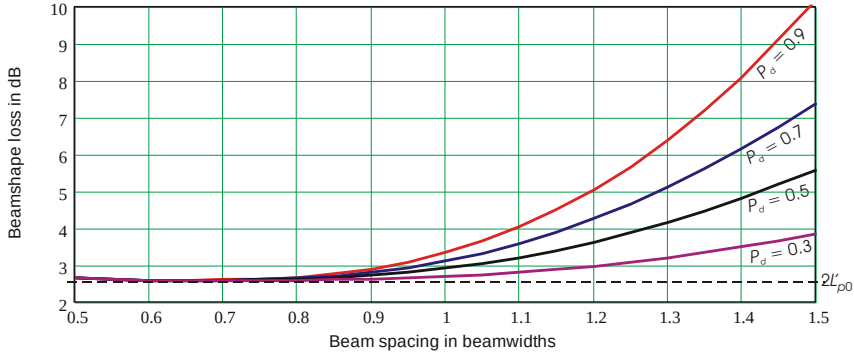

Figure 5.20 Beamshape loss L_{p2} versus sample spacing Δ_k for Case 2 with integration.

5.4.4.2 Case 2 Target with Cumulative Detection

The Case 2 target loss with cumulative detection over the entire scan is shown in Figure 5.21. The optimum spacing for $P_d = 0.9$ is $\Delta \approx 0.9$, giving $L_{p2} = 5.8$ dB, and the optimum shifts upward with decreasing P_d to $\Delta \approx 1.1$ for $P_d = 0.3$. The relatively large loss for $\Delta < 0.7$ is the result of the inefficient cumulative detection process. The loss with cumulative detection is greater for Case 2 than for Case 1, but this is the result of the lower reference level D_{r2} for Case 2, and does not imply that Case 2 requires a greater snr for a given level of detection performance.

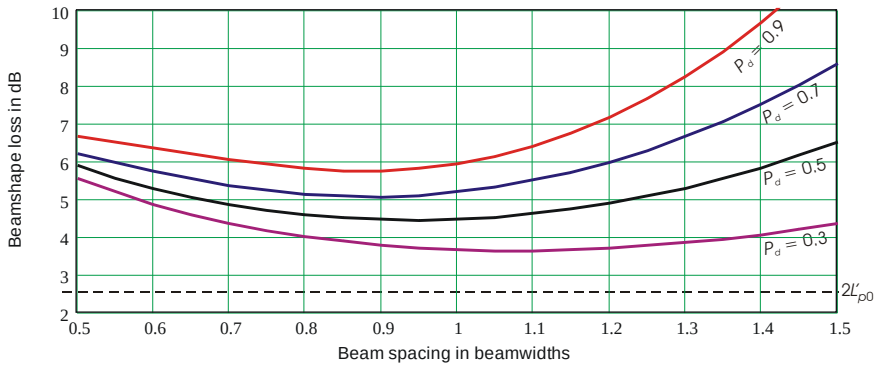

Figure 5.21 Beamshape loss L_{p2} versus sample spacing Δ_k for Case 2 with cumulative detection.

5.4.4.3 Case 2 with Mixed Processing

The steps in calculating beamshape loss for the Case 2 target with mixed processing are listed in Table 5.7. Step (1) performs integration over each line a = 1, 2, 3. Step (2) gives the corresponding Case 2 detection probabilities, where n_{e1} is the number of independent target samples in a single line, given by (5.34) and Figure 5.7. Step (3) forms the Case 2 cumulative probability $P_{m\{2\}}$. Steps (4)–(7) parallel (3)–(6) of Table 5.4.

Table 5.7 Steps in Calculating Beamshape Loss for Case 2 with Mixed Processing

(1) Add signals from beams in line a (5.47)	$S_i(i,j,k,a) = \sum_{m=m_1(a)}^{m_2(a)} s(i,j,k,m,a)$	
(2) Case 2 target detection probability for integrated signal in line a	$P_{d\{2\}}(i,j,k,a) = 1 - P_\gamma\left\{\dfrac{P_\gamma^{-1}(1-P_{fa},1) - \left[1-n_{e1}(k)\right]}{\left[1/n_{e1}(k)\right]S_i(i,j,k,a)+1}, n_{e1}(k)\right\}$	(5.60)
(3) Case 2 target cumulative probability over all lines	$P_{c\{2\}}(i,j,k) = 1 - \prod_{m=m_1(a)}^{m_2(a)} \left\{1 - P_{d\{2\}}\left[s(i,j,k,a)\right]\right\}$	(5.61)
(4) Average $P_{mi\{1\}}$ over all target positions	$\overline{P_{c\{2\}}}(i,k) = \dfrac{1}{j_{\max}} \sum_j P_{c\{2\}}(i,j,k)$	(5.62)
(5) Detectability factor with beamshape loss	$D_{p\{2\}}(k,u) = s_x,\ x = \text{root}_i\left[\overline{P_{c\{2\}}}(i,k) = P_{du}\right]$	(5.63)
(6) Reference detectability factor	$D_{r2}(k,u) = \Delta_k\left\{\dfrac{P_\gamma^{-1}(1-P_{fa},1) - \left[1-n_e(k)\right]}{P_\gamma^{-1}\left[1-P_{d_u},n_e(k)\right]} - 1\right\} n_e(k)$	(5.64)
(7) Beamshape loss	$L_{p2\{2\}}(k,u) = D_{p\{2\}}(k,u) / D_{r\{2\}}(k,u)$	(5.65)

The beamshape loss for Case 2 with mixed processing is shown in Figure 5.22. The curves are similar to those of the Case 1 target (Figure 5.17). Optimum spacings vary from $\Delta = 0.8$ for $P_d = 0.9$ to $\Delta = 1.05$ for $P_d = 0.3$.

5.4.5 Diversity Target Beamshape Loss for 2-D Scan

The steps in calculating beamshape loss for the diversity target are listed in Table 5.8 for integration and for cumulative detection over the entire scan. This target is defined as having Rayleigh fluctuation, with amplitudes correlated over each line but decorrelated from one line to the next. Hence, its correlation properties lie between Case 1 and Case 2.

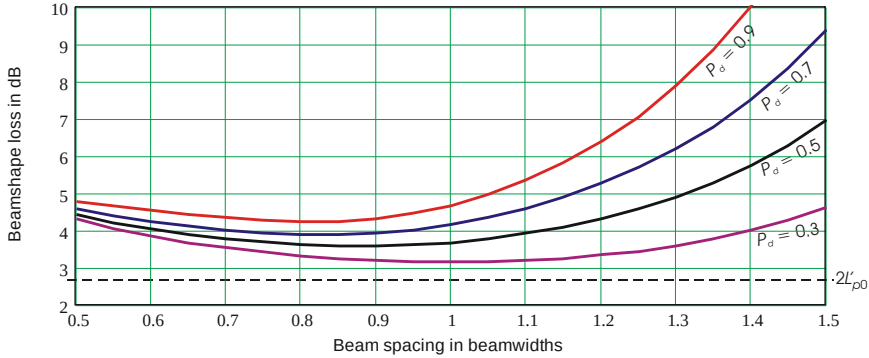

Figure 5.22 Beamshape loss L_{p2} versus sample spacing Δ_k for Case 2 with mixed processing.

Table 5.8 Method of Calculating Beamshape Loss for Diversity Target

	Integration over entire scan	
(1) Add signals from m beams	$S_i(i,j,k) = \sum_m s(i,j,k,m)$	(5.66)
(2) Detection probability for signal with $n_{e1}(k)$ target samples (5.36)	$P_{d\{D\}}(i,j,k) = 1 - P_\gamma\left\{\dfrac{P_\gamma^{-1}(1-P_{fa},1) - \left[1-n_{e1}(k)\right]}{\left[1/n_{e1}(k)\right]S_i(i,j,k)+1}, n_{e1}(k)\right\}$	
(3) Average $P_{d\{2\}}$ over target positions	$\overline{P_{d\{D\}}}(i,k) = \dfrac{1}{j_{\max}}\sum_j P_{d\{D\}}(i,j,k)$	(5.67)
(4) Detectability factor with beamshape loss	$D_{p\{D\}}(k,u) = s_x,$ where $x = \text{root}_i\left[\overline{P_{d\{D\}}}(i,k) = P_{du}\right]$	(5.68)
(5) Reference detectability factor	$D_{rD}(k,u) = \Delta_k\left\{\dfrac{P_\gamma^{-1}(1-P_{fa},1) - \left[1-n_e(k)\right]}{P_\gamma^{-1}\left[1-P_{d_u}, n_e(k)\right]} - 1\right\} n_e(k)$	(5.69)
(6) Beamshape loss	$L_{p1\{D\}}(k,u) = D_{p\{D\}}(k,u) / D_{r\{D\}}(k,u)$	(5.70)
	Cumulative detection over entire scan	
(1) Detection probability for single steady sample	$P_{d\{0\}}(i,j,k,m) = \Phi\left[\sqrt{2\ln(1/P_{fa})} - \sqrt{2s(i,j,k,m)+1}\right]$	(5.71)
(2) Cumulative probability over lines a = 1, 2, 3	$P_{c\{0\}}(i,j,k) = 1 - \prod_{m=m_1(a)}^{m_2(a)}\left[1 - P_{d\{0\}}(i,j,k,m)\right]$	(5.72)
(3) Case 1 cumulative probability over lines a = 1, 2, 3 (5.32)	$P_{c\{1\}}(i,j,k) = (1/s)\int_0^\infty \exp(-p/s) P_{c\{0\}}(p,j,k)\, dpv$	
(4) Cumulative probability over all lines	$P_{c\{D\}}(i,j,k) = 1 - \prod_{a=1}^{3}\left\{1 - P_{c\{1\}}\left[s(i,j,k)\right]\right\}$	(5.73)
Steps (5–8) are the same as steps (3–6) for integration, using $P_{c\{D\}}$ in place of $P_{d\{D\}}$.		

Integration is carried out over all m beams, as for other target models. However, the number of independent target samples used in step (2) is the number for a single line in the scan, as given by (5.34) and plotted in Figure 5.7. (The samples are actually those in the central column of beams, m = 2, 5, 8, but the symmetry is such that beams m = 4, 5, and 6 have the same correlation properties.) The steps in integration are then equivalent to those of the 1-D scan on a Case 2 target.

Calculations for cumulative detection start in step (1) with the steady-target detection probability for each individual beam. A cumulative probability for the steady target in each scan line is given by step (2), and in step (3) this is integrated over the exponential distribution to obtain the single-line cumulative probability of the fluctuating target. This in turn is used in step (4) to find the cumulative probability over the three lines, whose signals are uncorrelated.

As with the other target models, the signals can be processed in any of the three ways: integration over the scan, cumulative detection over the scan, or integration over each line (mixed processing).

5.4.5.1 Diversity Target with Integration

The beamshape loss for the diversity target with integration is shown in Figure 5.23. The losses for this target are almost indistinguishable from those of Case 2, which in turn is barely distinguishable from Case 1 when integration is used over the entire scan.

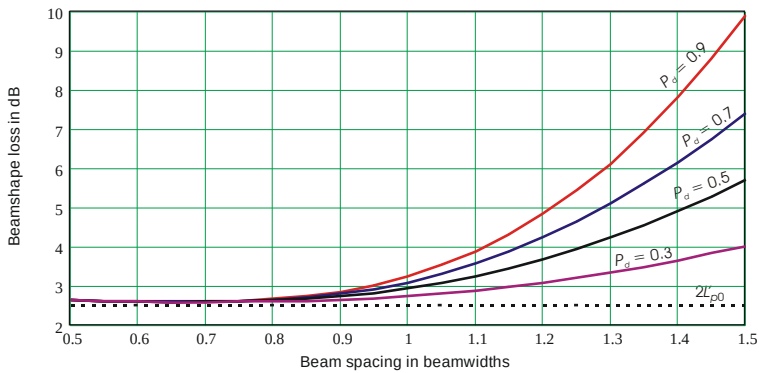

Figure 5.23 Beamshape loss L_{p2} versus sample spacing Δ_k for diversity target with integration.

5.4.5.2 Diversity Target with Cumulative Detection

The diversity target loss with cumulative detection over the entire scan is shown in Figure 5.24. The optimum spacing for P = 0.9 is $\Delta \approx 0.9$, where L_{p2} = 5.3 dB, and the optimum shifts upward with decreasing P_d to $\Delta \approx 1.15$ for P_d = 0.3.

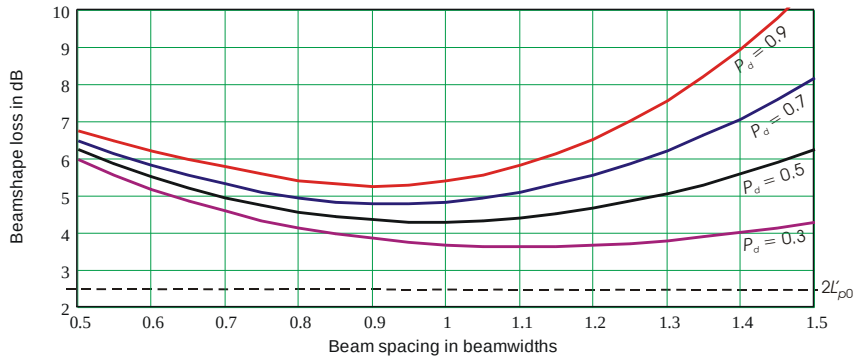

Figure 5.24 Beamshape loss L_{p2} versus sample spacing Δ_k for diversity target with cumulative detection.

5.4.5.3 Diversity Target with Mixed Processing

The diversity target loss with mixed processing is shown in Figure 5.25. The loss is very similar to that of the Case 2 target. The optimum spacing for $P_d = 0.9$ is $\Delta = 0.85$, where the loss is 4.7 dB. Spacings $\Delta > 1.3$ introduce losses that are not tolerable for applications requiring high P_d.

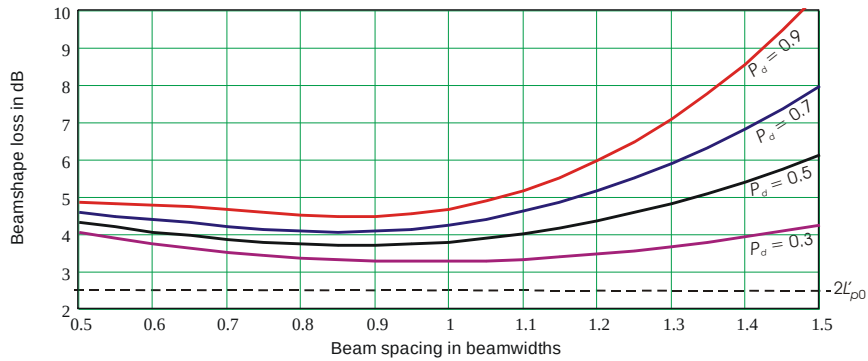

Figure 5.25 Beamshape loss L_{p2} versus sample spacing Δ_k for diversity target with mixed processing.

5.4.6 Beamshape Loss in the Search Radar Equation for 2-D Raster Scan

As discussed in Section 5.3.5 for the 1-D scan, a net beamshape loss must be adopted for use in the search radar equation:

$$L_{pn2}(k,u) = \frac{L_{p2}(k,u)}{\Delta_k^2} \tag{5.74}$$

This loss includes the effect of reapportioning the energy transmitted during the search frame time into the larger or smaller number of beams required as the spacing is varied. The net effect of reapportionment of energy and beamshape loss is shown in Figures 5.26 and 5.27 for Case 1 and Case 2 targets with cumulative detection. The data suggest that the optimum beam spacing is $\Delta > 1$ for both targets with cumulative detection. It can be seen that relatively sparse sampling is advantageous, especially for Case 2, even when high P_d is required.

Integration of signals gathered over a 2-D scan that covers a large sector may not be easily implemented (e.g., on high-velocity targets that may move through the range resolution cell during the scan period). More practical is mixed pro-

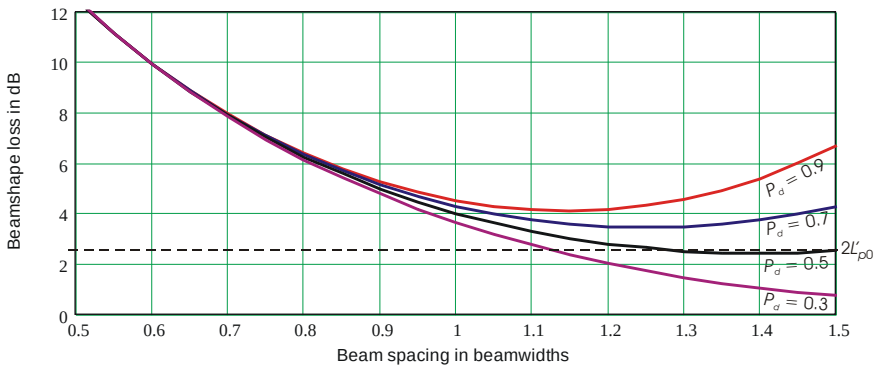

Figure 5.26 Net beamshape loss L_{pn2} versus sample spacing Δ_k for Case 1 with cumulative detection.

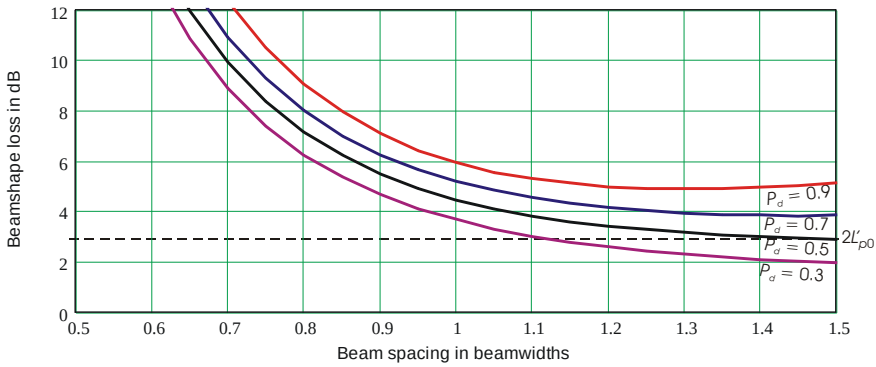

Figure 5.27 Net beamshape loss L_{pn2} versus sample spacing Δ_k for Case 2 with cumulative detection.

cessing: integration over contiguous beams on each line in the raster, with successive lines combined by cumulative detection over the scan. The net beamshape loss for this case is shown in Figures 5.28 and 5.29 for Case 1 and Case 2 targets.

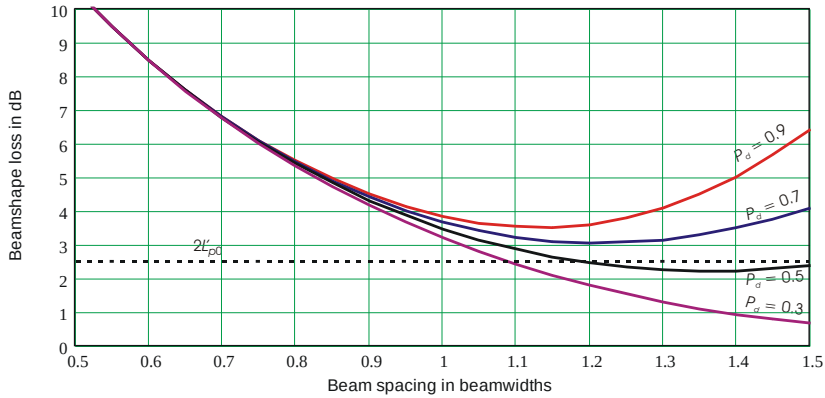

Figure 5.28 Net beamshape loss L_{pn2} versus sample spacing Δ_k for Case 1 with mixed processing.

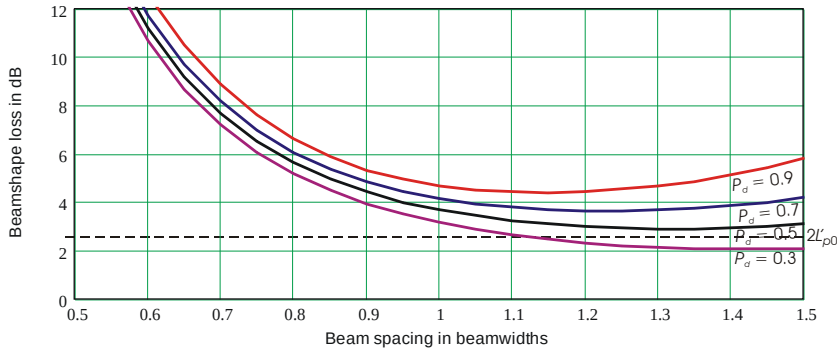

Figure 5.29 Net beamshape loss L_{pn2} versus sample spacing Δ_k for Case 2 with mixed processing.

Not considered in these comparisons of net beamshape loss is the advantage of greater accuracy in angle estimation for scans with dense sampling. When track-while-scan techniques are used to form track files with the detection data from overlapping beams, the improved accuracy may justify the extra energy required. However, when designing a search scan to minimize both power and time, it appears that spacings of one beamwidth or more are advantageous. In systems that can assign validation and track initiation beams immediately after the first detection, the range at which track initiation occurs with probability P_{track} can be extended to the range that gives a cumulative probability of detection equal to

P_{track} over several scans. A further advantage of using several scans with the reduced scan time of sparse sampling is that fluctuating targets will normally become decorrelated from scan to scan, reducing the fluctuation loss.

5.5 SPARSE SAMPLING USING A TRIANGULAR GRID

The geometry for the triangular grid is similar to that for the rectangular grid, Section 5.4, but the beams in successive scan lines are offset from each other in the x coordinate by 0.5Δ, and the y coordinate spacing is reduced from Δ to $\sqrt{0.75}\Delta$ to form the equilateral triangles shown in Figure 5.30. The target locations occupy one quadrant of the central beam, but the vertical spacing has been changed by a factor $\sqrt{0.75}$ relative to those in the rectangular raster. The results is a more uniform distribution of energy within the scan sector, and reduced beamshape loss. The method of calculation follows that for the rectangular grid, but with the following changes.

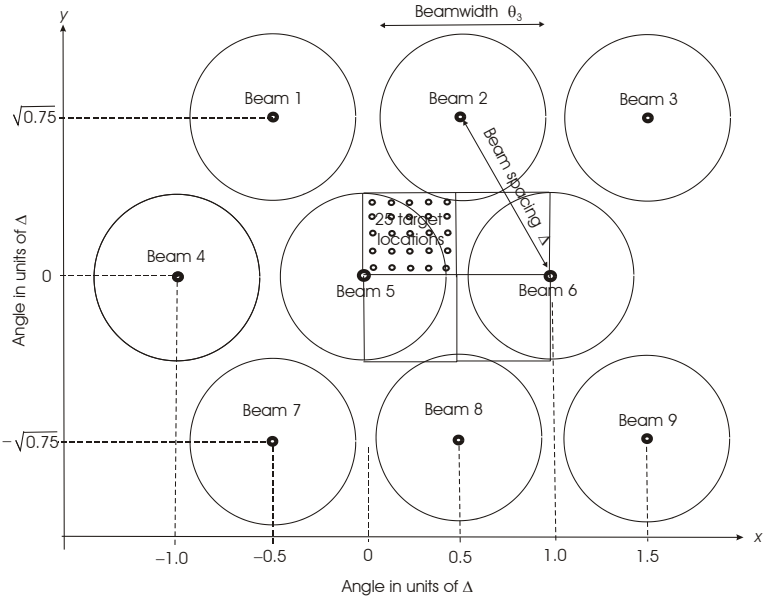

Figure 5.30 Beam grids and target sample positions for triangular scan grid.

5.5.1 Method of Calculation for Triangular Grid

The steps for each type of processing remain as for the rectangular grid (Tables 5.2–5.8), but with $\sqrt{0.75}\Delta_k^2$ replacing Δ_k^2 in the reference detectability factors,

and a loss denoted by L_{pT2} rather than L_{p2}. The upper limits for m and j are 9 and 25, respectively. The beam spacing Δ varies from 0.5 to 1.5 beamwidths, as for the rectangular grid, but now applies to the length of each side of the equilateral triangle shown in Figure 5.35.

5.5.2 Steady-Target Beamshape Loss for Triangular Grid

Results for this target model are not presented here, as it is seldom applicable to actual radar. Analytic approximations to the loss are presented in Appendix 5A.

5.5.3 Case 1 Beamshape Loss for Triangular Grid

5.5.3.1 Case 1 with Integration

The beamshape loss for Case 1 with integration is shown in Figure 5.31. The loss for high P_d is substantially less than that shown in Figure 5.15 for the rectangular grid. The additional power required for the closer spacing of adjacent rows is $1/\sqrt{0.75}$ or 0.63 dB, and the reduction in loss for $P_d = 0.9$ is 2 dB at $\Delta = 1.2$. The apparent slight rise for $\Delta \to 0.5$ results from failure to include contributions from beyond the nine-beam grid shown in Figure 5.30, whose inclusion is assumed in calculation of the reference detectability factor. Extension of integration over those beams might or might not actually occur in a practical processing system.

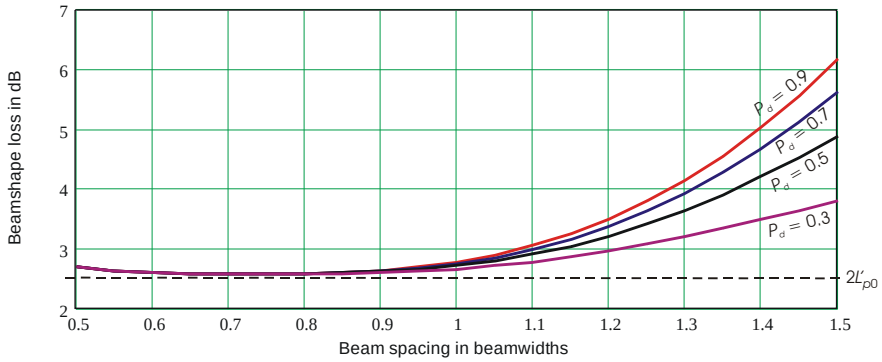

Figure 5.31 Beamshape loss L_{pT2} versus sample spacing Δ_k for Case 1 with integration over the entire scan.

5.5.3.2 Case 1 with Cumulative Detection

The loss for Case 1 with cumulative detection is shown in Figure 5.32. Again, the loss for high P_d and $\Delta > 1.1$ is substantially lower than for the rectangular grid.

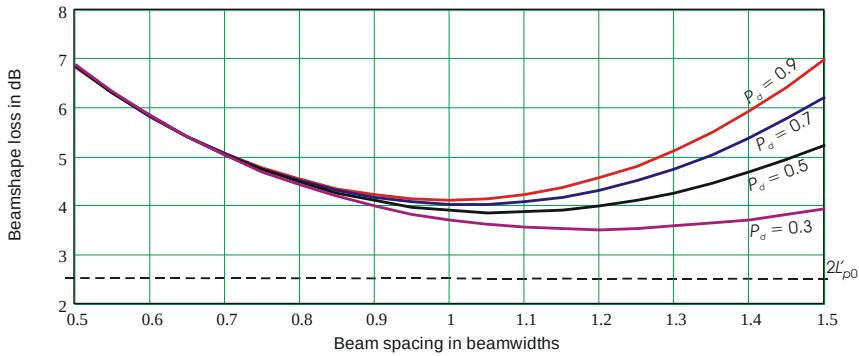

Figure 5.32 Beamshape loss L_{pT2} versus sample spacing Δ_k for Case 1 with cumulative detection.

5.5.3.3 Case 1 with Mixed Processing

The Case 1 loss with mixed processing, shown in Figure 5.33, exhibits the same reduction for $\Delta > 1.1$ compared with the rectangular grid, with small increases as $\Delta \rightarrow 0.5$.

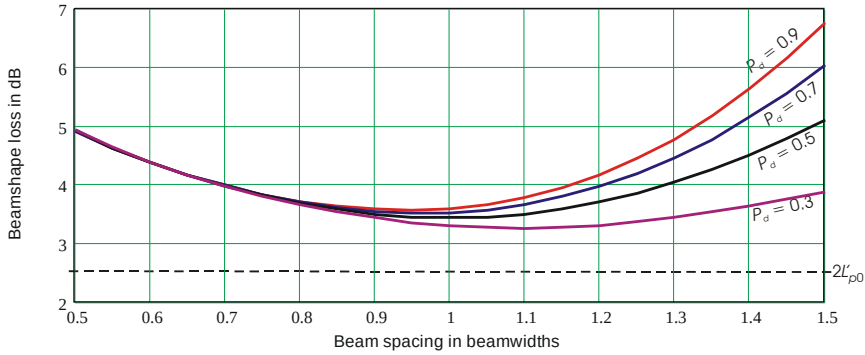

Figure 5.33 Beamshape loss L_{pT2} versus sample spacing Δ_k for Case 1 with mixed processing.

5.5.4 Case 2 Beamshape Loss for Triangular Grid

The number of independent samples for Case 2 is slightly increased by the closer spacing of rows in the scan, compared with the rectangular grid, resulting in a slight decrease in the reference detectability factor, and shown in Figures 5.34 and 5.35.

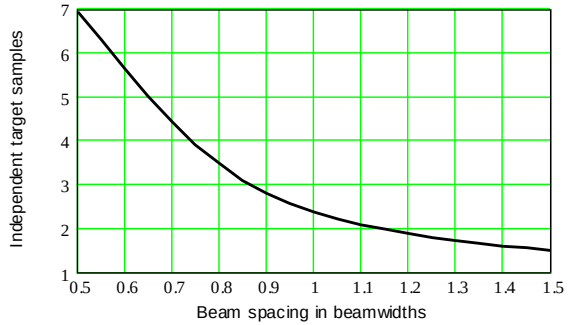

Figure 5.34 Number of independent target samples as a function of beam spacing, for triangular grid.

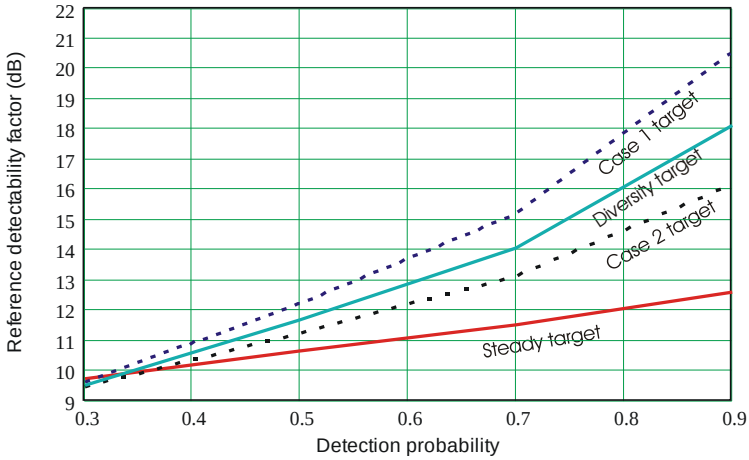

Figure 5.35 Reference detectability factors $D_{r\{0,1,2,D\}}(P_d)$ for triangular grid with $\Delta_k = 1$.

5.5.4.1 Case 2 with Integration

The Case 2 beamshape loss with integration is shown in Figure 5.36. The loss is slightly higher than that for Case 1, because the samples do not include quite as many independent target samples as used in calculating the reference detectability factor.

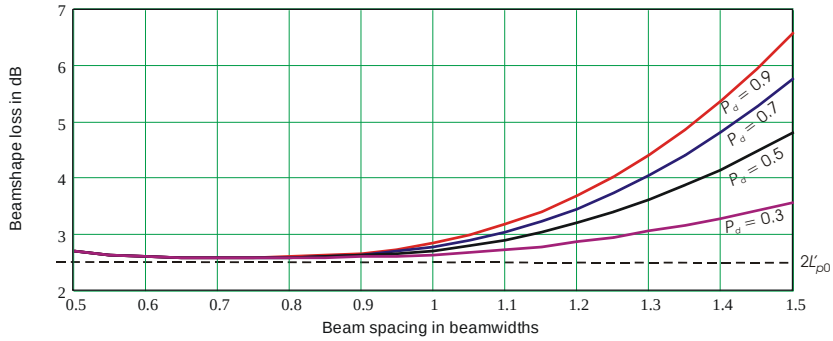

Figure 5.36 Beamshape loss L_{pT2} versus sample spacing Δ_k for Case 2 with integration.

5.5.4.2 Case 2 with Cumulative Detection

The Case 2 loss with cumulative detection is shown in Figure 5.37. The loss is lower than with the rectangular grid for all P_d when $\Delta > 1$.

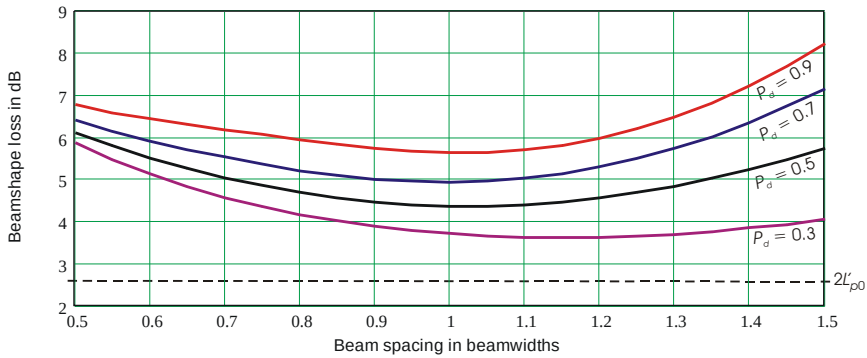

Figure 5.37 Beamshape loss L_{pT2} versus sample spacing Δ_k for Case 2 with cumulative detection.

5.5.4.3 Case 2 with Mixed Processing

The Case 2 loss for mixed processing, shown in Figure 5.38, has also been reduced relative to that for the rectangular grid for $\Delta > 1$.

5.5.5 Diversity Target Beamshape Loss for Triangular Grid

The beamshape loss for the diversity target is shown in Figures 5.39–5.41 for the three processing methods. In each case, the loss is similar to that for the Case 1 target, as shown in Figures 5.36–5.39.

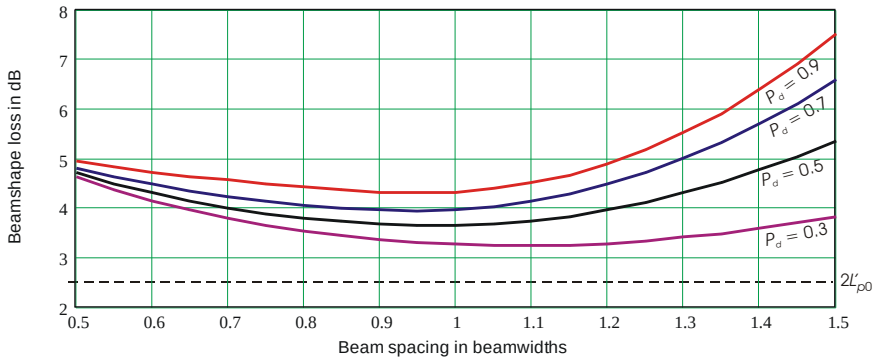

Figure 5.38 Beamshape loss L_{pT2} versus sample spacing Δ_k for Case 2 with mixed processing.

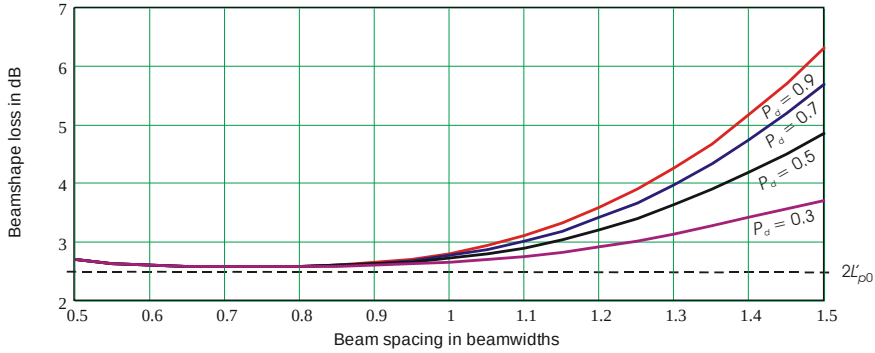

Figure 5.39 Beamshape loss L_{pT2} versus sample spacing Δ_k for diversity target with integration.

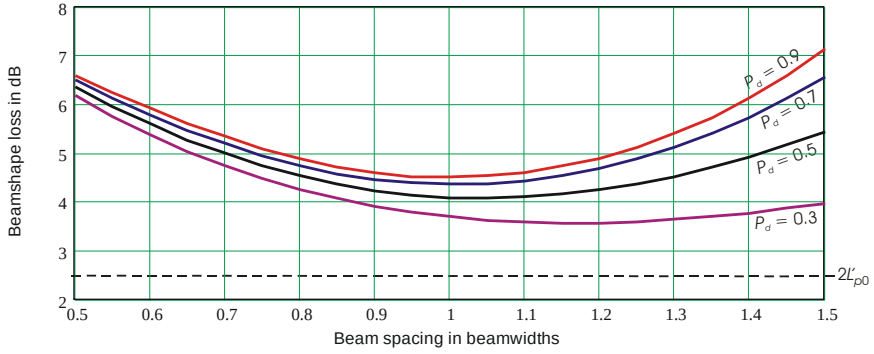

Figure 5.40 Beamshape loss L_{pT2} versus sample spacing Δ_k for diversity target with cumulative detection.

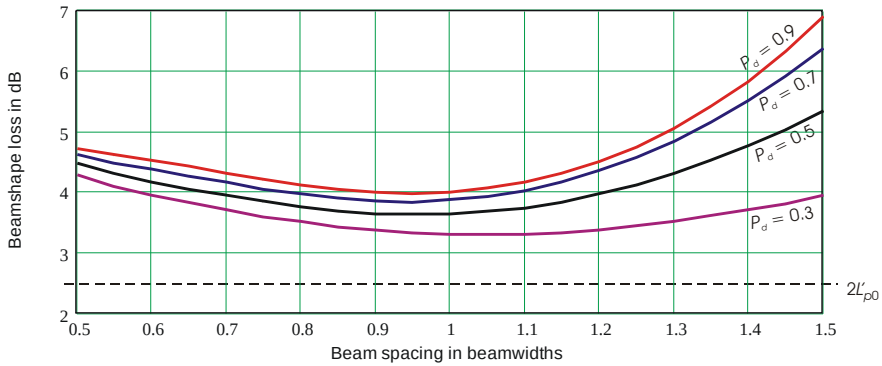

Figure 5.41 Beamshape loss L_{pT2} versus sample spacing Δ_k for diversity target with mixed processing.

5.5.6 Beamshape Loss in Search Radar Equation for Triangular Grid

For use in the search radar equation, the net beamshape loss is calculated on the basis of maintaining constant energy over the scan as beam spacing changes. This loss is shown in Figures 5.42–5.44 for the diversity target with three methods of processing. The results for this target model are approximately equal to those for Cases 1 and 2, and provide a basis for estimating the effects of different spacing of samples.

The major conclusion from Figures 5.42–5.44 is that the net beamshape loss to be included in the search radar equation for a 2-D scan with a triangular grid must significantly exceed the value L_{p2} = 1.77 = 2.48 dB commonly used for dense sampling. Given the usual spacing of ≈0.71 beamwidth, the loss will vary from 7.5 dB for mixed processing to 8.5 dB for cumulative detection. Achieving the minimum loss of 2–4 dB requires that the spacing be increased to ≈ 1.3 beam-

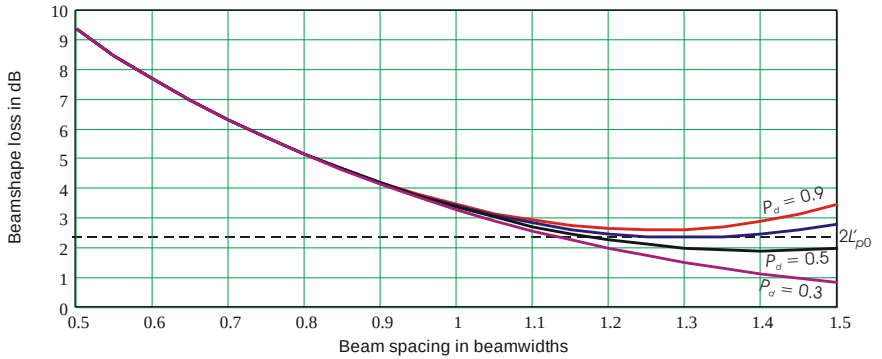

Figure 5.42 Net beamshape loss L_{pTn2} versus sample spacing Δ_k for diversity target with integration.

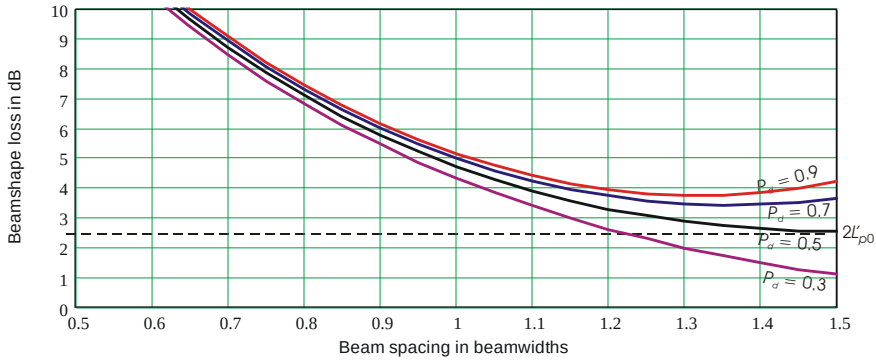

Figure 5.43 Net beamshape loss L_{pTn2} versus sample spacing Δ_k for diversity target with cumulative detection.

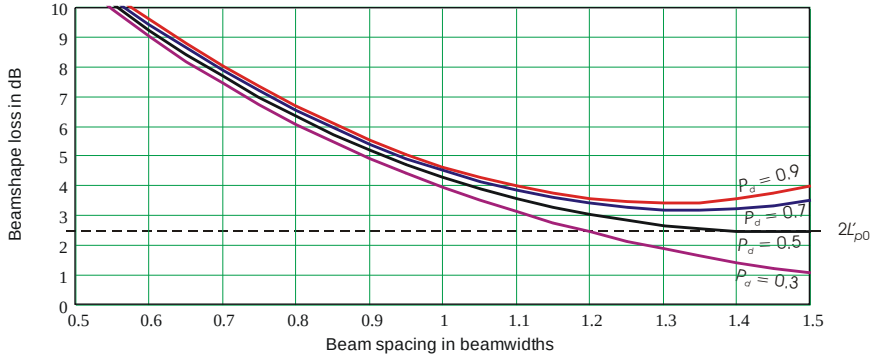

Figure 5.44 Net beamshape loss L_{pTn2} versus sample spacing Δ_k for diversity target with mixed processing.

width. Such large spacing would result in reduced accuracy of angle estimation, but would significantly decrease the time required to scan a given search volume. This might be an advantage, especially in the case of multifunction radars that follow up on an initial detection with an immediate track acquisition process.

5.6 SUMMARY OF BEAMSHAPE LOSS

5.6.1 Beamshape Loss for Dense Sampling

Sample spacing $\Delta < 0.71$ beamwidth in the scanned coordinate constitutes dense sampling. The loss for dense sampling in one coordinate is $L_{p0} = 1.33 = 1.24$ dB for any target type and processing using integration or cumulative detection. For 2-D scanning it is $L_{p2} = L_{p0}^2 = 1.77 = 2.48$ dB. Separate integration loss (see Sec-

tion 4.4.3), and integrator weighting loss or cumulative detection loss (Section 10.2.5) is included in the usual forms of the radar equation.

5.6.2 Beamshape Loss for Sparse Sampling

Sample spacing $\Delta > 0.71$ beamwidth in the scanned coordinate constitutes sparse sampling. The loss for sparse sampling is a function of spacing Δ, detection probability P_d, target type, and processing method.

5.6.2.1 One-Dimensional Scanning

Figures 5.45 and 5.46 illustrate the variation in 1-D beamshape loss between steady and Case 1 fluctuating targets for integration and cumulative detection. For sparse sampling the loss is seen to be much more dependent on P_d for the steady target than for Case 1.

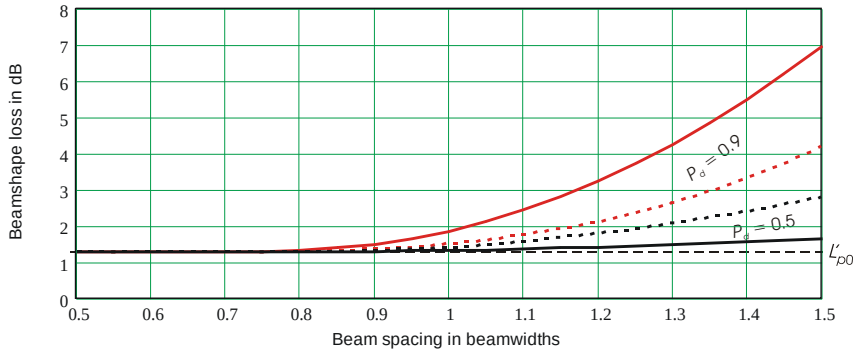

Figure 5.45 Beamshape loss L_{p1} versus sample spacing Δ_k for 1-D scan with integration for steady target (solid lines) and Case 1 (dotted lines).

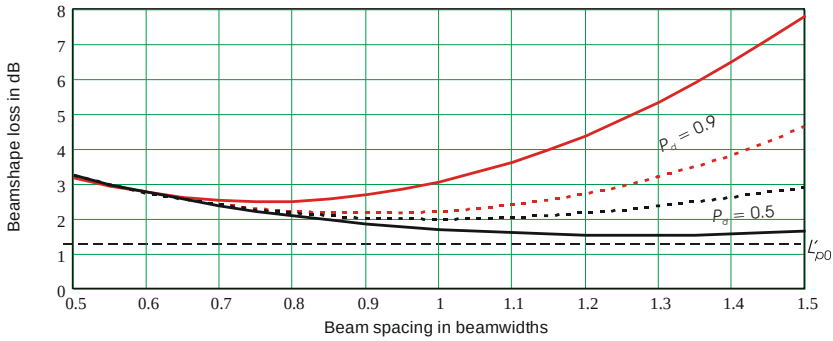

Figure 5.46 Beamshape loss L_{p1} versus sample spacing Δ_k for 1-D scan with cumulative detection for steady target (solid lines) and Case 1 (dotted lines).

5.6.2.2 Two-Dimensional Scan with Rectangular Grid

The beamshape loss for 2-D scan with a rectangular grid is shown in Figures 5.47 and 5.48 for integration and cumulative detection. In both cases the loss is approximately the square (twice the decibel value) of the corresponding 1-D loss at high P_d. For the steady target at $P_d = 0.5$, the 2-D loss exceeds that relationship.

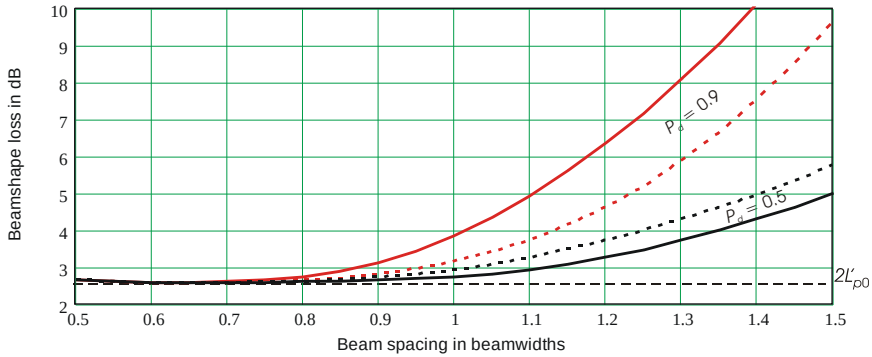

Figure 5.47 Beamshape loss L_{p2} versus sample spacing Δ_k for 2-D scan with integration for steady target (solid lines) and Case 1 (dotted lines).

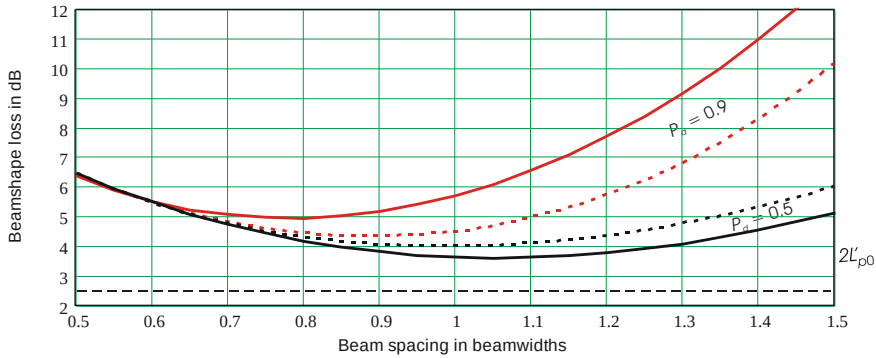

Figure 5.48 Beamshape loss L_{p1} versus sample spacing Δ_k for 2-D scan with cumulative detection for steady target (solid lines) and Case 1 (dotted lines).

5.6.2.3 Two-Dimensional Scanning with Triangular Grid

Location of beams on an equilateral triangular grid, with scan lines offset by half the spacing in the rapid-scan coordinate and spaced by $\sqrt{0.75}$ beamwidth in the other coordinate, substantially reduces beamshape loss. The energy required to

obtain a given beam-axis snr is increased by only 0.6 dB for this scan. The loss for sparse sampling increases much more slowly than with the rectangular grid, especially for high P_d, as shown in Figures 5.49 and 5.50. In these plots, the reference detectability factor has been adjusted to account for the additional energy required, so the loss for integration remains $2L_{p0} = 2.48$ dB in the transition to dense sampling. The difference between the two grids is more extreme for the steady target than for Case 1 as shown in these figures.

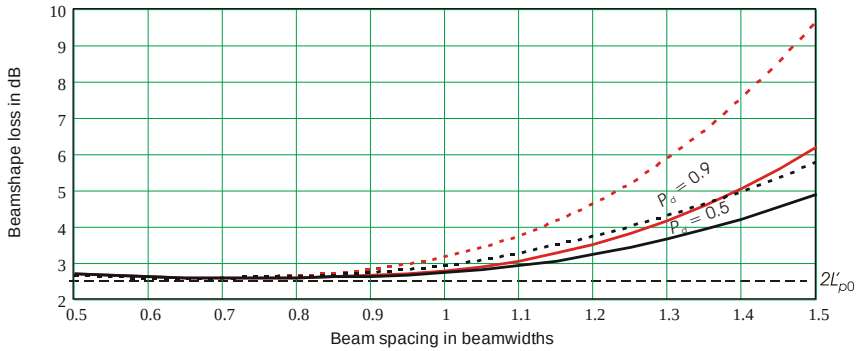

Figure 5.49 Beamshape loss L_{p2} versus sample spacing Δ_k for 2-D scan with integration for Case 1 with triangular grid (solid lines) and rectangular grid (dotted lines).

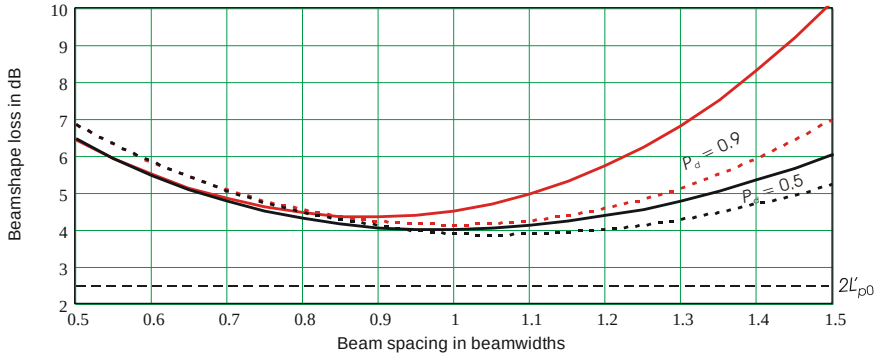

Figure 5.50 Beamshape loss L_{p2} versus sample spacing Δ_k for 2-D scan with cumulative detection for Case 1 with triangular grid (solid lines) and rectangular grid (dotted lines).

5.6.3 Processing Methods

Three processing methods have been considered in calculating beamshape loss: integration of samples from each beam dwell, combination of detection probabilities from each dwell into a cumulative probability of detection, and (for 2-D scan)

a mixed process in which detection is performed on signals integrated over each scan line, with results combined in a cumulative probability of detection over successive lines.

The use of integration (either coherent or noncoherent) is obviously the most efficient of the three methods, but it may not be possible on 2-D scans that cover large sectors. When each line of the scan requires a time longer than the correlation time of the target (see Section 4.5.2), coherent integration cannot be performed beyond a single line. When the scan time for a line exceeds the time in which the target stays within a range or Doppler resolution cell, even noncoherent integration becomes difficult. It is possible to perform integration over a string of cells that follow the target dynamics (so-called retrospective, or "track-before-detect" processing), but this requires much higher processing power than conventional integration within each cell. Hence, the mixed processing option may be substituted.

Mixed processing performs integration over each line, but combines results of successive lines through the process of cumulative detection. Since there are not normally more than two or three scan lines in which the target appears, the loss from the cumulative process is moderate (see Section 10.2.5). The plots of beamshape loss using this procedure include the cumulative detection loss. For spacing $\Delta = 0.5$ beamwidth, there are basically four beams with significant target energy (two per line, over two lines). Integration within the line provides a gain approaching 3 dB, and the cumulative process gains an additional 1–1.5 dB, leaving 1.5–2 dB of cumulative loss relative to ideal integration. Thus, the plotted results show a total beamshape loss of 4–4.5 dB at $\Delta = 0.5$, of which the basic dense sampling loss $2L_{p0} = 2.5$ dB.

The least efficient process is to make a detection decision within each dwell, with no dwell-to-dwell memory but an increase in cumulative detection probability over all dwells that contain target signals. The curves typically show a total beamshape loss of 6 dB at $\Delta = 0.5$, of which the basic dense-sampling loss $2L_{p0} = 2.5$ dB, the other 3.5 dB being attributable to the cumulative process.

Not all scan patterns use regular rasters such as the rectangular or triangular grid. Acquisition scans for a tracking radar may use arbitrary clusters of beams centered on the designated target position. In general, the beamshape loss for such scans can be estimated using the data obtained for triangular 2-D scan grids (e.g., Figures 5.31–5.44) with the spacing and the processing method by which the signals are combined in the acquisition scan.

5.6.4 Net Beamshape Loss for the Search Radar Equation

In the loss budget for the search radar equation, the net beamshape loss L_{pn1} (Section 5.3.5) or L_{pn2} (Sections 5.4.6, 5.5.6) replaces the product of L_{p0} or L_{p2} and the

cumulative detection loss. The result is to multiply the loss values plotted in this summary by a factor $1/\Delta$ (for 1-D scan), $1/\Delta^2$ (for 2-D scan with rectangular grid), or $1/\sqrt{0.75}\Delta^2$ (for 2-D scan with triangular grid). The result is to increase the contribution of net beamshape loss for the normally used sample spacings $\Delta < 1$. For example, at $\Delta = 0.71$, the loss for 1-D scan is not $L_{p0} = 1.24$ dB but rather $L_{pn} = 3$–4 dB, depending on the target model and processing (see Figures 5.10–5.13). For 2-D scan these values increase to $L_{pn}^2 = 6$–12 dB (see Figures 5.26–5.29 and 5.42–5.44), well above $L_{p0}^2 = 2.48$ dB (or the 3.2 dB derived from Blake's work). Part of the net beamshape loss is explained by inclusion of the cumulative detection.

The minimum net beamshape loss appears in all cases at $\Delta \geq 1$, even for $P_d \rightarrow 0.9$, suggesting that sparse sampling provides a more efficient search mode than the conventional $\Delta \approx 0.71$. As noted earlier, however, this efficiency may compromise the angular accuracy of the target data.

5.6.5 Beamshape Loss for Unequally Spaced 2-D Scan

All the 2-D beamshape loss data presented above are based on the assumption that sample spacings, in beamwidths, were either equal in the two coordinates or were on equilateral triangles. Where this condition is not met, an approximation of the loss can be made in either of two ways. For a rectangular grid, the loss is approximately the product (sum, in decibels) of the 1-D loss values for the two spacings. Alternatively, and for the triangular grid, the loss may be estimated by averaging the decibel values of the 2-D losses calculated for the two spacings.

If more accurate data are needed, the procedures described in Sections 5.4.1, 5.4.2, and 5.5.1 may be modified to include the two spacings.

References

[1] IEEE Standard 100, *The Authoritative Dictionary of IEEE Standards Terms*, 7th ed., New York: IEEE Press, 2000.

[2] Blake, L. V., "The Effective Number of Pulses Per Beamwidth for a Scanning Radar," *Proc. IRE*, Vol. 41, No. 6, June 1953, pp. 770–774.

[3] Blake, L. V., "Addendum to 'Pulses Per Beamwidth for Radar,'" *Proc. IRE*, Vol. 41, No. 12, December 1953, p. 1785.

[4] Blake, L. V., "Recent Advancements in Basic Radar Range Calculation," *IRE Trans. on Military Electronics*, Vol. MIL-5, No. 2, April 1961, pp. 154–164.

[5] Hall, W. M. and Barton, D. K., "Antenna Pattern Loss Factor for Scanning Radars," *Proc. IEEE*, Vol. 53, No. 9, September 1985, pp. 1257–1258.

[6] Hall, W. M., "Antenna Beam-Shape Factor in Scanning Radars," *IEEE Trans. on Aerospace and Electronic Systems*, Vol. AES-4, No. 3, May 1968, pp. 402–409.

[7] Barton, D. K. and Barton, W. F., *Modern Radar System Analysis Software and User's Manual Version 2.0*, Norwood, MA: Artech House, 1993.

[8] Barton, D. K., *Radar System Analysis and Modeling*, Norwood, MA: Artech House, 2005.

[9] Barton, D. K., *Modern Radar System Analysis Software and User's Manual*, Version 3.0, Norwood, MA: Artech House, 2005.

[10] Doviak, R. J. and Zrnic, D. S., *Doppler Radar and Weather Observations*, 2nd ed., New York: Academic Press, 1993.

Appendix 5A Analytical Approximations for Beamshape Loss

While the calculation procedures presented in Sections 5.3.1–5.3.7 yield accurate estimates of beamshape loss, they can be time-consuming and impractical for inclusion in radar analysis programs. The following approximations were derived to match the calculated beamshape loss with a beam from a cosine-illuminated rectangular aperture. That pattern was used rather than the Gaussian beam because it better captures the increased loss from sparse sampling that results from the steep slope as the target approaches the first null on each side of the mainlobe. The approximations give L'_p to within 0.1–0.2 dB for each case discussed in the previous sections, merging with the dense-sampling value as the spacing $\Delta \to 0.71$. Primed symbols denote values in decibels, and the dense-sampling value for 1-D scan is denoted by L'_{p0}.

5A.1 1-D Beamshape Loss

The following expressions apply for $\Delta > 0.71$; $L'_{p1} = L'_{p0}$ = 1.24 dB for $\Delta \le 0.71$.

5A.1.1 Approximation for Steady Target with Integration

$$L'_{p1}(P_d,\Delta) = L'_{p0} + 23(P_d - 0.3)^{1.7}(\Delta - 0.71)^{2.25} - 2.1(0.9 - P_d)^{1.3}(\Delta - 0.71)^{1.8} \quad (5.75)$$

5A.1.2 Approximation for Steady Target with Cumulative Detection

In the subsequent equations, the term $C(P_d,\Delta)$ represents the difference between the spacing Δ and the spacing at which minimum loss occurs for given P_d. The loss follows different functions, defined by $A(P_d,\Delta)$, for positive and negative values of this term.

$$L'_{p1}(P_d,\Delta) = \Delta L(P_d) + A(P_d,\Delta)$$

$$\Delta L(P_d) = L'_{p0} - 0.67 + 2.61(P_d - 0.3)^{0.63}$$

$$A(P_d,\Delta) = 0.7\left[3.25 - \Delta L(P_d)\right](1.5 - P_d)\left[\frac{C(P_d,\Delta)}{C(P_d,0.5)}\right]^{1.5+P_d}, \text{ if } C(P_d,\Delta) < 0, \quad (5.76)$$

$$= 12(P_d - 0.25)^{0.8}\left[C(P_d,\Delta)\right]^{1.8}, \text{ if } C(P_d,\Delta) \ge 0$$

$$C(P_d,\Delta) = \Delta + 1.15(P_d - 0.3)^{0.83} - 1.5$$

5A.1.3 Approximation for Case 1 Target with Integration

$$L'_{p1}(P_d,\Delta) = L'_{p0} + 5.6P_d^{0.6}(\Delta - 0.71)^{2.5} - 3.7(0.9 - P_d)^{1.5}(\Delta - 0.71)^3 \quad (5.77)$$

5A.1.4 Approximation for Case 1 Target with Cumulative Detection

$$\begin{aligned} L'_{p1}(P_d,\Delta) &= L'_{p0} + 0.49 + 0.51(P_d - 0.3)^{0.49} + A(P_d,\Delta) \\ A(P_d,\Delta) &= \left[3.25 - \Delta L(P_d)\right] P_d^{0.05} \left[\frac{C(P_d,\Delta)}{C(P_d,0.5)}\right]^{2.5} \text{ if } C(P_d,\Delta) < 0 \\ &= 7.6P_d^{0.9}\left[C(P_d,\Delta)\right]^2, \text{ if } C(P_d,\Delta) \ge 0 \\ C(P_d,\Delta) &= \Delta + 0.36(P_d - 0.3)^{0.37} - 1.2 \end{aligned} \quad (5.78)$$

5A.1.5 Approximation for Case 2 Target with Integration

$$L'_{p1}(P_d,\Delta) = L'_{p0} + 6P_d(\Delta - 0.71)^{2.4} - 4.5(0.9 - P_d)^{2.5}(\Delta - 0.71)^{3.8} \quad (5.79)$$

5A.1.6 Approximation for Case 2 Target with Cumulative Detection

$$\begin{aligned} L'_{p1}(P_d,\Delta) &= L'_{p0} + 0.58 + 1.9(P_d - 0.3)^{0.85} + A(P_d,\Delta) \\ A(P_d,\Delta) &= 1.4(1.5 - P_d)(1-\Delta)^{2.2-P_d}, \text{ if } \Delta < 1 \\ &= 12.5(P_d - 0.29)^{0.8}\left[\Delta - 1\right]^{1.9}, \text{ if } \Delta > 1 \end{aligned} \quad (5.80)$$

The net beamshape loss for use in the search radar equation, for all cases listed above, is $L'_{pn1}(P_d,\Delta) = L'_{p1}(P_d,\Delta) - 10\log(\Delta)$.

5A.2 2-D Beamshape Loss with Rectangular Grid

The 2-D beamshape loss in dB is denoted by L'_{p2}. All expressions apply for $\Delta > 0.71$; $L'_{p2} = 2L'_0 = 2.48$ for $\Delta \le 0.71$.

5A.2.1 Approximation for Steady Target with Integration

$$L'_{p2}(P_d,\Delta) = 2L'_{p0} + 21P_d^{2.7}(\Delta - 0.71)^2 - 6(0.9 - P_d)^4(\Delta - 0.71)^{1.5} \quad (5.81)$$

5A.2.2 Approximation for Steady Target with Cumulative Detection

$$\begin{aligned} L'_{p2}\left(P_d,\Delta\right) &= 2L'_{p0}+3.58\left(P_d-0.3\right)^{0.63}+18P_d^{1.2}\left|C\left(P_d,\Delta\right)\right|^{2.3}A\left(P_d,\Delta\right) \\ A\left(P_d,\Delta\right) &= 1+P_d^{0.8}\ \text{, if } C\left(P_d,\Delta\right)<1; \\ &= 1\ \text{, if } C\left(P_d,\Delta\right)\geq 1 \\ C\left(P_d,\Delta\right) &= \Delta+0.81\left(P_d-0.3\right)^{0.6}-1.35 \end{aligned} \tag{5.82}$$

5A.2.3 Approximation for Steady Target with Mixed Processing

$$\begin{aligned} L'_{p2}\left(P_d,\Delta\right) &= 2L'_{p0}-1.17+2.58\left(P_d-0.3\right)^{0.56}+A\left(P_d,\Delta\right) \\ A\left(P_d,\Delta\right) &= 0.85\left(1.9-P_d\right)^{2.6}\left[\frac{C\left(P_d,\Delta\right)}{C\left(P_d,0.5\right)}\right]^2\text{, if } C\left(P_d,\Delta\right)<0 \\ &= 17.5\left[C\left(P_d,\Delta\right)\right]^2\text{, if } C\left(P_d,\Delta\right)\geq 0 \\ C\left(P_d,\Delta\right) &= \Delta+0.79\left(P_d-0.3\right)^{0.72}-1.3 \end{aligned} \tag{5.83}$$

5A.2.4 Approximation for Case 1 with Integration

$$L'_{p2}\left(P_d,\Delta\right)=2L'_{p0}+13.5P_d^{0.75}\left(\Delta-0.71\right)^{2.6}-5\left(0.9-P_d\right)^{0.8}\left(\Delta-0.71\right)^3 \tag{5.84}$$

5A.2.5 Approximation for Case 1 with Cumulative Detection

$$\begin{aligned} L'_{p2}\left(P_d,\Delta\right) &= 2L'_{p0}+1.08+1.02\left(P_d-0.3\right)^{0.52}+A\left(P_d,\Delta\right) \\ A\left(P_d,\Delta\right) &= 1.5\left(1.9-P_d\right)^{1.4}\left[\frac{C\left(P_d,\Delta\right)}{C\left(P_d,0.5\right)}\right]^2\text{, if } C\left(P_d,\Delta\right)<0; \\ &= 17.8P_d^{1.35}\left[C\left(P_d,\Delta\right)\right]^2\text{, if } C\left(P_d,\Delta\right)\geq 0 \\ C\left(P_d,\Delta\right) &= \Delta+0.23\left(P_d-0.3\right)^{0.26}-1.1 \end{aligned} \tag{5.85}$$

5A.2.6 Approximation for Case 1 with Mixed Processing

$$
\begin{aligned}
L'_{p2}\left(P_d,\Delta\right) &= 2L'_{p0}+0.71+0.45\left(P_d-0.3\right)^{0.54}+A\left(P_d,\Delta\right)\\
A\left(P_d,\Delta\right) &= 0.95\left(1.9-P_d\right)^{0.7}\left[\frac{C\left(P_d,\Delta\right)}{C\left(P_d,0.5\right)}\right]^2,\ \text{if } C\left(P_d,\Delta\right)<0;\\
&= 15P_d\left[C\left(P_d,\Delta\right)\right]^{2.2},\ \text{if } C\left(P_d,\Delta\right)\geq 0;\\
C\left(P_d,\Delta\right) &= \Delta+0.28\left(P_d-0.3\right)^{0.63}-1
\end{aligned}
\tag{5.86}
$$

5A.2.7 Approximation for Case 2 with Integration

$$
L'_{p2}\left(P_d,\Delta\right)=2L'_{p0}+15P_d^{1.55}\left(\Delta-0.71\right)^{2.3} \tag{5.87}
$$

5A.2.8 Approximation for Case 2 with Cumulative Detection

$$
\begin{aligned}
L'_{p2}\left(P_d,\Delta\right) &= 2L'_{p0}+1.15+3.28\left(P_d-0.3\right)^{0.87}+A\left(P_d,\Delta\right)\\
A\left(P_d,\Delta\right) &= 0.95\left(1.9-P_d\right)^{1.4}\left[\frac{C\left(P_d,\Delta\right)}{C\left(P_d,0.5\right)}\right]^2,\ \text{if } C\left(P_d,\Delta\right)<0;\\
&= 16.5P_d^{1.35}\left[C\left(P_d,\Delta\right)\right]^2,\ \text{if } C\left(P_d,\Delta\right)\geq 0;\\
C\left(P_d,\Delta\right) &= \Delta+0.23\left(P_d-0.3\right)^{0.26}-1.05
\end{aligned}
\tag{5.88}
$$

5A.2.9 Approximation for Case 2 with Mixed Processing

$$
\begin{aligned}
L'_{p2} &= 2L'_{p0}+0.67+1.68\left(P_d-0.3\right)^{0.86}+A\left(P_d,\Delta\right)\\
A\left(P_d,\Delta\right) &= 0.6\left(1.9-P_d\right)^{1.4}\left[\frac{C\left(P_d,\Delta\right)}{C\left(P_d,0.5\right)}\right]^2,\ \text{if } C\left(P_d,\Delta\right)<0\\
&= 22P_d^{1.25}\left[C\left(P_d,\Delta\right)\right]^{2.4},\ \text{if } C\left(P_d,\Delta\right)\geq 0\\
C\left(P_d,\Delta\right) &= \Delta+0.18\left(P_d-0.3\right)^{0.37}-0.95
\end{aligned}
\tag{5.89}
$$

5A.2.10 Approximation for Diversity Target with Integration

$$L'_{p2}\left(P_d,\Delta\right)=2L'_{p0}+13.5P_d^{1.2}\left(\Delta-0.71\right)^{2.3}-2.3\left(0.9-P_d\right)^2\left(\Delta-0.71\right)^3 \quad (5.90)$$

5A.2.11 Approximation for Diversity Target with Cumulative Detection

$$\begin{aligned} L'_{p2} &= 2L'_{p0}-1.1+2.53\left(P_d-0.3\right)^{0.83}+A\left(P_d,\Delta\right) \\ A\left(P_d,\Delta\right) &= 1.2\left(2.1-P_d\right)^{1.1}\left[\frac{C\left(P_d,\Delta\right)}{C\left(P_d,0.5\right)}\right]^2, \text{ if } C\left(P_d,\Delta\right)<0 \\ &= 17.5P_d^{1.4}\left[C\left(P_d,\Delta\right)\right]^{1.4}, \text{ if } C\left(P_d,\Delta\right)\geq 0 \\ C\left(P_d,\Delta\right) &= \Delta+0.18\left(P_d-0.3\right)^{0.37}-1.1 \end{aligned} \quad (5.91)$$

5A.2.12 Approximation for Diversity Target with Mixed Processing

$$\begin{aligned} L'_{p2} &= 2L'_{p0}+0.77+1.94\left(P_d-0.3\right)^{0.93}+A\left(P_d,\Delta\right) \\ A\left(P_d,\Delta\right) &= 0.8\left(1.25-P_d\right)^{0.5}\left[\frac{C\left(P_d,\Delta\right)}{C\left(P_d,0.5\right)}\right]^2, \text{ if } C\left(P_d,\Delta\right)<0 \\ &= 17P_d^{1.3}\left[C\left(P_d,\Delta\right)\right]^{1.3}, \text{ if } C\left(P_d,\Delta\right)\geq 0 \\ C\left(P_d,\Delta\right) &= \Delta+0.13\left(P_d-0.3\right)^{0.17}-1 \end{aligned} \quad (5.92)$$

The net beamshape loss for use in the search radar equation, for all cases listed above, is $L'_{pn2}(P_d,\Delta) = L'_{p2}(P_d,\Delta) - 20\log(\Delta)$.

5A.3 2-D Beamshape Loss with Triangular Grid

The beamshape loss in dB for the triangular grid is denoted by L'_{pT2}. The following expressions apply for $\Delta > 0.71$; $L'_{pT2} = 2L'_0 = 2.48$ for $\Delta \leq 0.71$.

5A.3.1 Approximation for Steady Target with Integration

$$L'_{pT2}\left(P_d,\Delta\right)=2L'_{p0}+12P_d^{1.75}\left(\Delta-0.71\right)^{2.4}-9.5\left(0.9-P_d\right)^{3.7}\left(\Delta-0.71\right)^2 \quad (5.93)$$

5A.3.2 Approximation for Steady Target with Cumulative Detection

$$\begin{aligned} L'_{pT2}(P_d,\Delta) &= 2L'_{p0} + 3.18(P_d - 0.3)^{0.58} + A(P_d,\Delta) \\ A(P_d,\Delta) &= 1.6(2-P_d)^{1.85}\left[\frac{C(P_d,\Delta)}{C(P_d,0.5)}\right]^2, \text{ if } C(P_d,\Delta) < 1, \\ &= 11P_d^{0.9}\left[C(P_d,\Delta)\right]^{1.8}, \text{ if } C(P_d,\Delta) \geq 1 \\ C(P_d,\Delta) &= \Delta + 0.69(P_d - 0.3)^{0.63} - 1.4 \end{aligned} \tag{5.94}$$

5A.3.3 Approximation for Steady Target with Mixed Processing

$$\begin{aligned} L'_{pT2}(P_d,\Delta) &= 2L'_{p0} - 0.14 + 1.86(P_d - 0.3)^{0.43} + A(P_d,\Delta) \\ A(P_d,\Delta) &= 0.7(2-P_d)^{2.3}\left[\frac{C(P_d,\Delta)}{C(P_d,0.5)}\right]^2, \text{ if } C(P_d,\Delta) < 0 \\ &= +10.5P_d^{1.2}\left[C(P_d,\Delta)\right]^{1.8}, \text{ if } C(P_d,\Delta) \geq 0 \\ C(P_d,\Delta) &= \Delta + 0.77(P_d - 0.3)^{0.33} - 1.5 \end{aligned} \tag{5.95}$$

5A.3.4 Approximation for Case 1 with Integration

$$L'_{pT2}(P_d,\Delta) = 2L'_{p0} + 7P_d^{0.5}(\Delta - 0.71)^{2.7} - 8.5(0.9 - P_d)^3(\Delta - 0.71)^4 \tag{5.96}$$

5A.3.5 Approximation for Case 1 with Cumulative Detection

$$\begin{aligned} L'_{pT2}(P_d,\Delta) &= 2L'_{p0} + 1.03 + 0.79(P_d - 0.3)^{0.51} + A(P_d,\Delta) \\ A(P_d,\Delta) &= 2.9(1.7 - P_d)^{0.3}\left[\frac{C(P_d,\Delta)}{C(P_d,0.5)}\right]^2, \text{ if } C(P_d,\Delta) < 0; \\ &= 13P_d\left[C(P_d,\Delta)\right]^2, \text{ if } C(P_d,\Delta) \geq 0 \\ C(P_d,\Delta) &= \Delta + 0.23(P_d - 0.3)^{0.26} - 1.2 \end{aligned} \tag{5.97}$$

5A.3.6 Approximation for Case 1 with Mixed Processing

$$
\begin{aligned}
L'_{pT2}\left(P_d,\Delta\right) &= 2L'_{p0}+0.8+0.38\left(P_d-0.3\right)^{0.55}+A\left(P_d,\Delta\right)\\
A\left(P_d,\Delta\right) &= 1.4\left(1.9-P_d\right)^{0.3}\left[\frac{C\left(P_d,\Delta\right)}{C\left(P_d,0.5\right)}\right]^2,\ \text{if } C\left(P_d,\Delta\right)<0;\\
&= 11P_d^{0.7}\left[C\left(P_d,\Delta\right)\right]^2,\ \text{if } C\left(P_d,\Delta\right)\geq 0\\
C\left(P_d,\Delta\right) &= \Delta+0.23\left(P_d-0.3\right)^{0.26}-1.15
\end{aligned}
\tag{5.98}
$$

5A.3.7 Approximation for Case 2 with Integration

$$
L'_{pT2}\left(P_d,\Delta\right)=2L'_{p0}+8P_d^{0.9}\left(\Delta-0.71\right)^{2.5}-6\left(0.9-P_d\right)^4\left(\Delta-0.71\right)^{2.5} \tag{5.99}
$$

5A.3.8 Approximation for Case 2 with Cumulative Detection

$$
\begin{aligned}
L'_{pT2}\left(P_d,\Delta\right) &= 2L'_{p0}+1.13+3.2\left(P_d-0.3\right)^{0.91}+A\left(P_d,\Delta\right)\\
A\left(P_d,\Delta\right) &= 5\left(1.6-P_d\right)^{0.2}\left[\frac{C\left(P_d,\Delta\right)}{C\left(P_d,0.5\right)}\right]^2,\ \text{if } C\left(P_d,\Delta\right)<0;\\
&= 13.5\left(P_d-0.2\right)^{0.4}\left[C\left(P_d,\Delta\right)\right]^{2.2},\ \text{if } C\left(P_d,\Delta\right)\geq 0\\
C\left(P_d,\Delta\right) &= \Delta+0.18\left(P_d-0.3\right)^{0.37}-1.15
\end{aligned}
\tag{5.100}
$$

5A.3.9 Approximation for Case 2 with Mixed Processing

$$
\begin{aligned}
L'_{pT2} &= 2L'_{p0}+0.75+1.66\left(P_d-0.3\right)^{0.87}+A\left(P_d,\Delta\right)\left[C\left(P_d,\Delta\right)\right]^2\\
A\left(P_d,\Delta\right) &= 3.7\left(1.6-P_d\right)^{0.22},\ \text{if } C\left(P_d,\Delta\right)<0\\
&= 12.5\left(P_d-0.2\right)^{0.5},\ \text{if } C\left(P_d,\Delta\right)\geq 0\\
C\left(P_d,\Delta\right) &= \Delta+0.18\left(P_d-0.3\right)^{0.37}-1.1
\end{aligned}
\tag{5.101}
$$

5A.3.10 Approximation for Diversity Target with Integration

$$
L'_{pT2}\left(P_d,\Delta\right)=2L'_{p0}+\left(\Delta-0.71\right)^{2.7}\left[7.5P_d^{0.7}-12\left(0.9-P_d\right)^5\right] \tag{5.102}
$$

5A.3.11 Approximation for Diversity Target with Cumulative Detection

$$
\begin{aligned}
L'_{pT2} &= 2L'_{p0} + 1.09 + 1.24\left(P_d - 0.3\right)^{0.56} + A\left(P_d, \Delta\right) \\
A\left(P_d, \Delta\right) &= 2.1\left(2 - P_d\right)^{0.35}\left[\frac{C\left(P_d, \Delta\right)}{C\left(P_d, 0.5\right)}\right]^2, \text{ if } C\left(P_d, \Delta\right) < 0 \\
&= 13.5\left(P_d - 0.15\right)^{0.7}\left[C\left(P_d, \Delta\right)\right]^2, \text{ if } C\left(P_d, \Delta\right) \geq 0 \\
C\left(P_d, \Delta\right) &= \Delta + 0.18\left(P_d - 0.3\right)^{0.37} - 1.15
\end{aligned}
\tag{5.103}
$$

5A.3.12 Approximation for Diversity Target with Mixed Processing

$$
\begin{aligned}
L'_{pT2} &= 2L'_{p0} + 0.82 + 0.94\left(P_d - 0.3\right)^{0.66} + A\left(P_d, \Delta\right) \\
A\left(P_d, \Delta\right) &= 0.75\left(2 - P_d\right)^{0.4}\left[\frac{C\left(P_d, \Delta\right)}{C\left(P_d, 0.5\right)}\right]^2, \text{ if } C\left(P_d, \Delta\right) < 0; \\
&= 14.5\left(P_d - 0.2\right)^{0.7}\left[C\left(P_d, \Delta\right)\right]^{2.2}, \text{ if } C\left(P_d, \Delta\right) \geq 0 \\
C\left(P_d, \Delta\right) &= \Delta - 0.9
\end{aligned}
\tag{5.104}
$$

The net beamshape loss for use in the search radar equation, for all cases listed above, is $L'_{pTn2}(P_d, \Delta) = L'_{pT2}(P_d, \Delta) - 20\log(\Delta)$.

CHAPTER 6

System Noise Temperature

6.1 NOISE IN THE RADAR BANDS

A significant contribution made by Blake [1–3] is his treatment of noise in radar receiving systems. The reader is referred to the referenced publications for a thorough discussion. Two major points on the subject are:

> Thermal and quasi-thermal noise cannot be eliminated or filtered out by any special circuitry or devices, while many manmade noises can be. Although the signal-to-thermal-noise ratio can be maximized by good receiver design and optimum signal processing, the residual thermal noise still imposes a fundamental limit on how small a signal can be detected.
>
> A basic cause of the voltage fluctuation known as electrical noise is thermal agitation of electrons in imperfect conductors. The phenomenon of temperature, according to the science of thermodynamics, is the result of the kinetic energy (motion) of particles of matter—solid, liquid, or gaseous. [3, pp. 131–132]

6.1.1 Noise Spectral Density

Radio noise originates in a conductor of resistance R ohms at thermodynamic temperature T, which generates thermal noise with uniform power spectral density N_0 over a broad RF band. Exact quantum mechanical analysis gives a noise power density that is a function of frequency and temperature:

$$N_0 = \frac{hf_0}{\exp\left(hf_0/kT\right)-1} \approx kT \tag{6.1}$$

where

$h = 6.63 \times 10^{-34}$ W·s^2 is Planck's constant;
f_0 = frequency in Hz;
$k = 1.38 \times 10^{-23}$ W·s is Boltzmann's constant.

The frequency-independent (white-noise) approximation in (6.1) is obtained by expanding the exponential, assuming that $hf_0/kT << 1$, and retaining only the first two terms of the expansion:

$$\exp\left(hf_0/kT\right) \approx 1 + hf_0/kT \tag{6.2}$$

The error in approximation is –0.1 dB for $f_0/T = 10^9$, corresponding to X-band (10 GHz) at 10K temperature, and for W-band (100 GHz) at 100K. It increases to –1.1 dB for $f_0/T = 10^{10}$, corresponding to W-band at 10K. Hence the approximation is adequate for almost all radar calculations, and will be used here. The full expression (6.1) is needed in the terahertz, infrared, and optical bands.

The noise spectral density N_0 used in the radar equation is referred to the output port of the receiving antenna, where the system noise temperature T_s is defined for entry into (6.1). The receiver that accepts signals from the antenna is characterized by its frequency response $H(f)$ and *noise bandwidth* B_n, defined as

$$B_n \equiv \frac{1}{\left|H\left(f_0\right)^2\right|} \int_{-\infty}^{\infty} \left|H\left(f\right)^2\right| df \tag{6.3}$$

where f_0 is the center frequency of the response.

Given the noise bandwidth B_n and a power gain G measured to a specific point in the receiver chain, the noise power at that point is

$$N = kT_s B_n G \tag{6.4}$$

The noise voltage across a resistance at that point is then

$$E_n = \sqrt{N/R} = \sqrt{kT_s B_n G/R} \tag{6.5}$$

It is customary in analysis of radar performance, as opposed to circuit design, to simplify discussions by setting $R = 1$, thereby expressing power simply as the square of voltage.

6.1.2 Noise Statistics

The probability density function (pdf) of thermal noise voltage is Gaussian [3, p. 135, Eq. (4.8)]:

$$p(E_n) = \frac{1}{\sqrt{2\pi}\sigma} \exp\left(-\frac{E_n^2}{2\sigma^2}\right) \tag{6.6}$$

where σ is the rms value of the noise voltage.[1] The average voltage is zero. Blake states [3, p. 135] that "quasi-thermal noise" introduced by some radio circuits is "virtually indistinguishable from thermal noise within the passband of a radar receiver," and can be modeled as thermal noise. Ultrawideband (UWB) radar may require use of different spectral and statistical treatment of noise.

Video noise (envelope detected Gaussian noise) has a Rayleigh distribution:

$$\begin{aligned} p(v) &= \frac{v}{\sigma^2} \exp\left(-\frac{v^2}{2\sigma^2}\right), \quad v \geq 0 \\ &= 0, \qquad\qquad\qquad v < 0 \end{aligned} \tag{6.7}$$

where σ is the standard deviation of the IF noise applied to the envelope detector. Video noise has a DC component:

$$\bar{v} = \int_0^\infty v p(v)\, dv = \sigma\sqrt{\pi/2} \tag{6.8}$$

The DC component is removed in signal processing, leaving the noise (AC) component of video noise:

$$\sigma_{\text{video}} = \left[\int_0^\infty (v - \bar{v})^2\, p(v)\, dv\right]^{1/2} = \sigma\sqrt{2 - \pi/2} = 0.6551\sigma \tag{6.9}$$

These values are used in the calculation of threshold settings for detection (Chapter 4).

---

[1] In [3, Eq. (4.8)], a typographical error in the D. C. heath edition, corrected in the subsequent Artech edition, places $2\pi\sigma^2$ instead of $2\sigma^2$ in the denominator of the exponential. In the subsequent integration for the rms value of E_n the lower limit of integration is given as 0 rather than the correct value $-\infty$, in both editions. The lower limit is correctly zero in integrations for video noise.

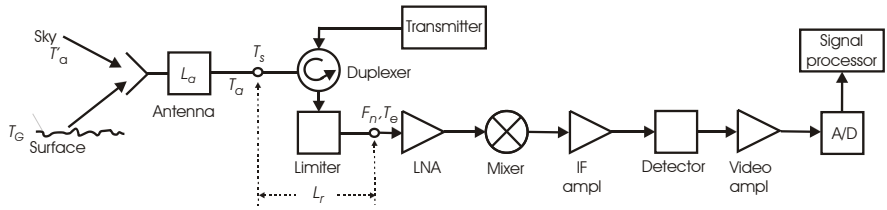

Figure 6.1 Sources of receiving system noise.

6.2 SOURCES OF NOISE IN RADAR RECEPTION

Sources of noise in a radar receiving system are shown in Figure 6.1. The first radar element through which the received signal passes is the antenna. Its pattern has lobes that are directed partly toward the sky and partly toward the surface. Noise sources in the sky include molecules of the tropospheric gases, ions at altitudes above the troposphere, cosmic sources, and sometimes solar radiation. The physical temperature of the troposphere is coupled to an RF noise temperature by the one-way attenuation $L_{\alpha 1}$ applicable to passage of a ray from space through the troposphere, contributing the sky noise T'_a. Antenna pattern lobes reaching the Earth's surface accept noise from molecular agitation of the surface material that is at a physical temperature T_g, along with sky noise reflected from the surface. Within the antenna are resistive elements whose loss L_a contributes to the antenna noise temperature T_a, which is measured at the antenna output terminal. This is the reference point to which system noise temperature T_s is referred.

Each subsequent hardware element through which the received signal passes contains additional sources of noise. These are referred to the antenna terminal, and are grouped into two terms: T_r, the contribution of RF elements that introduce a loss L_r between the antenna terminal and the receiver input, and $L_r T_e$, the contribution of the receiver (and possibly subsequent circuits), increased by the loss L_r to refer T_e to the antenna terminal. The system noise temperature is given by

$$T_s = T_a + T_r + L_r T_e \tag{6.10}$$

This expression is used, for example, in the Blake chart, Figure 1.1, and in the modified chart of Figure 1.2. The remainder of this chapter discusses the calculation of the terms in (6.10) for different environments and radar types.

The noise temperature contributed in passing through a circuit element or path with loss L can be referred to the input of that element as

$$T_{\text{in}} = T_p \left(L - 1 \right) \tag{6.11}$$

where T_p is the physical temperature of the lossy material. Thus, the temperature at the output of the element is

$$T_{\text{out}} = \frac{T_{\text{in}}}{L} = T_p\left(1 - \frac{1}{L}\right) \tag{6.12}$$

These relationships are used to calculate noise temperature components at successive stages in the receiving path.

6.3 ANTENNA NOISE TEMPERATURE

The *antenna noise temperature* T_a is the result of the loss within the antenna itself and several noise sources in the environment surrounding the antenna. Early forms of the radar equation assumed $T_a \approx 300$K. Blake's work was instrumental in refining that assumption, and providing a method of assigning to T_a an accurate value that is often a small fraction of the "standard temperature" $T_0 = 290$K used in defining receiver noise figure.

6.3.1 Sources of Antenna Noise Temperature

6.3.1.1 Transmitted Power Coupling to Environment

The contributions of the antenna and its environment to T_a may be identified by looking outward from the antenna port, considering the way in which transmitted power applied to that port would be distributed among four dissipative loads, and invoking reciprocity to apply that same distribution to the input noise. In Figure 6.2, a power of 1W enters the antenna from the right and is split into four components. An initial power divider routes power $1/L_a < 1$W into radiation from the antenna, while the remaining $P_{a4} = 1 - 1/L_a$ goes the ohmic loss L_a within the antenna. The radiated power in turn is divided between two angular regions: a fraction a_s appears in lobes that reach the surface (the lower hemisphere), while $1 - a_s$ is directed to the sky (the upper hemisphere). The power radiated directly toward the sky is $P_{a1} = (1 - a_s)/L_a$, while a_s/L_a goes to the surface. When the radar beam axis is elevated to an elevation angle $\theta_b > 0$, only the lower sidelobes, and possibly the lower skirt of the mainlobe, contribute to a_s.

For a surface with the surface reflection coefficient ρ, a fraction ρ^2 of the power reaching the surface is reflected upwards toward space, while $1 - \rho^2$ is absorbed. The power absorbed in the surface is $P_{a3} = a_s(1 - \rho^2)/L_a$. The upward component is $P_{a2} = a_s\rho^2/L_a$, and this is added to P_{a1} in the sky in front of the antenna. A fraction $1/L_{\alpha 1}$ of $P_{a1} + P_{a2}$ passes outward through the galaxy to the cos-

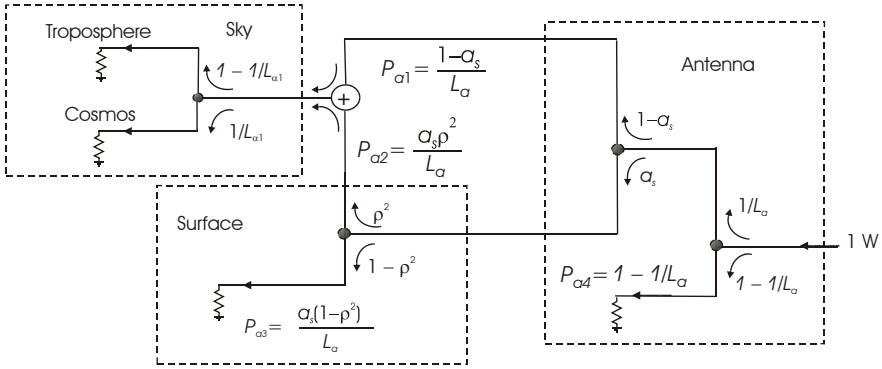

Figure 6.2 Distribution of transmitted power applied to the antenna.

mos, while the fraction $1 - 1/L_{\alpha 1}$ is absorbed by the one-way tropospheric attenuation $L_{\alpha 1}$ (see Chapter 7). Thus the sky component is divided between power dissipated in the troposphere and power passing into space. The ionosphere need not be considered, because it has negligible attenuation at frequencies above 300 MHz. Even at 100 MHz the maximum ionospheric loss of ≈1 dB makes a negligible contribution to noise, compared with galactic sources.

Blake in [3] considers the issue of upward reflections from the surface, in terms of a reflectivity $\mathcal{R}$ and emissivity $\mathcal{E}$, but provides little guidance as to how these terms should be evaluated. Formulation using the reflection coefficient ρ, calculated in Section 8.3 for different surfaces, polarizations, and grazing angles, provides a practical procedure that is used here.

6.3.1.2 Environmental Noise Coupling to Antenna Port

For a system in thermal equilibrium, the principle of reciprocity establishes that the thermal noise received from the galaxy, the troposphere, the surface, and the antenna loss will be combined at the antenna output port, each noise component weighted by the same coefficients that control the transmitted power distribution. Figure 6.3 illustrates this receiving process.

Four sources of noise, entering from the left, are coupled to the antenna output port. These are the troposphere, at physical temperature T_α; the cosmos at T_c; the surface at T_G; and the antenna loss at T_p. The *physical temperatures* are the temperatures of the molecules contributing the noise, as distinguished from the resulting RF *noise temperature*. The temperature components from the troposphere and galaxy are added to form *sky noise* T'_a, which enters directly into the antenna lobes of the upper hemisphere with weight $1 - a_s$. It is further weighted by $1/L_a$ to form the first noise temperature component T_{a1}:

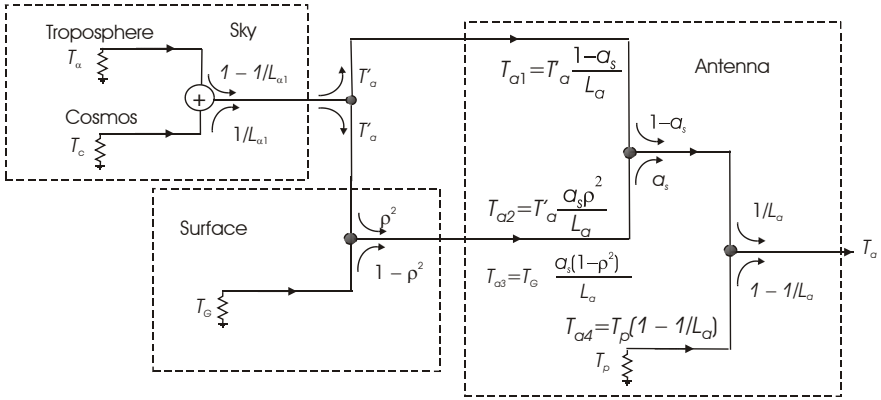

Figure 6.3 Combination of antenna thermal noise components. The four output components T_{a1-4} are defined as they appear at the output terminal to form T_a

$$T_{a1} = T_a' \frac{1-a_s}{L_a} \tag{6.13}$$

The sky noise also enters lower lobes through surface reflections, with weight $a_s\rho^2$, and is further weighted by $1/L_a$ form the second component T_{a2}:

$$T_{a2} = T_a' \frac{a_s\rho^2}{L_a} \tag{6.14}$$

The surface temperature T_g, is received in the lower lobes with weight $a_s(1 -\rho^2)$, and is further weighted by $1/L_a$ to form the third component T_{a3}:

$$T_{a3} = T_G \frac{a_s\left(1-\rho^2\right)}{L_a} \tag{6.15}$$

The internal antenna noise, referred to the output port, is the fourth component:

$$T_{a4} = T_p\left(1-\frac{1}{L_a}\right) \tag{6.16}$$

The antenna temperature T_a at the output terminal is the sum of these four components:[2]

$$\begin{aligned} T_a &= T_{a1} + T_{a2} + T_{a3} + T_{a4} \\ &= \frac{T_a' + (T_G - T_a')\, a_s \left(1 - \rho^2\right) + T_p \left(L_a - 1\right)}{L_a} \end{aligned} \tag{6.17}$$

Blake [3, p. 172, Eq. (4.76a)] assumes $\rho = 0$, expressing antenna noise as:[3]

$$\begin{aligned} T_a &= \frac{(1 - a_s) T_a' + a_s T_G}{L_a} + T_p \left(1 - \frac{1}{L_a}\right) = \frac{(1 - a_s) T_a' - T_p + a_s T_G}{L_a} + T_p \text{ (K)} \\ &= \frac{0.876 T_a' - 254}{L_a} + 290 \text{ , for } T_G = T_p + T_0 = 290\text{K} \end{aligned} \tag{6.18}$$

We discuss next the methods by which the noise temperature inputs are calculated.

6.3.2 Sky Noise Temperature

The sky noise temperature T_a' is the sum of tropospheric, cosmic, and solar noise temperatures:

$$T_a' = T_\alpha + T_c + T_{\text{sun}} \tag{6.19}$$

6.3.2.1 Tropospheric Noise Temperature T_α

Molecules of atmospheric gas and water vapor in a tropospheric volume element emit part of their thermal energy as electromagnetic noise with a density given by (6.1), in which T represents the noise temperature of the element. An antenna lobe at elevation angle $\theta \geq 0$ from a receiving antenna at altitude h_r passes through elements of the troposphere at altitudes h above sea level that increase with range r approximately as

---

[2] But note that a recently discovered 5th component will be discussed in Section 6.3.5.

[3] Blake [3, p. 168] uses the symbol T_G for the physical temperature of the surface, as we do here. On p. 171 he uses that same symbol for the product $a_s T_G$, and [3, Eq. (4.76)] includes $T_g = a_s T_G$, which becomes 36K in [3, (4.76a)].

$$h(r,\theta) = h_r + \frac{(r\cos\theta)^2}{2k_e a_e} + r\sin\theta \text{ (km)} \tag{6.20}$$

where

a_e = radius of the Earth = 6,378 km;
k_e = Earth's radius factor ≈ 4/3, accounting for tropospheric refraction (see Section 7.1.4);
r = range in km.

The variation in physical temperature of the tropospheric gases as a function of h can be described using the 1976 U.S. Standard Atmosphere [4, p. 14-3] discussed in Section 7.1.2 and shown in Figure 6.4.

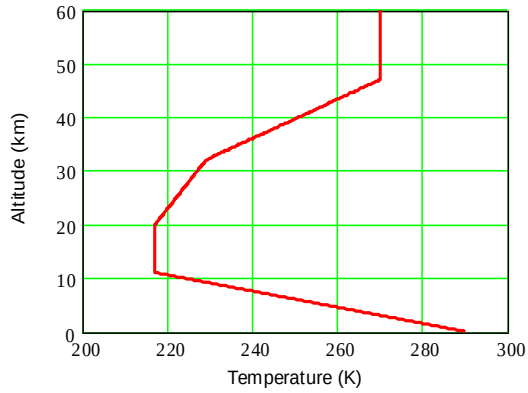

Figure 6.4 Physical temperature T_{tr} of the troposphere as a function of altitude [4, p. 14-3].

The noise temperature over an incremental distance along the path at angle θ is the product of the tropospheric temperature and attenuation over that distance, and its contribution to antenna noise temperature is proportional to that product, reduced by the attenuation over the earlier portion of the path. This is the basis of Blake's analysis that led to the expression for antenna temperature [3, p. 165, Eq. (4.65)]:

$$T_\alpha(f_0,\theta) = 0.2303\int_0^\infty k_{\alpha 1}\left[f_0, h(r,\theta)\right] T_{tr}\left[h(r,\theta)\right] \times \exp\left\{-0.2303\int_0^r k_{\alpha 1}\left[f_0, h(r',\theta)\right] dr'\right\} dr \tag{6.21}$$

where $k_{\alpha 1}(f_0, h)$ is the one-way attenuation coefficient in dB/km of the troposphere at frequency f_0 and altitude h. The constant 0.2303 = 0.1 ln(e) multiplies the outer integral to give the noise temperature in kelvins generated in passage of the beam through the entire atmosphere into space. The exponential with argument −0.2303 times the inner integral gives the fraction of this temperature reaching the antenna from range r, after attenuation in the intervening troposphere. The effect is to decrease the contribution from higher altitudes of the troposphere.

The one-way attenuation coefficient $k_{\alpha 1}$ in dB/km is found from the two-way coefficient k_α, which is:

$$k_{\alpha 1}(f_0, h) = 0.5\left[\frac{P(h)}{P(0)} k_{\alpha O}(f_0) + \frac{\rho_w(h)}{\rho_w(0)} k_{\alpha W}(f_0)\right] \text{ (dB/km)} \qquad (6.22)$$

where

$k_{\alpha O}$ = two-way, sea-level attenuation coefficient of oxygen (see Section 7.2.1);
$k_{\alpha W}$ = two-way, sea-level attenuation coefficient of water vapor (see Section 7.2.1);
P = air pressure;
ρ_w = density of water vapor.

Expressions for the atmospheric pressure profile $P(h)$ and water-vapor density $\rho_w(h)$ are given in Sections 7.1.2 and 7.1.3.

A computational problem in application of (6.21) results from the need to find $h(r', \theta)$ by the ray-tracing integral, followed by root-finding to solve for $r'(h, \theta)$. This is then integrated over r', and the entire process repeated for the integration over r. A practical procedure that introduces only slight error in the evaluation of T_α uses the effective Earth radius approach to obtain a closed-form expression

$$h(r, \theta) = \sqrt{(k_e a_e + h_s)^2 + r^2 + 2(k_e a_e + h_s) R \sin\theta} - k_e a_e \qquad (6.23)$$

By avoiding the ray-tracing and root-finding within each integral, the time required for the nested integration is greatly reduced. Plots of sky temperature as functions of frequency and beam elevation angle, such as Figure 6.7, can then be generated for any selected atmospheric model.

6.3.2.2 Noise Temperature from Weather Attenuation

The attenuation coefficient $k_{\alpha 1}$ in (6.21) applies to an atmospheric model for clear air, including water vapor but without allowance for precipitation or clouds along

the tropospheric path into space. An accurate estimate of performance of the radar in the presence of precipitation requires the appropriate two-way attenuation coefficient $k_{\alpha r}(f_0,h)$ for rain or $k_{\alpha s}(f_0,h)$ for snow, determined from data in Sections 7.3.1 or 7.3.4. The one-way values $k_{\alpha 1r,s}(f_0,h) = 0.5k_{\alpha r,s}(f_0,h)$ dB/km are then added to $k_{\alpha 1}(r,\theta)$ in (6.21). A known relationship between $k_{\alpha r,s}$ and altitude $h(r,\theta)$ reduces the precipitation coefficient to zero beyond the weather volume, and permits integration over ranges r' and r.

6.3.2.3 Cosmic Noise Temperature T_c

Cosmic noise includes temperature components from the galaxy, the background of distant space, and the sun:

$$T_c = T_{\text{gal}} + T_{\text{sp}} + T_{\text{sun}} \tag{6.24}$$

The galactic component of noise is greatest within ≈ 2° of the plane of our galaxy (the Milky Way). The noise temperature thus depends on the direction of the antenna lobe with respect to that plane and center of the galaxy. The model for galactic noise temperature [3, p. 162, Eq. (4.60)] is based on a reference temperature $T_{0.1}$ that is measured at f = 0.1 GHz:

$$T_{\text{gal}}(f_0) = T_{0.1}\left(\frac{0.1}{f_0}\right)^{2.5} \text{ (K)} \tag{6.25}$$

where f_0 is in GHz. The reference level varies with direction over the following limits:

$T_{0.1\text{max}}$ = 18,650K at the center of the galaxy;
$T_{0.1\text{mid}}$ = 3,050K elsewhere in the galactic plane;
$T_{0.1\text{min}}$ = 500K outside the galactic plane.

The second component of cosmic noise is a constant T_{sp} = 2.7K, making only a small contribution.

The angles of the beam axis relative to the plane and center of the galaxy are unpredictable, so radar analysis is normally carried out using $T_{0.1\text{mid}}$ = 3,050K in the mainlobe. The maximum value may be substituted for a conservative estimate of performance. In any case, the contribution of galactic noise to the final system noise temperature for microwave radar is insignificant, amounting to less than 10K at S-band.

The solar contribution is calculated using the noise brightness temperature T_B of the quiet sun's disc, based on calculations made by Blake, as shown in Figure

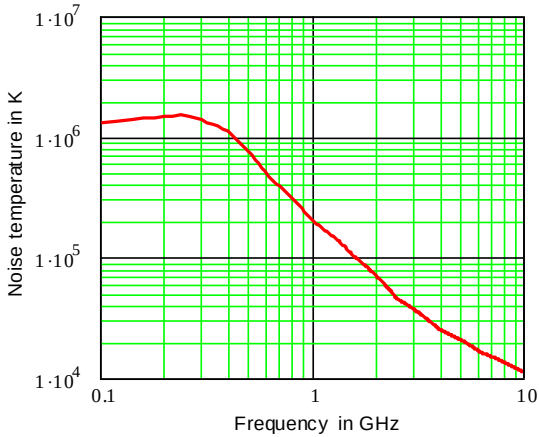

Figure 6.5 Noise brightness temperature of the quiet sun's disc as function of frequency.

6.5. The solar disk as observed from the Earth has an angular diameter of 0.5°, corresponding to a solid angle $\Omega_s = 5.98 \times 10^{-5}$ steradian.

The contribution to sky noise T_a' when observing the sun with antenna gain pattern $G(A,\theta)$ is

$$T_{\text{sun}} = \frac{1}{4\pi}\int_{\Omega_s} T_B(A,\theta)G(A,\theta)\,d\Omega \approx 4.76\times10^{-6} G_{\text{far}} T_B, \quad \text{for } \Omega_s \text{ in lobes with gain } G_{\text{far}} \tag{6.26}$$

The approximation applies when the sun lies in a far-sidelobe region where the gain is uniform at a level G_{far}. Even for an antenna with a relatively high far-sidelobe level (e.g., $G_{\text{far}} = -5$ dB), $T_{\text{sun}} < 2$K at $f_0 \geq 0.1$ GHz, and this component is negligible. Larger sidelobes or the mainlobe see significant increases for the quiet sun, especially in the lower radar bands. During sunspot activity, temperatures up to ten times the level of the quiet sun may be observed over periods of several hours. Solar noise is thus a problem in limited angular regions and for brief time periods, and is usually omitted from radar analysis.

6.3.2.4 Total Sky Temperature T_a'

The total sky temperature T_a', given by (6.19), is shown in Figure 6.6 as a function of frequency, for different beam elevation angles. Elevation beamwidths $\theta_e > 1°$ require use of an average over the elevation angles within the mainlobe, weighted by the antenna power gain for each angle.

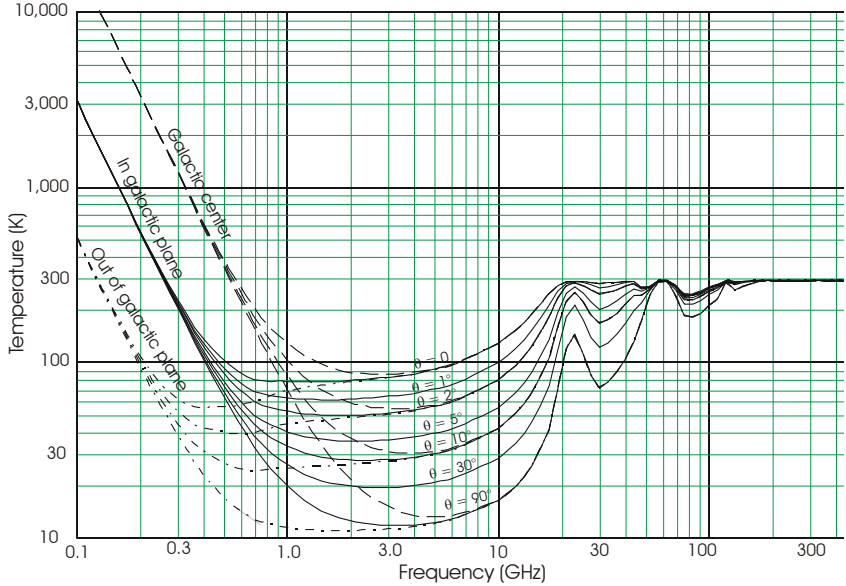

Figure 6.6 Total sky temperature T_a' as function of frequency, for different elevation angles θ. Three sets of results for the low radar bands are shown, corresponding to galactic contributions to a mainlobe directed at the center of the galaxy, any point within the Milky Way, or outside the galactic plane.

6.3.3 Noise Temperature from the Surface

The surface in which the noise component T_{a3} originates is generally assumed to be at a physical temperature $T_G = T_0 = 290$K. A different local value may be used to account for extreme climatic conditions, but variation from 290K is small when compared with uncertainty in the fraction a_s of the antenna pattern that accepts the surface noise. In his approximate expression, Blake assigns a value $a_s = 0.124$ for that fraction, obtaining a surface noise temperature $T_G a_s(1 - \rho^2) = 36$K.

Given the more recent developments in low-sidelobe antennas and array systems, it is appropriate to evaluate the fraction more exactly for the antenna pattern of a specific radar. For a power directivity pattern $G(A, \theta)$, defined over the entire hemisphere surrounding the antenna and normalized to unity total radiated power is

$$P = \int_{-\pi}^{\pi} \int_{-\pi/2}^{\pi/2} G(A,\theta) \cos\theta \, d\theta \, dA = 1 \tag{6.27}$$

where A is azimuth angle and θ is elevation angle. If the beam axis is elevated to an angle θ_b, the fraction of the power radiated into the lower hemisphere is

$$a_s = \int_{-\pi}^{\pi} \int_{-\pi/2}^{0} G\left(A, \theta - \theta_b\right) \cos\theta \, d\theta \, dA \tag{6.28}$$

and the remaining fraction $1 - a_s$ is in the upper hemisphere, $0 < \theta \leq \pi/2$.

Figure 6.7 shows the results of applying (6.28) to patterns of a cosine-illuminated aperture with 2° beamwidth and with uniform far-sidelobe levels −5, −10, and −15 dBi. The normalization of the curves to the beamwidth makes them applicable to most radar antennas. With the axis of a symmetrical beam directed horizontally, 50% of the power from an antenna at low altitude reaches the surface. Upward tilt of the beam axis to one beamwidth reduces the fraction of power on the surface to the level set by the far sidelobes, which is 13.5%, 5.2%, and 1.8% for the three sidelobe levels plotted. If the antenna is a front-fed reflector, about half the spillover power is added to the surface fraction, which may increase a_s from values calculated here using theoretical patterns for the illumination function. Ultralow-sidelobe reflector antennas, discussed in [5, pp. 175–179], are designed to minimize spillover and other sources of surface illumination, which may approach the curve for −15 dBi far sidelobes.

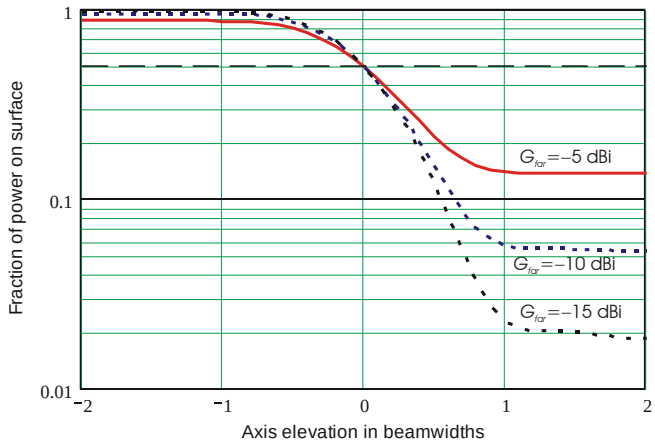

Figure 6.7 Fraction a_s of antenna power on surface as a function of beam-axis tilt, for typical antenna patters with far sidelobe levels G_{far}.= −5, −10, and −15 dBi.

Radars operating over barren land or the sea, for which the reflection coefficient ρ in (6.17) approaches unity, observe reduced surface noise temperature. As pointed out in Section 8.3, the specular reflection coefficient is the product of three factors:

$$\rho = \rho_0 \rho_s \rho_v \tag{6.29}$$

where

ρ_0 = Fresnel reflection coefficient of the surface material;
ρ_s = specular scattering factor of a rough surface;
ρ_v = vegetation factor for the surface cover.

Only the factors ρ_0 and ρ_v should be included in applying (6.29) to (6.17), because the diffuse scattering that results for $\rho_s < 1$ appears in a narrow cone centered on the specular ray in the upper hemisphere, and is unlikely to spread far enough for significant power to reach the surface. Horizontal polarization gives ρ_0 near unity over most grazing angles, resulting in less absorption by the surface and lower surface-temperature than for vertical polarization.

The beam of a 2-D search radar or the lowest beam of a 3-D radar typically has its axis elevated 0.3–0.4 beamwidths above the horizontal, resulting in a_s = 0.2–0.3. In a 2-D radar using a $\csc^2$ pattern, the fraction of the pattern reaching the surface is reduced by L_{csc}, the $\csc^2$ pattern loss (typically $L_{csc} \approx 1.6$; see Section 2.2.4) The upper beams of 3-D radars are more than one beamwidth above the surface, as are tracking-radar beams on most targets. For those cases it is the far sidelobe level that controls a_s, as shown on the right side of Figure 6.7.

6.3.4 Noise Temperature from Antenna Ohmic Loss

The term *ohmic loss* is used to distinguish loss components that dissipate energy in the antenna structure from those that broaden the beam (e.g., illumination loss) or increase sidelobes (e.g., loss from $\csc^2$ pattern shaping or from phase and amplitude errors in the aperture illumination). Components contributing to the antenna loss L_a include waveguide or transmission line between the antenna port and radiation into space, along with rotary joints, dielectric coverings or windows, phase shifters (in steerable arrays), and any resistive components to which signal energy may be coupled.

The fourth component T_{a4} of antenna noise results from this internal loss. It is usually small in reflector or lens antennas, for which typical $L_a \approx 0.05$ dB and physical temperature $T_p \approx T_0$. Insertion of those values in (6.16) gives T_{a4} = 13K. It is a more significant source of noise temperature in array systems, where contributors to ohmic loss may be larger, as discussed below. Array components are usually assumed to be at a temperature $T_p \approx T_0$, but may be higher as a result of

dissipation of RF power from the transmitter and control power in the phase-shifters. In active electronically scanned arrays (AESAs), the effects of feed and phase-shifter losses are negligible because those components follow the LNA in the T/R module.

6.3.4.1 Feed Loss

In a passive array, whether electronically or mechanically scanned, the antenna elements are connected to the receiver through networks of power combiners that establish the desired illumination (or weighting) function across the aperture. Array designers minimize the dissipative loss by using waveguide in the feed components and coupling as much energy as possible into the signal output, but the remaining loss is still significant in most array radars (other than AESAs).

6.3.4.2 Phase Shifter Loss

The passive electronically scanned array requires a phase shifter in the feed line of each radiating element. Phase shifter loss is typically 0.7–1 dB for a ferrite device, or 1.0–1.5 dB for a diode device. That loss is multiplies (adds in dB) directly to the feed loss and other antenna losses.

6.3.4.3 Loss from Water Films

Precipitation or condensation may form a water film on components such as dielectric covers on the array face or feed horn, the exposed surface of a reflector, or a radome covering the entire antenna. The loss in liquid water films is discussed in Section 10.1.5. Ice and snow crystals have relatively low loss, but as melting occurs they may contain liquid water with high loss. A water film on a reflector surface has only small effect, because the electric field falls to zero at the surface and there is little coupling between RF energy and the water.

6.3.5 Noise Temperature from Antenna Mismatch

Figure 6.8 shows the components contributing to the noise temperature T_a of a mismatched antenna. Matching the impedance of the radiating element to space and to the line that connects to the circulator maximizes the echo signal power and minimizes the noise temperature. Brookner [6] discusses the contribution of mismatch to noise temperature for both reflector and array antennas.

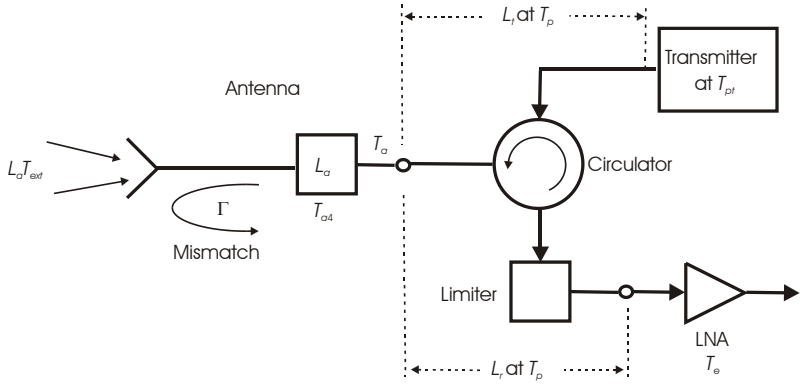

Figure 6.8 Noise temperature components with mismatched antenna (after [6]).

The external portion of the noise temperature $T_{ext} = T_{a1} + T_{a2} + T_{a3}$ at the antenna output appears in (6.17), and also (increased by the factor L_a) at the input in Figure 6.8. The temperature T_{a4} is from ohmic loss L_a, while T_r and T_e are the receiving line and receiver temperatures (see Sections 6.4 and 6.5). The physical temperature T_p is that of the receiving line losses L_r and L_t. The physical temperature characterizing termination within the transmitter (in the absence of the transmitted pulse) is T_{pt}. This differs from the presentation in [6], where the transmitter is represented by a resistive load at physical temperature T_p, without considering the possibility of higher transmitter temperature. Also, the antenna loss L_a in [6] is placed between the mismatch and the radiating element, rather than between the mismatch and the antenna output terminal as in Figure 6.8.

The temperature presented to the antenna port via the transmitter path through the circulator is

$$T_{tr} = T_p\left(1 - \frac{1}{L_t}\right) + \frac{T_{pt}}{L_t} \tag{6.30}$$

A fraction $(1 - 1/L_a)$ of T_{tr} reaches the mismatched radiating element and is reflected back to the output port by the reflection coefficient Γ:

$$|\Gamma| = \frac{\text{VSWR} - 1}{\text{VSWR} + 1} \tag{6.31}$$

Applying our notation to the expression developed in [6], with adjustments for different transmitter and line temperatures and for two-way passage through

L_a, the antenna temperature is modified to include noise reflected by the antenna mismatch:

$$T_a = \left[1 - |\Gamma|^2\right] T_{ext} + T_{a4} + \frac{|\Gamma|^2}{L_a^2}\left(T_p + \frac{T_{pt} - T_p}{L_t}\right) \tag{6.32}$$

The effect of the mismatch is thus to reduce the external noise by the fraction $|\Gamma|^2$, replacing it with $|\Gamma|^2/L_a^2$ times the physical temperature presented by the transmitter arm of the circulator. This mismatch leads to a fifth input temperature component given by

$$T_{a5} = |\Gamma|^2\left(\frac{T_{tr}}{L_a^2} - T_{ext}\right) = |\Gamma|^2\left(\frac{T_p}{L_a^2} + \frac{T_{pt} - T_p}{L_t L_a^2} - T_{ext}\right) \tag{6.33}$$

The appearance of L_a^2 in these expressions results from the two-way passage of the transmitter noise through the lossy components of the antenna. The term T_{a5} is a new temperature component not included in Blake's analysis, but potentially significant in radars using array antennas.

6.3.5.1 Mismatched Mechanically Steered Antenna

For unity VSWR, $|\Gamma| = 0$ and (6.32) reverts to (6.17). For a mechanically steered antenna with typical VSWR = 1.5, $|\Gamma|^2 = 0.04$, so the change in noise temperature is approximately 4% of the difference between transmitter temperature T_{tr} and external temperature. For the typical mechanically steered reflector or array, $T_{pt} \approx T_0$, and this increase does not exceed 11K even as the external temperature $T_{ext} \to 0$. However, depending on transmitter design, T_{pt} may significantly exceed T_0. In a solid-state transmitter, for example, T_{pt} can be taken as the junction temperature of the final amplifier devices, which may approach 400K.

6.3.5.2 Mismatched Electrically Steered Array (ESA)

The significance of Brookner's paper [6] is greatest when applied to the varying mismatch that results when an ESA is steered from broadside. The array area (projected normal to the beam axis) varies with the cosine of the steering angle θ. However, the typical element pattern $G_e(\theta)$ has a gain given by

$$G_e(\theta) = \cos^{\beta}(\theta) \tag{6.34}$$

where $\beta \approx 1.5$ is typical. The departure of the exponent from unity describes the loss in gain caused by antenna mismatch. For an array with power reflection coefficient $|\Gamma_0|^2$ on broadside, the off-broadside coefficient varies with the steering angle θ according to [6, Eq. (10)]:

$$\left|\Gamma(\theta)\right|^2 = 1 - \left(1 - \left|\Gamma_0\right|^2\right)\cos^{\beta-1}\theta \tag{6.35}$$

For $\beta = 1.5$, this gives $|\Gamma(60°)|^2 = 0.32$, so with $T_{pt} \rightarrow 400$K the increase in antenna noise temperature from (6.33) can approach $T_{a5} = 120$K in a system with low T_{ext}. For smaller scan angles the problem is less severe, but $|\Gamma(45°)|^2 = 0.19$, and most ESAs reach that scan angle. The average increase in noise temperature over a sector extending θ_{max} from broadside is

$$\overline{T}_{a5} = \left(\frac{T_p}{L_a^2} + \frac{T_{pt} - T_p}{L_t L_a^2} - T_{ext}\right)\frac{1}{\theta_{max}}\int_0^{\theta_{max}} \left|\Gamma(\theta)\right|^2 d\theta \tag{6.36}$$

This average approaches 50K, as L_a and $T_{ext} \rightarrow 0$, for $\beta = 1.5$, $\theta_{max} = 60°$.

In the radar equation, the primary effects of the mismatch Γ_0 are included as reductions in antenna gains G_t and G_r, and as $\Gamma(\theta)$ in the pattern-propagation factors for $|\theta| > 0$. However, neither the maximum nor the average noise temperature increase should be neglected in estimating performance of an ESA, and especially an AESA in which low system noise is relied upon to achieve a specified performance.

A recent text [7] discusses the temperature contribution of antenna mismatch, as well as the other sources of antenna noise, in the context of deep space communications. Because of the very low noise contributed to such a system by a receiver using a maser or high-electron-mobility transistor (HEMT), for which $T_e < 10$K, the space communication community has placed great emphasis on design and modeling methods for reducing antenna noise. The same considerations can be applied to radar systems in which the beam is elevated well above the horizon and which are not subject to active jamming.

6.3.6 Approximation for Antenna Noise Temperature

Given the complexity of the full expression for antenna noise temperature resulting from the preceding sections, Blake's approximation (6.18) from [3, p. 172, Eq. (4.76a)] is often used:

$$T_a \approx \frac{0.876T_a' - 254}{L_a} + 290 \ \text{(K)} \tag{6.37}$$

The assumptions applicable to this approximation are:

Fraction of antenna pattern on surface: $a_s = 0.124$;
Physical temperature of surface and antenna: $T_G = T_p = T_0$;
Reflection coefficient of surface: $\rho = 0$;
Noise temperature from lower hemisphere: $T_{a2} + T_{a3} = a_s T_0 = 36\text{K}$;
Antenna ohmic loss: L_a is constant and includes any mismatch effect.

An example showing the difference between this approximation and the more exact treatment, consider the radar and environmental parameters listed in Table 6.1. Comparing the results of the exact treatment with the approximation:

Exact:	$T_a = 78\text{K}$,	$T_s = 341\text{K}$ (based on $a_s = 0.111$);
Approximation	$T_a \approx 88\text{K}$,	$T_s \approx 350\text{K}$.

If the $\csc^2$ loss is eliminated and the beam elevation is raised to 10° for an elevated 3-D or tracking radar beam, the comparison gives the following temperatures:

Exact:	$T_a = 48\text{K}$,	$T_s = 311\text{K}$ (based on $a_s = 0.175$);
Approximation	$T_a \approx 57\text{K}$,	$T_s \approx 320\text{K}$.

For both these cases, the approximation for antenna temperature is within 0.8 dB of the more exact calculation, and for system temperature it is within 0.15 dB, which is adequate for many purposes. It would be less accurate for an ultralow-sidelobe antenna or a receiver with very low noise.

Table 6.1 Example Radar

Carrier frequency f_0	3.0 GHz	Wavelength λ	0.1m
Transmitter line loss L_t	0.5 dB	Transmitter temperature T_{pt}	400K
Antenna beamwidths θ_a, θ_e	1.0°, 2.0°	Beam axis elevation θ_b	1.2°
Far sidelobe level G_{far}	–15 dB	$\csc^2$ loss L_{csc}	2 dB
Antenna VSWR	1.5	Scan method	Mechanical
Antenna altitude h_r	10m	Antenna ohmic loss L_a	0.2 dB
Physical temperature T_p	290K	Receiving line loss L_r	1.0 dB
Galactic background $T_{0.1}$	3,050K	Receiver noise figure F_n	1.8 dB
Surface reflection coefficient ρ	0.9		

6.4 RECEIVING LINE NOISE TEMPERATURE

Compared with antenna noise temperature, the calculation of the noise temperature contribution of the receiving line is simple: (6.11) gives:

$$T_r = T_p \left(L_r - 1 \right) \tag{6.38}$$

where T_p is the physical temperature of the receiving line loss L_r. Included in L_r are the RF components between the antenna output port and the point in the receiver where noise figure is defined. These components include the transmission line itself, the duplexer receiving path, any additional receiver protection such as a solid-state limiter or attenuator (which may also be provided for gain control), an RF filter, and possibly a directional coupler used for test purposes.

6.5 RECEIVER NOISE TEMPERATURE

Given the noise figure F_n of the receiver, the corresponding noise temperature T_e is

$$T_e = T_0 \left(F_n - 1 \right) \tag{6.39}$$

where T_0 is used to conform to the definition of noise figure [8]:

> The ratio of: a) the total noise power per unit bandwidth (at a corresponding output frequency) delivered by the system into an output termination, to b) the portion thereof engendered at the input frequency by the input termination, whose noise temperature is standard (290°K) at all frequencies.

Referring T_e to the antenna port, it is multiplied by the receiving line loss L_r to give the receiver contribution to system temperature in (6.10).

6.5.1 Noise in Cascaded Receiver Stages

The radar receiver typically consists of the stages shown in Figure 6.9. The noise input power from the duplexer and receiving line is typically –110 to –115 dBm, corresponding to tenths of one microvolt in a 50-ohm circuit. Minimum detectable signal levels may approach this noise level. The low-noise amplifier (LNA) operates at the carrier frequency f_0, and is designed with a low noise figure $F_{n1} \approx 1$ dB, and gain G_1 = 15 –20 dB. This brings the input noise several decibels above circuit noise at the mixer output, after a mixer loss of ≈6 dB. IF amplifier stages following the mixer increase the noise voltage at the envelope detector output to

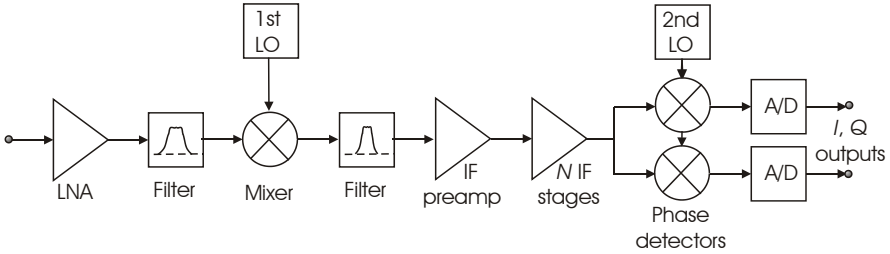

Figure 6.9 Stages in typical radar receiver.

above the least bit of the analog-to-digital (A/D) converter, typically tenths of one millivolt. The net receiver gain is in the order of 60 dB.

Calculation of receiver noise temperature T_e and noise figure F_n can be carried out by considering the noise temperature T_{ej} or noise figure F_{nj} of each of the m circuits that make up the receiver, where $j = 1, 2, \ldots m$:

$$T_e = T_{e1} + \frac{T_{e2}}{G_1} + \frac{T_{e3}}{G_1 G_2} + \ldots + \frac{T_{em}}{G_1 G_2 \ldots G_{m-1}} \tag{6.40}$$

$$F_n = F_{n1} + \frac{F_{n2} - 1}{G_1} + \frac{F_{n3} - 1}{G_1 G_2} + \ldots + \frac{F_{nm} - 1}{G_1 G_2 \ldots G_{m-1}} \tag{6.41}$$

As an example, $m = 7$ circuits precede the A/D converters in Figure 6.8. These might have the typical parameters shown in Table 6.2.

Table 6.2 Description of Typical Receiver Circuits

j	*Description*	F_{nj}		T_{ej} (K)	G_j		$T_{oj}\prod_2^m G_{j-1}^{-1}$
		Ratio	*dB*		*Ratio*	*dB*	
1	LNA	1.26	1.0	75.09	100	20.0	75.09
2	RF filter	1.12	0.5	35.39	0.89	–0.5	0.71
3	Mixer (r = 1.6)	6.31	8.0	1,539.78	0.25	–6.0	51.83
4	IF filter	1.26	1.0	75.09	0.79	–1.0	13.42
5	IF preamp	1.12	0.5	35.39	31.6	15.0	9.95
6	IF stages	1.26	1.0	75.09	10,000	40.0	0.80
7	Phase detectors (r = 1.3)	5.01	7.0	1,163.44	0.25	–6.0	0.00
Receiver, from (6.40), (6.41)		1.52	1.83	151.80	1.4×10^6	61.5	151.80

Noise figures and gains are determined for different circuits as follows:

For passive circuits: $F_{nj} = L_j = 1/G_j$;
For a mixer: $F_{nj} = rL_j$, $= r/G_j$, where r is the *noise-temperature ratio* [9, p. 33], typically 1.2 –2.0 = 2 ± 1 dB;
For amplifiers: F_{nj} and G_j are as specified in the table.

The noise temperature T_{ej} is calculated as $T_0(F_{nj} - 1)$. Note that placing the RF filter after the LNA minimizes the effect of its loss, and that the IF stages after the preamplifier make an insignificant contribution to noise temperature in a typical receiver. In spite of the LNA gain of 20 dB, the mixer in this case makes a significant contribution to the overall receive noise figure.

6.5.2 Input and Output Levels

The output noise power from the receiver to the A/D converter is the product of input noise $N = kT_sB_n$ and the net gain in the receiving path from the antenna, including the factor $1/L_r$. As an example, assume from the example radar of Table 6.1 the values T_a = 79K, L_r = 1.0 dB, and T_r = 75K. The system noise temperature from (6.10) is:

$$T_s = T_a + T_r + L_rT_e = 79 + 75 + 1.26 \times 151.8 = 345\text{K}$$

Assuming a noise bandwidth B_n = 1 MHz, the corresponding noise power and rms noise voltage in a 50-ohm circuit at the antenna terminal are:

$$N = kT_sB_n = -113.2 \text{ dBm}, E_{n\text{in}} = 0.49 \ \mu\text{V}$$

The net gain of the receiving system, from the antenna terminal to the detector output, is

$$61.5 - 1.0 = 60.5 \text{ dB}.$$

The resulting output noise power is

$$N_{\text{out}} = -113.2 + 60.5 = -52.7 \text{ dBm},$$

and the corresponding rms output voltage is

$$E_{n\text{out}} = 0.52 \text{ mV (in a 50-ohm circuit)}.$$

6.5.3 Quantizing Noise

Modern radars use digital signal processing in which the analog inputs are converted to digital form either after downconversion to baseband, as shown in Figure 6.8, or by direct conversion of the IF voltage. The A/D converter adds a *quantizing noise voltage* E_q to the thermal noise at the output:

$$E_q = \frac{\Delta E}{\sqrt{12}} = \frac{E_{\max}}{2^{b-1}\sqrt{12}} \tag{6.42}$$

where

ΔE is the voltage corresponding to the least bit of the A/D converter;
$E_{\max}$ is the peak voltage that corresponds to the full A/D output;
b is the number of A/D bits that express the peak voltage that varies over $\pm E_{\max}$.

The gain prior to the A/D converter is adjusted so that the rms noise voltage is $q\Delta$E:

$$E_{n\text{out}} = q\Delta E = \sqrt{12}qE_q \tag{6.43}$$

where $q \approx 1.5$ is a constant chosen to balance the competing needs for large dynamic range and small quantizing noise. The thermal noise power is $12q^2$ times the quantizing noise power. This is equivalent to an added input noise temperature term given by

$$T_q = \frac{T_s}{12q^2} \tag{6.44}$$

The dynamic range DR is defined as the ratio of (1) the average power of a sinusoidal output signal above which the A/D converter saturates to (2) the mean thermal noise power, referred to the receiver output. From (6.42) and (6.43) this is

$$\text{DR} = \frac{P_{\text{out max}}}{E_{n\text{out}}^2} = \frac{E_{\max}^2/2}{E_{n\text{out}}^2} = \frac{1}{8}\left(\frac{2^b}{q}\right)^2 \tag{6.45}$$

Both the quantizing noise temperature and the dynamic range vary inversely as q^2, so the need for large dynamic range and small temperature contribution are in conflict.

As an example, assume that the thermal noise at the output is set to $q = \sqrt{2}$ = 3 dB above the quantizing noise. From (6.44)

$$T_q = \frac{T_s}{12q^2} = \frac{T_s}{24}$$

Added to T_s, this increases the input noise temperature by a factor 1 + 1/24 = 1.04, or 0.18 dB relative to the result of (6.10). For this same value of q, with b = 12, the dynamic range from (6.45) becomes

$$\text{DR} = \frac{1}{8}\left(\frac{2^b}{\sqrt{2}}\right)^2 = 1,049\times 10^6 = 60.2 \text{ dB}$$

Combining (6.44) and (6.45), the quantizing noise temperature at the input can be expressed in terms of the dynamic range as

$$T_q = \frac{\text{DR}}{2^{2(b-1)}}\frac{T_s}{6} \tag{6.46}$$

The dynamic range available for b-bit converters has been given in the literature as

$$\text{DR} = 2^{2(b-x)} = 6.02\left(b-x\right) \text{ dB} \tag{6.47}$$

where different authors use x = 0, 1, or 2. Results of (6.46) are shown in Figure 6.10, for b = 10 –14 bits. The dashed lines show the increase in dB resulting from different values of x in (6.47): 2.22 dB for x = 0, 0.67 dB for x = 1, and 0.18 dB for x = 2. Depending on the investment in the transmitter and antenna, selection of the gain prior to the A/D converter to achieve the dynamic range given by x = 2 is often the best choice in receiver design.

6.6 SUMMARY OF RECIVING SYSTEM NOISE

6.6.1 Thermal Noise Dependence on Carrier Frequency

The noise spectral density resulting from an input noise temperature T_s, as calculated by the simple expression $N_0 = kT_s$, is correct to within 0.1 dB for receivers in which the ratio of carrier frequency to noise temperature $f_0/T_s \le 10^9$ (e.g., X-band at 10K). The simple expression underestimates N_0 by 1.1 dB for $f_0/T_s \le 10^{10}$ (e.g., W-band at 10K), and the error increases for larger ratios as may be encountered in terahertz and optical-band radar.

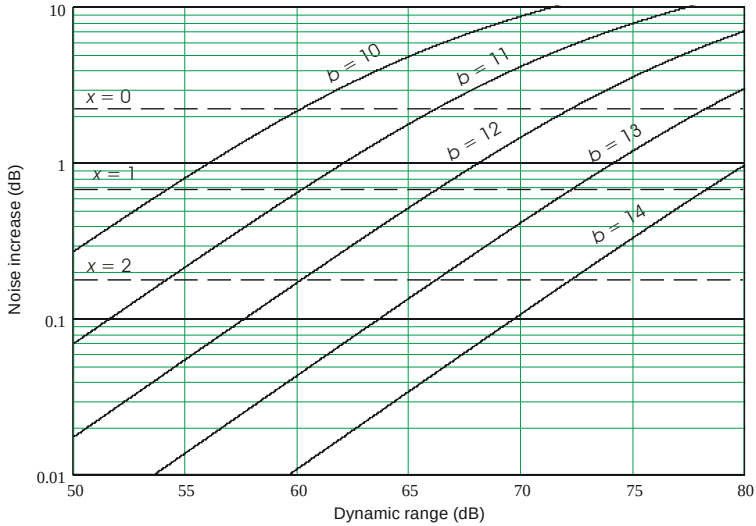

Figure 6.10 Noise temperature increase as a function of dynamic range.

6.6.2 Applicability of Blake's Method

The many external and internal sources of radar noise are identified in this chapter, and expressions given for estimating their contribution to input noise temperature. Blake's method provides a sound basis for evaluation of the noise temperature, which he expresses in the form of (6.10).

Blake also gives the approximation (6.18), based on 12.4% of the antenna pattern's power lying in the lower hemisphere, which gives adequate results for most practical radar situations.

6.6.3 Refined Method for Modern Radar

To refine Blake's method and adapt it to modern radar situations, more exact models of the troposphere are used, and the contribution of the surface is refined in Section 6.3.3, accounting for the antenna's elevation pattern and the reflection coefficient of the surface. The effect of antenna mismatch, especially significant in electronically steered arrays, is discussed in Section 6.3.5 and is based on Brookner's recent work. The added noise temperature term from mismatch, including the effect of transmitter temperature, typically approaches 120K at the edge of the scanned volume, or 50K when averaged over that volume.

6.6.4 Receiver and Quantization Noise Temperature

The modeling of receiver noise, including the effect of quantization in an A/D converter at the output, is presented in Section 6.5. A new relationship between quantizing noise temperature, the number of bits in the A/D converter, and the dynamic range of the receiver is developed. This relationship justifies use of a simple expression for the available dynamic range:

$$\mathrm{DR} = 2^{2(b-2)} = 6.02(b-2)\ \mathrm{dB} \tag{6.48}$$

The expression should be used when the input noise temperature is to be held within tenths of a decibel of the value given by (6.10).

References

[1] Blake, L. V., "Antenna and Receiving System Noise-Temperature Calculation," *NRL Report 5668*, September 19, 1961.

[2] Blake, L. V., "Radar/Radio Tropospheric Absorption and Noise Temperature," *NRL Report 7461*, October 30, 1972.

[3] Blake, L. V., *Radar Range-Performance Analysis*, Lexington, MA: D. C. Heath, 1980; Dedham, MA: Artech House, 1986.

[4] Air Force Geophysics Laboratory, *Handbook of Geophysics*, 1985, Document No. ADA 167,000, Springfield, VA: National Technical Information Service.

[5] Barton, D. K., *Radar System Analysis and Modeling*, Norwood, MA: Artech House, 2005.

[6] Brookner, E., "Right Way to Calculate Reflector and Active-Phased-Array Antenna System Noise Temperature Taking into Account Antenna Mismatch," *IEEE International Symposium on Phased Array Systems and Technology 2003*, Boston, MA, October 14–17 2003, pp. 130–135.

[7] Otoshi, T. Y., *Noise Temperature Theory and Applications for Deep Space Communications Antenna Systems*, Norwood, MA: Artech House, 2008.

[8] IEEE Standard 100, *The Authoritative Dictionary of IEEE Standards Terms*, 7th ed., New York: IEEE Press, 2000.

[9] Skolnik, M. I., *Introduction to Radar Systems*, 3rd ed., New York: McGraw-Hill, 2001.

CHAPTER 7

Atmospheric Effects

Atmosphere affects on radar propagation include:

- Refraction (bending) of the rays between the radar and the target;
- Attenuation the waves that travel those paths;
- Rotation in the polarization of waves in the ionosphere (at frequencies below S- band).

Attenuation and Faraday rotation have obvious relevance to the radar equation, but refraction must also be considered because the refracted ray from the radar lies above the geometric straight line to the target, reducing the attenuation relative to that applicable to the straight-line path. In addition, the bundle of rays leaving the radar within the elevation beamwidth is spread by greater bending in the lower portion of the beam, causing the power density to be reduced more than by the factor $1/R^2$ for free-space transmission.

Blake in [1] presents a thorough treatment of the atmospheric effects that remains valid today. The purpose of this chapter is to summarize and update the data, discuss practical modeling and computational methods, and present the results in metric units and in graphical formats that improve reading accuracy and interpretation.

7.1 TROPOSPHERIC REFRACTION

Blake's method of calculating attenuation uses integration along paths determined by *ray-tracing* through the troposphere. A model for the tropospheric refractive index as a function of altitude is required, and we present alternative models that

permit evaluation of different radar siting and weather effects in all radar frequency bands.

7.1.1 Refractive Index of Air

The complex refractive index is defined [2] as:

> A dimensionless complex quantity, characteristic of a medium and so defined that its real part is the ratio of the phase velocity in free space to the phase velocity in the medium. The product of the imaginary part of the refractive index and the free-space propagation constant is the attenuation constant of the medium.

Refraction of radar waves in the troposphere depends on the real part n of the refractive index, which is a function of temperature T, air pressure P, and partial pressure e of the water-vapor content.[1]

The real part of the refractive index is usually expressed in terms of the *refractivity N*, the departure of n from unity and given by [3, p. 7, Eq. (1.15)]:

$$\begin{aligned} N &= (n-1)\times 10^6 = 77.6\frac{P_{da}}{T} + 72\frac{e}{T} + 3.75\times 10^5 \frac{e}{T^2} \quad \text{(ppm)} \\ &\approx \frac{77.6}{T}\left(P + \frac{4820e}{T}\right) \end{aligned} \tag{7.1}$$

where

T = temperature in K;
P_{da} = partial pressure of dry air in mbar;
e = partial pressure of water vapor in mbar;
P = $P_{da} + e$ = air pressure in mbar.

This equation is accurate to within ≈ 0.5% at all radar frequencies, decreasing slightly for frequencies above the 60-GHz oxygen-absorption region.

The partial pressure e can be expressed as a function of the water vapor density ρ [4, p. 16-3]:

$$\frac{e}{T} = \frac{\rho_w}{216.68} \tag{7.2}$$

where ρ is in g/m^3. Thus (7.1) can be written as

$$N = 77.6\frac{P_{da}}{T} + \left(\frac{1,730.7}{T} + 0.332\right)\rho_w \tag{7.3}$$

[1] The unit of pressure commonly used is the millibar (mbar), defined as 100 pascals or 1,000 dyne/cm^2. It is approximately 1/1000 times the atmospheric pressure at sea level.

7.1.2 Standard Atmosphere

The standard atmosphere was defined by a committee of U.S. experts during the 1950s, and the 1976 version [5] that remains in effect at this writing was updated by experts from NOAA, NASA, and USAF. It is identical to the ICAO 1964 standard up to 32-km altitude and to the ISO 1973 standard up to 50 km. Temperature and pressure data below 30-km altitude, shown in Figure 7.1, are relevant to radar. Note that the pressure profile is close to an exponential, although its slope changes at ≈ 11 km altitude.

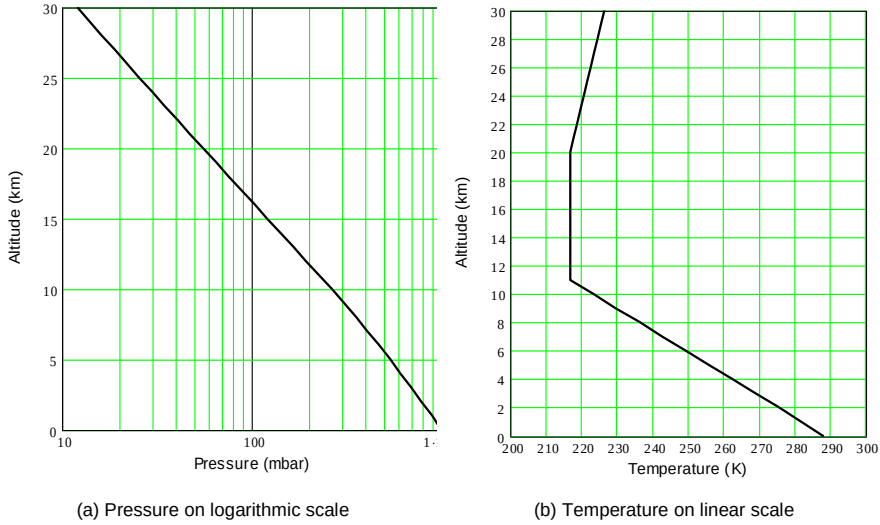

(a) Pressure on logarithmic scale (b) Temperature on linear scale

Figure 7.1 Temperature and pressure from U.S. Standard Atmosphere, 1976.

Temperature is characterized by three linear segments with slopes changing at 11 km and 20 km. The parameters at sea level are:

Temperature $T(0)$	288K;
Pressure $P(0)$	1,013.25 mbar.

where (0) denotes the altitude of sea level. The pressure profile can be approximated by two exponential sections:[2]

[2] Blake [1, p. 205] presents an atmospheric model with equations that contain obvious typographical errors; we will use here the model given by Figure 7.1 and (7.4), along with Blake's Table 5-4 for water-vapor density, expressed by (7.5).

$$P(h) = P(0)\exp\left(-\frac{h}{7.354}\right), \qquad h \le 11 \text{ km}$$
$$= 0.224P(0)\exp\left(-\frac{h}{6.457}\right), \quad h > 11 \text{ km} \tag{7.4}$$

7.1.3 Inclusion of Water Vapor

The standard atmosphere does not specify the water-vapor content of the air, but the sea-level value for the standard atmosphere is ρ_0 = 7.75 g/m^3. This can be compared with the density of saturated water vapor, 12.8 g/m^3 at 288K. When combined with the standard atmosphere, this leads to the following sea-level parameters

Density of water vapor ρ_{w0}	7.75	g/m^3;
Density of saturated water vapor $\rho_{w\max}$	12.8	g/m^3;
Relative humidity RH	60	%,
Partial pressure of water vapor e_0	10.3	mbar (from (7.2);
Partial pressure of dry air P_{da0}	1,002.7	mbar.

The sea-level refractivity and its dry-air and water-vapor components can be calculated using (7.1):

Refractivity N_0	319.2	ppm;
Dry-air refractivity N_{d0}	70.1	ppm;
Water-vapor refractivity N_{w0}	49.1	ppm.

Thus 85% of the sea-level refractivity results from the dry air and 15% from water vapor, even though the partial pressure of water vapor is only 1% of the total pressure.

Blake [1, p. 207] presented a vertical profile of measured ρ_w as a function of altitude, which can be scaled to the sea-level value ρ_{w0} = 7.75 g/m^3 to obtain Figure 7.2. The profile for water-vapor density can be expressed by a three-section model:

$$\rho_w(h) = \rho_{w0}(1 - 0.2523h), \quad h \le 2 \text{ km}$$
$$= 0.4954\rho_{w0}\exp\left(-\frac{h-2}{1.861}\right), \quad 2 < h \le 8 \text{ km} \tag{7.5}$$
$$= 0.0197\rho_{w0}\exp\left(-\frac{h-8}{1.158}\right), \quad 8 < h \text{ km}$$

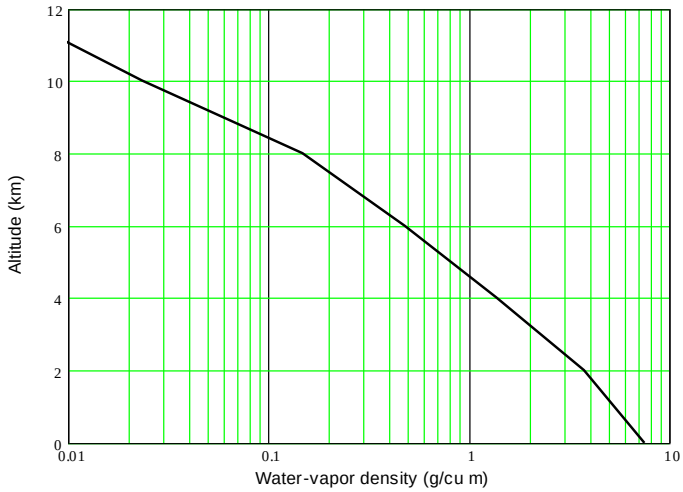

Figure 7.2 Water-vapor density versus altitude for $\rho_{w0} = 7.75$ g/m^3.

where the sea-level water-vapor density is $\rho_{w0} = 7.75$ g/m^3, for 60% relative humidity in the standard atmosphere. Separate profiles must be used for air pressure and water-vapor density to account for the concentration of water vapor at low altitudes.

7.1.4 Vertical Profile of Refractivity

Given profiles of T, P, and ρ_w, (7.3) is applied to obtain the refractivity profile of the standard atmosphere. In Figure 7.3 that profile is compared with a dashed line representing a single-section exponential fit to the low-altitude refractivity values that dominate the effect of the troposphere. This is one of a family of refractivity profiles known as the *CRPL Exponential Reference Atmospheres*, developed by the Central Radio Propagation Laboratory.[3]

The CRPL Exponential Reference Atmospheres are defined by [3, p. 65, Eq. (3.43)]:

$$N(h) = N_s \exp\left[-\frac{h-h_s}{h_0}\right] \approx N_0 \exp\left[-\frac{h}{h_0}\right] \tag{7.6}$$

where

[3] CRPL was a branch of the U.S. National Bureau of Standards in Boulder, Colorado, where extensive efforts to measure and model the atmosphere were carried out. The laboratory was transferred to the Environmental Science Services Administration in 1965, and subsequently to the National Oceanic and Atmosphere Agency (NOAA).

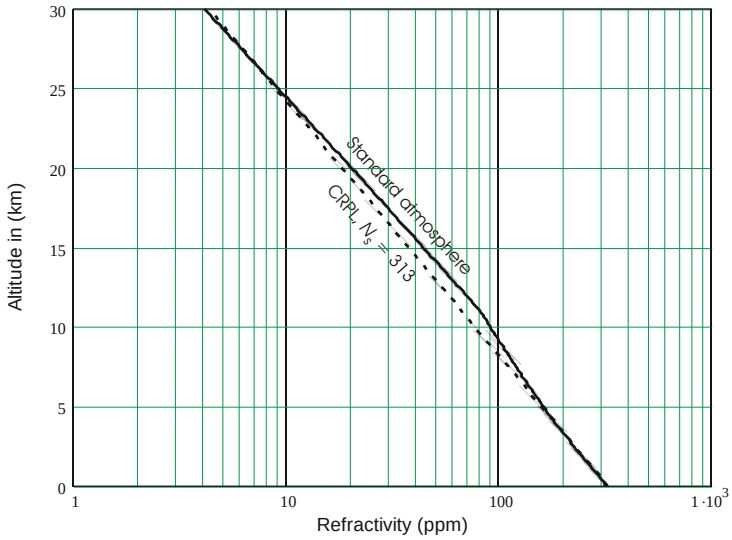

Figure 7.3 Refractivity versus altitude, for $\rho_{w0} = 7.75$ g/m^3.

h = altitude in km above sea level;
N_0 = sea-level refractivity in ppm;
h_0 = atmospheric scale height in km; [4]
N_s = refractivity at altitude h_s;
h_s = surface altitude in km above sea level.

The approximation symbol appears in the last form of (7.6) because the scale height h_0 used with N_0 should be slightly higher than for N_s. The scale heights h_0 given in [3, p. 66, Table 3.3] are shown in Table 7.1, and can be expressed for $200 \le N \le 450$ to an accuracy of 0.02 km by

$$h_0(N) = 4.479 + 8.17\left(1 - \frac{N}{450}\right) - 19\left(1 - \frac{N}{450}\right)^6 \tag{7.7}$$

The CRPL models are based on many measurements conducted during the 1950s. The dashed line in Figure 7.3 is for a surface refractivity $N_s = 313$ ppm, used by Blake [1, p. 183] as the average for the United States. The parameters presented in Table 7.1 are applicable to different site altitudes and weather condi-

[4] The scale height h_0 in [1, 3] is expressed by its reciprocal c in km^{-1}, but the scale height h_0 (defined as the altitude in km at which N falls to $1/e$ of its surface value) has a clear physical interpretation.

Table 7.1 Parameters of CRPL Exponential Reference Atmospheres

Surface Refractivity N_s (ppm)	*Scale Height* h_0 (km)	*Earth Radius Constant* k_e
450.0	4.479	2.784
400.0	5.356	1.910
350.0	6.276	1.552
313.0	6.951	1.403
301.0	7.162	1.366
250.0	7.960	1.251
200.0	8.446	1.178

tions. The parameter k_e represents the ratio of effective Earth's radius to true radius a_e = 6,378 km, and k_e = 4/3 is the value commonly used in radar calculations.

The motivation for and development of the CRPL exponential reference atmospheres are discussed in detail in [6], which also presents climatic charts of the U. S. showing contours of refractivity for day and night conditions in February and August, adjusted to sea-level values N_0. Extreme values on these charts are as follows:

Maximum N_0 = 390 on the Gulf Coast on an August day;
Minimum N_0 = 285 in southern Nevada on a February day.

The entry N_s = 450 in Table 7.1 is observed only in hot, humid environments. The entry N_0 = 200 is associated in [3] with an altitude of 3 km, near the maximum altitude for land-based radar. The U.S. average N_s = 313 is associated in the CRPL data with a surface altitude of 700 ft (213m), for which the corresponding sea-level N_0 = 323.

The CRPL data suggest that $250 \le N_0 \le 400$ covers the likely variation in sea-level conditions, with $N_0 \approx 320$ a nominal value. The refractive index profile for a given site altitude is then found from (7.6) using the selected N_0.

7.1.5 Ray Paths in the Troposphere

7.1.5.1 Ray-Tracing Method

A ray leaving the radar at elevation angle θ_0 is gradually bent downward as a result of the decrease in the tropospheric refractive index with altitude h. The path is calculated for a known vertical profile of refractive index by *ray-tracing*, in which the range $R_d = ct_d/2$, as measured by the time delay t_d of the radar echo, is given by [1, p. 182, Eq. (5.9)]:

$$R_d(h,\theta_0) = \int_{h_s}^{h} n(h)\left\{1-\left[\frac{n(h_s)\cos\theta_0}{n(h)(1+h/a_e)}\right]^2\right\}^{-1/2} dh \text{ (km)} \tag{7.8}$$

where

$n(h)$ = $1 + N(h) \times 10^{-6}$ =vertical profile of refractive index;
h_s = altitude in km above sea level of the radar;
h = altitude in km above sea level along the path;
a_e = 6,378 km = radius of the Earth.

In order to use the result of (7.8) in calculation of attenuation along the path, it must be inverted to yield altitude $h(R,\theta_0)$. There is no closed-form equation for this, so root-finding methods must be used.

7.1.5.2 Altitude Based on Effective Earth's Radius

The effective Earth's radius $k_e a_e$ is defined so that a ray leaving a radar antenna at altitude h_s above sea level at elevation angle θ_0 reaches an altitude h at range R given by [1, p. 187, Eq. (5.15)]

$$h(R,\theta_0) = \sqrt{(k_e a_e + h_s)^2 + R^2 + 2(k_e a_e + h_s)R\sin\theta_0} - k_e a_e \tag{7.9}$$

For radar ranges at which the effective Earth's radius can be used, the following approximation is valid [1, p. 188, Eq. (5.16)]:

$$h(R,\theta_0) \approx R\sin\theta_0 + \frac{(R\cos\theta_0)^2}{2k_e a_e} + h_s \tag{7.10}$$

For example, at R = 1,000 km the altitude error is less than 0.4% of the value from (7.9). The approximation permits attenuation calculations to be performed with acceptable accuracy over many ranges and elevation angles without the complexity of ray-tracing.

7.2 ATTENUATION IN THE TROPOSPHERE

The attenuation for a radar path is expressed as the product of a two-way attenuation coefficient in dB/km and the pathlength in km through the attenuating medium. In the equations that follow, the two-way tropospheric attenuation coefficient denoted by k_α is used in place of γ, which in the referenced literature denotes the one-way coefficient in dB/km.

7.2.1 Sea-Level Attenuation Coefficients of Atmospheric Gases

Attenuation results from the imaginary part of the complex refractive index, which varies with radar frequency f and with atmospheric pressure P, temperature T, and water-vapor density ρ. The relationships between these quantities and attenuation (absorption) were developed in an MIT Radiation Laboratory report by J. H. Van Vleck, condensed in [7]. That theory is used as the basis for the treatment in [3, Chapter 7] and by Blake [1, pp. 200–204].

Oxygen and water vapor cause attenuation, both having strong, narrow absorption lines within the millimeter-wave spectrum (and at 22.2 GHz for water vapor). The absorption extends at lower levels throughout bands used by radar.

7.2.1.1 Oxygen Attenuation

The primary oxygen absorption lines are centered near $f_{O1} \approx 60$ GHz ($\lambda_{O1} = 0.50$ cm). Rather than a single line, there are actually a sequence of resonances corresponding to odd values of the rotational quantum number N, listed in Table 7.2 up to order 45, beyond which the contributions to attenuation are negligible. Note the well separated resonance at $f_{1-} = 118.75$ GHz, which will appear in subsequent plots.

Table 7.2 Oxygen Resonance Frequencies (GHz)

N	f_{N+}	f_{N-}	N	f_{N+}	f_{N-}
1	56.2648	118.7505	25	65.7626	53.5960
3	58.4466	62.4863	27	66.2978	53.0695
5	59.5910	60.3061	29	66.8313	52.5458
7	60.4348	59.1642	31	67.3627	52.0259
9	61.1506	58.3239	33	67.8923	51.5091
11	61.8002	57.6125	35	68.4205	50.9949
13	62.4112	56.9682	37	68.9478	50.4830
15	62.9980	56.3634	39	69.4741	49.9730
17	63.5685	55.7839	41	70.0000	49.4648
19	64.1272	55.2214	43	70.5249	48.9582
21	64.6779	54.6728	45	71.0497	48.4530
23	65.2240	54.1294			

Values of $f_{N\pm}$ from [8], as listed in [1, Table 5-3].

The oxygen attenuation coefficient $k_{\alpha 0}$ was derived by Van Vleck [7 pp. 646–656], whose equations as given in [1, pp. 200–201] (with the initial constant doubled for two-way attenuation) are as follows:

$$k_{\alpha O}(f,h) = 4.0116\frac{Pf^2}{T^3}\sum_N \left(F_0\mu_{N0}^2 + F_{N+}\mu_{N+}^2 + F_{N-}\mu_{N-}^2\right)\exp\left[-\frac{2.06844N(N+1)}{T}\right] \tag{7.11}$$

$$F_0(f,h) = \frac{\Delta f}{f^2 + (\Delta f)^2} \tag{7.12}$$

$$\Delta f(h) = g(h)\frac{P(h)}{P(0)}\frac{T(0)}{T(h)} \tag{7.13}$$

$$\begin{aligned} g(h) &= 0.640, && h \le 8 \\ &= 0.640 + 0.04218(h-8), && 8 < h \le 25 \\ &= 1.357, && 25 < h \end{aligned} \tag{7.14}$$

$$F_{N\pm}(f,h) = \frac{\Delta f}{(f_{N\pm} - f)^2 + (\Delta f)^2} + \frac{\Delta f}{(f_{N\pm} + f)^2 + (\Delta f)^2} \tag{7.15}$$

$$\mu_{N0}^2 = \frac{2(N^2+N+1)(2N+1)}{N(N+1)} \tag{7.16}$$

$$\mu_{N+}^2 = \frac{N(2N+1)}{N+1} \tag{7.17}$$

$$\mu_{N-}^2 = \frac{(N+1)[2N-1]}{N} \tag{7.18}$$

where

$k_{\alpha O}$ = two-way attenuation in dB/km;
f = frequency in GHz;
P = air pressure in mbar;
h = altitude in km;
T = temperature in K.

The term $F_0\mu_{N0}^2$ in (7.11) gives the nonresonant absorption, while $F_{N\pm}\mu_{N\pm}^2$ result from the resonances listed in Table 7.2. The altitude factor $g(h)$ in (7.13), (7.14) is included in the Blake's equations, based on [8]. The results for the sea-level atmosphere are shown in Figure 7.4.

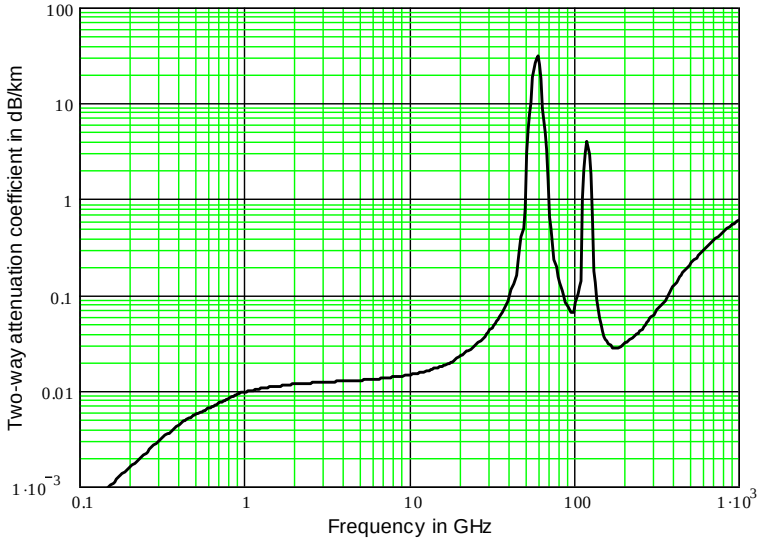

Figure 7.4 Sea-level attenuation coefficient $k_{\alpha O}$ of atmospheric oxygen.

7.2.1.2 Water-Vapor Attenuation

The attenuation coefficient of water vapor was also derived by Van Vleck [7, pp. 656 –664], based on the primary water-vapor absorption line at f_{W1} = 22.235 GHz. Subsequent work has included additional absorption lines at frequencies f_{W2} = 183.3 GHz and f_{W3} = 323.8 GHz. The expression for two-way water-vapor attenuation in dB/km is

$$k_{\alpha W}(f,h) = \frac{\rho_w(h)}{7.75}\left(\frac{288}{T(h)}\right)^{5/2}\left\{\left(\frac{f}{100}\right)^2\frac{P(h)}{1{,}013}+\left(\frac{f}{f_{r1}}\right)^2\times \exp\left[2.144\left(1-\frac{288}{T(h)}\right)\right]\right\}\sum_{z=1}^{3}F_{Wz} \tag{7.19}$$

$$F_{Wz}(f,h) = \frac{\Delta f_W}{(f_{Wz}+f)^2+(\Delta f_W)^2}+\frac{\Delta f_W}{(f_{Wz}-f)^2+(\Delta f_W)^2} \tag{7.20}$$

$$\Delta f_W(h) = 0.0187\rho_w(h)+0.00385\left[0.75P(h)-\rho_w(h)\right]\left[\frac{288}{T(h)}\right]^{0.63} \tag{7.21}$$

where

h = altitude in km;
$\rho_w(h)$ = density of water vapor in g/m^3 at altitude h;
$P(h)$ = air pressure in mbar at altitude h;
$T(h)$ = temperature in K at altitude h;
F_{Wz} = resonant line structure;
f_{Wz} = resonant frequencies $f_{W1\ldots3}$ in GHz;
Δf_W = resonant line width in GHz.

The term in (7.19) involving $f/100$ is the nonresonant (residual) water-vapor coefficient from lines above 100 GHz, while that with f/f_{r1} is the sum of resonant contributions defined by (7.20).[5] The water-vapor attenuation coefficient for a standard density $\rho_w(0) = 7.75$ g/m^3 is shown in Figure 7.5.

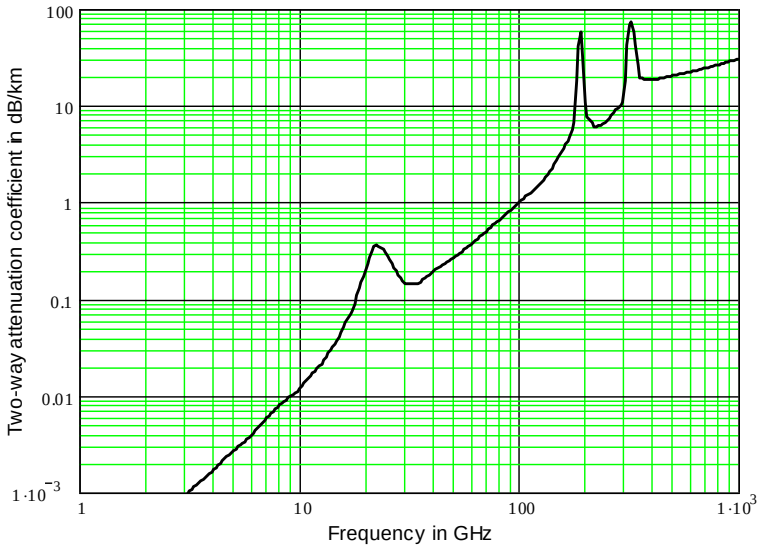

Figure 7.5 Sea-level attenuation coefficient $k_{\alpha W}$ of water vapor with density $\rho_{w0} = 7.75$ g/m^3.

7.2.1.3 Total Tropospheric Attenuation Coefficient

Figure 7.6 shows the combined attenuation coefficient for the sea-level atmosphere with water-vapor density of 7.75 g/m^3, and the individual contributions of oxygen and water vapor.

---

[5] Constants in (7.19)–(7.21) have been changed from those in the literature to be consistent with use of a single temperature reference $T(0) = 288$K, rather than both 288K and 300K appearing in some literature; water-vapor density ρ in g/m^3 rather than partial pressure in torr; and air pressure in mbar, rather than in torr.

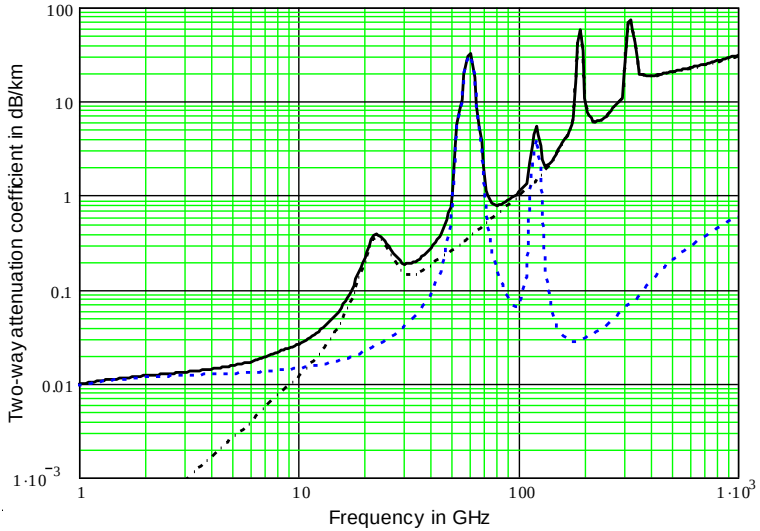

Figure 7.6 Sea-level attenuation coefficients of atmosphere: combined attenuation k_α (solid line); oxygen $k_{\alpha O}$ (dashed line), water-vapor $k_{\alpha W}$ for density $\rho_{w0} = 7.75$ g/m^3 (dash-dot line).

7.2.2 Variation of Attenuation Coefficients with Altitude

The attenuation coefficients of oxygen and water vapor vary in different ways as the radar beam passes upwards through the troposphere. The atmospheric and geometric models developed in Section 7.1 provide the data needed to calculate the attenuation on a path to a target, or through the entire atmosphere into space.

Equations (7.11)–(7.21) for attenuation coefficients include several terms that depend on altitude above sea level. We can find the coefficients for any altitude within the troposphere using vertical profiles of pressure $P(h)$, temperature $T(h)$ and water-vapor density $\rho_w(h)$ given by (7.4), Figure 7.1(b), and (7.5). Typical results are shown in Figure 7.7, for altitudes $h = 0$, 3 km, and 10 km. Note that the attenuation at resonant frequencies is reduced much more slowly than the nonresonant term as altitude increases. For this reason, a simple scaling of attenuation coefficients with altitude or atmospheric pressure cannot be used. Instead, the attenuation must be calculated by integration over the actual ray path, using coefficients that vary with altitude.

7.2.3 Attenuation Through the Troposphere

The total two-way attenuation $L_{\alpha t}(h_m)$ along a path leaving the radar at elevation angle θ_0 and reaching altitude h_m km is given by [1, p. 209, Eq. (5.46)]:

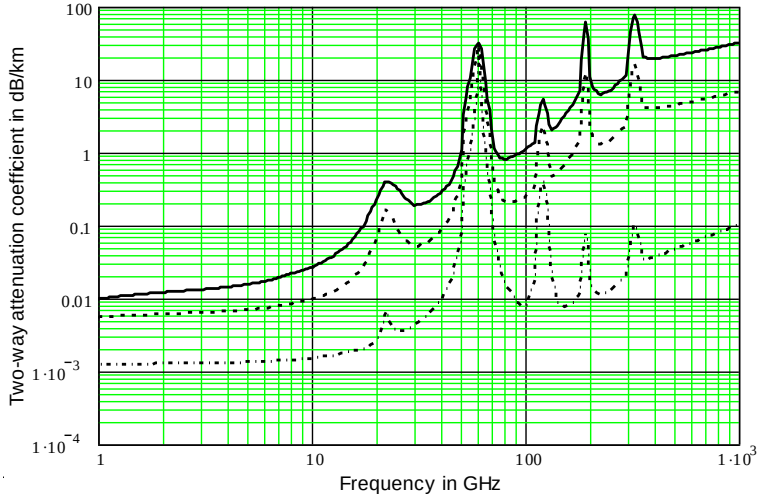

Figure 7.7 Attenuation coefficient k_α as a function of frequency at different altitudes, for an atmosphere with sea-level water-vapor density $\rho_{w0} = 7.75$ g/m^3: $h = 0$ (solid line); $h = 3$ km (dashed line), $h = 10$ km (dash-dot line).

$$L_{\alpha t}(h_m) = \int_{h_s}^{h_m} k_\alpha(h) \left\{ 1 - \left[\frac{a_e n(h_s) \cos\theta_0}{n(h)(a_e + h - h_s)} \right]^2 \right\} dh \quad \text{(dB)} \tag{7.22}$$

where

$n(h)$ = refractive index profile;
$k_\alpha(h)$ = attenuation coefficient in dB/km at altitude h km;
a_e = 6,378 km = radius of Earth
θ_0 = elevation angle of beam leaving radar;
h_s = altitude of radar site in km.

For a path from sea level into space, the lower altitude limit $h_s = 0$ and the upper altitude limit can be taken as $h_m = 100$ km. Figure 7.8 shows the attenuation into space for different beam elevations as a function of frequency.

7.2.4 Attenuation to Range *R*

Attenuation $L_\alpha(R, \theta)$ for a path to range R at beam elevation θ can be found by plotting the results of (7.22) as a function of $R(h_m, \theta)$ from (7.8). The results, shown in Figures 7.9–7.18 are equivalent to those presented by Blake [1, pp. 210–216, Figures 5.12–519], widely used to obtain the atmospheric attenuation used in

the radar equation. The plots presented here are based on a sea-level water-vapor density ρ_{w0} = 7.75 g/m^3, corresponding to a relative humidity of 60% in the standard atmosphere, and are plotted on log-log scales for better reading accuracy.

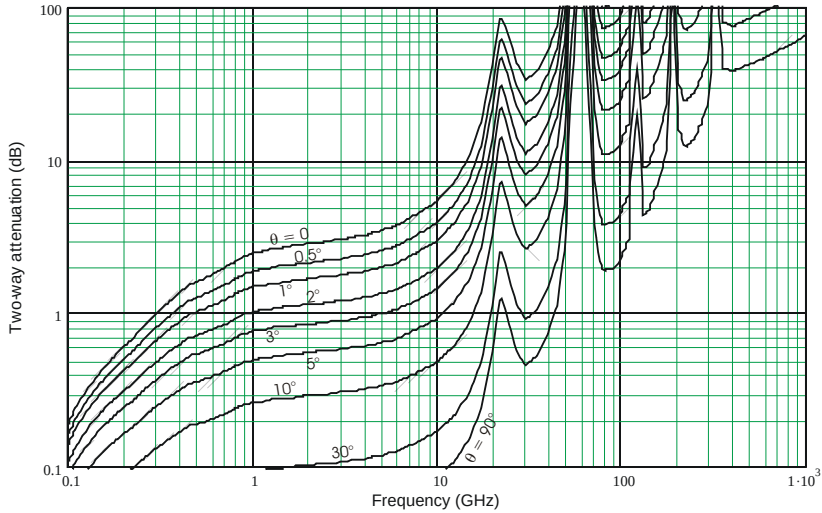

Figure 7.8 Atmospheric attenuation from sea level through the troposphere as a function of frequency at different beam elevation angles: standard atmosphere with water-vapor density ρ_{w0} = 7.75 g/m^3.

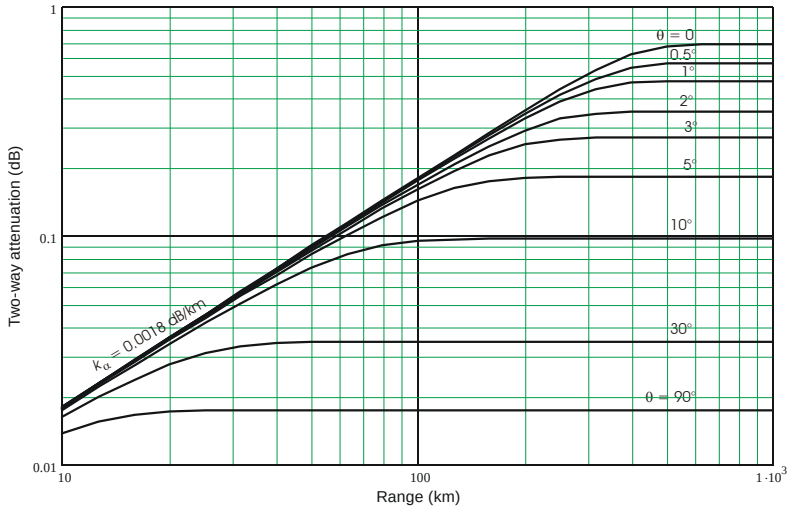

Figure 7.9 Atmospheric attenuation to range R for frequency f_0 = 225 MHz at different beam elevation angles, for a standard atmosphere with water-vapor density ρ_{w0} = 7.75 g/m^3.

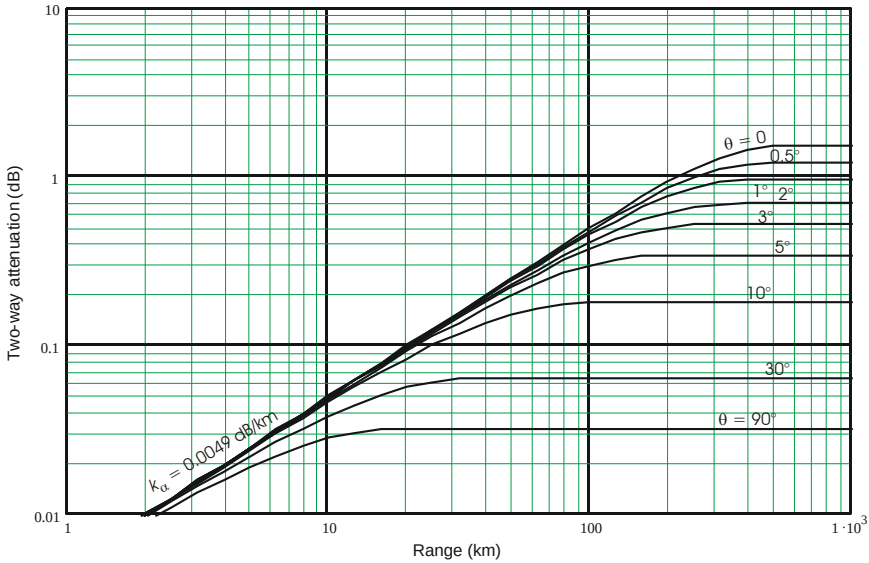

Figure 7.10 Atmospheric attenuation to range R for frequency f_0 = 450 MHz at different beam elevation angles, for a standard atmosphere with water-vapor density ρ_{w0} = 7.75 g/m^3.

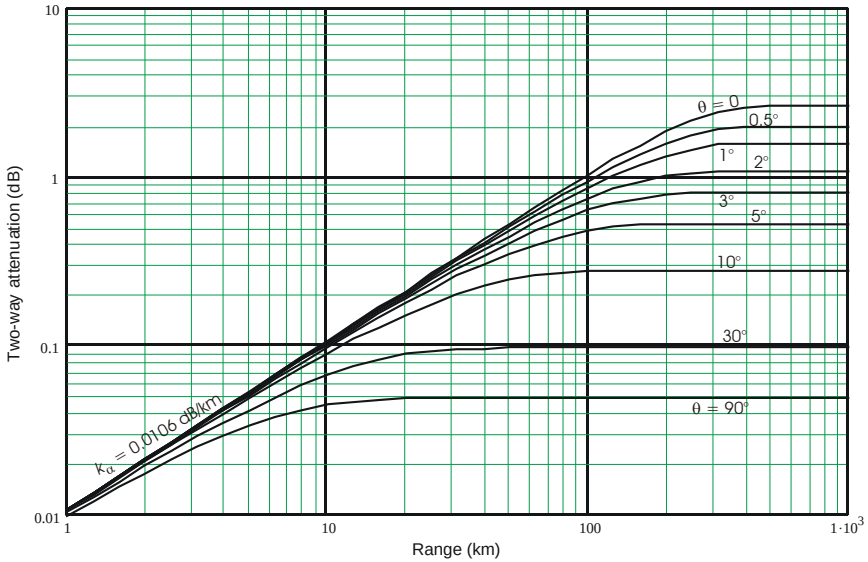

Figure 7.11 Atmospheric attenuation to range R for frequency f_0 = 1.3 GHz at different beam elevation angles, for a standard atmosphere with water-vapor density ρ_{w0} = 7.75 g/m^3.

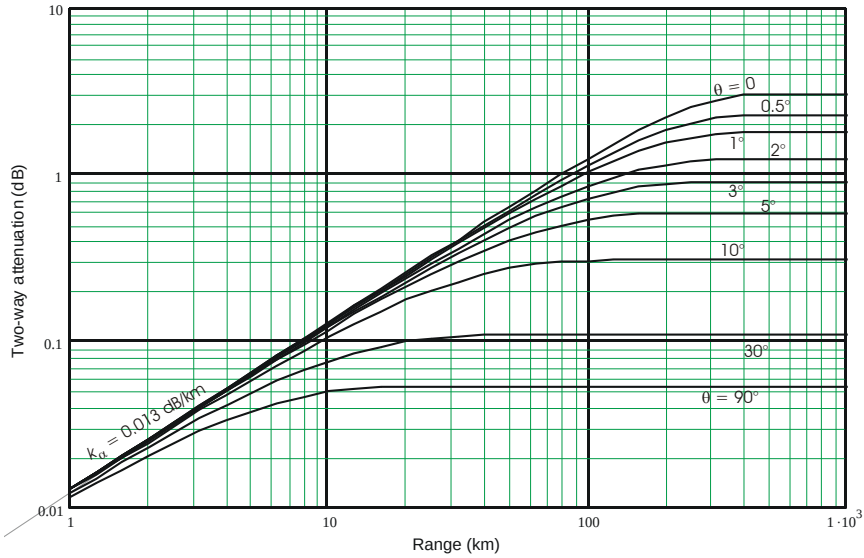

Figure 7.12 Atmospheric attenuation to range R for frequency f_0 = 3.0 GHz at different beam elevation angles, for a standard atmosphere with water-vapor density ρ_{w0} = 7.75 g/m^3.

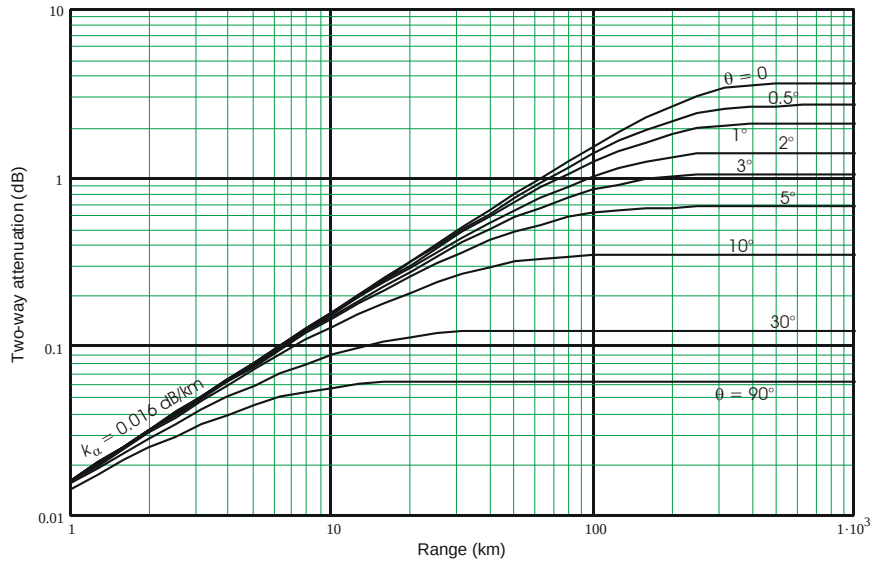

Figure 7.13 Atmospheric attenuation to range R for frequency f_0 = 5.6 GHz at different beam elevation angles, for a standard atmosphere with water-vapor density ρ_{w0} = 7.75 g/m^3.

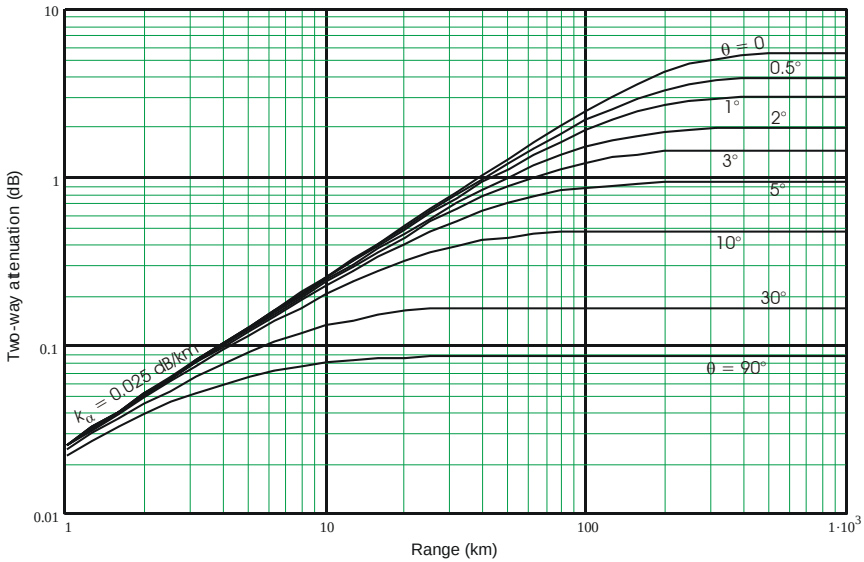

Figure 7.14 Atmospheric attenuation to range R for frequency f_0 = 10 GHz at different beam elevation angles, for a standard atmosphere with water-vapor density ρ_{w0} = 7.75 g/m^3.

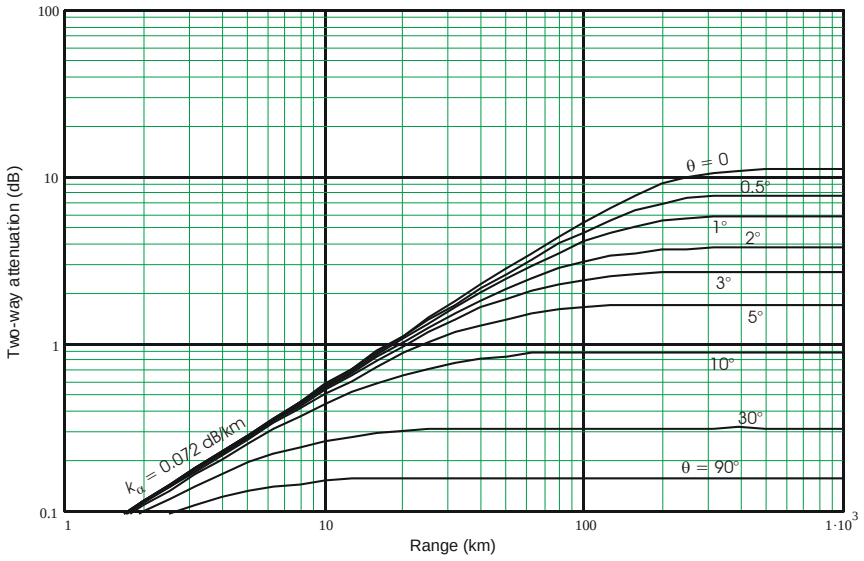

Figure 7.15 Atmospheric attenuation to range R for frequency f_0 = 15 GHz at different beam elevation angles, for a standard atmosphere with water-vapor density ρ_{w0} = 7.75 g/m^3.

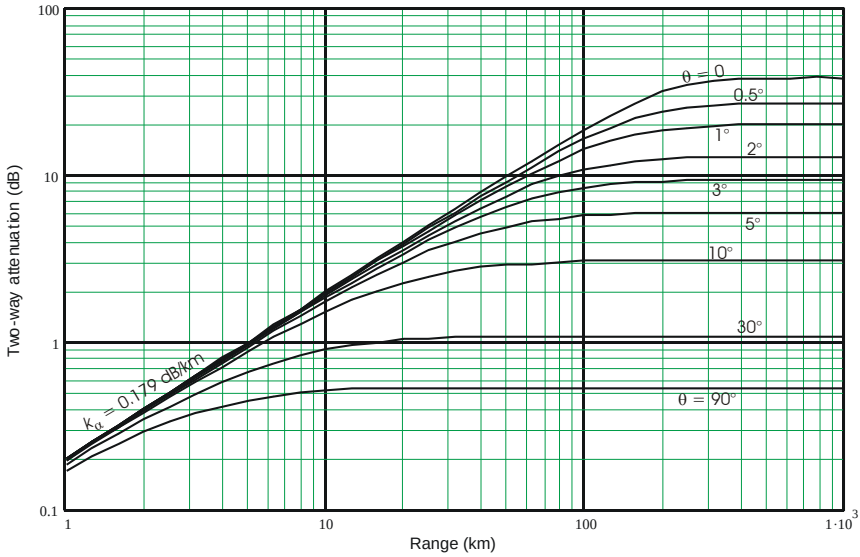

Figure 7.16 Atmospheric attenuation to range R for frequency f_0 = 35 GHz at different beam elevation angles, for a standard atmosphere with water-vapor density ρ_{w0} = 7.75 g/m^3.

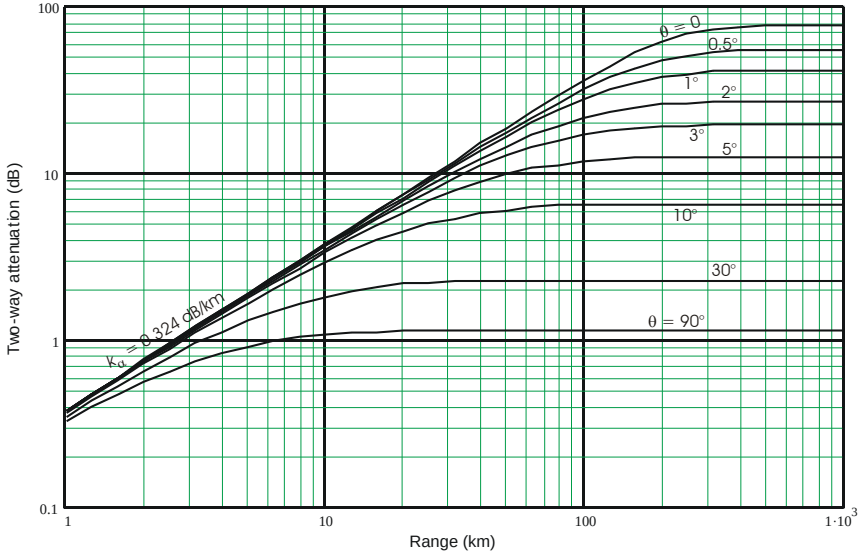

Figure 7.17 Atmospheric attenuation to range R for frequency f_0 = 45 GHz at different beam elevation angles, for a standard atmosphere with water-vapor density ρ_{w0} = 7.75 g/m^3.

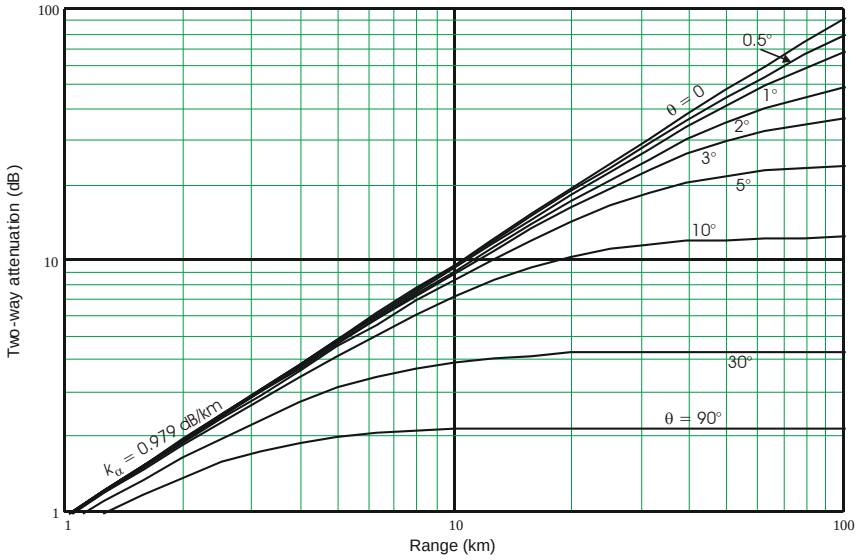

Figure 7.18 Atmospheric attenuation to range R for frequency f_0 = 95 GHz at different beam elevation angles, for a standard atmosphere with water-vapor density ρ_{w0} = 7.75 g/m^3.

7.2.5 Attenuation for Dry and Moist Atmospheres

Attenuation data are sometimes needed for water-vapor densities other than the ρ_{w0} = 7.75 g/m^3 used in Figures 7.8–7.18. Because the relative contributions of oxygen and water vapor vary with frequency and altitude, exact attenuation curves for other water-vapor densities require that calculations using (7.22) be repeated for other moisture conditions. Blake's solution to this problem is to plot separate families of curves for $k_{\alpha O}$ and for $k_{\alpha W}$ at 7.75 g/m^3 at frequencies above L-band. The total attenuation k_α is then found by multiplying the plotted $k_{\alpha W}$ in decibels by the ratio ρ_w/7.75 g/m^3 and adding it to $k_{\alpha O}$ for oxygen.

An alternative to Blake's method of adjusting for water-vapor content, which avoids the multistep procedure, is to scale readings from the curves of Figures 7.8–7.18 directly by a *water-vapor factor* W_ρ, defined as

$$W_\rho = \frac{1}{k_\alpha(0)}\left[k_{\alpha O}(0) + \frac{\rho_w}{7.75}k_{\alpha W}(0)\right] \tag{7.23}$$

where $k_\alpha(0)$, $k_{\alpha O}(0)$, and $k_{\alpha W}(0)$ are the attenuations coefficients at sea level. Figure 7.19 shows W_ρ for several values of ρ. The scaled attenuation given by $L_\alpha(h_m, \rho_w) = W_\rho(\rho_w)\, L_\alpha(h_m, 7.75)$ is only approximate, because it fails to model the

variation in the relative coefficients as a function of altitude, but as shown in Figure 7.20 it is close to exact values. The differences are less than the typical errors in knowledge of water-vapor density. For average atmospheric conditions the curves given in Figures 7.8–7.18 may be used directly.

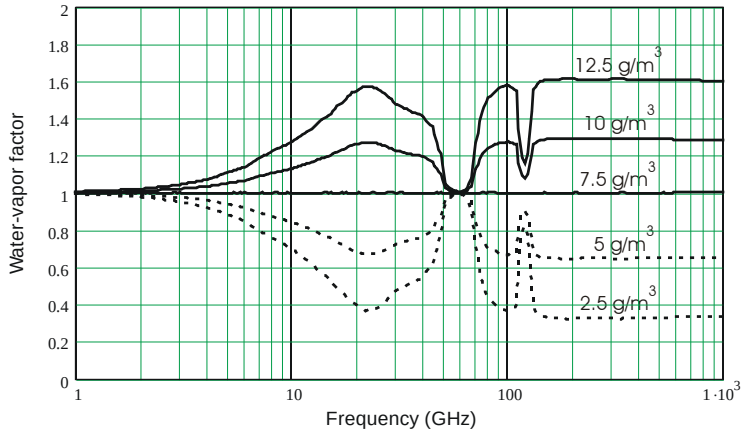

Figure 7.19 Water-vapor factor W_ρ as a function of frequency for different water-vapor densities.

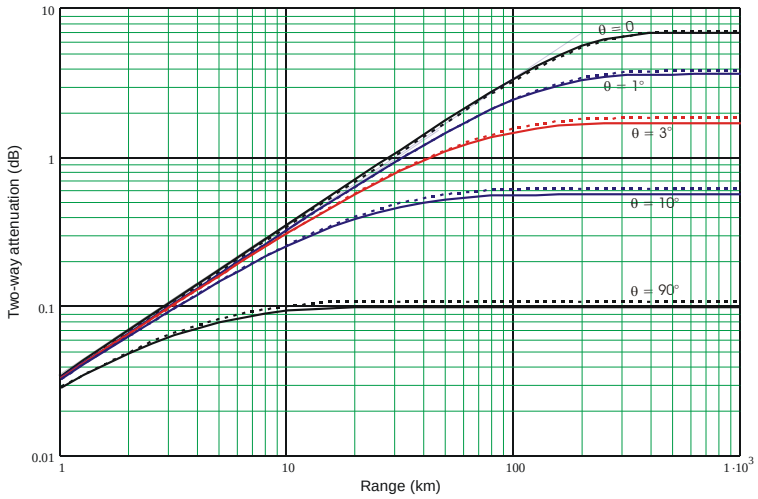

Figure 7.20 Atmospheric attenuation L_α as a function of range for f_0 = 10 GHz at different elevation angles, with water-vapor density ρ_{w0} = 12.5 g/m^3. Solid lines: exact results of (7.22); dashed lines: approximation using product of attenuation for ρ_{w0} = 7.75 g/m^3 and water-vapor factor W_ρ.

7.3 ATTENUATION FROM PRECIPITATION

7.3.1 Rain Attenuation Coefficient at 293K

Theoretical studies of rain attenuation are presented by Goldstein [11] and Gunn and East [12], whose results remain in extensive use. Much of that analysis and the today's models of weather attenuation originated in a 1945 company report by Ryde and Ryde [13] and their subsequent paper published in 1946 by the Physical Society, London [14], neither of which is available today. More recent adjustments are presented by Blake [1, pp. 214–221], and Nathanson [15, pp. 226–228].

The standard model that relates attenuation coefficient $k_{\alpha r}$ to rainfall rate takes the form [1, p. 215, Eq. (5.47)]:

$$k_{\alpha r}\left(r_r\right) = a r_r^b \text{ dB/km} \tag{7.24}$$

where

r_r = rainfall rate in mm/h;
a = multiplicative factor that depends on frequency f_0;
b = exponent that depends on frequency f_0.

Blake presents equations for a and b that apply for a temperature of ≈291K, and are updated here to match data in [1, p. 228, Table 6.4]:

$$a\left(f_0\right) = \frac{C_0 f_0^2 \left(1 + f_0^2 / f_1^2\right)^{1/2}}{\left(1 + f_0^2 / f_2^2\right)^{1/2} \left(1 + f_0^2 / f_3^2\right)^{1/2} \left(1 + f_0^2 / f_4^2\right)^{0.65}} \tag{7.25}$$

$$b\left(f_0\right) = 1.30 + 0.0372\left[1 - \left(1 + x_f^2\right)\right]^{1/2} \tag{7.26}$$

where

C_0 = 6.2×10^{-5}, f_1 = 3 GHz, f_2 = 35 GHz, f_3 = 50 GHz, f_4 = 110 GHz, and
x_f = $16.7 \log(0.13 f_0)$.

The changes made here to Blake's equations are that the last term in the denominator of (7.25) has an exponent 0.65 rather than 0.5, and the parameter x_f is now $16.7\log(0.13f_0)$ rather than $16.7\log(0.1f_0)$. The effect decreases $a(f_0)$ for $f_0 > 90$ GHz, and shifts the peak of the curve for $b(f_0)$ from 10 GHz to 7.75 GHz. The resulting two-way rain attenuation coefficient $k_{\alpha r}$ is shown as a function of frequency in Figure 7.21, for different rainfall rates.

Nathanson's table gives slightly different values of a and b for horizontal and vertical polarization, consistent with observations that predict a gradual shift of circularly polarized waves to elliptical polarization. That is a critical issue in

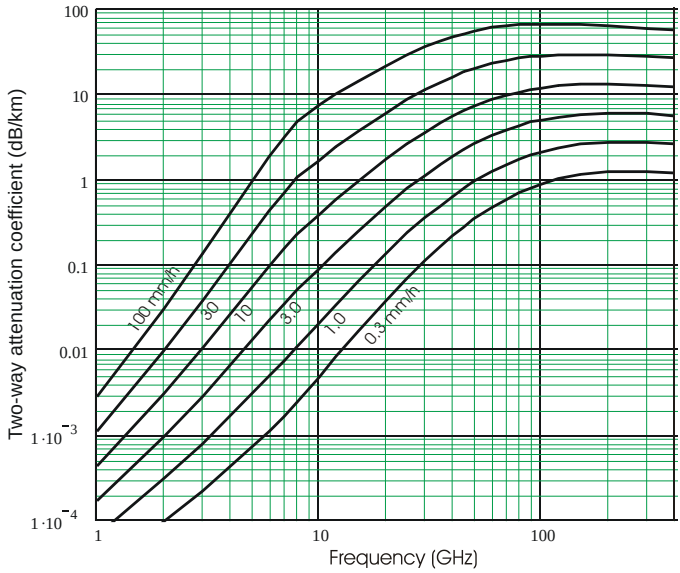

Figure 7.21 Two-way rain attenuation coefficient at T = 293K as a function of frequency for different rainfall rates, calculated using (7.24) with a and b from (7.25) and (7.26).

communications systems with polarization diplexing, but the average of each constant over both polarizations is adequate for calculating radar attenuation in rain, giving accuracy better than can be justified by weather models. Medhurst [16] and Blake note that measured attenuation often exceeds that predicted by theory. Blake suggests that this may result from relative humidity approaching 300% during rainstorms, an effect that can be modeled by increasing ρ_w in (7.23) and applying the resulting W_ρ to increase the attenuation of the atmospheric gases.

7.3.2 Temperature Dependence of Rain Attenuation

Several studies [10–13, 17, 18] have shown that rain attenuation varies significantly with the temperature of the water droplets. Ryde's results, presented in [17, p. 19-12, Table 19-1] indicate that the attenuation coefficients for T = 291K, used in the model of the preceding section, should be multiplied by correction factors listed in Table 7.3. While these values differ significantly from some earlier results in [12, 13], especially for the longer wavelengths at low temperatures, they appear to represent an adequate model. The data in Table 7.3 can be approximated by the following approximation:

$$C_T(\lambda) = 1 + a_T(100\lambda - 1.5)^{b_T}, \quad \lambda \geq 0.015 \text{ m}$$
$$= 1, \qquad \lambda < 0.015 \text{ m} \tag{7.27}$$

where the constants are given by:

$a_{273} = 0.2$, $a_{283} = 0.1$, $a_{291} = 0$, $a_{303} = -0.12$, $a_{313} = -0.21$;
$b_{273} = 0.6$, $b_{283} = 0.5$, $b_{291} = 0$, $b_{303} = 0.27$, $b_{313} = 0.25$.

Table 7.3 Temperature Correction Factor C_T for Rain Attenuation

Rainfall Rate (mm/h)	*Wavelength* (m)	*Temperature* (K)				
		273	283	293	3003	313
2.5	0.0003	1.00	1.00	1.00	1.00	1.00
	0.001	1.00	1.00	1.00	1.00	1.01
	0.005	1.01	1.01	1.00	0.99	0.98
	0.0125	0.95	0.96	1.00	1.05	1.10
	0.032	1.28	1.14	1.00	0.86	0.72
	0.10	1.73	1.30	1.00	0.79	0.64
50.0	0.0003	1.00	1.00	1.00	1.00	1.00
	0.001	1.00	1.00	1.00	1.00	1.01
	0.005	1.02	1.01	1.00	0.98	0.97
	0.0125	0.99	0.99	1.00	1.02	1.04
	0.032	0.91	0.96	1.00	1.01	1.01
	0.10	1.75	1.31	1.00	0.78	0.62

The results of (7.27) are plotted in Figure 7.22 as functions of wavelength in m and frequency in GHz. The abrupt transition to unity at 0.015m wavelength is unrealistic, but for shorter wavelengths the actual correction is less than ±10% and does not require accurate modeling.

The effects of higher and lower temperatures are compared in Figure 7.23 for high and low rainfall rates. It can be seen that only the microwave and lower radar bands are affected significantly by changing temperatures, but that the coefficient can increase or decrease by a factor of two at L-band and by 1.6 for S-band. Uncertainties in the temperature profile over the extent of the rain region thus prevent accurate estimation of losses for X-band and lower frequencies, but the largest percentage errors occur where the attenuation is low, and the resulting errors in range calculation are moderate.

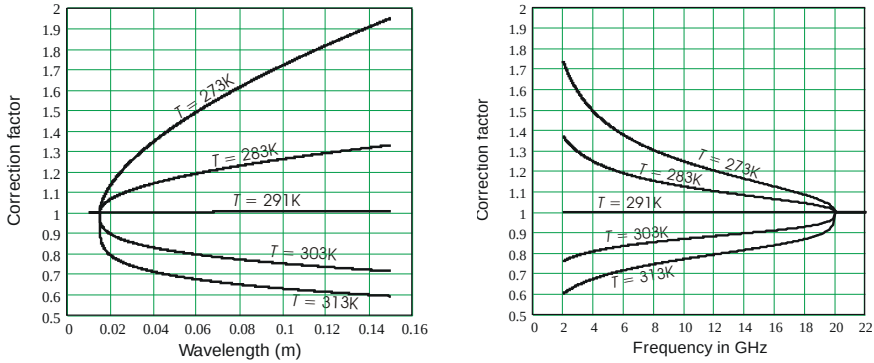

Figure 7.22 Temperature correction factors for rain attenuation as a function of wavelength and frequency.

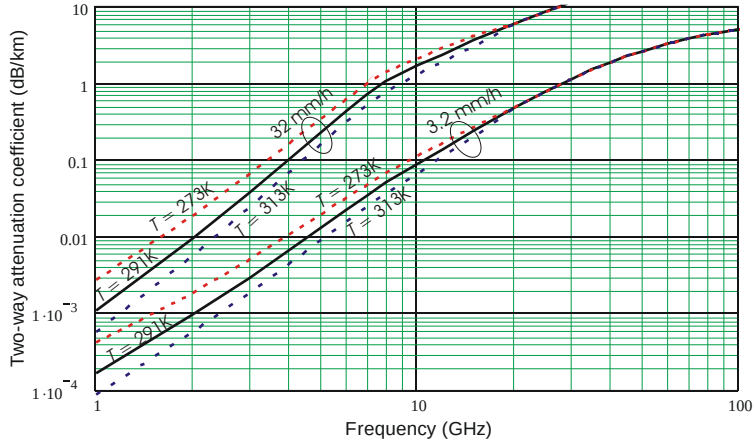

Figure 7.23 Comparison of rain attenuation coefficients at T = 273K, 291K, and 313K.

7.3.3 Rainfall Rate Statistics

The probability of encountering a given rain attenuation depends of the type of climate in which the radar is operated. Figure 7.24 shows the percentage of time and corresponding hours per year in which rainfall exceeds a given rate for four climates. Taking the continental temperate climate as an example, a "moderate" rate of 3 mm/h can be expected about 1% of the time, or 90 hours per year. The probability of rain considered "heavy," 16 mm/h, is about 0.2%, corresponding to 18 hours per year. The need to include these levels of attenuation in a range calcu-

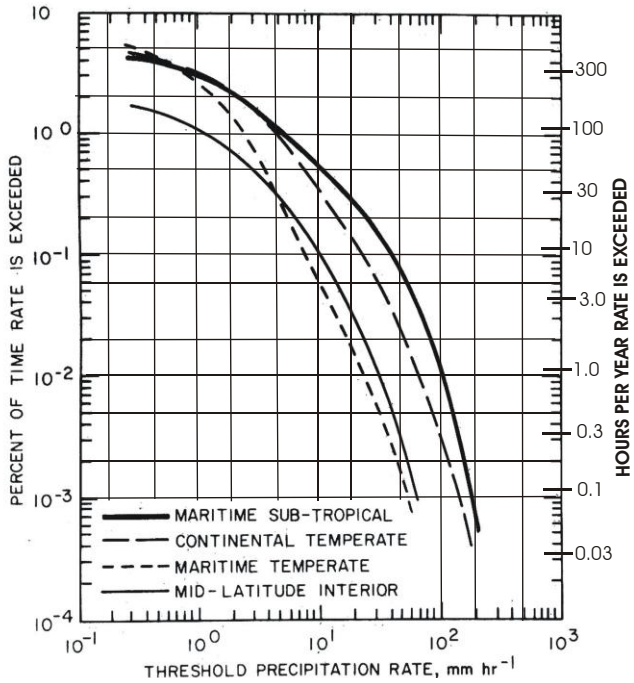

Figure 7.24 Occurrence of rainfall rates in four types of climate [after 18, p. 16-11, Figure 16-8].

lation depends on the required reliability of the radar service. For example, significant range reduction for 18 hours per year might be unacceptable for an airport surveillance radar at a heavily used location, but acceptable for other radars.

Much more detailed statistics on rain can be found in the book devoted to this subject by Crane [19], intended to describe rain attenuation problems on communications paths. Among the data he presents are the maximum altitudes of the rain cells corresponding to the rainfall rates observed with 0.001% and 1.0% probability. At latitudes between ±40° those altitudes are 4–5.5 km and 2.7–4.6 km, respectively. Nathanson [15, p. 223] presents a plot of altitude as a function of rainfall rate, showing maximum altitude up to ≈9 km. He suggests that a model using uniform rate up to 4-km altitude is adequate in many cases. On the other hand, there have been measurements of rain reflectivity corresponding to rates exceeding 250 mm/h in thunderheads, supported by updrafts at altitudes near 12 km, during times when the surface received no rain.

Nathanson notes that "design of air defense, air traffic control, or multimode airborne systems is quite different with anything near a 20-mm/h rainfall rate. It is also a question as to the enemy's ability to operate in such an environment. Mili-

tary and civil air surveillance radars usually specify widespread 1- to 4-mm/h rain and sometimes a storm of perhaps 16 mm/h over a diameter of 10 to 20 km. Heavier storms have smaller diameters." He suggests an approximate relationship that in metric units converts to

$$d = 41.7 - 23.7 \log r_r \tag{7.28}$$

where d = storm diameter in km and r_r = rainfall rate in mm/h.

Data on the areas occupied by rainstorms are sparse. The higher rainfall rates are more limited in horizontal extent, with areas near 5 km^2 for intense rain cells. Table 7.4 shows typical pathlengths and attenuations for large regions of light rain and small regions of intense rain. The pathlengths and attenuations apply to elevation angles such that the path remains below the maximum rain altitude as it passes within the rain volume. For comparison, the atmospheric attenuation of the air is shown in the last row of the table. It can be seen that the presence of light rain has a small effect at X-band over the extent of the rain volume compared to that of the air, while heavy rain more than triples the attenuation in that small distance. That comparison would change for other bands.

Rain clutter effects on detection range must be considered, of course, along with the attenuation discussed here (see Chapter 9).

Table 7.4 Pathlengths and Attenuations (X-band) of Typical Rainstorms

		Large Region of Light Rain	*Small Region of Heavy Rain*
Rain area	km^2	1,400	35
Maximum rain altitude	km	4	5
Pathlength in rain	km	42	7
Rainfall rate	mm/h	1.0	30
Rain attenuation coefficient	dB/km	0.02	1.6
Rain attenuation	dB	0.8	10.7
Air attenuation coefficient	dB/km	0.027	0.027
Air attenuation	dB	3.1	3.1

7.3.4 Attenuation in Snow

Water in frozen form has a much lower attenuation coefficient than rain. Blake presents an expression [1, p. 221, Eq. (5.53)] derived from Gunn and East [12, p. 536] that gives the two-way attenuation, using λ in m:

$$k_{\alpha s}\left(r_s\right) = 7.4\times10^{-11}\frac{r_s^{1.6}}{\lambda^4} + 4.4\times10^{-5}\frac{r_s}{\lambda}\ \text{(dB/km)} \tag{7.29}$$

where r_s in mm/h is the equivalent liquid water content and λ is in m.[6] Figure 7.25 shows results of (7.29) for snowfall rates r_r = 0.32, 1.0, and 3.2 mm/h, with a curves for rain at 1 mm/h for comparison. Rates in excess of 3.2 mm/h are rare, but the coefficient increases steeply for melting snow in the narrow layer below the level where the air temperature reaches 273K. Above that layer, a temperature corrected value to replace the constant 4.4×10^{-5} in (7.29) can be derived from data in [11]:

$$C_{Ts} = \left[4.4 - 1.7\left(273 - T\right)^{0.23}\right]\times10^{-5},\quad T < 273 \tag{7.30}$$

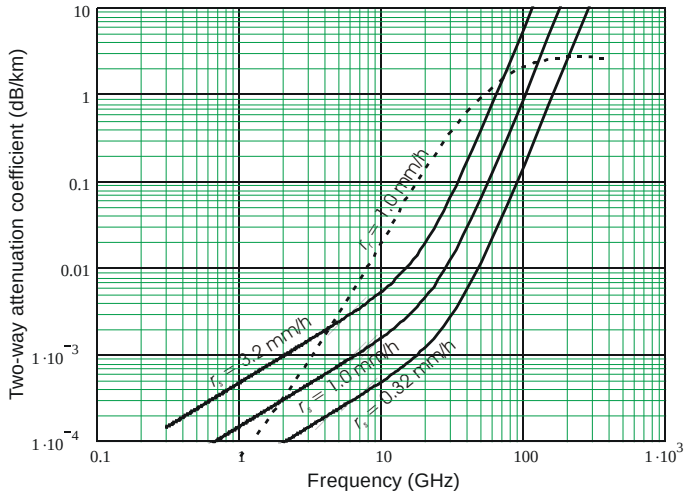

Figure 7.25 Attenuation coefficient for dry snow as a function of frequency, compared with light rain (dashed curve).

The result is

$$k_{\alpha s}\left(r_s\right) = 7.4\times10^{-11}\frac{r_s^{1.6}}{\lambda^4} + \times10^{-5}\left[4.4 - 1.7\left(273 - T\right)^{0.23}\right]\frac{r_s}{\lambda}\ \text{(dB/km)} \tag{7.31}$$

[6] Based on a personal communication from East, the factor multiplying $r_r^{1.6}$ has been increased here by 5.6%.

The effect of the temperature correction is to reduce the snow attenuation in the microwave band in regions where the temperature is significantly below 273K, as shown in Figure 7.25.

7.3.5 Attenuation in Clouds

Goldstein's derivation of cloud attenuation [11] remains definitive, confirmed by Gunn and East [12]. Both are based on work of Ryde [13, 14] and the classic Mie theory on scattering from spherical objects [20].

The attenuation of small, spherical water droplets is calculated from the complex dielectric constant ε_c of water, given as a function of wavelength by the Debye formula [21]:

$$\varepsilon_c = \frac{\varepsilon_0 - \varepsilon_\infty}{1 + \frac{j\Delta\lambda}{\lambda}} + \varepsilon \tag{7.32}$$

where ε_0, ε_∞, and $\Delta\lambda$ are functions of temperature, plotted in Figure 7.26. The two-way attenuation coefficient for a cloud is given as a function of the water density M in g/m^3 and ε_c:

$$k_{\alpha c} = 0.052\pi \frac{M}{\lambda} \mathrm{Im}(K) \tag{7.33}$$

where $K = (\varepsilon_c - 1)/(\varepsilon_c + 2)$ is the parameter used in [12]. Figure 7.27 shows the normalized attenuation coefficient $k_{\alpha c}/M$ as a function of frequency for temperatures T = 273, 293, and 313K.

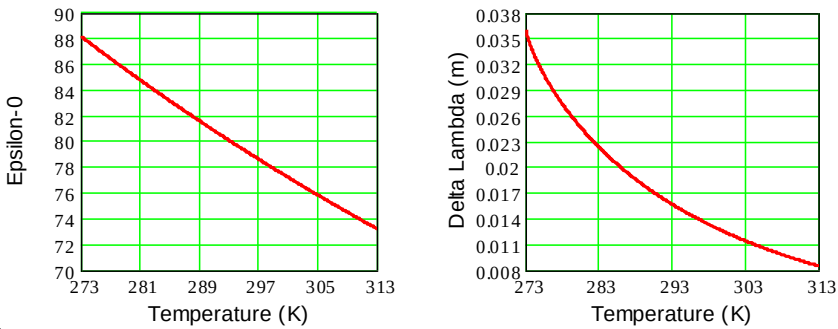

Figure 7.26 Temperature-dependent parameters ε_0 and $\Delta\lambda$ of Debye formula; ε_∞ = 5.5 for all T.

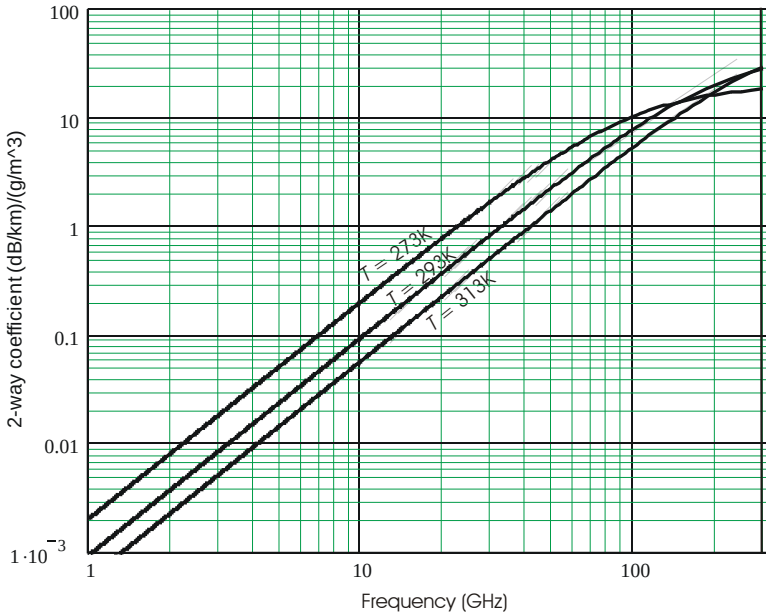

Figure 7.27 Cloud attenuation coefficient $k_{\alpha c}/M$ as a function of frequency for three temperatures.

An approximation for Im(–*K*), valid for $f < 60$ GHz, is

$$\mathrm{Im}(-K) = \frac{0.0011}{\lambda}\exp\left[-0.067(T-273)^{0.8}\right], \quad \lambda > 0.005\text{m} \tag{7.34}$$

which leads to

$$k_{\alpha c} = 1.64\times10^{-4}\frac{M}{\lambda^2}\exp\left[-0.067(T-273)^{0.8}\right], \quad \lambda > 0.005\text{m} \tag{7.35}$$

Comparing this with Goldstein's equation [11, p. 676, Eq. (41)], applicable to $T = 291$K, we find:

$$k_{\alpha c} = \frac{9.76\times10^{-5}M}{\lambda^2} \qquad \text{[2-way, } T = 291\text{K, from Goldstein]} \tag{7.36}$$

$$k_{\alpha c} = \frac{9.15\times10^{-5}M}{\lambda^2} \qquad \text{[2-way, } T = 291\text{K, from (7.35)]} \tag{7.37}$$

This represents a 5% difference in the decibel value of cloud attenuation, which lies within the accuracy of temperature and water-content models for clouds.

7.3.6 Weather Effects on System Noise Temperature

The sky temperature calculation of Section 6.3.2 considered only the attenuation in a clear atmosphere. Any increase in attenuation from precipitation or clouds carries with it an increase in system noise temperature. The total noise temperature is found by adding the one-way weather attenuation coefficient $k_{w1}(f_0, h)$ from (7.24), (7.29), or (7.35) to that of the troposphere in the integral of (6.21):

$$T_\alpha(f_0,\theta) = 0.2303\int_0^\infty \left\{k_{\alpha 1}\left[f_0, h(r,\theta)\right] + k_{w1}\left[f_0, h(r,\theta)\right]\right\} T_{tr}\left[f_0, h(r,\theta)\right] \times$$
$$\times \exp\left(-0.2303\int_0^r \left\{k_{\alpha 1}\left[f_0, h(r',\theta)\right] + k_{w1}\left[f_0, h(r',\theta)\right]\right\} dr'\right) dr \tag{7.38}$$

In many cases a constant physical temperature T_{pw} applies to the weather, and the noise temperature component is expressed approximately by adding to the tropospheric temperature a weather component given by

$$T_w \approx T_{pw}\left(1 - \frac{1}{L_w}\right) = T_{pw}\left[1 - \exp\left(-0.2303 k_{w1}\Delta_w\right)\right] \tag{7.39}$$

where

$L_w = \exp(0.2303 k_{w1}\Delta_w)$ = loss (as a ratio) due to the weather;
Δ_w = radial depth of the weather region in km.

For example, a loss $k_{w1}\Delta_w$ = 1 dB in particles at T_w = 290K contributes ≈ 60K to the noise temperature. Clear-air attenuation from shorter ranges reduces T_w, while the weather attenuation from ranges beyond the weather reduces the clear-air temperature contribution, according to the second integral in (7.38).

7.4 TROPOSPHERIC LENS LOSS

Rays leaving the radar antenna are refracted downward in the troposphere, as shown in Figure 7.28. A ray leaving the surface at elevation angle θ_0 arrives at the target point (R, h_t) for which the true elevation angle is θ_t. The time delay over this path exceeds that of a vacuum path by $\delta_t = (R_d - R)/c$, where R_d is given by the

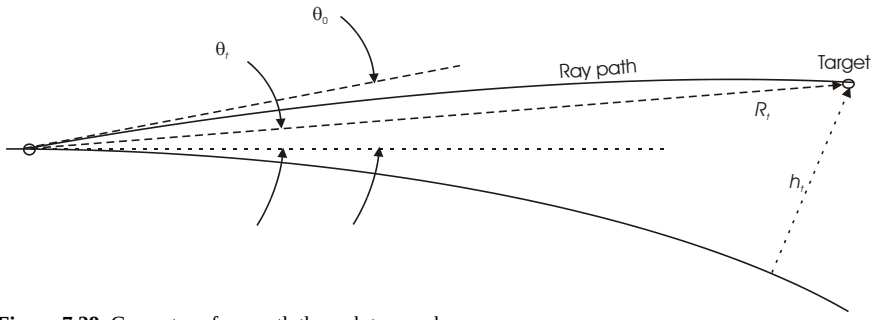

Figure 7.28 Geometry of ray path through troposphere.

ray-tracing formula (7.8). The bending of the ray path is greatest for $\theta_0 = 0$ and decreases monotonically as θ_0 increases. The result is that energy radiated from the surface within an angular extending from θ_0 to $\theta_0 + \Delta_0$ is distributed over a slightly greater angular sector θ_t to $\theta_t + \Delta_t$ at the target, reducing the energy density relative to that that predicted for propagation in a vacuum. This effect is described by Weil [22], who presents plots of the two-way loss as a function of target elevation angle and range.

The loss can be computed in different ways, but a straightforward method is to express the one-way lens loss as the derivative of the ray's final elevation angle θ_t with respect to its value θ_0 as it leaves the antenna:

$$L_{\text{lens1}}(\theta_0) = \lim \left[\frac{\Delta\theta_t(R,h)}{\Delta\theta_0(R,h)} \right]_{\Delta\theta_0 \to 0} \tag{7.40}$$

where θ_0 is the launching angle from the antenna, $\Delta\theta_0$ is a small increment in that angle, and $\Delta\theta_t$ is the corresponding increment in the true elevation of the ray arrival angle at the target range. Since (7.8) cannot be inverted to evaluate the derivative represented by (7.40), θ_t is obtained using a root-finding algorithm, allowing its derivative to be approximated over a small angular difference $\Delta\theta_0$ in the launch angle of the ray from the surface. The results are in Figure 7.29 as the two-way lens loss L_{lens2} in decibels. The corresponding lens factor used in (1.25) is

$$F_{\text{lens}} = \frac{1}{\sqrt{L_{\text{lens1}}}} \tag{7.41}$$

These results are in close agreement with the data presented in [22] and [1, p. 192, Figure 5.7]. The latter, however, extends in range only to 750 km and losses for

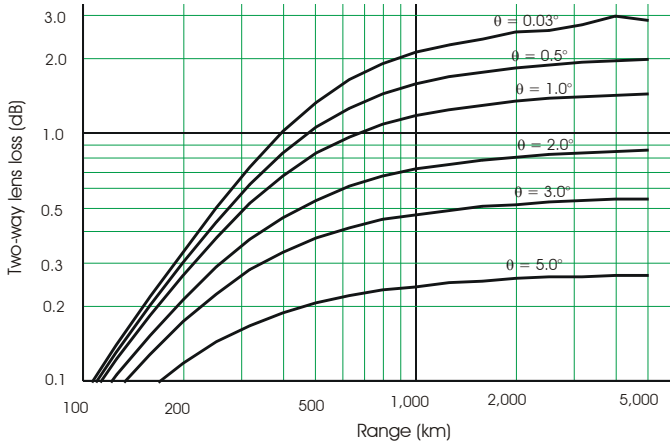

Figure 7.29 Two-way tropospheric lens loss as a function of range for different beam elevations.

angles near zero fail to show the continuing increase that reaches its maximum for $R > 2{,}000$ km.

The curve for the minimum plotted beam elevation 0.03° in Figure 7.28 departs at long ranges from a smooth curve because of difficulty in the algorithm for finding the derivative in (7.40) from ray-tracing expression (7.8) at $\theta < 0.1°$. However, variations normally encountered in the refractive index profile lead to variations in lens loss in this region that mask these computational errors.

The conclusion in [1] that reciprocity is applicable to the lens loss on the return path of the echo is correct, because the refractive process is linear and is equivalent to an increase in the antenna beamwidth, with corresponding loss as the rays pass through and beyond the troposphere and return to the radar along the same path.

Lens loss does not result from dissipation of energy in the troposphere, and in contrast to other atmospheric losses it does not contribute to the system noise temperature. For this reason, it is included in the radar equation as a range-dependent response factor F_{lens} to keep it separate from the tropospheric absorption L_α.

7.5 IONOSPHERIC EFFECTS

The ionosphere affects radar range performance in two ways: it introduces Faraday rotation of the wave polarization, causing the received polarization to differ from that transmitted, and it causes dispersion of different components of the signal spectrum, broadening the pulse and reducing its amplitude. Both these effects

are variable, depending on the path through the layers of the ionosphere and the electron density of these layers. Faraday rotation also depends on the strength and direction of the magnetic field with respect to the direction of the ray.

7.5.1 Geometry of Ray in Ionosphere

The geometry of the ray path through an ionospheric layer is shown in Figure 7.30. The ray leaves the Earth's surface at elevation angle θ, enters the layer at altitude h_1 and exits at h_2. The maximum electron density of the layer occurs at altitude h_m, where the ray elevation angle relative to the local horizontal is θ′. The pathlength through the layer is ΔR, given by

$$\Delta R = \left(h_2 - h_1\right)\sec\theta' \tag{7.42}$$

The Earth's magnetic field H is directed at some angle relative to the local horizontal, differing by Δθ from the ray direction.

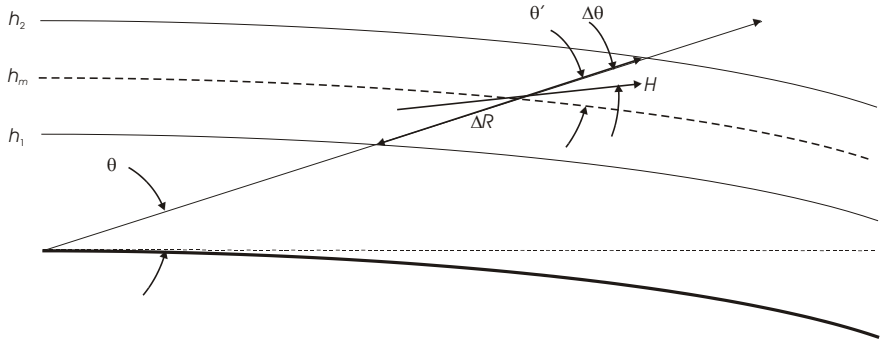

Figure 7.30 Geometry of ray path through an ionospheric layer.

7.5.2 Ionospheric Structure

The daytime ionosphere consists of three layers, known as the E, F_1, and F_2 layers (a lower, weak D layer is of no importance in radar operation). At night, the E layer disappears and the F_1 and F_2 layers merge into a single F layer. The electron density N_e of the ionosphere was described in 1927 by Sydney Chapman, and his equations have been used by Millman [23] to derive the effects on radar transmissions:

$$N_e = N_m \exp\left[\frac{1}{2}\left[\left(1 - Z - \exp Z\right)\right]\right] \tag{7.43}$$

where

N_m = maximum electron density in electrons/m^3;
Z = $(h - h_m)/h_0$ = normalized altitude;
h = altitude in m;
h_m = altitude of maximum density in m;
h_0 = scale altitude in m.

Values of N_m, h_m, and h_0 for typical day and night conditions are shown in Table 7.5, and the total density is shown in Figure 7.31 as a function of altitude.[7]

Table 7.5 Chapman Parameters of Ionospheric Layers

Layer	N_m (m^{-3})	h_m (km)	h_0 (km)
Daytime E	1.5×10^{11}	100	10
Daytime F_1	3.0×10^{11}	200	40
Daytime F_2	1.25×10^{12}	300	50
Nighttime E	8×10^{9}	120	10
Nighttime F	4×10^{11}	300	45

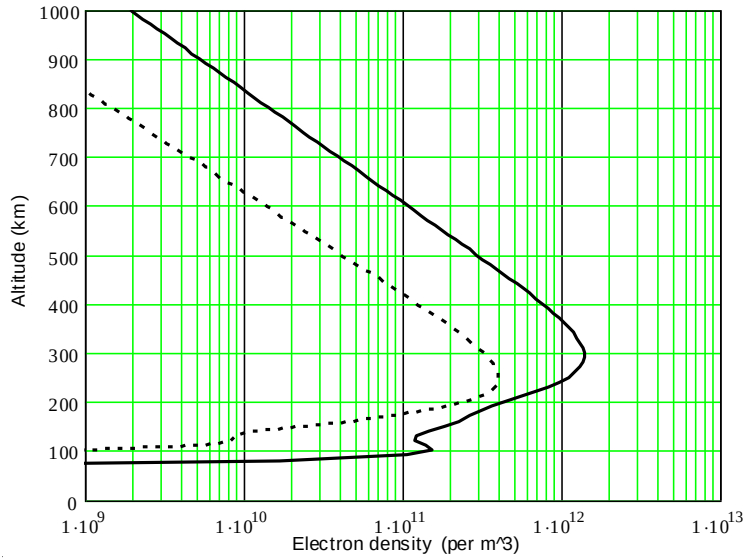

Figure 7.31 Typical ionospheric electron densities N_e: daytime (solid line), nighttime (dashed line).

[7] Much of the literature expresses electron densities per cm^3 and altitude in cm; to avoid conversion errors in computation of many ionospheric effects, densities per m^3 and altitudes in m are used here.

The electron densities vary upwards and downwards by factors up to about two, depending on solar condition and latitude, but the values shown in Figure 7.30 can be used to calculate typical effects on radar signals.

7.5.3 Total Electron Count

The effects of the ionosphere on the radar signal are proportional to the total electron count N_t in a column having a cross section of one cm^2 extending from the radar to the target:

$$N_t = \int_0^\infty F(h,\theta) N_e dh \text{ (electrons/m}^2\text{)} \tag{7.44}$$

where

$$F(h,\theta) = \frac{a_e + h}{\sqrt{(a_e + h)^2 - (a_e \cos\theta)^2}} \tag{7.45}$$

where a_e is the radius of the Earth in m. The function F is the cosecant of the local elevation angle of the beam at altitude h. It describes the ratio of the pathlength through each altitude element dh at local ray elevation θ' to the thickness of that element, allows integration with respect to altitude rather than range. Integration of (7.44) to an altitude of 10^6 m is sufficient to capture the effect of the ionosphere, since the electron density above that altitude is low enough to be neglected.

The total electron count is shown as a function of target altitude in Figure 7.32 for typical daytime and nighttime conditions. Signals from targets below 100 km will experience negligible ionospheric effects, as will be shown when Faraday rotation and dispersion effects are calculated in the following sections.

7.5.4 Faraday Rotation

Millman gives the equation for Faraday rotation $\phi(h)$ experienced on a two-way path between the radar and a target [24, p. 362, Eq. (1-138)]:

$$\phi(h) = \frac{e^3}{\pi m^2 c^2 f^2} \int_{h_1}^{h_2} F(h) H(h) \cos\theta N_e(h) dh \quad \text{(rad)} \tag{7.46}$$

where

e = 4.8×10^{-10} = electron charge in esu;

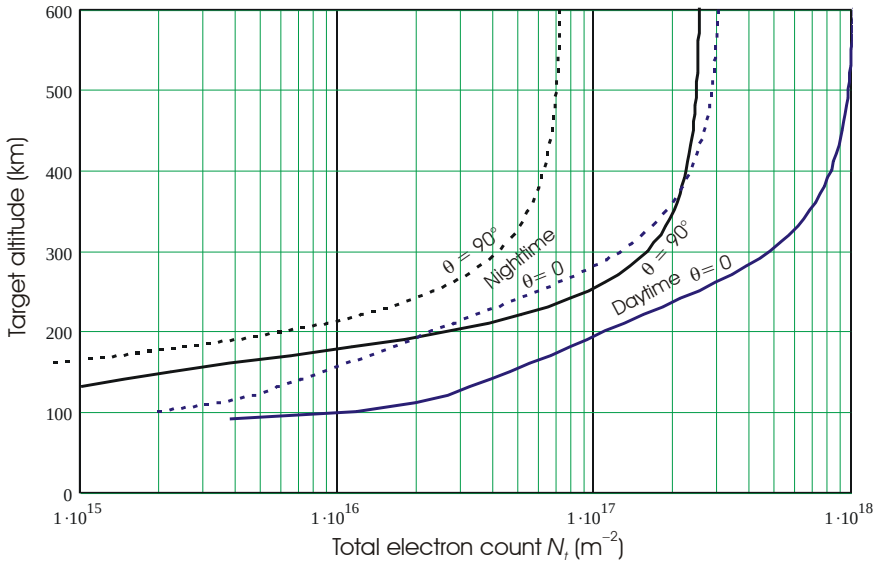

Figure 7.32 Typical total electron counts for daytime and nighttime ionosphere at elevation angles 0° and 90°.

m	=	9.1×10^{-28} = electron mass in g;
c	=	3×10^{10} = velocity of light in cm/s;
f	=	frequency in Hz;
$F(h)$	=	factor defined by (7.45);
H	=	Earth's magnetic field in gauss;
θ	=	angle between the ray and the magnetic field;
$N_e(h)$	=	electron density per cm^3;
h_1, h_2	=	altitude limits in cm of significant electron density;
h	=	altitude in cm.

The magnetic field varies with altitude as

$$H(h) = H_0 \left(\frac{a_e}{a_e + h} \right)^3 \tag{7.47}$$

where $H_0 \approx 0.65$ gauss is the sea-level value at latitudes of greatest interest. The constant in (7.46) becomes 4.73 when h is expressed in m, c in m/s, and N_e in electrons per m^3. Although the angle θ varies with the direction in which the radar view the target, the maximum Faraday rotation angle can be found for $\theta = 0$, for which (7.46) can be written as

$$\phi_{\max}(h) = \frac{4.73}{f^2}\int_0^{\infty} F(h)H(h)\,N_e(h)\,dh$$
$$\approx \frac{2.7}{f^2}N_t(h) \quad \text{(rad)} \tag{7.48}$$

The Faraday rotation angles $\phi_{max}(h)$ for f = 100 MHz under typical daytime and nighttime conditions at 0° and 90° elevation are shown as a function of target altitude in Figure 7.33. For altitudes above 600 km the Faraday rotation is shown in Figure 7.34 as a function of frequency. The average loss as polarization varies from zero to the maximum for a radar using linear polarization is given by

$$L_{\text{Far}} = \frac{1}{\phi_{\max}}\int_0^{\phi_{\max}} \cos^2\phi\, d\phi \tag{7.49}$$

and this loss is shown in Figure 7.35 as a function of frequency for a target at h = 300 km. The loss is 3 dB when averaged over more than 20 rotations, and oscillates as that number decreases, peaking near 4 dB when averaged between 0°

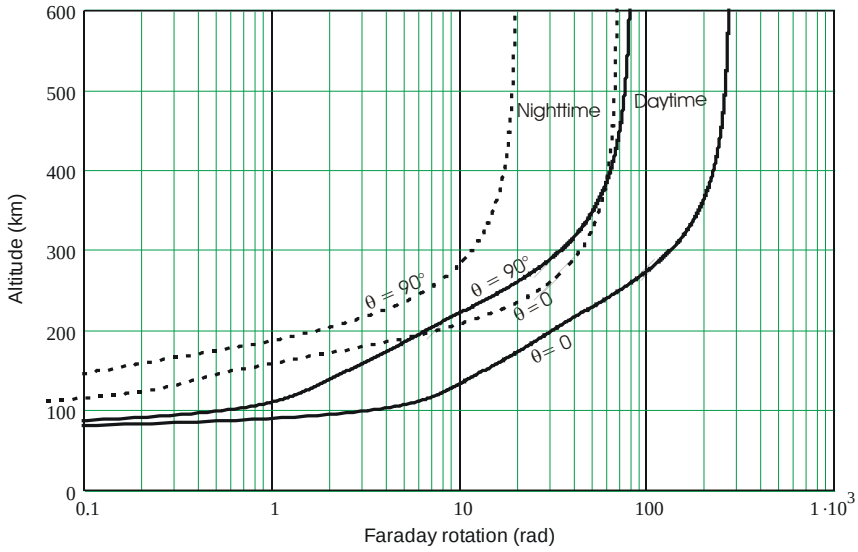

Figure 7.33 Typical Faraday rotation angles for daytime (solid lines) and nighttime (dashed lines) at 0° and 90° elevation angles, as a function of altitude, for f = 100 MHz.

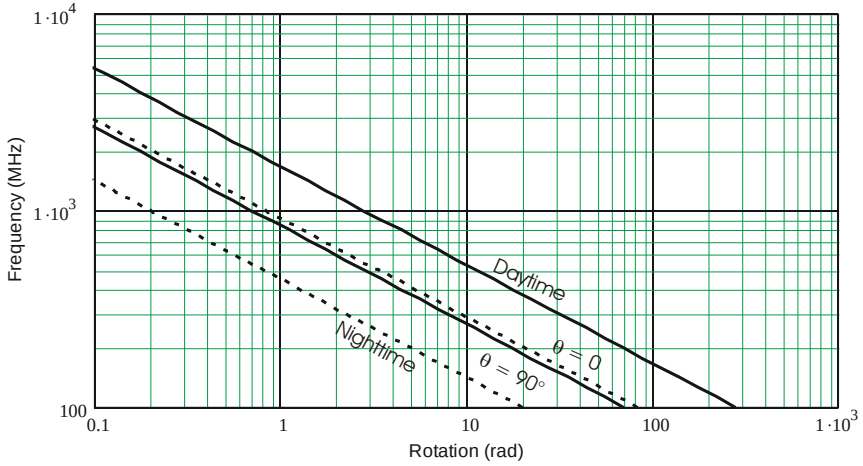

Figure 7.34 Typical Faraday rotation angles for daytime (solid lines) and nighttime (dashed lines) ionosphere at 0° and 90° elevation angles, as a function of frequency, for $h \geq 600$ km.

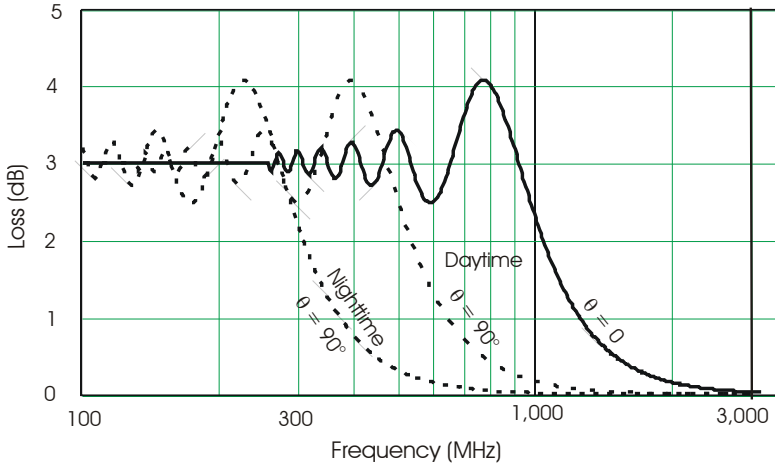

Figure 7.35 Faraday rotation loss as a function of frequency.

and 130° of rotation. As the maximum rotation is further reduced, the loss is reduced, approaching 0 dB for maximum rotation less than 20°.

For the daytime ionosphere at zero elevation, Figure 7.34 indicates that the rotation angle is less than 20° for $f \geq 3$GHz. It is necessary at L-band (1.3 GHz) and below to allow for Faraday rotation in applying the radar equation to targets above about 250-km altitude. The loss may be eliminated by using circular polari-

zation, where rotation merely changes the phase of the received signal. If linear polarization is used for transmission, a dual-polarized receiving antenna may be used, the two linear polarizations being combined either adaptively, to follow the rotated signal polarization, or by noncoherently summing outputs of a two-channel receiver, incurring a small integration loss.

Because the Faraday rotation angle cannot be predicted accurately its effect on detection probability must be treated as a statistical quantity and the corresponding loss (Figure 10.5) evaluated as a function of P_d, as discussed in Section 10.2.1.

7.5.5 Dispersion Across Signal Spectrum

7.5.5.1 Refractivity in the Ionosphere

A second source of ionospheric loss in the radar equation results from dispersion across the signal spectrum, causing distortion of the received pulse. The refractivity N_i of the ionosphere is a function of the electron density:

$$N_i\left(f_0,h\right)=\left(n_i-1\right)\times10^6=\left(\sqrt{1-\frac{N_e\left(h\right)e^2}{\pi m f_0^{\,2}}}-1\right)\times10^6$$
$$\approx -40.3\times10^6\,\frac{N_e\left(h\right)}{f_0^{\,2}}\quad\text{(ppm), assuming } N_i<<10^6 \tag{7.50}$$

where

f_0 = carrier frequency in Hz;
$N_e(h)$ = electron density per m^3;
h = altitude.

7.5.5.2 Time Delay through the Ionosphere

The time delay of the echo signal from a target exceeds the value for empty space above the troposphere by Δ_t, which varies with frequency, for given total electron count N_t:

$$\Delta_t=\frac{-2\times10^{-6}}{c}\int_0^h F\left(h',\theta\right)N_i\left(f_0,h'\right)dh'\ \text{(s)}$$
$$=80.6\,\frac{N_t}{cf_0^{\,2}}\ \text{(s)}=0.2688\,\frac{N_t}{f_0^{\,2}}\ \ (\mu\text{s}) \tag{7.51}$$

where

N_t = total electron count per m^2 given by (7.44);
c = velocity of light in m/s.

The delay is positive because the group velocity in the ionosphere is $v_g = n_i c$. The delay in microseconds is shown in Figure 5.36 as a function of the ratio N_t/f_0^2 where f is in Hz.

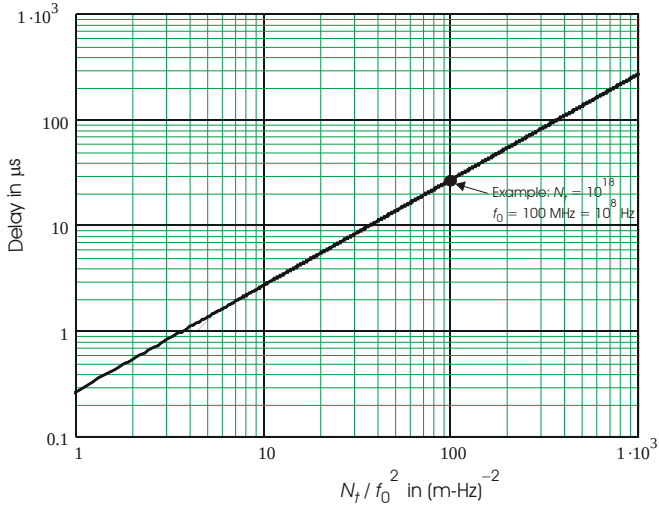

Figure 7.36 Ionospheric time delay in μs as a function of the ratio N_t/f_0^2, for N_t in m^{-2}, f_0 in Hz.

For example, a signal at carrier frequency f_0 = 100 MHz, echoed from a target beyond the typical daytime ionosphere at zero elevation with $N_t = 10^{18}/m^2$, returns to the radar with 28 μs extra delay, corresponding to a range 4.2 km beyond the actual target.

The extra range is not significant in using the radar equation, but in the process of passing through the ionosphere the different frequencies in the pulse spectrum experience a differential delay. Letting f_0 be the carrier frequency, and f the offset from that frequency of a spectral component of the waveform, we can express the differential delay δ_t as:

$$\delta_t(f_0, f) = \left[\left(\frac{f_0}{f_0 + f}\right)^2 - 1\right]\Delta_t \approx \frac{-2f}{f_0}\left(1 - \frac{3}{2}\frac{f}{f_0}\right)\Delta_t$$
$$= -5.377\times10^{-7} N_t \frac{f}{f_0^3}\left(1 - \frac{3}{2}\frac{f}{f_0}\right) \tag{7.52}$$

where

δ_t = differential time delay in s;
f = frequency offset in Hz from carrier frequency f_0.

The first-order term for differential delay is thus proportional to the delay Δ_t of the carrier-frequency f_0 multiplied by the frequency deviation as a fraction of the carrier. In the previous example of the pulse at f_0 = 100 MHz, the delay at the carrier frequency was Δ_t = 28 μs. For a waveform with spectral width B = 1 MHz, in this ionosphere, the extreme spectral components separated by ±0.5 MHz from the carrier would have delays differing by $\delta_t = \mp 0.01\Delta_t = \mp 0.28$ μs from that of the central component of the spectrum. At f_0 = 100 MHz, this corresponds to shifts of ∓28 cycles = ∓176 rad in phase across the signal spectrum.

7.5.5.3 Effect of Ionosphere on Received Pulse

The result of spectral dispersion is a differential phase shift δ_ϕ across the echo signal spectrum, given for f and f_0 in Hz by

$$\delta_\phi(f, f_0) = 2\pi(f_0 + f)\delta_t(f, f_0) = -2\pi(f_0 + f)\frac{2f}{f_0}\left(1 - \frac{3}{2}\frac{f}{f_0}\right)\Delta_t \tag{7.53}$$

The signal spectrum is normally described by a function $A(f)$, where f denotes frequency relative to the carrier at f_0. The received signal spectrum is then

$$A_r(f) = A(f)\exp\left[j\left[\phi_0 + \delta_\phi(f, f_0)\right]\right]$$
$$= A(f)\exp\left\{-j2\pi(f_0 + f)\left[1 - \frac{2f}{f_0}\left(1 - \frac{3}{2}\frac{f}{f_0}\right)\right]\Delta_t\right\} \tag{7.54}$$
$$= A(f)\exp\left\{-j2\pi\frac{(f_0 + f)}{f_0^2}\left[1 - \frac{2f}{f_0}\left(1 - \frac{3}{2}\frac{f}{f_0}\right)\right]\times 2.688\times10^{-7} N_t\right\}$$

where $\phi_0 = -2\pi(f_0 + f)\Delta_t$ is the phase delay of the carrier. The unit term in square brackets corresponds to the phase of the carrier, the second to the dispersive effect across the signal bandwidth.

Assuming a filter response $H(f)$, we can write the expression for the output waveform on a target with free-space delay t_d as

$$\chi(t_d) = \int_{-\infty}^{\infty} A_r(f) H(f) \exp(-j2\pi f t_d) df \tag{7.55}$$

In the absence of the ionosphere $\chi(t_d)$ would be the output waveform of the matched filter.

The effects of dispersion on the received waveform are shown in Figure 7.37, as calculated for carrier frequencies that give the indicated products of differential delay and bandwidth over a path with total electron count 3×10^{17} per m^2. In Figure 7.38 the excess carrier time delay Δ_t has been removed to align the waveforms, to compare the effects on pulse shape and amplitude. The transmitted pulse assumed for these plots is rectangular with width $\tau = 0.1$ μs, such that the noise bandwidth of the transmission and the matched-filter is $B_n = 10$ MHz. As the carrier frequency is reduced toward 145 MHz from 10 GHz, where the ionospheric delay is negligible ($\Delta_t = 0$), the delay increases to 4 μs, the differential delay time increases to $\delta_t = 0.5$ μs $= 5/B$, the pulse broadens to ≈ 0.5 μs, and its amplitude decreases to less than half its original voltage.

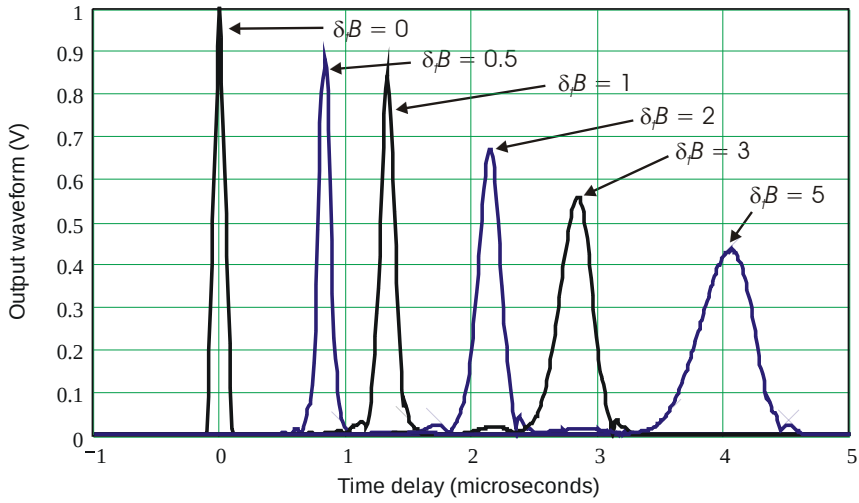

Figure 7.37 Waveforms of rectangular 0.1 μs pulse passed through ionosphere and a filter matched to the transmitted waveform ($B_n\tau = 1$).

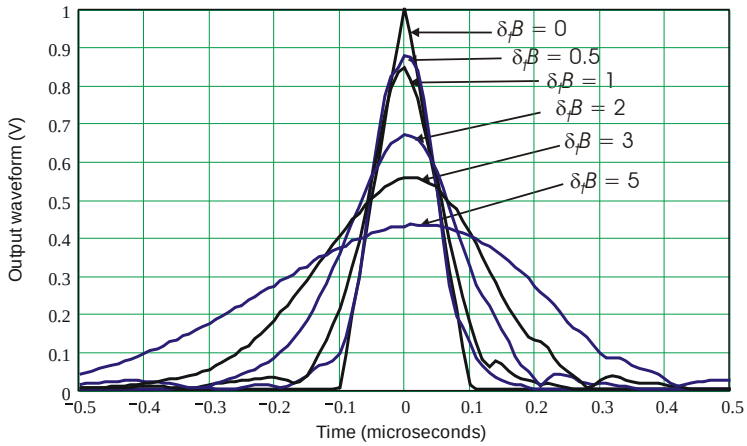

Figure 7.38 Detail of waveforms from Figure 7.37 with time delay removed.

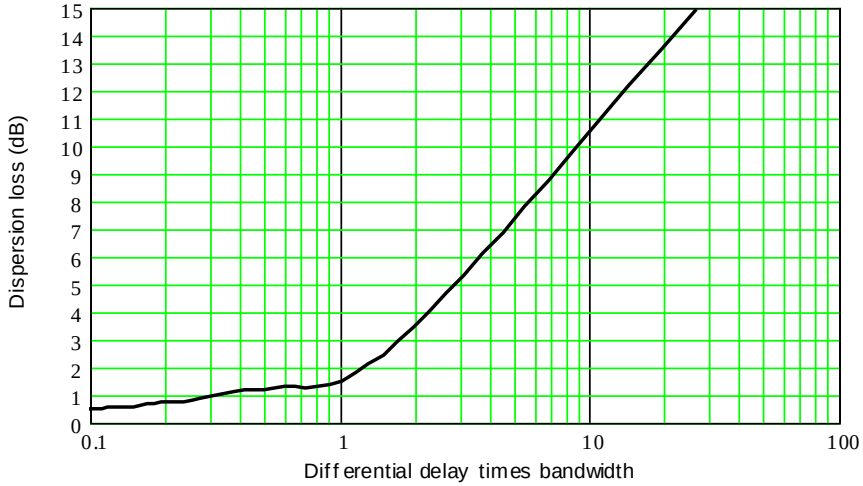

Figure 7.39 Ionospheric dispersion loss as a function of $\delta_t B_n$.

Since the filter response cannot be adjusted to compensate for phase shift over the signal bandwidth, there is a loss in signal amplitude, shown in Figure 7.39. This loss is discussed by Brookner [25], who illustrates the broadening and loss on Gaussian pulses. His curves show, for example, that the "available bandwidth" for propagation at low elevation angle through a severe daytime ionosphere is limited to about 1 MHz at f_0 = 100 MHz, consistent with the curve for $\delta_t B_n$ = 0.5 in Figure 7.37 and the loss of 1.3 dB shown in Figure 7.38.

For pulse compression and other waveforms, the appropriate transmitted spectrum $A(f)$ of the transmitted signal and its matched filter $H(f)$ may be entered into (7.55) to obtain the waveform of the received echo. The loss, when expressed as a function of the product $\delta_t B_n$ should follow a curve close to that of Figure 7.37.

7.6 SUMMARY OF ATMOSPHERIC EFFECTS

Tropospheric refraction is the cause of errors in measurement of target position, but the radar equation is not affected by those problems. It is affected, however, by the fact that the ray paths through the troposphere lie above the direct geometric line to the target, which reduces the density, and hence the attenuation, along the path. Hence, calculations of attenuation must be carried out with the appropriate ray-tracing model for the troposphere.

The attenuation coefficients of atmospheric gases can be found from theory developed during World War II by J. H. Van Vleck, and extended subsequently to cover the millimeter-wave region. Blake [1] gave the necessary equations and plotted the results. The same results are plotted here as a function of range in kilometers. An alternative to his procedure for adjusting to moisture content is presented that holds accuracies within the limits set by uncertainties in atmospheric models.

Precipitation and clouds add to attenuation of the clear air, and the model used by Blake is extended here to include temperature effects. The normal variations in temperature can change the attenuation coefficient of rain, expressed in dB/km, over the 3:1 range represented by factors between 1.8 and 0.6 relative to the values at 291K that are often cited. The literature on this effect is far from unified, but an approximate model is developed here to estimate this correction.

To describe radar performance when weather is present, the effect of its attenuation on the sky temperature is expressed here by an addition to the integral presented in Chapter 6 that gives the conventional clear-air sky temperature. This correction becomes increasingly important as receiver noise temperatures are reduced to near or below the temperature of the clear sky.

The effect of the ionosphere on the radar equation is important for radars operating below S-band on targets in or beyond the F layer. Faraday rotation of the echo signal polarization causes a loss when other than circular polarization is used. There is also a dispersion limit on signal bandwidth that can be supported by transmission paths through the ionosphere, and the echo signal power is reduced steeply as the bandwidth exceeds the reciprocal of the differential delay across the spectrum.

Ionospheric effects are especially important in VHF and UHF radars when they are used for detection and tracking of ballistic missiles, but must be considered in those applications even for L-band radars.

References

[1] Blake, L. V., *Radar Range-Performance Analysis*, Lexington, MA: D. C. Heath, 1980; Dedham, MA: Artech House, 1986.

[2] IEEE Standard 100, *The Authoritative Dictionary of IEEE Standards Terms*, 7th ed., New York: IEEE Press, 2000.

[3] Bean, B. R., and Dutton, E. J., *Radio Meteorology*, National Bureau of Standards Monograph 92, March 1, 1966, Washington, DC: U. S. Gov't. Printing Office.

[4] Air Force Geophysics Laboratory, *Handbook of Geophysics*, 1985, Document No. ADA 167,000, Springfield, VA: National Technical Information Service.

[5] U.S. Standard Atmosphere, 1976, U.S. Government Printing Office, Washington, D.C., 1976.

[6] Bean, B. R., and G. D Thayer, "Models of the Atmospheric Radio Refractive Index," *Proc. IEEE*, Vol. 47, No. 5, May 1959, pp. 740–775.

[7] Van Vleck, J. H., "Atmospheric Attenuation," Chapter 8, Sections 8.1–8.3 in *Propagation of Short Radio Waves*, (D. E. Kerr, ed.), Vol. 13 in MIT Radiation Laboratory Series, New York: McGraw-Hill, 1951. Reprinted, (CR ROM edition), Norwood, MA: Artech House, 1999.

[8] Meeks, M. L., and A. E. Lilley, "The Microwave Spectrum of Oxygen in the Earth's Atmosphere," *J. Geophys. Res.*, Vol. 68, No. 6, March 15, 1963, pp. 1603–1703.

[9] Brussaard, G., and P. A. Watson, *Atmospheric Modelling and Millimetre Wave Propagation*, London: Chapman and Hall, 1995

[10] Kirby, R. C., and K. A. Hughes, "Propagation Over the Earth Through the Nonionized Atmosphere," Section 22.11 in *Electronics Engineers' Handbook*, 4th ed., (D. Christiansen, ed. in chief), McGraw-Hill, 1997.

[11] Goldstein, H., "Attenuation by Condensed Water," Sections 8.6–8.9 in *Propagation of Short Radio Waves*, (D. E. Kerr, ed.), Vol. 13 in MIT Radiation Laboratory Series, New York: McGraw-Hill, 1951. Reprinted, (CR ROM edition) , Norwood, MA: Artech House, 1999.

[12] Gunn, K. L. S., and T. W. R. East, "The Microwave Properties of Precipitation Particles," *Quart. J. Royal Meteorol. Soc*., Vol. 80, October 1954, pp. 522–545.

[13] Ryde, J. W., and D. Ryde, "Attenuation of Centimetre and Millimetre Waves by Rain, Hail, Fogs and Clouds," *GEC Report No. 8670*, May 1945.

[14] Ryde, J. W., 1946: "The Attenuation and Radar Echoes Produced at Centimetric Wavelengths by Various Meteorological Phenomena," *Meteorological Factors in Radio Wave Propagation*, , London: Physical Society, pp. 169–188.

[15] Nathanson, F. E., J. P. Reilly, and M. N. Cohen, *Radar Design Principles, Signal Processing and the Environment*, (2nd ed.), New York: McGraw Hill, 1991.

[16] Medhurst, R. G., "Rainfall Attenuation of Centimeter Waves: Comparison of Theory and Measurement," *IEEE Trams. on Antennas and Propagation*, Vol. AP-13, No. 4, July 1965, pp. 550–564.

[17] Burrows, C. R., and S. S. Atwood, *Radio Wave Propagation*, New York: Academic Press, 1949.

[18] Jursa, A. S. (ed.), *Handbook of Geophysics and the Space Environment*, Air Force Geophysics Laboratory, 1985.

[19] Crane, R. K., *Electromagnetic Wave Propagation Through Rain*, New York: John Wiley, 1996.

[20] Mie, G., "Contributions to the Optics of Suspended Media, Specifically Colloidal Metal Suspensions," (in German), *Ann. Phys*., 1908, pp. 377–445.

[21] Debye, P., *Polar Molecules*, New York: Chemical Catalog Co., 1929.

[22] Weil, T. A., Atmospheric Lens Effect: Another Loss for the Radar Range Equation," *IEEE Transactions on Aerospace and Electronic Systems*, Vol. AES-9, No. 1, January 1973, pp. 51–54.

[23] Millman, G. H., "Atmospheric Effects on VHF and UHF Propagation," *Proc. IRE*, Vol. 46, No. 8, August 1958, pp. 1491–1501.

[24] Millman, G. H., "Atmospheric Effects on Radio Wave Propagation," Part V, Chapter 1, in *Modern Radar*, (R. S. Berkowitz, ed.), New York: John Wiley, 1965.

[25] Brookner, E., "Ionospheric Dispersion of Electromagnetic Pulses," *IEEE Trans. on Antennas and Propagation*, Vol. AP-21, No. 5, May 1973, pp. 402–405.

CHAPTER 8

The Pattern-Propagation Factor

Chapter 1 derived the radar equation for free-space detection range, and noted the importance of including the pattern-propagation factors F_t and F_r that describe the effects of the transmitting and receiving antenna patterns in elevation and interaction with the Earth's surface. This chapter considers those factors in detail, including both reflections from the surface and diffraction on paths that graze the surface. For brevity, we will use the term *F*-factor.

The original radar equation [1, Eq. (31)] included the *F*-factor, which had been developed during World War II and defined in [2, p. 35] as

> the ratio of the amplitude of the electric field at a given point under specified conditions to the amplitude of the electric field under free-space conditions with the beam of the transmitter directed toward the point in question.

Radar equations for modern radar must include this factor unless the radar beam is elevated well above the surface and has negligible sidelobes that illuminate the surface. There are four regions in which the *F*-factor varies differently with range:

- Near region, where a clear path exists and $F \approx 1$;
- Interference region, where surface reflections interfere with the direct ray;
- Intermediate region, where both interference and diffraction are applicable;
- Diffraction region, where diffraction is dominant.

Blake [3, Chapter 6] described *multipath* (surface-reflection) effects on propagation, and extended the discussion to a simple model of smooth-sphere diffraction. We will follow Blake's methods, which present several levels of complexity and accuracy of modeling the *F*-factor, discuss the errors that result from simplifications and imperfect knowledge of the several parameters involved, and extend the discussion to knife-edge diffraction, which may modify the results obtained from the smooth-sphere model.

8.1 *F*-FACTOR IN THE INTERFERENCE REGION

8.1.1 Derivation of the Interference *F*-Factor

The free-space field of the direct transmitted wave at range R and elevation θ_t, with the antenna beam axis at elevation θ_b, is

$$E_d = f(\theta_t - \theta_b) E_0 \exp\left(-j\frac{2\pi R}{\lambda}\right) \text{ (V/m)} \tag{8.1}$$

where $f(\theta)$ is the voltage pattern of the antenna, $|E_0| = \sqrt{30 P_t G_t}/R$ is the magnitude of the field on the beam axis, P_t is the transmitted power in W, G_t is the transmitting antenna gain, R is in m, λ is the wavelength in m, and $f(\theta)$ is the elevation voltage pattern of the antenna, normalized to unity on the axis at which G_t is calculated.

The field of a wave reflected from the surface at angle ψ below the axis is

$$E_r = \Gamma f(-\psi - \theta_b) E_0 \frac{R}{R_r} \exp\left(-j\frac{2\pi R_r}{\lambda}\right) \text{ (V/m)} \tag{8.2}$$

where Γ is the complex surface reflection coefficient, R_r is the pathlength of the reflected ray and ψ is the grazing angle at the reflection point. The difference between the reflection and direct paths is

$$\delta = R_r - R \text{ (m)} \tag{8.3}$$

It is normally assumed that $\delta/R << 1$, $R_r/R \approx 1$, giving [3, p. 241, Eq. (6.2)]:

$$E_r = \rho f(-\psi - \theta_b) E_0 \exp(-j\alpha) \text{ (V/m)} \tag{8.4}$$

where ρ is the magnitude of Γ and α is the phase angle of the reflection relative to the direct ray:

$$\alpha = \alpha_0 + \phi = \frac{2\pi\delta}{\lambda} + \phi \text{ (rad)} \tag{8.5}$$

Here ϕ is the phase angle of Γ and δ is the extra pathlength of the reflected ray.

The magnitude of the vector sum of the direct and reflected rays is [3, p. 241, Eq. (6.3)]:

$$|E| = |E_d + E_r| = \left|E_0 \left[f\left(\theta_t - \theta_b\right) + \rho f\left(-\psi - \theta_b\right) \exp\left(-j\alpha\right)\right]\right| \quad \text{(V/m)} \qquad (8.6)$$

The *F*-factor resulting from constructive and destructive interference by a reflected signal is then defined as [3, p. 241, Eq. (6.4)]:

$$F_i = \left| f\left(\theta_t - \theta_b\right) + \rho f\left(-\psi - \theta_b\right) \exp\left(-j\alpha\right)\right| \qquad (8.7)$$

where the subscript *i* identifies the factor as resulting from the interference phenomenon. Absolute values are used for F_i because the phase of the resultant field does not affect the results of the radar equation.

When a common antenna is used for transmission and reception, the same function *f* applies to the outgoing and incoming paths, resulting in a single *F*-factor. In other cases, separate F_{it} and F_{ir} are calculated, and

$$F_i \equiv \sqrt{F_{it} F_{ir}} \qquad (8.8)$$

Blake noted that the difference in antenna pattern phase angles may be included in α, permitting (8.7) to be written such that all terms are real except the phase angle α:

$$\begin{aligned} F_i &= f\left(\theta_t - \theta_b\right) \left| 1 + \rho \frac{f\left(-\psi - \theta_b\right)}{f\left(\theta_t - \theta_b\right)} \exp\left(-j\alpha\right) \right| \\ &= f\left(\theta_t - \theta_b\right) \sqrt{1 + x^2 + 2x\cos\alpha} \end{aligned} \qquad (8.9)$$

where

$$x = \rho \frac{f\left(-\psi - \theta_b\right)}{f\left(\theta_t - \theta_b\right)} \qquad (8.10)$$

The calculation requires knowledge of the antenna elevation patterns for transmitting and receiving, the pathlength difference δ, and the complex surface reflection coefficient Γ. Those parameters are discussed in subsequent sections of this chapter. Most conventional radars use a common antenna for which a single calculation of *F* is sufficient. In phased array radars, the transmitting and receiving patterns often differ even when the are generated by a common array, requiring separate calculations for F_{it} and F_{ir}.

8.1.2 Application of the *F*-Factor

The *F*-factor is applied in the Blake chart (Figure 1.1 or 1.2) as an adjustment to the free-space range R_0 to obtain $R' = R_0 F_i$. This is followed by application of a factor for atmospheric attenuation based on the range R'. The iterative process in steps 9–13 of the chart leads to an accurate result for any specified target elevation angle. A range-height-angle (coverage) plot may then be prepared by scaling range to the *F*-factor, with adjustments as needed for variation of attenuation with elevation angle and range.

At elevation angles $\theta_t << 1$, $\delta \approx 2h_r \sin\theta_t$, and for a horizontally polarized radar the reflection coefficient (see Section 8.3) is $\Gamma \approx -1.00$, leading to

$$\cos\alpha = \cos\left[\left(\frac{4\pi h_r}{\lambda}\sin\theta_t - \pi\right)\right] = -\cos\left(\frac{4\pi h_r}{\lambda}\sin\theta_t\right) \approx -\cos\frac{4\pi h_r \theta_t}{\lambda}$$

and

$$x \approx \frac{f\left(-\psi - \theta_b\right)}{f\left(\theta_t - \theta_b\right)} \approx 1$$

For this case, (8.9) becomes

$$F_i \approx f\left(\theta_t - \theta_b\right)\sqrt{2 - 2\cos\frac{4\pi h_r \theta_t}{\lambda}} = 2\left| f\left(\theta_t - \theta_b\right)\sin\left(\frac{2\pi h_r \theta_t}{\lambda}\right)\right| \qquad (8.11)$$

Nulls and peaks appear in the resulting coverage pattern at elevation angles given by

$$\theta_{\text{null}} \approx \sin\theta_{\text{null}} = \frac{(i-1)\lambda}{2h_r}, \quad i = 1, 2, 3\ldots \qquad (8.12)$$

$$\theta_{\text{peak}} \approx \sin\theta_{\text{peak}} = \left(\frac{2i-1}{2}\right)\frac{\lambda}{2h_r}, \quad i = 1, 2, 3\ldots \qquad (8.13)$$

where $i = 1$ corresponds to the null at the horizon and to the first reflection lobe.

As an example, consider a horizontally polarized S-band radar with elevation beamwidth $\theta_e = 6°$, operating at height $h_r = 10$m over a sea surface. The axis of the elevation beam is normally set to $\theta_b \approx \theta_e/3$ above the horizon. The lower lobes of the *F*-factor, shown in Figure 8.1, are approximately sinusoidal, as predicted by (8.11). When applied to the radar equation this results in a range at the center of

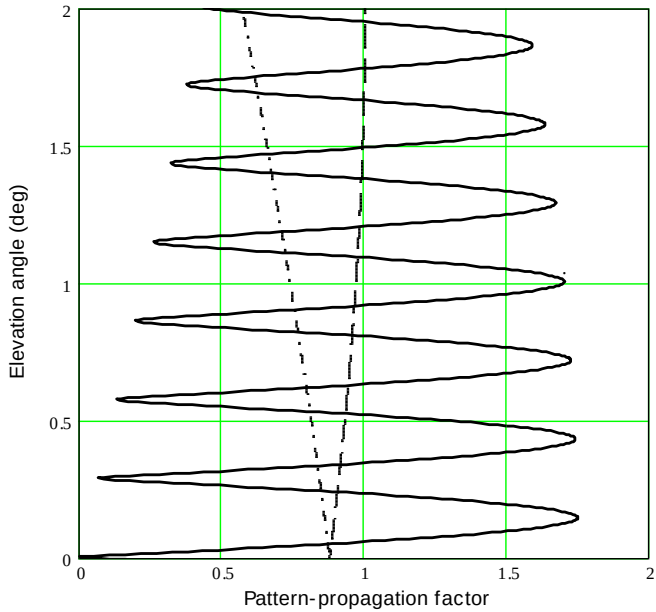

Figure 8.1 Interference pattern-propagation factor for a typical search radar over a sea surface (solid line), with antenna voltage pattern $f(\theta_t)$ (dashed line) and $f(-\theta_r)$ (dot-dash line).

the lowest lobe that is approximately twice the free-space range for that elevation angle. For zero axis tilt, $f(\theta) = 1$ at the horizon, and the first lobe would have amplitude $F_i = 2.0$, rather than the somewhat lower value shown in the figure. If the elevation angle scale is converted to target altitude at a given range, the plot will show the *height-gain factor* for the radar-target path.

Computer methods of solving for detection range are based on calculating the received and required signal energies as functions of range and identifying the longest range at which the requirement is met. Range-dependent parameters in the radar equation, including atmospheric attenuation and *F*-factor, are determined for each range, based on the assumed target trajectory. If that trajectory maintains a constant elevation from the radar, repeated calculations of the *F*-factor may be unnecessary as long as the resulting detection range remains large enough to give a constant pathlength difference δ (see Section 8.2).

8.2 GEOMETRICAL MODELS OF THE RAY PATHS

A model of radar and target location over the Earth's surface is needed to find the pathlength difference δ and the grazing angle ψ for which the reflection coeffi-

cient is to be calculated. Depending on the target ranges of interest and the accuracy required of the calculation, there are several modeling methods that may be used, starting with a distant target over a flat Earth, proceeding to targets at arbitrary range, and then to spherical-Earth models of increasing complexity.

8.2.1 Method 1: Flat-Earth Approximation with Distant Target

The geometry is shown in Figure 8.2. For this simple model, the input parameters are the radar wavelength λ, antenna height h_r above the surface, and target elevation θ_t.

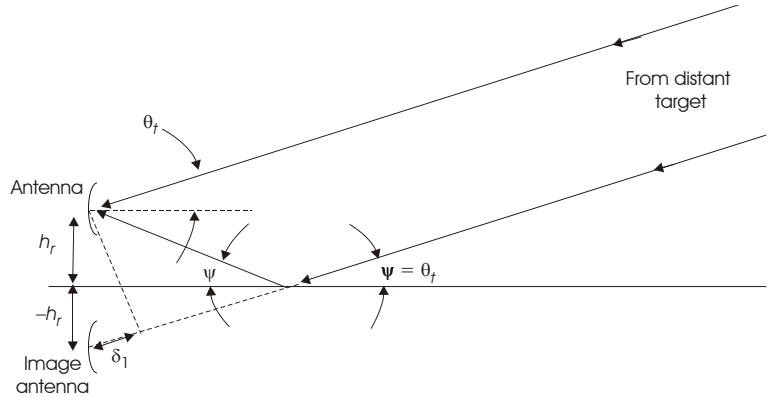

Figure 8.2 Geometry of distant target over flat Earth, with arrows drawn for the receiving case.

The reflected ray, arriving at the radar site parallel to the direct ray, can be considered as passing in a straight line through the surface at the point of specular reflection to an *image antenna* located h_r below the surface. The grazing angle ψ of that ray relative to the surface is equal to the elevation θ_t and the pathlength difference is

$$\delta_1 = 2h_r \sin\theta_t \quad \text{(m)} \tag{8.14}$$

The altitude of a target at range R above the flat Earth is

$$h_{t1} = h_r + R\sin\theta_t \quad \text{(m)} \tag{8.15}$$

and the pathlength difference is

$$\delta_1 = \frac{2h_r h_{t1}}{R} \quad \text{(m)} \tag{8.16}$$

The following parameters will be assumed in comparing this approximation with others and with exact methods to be described in subsequent sections:

$$h_r = 10\text{m}, \lambda = 0.1\text{m}, \text{ and } \theta_t = 2°.$$

This is the case used as an example in Figure 8.1. At 2° elevation, the phase reversal introduced by the reflection coefficient shifts the reflected ray by π radians, relative to the direct ray, causing a deep null to appear near that elevation.

8.2.2 Method 2: Flat-Earth Approximation with Target at Arbitrary Range

Relaxing the assumption that the target is at range long enough that the rays can be considered parallel on arrival at the radar site, the geometry is as shown in Figure 8.3. The target is at range R and elevation θ_t, and in rectangular coordinates it is characterized by altitude h_{t1} and ground range G:

$$\begin{aligned} h_{t1} &= h_r + R\sin\theta_t \quad \text{(m)} \\ G &= R\cos\theta_t = \sqrt{R^2 - \left(h_{t1} - h_r\right)^2} \quad \text{(m)} \end{aligned} \tag{8.17}$$

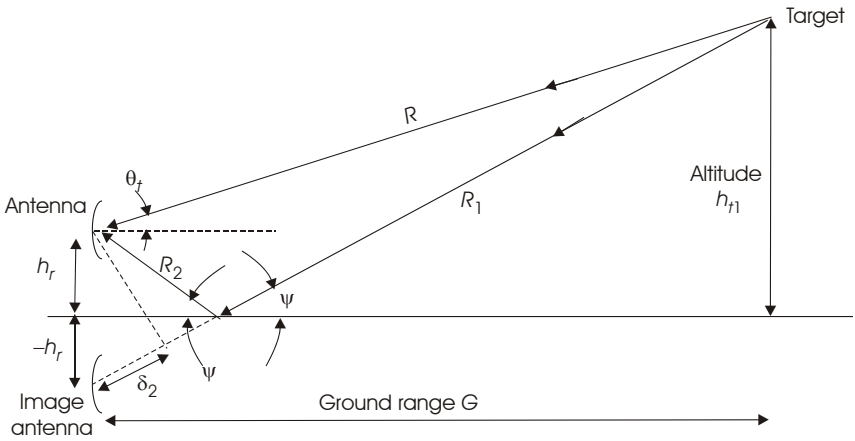

Figure 8.3 Geometry of target at arbitrary range over flat Earth.

The reflected ray arrives at and is reflected from the flat surface at a grazing angle ψ exceeding the elevation angle of the target:

$$\psi = \sin^{-1}\frac{h_{t1}+h_r}{R} \quad \text{(rad)} \tag{8.18}$$

The reflected pathlength is the sum of two segments, $R_r = R_1 + R_2$, where R_2 is the distance from the reflection point to the antenna and also to the image antenna:

$$R_r = \sqrt{G^2 + \left(h_{t1}+h_r\right)^2} = \sqrt{R^2 + 4h_{t1}h_r} \tag{8.19}$$

The pathlength difference is

$$\delta_2 = R_r - R = R\left(\sqrt{1+\frac{4h_{t1}h_r}{R^2}} - 1\right) = R\left(\sqrt{1+\frac{2\delta_1}{R}} - 1\right) \quad \text{(m)} \tag{8.20}$$

Expanding the radical for $2\delta_1/R << 1$ and retaining the second-order term, we find

$$\delta_2 = R\left[\sqrt{1+\frac{4h_t'h_r}{R^2}}\right] \approx \delta_1\left(1-\frac{h_r}{R}\sin\theta_t\right) = \delta_1\left(1-\frac{\delta_1}{2R}\right) \quad \text{(m)} \tag{8.21}$$

where δ_1 is the result of the distant-target approximation (8.16). The reduction in the pathlength difference by inclusion of the second-order term in (8.21) is about one part in 10^5 at 2° elevation, but can be significant at higher elevation angles. The *F*-factor plot for this case is indistinguishable from Figure 8.1.

Blake [3, p. 245, Eqs. (6.17)–(6.19)] uses an approximation that results in

$$\delta \approx \frac{2h_r h_{t1}}{G} = \frac{\delta_1}{\cos\theta_t} \quad \text{(m)} \tag{8.22}$$

The pathlength predicted by this approximation is in error by 6 parts in 10^4 at 2°.

8.2.3 Method 3: First-Order Approximation for Spherical Earth

A simple, first-order correction for the spherical Earth with effective radius $k_e a_e$ uses the target altitude h_{t1} above a plane tangent to the Earth's surface at the radar site, as shown in Figure 8.4.

The surface at the target range lies below the tangent plane by

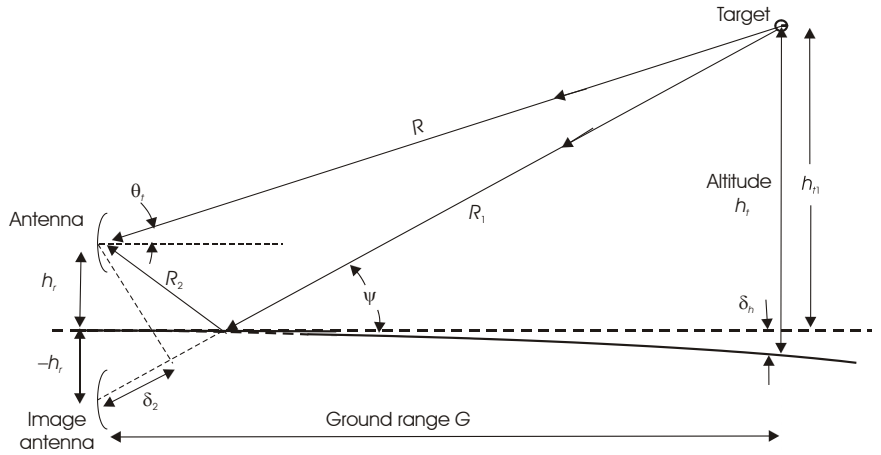

Figure 8.4 First-order correction for spherical Earth.

$$\delta_h = \frac{G^2}{2k_e a_e} \quad \text{(m)} \tag{8.23}$$

where $k_e a_e$ is the effective Earth's radius. Here and subsequently, the constant $k_e \approx 4/3$ appears along with the actual radius a_e, making the results dependent on the tropospheric refractivity gradient (see Section 7.1.4). As the target altitude increases, this method of modeling the effects of tropospheric refraction becomes less accurate, resulting in errors in the geometric models discussed. However, the results may still be used to compare the relative accuracies of different methods, keeping in mind that the error in refractive modeling may exceed that of geometric approximations. Blake developed a method of using the exponential reference atmosphere to relate R, h_t, and θ_t, but found it unnecessary to apply this to calculation of the F-factor, basing it instead on the effective radius $k_e a_e$.

The target altitude above the tangent plane is

$$h_{t1} = h_t - \delta_h = h_t - \frac{G^2}{2k_e a_e} \quad \text{(m)} \tag{8.24}$$

It is assumed in this method that the reflection point is close enough to the radar that it can be modeled as lying on a plane tangent to the surface at the radar. This allows the grazing angle ψ to be calculated by substitution of h_{t1} for h_t in (8.18):

$$\psi = \sin^{-1}\frac{h_{t1}+h_r}{R} \quad \text{(rad)} \tag{8.25}$$

The target elevation angle is reduced to

$$\theta_t = \sin^{-1}\frac{h_{t1}-h_r}{R} \quad \text{(rad)} \tag{8.26}$$

Substituting h_{t1} in (8.16) gives the pathlength difference δ_1'. Analogous to (8.20), we find

$$\delta_3 = R\left[\sqrt{1+\frac{2\delta_1'}{R}}-1\right] \approx \delta_1'\left(1-\frac{\delta_1'}{2R}\right) \quad \text{(m)} \tag{8.27}$$

8.2.4 Method 4: Approximation for Spherical Earth with Distant Target

Blake [3, pp. 249–253] develops expressions for the pathlength difference and grazing angle when a distant target is observed at elevation angle θ_t over the spherical Earth. The geometry is shown in Figure 8.5.

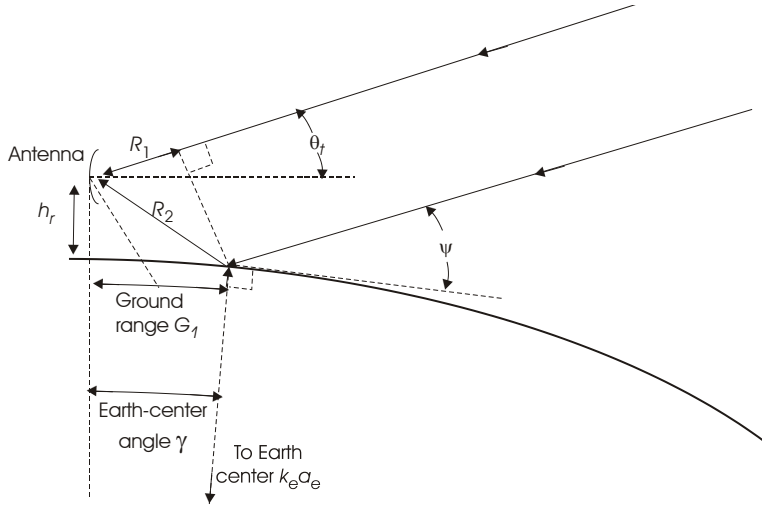

Figure 8.5 Geometry of distant target over spherical Earth.

Blake gives the Earth-center angle subtended by the ground range to the reflection point as [3, p. 252, Eq. (6.40)]:

$$\gamma = \frac{2h_r/3k_e a_e}{\sqrt{(\tan\theta_t/3)^2 + 2h_r/3k_e a_e} + \tan(\theta_t/3)} \quad \text{(rad)} \tag{8.28}$$

The ground range and grazing angle are:

$$G_1 = k_e a_e \gamma \quad \text{(m)} \tag{8.29}$$

$$\psi = \theta_t + \gamma \quad \text{(rad)} \tag{8.30}$$

The pathlength difference is

$$\delta_4 = R_2 - R_1 \quad \text{(m)} \tag{8.31}$$

where the range segments are

$$R_1 = R_2 \cos(2\theta_t + 2\gamma) \quad \text{(m)} \tag{8.32}$$

$$R_2 = \sqrt{h_r^2 + k_e a_e (k_e a_e + h_r)\gamma^2} \quad \text{(m)} \tag{8.33}$$

The result is [3, p. 252, Eqs. (6.44), (6.45)]:

$$\delta_4 = 2R_2 \sin^2(\theta_t + \gamma) = 2\sqrt{h_r^2 + k_e a_e (k_e a_e + h_r)\gamma^2} \sin^2(\theta_t + \gamma) \quad \text{(m)} \tag{8.34}$$

Method 4, not requiring target altitude or range as inputs, is insensitive to the position of the target along the line of constant elevation.

8.2.5 Method 5: Approximation for Spherical Earth with Target at Arbitrary Range

The geometry for general case is shown in Figure 8.6. Fishback, in [2, p. 113] presents the solution of the cubic equation that yields the pathlengths and grazing angle based on knowledge of the altitudes h_t and h_r and the ground rage $G = G_1 + G_2$. For this purpose, two intermediate parameters are defined:

$$p = \frac{2}{\sqrt{3}} \sqrt{k_e a_e (h_t + h_r) + \left(\frac{G}{2}\right)^2} \quad \text{(m)} \tag{8.35}$$

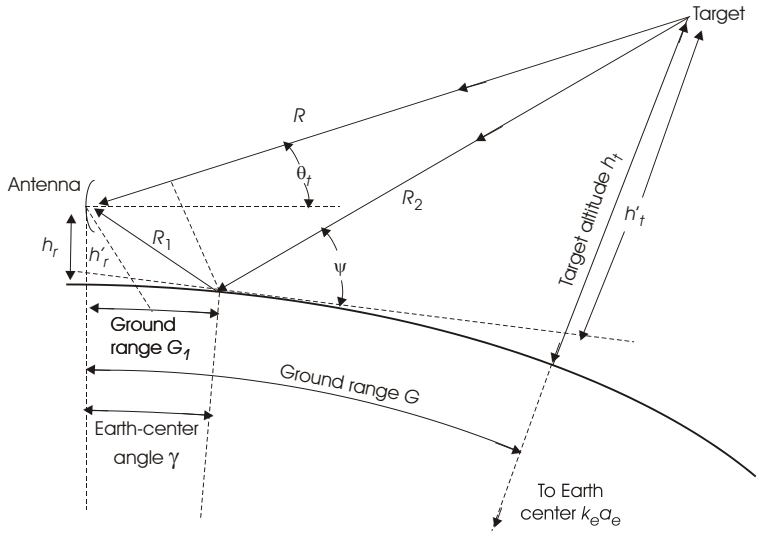

Figure 8.6 Geometry of target at arbitrary range over spherical Earth.

$$\Phi = \cos^{-1}\left[\frac{2k_e a_e G\left(h_t - h_r\right)}{p^3}\right] \text{ (rad)} \tag{8.36}$$

Using these parameters, and assuming that the grazing angle is small, the ground range to the reflection point is[1]

$$G_1 = \frac{G}{2} - p\cos\frac{\Phi + \pi}{3} \text{ (m)} \tag{8.37}$$

The altitudes referred to a plane tangent to the surface at the reflection point are then

$$\begin{aligned} h_r' &= h_r - \frac{G_1^2}{2k_e a_e} \text{ (m)} \\ h_t' &= h_r \frac{G - G_1}{G_1} \text{ (m)} \end{aligned} \tag{8.38}$$

[1] A typographical error in [2, p. 113] shows a + sign rather than − for the second term in our (8.37).

The approximations for pathlength difference, grazing angle, and target elevation angle are:

$$\delta_5 = \frac{2h_r' h_t'}{G} \tag{8.39}$$

$$\psi = \tan^{-1}\frac{h_r'}{G_1} \tag{8.40}$$

$$\theta_t = \frac{h_t' - h_r'}{G} - \frac{G}{2k_e a_e} \quad \text{(rad)} \tag{8.41}$$

If the slant range R is given, the ground range G is found from Blake's expression [3, p. 256, Eqs. (6.57), (6.58)]:

$$G = 2k_e a_e \sin^{-1}\sqrt{\frac{R^2 - (h_t - h_r)^2}{4(k_e a_e + h_t)(k_e a_e + h_r)}} \approx \sqrt{\frac{R^2 - (h_t - h_r)^2}{1 + (h_t + h_r)/k_e a_e}} \quad \text{(m)} \tag{8.42}$$

where the approximation is accurate to one part in 10^4 for practical radar cases.

8.2.6 Method 6: Exact Expressions for Spherical Earth with Target at Arbitrary Range

Blake presents a method that avoids the restriction $\psi << 1$. Fishback's solution to the cubic equation is used, and the first ground-range segment G_1 is found from (8.37). Using G_1 and other known parameters, the two segments of the reflected path are

$$\begin{aligned} R_1 &= \sqrt{k_e^2 a_a^2 + (k_e a_e + h_r)^2 - 2k_e a_e (k_e a_e + h_r)\cos(G_1/k_e a_e)} \\ &= \sqrt{h_r^2 + 4k_e a_e (k_e a_e + h_r)\sin^2(G_1/2k_e a_e)} \quad \text{(m)} \end{aligned} \tag{8.43}$$

$$\begin{aligned} R_2 &= \sqrt{k_e^2 a_a^2 + (k_e a_e + h_t)^2 - 2k_e a_e (k_e a_e + h_t)\cos(G_2/k_e a_e)} \\ &= \sqrt{h_t^2 + 4k_e a_e (k_e a_e + h_t)\sin^2(G_2/2k_e a_e)} \quad \text{(m)} \end{aligned} \tag{8.44}$$

where $G_2 = G - G_1$. If the ground range G is given rather than R, the latter may be found as

$$R = \sqrt{\left(h_t - h_r\right)^2 + 4\left(k_e a_e + h_r\right)\left(k_e a_e + h_t\right)\sin^2\left(G/2k_e a_e\right)} \quad \text{(m)} \tag{8.45}$$

The pathlength difference is

$$\delta_6 = R_1 + R_2 - R \quad \text{(m)} \tag{8.46}$$

The angles θ_t and ψ are:

$$\begin{aligned} \theta_t &= \sin^{-1}\frac{2k_e a_e\left(h_t - h_r\right) + h_t^2 - h_r^2 - R^2}{2\left(k_e a_e + h_r\right)R} \\ &\approx \sin^{-1}\left(\frac{h_t - h_r}{R} - \frac{R}{2k_e a_e}\right) \quad \text{(rad)} \end{aligned} \tag{8.47}$$

$$\psi = \sin^{-1}\frac{2k_e a_e h_r + h_r^2 + R_1^2}{2\left(k_e a_e + h_r\right)R_1} \quad \text{(rad)} \tag{8.48}$$

8.2.7 Comparison of Approximate Methods

The results of the six methods are compared in Table 8.1, where all values are calculated for an elevation angle $\theta_t = 2°$. Two antenna altitudes and two ranges are considered. The variation among results is negligible for the low-sited radar (h_r = 10m), except that the Fishback solution for the spherical Earth gives a lower elevation when the same target altitude is used as in the more approximate methods. Over typical land surfaces, there is likely to be some variation in the surface which, along with uncertainty in the refractivity profile, will mask any difference in the geometrical model.

At the higher antenna altitude (h_r = 100m), Method 1 fails to capture the divergence of grazing angle from target elevation, which is ≈ 0.1° in these examples. It also underestimates the pathlength difference, as does the distant-target approximation.

The Fishback method and Blake's modification are not excessively burdensome for today's computers, and may be included in programs for solution of the radar equation. For surface-based radars at other than high altitudes, any of the approximate methods may be used without introducing large errors in the grazing angle and pathlength difference.

Table 8.1

Inputs		*Method*	*Outputs*			
h_a m	R km		h_t m	ψ °	δ m	α rad
10	Any	1. Flat Earth, distant target		2.00	0.698	43.86
	100	2. Flat Earth, arbitrary range	3,500	2.01	0.700	43.98
		3. Spherical Earth, 1st-order	3,500	2.01	0.700	43.98
		4. Spherical Earth, distant target	3,500	2.00	0.699	43.89
		5. Spherical Earth, Fishback	4,084	2.01	0.701	44.01
		6. Spherical Earth, Blake	4,088	2.01	0.701	44.01
	Any	1. Flat Earth, distant target		2.00	0.698	43.86
	20	2. Flat Earth, arbitrary range	708	2.06	0.708	44.48
		3. Spherical Earth, 1st-order	708	2.06	0.708	44.48
		4. Spherical Earth, distant target	708	2.00	0.699	43.89
		5. Spherical Earth, Fishback	731	2.06	0.708	44.51
		6. Spherical Earth, Blake	732	2.06	0.708	44.51
100	Any	1. Flat Earth, distant target		2.00	6.98	438.56
	100	2. Flat Earth, arbitrary range	3,590	2.11	7.18	451.12
		3. Spherical Earth, 1st-order	3,590	2.11	7.18	451.12
		4. Spherical Earth, distant target	3,500	2.02	7.02	440.83
		5. Spherical Earth, Fishback	4,174	2.13	7.21	453.21
		6. Spherical Earth, Blake	4,177	2.13	7.21	453.09

8.3 REFLECTION COEFFICIENT

Having determined the angles required to express $f(\theta_t)$ and $f(\theta_r)$ of (8.9), the pathlength difference that determines α in that equation, and the grazing angle ψ at the surface, the next step is to calculate the magnitude ρ and phase ϕ of the surface reflection coefficient. The magnitude is the product of three terms:

$$\rho = \rho_0 \rho_s \rho_v \tag{8.49}$$

where

ρ_0 = $|\Gamma|$ = magnitude of the Fresnel reflection coefficient;
ρ_s = specular scattering coefficient;
ρ_v = vegetation factor for land surfaces.

8.3.1 Fresnel Reflection Coefficient

The Fresnel reflection coefficient Γ describes the ratio of the field reflected from a smooth surface to that incident on it. Values are different for horizontal and vertical polarizations:

$$\Gamma_h = \frac{\sin\psi - \sqrt{\varepsilon - \cos^2\psi}}{\sin\psi + \sqrt{\varepsilon - \cos^2\psi}} \tag{8.50}$$

$$\Gamma_v = \frac{\varepsilon\sin\psi - \sqrt{\varepsilon - \cos^2\psi}}{\varepsilon\sin\psi + \sqrt{\varepsilon - \cos^2\psi}} \tag{8.51}$$

where

Γ_h = coefficient for horizontal polarization;
Γ_v = coefficient for vertical polarization;
ψ = grazing angle;
ε = $\varepsilon_r + j\varepsilon_i$ = complex dielectric constant of the surface material;
ε_r = relative dielectric constant.

The imaginary component of the dielectric constant is

$$\varepsilon_i = -j60\lambda\sigma_e \tag{8.52}$$

where

λ = wavelength in m;
σ_e = conductivity in siemens/m.

For sea water, of greatest concern in naval and marine radar, Blake used data from an early paper [4], which gave the following expressions for the real and imaginary parts of the dielectric constant [3, p. 260, Eqs. (6.70), (6.71)]:

$$\begin{aligned}\varepsilon_r &= \frac{\varepsilon_s - \varepsilon_0}{1+x^2} + \varepsilon_0 \\ \varepsilon_i &= \frac{(\varepsilon_s - \varepsilon_0)x}{1+x^2} + \frac{2\sigma_i}{f}\end{aligned} \tag{8.53}$$

where

x = $2\pi f\tau$;
τ = relaxation constant = 12.1×10^{-12} at T = 10°C, or 9.2×10^{-12} at T = 20°C;
ε_s = static dielectric constant = 72.2 at T = 10°C, or 69.1 at T = 20°C;

ε_0 = 4.9;
σ_i = ionic conductivity = 3.6×10^{10} at T = 10°C, or 4.7×10^{10} at T = 20°C;
f = frequency in Hz.

These expressions give the values for salt water shown as a function of frequency in Figure 8.7.

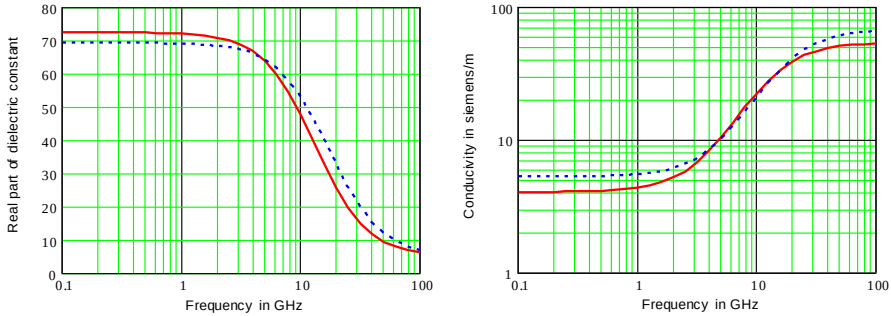

Figure 8.7 Components of dielectric constant for salt water: T = 10°C (solid lines); T = 20°C (dashed lines).

The resulting reflection coefficients are plotted in Figures 8.8. and 8.9, for different surfaces at X-band and at VHF as listed in Table 8.2, where data for fresh water and land surfaces have been added. Data on land surfaces were taken from [5]. The curves for salt water in the microwave band follow those for fresh water, but diverge as wavelengths increase.

Coefficients for snow and ice, not plotted, are essentially the same as for poor soil.

Table 8.2 Electrical Properties of Typical Surfaces

	ε_r		σ_e (siemens/m)	
Material	(λ = 0.03m)	(λ = 1m).	(λ = 0.03m)	(λ = 1m)
Fresh water	81	65	0.7	15
Salt water	48	72	22	4
Good soil (wet)	13	15	3	0.05
Average soil	7	8	1	0.02
Poor soil (dry)	3.5	4	0.3	0.005
Snow, ice	3	3	0.001	0.001

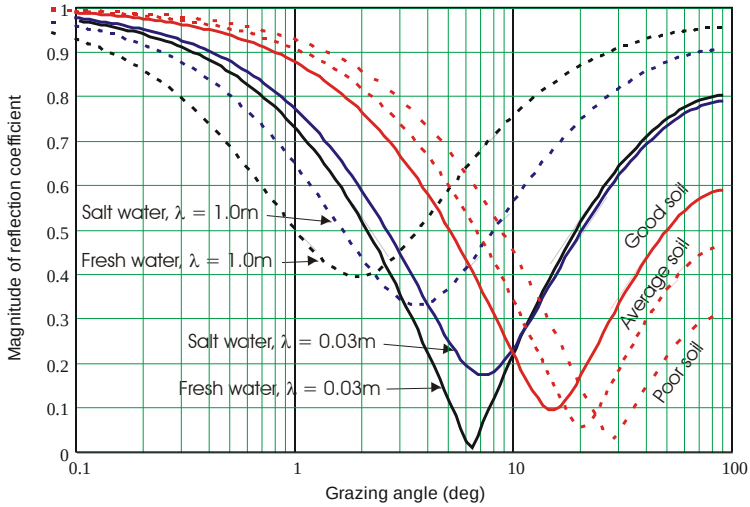

(a) Magnitude ρ_{0v} of reflection coefficient

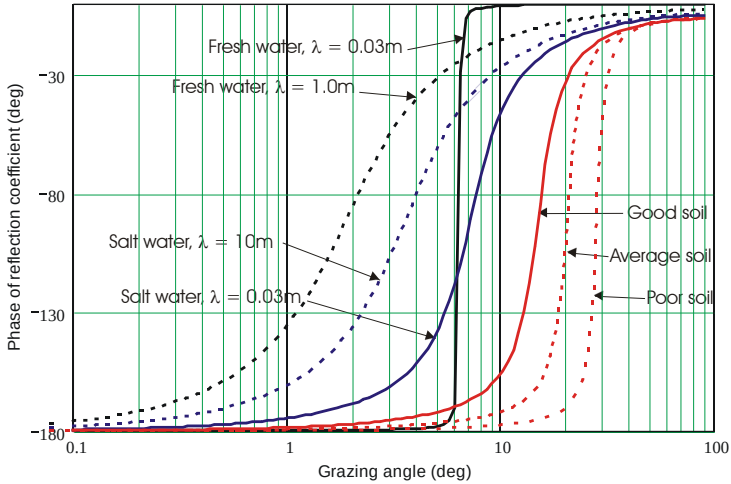

(b) Phase ϕ_v of reflection coefficient

Figure 8.8 Magnitude and phase of reflection coefficient for vertical polarization.

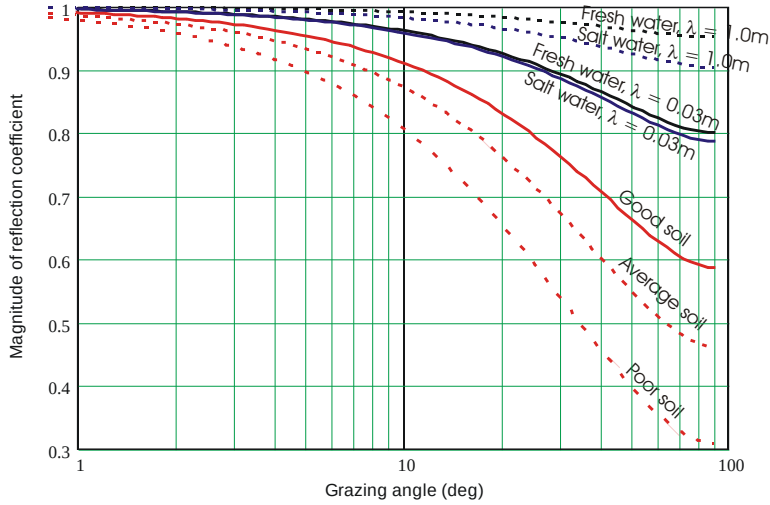

(a) Magnitude ρ_{0h} of reflection coefficient

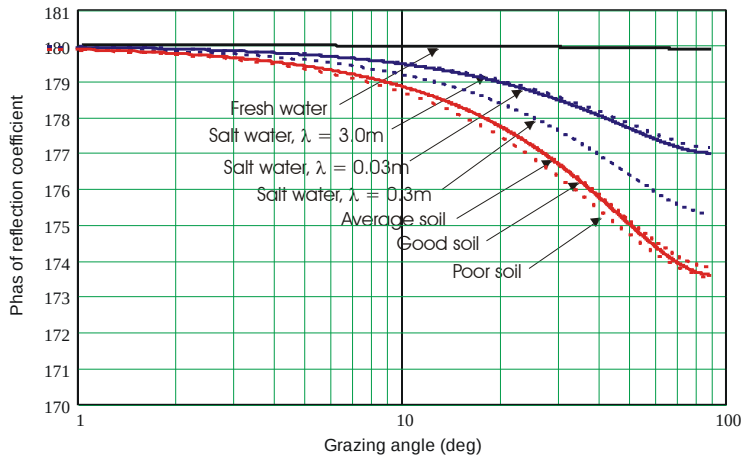

(b) Phase ϕ_h of reflection coefficient

Figure 8.9 Magnitude and phase of reflection coefficient for horizontal polarization.

For vertical polarization the magnitude ρ_{0v} drops to a minimum at the *pseudo-Brewster angle* ψ_B, where the phase passes through 90° while going from near 180° to 0°. An approximate expression for this angle is

$$\psi_B = \sin^{-1} \frac{1}{\sqrt{\varepsilon_r + 1}} , \quad \frac{\varepsilon_r}{\varepsilon_i} > 2 \tag{8.54}$$

That approximation breaks down for salt water at long wavelengths, but gives a good estimate for the other cases illustrated. For horizontal polarization the magnitude ρ_{0h} remains near unity for grazing angles below about 10°, and the phase angle remains near 180° at all grazing angles. It is for this case that the approximation (8.11) for the *F*-factor applies.

The reflection coefficient for circular polarization is discussed by Blake [3, p. 264]. Defining the reflection coefficient for the same sense of circular polarization as the direct ray as Γ_{cs}, this is given by

$$\Gamma_{cs} = \frac{1}{2}\left(\Gamma_v + \Gamma_h\right) \tag{8.55}$$

while for the opposite sense Γ_{os} it is

$$\Gamma_{os} = \frac{1}{2}\left(\Gamma_v - \Gamma_h\right) \tag{8.56}$$

8.3.2 Reflection from Rough Surfaces

The magnitude of the surface reflection coefficient is equal to the Fresnel coefficient for smooth surfaces, but for rough surfaces is reduced by a *specular scattering coefficient* [6, p. 316]:

$$\rho_s = \exp\left[-\frac{1}{2}\left(\frac{4\pi\sigma_h}{\lambda}\sin\psi\right)^2\right] \tag{8.57}$$

where σ_h is the rms height deviation of the surface relative to its mean. The value of σ_h to be used is that within the *first Fresnel zone* that surrounds the point of specular reflection at ground range G_1 from the antenna (see Figure 8.5). That zone is defined as the elliptical surface area from which the delay of the reflected ray deviates by < $\lambda/2$ from that at the specular point [2, pp. 412–418].

The *Rayleigh roughness criterion* is commonly used to describe the height h_s of surface irregularities below which the surface can be considered "smooth":

$$h_s = \frac{\lambda}{8\sin\psi} \tag{8.58}$$

Letting $\sigma_h = h_s/2$ gives

$$\rho_s = \exp\left[-\frac{1}{2}\left(\frac{2\pi h_s}{\lambda}\sin\psi\right)^2\right] = \exp\left(-\frac{\pi^2}{32}\right) = 0.735$$

The fraction of power in the specular reflection is $\rho_s^2 = 0.54$ when the Rayleigh criterion is met, using the 2σ value for h_s. Other scaling of σ_h to h gives slightly different results, but that used here gives a reasonable physical interpretation, and (8.57), based on a Gaussian distribution of height deviations, is commonly used. The grazing angle ψ is found from the geometrical models of Section 8.2.

Blake comments on the departure of some experimental data on ρ_s in [7] from the value given by (8.57), at larger values of the normalized roughness $x = (\sigma_h/\lambda)\sin\psi$, where $\rho_s \to 0$. There are several possible explanations of this, but in the development of the theory of multipath tracking errors [8] it was found that the experiment described in [7], conducted on a path between oil platforms in the Gulf of Mexico, was limited to a constant, small value of grazing angle ψ, and achieved high values of $(\sigma_h/\lambda)\sin\psi$ only as a result of large wave heights. This introduced shadowing of the wave troughs, which in turn reduced the σ_h of the visible reflecting surfaces [8, p. 516, Eq. (11.2.6)]:

$$\sigma_h' = \sigma_h \sqrt[5]{2\psi/\beta_0}\ , \quad \text{for } 2\psi/\beta_0 < 1 \tag{8.59}$$

where β_0 is 1.4 times the rms slope of the wave surfaces. The experimental data match (8.57) more closely when the corrected value σ_h' is used for high sea states.

Energy reaching the surface is divided among three components:

$1-\rho_0^2$ = fraction of energy absorbed by the surface;
$\rho_0^2\rho_s^2$ = fraction of energy in specular component of reflection;
$\rho_0^2\rho_d^2$ = fraction of energy in diffuse component of reflection.

where ρ_d is the *diffuse reflection coefficient*. Conservation of energy requires that the sum of these three components be unity, or

$$\rho_s^2 + \rho_d^2 = 1$$

The plot of the specular and diffuse scattering coefficients as a function of the normalized roughness $(\sigma_h/\lambda)\sin\psi$ is shown in Figure 8.10.

Experimental values of ρ_d reported in [7] did not exceed 0.4. This was partly the result of failure to correct for shadowing at high sea states, but also because most of the diffuse energy between low-altitude terminals tends to be reflected from surface areas near the two ends of a path. In the experiment, almost half the

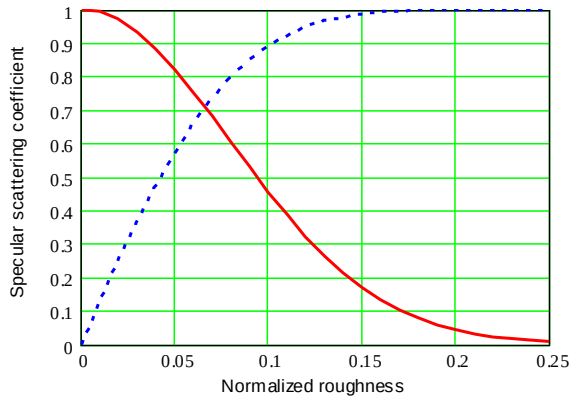

Figure 8.10 Scattering coefficients as a function of normalized surface roughness $(\sigma_h/\lambda)\sin\psi$: specular scattering coefficient ρ_s (solid line) and diffuse scattering coefficient ρ_d (dashed line).

total diffuse energy arrived at negative elevation angles on the lower skirts or below the mainlobe of the antenna, reducing the measured ρ_d. That situation applies also in many radar applications, limiting the diffuse energy actually received by the antenna. Procedures outlined in [8, pp. pp. 519–520] give the elevation density η_d of diffuse energy and the fraction of $(\rho_0\rho_d)^2$ that is received by the antenna power gain pattern.

As noted by Blake [3, p. 268], the diffuse reflections introduce or increase random fluctuations in the target echo, adding to the direct power while reducing the strength of the lobing caused by the specular component.

When the diffuse reflection are strong, the expression for the *F*-factor may be modified to include that term:

$$F_i = \sqrt{F_{\text{spec}}^2 + F_{\text{dif}}^2} = f\left(\theta_t - \theta_b\right)\left[\left|1 + \rho_0\rho_s \frac{f\left(\theta_r - \theta_b\right)}{f\left(E - \theta_b\right)}\exp\left(-j\alpha\right)\right|^2 + \right.$$
$$\left. + \int_{-\pi/2}^{0} \rho_0^2 \eta_d\left(\theta_r\right)\frac{f^2\left(\theta_{rd} - \theta_b\right)}{f^2\left(E - \theta_b\right)}d\theta_{rd}\right]^{1/2} \tag{8.60}$$

where F_{spec} and F_{dif} are the coherent and incoherent components of the *F*-factor and θ_{rd} is the elevation angle of the diffuse reflections. The target fluctuation model must then consider the relative energy contributed by the two components. If the diffuse term is large, statistics of the *F*-factor become Rician [9], and that distribution will be imposed on steady targets. Statistics of fluctuating targets will

be significantly affected only if their probability density function is narrowed to within the width of the Rician distribution by averaging over the observation time. No studies of this effect have been identified.

8.3.3 Land Surfaces with Vegetation

For land- or air-based radar, the effect of vegetation must be included in calculating the surface-reflected energy. Experimental data reported in [10], along with a survey of related literature, permitted generation of an empirical model [11, p. 287 and Appendix 6B]. The absorption is modeled as a *vegetation factor* ρ_v that multiplies ρ_0 in calculating the reflection coefficient for both specular and diffuse reflection:

$$\rho_v = \left(1 - \sqrt{a\lambda}\right) \exp\left(-\frac{b \sin\psi}{\lambda}\right) + \sqrt{a\lambda} \le 1.0 \tag{8.61}$$

where the coefficients a and b are

$a = 3.2$, $b = 1$ for thin grass;
$a = 0.32$, $b = 3$ for brush or dense weeds;
$a = 0.032$, $b = 5$ for dense trees.

The results for X-band ($\lambda = 0.03$m), S-band ($\lambda = 0.1$m), and VHF ($\lambda = 1$m) are shown in Figure 8.11. The reduction in reflection coefficient increases with frequency and depth of vegetation, and is minimal in the VHF band unless dense trees cover the otherwise visible surface. Even a thin layer of grass introduces up to 10 dB reduction at X-band, at grazing angles greater than a few degrees. The model is necessarily approximate, given the wide variation in foliage density and water content. However, the author has personally observed that two-foot layer of weeds in the first Fresnel zone virtually eliminates reflection lobing on an L-band air surveillance radar, and that sparse grass drops the X-band reflection coefficient by ≈ 10 dB.

8.3.4 The Divergence Factor

Another factor affecting the reflected rays is the *divergence factor D* [2, p. 99; 3, p. 270], expressed approximately by [3, p. 270, Eq.(6.79)]:

$$D \approx \left(1 + \frac{2G_1G_2}{k_e a_e G \sin\psi}\right)^{-1/2} \tag{8.62}$$

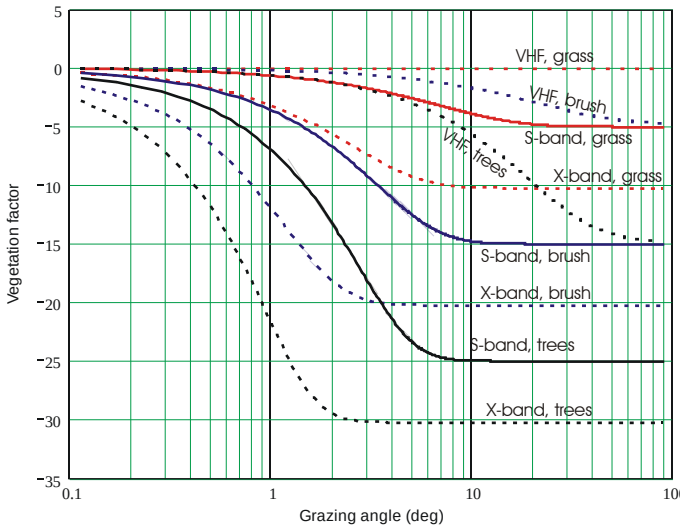

Figure 8.11 Vegetation factor ρ_v as a function of grazing angle for different surfaces at VHF, S-band, and X-band.

This factor results from the Earth's curvature within the first Fresnel zone surrounding the point of specular reflection, and appears as a multiplier to the reflection coefficient ρ in equations for the F_i.

The factor is near unity and can be ignored for most surface-based radars, because the geometric conditions leading to $D < 1$ correspond to values of pathlength difference δ that are in the intermediate region, where interpolation between the interference and diffraction factors masks the effects of D (see Section 8.6.1). However, for sites or airborne radars elevated to $h_r > 100$m above the reflecting surface it can reduce reflections.

8.4 DIFFRACTION

8.4.1 Smooth-Sphere Diffraction

Diffraction over the spherical Earth affects the F-factor when the pathlength difference δ from Section 8.2 is less than about $\lambda/6$, and becomes dominant at and below the horizon. The expression for the diffraction factor, assuming full antenna gain toward the horizon and using only the first mode of the diffraction equation, is [2, p. 122]:

$$\begin{aligned} F_{d0} &= 2\sqrt{\pi X}\,\exp\left(-2.02X\right)\left|U\left(Z_r\right)U\left(Z_t\right)\right| \\ &= V\left(X\right)\left|U\left(Z_r\right)U\left(Z_t\right)\right| \end{aligned} \tag{8.63}$$

where

X	=	R/L = range in natural units;
$Z_{r,t}$	=	$h_{r,t}/H$ = terminal heights in natural units;
$V(X)$	=	attenuation (range) factor;
$U_{r,t}$	=	height-gain factors for the two terminals.

The constant 2.02 in the argument of the exponential of (8.63) is based on the refractivity profile of the standard atmosphere, but the result should be generally applicable.

The natural units are given as a function of wavelength and effective Earth radius as

$$L = \sqrt[3]{\frac{\left(k_e a_e\right)^2 \lambda}{\pi n_0}} \quad \text{(m)} \tag{8.64}$$

$$H = \sqrt[3]{\frac{k_e a_e \lambda^2}{8\pi^2 n_0}} \quad \text{(m)} \tag{8.65}$$

where $n_0 \approx 1.000313$ is the refractive index at the surface (see Section 7.1.4).

Blake fits the following approximations to the diffraction height-gain factor U [3, p. 273, Eq. (6.87)]:

$$\begin{aligned} 20\log U\left(Z\right) &= 20\log Z, && Z \le 0.6 \\ &= -4.3 + 51.04\left(\log\frac{Z}{0.6}\right)^{1.4}, && 0.6 < Z < 1 \\ &= 19.85\left(Z^{0.47} - 0.9\right), && Z \ge 1 \end{aligned} \tag{8.66}$$

He expresses the range factor $V(X)$ in logarithmic form:

$$20\log V\left(X\right) = 10.99 + 10\log X - 17.55X \tag{8.67}$$

Thus, using (8.63)–(8.67), the diffraction factor can be expressed in decibels as the sum of the range factor and the two height-gain factors

$$20\log F_{d0} = 20\log V\left(\frac{R}{L}\right) + 20\log U\left(\frac{h_r}{H}\right) + 20\log U\left(\frac{h_t}{H}\right) \text{ dB} \qquad (8.68)$$

A typical plot of the F_{d0} is shown in Figure 8.12. Dashed vertical lines bound the *intermediate region* that extends between R_δ, the limit of the interference region, and R_h, the 4/3-Earth horizon range beyond which the single-mode diffraction values are adequate. Those ranges are 128 km and 143 km, respectively, in this example. For interpolation between the diffraction and reflection results in the intermediate region, it has been found useful to place a limit $F'_{d0} \le 1$, as shown by the dashed line in the figure, using

$$F'_{d0} = \sqrt{\frac{F_{d0}^2}{F_{d0}^2 + 1}} \qquad (8.69)$$

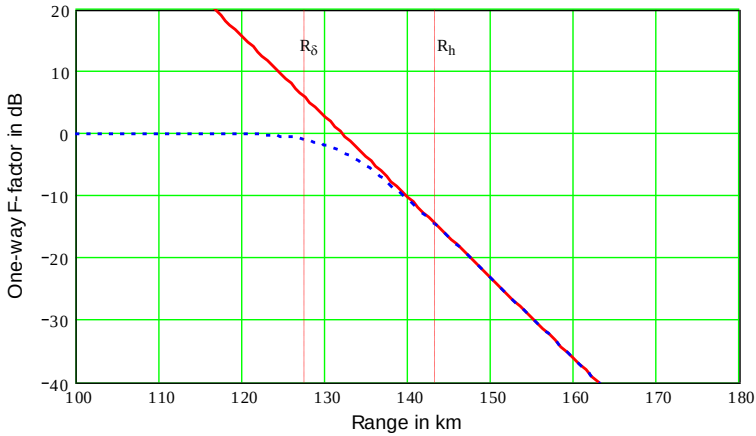

Figure 8.12 Typical one-way diffraction factor: Single-mode value F_{d0} (solid curve), adjusted factor F'_{d0} (dashed curve). Drawn for target altitude h_t = 1 km, radar altitude h_r = 10m, λ = 0.1m. The interference and diffraction regions meet at range R_δ at which $\delta = \lambda/6$, and the horizon range is R_h.

Methods have been developed using higher-order modes that yield accurate values of F_{d0} within the intermediate region without interpolation. One example is the Smooth-Earth and Knife-Edge (SEKE) program [12], which includes multiple smooth-sphere diffraction modes, along with reflection and knife-edge diffraction, to calculate the *F*-factor for arbitrary terrain profiles. A version of SEKE that runs on personal computers was created, but it is not widely available.

The pattern-propagation factor in the diffraction region is the product of F'_{d0} and the antenna pattern factor:

$$F_d = f\left(\theta_t - \theta_b\right) F'_{d0} \tag{8.70}$$

where θ_t is the target elevation angle and θ_b that of the beam axis.

8.4.2 Knife-Edge Diffraction

Land-based radars often operate at sites where the horizon is established by a discrete obstacle, as shown in Figure 8.13. The object need not have a sharp contour, because for radar wavelengths almost any surface feature diffracts as a knife-edge at low grazing angle. Trees, buildings, and even low ridges and raised ledges can establish a horizon at a masking angle above the surface of the smooth sphere. The propagation factor at this horizon is $F_{dk} = 0.5$, giving $F_{dk}^4 = -12$ dB for two-way propagation. Below the mask angle, F_{dk} drops to zero more slowly than for the smooth sphere, enabling some radars to detect targets in the shadow region. This capability is most pronounced for the longer radar wavelengths and for obstacles projecting well above the surface, but it has been exploited even at microwaves in communications systems using the *obstacle gain* of a mountain or ridge.

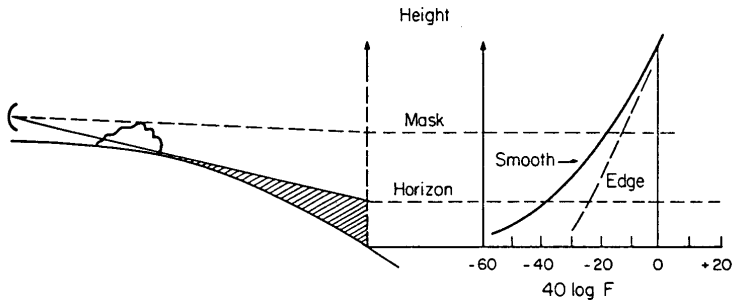

Figure 8.13 Comparison of knife-edge and smooth-sphere diffraction.

The propagation factor for knife-edge diffraction depends on the vertical distance h between the top of the obstacle and the direct path between the radar and the target (Figure 8.14). A diffraction parameter v is defined as

$$v = \sqrt{\frac{2h\theta}{\lambda}} = h\sqrt{\frac{2}{\lambda}\left(\frac{1}{d_1} + \frac{1}{d_2}\right)} \tag{8.71}$$

where θ is the elevation angle relative to the edge, h is the obstacle height above the direct path, and $d_{1,2}$ are the ground ranges from the terminals to the edge. Posi-

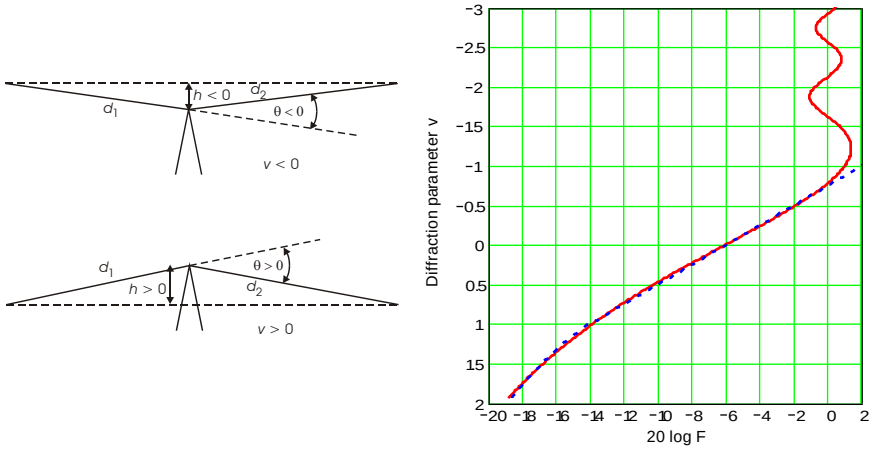

(a) Geometry of knife-edge diffraction (b) Diffraction factor F_{dk}

Figure 8.14 Knife-edge diffraction. The dashed line in (b) shows the approximation (8.73)

tive v implies a blocked path. The propagation factor for knife-edge diffraction is expressed in terms of Fresnel integrals as

$$F_{dk}(v) = \frac{1}{\sqrt{2}}\left|C(v) - 0.5 + j\left[S(v) - 0.5\right]\right| \tag{8.72}$$

where $C(v) = \int_0^v \cos\left(\pi t^2/2\right) dt$ and $S(v) = \int_0^v \sin\left(\pi t^2/2\right) dt$

Approximations to F_{dk} can be written

$$\begin{aligned} 20\log F_{dk}(v) &= -(6 + 8v), \quad -1 < v < 1 \\ 20\log F_{dk}(v) &= -\left[11.1 + 20\log\left(\sqrt{v^2+1} + v\right)\right], \quad v \geq 1 \end{aligned} \tag{8.73}$$

Obstacle gain occurs when this factor is greater than the corresponding value for smooth-sphere diffraction in the absence of the obstacle. However, it is important to establish that the top of the obstacle is in a free-space field. For example, Figure 8.15 shows a typical diffraction situation with an isolated obstacle. In this case, the extra path length for reflections from the terrain between the radar and the obstacle is δ_0 = 0.6m, and knife-edge diffraction should be used describe the fields beyond the obstacle when $\lambda < 6\delta_0$. For longer wavelengths or lower antenna or obstacle heights, the top of the obstacle would not be fully illuminated,

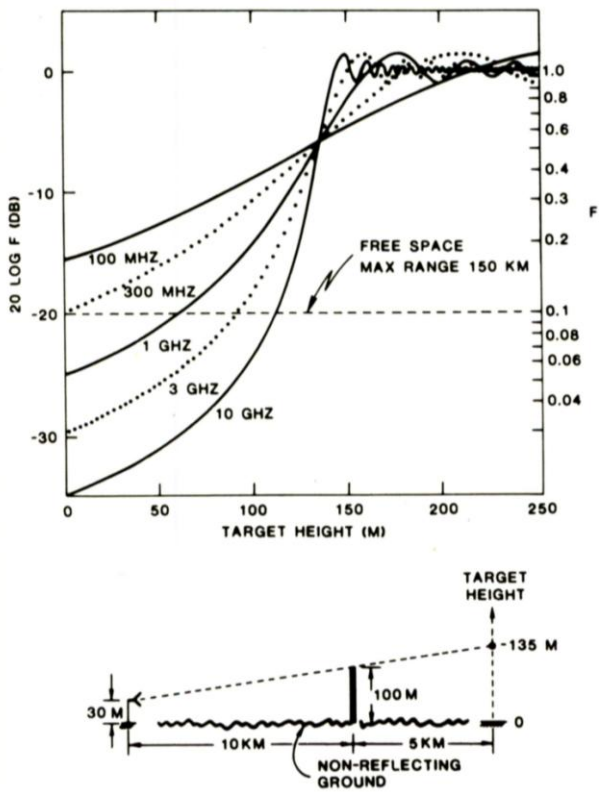

Figure 8.15 Example of knife-edge diffraction. (From: [3, p. 31]. © 1982, Artech House. Reprinted with permission.)

and the contribution of the knife edge to F_{dk} would be reduced by reflection-interference or smooth-sphere diffraction from the intervening terrain.

The obstacle need not be visibly sharp to qualify as a "knife edge" for diffraction purposes. Analysis of diffraction over cylinders of different radii shows that the diffraction field is essentially at its knife-edge value when the radius of curvature r of the obstacle meets the criterion

$$r < 0.0024\sqrt{d_2^3/\lambda} \tag{8.74}$$

where d_2 is the shorter of the two paths to the obstacle, and all lengths are in meters. For the example shown in Figure 8.16, the radius of curvature of the obstacle can be as great as 4.9 km (for X-band) or 1.8 km (for L-band) without significantly reducing the fields produced at a target masked by the obstacle.

The pattern-propagation factor F_d for knife-edge diffraction is $F_i F_{fk}$, where F_i is the interference factor that establishes the field at the top of the obstacle. The interference factor is discussed in the following section, but the criterion for full illumination of the knife edge can be expressed as an obstacle with height above the average surface exceeding

$$h_{\min} \approx \sqrt{\lambda d_1} \tag{8.75}$$

For X-band radar this corresponds to a height $h_{\min}$ = 17m at d_1 = 10 km, which is a reasonable minimum value for a path near the horizon.

8.5 THE INTERFERENCE REGION

In the interference region there is an unobstructed line of sight between the radar and the target, with enough clearance above the surface that diffraction effects are negligible. This clearance corresponds to a pathlength difference δ between the direct and reflected rays that exceeds $\lambda/6$. The interference F-factor, including the divergence factor, is given by (8.9), and substitution of the more complicated expression (8.60) for strong diffuse reflections is seldom necessary.

A plot of F_i as a function of range for a typical case is shown in Figure 8.16, where the target is flying at an altitude h_t = 1 km over a bare land surface with roughness σ_h = 1m, and a broad elevation beam is assumed. Two dashed vertical lines identify the intermediate region that extends from R_δ = 128 km to R_h = 143.5 km. The sharp increase near R_h results from applying the divergence factor, but as

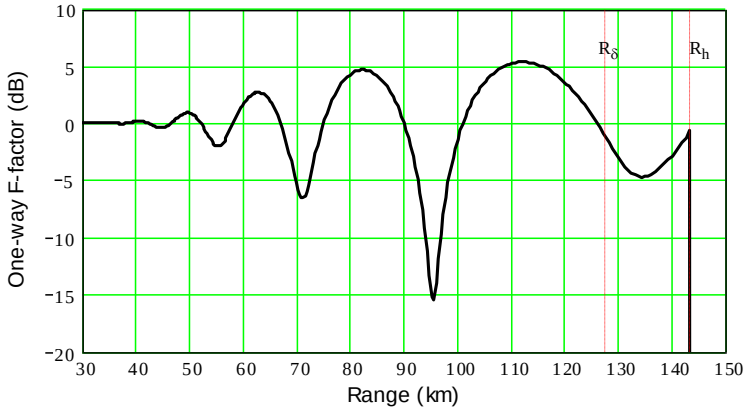

Figure 8.16 Typical one-way F_i for target altitude h_t = 1 km, radar altitude h_r = 10m, λ = 0.1m, surface roughness σ_h = 1m. The upturn near the horizon results from the divergence factor.

will be shown in Section 8.6.1 this will not affect the end result. The decay of the lobing structure for short ranges results from the reduction in the specular scattering coefficient as grazing angle increases. For smooth surfaces without vegetation, these lobes would continue to peak at +6 dB until reduced by the shaped antenna pattern. Rougher surfaces tend to limit the reflection effects to the initial lobe shown here at ≈ 115 km.

8.6 THE INTERMEDIATE REGION

Unless a multiple-mode diffraction model is used, the *F*-factor for the intermediate region must be estimated by interpolation between the interference and diffraction values. Fishback in [2, pp. 125–129] states that

> To determine the field strength in this region, it is necessary to prepare a plot of field strength as a function of distance for given terminal heights, extending the plot from the region in which interference-region methods are valid through the intermediate region into the region of validity for diffraction methods by bold interpolation.

To define the region, it is necessary first to solve for the range R_δ at which the pathlength difference between the direct and reflected paths reaches λ/6. At that point, the direct and reflected fields are 120° out of phase, and the interference *F*-factor is approximately unity. An accurate spherical-Earth model must generally be used for calculation R_δ, requiring either graphical or root-finding methods, based on (8.42)–(8.46). The solution for the horizon range R_h is more straightforward:

$$R_h = \sqrt{2k_e a_e}\left(\sqrt{h_r} + \sqrt{h_t}\right) \tag{8.76}$$

8.6.1 *F*-Factor as a Function of Target Range

One method for interpolation is to calculate the interference and diffraction factors $F_{i\,\mathrm{dB}}(R_\delta) = 20\log F_i(R_\delta)$ and $F_{d\,\mathrm{dB}}(R_h') = 20\log F_d(R_h')$ in decibels, and connect them with a straight line. This is done by applying a weight x to the diffraction factor and $1 - x$ to the interference factor in the intermediate region:

$$x = \left(\frac{R - R_\delta}{R_h' - R_\delta}\right)^{1+0.2\lambda} \tag{8.77}$$

$$
\begin{aligned}
F_{\mathrm{dB}}(R) &= F_{i\mathrm{dB}}(R), \quad R \le R_\delta \quad \text{(interference region)} \\
&= (1-x)\, F_{i\mathrm{dB}}(R_\delta) + x\, F'_{d\,0\,\mathrm{dB}}(R'_h), \quad R_\delta < R < R_h \\
&= F_{d\,0\,\mathrm{dB}}(R), \quad R_h \le R \quad \text{(diffraction region)}
\end{aligned}
\tag{8.78}
$$

The interference factor $F_i(R)$ is calculated by substituting in (8.9) the target elevation angle θ_t as a function of R from (8.47). An example for the same target trajectory as in Figures 8.14 and 8.18 is shown in Figure 8.17. Note that the effect of the divergence factor has been eliminated by the interpolation process, which gives heavy weight to F_d as range approaches R_h.

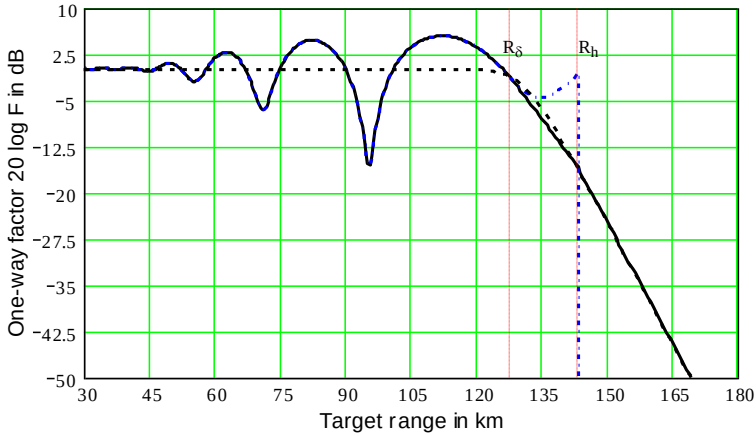

Figure 8.17 Typical one-way F for geometry used in preceding plots: interference factor (dash-dot line), diffraction factor (dashed line), interpolated result (solid line). Note that the effect of the divergence factor is eliminated.

This interpolation method is somewhat less satisfactory when used with a VHF radar, as shown in Figure 8.18. The F-factor of the interpolated curve is probably below that which would be obtained from a more accurate multimode diffraction model without interpolation. However, the curve does capture the essential difference between microwave and VHF propagation, showing an extended intermediate region with F going below unity at much shorter range (higher elevation), but falling more slowly as range increases into the diffraction region.

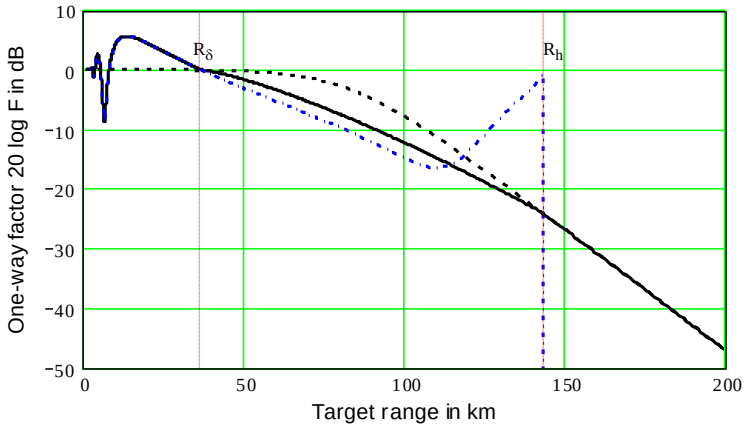

Figure 8.18 Typical one-way *F* for VHF radar, λ = 3m, with geometry used in preceding plots: interference factor (dash-dot line), diffraction factor (dashed line), interpolated result (solid line).

8.6.2 *F*-Factor as a Function of Altitude

A second method of presenting *F* is to plot it as a function of target altitude h_t at a selected constant range *R*. The interpolation procedure here differs from that for the constant-altitude target trajectory, in that the weighting factor *y* is based on altitude:

$$y = \left(\frac{h_\delta - h_t}{h_\delta - h_0} \right)^{1.5} \tag{8.79}$$

where h_δ is the altitude that results in δ = λ/6 at range *R*, and h_0 is the altitude at which the target reaches the horizon. The weighting is used in interpolation between F'_d at h_0 and F_i at h_δ:

$$\begin{aligned} F_{\mathrm{dB}}(h_t) &= F'_{d\,\mathrm{dB}}(h_t), \quad h_t \le h_0 \qquad \text{(diffraction region)} \\ &= (1-y)\,F_{i\,\mathrm{dB}}(h_\delta) + y\,F'_{d\,\mathrm{dB}}(h_0), \quad h_0 < h_t < h_\delta \\ &= F_{i\,\mathrm{dB}}(h_t), \quad h_\delta < h_t \qquad \text{(interference region)} \end{aligned} \tag{8.80}$$

The functions $F'_d(h_t)$and $F_i(h_t)$ are found for the selected range *R* by varying h_t in (8.68) and (8.47). Figure 8.19 shows the result, which is the height-gain factor at

range *R*. This presentation shows the very rapid reduction in signal power as the target drops below the horizon.

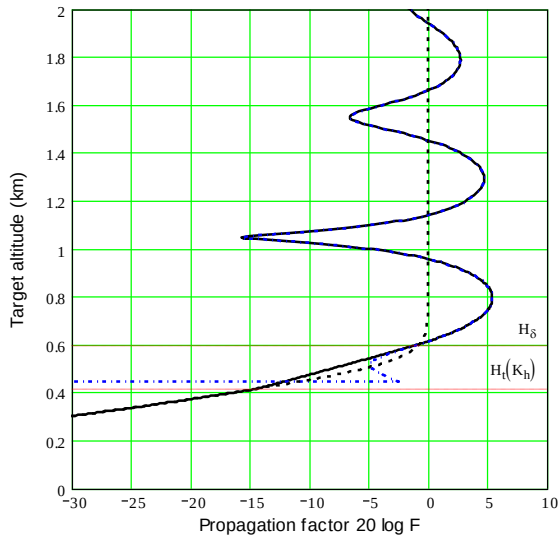

Figure 8.19 One-way *F* as a function of altitude at *R* = 100 km, radar altitude h_r = 10m, λ = 0.1m, surface roughness σ_h = 1m: interference factor (dash-dot line), diffraction factor (dashed line), interpolated result (solid line).

8.6.3 Vertical-Plane Coverage Plots

For search radars, the desired output is usually a plot showing the contour of coverage in the vertical plane, sometimes called a *range-height-angle plot*. An example was shown in Figure 1.6.

8.6.3.1 Approximate Method of Creating Coverage Plot

An approximation of the coverage chart can be prepared from the maximum free-space detection range R_0 given by the Blake chart (Figures 1.1, 1.2) with the target elevation angle θ_t on the beam axis:

$$f\left(\theta_t - \theta_b\right) = f\left(0\right) = 1$$

Calculations of range for elevation angles to be covered by the plot are calculated from this as

$$R'(\theta_t) = R_0 F(\theta_t), \quad 0 \le \theta_t \le \theta_{t\max} \tag{8.81}$$

The imposes the lobing structure of the *F*-factor on the plot. These values may then be adjusted for atmospheric attenuation that varies with R' and θ_t as shown in Chapter 7, using the one- or two-step iterative method of the Blake chart.

8.6.3.2 Accurate Method of Creating Coverage Plot

A more accurate coverage chart is produced using (1.26), which includes not only the *F*-factor and atmospheric attenuation for each elevation angle but also range variation in the detectability factor D_x and in the factor F_{rdr} that contains the lens factor, along with sensitivity time control, eclipsing, and other factors.

The procedure for computer generation of the accurate coverage chart, once radar and environmental parameters have been specified in sufficient detail, is as follows:

- A maximum range of calculation $R_{c\max}$ is established that exceeds the detection range of the peak lobe in the coverage;
- A set of ranges R_{ci} is established that that covers 0–$R_{c\max}$ at intervals δ_R that produce smooth plotted curves:

$$\begin{aligned} R_{ci} &= R_{c\max} - i\delta_R, \quad i = 0,1,2,\cdots,i_{\max}-1 \\ i_{\max} &= \frac{R_{c\max}}{\delta_R} \end{aligned} \tag{8.82}$$

  (calculations at $R_c = 0$ are excluded to avoid division by zero);

- A set of target elevation angles θ_{tj} is established that covers the desired sector with intervals δ_θ that produce smooth plotted curves:

$$\begin{aligned} \theta_{tj} &= j\delta_\theta, \quad j = 0,1,2,\cdots, j_{\max} \\ j_{\max} &= \frac{\theta_{t\max}}{\delta_\theta} \end{aligned} \tag{8.83}$$

- For each θ_{tj}, the available and required signal-to-noise energy ratios $(E/N_0)_{i,j}$ and D_{xi} are calculated, and range R_{cx} is identified at which $(E/N_0)_{i,j} > D_{xi,}$;
- Interpolation between $R_{cx-1}$and R_{cx} gives the range R_{mj} at which the requirement $(E/N_0)_{i,j} = D_{xi,}$ is met;

- The process is repeated to cover all elevation angles up to $\theta_{tj\max}$;
- For each θ_{tj} the altitude h_{t1} above the plane tangent to the surface at the radar site is calculated:

$$\left(h_{t1}\right)_j = \left(R_m\right)_j \sin\left(\theta_t\right)_j \tag{8.84}$$

- The continuous coverage envelope is plotted in rectangular coordinates R_m, h_{t1};
- A set of lines at ranges is overlaid on the coverage envelope at convenient intervals out to $R_{c\max}$;
- A second set of lines is overlaid at constant altitude intervals δ_h above the spherical Earth, where

$$h = k\delta_h - \frac{R^2}{2k_e a_e}, \quad k = 0,1,2\ldots \tag{8.85}$$

- An optional feature of some coverage charts is a plot of the free-space coverage, varying as a function of the elevation pattern of the antenna.

Figure 8.20 shows an example of a computer-generated coverage chart using [13].

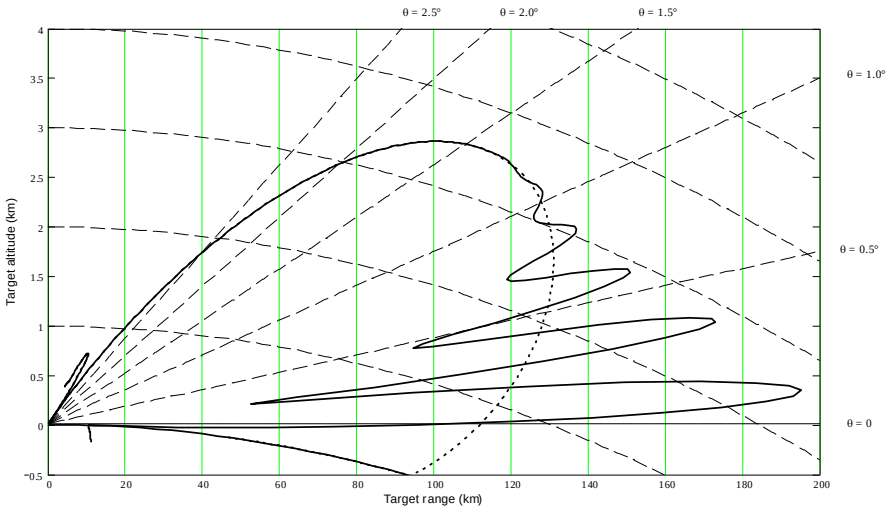

Figure 8.20 Example of coverage chart for low-altitude surveillance radar: coverage with *F*-factor (heavy solid line), free-space coverage (heavy dashed line).

This format, in which slant range is the ordinate and altitude above the tangent plane is the abscissa, is more convenient for plotting than that used by Blake, in which the ordinate is ground range and lines of constant slant range curve inwards at high altitude. The latter format, described in [14], preserves the shape of the coverage contour when the plotted coverage extends to altitudes comparable to the slant range.

8.7 SUMMARY OF PATTERN-PROPAGATION FACTOR

The interference factor F_i expresses the magnitude of the vector sum of the direct ray and a ray reflected from the Earth's surface, and is applicable to targets to which the path has adequate clearance above the surface. In the interference region, where adequate clearance exists, the pathlength difference δ between the direct and reflected rays is greater than $\lambda/6$.

The smooth-sphere diffraction factor F_{d0} expresses the magnitude of the field on the path to a target that lies below the horizon, and is applicable to targets beyond the horizon range given, for a path that does not encounter an obstacle that rises significantly above the surface, by

$$R_h = \sqrt{2k_e a_e}\left(\sqrt{h_r} + \sqrt{h_t}\right) \tag{8.86}$$

In the diffraction region, field is greater than zero but drops rapidly below that of the free-space path to the horizon range.

The knife-edge diffraction factor F_{dk} expressed the magnitude of the field beyond an obstacle that extends above the smooth spherical surface enough to form a horizon at range less than R_h. The criteria for such an obstacle are a radius of curvature less than that given by (8.74) and a height greater than that given by (8.75). The field beyond the obstacle exceeds that given by smooth-sphere diffraction at the same range.

In the intermediate region, where a line-of-sight direct path exists but has inadequate clearance from the surface, the field can be approximated by interpolation between the diffraction and interference fields.

A plot of the F-factor as a function of range, for a given target trajectory (e.g., constant altitude), exposes the nature of propagation condition as the target moves through the three regions: interference, intermediate, and diffraction. If the free-space factor R^{-4} is combined with the F-factor, the plot serves as the basis for graphical solution of the range equation, as was shown in Figures 1.3–1.5. A plot of the F-factor as a function of target altitude for a given range, as shown in Fig-

ure 8.21, provides a means of exploring details of the low-altitude propagation effects.

The most useful method of presenting surveillance radar coverage is the range-height-angle plot shown in Figure 8.22. Data for such plots can be assembled with relatively simple calculations based on the Blake chart, but today are more easily obtained by computer programs such as [13] or [14].

References

[1] Norton, K. A. and Omberg, A. C., "The Maximum Range of a Radar Set," *Proc. IRE*, Vol. 35, No. 1, January 1947, pp. 4–24.

[2] Kerr, D. E. (ed.), *Propagation of Short Radio Waves*, Vol. 13 in MIT Radiation Laboratory Series, New York: McGraw-Hill, 1951. Reprinted (CD ROM edition), Norwood, MA: Artech House, 1999.

[3] Blake, L. V., *Radar Range-Performance Analysis*, Lexington, MA: D. C. Heath, 1980; Dedham, MA: Artech House, 1986.

[4] Saxton, J. A. and Lane, J. A., "Electrical Properties of Sea Water," *Wireless Engineer*, Vol. 29, 1952, pp. 269–275.

[5] Montoya, T. P. and Smith, G. S., "Land Mine Detection Using a Ground-Penetrating Radar Based on Resistively Loaded Vee Dipoles," *IEEE Trans. on Antennas and Propagation*, Vol. 47, No. 12, December 1999, pp. 1795–1806 .

[6] Beckmann, P. and Spizzichino, A., *The Scattering of Electromagnetic Waves from Rough Surfaces*, London: Pergamon Press, 1963; reprinted, Norwood, MA: Artech House, 1987.

[7] Beard, C. I., "Coherent and Incoherent Scattering of Microwaves from the Ocean," *IRE Trans. on Antennas and Propagation*, Vol. AP-9, No. 2, April 1961, pp. 470–483.

[8] Barton, D. K., *Modern Radar System Analysis*, Norwood, MA: Artech House, 1988.

[9] Blake, L. V., "Reflection of Radio Waves from a Rough Sea," *Proc. IRE*, Vol. 38, No. 3, March 1950, pp. 301–304.

[10] Cornwell, P. E. and Lancaster, J., "Low Altitude Tracking over Rough Surfaces II: Experimental and Model Comparisons," *IEEE Eascon-79*, Washington, DC, October 9–11, 1979, pp. 235–248.

[11] Barton, D. K., *Radar System Analysis and Modeling*, Norwood, MA: Artech House, 2005.

[12] Ayasli, S., "SEKE: A computer model for low altitude radar propagation over irregular terrain," *IEEE Trans AP-34*, No. 8, Aug 1986, pp. 1013–1023.

[13] Barton, D. K., *Modern Radar System Analysis Software and User's Manual, Version 3.0*, Norwood, MA: Artech House, 2007.

[14] Blake, L. V., "Machine Plotting of Radio/Radar Vertical-Plane Coverage Diagrams," *Naval Research Laboratory Report 7098*, Washington, DC: Gov't. Printing Office, June 1970.

CHAPTER 9

Clutter and Signal Processing

Chapter 3 presented radar equations for the maximum detection range when clutter and jamming add to the interference created by thermal noise. In those equations, the effective spectral density of interference I_{0e} used in the equations is the sum of the densities of thermal noise, clutter, and jamming. In this context, *effective* refers to the density of white Gaussian interference that would have the same effect on detection probability as does the actual interference component, for which the spectral density may be uneven and the amplitude probability density function may be broader than the normal distribution.

This chapter presents models of surface, volume, and discrete clutter for use in determining their energy levels at the receiver input and the extent of their statistical departures from white, Gaussian noise, as functions of range from the radar. The models are general in nature. References are provided to literature discussing in greater detail the peculiarities of different types of clutter, from which more refined models can be constructed as necessary and as justified by knowledge of a particular environment.

Most radars incorporate some type of special signal processing designed to minimize the clutter at the output to display or detection circuits. The effect of such circuits is included in the radar equations of Chapter 3 through the clutter improvement factor I_m, for which calculation methods are discussed here in Section 9.6.

9.1 MODELS OF SURFACE CLUTTER

9.1.1 Clutter Cross Section and Reflectivity

The geometry of surface clutter as observed by the mainlobe of a radar sited on or above the surface is discussed in Section 3.3. The radar cross section is given by

the product of the area A_c of the surface within the radar resolution cell and the intrinsic surface clutter *reflectivity* σ^0:

$$\sigma_c = A_c \sigma^0 \tag{9.1}$$

where the area A_c is given by (3.18).

The reflectivity is best modeled as the product of a *intrinsic clutter reflectivity* γ and the sine of the local grazing angle ψ with which the radar ray reaches the surface:

$$\sigma^0 = \gamma \sin \psi \tag{9.2}$$

This *constant-*γ model is generally applicable when combined with a clutter propagation factor discussed in Section 9.1.2, and when ψ is not near 90°. The reflectivity described by (9.1) and (9.2) results from interaction of the radar ray with small-scale surface features that scatter a small fraction of the incident wave back to the source. To describe the persistence of clutter as $\psi \to 0$, a small constant value in the order of 10^{-6} is sometimes added to (9.2), or an increment 0.0001 rad is added to the grazing angle ψ, as in [1, p. 405]. The equations are inapplicable to scattering from surfaces that support specular reflection back toward the radar, such as discrete clutter from some manmade objects, as discussed in Section 3.5, or surface clutter viewed near vertical incidence.

Sea and land surfaces also produce a specular reflection component when viewed near vertical incidence, where a facet component σ_f^0 must be added to σ^0 to account for quasi-specular reflection from surface facets [2, p. 108, Eq. (3.32)]:

$$\sigma_f^0(\beta) = \frac{\rho_0^2 \rho_v^2}{\beta_0^2} \exp\left(-\frac{\beta^2}{\beta_0^2}\right) \tag{9.3}$$

where

ρ_0 = Fresnel reflection coefficient (see Section 8.3.1);
ρ_v = vegetation factor (see Section 8.3.3);
β = $(\pi/2) - \psi$ = slope of facet giving specular reflection;
β_0 = $\sqrt{2}$ times the rms slope of the surface

The facet angle β that gives specular reflection is equal to the angle from vertical at which the facet is observed. Values of β_0 for typical sea and land surfaces are in the order of 0.05 rad, so for the sea and bare land surfaces for which $\rho_0 \rho_v \approx 1$ the facet component has a sharp peak of magnitude $\approx 1/\beta_0^2$ and angular width $\approx \beta_0$

centered at $\psi = \pi/2 = 90°$. This will be illustrated in graphs of reflectivity for sea and land surfaces in Sections 9.2.2 and 9.3.1.

Most measured data do not show the large peak value predicted by (9.3), because the beamwidth of the measuring antenna observes the surface over an angle sector approaching or exceeded β_0, averaging the measured σ^0 over angles beyond the narrow quasi-specular lobe. Convolution of the measuring beamwidth θ_3 with the facet slope deviation leads to the expression for the product of measured reflectivity and the pattern-propagation factor F_c^4 (discussed further in the next section, but in this case representing the results of integration over the antenna pattern) [2, p. 109, Eq. (3.23)]:

$$\sigma_f^0 F_c^4 = \frac{\rho_0^2 \rho_v^2}{\beta_0^2 + 0.36\theta_3^2} \exp\left(-\frac{\beta^2}{\beta_0^2 + 0.36\theta_3^2} \right) \tag{9.4}$$

This equation also applies to prediction of clutter at near vertical incidence for a radar with beamwidth θ_3.

9.1.2 Surface Clutter Pattern-Propagation Factor

When the path between radar and clutter departs from free-space conditions, radar equations for clutter, such as (3.4), require the inclusion of the clutter pattern-propagation factor F_c and the atmospheric attenuation $L_{\alpha c}$ on the two-way path.[1] The departures from free-space propagation that enter F_c include interference between the direct ray and rays reflected in the forward direction from the surface beneath the path, and diffraction on paths near the surface. For simplicity, it is normally assumed that the antenna pattern terms in (8.9) and (8.10) for direct and reflected rays the interference region are equal. This permits the following discussions to treat a *clutter propagation factor* that will be denoted by F_c', separating the antenna pattern factor $f(-\theta_r - \theta_b)$ in the direction of the surface as a term to be applied for a specific radar and its beam elevation angle.

Measurements of surface clutter reflectivity are actually measurements of the product $\sigma_c F_c^4$. Hence the values of F_c^4 applicable to the measurement geometry and antenna must be known if σ^0 is to be modeled for use with other radars and paths. In order to interpret the measured data on which the models Sections 9.2–9.4 are based, it will be assumed that antenna pattern effects were taken into account in calculating the reported reflectivity, and that the quantity reported as σ^0 is actually the product $\sigma_c F_c'^4$, except in rare instances where F_c' is specifically addressed as a separate factor.

---

[1] Blake in [2, p. 27, Eq. (1.44)] notes that "the factor F_c^4 has been omitted because by convention it is included in the evaluation of σ^0." It is considered here as a separate factor.

Five regions for surface clutter measurement and modeling may be identified, based on the range from the radar. In order of increasing range, these are:

- Zenith region (from airborne radar), where (9.3) or (9.4) applies;
- Near region[2], $R < R_1$, where a clear path exists and $F_c' \approx 1$;
- Interference region, $R_1 < R < R_\delta$, where reflections interfere with the direct ray;
- Intermediate region, $R_\delta < R < R_h$, where both interference and diffraction are applicable;
- Diffraction region, $R_h < R$, where diffraction is dominant.

Figure 9.1 shows the geometry of a surface-based radar viewing clutter from the last four of these regions (the first being applicable only to airborne radars).

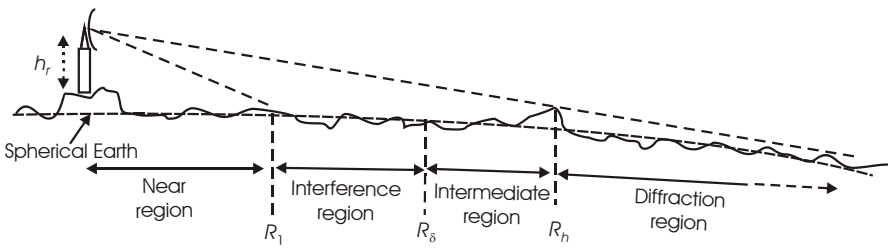

Figure 9.1 Surface-clutter propagation regions for surface-based radar.

The transition between near and interference regions takes place at range R_1, where

$$\psi_c = \frac{\lambda}{4\pi\sigma_h} = \frac{h_r'}{R_1} - \frac{R_1}{2k_e a_e}, \quad \text{or}$$
$$\frac{R_1^2}{2k_e a_e} + \frac{\lambda R_1}{4\pi\sigma_h} - h_r' = 0 \tag{9.5}$$

Solving the quadratic equation for R_1 we find

[2] Blake refers to this as the *plateau region*, but the plateau has a well defined slope in which σ^0 is proportional to the grazing angle.

$$R_1 = \frac{k_e a_e \lambda}{4\pi\sigma_h}\left[\sqrt{1+\frac{2h_r'}{k_e a_e}\left(\frac{4\pi\sigma_h}{\lambda}\right)^2}-1\right] \approx \frac{4\pi h_r'\sigma_h}{\lambda} \tag{9.6}$$

where $h_r' = h_r + 2\sigma_h$ is the antenna phase-center height above the average surface, h_r is the phase-center height above the surface beneath the antenna, and that surface is assumed to be $2\sigma_h$ above the average. The approximation applies for a flat-Earth model, which is often adequate for low-sited radar:

$$\frac{h_r'}{R_1} >> \frac{R_1}{2k_e a_e} \tag{9.7}$$

At range R_1, the ray reaches the surface at the *critical grazing angle* given by[3]

$$\psi_c = \sin^{-1}\frac{\lambda}{4\pi\sigma_h} \tag{9.8}$$

At the critical angle the specular scattering coefficient ρ_s defined in (8.57) is 0.607 and the reflected power ρ_s^2 is $1/e$ times that for a smooth surface.

Where the depression angle θ to the surface clutter rather than the range is known, the grazing angle can be calculated from [3, p. 312, Eq. (7.34)]:

$$\psi = \cos^{-1}\left(\frac{k_e a_e + h_r'}{k_e a_e}\cos\theta\right) \tag{9.9}$$

Figure 9.2 shows the propagation factor for the near and far regions, for X- and L-band radars with σ_h = 1m. Just within the transition range, a reflection lobe begins to form, but disappears at shorter ranges as ρ_s is reduced by the higher grazing angle. The full expression for the clutter propagation factor in these two regions is derived from (8.9), setting the antenna pattern terms $f(\theta)$ to unity:

$$F_c' = \sqrt{1+\rho^2+2\rho\cos\alpha} \tag{9.10}$$

A close approximation for F_c is shown by the dashed lines:

[3] Blake gives this as $\sin^{-1}(\lambda/5h_{av}) = \sin^{-1}(\lambda/13\sigma_h)$, essentially the same as (9.8).

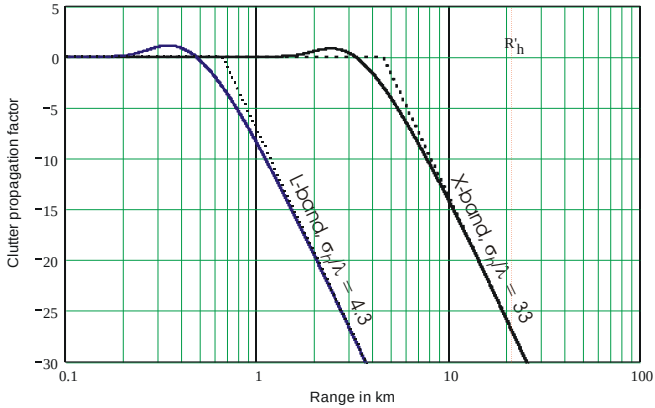

Figure 9.2 Clutter propagation factor F_c' (solid line), and approximation (dashed line) for near and interference regions. Drawn for σ_h = 1m, h_r = 10m, λ = 0.03m, for which R_1 = 4.5 km, ψ_c = 0.14°; and λ = 0.23m, for which R_1 = 0.65 km, ψ_c = 1.0°; and $\rho_0\rho_v$ = 1. The horizon range R_h = 21.5 km.

$$\begin{aligned} F_c' &\approx 1, \qquad R < R_1 \\ &\approx R_1/R, \quad R_1 < R \end{aligned} \tag{9.11}$$

The integrated area under $F_c'^4$ for the approximation exceeds the more exact value by ≈ 10%, indicating that clutter energy estimates using the approximation would exceed the exact values by about 0.4 dB.

The transition between the far and intermediate regions, where the influence of diffraction begins, occurs at range R_δ given by

$$R_\delta = \frac{k_e a_e \lambda}{12 h_c}\left[\sqrt{1+\frac{2h_r'}{k_e a_e}\left(\frac{12h_c}{\lambda}\right)^2}-1\right] \tag{9.12}$$

where $h_c \approx 3\sigma_h$ is the height of significant clutter scatterers above the average surface. For the conditions illustrated in Figure 9.2, R_δ = 8.9 km at X-band and 1.8 km at L-band. The curves for F_c' will begin to deviate from the interference value beyond those ranges, as will be shown below.

Both smooth-sphere and knife-edge diffraction must be considered for ranges beyond R_δ. The diffraction equations (8.63)–(8.75) are applied, substituting h_c for h_t, unless the horizon is established by an obstacle rising above the average surface by at least h_{min}, as given by (8.75). A random rough surface may also meet the knife-edge criterion if the rms roughness is large enough:

$$3\sigma_h > \sqrt{R_h \lambda} \tag{9.13}$$

For the conditions illustrated in Figure 9.2 this would require σ_h > 13m for X-band and 35m for L-band. For knife-edge diffraction, (8.71)–(8.75) are used, substituting h_c for h_t.

Figure 9.3 shows the effect of transition to smooth-sphere diffraction beyond R_δ for the conditions used in Figure 9.2. The diffraction term causes a slight increase in the propagation factor in the intermediate region, followed by a steeper decrease near and beyond the horizon. The two-segment approximation (9.11) and the full expression (9.10) for the near and interference regions are generally adequate within the horizon range but give overestimates beyond the horizon.

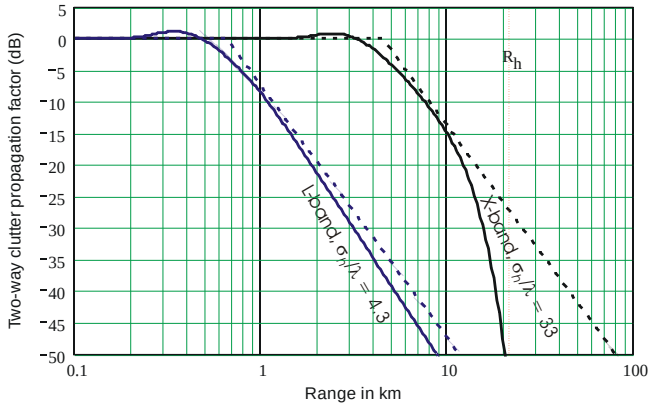

Figure 9.3 Clutter pattern-propagation factor (solid line) and approximation (dashed line) from (9.11), for near, interference, intermediate, and diffraction regions. Drawn for σ_h = 1m, h_r = 10m, λ = 0.03m, and λ = 0.23m, and $\rho_0\rho_v$ = 1. The horizon range R_h = 21.5 km.

There are situations in which surface clutter from antenna sidelobes causes interference that is not expressed by (9.1) using the area A_c from (3.18). The area occupied by sidelobes in the hemisphere forward or to the rear of the antenna aperture is

$$A_{cs} = \pi R_c \frac{\tau_n c}{2} \sec\psi \quad \text{m}^2 \tag{9.14}$$

A separate calculation of sidelobe clutter is necessary in order to evaluate the applicable improvement factor, which may differ from that of mainlobe clutter.

Within the forward hemisphere the pattern-propagation factor is the product of the two-way sidelobe level and the clutter propagation factor:

$$F_c^4 = f_{tsf}^2 f_{rsf}^2 F_c'^4 = \frac{G_{t_{sf,\,\mathrm{iso}}} G_{r_{sf,\,\mathrm{iso}}}}{G_t G_r} F_c'^4 \tag{9.15}$$

where f_{tsf} and f_{rsf} are the rms voltage gains of transmitting and receiving sidelobes in the forward hemisphere, and $G_{tsf,\,\mathrm{iso}}$ and $G_{tsf,\,\mathrm{iso}}$ are the corresponding forward-hemisphere power gains relative to an isotropic antenna. For the rear hemisphere, (9.15) is used with backlobe levels replacing forward sidelobe levels.

The clutter contributions from sidelobes are generally much smaller than those of the mainlobe, but become important when one or more of the following conditions is encountered:

- The mainlobe, for the range considered, does not illuminate the surface;
- The mainlobe clutter has a Doppler shift that allows it to be reduced by a larger improvement factor than can be obtained at the Doppler shift of sidelobe clutter;
- The two-way sidelobe gain ratio represented by the factors multiplying $F_c'^4$ in (9.15) exceeds $\approx 0.1\theta_a/\pi$.
- The sidelobes reach the surface at ranges less than does the mainlobe.

The second and last of these conditions are often encountered in airborne radar operating at medium or high PRF [2, pp. 245–248], extending clutter broadly across the blind-speed intervals $v_b = if_r\lambda/2$, where i is an integer.

9.1.3 Spectral Properties of Surface Clutter

The shape of the clutter spectrum affects the radar equation in two ways:

- The improvement factor I_m, which expresses the reduction in clutter energy as it passes through the signal processor, is critically dependent on the shape of the clutter input spectrum;
- The clutter detectability factor (see Section 3.2.3), which adjusts the radar equation for correlation of clutter samples at the output of the signal processor, is sensitive to the product of input spectral density and processor response function.

Measurements of the clutter spectrum of sea clutter are reported in [4, p. 579] as "roughly Gaussian in shape." Similar measurements on land clutter from wooded sites showed a deviation from Gaussian shape, but including also a steady component represented by an impulse function at zero velocity.

A Gaussian spectrum was assumed as the basis for calculating clutter effects in the early paper by Barlow [5] on CW radar:

$$W(f) = W_0 \exp\left(-a\frac{f^2}{f_0^2}\right) \tag{9.16}$$

where W_0 is the power density in W/Hz at the carrier frequency, f is the Doppler shift, f_0 is the carrier frequency, and a is a dimensionless width parameter of the clutter. Setting $a = c^2/8\sigma_{vc}^2$ and allowing for possible nonzero mean velocity v_0, this can be expressed is the power density in velocity:[4]

$$W(v) = \frac{C}{\sqrt{2\pi}\sigma_v}\exp\left[-\frac{(v-v_0)^2}{\sigma_{vc}^2}\right] \quad \frac{\text{W}}{\text{m/s}} \tag{9.17}$$

where σ_{vc} is the standard deviation in clutter velocity in m/s and C is the clutter power in W. The mean velocity can be the result of observation from a moving platform, or wind effect on a sea surface. Values of the half-power spectral widths reported in [4] and subsequent works are discussed in the following sections for different types of clutter.

Use of the Gaussian form for the intrinsic clutter spectrum is convenient, because it is easily combined with components of spread caused by radar parameters. These several components are:

- The antenna scan modulation component. A scanning radar beam modulates the echo with the one-way voltage pattern function given by (5.3), which becomes a two-way power function of time t:

$$f(t) = \exp\left(-8\ln 2\frac{\omega_s^2 t^2}{\theta_3^2}\right) \tag{9.18}$$

  where ω_s is the scan rate in rad/s and θ_3 is the beamwidth in the scanned coordinate in rad, and the Gaussian beamshape approximation is assumed. Transformed into frequency and converted to a velocity spectrum, this gives a Gaussian velocity spectral component with standard deviation given by

$$\sigma_{va} = \frac{\sqrt{\ln 2}\omega_s\lambda}{2\pi\theta_3} = 0.133\frac{\omega_s w}{K_\theta} \quad \text{m/s} \tag{9.19}$$

[4] We express the clutter spectrum in velocity because it is an inherent property of the clutter scatterers, independent of the radar frequency.

where $K_\theta = w\theta_3/\lambda \approx 1.2$ is the beamwidth constant in rad and w is the width in m of the aperture in the scan plane. Thus the velocity spread is directly proportional to the velocity of the edge of a mechanically scanning aperture, or the rate of change of phase shift for electronic scanning.

- The beamwidth component. A mean velocity v_0 of clutter relative to the radar introduces another spread component of clutter with standard deviation[5]

$$\sigma_{v\theta} = \frac{v_0\theta_3}{4\sqrt{\ln 2}}\sin\beta = 0.300\, v_0\theta_3 \sin\beta \quad \text{m/s} \tag{9.20}$$

where β is the angle between the beam axis and the relative velocity vector.

When the intrinsic clutter spectrum is Gaussian, the over-all velocity spread is found as the rss sum of the three components:

$$\sigma_v = \sqrt{\sigma_{vc}^2 + \sigma_{va}^2 + \sigma_{v\theta}^2} \tag{9.21}$$

If a zero-velocity (DC) impulse is included in the spectrum for land clutter, it spreads into a Gaussian component having the power of the impulse, with spread σ_{v0} given by

$$\sigma_{v0} = \sqrt{\sigma_{va}^2 + \sigma_{v\theta}^2} \tag{9.22}$$

The total spectrum of the clutter is the sum of a narrow Gaussian components containing the DC power with rms spread σ_{v0} and a wider Gaussian components containing the AC power with spread σ_v.

As discussed in Section 9.3, recent results for land clutter have shown spectra with an exponential, rather than Gaussian shape. The simple expression (9.17) must then be replaced by a spectrum representing the convolution of the exponential intrinsic spectrum with a Gaussian function of unit power given by (9.22), for which there is no convenient closed-form expression. The resulting spectrum falls off more slowly than would a Gaussian spectrum having the same half-power width, leading to degraded improvement factor in a Doppler-based processor.

When sidelobe or backlobe clutter is encountered at significant levels, it spectrum has a beamwidth component that extends over velocities between $-v_0$ and v_0, at levels determined by the envelopes of the corresponding lobe structure.

---

[5] Nathanson [6] gives this same expression as $0.42v_0\theta_2\sin\beta$, where θ_2 is the two-way half-power beamwidth.

9.1.4 Amplitude Distributions of Surface Clutter

The clutter detectability factor (see Section 3.2.3) also adjusts the radar equation for departures of the probability density function of clutter voltage from Rayleigh (corresponding to two quadrature Gaussian components). Measurement programs of clutter on sea and land surfaces, especially those carried out at grazing angles below the critical value defined by (9.8), or with high spatial resolution (small A_c), have found significant departures from Gaussian statistics. The families of distributions (probability density functions) used to describe surface clutter power are:

- Weibull distribution: a two-parameter distribution given by

$$P(x) = \frac{x^{1/a}}{a\alpha x} \exp\left(-\frac{x^{1/a}}{\alpha}\right); \quad x \geq 0 \tag{9.23}$$

  where a is the spread (or shape) parameter that determines the width of the distribution[6] and α is the scale factor. The mean and median values and their ratio are

$$\bar{x} = \alpha^a \Gamma(1+a) \tag{9.24}$$

$$x_{50} = (\alpha \ln 2)^a \tag{9.25}$$

$$\frac{\bar{x}}{x_{50}} = \frac{\Gamma(1+a)}{(\ln 2)^a} \tag{9.26}$$

  where Γ is the Gamma function. A spread parameter $a = 1$ gives the exponential distribution (corresponding to a Rayleigh voltage distribution) with $\bar{x} = \alpha$. In application to clutter, x is the product $\sigma^0 F_c^4$ of reflectivity and clutter propagation factor.

- Lognormal distribution: a two-parameter distribution expressed in terms of the natural logarithm, base-10 logarithm, or decibels, the last being most convenient for description of radar targets and clutter:

$$P(x_{\text{dB}}) = \frac{1}{\sqrt{2\pi}\sigma_{\text{dB}}} \exp\left[-\frac{(x_{\text{dB}} - \mu_{\text{dB}})^2}{2\sigma_{\text{dB}}^2}\right] \tag{9.27}$$

[6] The Weibull spread parameter is identified subsequently as a_w, but a is used here for compactness.

Here, for x representing a power term, $x_{dB} = 10\log x$, σ_{dB} is the standard deviation, and μ_{dB} is the mean (and also the median) of x_{dB}. The median and mean power ratios and their ratio are

$$\bar{x} = 10^{0.1\mu_{dB} + (0.005\ln 10)\sigma_{dB}^2} \tag{9.28}$$

$$x_{50} = 10^{0.1\mu_{dB}} \tag{9.29}$$

$$\frac{\bar{x}}{x_{50}} = 10^{(0.005\ln 10)\sigma_{dB}^2} \tag{9.30}$$

This ratio is expressed in decibels as

$$10\log\left(\frac{x_{av}}{x_{50}}\right) = (0.05\ln 10)\sigma_{dB}^2 = 0.12\sigma_{dB}^2 \tag{9.31}$$

- *K*-distribution: a two-parameter distribution used to describe the clutter power x, given by

$$P(x) = \frac{2b^{(v+1)/2}x^{(v-1)/2}}{\Gamma(v)}K_{v-1}\left(2\sqrt{bv}\right); \quad x \geq 0 \tag{9.32}$$

where v is the shape parameter, b is the scale parameter, and K is the modified Bessel function (or K-function). The properties of this distribution, most commonly applied to sea clutter, are described in [1, p. 279] and [6, p. 109].

When many comparable scattering sources lie within the radar resolution cell, the probability density function of surface clutter voltage tends to the Rayleigh distribution (exponential distribution for power). Schleher [7, p. 261] gives the conditions for this as linear dimensions of about 75m, corresponding to a pulsewidth $\tau_n \geq 0.5$ μs and azimuth beamwidth given in degrees by $\theta_a \geq 4.3/R_{km}$. These conditions are generally met for air surveillance radars, but radars used for tracking, marine navigation, and maritime patrol often have smaller resolution cells.

Barton [2] models the spread factors of both Weibull and lognormal distributions as a function of F_c' and area of the resolution cell, as shown in Figure 9.4. That model captures the effect of reduced grazing angle that is a major contributor to formation of sea clutter spikes. It shows significant increases in the spread fac-

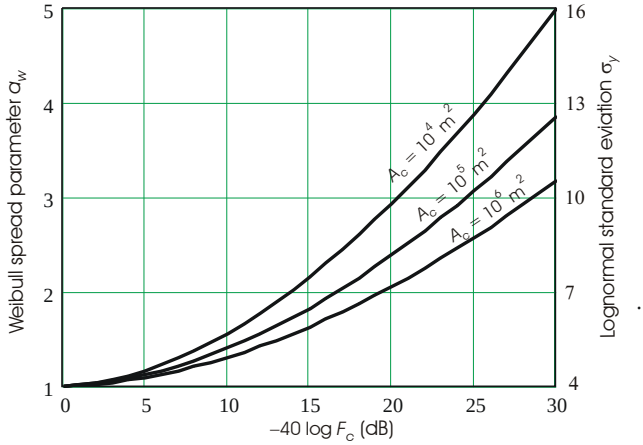

Figure 9.4 Variation in spread of clutter pdf with average propagation factor for different cell areas.

tor even for resolution cell areas much greater than the 5,000m^2 suggested by Schleher's criterion.

9.2 MODELS OF SEA CLUTTER

The several parameters for expressing a surface clutter model may now be applied to two types of distributed surface clutter: sea and land.

9.2.1 Physical Properties of the Sea Surface

Blake [3, pp. 306–308] lists the parameters used to describe the physical properties of the sea surface. The *wave height* is defined as the vertical distance between the wave to and the adjacent troughs. A Gaussian distribution of the vertical coordinate h of the surface about its mean is normally assigned:

$$p(h) = \frac{1}{\sqrt{2\pi}\sigma_h} \exp\left(-\frac{h^2}{2\sigma_h^2}\right) \tag{9.33}$$

where h is measured relative to the average surface and σ_h is its standard deviation. Blake lists three other measures of wave height:

h_{av} = $2.6\sigma_h$ is the average wave height;
$h_{1/3}$ = $4\sigma_h$ is the average wave height of the largest 1/3 of the waves;
$h_{1/10}$ = $5.2\sigma_h$ is the average wave height of the largest 1/10 of the waves.

Approximations for relationships between sea surface parameters and local wind velocity can be derived from data in Nathanson [8, p. 270]:

$$v_w \approx 1 + 2\text{SS} + \left(\frac{\text{SS}}{5.3}\right)^6 \tag{9.34}$$

$$\sigma_h \approx \left(\frac{v_w}{15}\right)^2 \approx 0.01 + \left(\frac{s}{7}\right)^2 + \left(\frac{s}{7}\right)^8 \text{ (m)} \tag{9.35}$$

$$\beta_0 \approx 0.055 + 0.007\text{SS} \text{ (rad)} \tag{9.36}$$

where

v_w = wind speed in m/s;
SS = Douglas sea-state number.

The same equations can be applied for the Beaufort wind scale number K_B by replacing SS with $K_B - 1$. Table 9.1 lists the results for sea states 0 to 8. The slow increase in slope β_0 with sea state results from the fact that both wavelength and wave height increase with wind speed, although not be the same factor.

Table 9.1 Sea Surface Parameters for Sea States 0 to 8

Sea State SS	*Wind Scale* K_B	*Wind Velocity* v_w (m/s)	*Rms Height Deviation* σ_h (m)	*Slope* β_0 (rad)
0	1	1.5	0.01	0.055
1	2	2.6	0.03	0.063
2	3	4.6	0.10	0.073
3	4	6.7	0.24	0.080
4	5	8.2	0.38	0.085
5	6	10.8	0.57	0.091
6	7	13.9	0.91	0.097
7	8	19.0	1.65	0.104
8	9	28.8	2.50	0.116

9.2.2 Reflectivity of Sea Clutter

When the constant-γ model is applied to sea clutter, averaging over all polarizations and directions relative to the wind, a first-order model for γ depends on the sea state or Beaufort wind scale K_B and radar wavelength [2, p. 110, Eq. (3.37)]:

$$10\log\gamma = 6\text{SS} - 10\log\lambda - 58 = 6K_B - 10\log\lambda - 64 \text{ dB} \tag{9.37}$$

This expression results in variation of the intrinsic reflectivity factor γ (and hence σ^0 for a specific grazing angle) with $SS^{0.6}$ and λ^{-1}. Blake [3, p. 311] accepts as "the present-day view" the inclusion of F_c^4 within σ^0, making it "customary to ascribe to σ^0 itself the frequency dependence that is actually the result of the interference effect." As we have stated in Section 9.1.2, the separation of the two terms and use of the constant-γ model improves the understanding of the physical factors involved in surface clutter measurement and modeling.

Based on (9.37) and using values in Table 9.1, the first-order model for the dependence on grazing angle of $\sigma_c F_c^4$ for sea clutter is shown for different radar wavelengths and for a medium sea in Figure 9.5. Three of the regions of defined in Section 9.1.2 can be identified:

1. The zenith region, a narrow region near vertical incidence, where quasi-specular reflection dominates.
2. The near (free-space) region covering most grazing angles below 70°, where the constant-γ model applies;
3. The interference region, where the interference propagation factor is dominant.

The product $\sigma^0 F_c'^4$ for sea clutter in the interference region reaches such low levels that intermediate and diffraction regions are seldom of interest, although the propagation factor models of Section 9.1.2 applicable. However, atmospheric conditions over the sea often create ducts that invalidate simple diffraction mod-

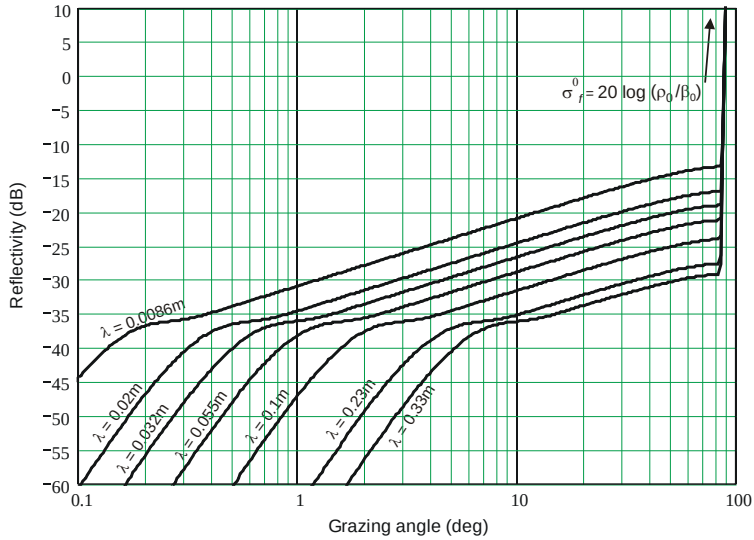

Figure 9.5 Reflectivity $\sigma^0 F_c'^4$ of clutter for a medium sea (sea state 4, σ_h = 0.38m, β_0 = 0.085 rad).

els.

Researchers [1, pp. 382–402] have explored the variation of σ^0 with polarization and wind direction, and have put forth detailed models in which these factors are considered. These variations are generally small enough that they are masked by uncertainties in the wind scale or sea state, and hence need not be considered in most models and analyses. Long [1, p. 353] states, with regard to sea clutter, that:

> Obtaining a valid description of the dependence of radar cross section on wavelength is difficult because one must make measurements simultaneously with at least two radars, while making quantitative sea state measurements. … The problem is further complicated by the rapid time variations of the average value of σ^0 which can occur. Observations at a single wavelength indicate that "average" radar cross section can change as much as 10 dB in a 1-minute interval. Therefore, the measurement errors and uncertainties tend to obscure the weak functional relationships that exist between σ^0 and λ for most incidence angles.

Given these uncertainties, it would appear that a first-order model such as (9.37) are adequate for most purposes. For those with interest in exploring second-order effects, Long's text and a recent book [6] that explores the details of sea clutter statistics and models are recommended.

9.2.3 Power Spectrum of Sea Clutter

The sea clutter for a surface wind velocity v_w has a mean velocity in the downwind direction that depends on the polarization, given approximately, from data in [8, p. 292], by:

$$\begin{aligned} v_{0H} &\approx 0.75\sqrt{v_w} \quad \text{(H-pol)} \\ v_{0V} &\approx 0.14 v_w \quad \text{(V-pol)} \\ v_0 &\approx 0.38 v_w^{0.7} \quad \text{(average of both polarizations)} \end{aligned} \tag{9.38}$$

These expressions, plotted in Figure 9.6, apply to clutter generated by the capillary waves. A different mean velocity applies to Bragg scattering in the lower radar bands, as observed by over-the-horizon radar [1, pp. 104–105].

The sea clutter spectrum is approximately Gaussian with a standard deviation [8, p. 286]:

$$\sigma_{vc} \approx 0.11 v_w \quad \text{(both polarizations)} \tag{9.39}$$

An approximation showing σ_w proportional to sea state, presented by Blake [3, p. 320, Eq. (7.40)], gives lower values than (9.39) for $v_w > 12$ m/s (SS > 5), but the linear relationship to v_w is a better match to Nathanson's data that were Blake's source.

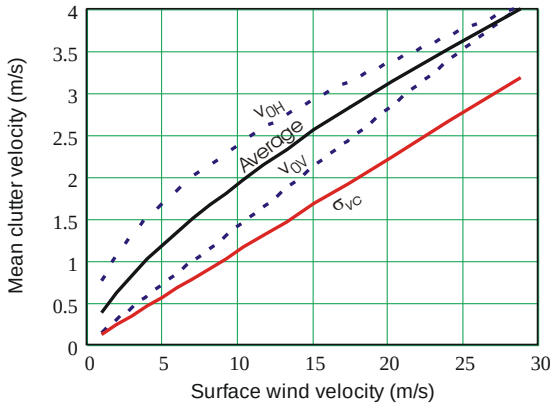

Figure 9.6 Mean and standard deviation sea clutter velocity for vertical and horizontal polarizations.

When passed through an envelope detector, the standard deviation of (9.39) is increased by $\sqrt{2}$. The intrinsic velocity spread σ_{vc} is inserted in (9.21) to find the total spread σ_v for a moving radar with a scanning antenna for use in (9.17).

9.2.4 Amplitude Distribution of Sea Clutter

Measurement programs have been carried out on sea clutter over grazing angles from below 1° to 90°. Most of the data have been collected in the interference region (above the critical grazing angle ψ_c and below the onset of specular facet reflections at $90° - 2\beta_0$). and represent σ^0 influenced only slightly by F_c^4. The measured distributions of power lie close to the exponential until the grazing angle approaches the interference region, where moderately spread versions of the lognormal, Weibull, or K-distributions appear.

High-resolution measurements [9], in which a single wave crest may dominate the resolution cell, have tended to show agreement with the lognormal distribution, with σ_{dB} between 4 and 6.1 dB. The corresponding ratios of average to median σ^0 are 1.8 and 4.3 dB, values that apply to Weibull spread factors $a = 1.06$ and 1.65, respectively. At very low grazing angles and with high-resolution radar, sea clutter may be "spikey" in nature, described by larger spread factors for Weibull or lognormal distributions.

9.3 Models of Land Clutter

Unlike sea clutter, there are no standard "states" that can be invoked to describe the physical properties of the land surface. Using a Gaussian model, it can be de-

scribed by its roughness (the standard deviation σ_h from the average surface), the slope β_0, and by the type and thickness of any vegetative cover. There are no standard terms that are associated with certain combinations of those parameters, but terms such as used in Table 9.2 can be used to describe several surface types as examples. The Gaussian model, however, fails to capture the effects of some natural and most manmade structures that rise from the surface, which are described separately as *discrete clutter* in Section 9.4.

Table 9.2 Land Surface Parameters

Surface Description	*Intrinsic Reflectivity* γ (dB)	*Rms Height Deviation* σ_h (m)	*Slope* β_0 (rad)
Mountains	–5	100	0.1
Urban	–5	10	0.1
Wooded hills	–10	10	0.05
Rolling hills	–12	10	0.05
Farmland, desert	–15	3	0.03
Flatland	–20	1	0.02
Smooth surface	–25	0.3	0.01

Agreement of measured land-clutter data with the constant-γ model is shown in Figure 9.7. The data agree within 1 dB with the model for grazing angles in the near region.

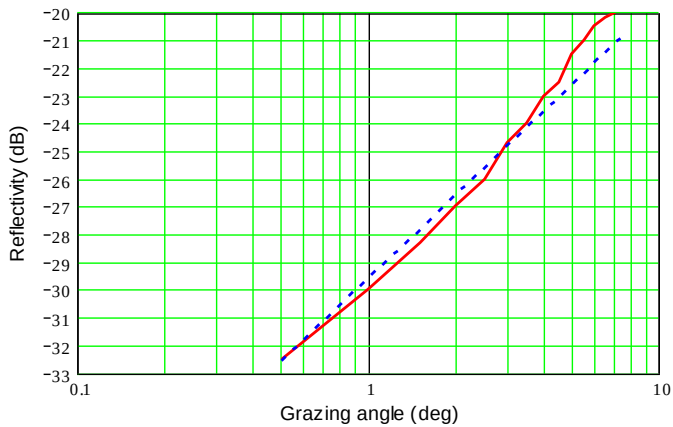

Figure 9.7 Measured X-band land clutter reflectivity σ^0 (solid line), compared to model with constant $\gamma = -12$ dB (dashed line). Measured data replotted with grazing angle on log scale from [10, p.103, Figure 2.44].

9.3.1 Reflectivity of Land Clutter

The reflectivity of land clutter is much more difficult to characterize than that of the sea. The constant-γ model applies at grazing angles in the interference region, giving the values of γ that are shown in Table 9.2. The reflectivity is almost independent of wavelength, whose effect appears instead in the propagation factor for the intermediate and diffraction regions. Propagation considerations become the dominant factor at the low grazing angles applicable to surface-based radars. One study [11] showed that practically all of the variations in measured reflectivity of terrain could be attributed to the propagation factor, permitting use of a constant σ^0 (e.g., –30 dB) to reproduce the measured mean and pdf, at least in the microwave region.

A first-order modeling approach [12] assumes a homogeneous surface with given σ_h and γ for each land type (Table 9.2), and assumes the radar antenna has been sited on a point $2\sigma_h$ above the mean local surface. This leads to an antenna altitude above the mean surface $h_r' = h_r + 2\sigma_h$. A single family of curves for σ^0 then results (Figure 9.8), which may be modified as needed for propagation factors at different wavelengths.

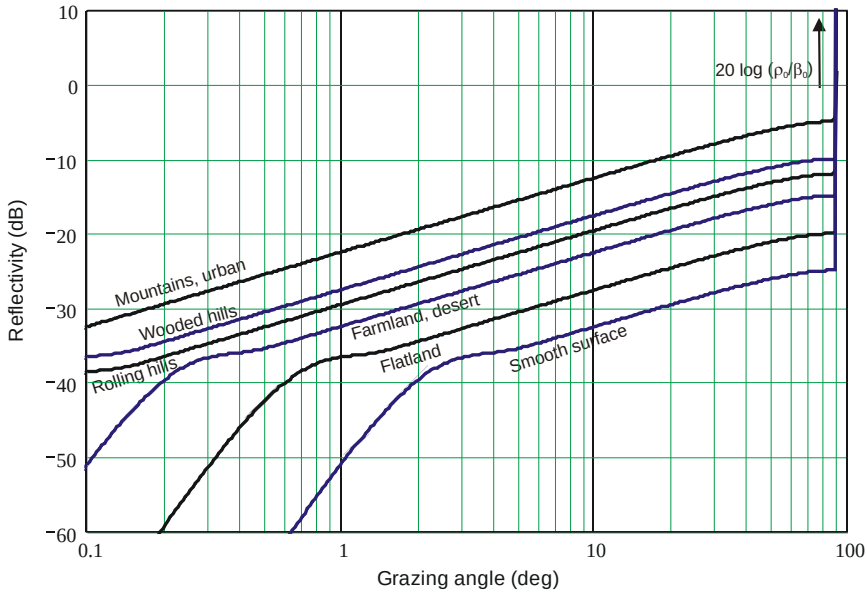

Figure 9.8 Land clutter reflectivity versus grazing angle. The transition ranges R_1 for propagation factor have been calculated here for $\lambda = 0.1$m, $h_r = 10$m.

Studies and measurement programs on land clutter have been complicated by the fact that properties of the terrain underlying the path to clutter may differ from that in the resolution cells for which clutter is to be predicted or measured. For example, hilly terrain may be observed either on a path over a similarly hilly surface, or over flat terrain with quite different properties. It is therefore essential to separate the propagation factor from the intrinsic reflectivity of the observed cell. In one major work on land clutter [10] where the product $\sigma^0 F_c'^4$ of these two factors was measured and analyzed statistically, it was found that the correlation between $\sigma^0 F_c'^4$ and grazing angle at the cell was weak and sometimes negative. Grazing angle was therefore excluded as a factor in the clutter model. The reason for absence of correlation is illustrated in Figure 9.9, which shows a simple case of corrugated terrain. The local surface slope is zero (by definition) at the tops of peaks and the bottoms of valleys, and maximum halfway between (where the mean surface level is shown by the dashed line). Thus, σ^0 is greatest halfway up the slopes facing the radar, drops to near zero at the peaks and valleys, and to zero on slopes facing away from the radar. The surfaces with maximum slope, however, are shadowed by the intervening peaks.

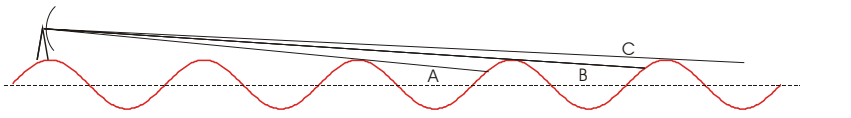

Figure 9.9 Propagation paths in simple sinusoidal terrain model.

Paths A and B in Figure 9.8, which arrive at the surface with the highest grazing angles, are subject to knife-edge diffraction from the preceding peaks, where the two-way propagation factors $F_c^4 \approx -12$ dB. That loss applies in spite of optical "visibility" of the surface. Path C, with grazing angle and σ^0 near zero, has path clearance sufficient to give $F_c'^4 \rightarrow 0$ dB. Diffraction theory predicts a continuous variation in F, rather than an abrupt drop from unity to zero, between the region of adequate clearance above the intervening terrain and the shadowed region. As a result, no positive correlation should be expected between grazing angle and $\sigma^0 F_c'^4$ for "visible terrain." The constant-γ model does not predict that there should be positive correlation with the product $\sigma^0 F_c'^4$ in the intermediate region, and suggests that the correlation may be negative for some surface contours.

This is only one example of the complexity introduced by the propagation factor that results from terrain between the radar and the cell being measured or modeled. A purely statistical analysis that ignores propagation theory cannot provide an adequate basic for land clutter modeling. The applicability of separate modeling of F_c' and σ^0, shown in [11], suggests that propagation alone contributed

most of the statistical spread in clutter echo power, so a model such as shown in Figure 9.4 should be useful.

Another misinterpretation of measured data leads to the idea that σ^0 in tree-covered terrain increases as the grazing angle approaches zero, attributed to specular scattering from vertically oriented cylindrical tree trunks [13]. The strong increase shown in these data are directly traceable to the terrain contour between the radar site and the clutter measured at the longest ranges in that experiment. The assumption was made that grazing angle varied inversely with measurement range, as would be true for terrain on a flat Earth (or spherical Earth at relatively short ranges). In the actual case, the terrain changed from a basically level surface to rising ground at the longest ranges measured, causing the local grazing angle to increase after having decreased with range over the level portion. It was the upward tilt of the terrain, and the accompanying increase in propagation factor, rather than the presence of vertically oriented tree trunks, that caused the increase in reflectivity.

As the next step beyond the first-order model of Table 9.2, it is often possible to model two or more surface regions in each azimuth sector of a specific radar site with different average surface slopes (not β_0, but averages over much larger regions), and different roughness parameters and vegetation. These can be used to estimate both F_c' and σ^0 for cells at different rages in an azimuth sector. Where surface features are present that can be not modeled by a Gaussian distribution of heights, discrete clutter sources may be added to the model. Beyond this step, a site- and azimuth-dependent propagation model such as SEKE [14], used in [11], can be used.

9.3.2 Power Spectrum of Land Clutter

The velocity spectrum of land clutter is narrow, and has been modeled as Gaussian with $\sigma_v < 0.5$ m/s for vegetation in windy conditions. However, excellent data have been gathered with a coherent clutter measurement system having large dynamic range [10, Chapter 6] that show the actual spectrum to have an exponential shape (Figure 9.10). The total power of all the spectra plotted in this figure is normalized to unity. The exponential spectrum for windy conditions has 94% of its power within ±0.5 m/s, compared to 95% for a Gaussian spectrum with σ_v = 0.20 m/s. Neither type of spectrum shows the broad spread of power predicted by power-law equations of the form $1/[1 + (f/f_a)^n]$, where $n = 2$ or 3. Reported clutter data [16] showing such spectra can be explained by presence of nonlinearity (e.g., logarithmic characteristics) in the receivers used for measurement.

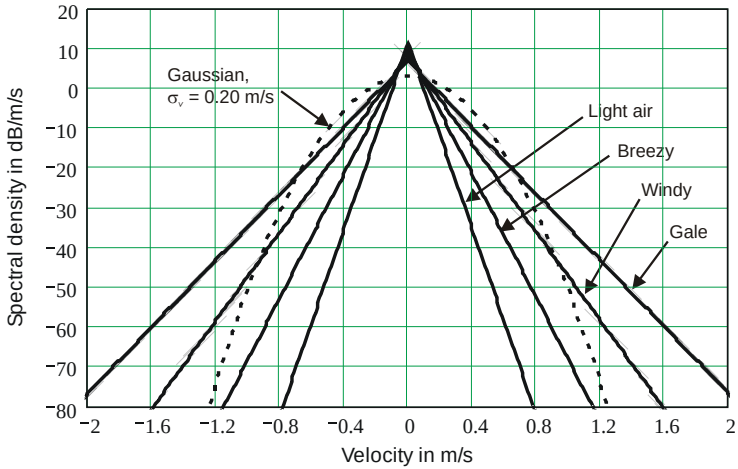

Figure 9.10 Exponential spectra of windblown trees for four wind conditions derived from models in [10, Table 6.1, p. 578], compared to a Gaussian spectrum with $\sigma_v = 0.2$ m/s.

The accurately measured data also show a nonfluctuating (DC) component with the power ratio r of dc to ac given by [10, p. 580, Eq. (6.4), modified for metric units]:

$$r = \frac{140}{v_w^{1.55} f_{\text{GHz}}^{1.21}} \tag{9.40}$$

where the constant in the numerator applies for v_w in meters per second. Spread components from antenna scan (9.19) and platform motion (9.20), with $v_s = 0$, must be combined with the spectra of Figure 9.10 and the DC component by convolution. Unless the internal motion component is dominant, the result is approximately Gaussian with a standard deviation given by (9.21) for the fluctuating component and (9.22) for the DC component. As noted earlier, the slowly falling spectra reported in [15] with velocities beyond the physical limits of scatterer motion should not be used.

9.3.3 Amplitude Distribution of Land Clutter

The measured amplitude distributions of land clutter in the zenith and near (plateau) regions are Rayleigh (exponential power), until near the transition to the interference region, where Weibull or lognormal distributions apply. The change from Rayleigh to more widely spread distributions follows the model shown in

Figure 9.4, with the most extreme spreads encountered in intermediate and diffraction regions.

9.4 DISCRETE CLUTTER

The broadly spread Weibull and lognormal distributions do not normally extend to the high peak values contributed by manmade and some natural land features. Birds in flight and land vehicles are also sources of clutter that require models separate from those of sea and land clutter.

9.4.1 Discrete Land Features

Of the several types of discrete clutter, buildings (including towers and water tanks) present the largest RCS. Table 9.3 shows different models of discrete land clutter taken from the literature [16–19], along with a recommended model for general use. Large, rigid sources can be regarded as having very small spatial extent (typically only one or a few meters) and spectra of essentially zero width. They establish the dynamic range at the input to the receivers of most systems, and place special requirements on methods of controlling false alarms.

Table 9.3 Models of Discrete Point Clutter

Parameter	*RRE* [16]	*Ward* [17]	*Mitre*		*Suggested Value*
			Rural [18]	*Metro* [19]	
Density (per km^3) for RCS:					
$\sigma_c F_c' = 10^2$ m^2	3.5	1.8			2
$\sigma_c F_c' = 10^3$ m^2	0.8	0.36	0.02	2	0.5
$\sigma_c F_c' = 10^4$ m^2	0.15	0.18	0.002	0.2	0.2
Resulting mean σ^0	–26	–26	–44	–24	–26
Number of points per 1° beam between 0 and 5 km:					
$\sigma_c F_c' = 10^2$ m^2	0.7	0.35			0.4
$\sigma_c F_c' = 10^3$ m^2	0.16	0.07	0.004	0.4	0.1
$\sigma_c F_c' = 10^4$ m^2	0.03	0.035	0.004	0.04	0.04

9.4.2 Birds and Insects

The clutter produced by birds was not discussed by Blake, although it poses a major problem for naval and other types of radar attempting to detect and track low-

altitude targets. The bird RCS for mid-microwave bands can be modeled by a lognormal pdf, with a median $\sigma_{50} = -30$ dBsm and a standard deviation $\sigma_y = 6$ dB. This implies that only 0.13% of the bird population exceeds −12 dBsm. However, populations of birds are such that there may be 10^5 birds within 50 km of the radar, of which 130 exceed −12 dBsm. Variation with radar wavelength and type of bird is discussed in [8, p. 184; 19]. Bird RCS is not sensitive to polarization, nor are the larger bird RCS values sensitive to wavelength (at least for $\lambda < 0.3$m). Small birds become resonant near that wavelength, and are in the Rayleigh region at longer wavelengths. Larger birds resonate in the UHF bands, but all are in the Rayleigh region for VHF and lower bands.

The most damaging feature of the bird population, in modern Doppler radar systems, is its velocity distribution. The birds move at air speeds as great as 25 m/s, and [21, 22] show an approximate Gaussian distribution with a mean of 15 m/s and a standard deviation of 5 m/s.

Migrating birds are generally distribution exponentially in altitude, with a scale height near 1 km, occasionally extending upwards to 5 km or more, although most local birds are at lower altitudes. This means that that the birds are often at altitudes high enough to provide free-space propagation, $F_c' = 1$, or even in reflection lobes for which $F_c' \rightarrow 2$. A bird with average $\sigma = -12$ dBsm may appear in the radar with $\sigma F_c'^4 = 0$ dBsm. This, and the presence of multiple birds in a flock, makes it impossible to reject birds on the basis of signal thresholding unless the desired targets lie well above 0 dBsm. Only filtering based on velocity can be relied upon to reject bird clutter, and this requires either a broad Doppler rejection notch or tracking to determine absolute velocity as a basis for discarding the information. It should be noted that track files on detectable birds cannot be dropped, because the entire detection and track initiation process would then have to be repeated on subsequent detections.

A similar consideration applies to insects [20], for which the median of the log-normal distribution may be −70 dBsm ±10 dB in microwave bands. For a standard deviation $\sigma_y = 6$ dB, the mean is increased to $-70 + 5 = -65$ dBsm. Clouds of thousands of insects then have mean ≈ -30 dBsm with a Rayleigh distribution. A propagation factor that can average up to +8 dB places insects also within the detection capabilities of modern systems.[7]

[7] This writer had occasion in 1947–49 to detect and automatically track individual insects at ranges of hundreds of meters, using an X-band variant of the World War II SCR-584 fire control radar at White Sands Proving Ground. The radar had a peak power of 60 kW, pulsewidth of 0.5 μs, and a reflector diameter of 1.8m. On close arrival at the radar, these insects proved to be dragonflies.

9.4.3 Land Vehicles

Land vehicles become a clutter problem for many air surveillance radars, because their RCS is comparable to that of aircraft, and their velocities lie in the passband of MTI and many pulsed Doppler systems. Here, at least, the propagation factor almost always favors the desired (aircraft) target, which necessarily lies at higher altitude than the land vehicle, which is often in the diffraction region. However, when there are dozens or hundreds of land vehicles within line of sight of the radar, false alarms are inevitable unless velocity filtering removes targets whose velocities are below ≈ 40 m/s.

9.4.4 Wind Turbines

A radar clutter problem that has risen since Blake's work is the wind turbine. These are increasingly appearing in farms of tens of turbines, with individual blade lengths up to 40m, mounted on towers that place the blades up to 200m above the local terrain. The towers themselves constitute strong discrete clutter sources with zero Doppler. The blades, rotating at 10–30 rpm, have tip velocities up to ≈75 m/s and peak RCS exceeding +40 dBsm, and hence can pass through most Doppler-based signal processors. At this writing, the *IEEExplore* database contains some 40 papers on radar interference caused by wind turbines. Only a few of these provide data that can be used for modeling and analysis. Some attempt to predict the effect of an extended shadowed region beyond the turbine, in which echo power from desired targets may be reduced, but the probability of a target lying within such a shadow is negligible. The primary effect of turbines is to create strong, discrete clutter accompanied by high-velocity components from periodic specular "flash" from the blades.

One useful paper from this set [23] includes a histogram of calculated RCS values, showing a continuous Rayleigh-like distribution with a peak (and median) value near +16 dBsm, combined with a low-probability values extending up to +44 dBsm, representing the periodic blade flashes. The paper emphasizes that objects like wind turbines are usually viewed at ranges shorter than their far-field range at which RCS is defined, and that surface reflections cause large departures from the plane wave on which most computational models are based.

9.5 MODELS OF VOLUME CLUTTER

Volume clutter appears in two forms: precipitation, and chaff. The methods of modeling are similar, as both occupy a volume in space and consist of huge numbers of scatterers distributed over the volume with slowly varying densities. With-

in a radar resolution cell, the density of scatterers can normally be considered constant, except when the lower edge of the elevation beam falls below the horizon, or the upper edge lies above the maximum elevation of the clutter volume. The result is a very close approximation to Rayleigh pdf, and a velocity spectrum determined by motion of the air mass in which the scatterers are embedded.

9.5.1 Volume Clutter Cross Section and Reflectivity

The radar cross section of volume clutter is given by the product of the volume V_c of the clutter within the radar resolution cell and the *volume reflectivity* η_v of the scattering particles, expressed in m^2/m^3:

$$\sigma_c = V_c \eta_v \tag{9.41}$$

When clutter extends beyond the resolution cell in all dimensions, its volume is

$$V_c = \frac{R_c \theta_a}{L_p} \frac{R_c \theta_e}{L_p} \frac{\tau_n c}{2} \quad \text{m}^3 \tag{9.42}$$

where

R_c = range from the radar in m;
θ_a, θ_e = azimuth and elevation half-power beamwidths in rad;
L_p = beamshape loss;
τ_n = width of the processed pulse in s;
c = velocity of light in m/s.

When the elevation beamwidth includes the surface beneath the clutter, or extends above the clutter, the second term in (9.42) is replaced by integration over the elevation sector, resulting in:

$$\begin{aligned} \sigma_c &= \frac{R_c \theta_a}{L_p} \frac{\tau_n c}{2} R_c \int_0^{\pi/2} \eta_v(R_c, \theta)\ f^4(\theta - \theta_b) d\theta \\ &= \frac{R_c \theta_a}{L_p} \frac{\tau_n c}{2} \eta_v(R_c) \int_0^{h_{\max}} f^4\left(\frac{h - h_r}{R_c} - \frac{R_c}{2 k_e a_e} - \theta_b \right) dh \end{aligned} \tag{9.43}$$

where

$f(\cdot)$ = one-way elevation voltage pattern of the antenna;
θ = elevation angle in beamwidths;
θ_b = elevation of beam axis in beamwidths;

θ_{max} = maximum elevation of clutter at range R_c;
$\eta(R_c,\theta)$ = clutter reflectivity at range R_c and angle θ, in m^2/m^3;
$\eta(R_c)$ = clutter reflectivity at range R_c, in m^2/m^3;
h = altitude in m;
h_{max} = maximum altitude of clutter at range R_c.

The integration over elevation angle in (9.43) is equivalent to that in (3.46), in that the clutter reflectivity is defined as zero outside the limits occupied by the scatterers. The integrals in (9.43) give the product of pattern-weighted extent of the clutter and the reflectivity of clutter when it is present. Except in rare cases, the clutter is assumed to extend beyond the azimuth beamwidth, so integrals in that coordinate are unnecessary.

9.5.2 Volume Clutter Pattern-Propagation Factor

The effect of the antenna's azimuth pattern is included in L_p, as is the elevation pattern when clutter fills the beam. The integrals in (9.43) replace L_p for clutter than does not fill the elevation beam. Inclusion of propagation effects is less critical for volume clutter than for surface clutter, but an interference pattern in elevation introduces a more complicated integral:

$$\begin{aligned}\sigma_c F_c^4 &= \frac{R_c\theta_a}{L_p}\frac{\tau_n c}{2}R_c\int_0^{\theta_{max}}\eta_v(R_c,\theta)\; f^4(\theta-\theta_b)\left(1+x^2+2x\cos\alpha\right)^2 d\theta \\ &= \frac{R_c\theta_a}{L_p}\frac{\tau_n c}{2}\eta_v(R_c)\int_0^{h_{max}} f^4\left(\frac{h-h_r}{R_c}-\frac{R_c}{2k_e a_e}-\theta_b\right)\left(1+x^2+2x\cos\alpha\right)^2 dh\end{aligned} \tag{9.44}$$

where, from (8.5) and (8.10):

$$x=\rho\frac{f(-\psi-\theta_b)}{f(\theta-\theta_b)} \tag{9.45}$$

$$\alpha=\frac{2\pi R_c}{\lambda}\left(\sqrt{1+\frac{4h_r h}{R_c^2}-\frac{2h_r}{k_e a_e}}-1\right)+\phi \tag{9.46}$$

The expression given by Blake [3, p. 300, Eqs. (7.18) and (7.19)] to express the power received from volume clutter includes within the integral the atmospheric attenuation coefficient, which may vary with range as a result of precipitation. This loss is expressed as a separate term in (3.4) and subsequent equations for received clutter energy, and evaluated in Section 7.3. We use calculations of the product σF_c^4 without involving the attenuation to clarify the origin of the clutter

echoes. It should be remembered that clutter energy from ambiguous ranges must be calculated using (3.5), using the attenuation applicable to each ambiguity.

The volume clutter propagation factor F_c' may be defined as the fourth root of the ratio of the integral in (9.44) to that in (9.43). In the presence of strong reflections over the elevation beam ($\rho \approx 1$), $F_c'^4 \approx 6$ (or +8 dB), a factor large enough to require inclusion in the radar equation.

9.5.3 Spectral Properties of Volume Clutter

The spectral properties of volume clutter have the same effects on the radar equation as did those of surface clutter: the improvement factor I_m depends on the location and shape of the clutter spectrum, and the clutter detectability factor depends on the correlation of clutter samples being integrated by the processor. Nathanson [8, p. 240, Eq. (6.10)] expressed the standard deviation of the volume clutter velocity spectrum as the sum of four components. We add here the component σ_{va} caused by antenna scanning:

$$\sigma_v = \sqrt{\sigma_{vc}^2 + \sigma_{va}^2 + \sigma_{vs}^2 + \sigma_{vb}^2 + \sigma_{vf}^2} \tag{9.47}$$

where

σ_{vc} = intrinsic spread from turbulence within the air mass;
σ_{va} = spread caused by scanning of the radar beam;
σ_{vs} = spread cause by wind shear effect across the elevation beamwidth;
σ_{vb} = spread caused by varying radial velocity across the azimuth beamwidth;
σ_{vf} = spread caused by projection of the particle fall velocity across the elevation beamwidth.

A value $\sigma_{vc} \approx 1$ m/s is normally assigned to the turbulence component, but Nathanson notes that extreme values vary over $0.5 < \sigma_{vc} < 2$ m/s. The antenna scanning component is given by (9.19), and the azimuth beam-broadening component by (9.20), as for surface clutter. The wind-shear component, when clutter fills the elevation beamwidth, is[8]

$$\sigma_{vs} = \frac{k_{sh} R_c \theta_e}{4\sqrt{\ln 2}} = 0.3 k_{sh} R_c \theta_e \tag{9.48}$$

where

k_{sh} = wind shear constant in m/s per km along the beam direction;

[8] Nathanson [8, p. 242] uses a two-way beamwidth, for which the constant factor in (9.48) is $1/\sqrt{8\ln 2} = 0.425$.

R = range in km;
θ_e = elevation beamwidth in rad.

The wind-shear spreading component when clutter occupies only a portion of the elevation beamwidth is reduced, and can be calculated by integrating the profile of velocity as a function of altitude, weighted by the fourth power of the pattern-propagation factor, to yield a velocity spectrum for a given range:

$$W(v) = \int_0^{h_{\max}} (v_w + k_{sh} h) f^4 \left(\frac{h - h_r}{R_c} - \frac{R_c}{2 k_e a_e} - \theta_b \right) \left(1 + x^2 + 2x \cos\alpha\right)^2 dh \qquad (9.49)$$

where h is in km. The power in the input spectrum is:

$$C_i = \int_{-\infty}^{\infty} W(v)\, dv \qquad (9.50)$$

The mean v_0 of this spectrum is:

$$v_0 = \frac{1}{C_i} \int_{-\infty}^{\infty} v W(v)\, dv \qquad (9.51)$$

and the variance σ_{vs}^2 is:

$$\sigma_{vs}^2 = \frac{1}{C_i} \int_{-\infty}^{\infty} (v - v_0)^2 W(v)\, dv \qquad (9.52)$$

The wind shear and azimuth beam-broadening components are the counterparts of the beamwidth component $\sigma_{v\theta}$ in (9.20) for surface clutter, appearing here as separate terms for particle velocities in each of the two angular coordinates. The azimuth beam-broadening component σ_{vb} is calculated, as for surface clutter, from (9.20), in which the azimuth beamwidth θ_a is used. The variation in fall velocities is estimated by Nathanson to be

$$\sigma_{vf} = 1.0 \sin\theta \quad \text{(m/s)} \qquad (9.53)$$

for rain, where θ is the elevation angle. For snow the initial constant is << 1 m/s.

The mean velocity of volume clutter is the projection of the wind velocity vector on the beam axis:

$$v_{0w} = -v_w \cos\left(A_w - A_b\right)\cos\theta \tag{9.54}$$

where

v_w = the wind speed;
A_w = azimuth angle of the wind vector;
A_b = beam-axis azimuth;
θ = elevation angle in rad.

When the wind vector is aligned with the beam axis, this mean velocity is a receding component, expressed by the minus sign in (9.54). Added to the horizontal component is a shift in the mean rain fall rate projected on the beam direction as an incoming velocity component

$$v_{0f} = v_f \sin\theta \quad \text{(m/s)} \tag{9.55}$$

where the fall velocity v_f can reach 9 m/s in heavy rain.

When sidelobe or backlobe clutter is encountered at significant levels, it spectrum has a beamwidth component that extends over velocities between $-v_0$ and v_0, at levels determined by the envelopes of the corresponding lobe structure.

9.5.4 Amplitude Distribution of Volume Clutter

In most case the huge number of scatterers contributing to volume clutter in the resolution cell ensures a Rayleigh distribution of amplitudes. One report [24] shows measurements of rain clutter following Weibull distributions with spread factors as high as $a_w = 1.6$. It is possible that such distributions will apply to a range interval extending over different portions of a cloud, from the edges to the center, for which the average reflectivity changes significantly. However, unless these gradients are quite steep the statistics over the typical CFAR window should adhere closely to the Rayleigh distribution, and a range-dell-averaging CFAR should not experience excessive false alarms.

9.5.5 Precipitation Clutter Models

Models of precipitation clutter are well defined, possibly due to the intensive application of weather radar to measurement of rainfall rates [25]. The radar cross section of a spherical drop of water with diameter $D \le \lambda/16$, meeting the Rayleigh small-sphere approximation, is [25, p. 35, Eq. (3.6)]:

$$\sigma_1 = \frac{\pi^5}{\lambda^4}\left|K_w\right|^2 D^6 \quad \text{m}^2 \tag{9.56}$$

where

D = drop diameter in m;
λ = wavelength in m;
K_w = $(m^2 - 1)/(m^2 + 2)$;
m = $n - jn\kappa$ = complex refractive index of water.

Values of $|K_w|^2$ are 0.91 to 0.93 for water in microwave and millimeter-wave bands. For ice the corresponding value is $|K_i|^2 = 0.18$.

Radar meteorologists define a *reflectivity factor Z* for precipitation as the weighted average of D^6 over volume:

$$Z = \frac{1}{\Delta V}\sum_i D_i^6 = \int_0^\infty n(D) D^6 dD \quad (\mathrm{m}^3) \tag{9.57}$$

where

ΔV = elementary volume in m^3 occupied by precipitation;
D_i = drop diameter in m;
$n(D)$ = number of drops in ΔV having diameter D.

The *volume reflectivity* is then

$$\eta_v = \frac{\pi^5}{\lambda^4}|K_w|^2 Z \quad \left(\mathrm{m}^2/\mathrm{m}^3\right) \tag{9.58}$$

When the Rayleigh approximation is not met, and *equivalent reflectivity factor* Z_e is substituted for Z. The value of Z is often expressed in radar meteorology as $\mathrm{dB}(Z) = 10\log Z$ ($\mathrm{mm}^6/\mathrm{m}^3$), which is $180\log Z$ ($\mathrm{m}^6/\mathrm{m}^3$). The commonly used Marshall-Palmer drop-size distribution leads to a relationship between Z and rainfall rate r_r in mm/h:

$$Z = 200 r_r^{1.6} \quad \mathrm{mm}^6/\mathrm{m}^3 \tag{9.59}$$

which with $|K_w|^2 = 0.93$ gives:

$$\eta_v = 5.7\times 10^{-14}\frac{r_r^{1.6}}{\lambda^4} \quad \mathrm{m}^2/\mathrm{m}^3 \tag{9.60}$$

For snow with a rate r_s in mm/h of water content

$$\eta_v = 1.2\times 10^{-13}\frac{r_s^2}{\lambda^4} \quad \mathrm{m}^2/\mathrm{m}^3 \tag{9.61}$$

A plot of (9.60) and (9.61) for rain and snow at different wavelengths is shown in Figure 9.11.[9] The values for rain in the millimeter-wave bands have been adjusted for drop sizes not meeting the Rayleigh approximation.

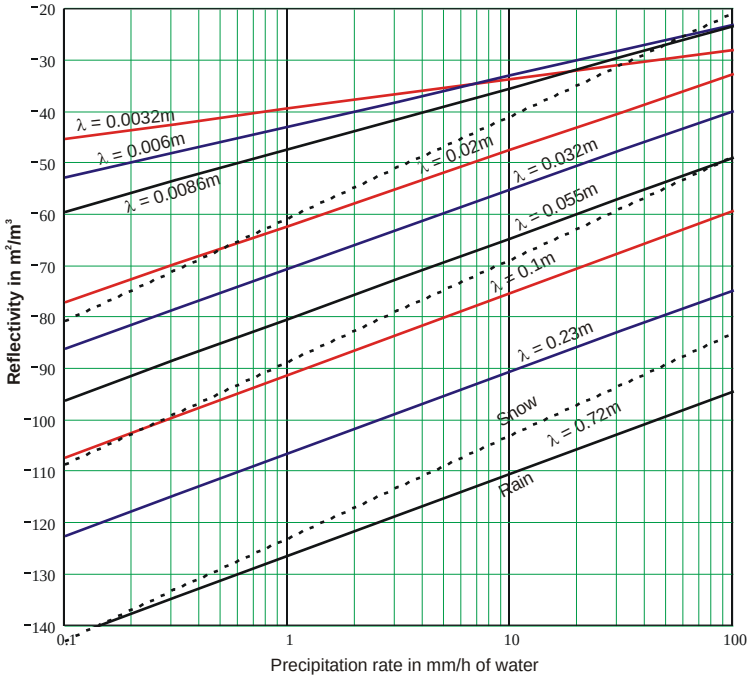

Figure 9.11 Volume reflectivity of rain (heavy lines) and snow (light lines).

The amplitude distribution of precipitation is Rayleigh, and the velocity spectrum is as discussed in Section 9.5.3. A significant property of precipitation clutter is that the echo of a circularly polarized (CP) transmission is returned with CP of the opposite sense. This permits the polarization factor F_{pc} in (3.4) and subsequent equations for clutter energy to be reduced, typically by 20–25 dB, by designing the receiving antenna to respond to the same CP sense that was transmitted, with lesser reduction for heavy rain and snow. The loss in target energy with this arrangement is 2–4 dB for aircraft targets, and hence a CP improvement factor in signal-to-clutter ratio can be as much as 20 dB, at the expense of reduced range in

[9] The constants and exponents in (9.60) and (9.61) require modification for the millimeter-wave bands. Adjusted values are derived as a function of wavelength in the Mathcad worksheet on the DVD, which was used in preparing Figure 9.11. The procedure can be reviewed in the PDF file of that worksheet by those lacking the Mathcad program.

thermal noise. A dual-polarized receiving system can be designed to switch between CP senses, avoiding the loss in target echo in regions not occupied by significant precipitation clutter.

9.5.6 Chaff Models

The RCS of an individual dipole of chaff viewed broadside is $0.86\lambda^2$. The average over all aspect angles drops to $0.15\lambda^2$. Early data on aluminum chaff gave a total RCS, as a function of its weight W in kilograms, frequency f_0 in GHz, and wavelength λ in m as

$$\sigma = 6,600\frac{W}{f_0} = 22,000\lambda W \quad \text{m}^2 \tag{9.62}$$

for chaff dipoles cut to resonate at λ. More recent data [26, p. 420] show that modern aluminized-glass chaff can achieve more than twice the RCS given by (9.62) over a two-octave band, with λ taken as the geometric mean value. The reflectivity across that bandwidth is shown in Figure 9.12. For $\lambda > 0.3$m, resonant dipoles may give way to long streamers called rope, producing lower RCS for its weight, but being less subject to breakage. Chaff falls slowly with a motion tending to randomize the orientation of individual dipoles, and hence is not very sensitive to the radar polarization, although stronger response is seen for horizontal

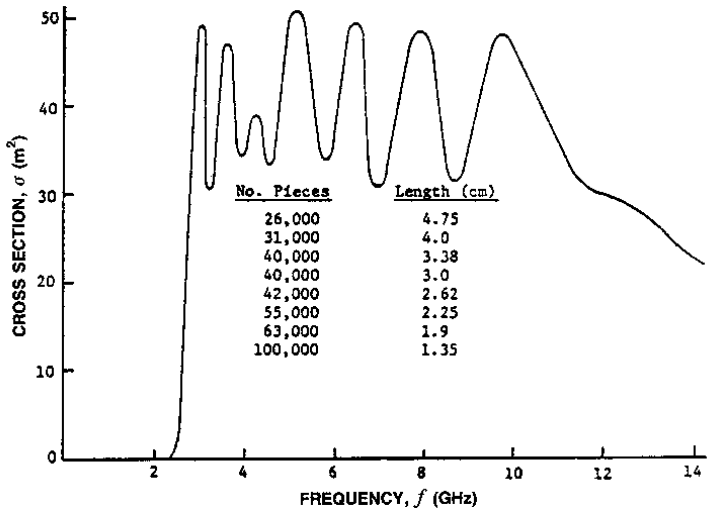

Figure 9.12 Radar cross section of a chaff package. (From: [26]. © 1999, Artech House, reprinted with permission.)

polarization, especially for times well after deployment.

The amplitude distribution of chaff is Rayleigh, and the spectral properties are as discussed in Section 9.5.3. Significant difference between chaff and precipitation clutter are that chaff echoes cannot be canceled by use of CP, and chaff can appear at much higher altitudes. The latter can be exploited by the attacking force to produce clutter beyond the unambiguous range of the radar waveform, where wind shear displaces the average velocity from that of shorter-range clutter [2, p. 121]. The resulting broad clutter spectrum requires a broader Doppler rejection notch than would be required for clutter in a single range ambiguity.

9.6 CLUTTER IMPROVEMENT FACTOR

Clutter can be reduced through filtering based on its relatively low Doppler shift. The voltage response of an arbitrarily defined Doppler filter as a function of velocity, normalized for unity power gain on white noise, can be expressed as a function of velocity:

$$H'(v) = \frac{1}{\sqrt{\bar{G}}} H(v) \tag{9.63}$$

where the average filter gain is $\bar{G} = \int_{-\infty}^{\infty} H^2(v)\,dv$.

The input energy C of the clutter spectrum $W(v)$is given by (9.50) and the energy at the output is

$$C_o = \int_{-\infty}^{\infty} W(v)\left[H'(v)\right]^2 dv \tag{9.64}$$

The clutter improvement factor is then defined as

$$I_m = \frac{C_i}{C_o} \tag{9.65}$$

These expressions can be applied to MTI and pulsed Doppler signal processors, and in special cases closed-form expressions can be written for the improvement factor. In general, the clutter spectrum in these special cases is Gaussian, characterized by a standard deviation σ_v and a mean velocity v_0.

9.6.1 Coherent MTI Improvement Factors

Coherent MTI refers to systems in which the transmitter is coherent over the number of pulses used in the canceler, and also to *coherent-on-receive* systems in which a coherent oscillator (COHO) in the receiver is locked to the transmitter pulse. The velocity response of an *m*-delay canceler using binary weights is

$$H_m(v) = \left(2\left|\sin\frac{\pi v}{v_b}\right|\right)^m \tag{9.66}$$

where the basic blind speed is

$$v_b = \frac{f_r \lambda}{2} \quad \text{(m/s)} \tag{9.67}$$

Voltage weights applied to the $m + 1$ pulses by the canceler are

$$\begin{aligned} w_i &= +1, -1 && \text{for } m = 1, \\ &= +1, -2, +1 && \text{for } m = 2, \\ &= +1, -3, +3, -1 && \text{for } m = 3, \end{aligned} \tag{9.68}$$

The average power gain is

$$\bar{G} = \sum_i w_i^2 = 2,\ 6,\ 20 \quad \text{for } m = 1,\ 2,\ 3 \tag{9.69}$$

The normalized response is

$$H'_m(v) = \frac{2^m}{\sqrt{\bar{G}}}\left|\sin\frac{\pi v}{v_b}\right|^m \tag{9.70}$$

For a Gaussian spectrum, the performance of a coherent MTI system using binary weights for two, three, and four pulses can be expressed in terms of the standard deviation and mean velocity of the clutter spectrum, the number of cascaded cancelers, and the velocity v_{0f} to which the null has been adjusted. To arrive at expressions that are independent of the radar wavelength λ and pulse repetition frequency f_r, it is convenient to normalize the spectral parameters to the basic blind speed v_b of the radar waveform:

$$v_z = \frac{2\pi v_0}{v_b} = \frac{4\pi v_0}{f_r \lambda} \tag{9.71}$$

$$\sigma_z = \frac{2\pi \sigma_v}{v_b} = \frac{4\pi \sigma_v}{f_r \lambda} \tag{9.72}$$

The normalized clutter spread from scanning, from (9.19), is

$$\sigma_{za} = \frac{2\sqrt{\ln 2}\,\omega_s}{\theta_3 f_r} = \frac{1.665}{n} \tag{9.73}$$

where $n = \theta_3/\omega_s$ is the number of pulses per beamwidth of scan. This spread places an upper limit on the improvement factor when other spread terms are absent.

MTI improvement factors for one-, two-, and three-pulse cancelers, as given by Raemer [27, p. 306], can be written in terms of the normalized parameters:

$$\begin{aligned} I_{m1} &= \left[1 - \exp\left(-\frac{\sigma_z^2}{2}\right)\cos\left(v_z - v_{zf}\right)\right]^{-1} \\ &\approx \frac{2}{\sigma_z^2} \quad \text{for } \sigma_z^2 << 1, \;\; v_{zf} = v_z \end{aligned} \tag{9.74}$$

$$\begin{aligned} I_{m2} &= \left[1 - \frac{4}{3}\exp\left(-\frac{\sigma_z^2}{2}\right)\cos\left(v_z - v_{zf}\right) + \frac{1}{3}\exp\left(-2\sigma_z^2\right)\cos 2\left(v_z - v_{zf}\right)\right]^{-1} \\ &\approx \frac{2}{\sigma_z^4} \quad \text{for } \sigma_z << 1, \;\; v_{zf} = v_z \end{aligned} \tag{9.75}$$

$$\begin{aligned} I_{m3} = \Bigg[1 &- \frac{3}{2}\exp\left(-\frac{\sigma_z^2}{2}\right)\cos\left(v_z - v_{zf}\right) + \frac{3}{5}\exp\left(-2\sigma_z^2\right)\cos 2\left(v_z - v_{zf}\right) + \\ &+ \frac{1}{10}\exp\left(-\frac{9}{2}\sigma_z^2\right)\cos 3\left(v_z - v_{zf}\right)\Bigg]^{-1} \\ \approx \frac{4}{3\sigma_z^6}, &\quad \text{for } \sigma_z << 1, \;\; v_{zf} = v_z \end{aligned} \tag{9.76}$$

The term v_{zf} is the normalized null velocity, which is zero unless some form of adaptation to the mean clutter velocity is used.

Blake considers the overall improvement factor that results from the clutter spread, as in (9.74)–(9.76), along with limitations from internal circuit instability, transmitter instability, and similar sources [3, p. 342, Eq. (7.60)]:

$$\frac{1}{I_m} = \frac{1}{I_{ma}} + \frac{1}{I_{mb}} + \cdots \tag{9.77}$$

This expression, which implies summing of output residue power calculated separately for two or more instability terms, applies only to single-pulse cancelers or when the second and subsequent terms result from instabilities that are random from pulse-to-pulse. If those terms are correlated, increasing the spread σ_z, or the factors $1/\sigma_z^4$ in (9.75) or $1/\sigma_z^6$ in (9.76) cause a much greater reduction in improvement factor than would result from random instabilities.

9.6.2 Noncoherent MTI Improvement Factors

Noncoherent MTI uses samples of the clutter itself to establish the reference phase against which targets and clutter are detected. The performance is generally inferior to that of coherent MTI, but it has the advantage of maintaining the null at v_0:

$$I_{mmn1} = 2\left[1 - \exp\left(-\sigma_z^2\right)\right]^{-1} \approx \frac{2}{\sigma_z^2} \quad \text{for } \sigma_z^2 << 1 \tag{9.78}$$

$$I_{mn2} = 2\left[1 - \frac{4}{3}\exp\left(-\sigma_z^2\right) + \frac{1}{3}\exp\left(-4\sigma_z^2\right)\right]^{-1} \approx \frac{1}{\sigma_z^4} \quad \text{for } \sigma_z << 1 \tag{9.79}$$

$$\begin{aligned} I_{mn3} &= 2\left[1 - \frac{3}{2}\exp\left(-\sigma_z^2\right) + \frac{3}{5}\exp\left(-4\sigma_z^2\right) - \frac{1}{10}\exp\left(-9\sigma_z^2\right)\right]^{-1} \\ &\approx \frac{1}{3\sigma_z^6}, \quad \text{for } \sigma_z << 1 \end{aligned} \tag{9.80}$$

9.6.3 Other MTI Considerations

In applying the improvement factor expressions of Sections 9.6.1 and 9.6.2, several issues listed below must be considered, extending beyond the models of clutter spectra and processor velocity response.

- *MTI losses*. The improvement factor from MTI processing is diluted by the presence of several MTI loss terms, discussed in Section 10.2.5. Those loss-

es apply over the entire range segment in which MTI processing is used, and they affect the detection range even for targets at ranges where no clutter is present unless steps are taken to apply the processing only in cluttered regions.

- *CFAR losses*. The presence of uncanceled clutter may require use of constant-false-alarm-rate (CFAR) detection, introducing another loss term (Section 10.2.5).
- *Multiple-time-around clutter*. All the expressions given in Sections 9.6.1 are limited to cases in which coherence is maintained for clutter over all the pulses used in the canceler process. If multiple-time-around clutter (returned from sources beyond the unambiguous range $R_u = c/2f_r$ of the waveform) is present, *fill pulses*, in addition to those used in the canceler, must be transmitted following each change in waveform (e.g., PRF, RF, or phase modulation within the pulse) or beam position (other than the small changes of a continuously scanning beam), so that the same clutter appears in each canceler pulse. Staggered PRF or pulse-to-pulse frequency agility are incompatible with MTI when multiple-time-around clutter is present. In addition, the coherent-on-receive technique cannot be used when multiple-time-around clutter is present. A theoretical solution to using coherent-on-receive with multiple-time-around clutter has been proposed, but the complexity and losses involved render it impractical for most applications.
- *Staggered PRF*. Use of staggered PRF imposes a limit to improvement factor [28, p. 2.44].
- *Nonlinearity*. The Gaussian spectrum appearing at the receiver input is modified by any nonlinearity prior to the MTI canceler [28, 29], greatly reducing the achievable improvement factor.

9.6.4 Pulsed Doppler Processing

In pulsed Doppler radar, n_c pulses are transmitted during a coherent processing interval (CPI). The processor combines the returns from $n_p = n_c - n_f$ pulses (after gating out a number n_f of *fill pulses* from the beginning of the CPI, where n_f varies from 0 to some fraction of n_c) to form a bank of n_p filters. The filter gains may be fixed or adjusted by a CFAR process to adapt the response to exclude (or reduce to noise level) the receiver output over the clutter spectrum. It is customary to describe the performance of the pulsed Doppler filter in terms of its *clutter attenuation* CA.

There is considerable variety in the velocity response of the PD processor, but in general it can be described as having the following properties:

- A rejection notch with voltage response $H_0 << 1$ and width Δ_v m/s, centered at or near $v = 0$;
- A transition region on each side of the notch of width Δ_v, over which response varies from H_0 at $v = \pm 0.5\Delta_v$ to $H = 0.5$ at $v = \pm(0.5\Delta_v + v_b/n_p)$, and to unity at $v = \pm(0.5\Delta_v + 2v_b/n_p)$;
- An full-response region in which response remains at unity out to $v = \pm 0.5v_b$;
- Repetition of this response at intervals v_b over the receiver bandwidth;
- Ability to adaptively shift the center of the clutter spectrum to the center of the notch.

The clutter attenuation CA is usually defined as

$$CA = \frac{C_i}{C_o} \tag{9.81}$$

where C_o is the output power of the filter whose voltage response $H(v) = 1$ over the frequencies of intended targets:

$$C_o = \int_{-\infty}^{\infty} W(v)\left[H(v)\right]^2 dv \tag{9.82}$$

Figure 9.13 shows an idealized response $H(v)$, with the notch and adjacent response regions for a clutter spread $\sigma_v = 1$ m/s. Notches for $n_p = 16$ and 8 pulses are shown that obtain CA = 40 dB with a blind speed $v_b = 60$ m/s. Notch widths are

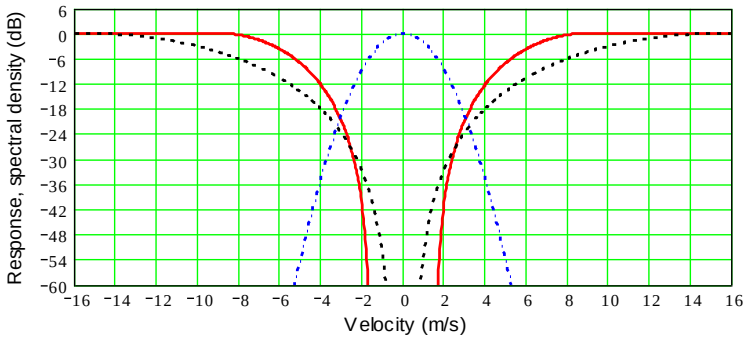

Figure 9.13 Clutter spectrum (dash-dot line) with $\sigma_v = 1$ m/s, and Doppler filter responses $H(v)$ for blind speed $v_b = 60$ m/s, CA = 40 dB with $n_p = 16$ pulses (solid line) and 8 pulses (dashed line).

Δ_v = 1.1 m/s for n_p = 8 and 3.1 m/s for n_p = 16. The sharper response obtained with 16 pulses reduces the width of the transition region, in which the response rises from the notch depth to −6 dB. In this case n_p = 16 gives acceptable target response over 82% of the blind speed, as opposed to 73% for 8 pulses. Adequate clutter attenuation would be available for blind speeds as low as 20 m/s, but the lost fraction of target response would increase, significantly reducing the probability of target detection.

In practice, the idealized response is approximated using a bank of Doppler filters such as shown in Figure 9.14, where several filters containing significant clutter are desensitized (e.g., by range-cell-averaging CFAR) to form a deep notch. Weighting of the inputs holds the filter sidelobes below the level of the rejection notch. The response envelope of the sensitive filters forms the target detection region, in which dips between filters introduce a small filter straddling loss (see Section 10.2.5). The width of the transition region on each side of the notch is approximately equal to the filter spacing v_b/n_p, while the −6-dB width of an individual filter is twice that spacing.

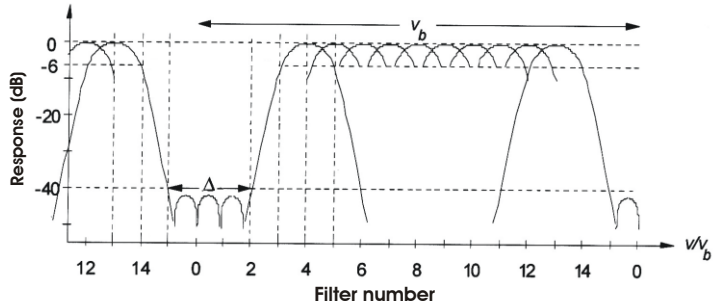

Figure 9.14 Doppler response formed from 16-point Fourier transform filter bank.

The conventional definition for pulsed Doppler clutter attenuation given by (9.81) and (9.82) differs from that of MTI, in which the improvement factor is defined using a *normalized* response $H'(v) = H(v)/\sqrt{\bar{G}}$, as in (9.63). The difference is small in most cases. For example, response of Figure 9.12 gives $\bar{G} = 0.82 = 0.84$ dB for 16 pulses and $\bar{G} = 0.73 = -1.4$ dB for 8 pulses. A more useful measure of pulsed Doppler performance is the *normalized clutter attenuation* CA′, equal to the improvement factor I_m given by (9.65) and given by $\mathrm{CA}' = \sqrt{\bar{G}}\,\mathrm{CA}$. The 0.8–1.4 dB difference in the case illustrated can be neglected, but the different definitions should be kept in mind for cases where $\bar{G}$ is significantly less than unity.

The fraction of velocities within each blind-speed interval with acceptable target response (above –6 dB) is

$$F_a = 1 - \frac{2\Delta_t + \Delta_v}{v_b} = 1 - \left(\frac{2}{n_f} + \frac{\Delta_v}{v_b} \right) \tag{9.83}$$

The clutter attenuation available in a pulse Doppler filter bank is directly related to the ratio of blind speed and the fraction of the velocity response that are allowed to fall below the –6 dB level. Figure 9.15 shows this relationship for a clutter spread σ_v = 1 m/s, with two blind speeds and 16 and 8 pulses. The curves may be applied to other cases with the same ratios of blind speed to clutter spread.

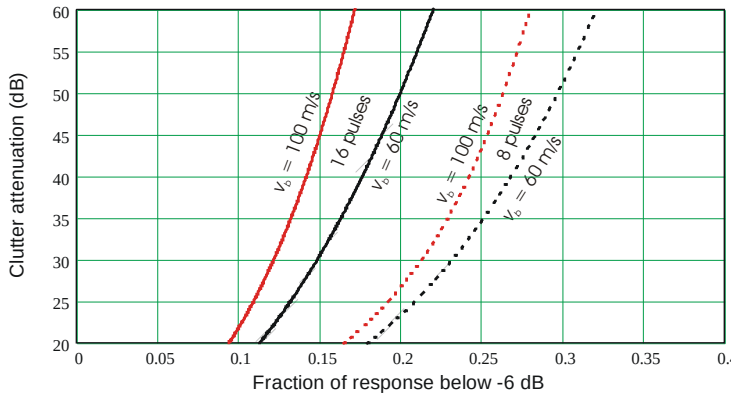

Figure 9.15 Clutter attenuation available as a function of fraction of velocity response below –6 dB,

From Figure 9.15 it can be seen that CA = 40 dB results in the loss of 14% to 18% of potential target velocities with 16 pulses, for $60 < v_b/\sigma_v < 100$, and 24% to 27% of velocities with 8 pulses. These fractions are increased if greater CA is required, or reduced for increased v_b/σ_v and numbers of pulses. They may be reduced and possibly eliminated, except for the zero-velocity region, through use of PRF diversity on a group-to-group basis [2, pp. 243–245], if the beam dwell provides adequate time for exchange of two or more pulse groups.

Further limitations in pulsed Doppler processor performance are similar to those described for MTI in Section 9.6.3.

9.6.5 Clutter Maps

A significant contribution of modern digital processing is the *clutter map*, which stores information on the level of input echoes in each small region in the radar coverage (ideally, each radar resolution cell), averaged over several antenna scans. Introduced originally by engineers at Lincoln Laboratory [30] as part of the so-called moving target detector (MTD), the clutter map is included in many modern signal processors. One map function is to control the receiver gain to preserve linearity in cells containing strong clutter, holding the echoes to the level at which the Doppler processing can suppress the output to the average noise level of the system. This avoids the need for threshold control based on both the average and variance of clutter within a range-cell-averaging CFAR detection circuit (see Sections 10.2.5 and 10.2.6) with the accompanying loss.

A second function of the clutter map is to select the processing mode to maximize detection probability as the clutter background changes (especially over land clutter). In cells containing only thermal noise, the signal is allowed to bypass the Doppler processor, providing detection of targets with radial velocities near zero or other blind speeds. Since targets moving tangentially to the radar pass from one resolution cell to the next without substantially affecting the average stored in the map, they are not suppressed by the processor. The map replaces the older procedure of manually selecting regions to which Doppler processing is applied (e.g., sector gating of MTI or normal video processing).

The potential exists for generalizing the mapping process to adapt the processing paths to different types of clutter and other interference. By using the recent history of the interference environment it is possible to improve the performance of adaptive processes that would otherwise be forced to rely on instantaneous response to interference that varies in time and spatial coordinates.

9.7 SUMMARY OF CLUTTER AND SIGNAL PROCESSING

Clutter can be described as originating from a surface, with RCS $\sigma_c = A_c\sigma^0$; from a volume, with RCS $\sigma_c = V_c\eta_v$; or from a discrete object with a specified σ_c. The terms σ^0 and η_v are the clutter reflectivities. In each case, the power received by the radar is proportional to the product $\sigma_c F_c^4$ of RCS and a clutter pattern-propagation factor. The factor F_c is the result of interaction of the antenna voltage pattern and a clutter propagation factor F_c' that can be expressed separately as a function of the path geometry and radar wavelength.

Five regions contributing surface clutter differ primarily by the nature of their pattern-propagation factors:

1. Near region, in which $F_c' \approx 1$ and is determined by the antenna elevation pattern;
2. Interference region, in which F_c' varies as a result of vector combination of direct and reflected rays;
3. Intermediate region, in which F_c' depends on both interference and diffraction,
4. Diffraction region, in which $F_c' = F_d$, the propagation factor for smooth-sphere or knife-edge diffraction;
5. Zenith region, in which the beam of an airborne radar encounters specular reflection from tilted facets on the surface. In this region a specular component σ_f^0 is defined, $F_c' \approx 1$, and the antenna pattern is applied to form the average of σ_f^0 over the illuminated area.

Measurements of surface clutter are commonly reported as representing σ^0, but in fact are $\sigma^0 F_c^4$, requiring the pattern-propagation factor applicable to the measurement system be evaluated and adjusted before the data are applied to estimate the surface clutter for a radar whose performance is to be estimated. First-order models of sea, land, and discrete clutter were presented in this chapter, considering the propagation effects on reported data. Models of precipitation clutter were presented that are relatively well defined as a result of extensive work in radar meteorology. A chaff model is taken from the electronic warfare literature.

Power spectra and amplitude distributions are modeled for different clutter types, as necessary to determine their effects on signal processing improvement factors and losses in target detection discussed in Chapter 10.

Clutter improvement factors of tens of decibels are available through use of Doppler processing, which also introduces blind speeds at multiples of the basic blind speed. Multiple-pulse dwells are required to support Doppler processing.

References

[1] Long, M. W., *Radar Reflectivity of Land and Sea*, 3rd ed., Norwood, MA: Artech House, 2001.

[2] Barton, D. K., *Radar System Analysis and Modeling*, Norwood, MA: Artech House, 2005.

[3] Blake, L. V., *Radar Range-Performance Analysis*, Lexington, MA: D. C. Heath, 1980; Dedham, MA: Artech House, 1986.

[4] Goldstein, H., "The Fluctuations of Clutter Echoes," Sections 6.18–6.21 in *Propagation of Short Radio Waves*, Vol. 13 in MIT Radiation Laboratory Series, New York: McGraw-Hill 1951. Reprinted (CD ROM Edition), Norwood, MA: Artech House, 1999, pp. 550–587.

[5] Barlow, E.J., "Doppler Radar," *Proc. IRE*, Vol. 37, No. 4, April 1949, pp. 340-355. Reprinted in *Radars*, Vol. 7, *CW and Doppler Radar*, (D. K. Barton, ed.), Dedham, MA: Artech House, 1978.

[6] Ward, K. D., R. J. Tough, and Simon Watts, *Sea Clutter: Scattering, the K-Distribution and Radar Performance*, London: The Institution of Engineering and Technology, 2006.

[7] Schleher, D. C., *MTI and Pulsed Doppler Radar*, 2nd ed., Norwood, MA: Artech House, 2010.

[8] Nathanson, F. E., with J. P. Reilly and M. N. Cohen, *Radar Design Principles–Signal Processing and the Environment*, 2nd ed., New York: McGraw-Hill, 1991.

[9] Trunk, G. V., "Radar Properties of Non-Rayleigh Sea Clutter," *IEEE Trans. on Aerospace and Electronics Systems*, Vol. AES-8, No. 2, March 1972, pp. 196–204. Reprinted in *Radars*, Vol. 5, *Radar Clutter*, (D. K. Barton, ed.), Dedham, MA: Artech House, 1975.

[10] Billingsley, J. B., *Low-Angle Radar Land Clutter–Measurements and Empirical Models*, Norwich, NY: Wm. Andrew Publishing, 2002.

[11] Ayasli, S., "Propagation Effects on Radar Ground Clutter," *IEEE Radar Conf.*, Los Angeles, CA, March 12–13, 1986, pp. 127–132.

[12] Barton, D. K., "Land Clutter Models for Radar Design and Analysis,", *Proc. IEEE*, Vol. 73, No. 2, February 1983, pp. 198–204.

[13] Krason, H. and G. Randig, "Terrain Backscattering Characteristics at Low Grazing Angles for X- and S-band," *Proc. IEEE*, Vol. 54, No. 12, December 1966, pp. 1964–1965 Reprinted in *Radars*, Vol. 5, *Radar clutter*, (D. K. Barton, ed.), Artech House, 1975, pp. 287–288.

[14] Ayasli, S., "SEKE: A Computer Model for Low Altitude Radar Propagation Over Irregular Terrain," *IEEE Trans AP-34*, No. 8, Aug 1986, 1013–1023.

[15] Fishbein, W., S. W. Gravelein, and O. E. Rittenbach, "Clutter Attenuation Analysis," *Technical Report ECOM-2808*, U.S. Army Electronics Command, Ft. Monmouth, NJ, March 1967. Reprinted in *MTI Radar*, (D. C. Schleher, ed.), Dedham, MA: Artech House, 1978, pp. 331–354.

[16] Edgar, A. K., Dodsworth, E. J., and Warden, M. P., "The Design of a Modern Surveillance Radar," *IEE Conf. Pub. No. 105, Radar-73*, October 1973, pp. 8–13. Reprinted in *Radars*, Vol. 5, *Radar clutter*, (D. K. Barton, ed.), Artech House, 1975, pp. 51–56.

[17] Ward, H. R., "A Model Environment for Search Radar Evaluation," *IEEE Eascon Record*, 1971, pp. 164–171. Reprinted in *Radars*, Vol. 5, *Radar clutter*, (D. K. Barton, ed.), Artech House, 1975, pp. 43–50.

[18] McEvoy, W. J., *Clutter Measurements Program: Operations in Western Massachusetts*, Mitre Corp. Rep. MTR-2074, March 1972, DDC Doc. AD742297.

[19] McEvoy, W. J., *Clutter Measurements Program: Operations in the Metropolitan Boston Area*, Mitre Corp. Rep. MTR-2085, March 1972, DDC Doc. AD 742,298.

[20] Vaughn, C. R., "Birds and Insects as Radar Targets – A Review," *Proc IEEE*, Vol. 73, No. 2, February 1985, pp. 205–227.

[21] Moon, J. R., "A Survey of Bird Flight Data Relevant to Radar Tracking Systems," *IEE Radar-2002*, Edinburgh, October 15–17, 2002, pp. 80–84.

[22] Moon, J. R., "Effects of Birds on Radar Tracking Systems," *IEE Radar-2002*, Edinburgh, October 15–17, 2002, pp. 300–304.

[23] Greving, G., and R. Mundt, "The Radar Cross Section and Wind Turbines–Definition and Effects of the Ground and Finite Distances," *Proc. 2011 International Radar Symposium*, September 7–9, 2011, pp. 803–808. Microwaves, Radar and Remote Sensing Symposium 2011, 25–27 August 2011, pp. 321–326.

[24] Sekine, M. et al., "On Weibull Distributed Weather Clutter," *IEEE Transactions on Aerospace and Electronic Systems*, Vol. AES-15, No. 6, November 1979, pp. 824–830.

[25] Doviak, R. J., and D. S. Zrnić, *Doppler Radar and Weather Observations*, New York: Academic Press, 1993.

[26] Schleher, D. C., *Electronic Warfare in the Information Age*, Norwood, MA: Artech House, 1999.

[27] Raemer, H. R., *Radar Systems Principles*, Boca Raton, FL: CRC Press, 1997.

[28] Shrader, W. W., and V. Gregers-Hansen, "MTI Radar," Chapter 2 in *Radar Handbook*, (3rd ed.), M. I. Skolnik, ed., New York: McGraw-Hill, 2008.

[29] Ward, H. R., "The Effect of Bandpass Limiting on Noise with a Gaussian Spectrum," *Proc. IEEE*, Vol. 57, No. 11, November 1969, pp. 2089–2090.

[30] Cartledge, L., and R. M. O'Donnell, *Description and Performance Evaluation of the Moving Target Detector*, MIT Lincoln Laboratory Project Report ATC-69, March 8, 1997.

CHAPTER 10

Loss Factors in the Radar Equation

The radar equation often produces an inaccurate estimate of radar detection range, even in the benign environment of thermal noise. Blake's formulation is an excellent start, and his rigorous treatment of receiver noise, atmospheric effects, and propagation factors reduces the opportunity for error in those terms of the equation. Other areas still remain the source of persistent errors in the range estimate: the loss factors that are either listed separately in the equation or implicit in the detectability factor and other radar parameters. This chapter discusses the many loss factors that must be evaluated if the detection range is to be estimated accurately.

The term *loss* may be defined in many ways, but it refers here not only to the dissipation of energy in a resistive circuit element but to any factor in the radar or the external environment that prevents the signal from being received and used to full effect. The *system loss L* is included in (1.16), (1.18), and (1.19) without detailed definition. Most radar texts include one or more loss actors, but leave it to the reader to identify and evaluate them. There is no standard procedure that ensures adequate accounting for losses, although [1] devotes a chapter to the loss budget.

Losses affect radar in different ways. Some reduce the signal energy received by the radar, some reduce the fraction of that energy passed to the detection device, and others reduce the response to target echoes, increasing the received energy required to obtain the desired detection performance. Some are identified specifically (e.g., the transmission line loss L_t in the Blake chart (Figure 1.1), while others can be identified as components of a specified term (e.g., components of the miscellaneous loss L_x, which increases the effective detectability factor D_x in the radar equation), or as changes in other terms from values that might be expected (e.g., antenna losses).

Some loss factors, denoted by the symbol L, increase the denominator of the equation, while others are expressed as voltage gain factors $F < 1$ in the numerator. The latter form is preferred when conditions can lead to $F = 0$. In the following discussions, symbols for loss factors use a subscript to identify their source, modified with an additional subscript t for the transmitting path, r for the receiving path, c when applied to received clutter energy, and j for received jammer energy.

10.1 REDUCTION IN RECEIVED SIGNAL ENERGY

Components of the loss L_1, included in (1.7)–(1.14) to describe reductions in received RF energy, are identified in this section.

10.1.1 Terms Specified in the Radar Equation

10.1.1.1 Transmission Line Loss L_t

The loss L_t is listed specifically in the Blake chart (Figures 1.1, 1.2) and in (1.20), (1.22), (1.23), and(1.26). It is defined as the ratio of power output of the transmitter (either peak or average) to that delivered to the antenna terminal at which G_t is defined. It includes dissipative losses listed in Table 10.1 and the effects of any impedance mismatch that reflects power back to the transmitter.

Table 10.1 Components of Transmission Line Loss

Component	*Typical Loss* (dB)	*Notes*
Waveguide or coaxial line	0.2	See Figure 10.1
Rotary joint(s)	0.1	Possibly two or three joints
Duplexer	0.5	Ferrite or gas device
Harmonic filter	0.2	Used with magnetron or CFA
Directional coupler	0.05	
Switch	0.05	Used with dummy load
Mismatch	0.1	Typical, for VSWR = 1.4

Loss coefficients for coaxial lines and waveguides are shown in Figure 10.1. In arrays using transmit/receive modules at each element, L_t may consist only of the duplexer and mismatch losses. The mismatch loss is given by

$$L_\Gamma = \frac{1}{1-\Gamma^2} = \frac{(\text{VSWR}+1)^2}{4\text{VSWR}} \tag{10.1}$$

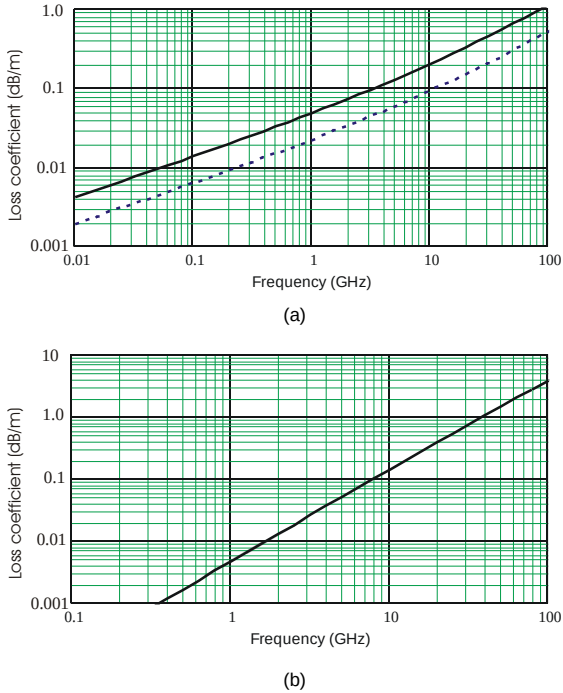

Figure 10.1 Loss versus frequency for (a) rigid coaxial transmission line and (b) rectangular waveguide, plotted using data from [2].

where Γ is the reflection coefficient and VSWR is the voltage standing-wave ratio.

In an electronically scanned phased array, (6.35) expresses the reflection coefficient Γ as a function of scan angle θ from broadside and the exponent β of the element gain pattern. From this, the varying loss over the scan sector is

$$L_{\Gamma}(\theta) = \left(1 - |\Gamma_0|^2 \cos^{\beta-1}\theta\right)^{-1} \tag{10.2}$$

10.1.1.2 Atmospheric Absorption L_α

The loss L_α is included specifically in the Blake chart (Figures 1.1, 1.2) and in (1.20), (1.22), (1.23), and (1.26). It is defined as the ratio of energy that would be received on a radar path through a vacuum to the actual received energy, excluding the lens-loss effect, and is discussed in Sections 7.2 and 7.3. There is no sig-

nificant ionospheric absorption at frequencies in the radar bands, but a dispersive effect may introduce a loss described in Section 7.5.5.

10.1.1.3 Pattern-Propagation Factor F

The pattern-propagation factor F is discussed in detail in Chapter 8.

10.1.1.4 Polarization Factor F_p

The polarization factor F_p is the ratio of the field intensity received by the polarized receiving antenna to the field intensity that would be received in a free-space environment if the receiving antenna polarization were matched to target reflection at the transmitted polarization. It is entered as a constant that depends on antenna polarization and the shape of the echo source.

Target cross section σ is normally specified for a linear (H or V) transmitted and received polarization. Values of the polarization factor for typical targets and for rain are shown in Table 10.2. The polarization factor for snow is closer to unity than for rain, because the snowflakes depart more from a spherical shape.

The polarization factor also describes the effect of ionospherically induced Faraday rotation when the antenna is linearly polarized, as discussed in Section 7.5.4. In this case, the loss varies with the ionospheric path, and must be treated as a statistical factor, as described in Section 10.2.1.

Jammer antennas are often linearly polarized at 45° or 135° to provide a polarization factor $F_{pj}^2 = -3$ dB against radars using H, V, LCP, or RCP (see Sections 3.7 and 3.8). If the victim radar uses an adaptively polarized receiving antenna,

Table 10.2 Polarization Factor

Polarization		*Target* F_p (dB)	*Rain* F_{pc} (dB)
Transmit	*Receive*		
H	H	0	0
H	V	–10	–15
V	V	0	0
V	H	–10	–15
RCP	RCP	–3	–20
RCP	LCP	0	0
LCP	LCP	–3	–20
L	R	0	0
H or V	RCP or LCP	–3	–3
RCP or LCP	V or H	–3	–3

separate jamming transmitters feeding any two orthogonally polarized antennas are necessary to ensure uniform $F_{pj}^2 = -3$ dB over all possible receiving polarizations.

10.1.2 Components of Range-Dependent Response Factor F_{rdr}

The factor F_{rdr}, introduced in (1.26), includes five range-dependent components, not separately listed and usually omitted in the radar equation, that reduce received energy.

10.1.2.1 Tropospheric Lens Factor F_{lens}

The component F_{lens} of the range-dependent response factor F_{rdr} is discussed in Section 7.4. It may be replaced by the lens loss $L_{\text{lens}} = 1/F_{\text{lens}}$ in the denominator, but should remain separated from the atmospheric absorption because only the latter affects the system noise temperature.

10.1.2.2 Sensitivity Time Control Factor F_{stc}

STC is applied at RF or early in the receiver to reduce the dynamic range required of subsequent receiver stages. The receiver power gain to echoes within some selected range R_{stc} varies as

$$\begin{aligned} F_{\text{stc}}^2(R) &= \left(\frac{R}{R_{\text{stc}}}\right)^{X_{\text{stc}}}, \quad R < R_{\text{stc}} \\ &= 1, \qquad\qquad R \geq R_{\text{stc}} \end{aligned} \tag{10.3}$$

relative to the full receiver gain, and $X_{\text{stc}} \leq 4$ is an exponent selected to maintain target detectability for $R < R_{\text{stc}}$. When the gain control is applied prior to the significant sources of receiver noise, the signal-to-noise ratio is assumed to vary as F_{stc}^2 relative to the value that would be obtained with full receiver gain.

A more complicated relationship may be derived in cases where significant noise originates prior to the gain-controlled stage. STC is used only in low-PRF radar, and its effect is illustrated in Figure 1.5. It should be noted that a target at constant altitude, flying above the antenna mainlobe into a region covered by the $\csc^2$ extension of the elevation pattern, closes on the radar with constant SNR in the absence of STC. To prevent the STC factor from dropping the echo below the detection threshold, the upper coverage may be provided by patterns in which the exponent of the csc function is less than two, as illustrated in Figure 2.1.

10.1.2.3 Beam-Dwell Factor F_{bd}

The factor F_{bd} is caused by beam motion occurring between transmission of a signal and reception of its echo. It varies with the target range R, and appears in systems that scan a beam continuously at a very rapid rate, and in those that step the beam to a new position prior to arrival of the echo from R.

For a radar scanning continuously through one beamwidth in time t_o, with a target at range R whose signal time delay $t_d = 2R/c$, the beam-dwell factor is

$$F_{\text{bd}}^2 = L_p \int_{-\infty}^{\infty} f^2(\theta) f^2(\theta - \delta) d\theta = L_p \int_{-\infty}^{\infty} f^2(\theta) f^2\left(\theta - \frac{t_d}{t_r}\right) d\theta \qquad (10.4)$$

where

L_p = beamshape loss;
δ = $t_d/t_o = t_d\omega_s/\theta_3$ = fractional beamwidth scanned during the delay;
ω_s = scan rate;
θ_3 = beamwidth in the scanned coordinate;
$f(\theta)$ = antenna voltage pattern.

The beamshape loss is included as a multiplier in (10.4) to normalize F_{bd} to unity for $\delta << 1$. For example, the beam-dwell factor for a Gaussian beam pattern with $t_d = 0.5t_o$ is $F_{\text{bd}}^2 = -1.5$ dB. This loss is absent from electronically scanned arrays that rapidly step the beam between dwells in each position after receipt of all desired echoes.

10.1.2.4 Frequency Diversity Factor F_{fd}

In frequency diversity, the frequency is changed between transmission of successive groups of n_{fd} pulses. The retuned receiver has zero response, $F_{\text{fd}} = 0$, on the final n_{rt} echo pulses of each group from targets at range $R > n_{tr}R_u$. With frequency agility, in which the radar frequency is changed from pulse to pulse, $F_{\text{fd}} = 0$ on all echoes from previous transmissions. This eliminates detection of clutter and responsive jammers as well as range-ambiguous targets. The effect does not appear in the standard radar equation, but should be included in computer programs that might otherwise include the rejected energy components from targets and interference lying beyond the unambiguous range. In most applications, this is considered a desirable feature that eliminates interference rather than a "loss" factor.

10.1.2.5 Eclipsing Factor F_{ecl}

Eclipsing occurs when the apparent time delay $t'_d = t_d$(modulo t_r) allows the echo pulse to overlap either the immediately preceding or following transmitted pulse.

Figure 10.2 shows in part (a) two successive transmitted pulses separated by the pulse repetition interval PRI = t_r, and an echo pulse with delay $t'_d = 0.5t_r$. The signal is subject to eclipsing for delays such that $|0.5t_r - t'_d| > 0.5t_r - \tau$. Part (b) of the figure shows the fraction of the echo pulse that passes uneclipsed. That fraction is given by

$$H_{\text{ecl}}\left(t'_d\right) = \frac{0.5_r - \left|\left(t'_d/t_r\right) - 0.5\right|}{D_u}, \quad \left|\left(\frac{t'_d}{t_r}\right) - 0.5\right| > 0.5 - D_u$$
$$= 1, \quad \left|\left(\frac{t'_d}{t_r}\right) - 0.5\right| \le 0.5 - D_u \tag{10.5}$$

where $D_u = \tau/t_r$ is the duty cycle.

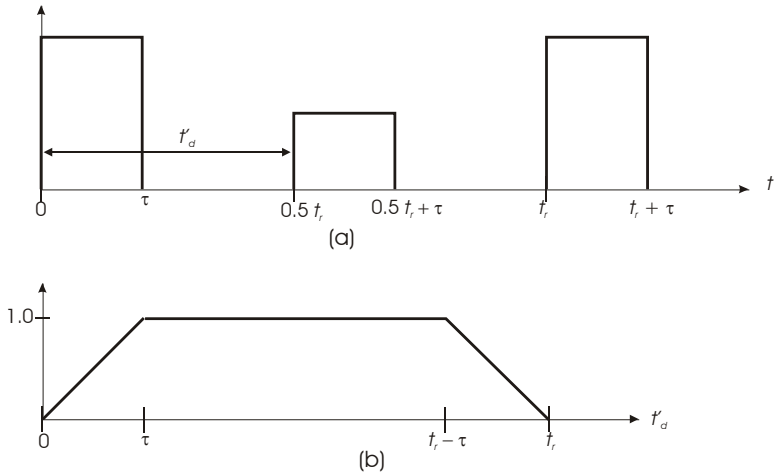

Figure 10.2 Eclipsing: (a) transmitted pulses with echo midway in PRI, (b) uneclipsed pulse fraction H_{ecl}.

For an uncoded rectangular pulse, the eclipsed pulse energy is H_{ecl} times its uneclipsed value, and the mismatched filter passes that fraction with efficiency H^2_{ecl}, resulting in an eclipsing factor given by:

$$F^2_{\text{ecl}}\left(t'_d\right) = H^3_{\text{ecl}}\left(t'_d\right) \tag{10.6}$$

A similar factor applies to waveforms using pulse compression.

In low- and medium-PRF radar using constant PRF, the deterministic factor given by (10.6) can be applied as a function of target range, producing identifiable regions adjacent to a transmitted pulse where P_d drops toward zero (see Figure 1.4). In high-PRF radar, the target passes rapidly through the eclipsed regions, and PRF diversity during each beam dwell is commonly used to shift those regions to preserve some of the target returns. For that case, and for other radars in which P_d is to be averaged over pulse groups at different PRFs, a statistical loss factor (Figure 10.4) is found using the procedure given in Section 10.2.1.

10.1.3 Losses Included in System Noise Temperature

Chapter 6 discussed the calculation of system noise temperature T_s. In addition to the receiver noise figure F_n, the three RF loss components listed below contribute to T_s.

10.1.3.1 Receiving Line Loss L_r

The loss L_r contains many of the components listed for L_t in Table 10.1, excluding the possible transmitter switch that connects to the dummy load. A bandpass filter to reduce out-of-band interference replaces the harmonic filter needed in some transmitters. An additional loss of 0.2–0.4 dB is often contributed by a solid-state limiter that protects the low-noise receiving amplifier.

10.1.3.2 Antenna Dissipative Loss L_a in Noise Temperature

The loss L_a varies significantly with antenna type, but may include the components listed in Table 10.3. The antenna mismatch for an electronically scanned array may greatly exceed that of a mechanically scanned antenna or an array at broadside, as shown in Section 6.3.5. Values shown in the table apply for an element pattern $G_e(\theta) = \cos^{3/2}\theta$.

10.1.3.3 Atmospheric Absorption Loss L_α in Noise Temperature

This loss, applied in calculating system noise temperature in Section 6.3.1, is discussed in Sections 7.2 and 7.3.

10.1.4 Losses in the Search Radar Equation

10.1.4.1 Cosecant Pattern Loss L_{csc}

Extension of the elevation coverage above the full-range coverage sector θ_1 of the mainlobe (see Figure 2.1) reduces the antenna gain. In the standard form of the radar equation, this appears as reduced G_t, G_r, or both, but in the search radar

Table 10.3 Components of Antenna Dissipative Loss

Location	*Component*	*Typical Loss* (dB)
Feed system	Feed horn	0.1
	Waveguide series feed	0.7
	Waveguide parallel feed	0.4
	Stripline series feed	1.0
	Stripline parallel feed	0.6
Phase shifter	Nonreciprocal or Faraday rotator	0.7
	Reciprocal ferrite	1.0
	Diode (per bit)	0.4
Array	Mismatch (no electronic scan)	0.2
	Mismatch (electronic scan 60°)	1.7
Exterior	Radome	0.5–1.0

equation the corresponding loss $L_{\csc}$ appears in both the solid angle ψ_s of search coverage and as a component of the search loss L_s. Losses for the $\csc^2$ and csc patterns are given in (2.11) and (2.12) and shown in Figure 2.2, along with those for intermediate cases.

10.1.4.2 Elevation Beamshape Loss L_{pe}

The loss L_{pe} appears as a component of search loss L_s in the search radar equation for 2-D radar. Figure 2.1 shows a fan beam that provides the specified full-range coverage at elevation angle $\theta_1 = \sin^{-1} H_m/R_m$. The half-power beamwidth θ_e required for this coverage exceeds the upper angle of full-range coverage θ_1 by the factor $L_{pe} \approx 1.5$, reducing the gain G_t relative to that assumed in derivation of the search radar equation. The same factor must also be included in selecting the height of the antenna, reducing the aperture area A relative to that required for a given wavelength if the elevation beamwidth were set to θ_1. An approximation for this loss as a function of the ratio θ_e/θ_1 is

$$L_{pe} = \sqrt{0.8\left(\frac{\theta_e}{\theta_1}\right)^2 + L_{p0}} \tag{10.7}$$

10.1.4.3 Antenna Dissipative Loss L_a in Search Radar Equation

Section 2.6.1 discusses the antenna gain assumptions made in derivation of the search radar equation. No dissipative loss within the antenna is included in those

assumptions, and hence L_a^2 must be included as component of L_s to account for the loss in transmission and reception, in addition to inclusion of L_a in system noise temperature calculation.

10.1.4.4 Pattern Constant L_n

Section 2.6.1 discusses also the need to include this factor as a component of L_s to correct for the fact that $G_t < 4\pi/\theta_a\theta_e$ in actual antennas (as opposed to the rectangular beam used in derivation of the search radar equation). The loss can be calculated from the beamwidth factor K_θ and aperture efficiency η_a as

$$L_n = \frac{1}{K_\theta^2 \eta_a} \tag{10.8}$$

Values L_n = 1.16–1.28 dB apply to all antennas, with additional spillover loss ≈ 0.5 dB for lens or reflector antennas and blockage loss 0.6–1.2 dB for reflector antennas with feeds centered in front of the reflector.

10.1.4.5 Antenna Illumination Loss L_η in Search Radar Equation

When the physical aperture A is used in the search radar equation (2.7) or (2.8), the search loss L_s must include the illumination loss, to be discussed in Section 10.1.5.1. That loss is applied only once to L_s, because the effect of illumination taper on the transmitting gain is included in the factor L_n.

10.1.4.6 Scan Distribution Loss L_d

The scan distribution loss describes the loss in integration performance when performing two or more scans of the search volume during the search time t_s. The detection requirements are met with a cumulative probability of detection rather than by P_d in a single scan. The loss is defined as the ratio of the SNR required when cumulative detection is performed over m scans with n/m pulses per scan to that required for a single scan with n pulses.

Marcum [3, pp. 13–14] discusses the effect of using m groups of separately integrated pulses to achieve detection. He states that "it is always best for [m] to equal 1." That observation is correct for a steady target under most conditions, but for fluctuating targets it may be possible to obtain better performance using two or more scans within the allocated search time.

The loss is calculated using the expression for binary integration loss (Section 10.2.5.1) with m = 1, modified by adjustment in other losses that are dependent on the single-scan P_d. For example, beamshape loss L_p and eclipsing loss L_{ecl} increase

steeply with increasing P_d. The method of calculating L_d is to define the effective detectability factor $D_{xm}(m)$ as

$$D_{xm}(m) = D(P_1, n/m) \prod_k L_{z_k}(P_1, n/m) \tag{10.9}$$

where

$D(P_1, n/m)$ = basic detectability factor for detection probability P_1 using integration of n/m pulses;
P_1 = $1 - (1 - P_c)^{1/m}$;
P_c = desired probability of detection after m scans;
$L_z(P_1, n/m)$ = statistical loss component for processing n/m pulses to achieve P_1;
k = number of statistical loss components contributing to D_x.

The scan distribution loss is

$$L_d = \frac{mD_{xm}(m)}{D_{xm}(1)} \tag{10.10}$$

This may result in $L_d < 1$, indicating a time-diversity gain for use of m scans of the volume during t_s.

10.1.4.7 Other Losses in Search Radar Equation

The other antenna losses discussed in Section 10.1.5.3 are also included in the search radar equation both for the transmitting and receiving directions, doubling their decibel contributions to L_s. In addition, all the losses contributing to D_x, as discussed below in Section 10.2, are included as components of L_s, since the denominator of that equation uses the detectability factor $D_0(1)$ for a single pulse on a steady target.

10.1.5 Losses Included in Antenna Gain

Several loss terms appear as reductions in antenna gains, but are listed here to ensure that they are included either there, in the pattern-propagation factor, or added separately to the radar equation.

10.1.5.1 Antenna Illumination Loss L_η

The antenna gains G_t and G_r are specified in the radar equation. They can calculated from the physical aperture area A using

$$G = G_0 \eta_a = \frac{4\pi A}{\lambda^2} \eta_a \tag{10.11}$$

where G_0 is the aperture gain for uniform illumination and η_a is the aperture efficiency. The illumination efficiency η_i is one component of aperture efficiency, and the illumination loss is defined as $L_\eta = 1/\eta_i$. This is shown in Figure 10.3 as a function of the sidelobe level, for rectangular apertures that use the same illumination taper in both coordinates and for elliptical apertures. For different illuminations, the loss is the geometric mean of the two losses. The Hansen illumination refers to the one-parameter circular illumination discussed in [4, pp. 107–111]. The circular illumination function with the steepest increase in loss has the form:

$$g(r) = \left(1 - 4r^2\right)^n \tag{10.12}$$

as tabulated in [5, p. 264]. This is representative of the illuminations produced by simple horn feeds for reflector or lens antennas.

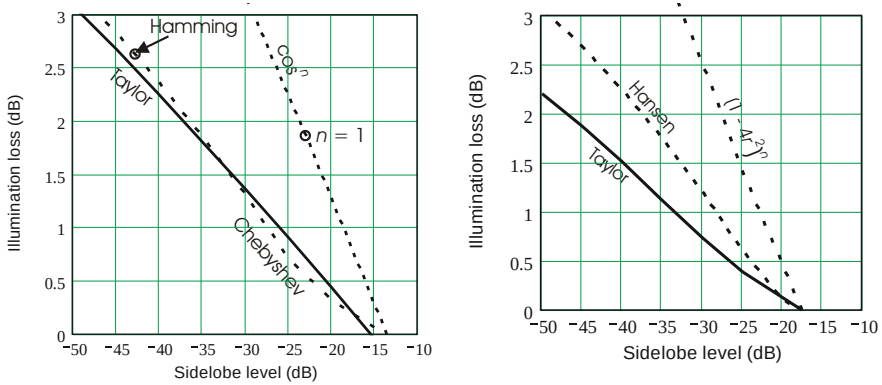

Figure 10.3 Two-coordinate illumination loss as a function of sidelobe level for different families of tapered illumination.

10.1.5.2 Antenna Dissipative Loss L_a in Antenna Gain

When the antenna gains are specified, it is assumed that the efficiency η_a has included the dissipative loss component $\eta_\Omega = 1/L_a$.

10.1.5.3 Other Losses in Antenna Gain

The aperture efficiency η_a is assumed to include also the following losses:

- Spillover loss: ≈ 0.5 dB for in a lens or reflector antenna;
- Blockage: 0.6–1.2 dB for a reflector antenna;
- Dimensional tolerance: rms phase errors σ_ϕ, describing deviations of the aperture by a distance σ_{as} from its assumed form, cause a loss given by

$$L_{as} = \exp\left(\sigma_{\phi s}^2\right) = \exp\left(k_{as}\frac{2\pi\sigma_{as}}{\lambda}\right) \tag{10.13}$$

  where k_{as} = 2 for reflector surfaces or 1 for planar arrays and lens surfaces. When the feed side and the radiating side of a lens have the same departure from their assumed form (e.g., bending of the entire structure), $k_{as} \to 0$.

- Signal bandwidth loss: While reflector and metallic lens antennas normally have bandwidths in excess of the signal bandwidth *B*, array antennas have limited bandwidth that can cause loss in gain for wideband signals, especially when scanned off broadside. This subject is discussed in [1, pp. 170–172.].
- Array phase error loss: the loss $L_\phi = \exp(\sigma_\phi^2)$, where σ_ϕ is the rms phase error of the feed and phase shifters.
- Phase-shifter quantization loss: quantization of phase-shift control to *m* bits causes a loss

$$L_{\phi q} = \exp\left(\sigma_{\phi q}^2\right) = \exp\left(\frac{\pi^2}{3\times 2^{2m}}\right) \tag{10.14}$$

- Antenna mismatch loss: the loss expressed by (10.1) applies also to antenna mismatch.
- Scan loss: the gain of an array scanned off broadside by the angle θ is reduced by the element factor

$$G(\theta) = f_e^2(\theta) = \cos^\beta(\theta)\,3.3 \tag{10.15}$$

$$L_{sc} = \frac{G(0)}{G(\theta)} = \cos^{-\beta}(\theta) \tag{10.16}$$

where $1 < \beta < 2$ (usually ≈1.5). When the radar equation is applied to targets at a specific off-broadside angle, the antenna gains are reduced by this loss. It also applies with $\beta \approx 1$ to electrically fixed arrays constructed of slotted waveguide, from which the beam is squinted from broadside by a frequency-dependent angle θ. When the radar equation uses the broadside gains, and detection performance is averaged over a sector extending θ_s from broadside, a scan loss is defined as the increase on on-axis SNR required to maintain the specified detection probability This is included as an increase in required signal energy (see Section 10.2.1).

- Cosecant pattern loss: the loss L_{csc} described in Section 10.1.4 reduces the antenna gains G_t and G_r in a 2-D radar, and G_t in a stacked-beam 3-D radar.

- Loss in water film: Most radar antennas pass the transmitted and received signals through a dielectric window or covering that separates the antenna or feed components from the environment. Loss in this dielectric material can be minimal, except in radomes that must withstand wind forces (see Table 10.3), but may increase when a water film is formed by condensation or precipitation. Table 10.4 shows losses calculated for different film thicknesses at S- and K_u-bands. Water films on a reflector surface are seldom thick enough to cause loss, as the electric field at the surface falls to zero and is incapable of transferring energy to the water unless the film thickness is greater than hundredths of a wavelength.

Table 10.4 Losses in Water Films

Film Thickness (mm)	*Radome Loss* (dB)		*Reflector Loss* (dB)	
	f = 3.7 GHz	f = 16 GHz	f = 3.7 GHz	f = 16 GHz
0.05	—	3.2*	—	—
0.13	1.1	5.3	≤ 0.01	0.03
0.25	1.1	5.3	≤ 0.01	0.2
0.38	4.2	10.9	≤ 0.01	0.9
0.5	5.6	12.3	≤ 0.01	2.7

Note: Theoretical data from [6]. * indicates experimental data reported in [7].

10.2 INCREASES IN REQUIRED SIGNAL ENERGY

10.2.1 Statistical Losses

Some loss factors do not appear directly in the radar equation, but instead cause an increase in the effective detectability factor D_x that represents the on-axis energy ratio required to achieve the desired detection probability P_d. Some of these are

constant, but others are *statistical losses*, in that their value depends on averaging detection probability P_d over a variable z that represents target position in one of the four dimensions of radar space (or in polarization angle of the echo). A loss L_z is defined in each case as the increase in input signal-to-noise energy ratio E/N_0 that is required to maintain the desired P_d as z varies between specified values. If the required energy ratio for the idealized system is D, the requirement increases to $L_z D$ when L_z is present. Each of the several components L_z is calculated for the desired P_d, and the loss product is applied to obtain the effective detectability factor appearing in the denominator of (1.20), (1.23), and similar equations:

$$D_x = D\prod_z L_z \tag{10.17}$$

The general procedure for calculation of statistical loss is to express the response of the radar system $H(z)$ as the voltage ratio of output signal to a reference value that would apply if the sensitivity to z were absent. The signal-to-noise power ratio s_o' applied to the detection device is then

$$s_o'(z) = s_o H^2(z) \tag{10.18}$$

where s_o is the SNR in the absence of the loss.

Theoretical probabilities of detection $p_d(s_o)$ for specified target models are given in Chapter 4. In the presence of loss p_d is reduced to

$$p_d'(z) = p_d\left[s_o'(z)\right] = p_d\left[s_o H^2(z)\right] \tag{10.19}$$

The detection probability when averaged over the possible values of z is

$$\begin{aligned} P_{av}(s_o) &= \frac{1}{z_{\max} - z_{\min}} \int_{z_{\min}}^{z_{\max}} p_t(z)\, p_d'(z)\, dz \\ &= \frac{1}{z_{\max} - z_{\min}} \int_{z_{\min}}^{z_{\max}} p_t(z)\, p_d\left[s_o H^2(z)\right] dz \end{aligned} \tag{10.20}$$

where $p_t(z)$ is the probability that the radar and target conditions lead to an echo at position z.

To calculate L_z, values of s_o in (10.20) are varied until the detection requirement is met: $P_{av} = P_d$, at a value $s_{d0}(P_d)$. This gives L_z as

$$L_z(P_d) = \frac{1}{D} s_{d0}(P_d) = \frac{1}{D} \text{root}_{s_o}\left[P_{av}(s_o) = P_d\right] \tag{10.21}$$

where the root function is the value of s_o that meets the equality in the brackets. In general there is no closed-form solution to (10.21), but computer programs are available to find this root for arbitrary $p_t(z)$, $H(z)$, and target statistics. The corresponding range-dependent response factor is $F^2_{\text{rdr}} = 1/L_z$.

10.2.1.1 Eclipsing Loss L_{ecl}

The eclipsing loss is derived statistically from the range-dependent factor F_{ecl}, and is used in the radar equation for high-PRF radar to find the range at which the average P_d for echoes whose apparent delay varies with z over specified limits (see Section 10.1.2.5). The factor $F_{\text{ecl}}(t'_d)$ replaces $H(z)$ in (10.21), with integration over $0 < t'_d < t_r$. Echoes are normally modeled as uniformly distributed over the PRI: $p_t(z) = 1$.

Figure 10.4 shows L_{ecl} when averages of P_d are taken for Case 1 targets distributed uniformly within the PRI. It can be seen that high P_d leads to large losses

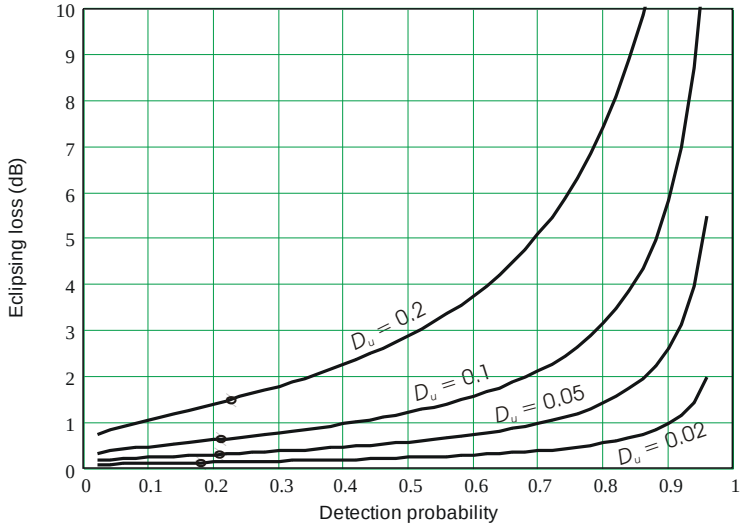

Figure 10.4 Eclipsing loss as a function of detection probability for different values of duty cycle. Values of L_{av} for each duty cycle are shown by the circles near $P_d = 0.2$.

as duty cycle is increased. High cumulative probability of detection could be obtained over two or more pulse groups with different PRIs, allowing reduced P_d per group with lower L_{ecl}.

This statistical loss may be compared with the loss L_{ecl} defined as the reciprocal of H_{av}^3 averaged over t_r, which are shown by the circles near the lower left portion of the figure. The statistical loss is greater for $P_d > 0.25$, and much greater for $P_d \to 1$.

10.2.1.2 Faraday Rotation Loss L_{Far}

The Faraday rotation angle $\phi(h)$ varies with the total electron count along the path to target altitude h, according to (7.44). The response of a linearly polarized radar antenna to this angle can be expressed as

$$H_{\text{Far}}(\phi) = \cos\phi \tag{10.22}$$

This expression is substituted for $H(z)$ in (10.21), and the integration is carried out over a region $0–\phi_m$ to calculate the Faraday rotation loss. Figure 10.5 shows L_{Far} as a function of P_d for rotations from zero to different maximum values ϕ_m. The worst case occurs at $\phi_m = 120°$ where $H_{\text{Far}} < -3$ dB over 67% of the interval 0 to ϕ_m. The average loss in received power for any number of full rotations is 3 dB,

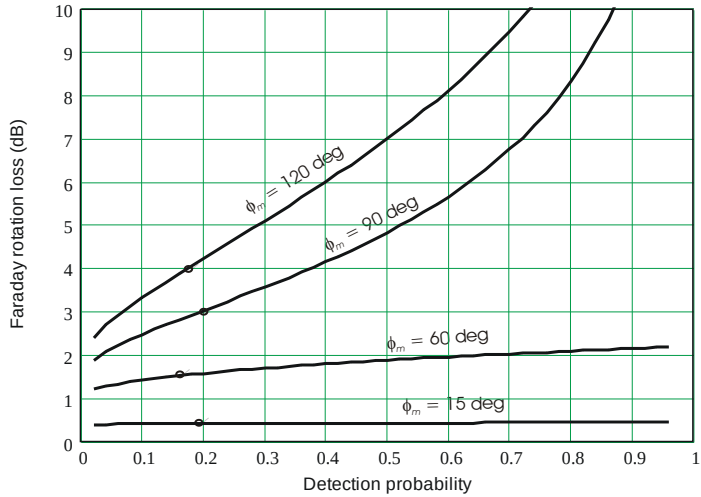

Figure 10.5 Faraday rotation loss for linearly polarized antenna as a function of average detection probability over rotation angles from zero to different values of ϕ_m. The average loss in received power is shown by circles on each curve near $P_d = 0.2$. For any number of full rotations the loss follows the curve for $\phi_m = 90°$.

but it can be seen that the statistical loss for $\phi_m = 90°$ is greater than that average value when $P_d > 20\%$.

10.2.1.3 Scan Sector Loss L_{sector}

Section 10.1.5.3 discussed the loss L_{sc} for the case where a specific scan angle is used. Where the scan is carried out over a sector in which a specified average P_d is to be obtained, the statistical loss procedure expression (10.21) is used over the limits of the scanned sector, with $H(\theta) = \cos^{\beta/2}(\beta)$ and $p_t(\theta)$ representing the probability density of target positions within the sector (normally assumed uniform).

Figure 10.6 shows the scan sector loss as a function of P_d for different maximum scan angles θ_m, for sectors extended over $\pm\theta_m$. For comparison, the average loss in power over each sector is shown by circles on each line, and those values are exceeded for $P_d > 20\%$.

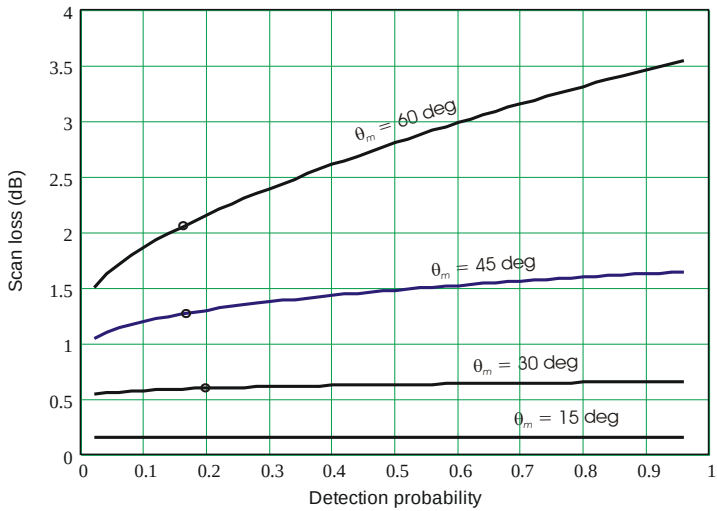

Figure 10.6 Scan sector loss as a function of detection probability averaged over sector $\pm\theta_m$. Average loss in power is shown by circles on each line near $P_d = 20\%$.

10.2.2 Losses in Basic Detectability Factor

The basic detectability factor, denoted by $D_{0,\ldots,4}$ for steady and Swerling targets, is the theoretical value before considering beamshape, matching, and signal processing losses. Values are calculated as shown in Chapter 4, which also extends the theory to the detectability factor D_e for targets observed with diversity. Within these factors are included two losses that are applied to the basic single-pulse,

steady-target factor D_{01} in deriving the factors for n-pulse integration and for fluctuating targets. These losses do not appear separately in the radar equation, but are useful in comparing the performance of different waveform and processing options. For example, Figure 4.12 shows the variation in their sum as a function of the number of diversity samples, with the optimum number of samples increasing from one to eight with detection probability.

10.2.2.1 Integration Loss L_i

Integration loss is discussed in Section 4.4.3, and plotted in Figure 4.9 as a function of n for different values of D_{01} whose detection performance is to be matched using the received energy ratio $nD_0(n)$.

10.2.2.2 Fluctuation Loss L_f

Fluctuation loss is discussed in Section 4.4.5, and plotted in Figure 4.10 for the Case 1 target. Section 4.4.7 discusses how the loss varies with the number of independent target samples n_e included in the n integrated pulses.

10.2.2.3 Detector Loss C_x

In Section 4.4.2 the loss in SNR resulting from the nonlinearity of the envelope detector was described by the detector loss C_x, defined relative to the SNR available from a coherent (phase sensitive) detector with an in-phase reference voltage. An empirical expression

$$C_x = \frac{s + 2.3}{s} \tag{10.23}$$

where s is the input SNR to the envelope detector, was found in [8] to reproduce with acceptable accuracy the performance of detection systems based on the output of an envelope detector. This loss is included in the integration loss term, and need not be calculated separately.

10.2.3 Matching and Bandwidth Losses

Blake's basic radar equation (1.16) includes a bandwidth correction factor C_b to multiply the detectability factor when nonoptimum receiver bandwidth is used. Subsequent forms of the equation from work of Hall and Barton replaced C_b with a matching loss L_m or a matching factor M for application to electronic detection.

10.2.3.1 Bandwidth Correction Factor C_b

Section 1.5.4 notes that the factor C_b given by (1.17) is unsuitable for use with electronic detection devices. It remains useful to multiply the visibility factor V_0 to characterize the visual detection process. The formal definition of C_b given by Blake [9, p. 366, Eq. (8.14)] would give the same result as the expression for matching loss in the following section, but the plotted value [9, p. 367, Figure 8-2] does not represent that result. Instead, it gives experimental values of the excess energy ratio required to maintain visibility of a display as receiver bandwidth is varied, as reported by Haeff [10]. Blake notes that the simple concept represented by the plots is inapplicable to radar that use "pulse bursts or other nonsimple waveforms."

10.2.3.2 Matching Loss L_m

Section 1.4.1 presents Hall's radar equation (1.20), in which the effective detectability factor is used to increase the basic detectability factor $D(n)$ by five loss factors: $D_x = D(n)L_mL_pL_cL_xL_o$. The matching loss L_m is defined as the ratio of peak output SNR of the matched filter to that of the mismatched filter, given the same input. It is calculated for a signal voltage spectrum $A(f)$ and filter response function $H(f)$ as

$$L_m = \frac{\int_{-\infty}^{\infty} |A(f)|^2 \, df \int_{-\infty}^{\infty} |H(f)|^2 \, df}{\left| \int_{-\infty}^{\infty} A(f)H(f) \, df \right|^2} \tag{10.24}$$

Figure 10.7 shows the loss as a function of the product of pulsewidth τ and receiver noise bandwidth B_n for an uncoded rectangular pulse with different filter types. Other than the $(\sin x)/x$ matched filter, the best performance is L_m = 0.5 dB obtained with a Gaussian filter, which represents a cascade of several single-pole filters with and overall response $B_n\tau = 0.8$.

Figure 10.8 shows the matching loss as a function of time-sidelobe level for a weighted linear-FM waveform with different weighting functions. The curves follow those for illumination taper loss given in Figure 10.2(a).

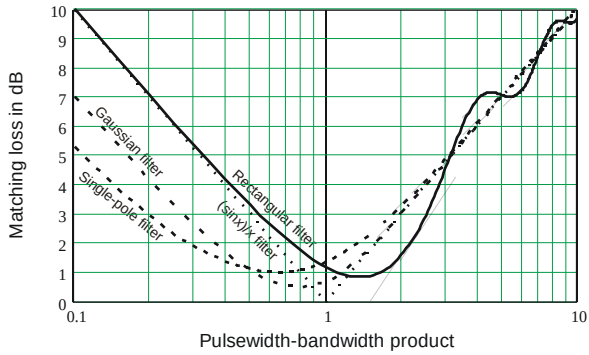

Figure 10.7 Matching loss L_m as a function of product τB_n for an unmodulated rectangular pulse with different IF filter types. From [1].

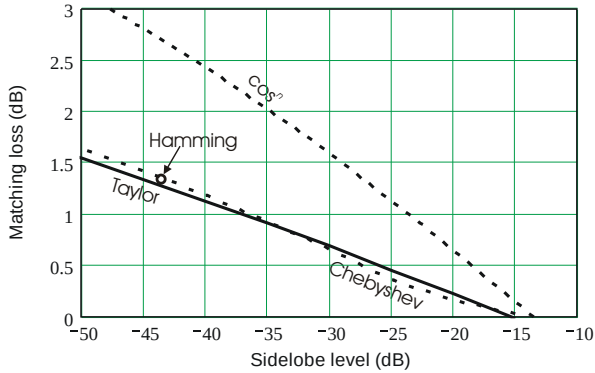

Figure 10.8 Matching loss L_m as a function of time sidelobe level for a weighted linear-FM waveform with different weighting functions.

10.2.3.3 Matching Factor *M*

In Barton's radar equation (1.23) and the accompanying modified Blake chart of Figure 1.2, L_m is replaced by the matching factor M. This factor includes two modifications to L_m:

- When the receiver filter has $B_n\tau > 1$ and the postdetection (video) bandwidth $B_v \geq B_n/2$, the matching loss L_m describes the reduction on SNR at the detection circuit. However, in many cases $B_v < B_n/2$ provides reduction in the noise leaving the receiver. The result is an *effective bandwidth* that is the lesser of B_n or $2B_v$ for rectangular filters, and otherwise is given by

$$B_{eff} = \left(\frac{1}{B_n^2} + \frac{1}{4B_v^2} \right)^{-1/2} \tag{10.25}$$

The greater noise entering the envelope detector leads to a collapsing ratio B_n/B_{eff} and causes a collapsing loss L_c (see Section 10.2.5.4). The product of L_m from (10.25) and L_c gives the correct matching factor M, which is generally less than L_m calculated from B_n alone. The difference is often small enough to be neglected.

- For $B_{eff}\tau < 1$ the peak SNR is reduced according to (10.24), but the output pulse is broadened and fewer noise samples reach the envelope detector during the periods when signal is absent. This reduces the false-alarm rate and permits increasing the false-alarm probability, reducing the threshold and the required detectability factor D_x relative to that calculated using L_m alone. Since small changes in P_{fa} have little effect on D, this difference is often small enough to be neglected.

In most cases, use of L_m from (10.25), Figure 10.7 or Figure 10.8 is sufficiently accurate for use without the extra calculations involved in finding the effective bandwidth and the adjustment for false-alarm probability.

10.2.4 Beamshape Loss L_p

The beamshape loss is the subject of Chapter 5, and applies to all radars during search and acquisition of a target unless the beam axis can be placed on the target within a small fraction of the beamwidth. In using the Blake chart or creating a vertical coverage chart (see Figure 1.6), the target position relative to the beam-axis in elevation is included in the pattern-propagation factor F, and only the one-dimensional beamshape loss appears as a multiplier of detectability factor in the denominator of the radar equation. However, when the search radar equation is used or when detection probability over a two-dimensional angle sector is calculated, the two-dimensional loss L_{p2} from Sections 5.4 and 5.5 is used instead of F.

Notations used in Chapter 5 to distinguish different beamshape losses are:

- L_{p0} = one-coordinate loss with dense sampling;
- L_{p1} = one-coordinate loss for general case;
- L_{p2} = two-coordinate loss for general case;
- L_{pn} = net beamshape loss after adjustment for beam spacing, as used in search radar equation;
- L_{pT} = two-coordinate loss for triangular beam grid.

10.2.5 Signal Processing Loss L_x

The miscellaneous loss L_x that appears in the Blake chart consists of several components listed below that result from signal processing that does not preserve the SNR at the receiver output. These are not necessarily the result of design defects, but may accompany steps necessary to reject false alarms from clutter and other interference.

10.2.5.1 Binary Integration Loss L_b

Binary integration uses a double-threshold system in which each of n pulses is applied to the first threshold to achieve probabilities of detection p_d and false alarm p_f. Outputs from the first threshold are accumulated over n pulses, and an alarm is issued when at least m outputs out of the n pulses are obtained. It is a substitute for video integration, and is sometimes called m-out-of-n integration.

The probability of obtaining j outputs from the first threshold is

$$P(j) = \frac{n!}{j!(n-j)!} p^j (1-p)^{n-j} \tag{10.26}$$

where $P(j)$ is the probability that exactly j crossings of the threshold occur in n trials, each with threshold crossing probability p. The probability of an output alarm is

$$P(j \geq m) = \sum_{j=m}^{n} P(j) \tag{10.27}$$

The output false-alarm probability is found by letting p in (10.26) be the probability p_{fa} that noise alone exceeds the threshold on each trial:

$$\begin{aligned} P_{fa} &= \sum_{j=m}^{n} \frac{n!}{j!(n-j)!} p_{fa}^j \left(1-p_{fa}\right)^{n-j} \\ &\approx \frac{n!}{m!(n-m)!} p_{fa}^m \left(1-p_{fa}\right)^{n-m}, \; p_{fa} \ll 1 \end{aligned} \tag{10.28}$$

Given the required P_{fa} at the integrator output, (10.28) is solved for the required single-pulse p_{fa}. Then, given the single-pulse SNR, the single-pulse p_d is found from expressions in Chapter 4 and used to find the output P_d from

$$P_d = \sum_{j=m}^{n} \frac{n!}{j!(n-j)!} p_d^j \left(1-p_d\right)^{n-j} \tag{10.29}$$

If a requirement for P_d is given, (10.29) must be solved for the required single-pulse p_d, and the detectability factor $D_b(n)$ corresponding to p_d and p_{fa} found from expressions in Chapter 4.

The range of optimum m is quite broad, lying near the value determined by Schwartz [11] for large n:

$$m_{\text{opt}} = 1.5\sqrt{n} \tag{10.30}$$

A comparison of the integration loss for optimum binary integration with the video integration loss $L_i(n)$ is shown in Figure 10.9. The *extra* loss with binary integration, beyond that for video integration, is the *binary integrator loss*, denoted by L_b, and is approximately 1.4 dB for $n \geq 5$. Accepting this approximation, the tedious processes of solving (10.29) for required single-pulse probabilities may be avoided by using the equations for video integration and increasing the signal processing loss by L_b = 1.5 dB. This loss is often considered acceptable, both because of the saving in hardware complexity and the fact that 1-bit A/D conversion offers significant protection against interference from random pulses of large amplitude. No matter how large the interfering pulse, it can only add one to the count of first-

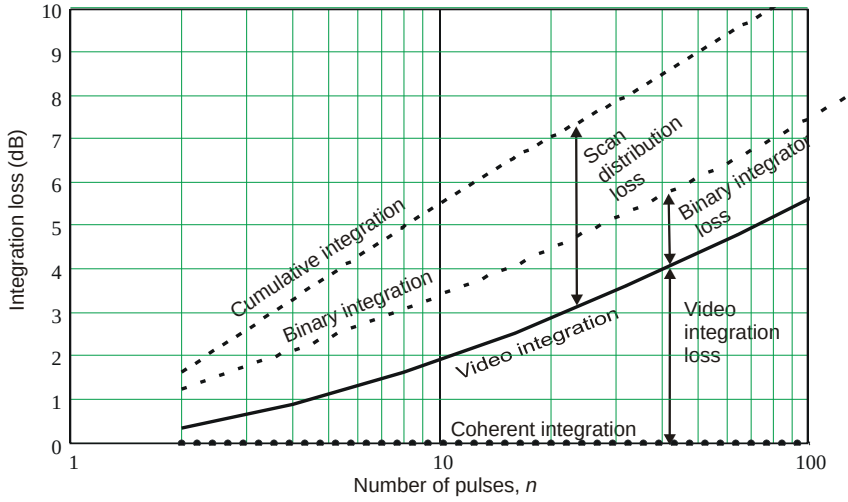

Figure 10.9 Comparison of integration loss for different methods of integration (calculated for P_d = 0.9, $P_{fa} = 10^{-6}$, $D_0(1)$ = 13.2 dB). From [1].

threshold crossings. For n 2, 3, and 4 the loss rises above the curve plotted in Figure 10.9, reaching 1.6, 2.2, and 2.4 dB, respectively.

Also shown in Figure 10.8 is the curve for binary integration with $m = 1$, sometimes called *cumulative integration*. When cumulative integration is performed over $n > 1$ scan, the difference between L_i for video integration and L_b for $m = 1$ is the scan distribution loss (see Section 10.1.4).

10.2.5.2 CFAR loss L_g

CFAR loss results from use of an adaptive threshold that reduces false alarms from variable or non-Gaussian interference. A typical implementation is the range-cell-averaging CFAR shown in Figure 10.10. The envelope-detected outputs of m adjacent range cells are available simultaneously from a tapped delay line in which the center tap represents the detection cell. The m reference taps are averaged to form an estimate w of the noise and interference near the target within the radar beam, and the ratio of the detection cell amplitude x_s to this average is used as the video output. In effect, the threshold level E_t is scaled to the estimate of local noise rather than to an a priori value as in previous discussions.

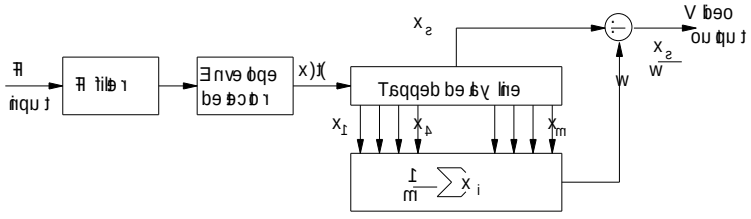

Figure 10.10 Range cell averaging CFAR. (After Gregers-Hansen: [12].)

The estimate of interference level as the average of m adjacent samples is subject to error, so the weight w applied to that average must be set higher than the value applicable to a perfect estimate. Hence, the threshold, varying about the correct estimate, is too high most of the time, reducing P_d relative to that for a fixed threshold at the correct level. This requires an increase in SNR, by an amount that is called the CFAR loss. Figure 10.11 shows that loss for single-pulse detection ($n = 1$).

The effective number of reference samples m_{eff} in Figure 10.11 is calculated as follows, where m is the number of taps in Figure 10.10:

- For m-cell averaging as in Figure 10.10:

  $m_{\text{eff}} = m$, for square-law detector;

$m_{\text{eff}} = (m + k)/(1 + k)$, where $k = 0.09$ for an envelope detector or 0.65 for a log detector.

- When using greatest-of selection:

  $k = 0.37$ for square-law detector, 0.5 for envelope detector, or 1.26 for log detector.

- For CFAR using hard limiting, add 1 dB limiting loss, and set

  $m_{\text{eff}} = (B_w/B_n) - 1$ for a Dicke-fix receiver, or
  $m_{\text{eff}} = B\tau - 1$ for dispersive or pulse-compression CFAR.

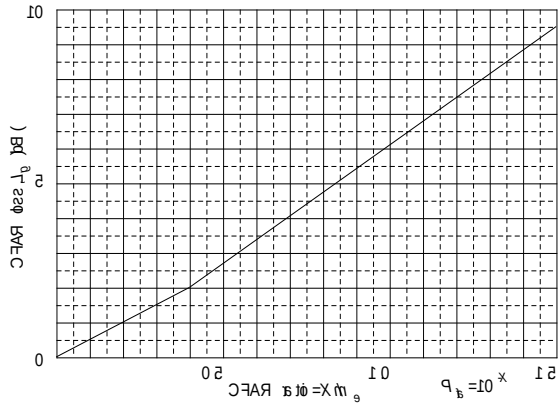

Figure 10.11 Universal curve for CFAR loss in single-hit detection, for steady or Rayleigh target. (After Gregers-Hansen: [12].)

An approximation for the curve of Figure 10.11 is

$$\begin{aligned} L_g &= 5X \ \text{dB}, && \text{for } X \le 0.5 \\ &= 7\left(X - 0.15\right) \ \text{dB}, && \text{for } X \le 0.5 \end{aligned} \tag{10.31}$$

10.2.5.3 Integrator Weighting Loss L_v

The ideal video integrator process applies weights to each of the n pulses that match the envelope of the two-way antenna gain of a scanning radar. This is the process used in Chapter 5 to calculate beamshape loss $L_{p0} = 1.33 = 1.24$ dB. Blake [13, 14] obtained a loss $L_p = 1.6$ dB by assuming an integrator with uniform weight over an optimum fraction of the half-power beamwidth, which added 0.27

dB of integrator weighting loss to the inherent beamshape loss. For other weighting functions (e.g., the exponential or double-exponential analyzed by Trunk [15, 16]), the loss L_v varies from 0.14 to 0.34 dB.

Uniform weights are optimum for pulses received during the fixed beam dwell of an electronically scanned radar.

10.2.5.4 Collapsing Loss L_c

Collapsing loss is defined [17] as

> The increase in required input signal-to-noise ratio to maintain a given probability of detection when resolution cells or samples containing only noise are integrated along with those containing signals and noise. *Note*: This type of loss occurs, for example, when radar returns containing range, azimuth and elevation information are constrained to a two-dimensional display.

The 2-D display *collapses* the information obtained from three dimensions.

The *collapsing ratio* ρ is defined as

$$\rho = \frac{m+n}{n} \tag{10.32}$$

where n is the number of samples containing signal and noise and m is the number containing noise alone. The collapsing loss, when using a square-law detector,[1] is calculated as in increase in integration loss L_i, given by

$$L_{c1}(\rho, n) = \frac{L_i(\rho n)}{L_i(n)} = \frac{L_i(m+n)}{L_i(n)} \tag{10.33}$$

when the false-alarm probability P_{fa} is held constant. In other cases, when the resolution cell is broadened by the collapsing process (e.g., excessive width of a range gate used for integration or broadening of the pulse from insufficient bandwidth or display resolution), the false-alarm *time* may be held constant by allowing an increased false-alarm probability ρP_{fa} and reducing the loss from (10.33) by the ratio of $D(\rho n)$ for P_{fa} to $D(\rho n)$ for ρP_{fa}:

$$L_{c2}(\rho, n) = \frac{L_i(\rho n)}{L_i(n)} \frac{D(\rho n, \rho P_{fa})}{D(\rho n, P_{fa})} \tag{10.34}$$

[1] Trunk [18] has shown that the collapsing loss in greater when a linear envelope detector is used.

10.2.5.5 MTI Losses L_{mti}

Three MTI losses are recognized:

- Noise correlation loss $L_{\text{mti}(a)}$. Use of MTI does not change the *average S/N* of targets that are broadly distributed in velocity, but nevertheless introduces a requirement for greater signal input that increases the detectability factor D_x. Passage of noise through an x-pulse MTI canceler introduces partial correlation over x successive outputs [19]. This reduces from n to an the number of independent noise samples available for integration in subsequent processing, where

$$\begin{aligned} a &= 2/3 && \text{for } x = 2 \\ &= 18/35 \approx 1/2 && \text{for } x = 3 \\ &= 20/47 \approx 0.43 && \text{for } x = 4 \end{aligned} \tag{10.35}$$

  The corresponding loss is the ratio of detectability factor for integration of an pulses to that for n pulses:

$$L_{\text{mti(a)}} = \frac{D(an)}{D(n)} \tag{10.36}$$

- An MTI system in which the signals are downconverted to baseband for processing is best implemented with two parallel cancelers for the in-phase (I-channel) and quadrature (Q-channel) components. If the quadrature canceler channel is not included, there is a further reduction factor of two in the number of independent noise samples integrated:

$$L_{\text{mti(a)}} = \frac{D(an/2)}{D(n)} \tag{10.37}$$

- When batch processing is used, with an x-pulse canceler operating on n/x batches at different PRFs, the number of outputs available for integration becomes n/x, giving

$$L_{\text{mti(a)}} = \frac{D(n/x)}{D(n)} \tag{10.38}$$

  Batch processing is not normally used with the *I*-channel canceler only, but a further reduction from n/x to $n/2x$ effective samples would apply in this case.

- Blind-phase loss $L_{mti(b)}$. Use of only the in-phase bipolar video leads to rejection of the quadrature components of both noise and signal. The effect on integration is given by (10.37), but there is also an increase in target fluctuation loss. The Rayleigh target, having a chi-square distribution with $2K = 2$ degrees of freedom, is converted to a Gaussian target ($K = 1$). The fluctuation loss is not significantly increased if the target changes phase sufficiently to appear at full amplitude in the I channel output at some time during t_o. However, in a batch-processed system where there is only one output sample, the fluctuation loss (in decibels) for a target with $2Kn_e$ degrees of freedom is doubled:

$$L_{\text{mti(b)}} = \frac{L_f\left(Kn_e/2\right)}{L_f\left(Kn_e\right)} \tag{10.39}$$

- Velocity response loss $L_{\text{mti}(c)}$. The S/N ratio remains the same in passage through the canceler system, when averaged over all target velocities, but individual targets lying near the response null may be canceled or significantly suppressed by the MTI. This is a statistical loss, calculated as shown in Section 10.2.5. The resulting loss is shown in Figure 10.12 as a function of detection probability, and is defined as the increase in input signal required to maintain the detection probability. Because of the high value of this loss at high P_d, PRF stagger or diversity is almost always used.

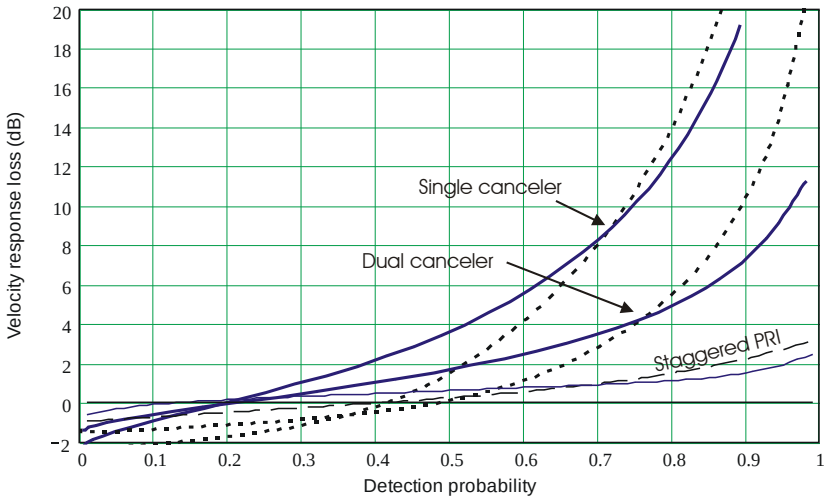

Figure 10.12 MTI velocity response loss versus detection probability for Case 1 targets (solid lines), and steady target (dashed lines). From [1].

10.2.5.6 Pulsed Doppler Losses

Several losses appearing in pulsed Doppler processors are discussed below.

- Doppler filter matching loss L_{mf}. This is the loss relative to a filter matched to the envelope of the input pulse train received during the coherent integration time t_f. It depends on the weighting applied during t_f to obtain the desired filter sidelobes. The filter performance for a given sidelobe level can be found using the curves of Figure 10.7, replacing the pulsewidth factor with a filter bandwidth factor, and calculating the loss from the plotted values of efficiency as

$$L_{mf} = \frac{1}{\eta_f} \tag{10.40}$$

- Range gate matching loss L_m. When a range gate of width τ_g is used at the input to the Doppler filters, the combined response of this gate and the preceding IF filter should match the transmitted pulse. If a wideband IF is used with a rectangular gate, the range gate loss is

$$\begin{aligned} L_m &= \frac{\tau_g}{\tau}, \quad \tau_g > \tau \\ &= \frac{\tau}{\tau_g}, \quad \tau > \tau_g \end{aligned} \tag{10.41}$$

  If a short sampling strobe is used in place of the range gate, L_m is determined by the preceding IF filter, as with other types of radar.

- Velocity response loss L_{vr} for pulsed Doppler. Section 9.6.4 discussed the fraction of target velocities within the blind speed of the waveform in which the response of a Doppler filter bank falls below –6 dB relative to response within the passband. In low- and medium-PRF radar, where target velocities may exceed the blind speed, PRF diversity is used to fill these regions of inadequate response, in order to preserve detection performance on targets that are aliased to within $\pm\Delta_v/2$ of the mean clutter velocity. In general, two or three PRFs are needed to fill all such regions out to the maximum target velocity. Detection performance is reduced at velocities where response is inadequate at one or more frequencies. The input signal energy ratio must be increased sufficiently to obtain the desired average P_d for targets distributed over the specified velocity region, and that increase is the velocity response loss. There is no general formula that expresses the velocity response loss, but the eclipsing-loss curves of Figure 10.4 also represent velocity response

loss as a function of detection probability if duty cycle D_u is replaced by the fraction of velocities having filter response less than −6 dB.

- Transient gating loss. When the coherent processing interval t_f includes n_f fill *pulses* to establish steady-state clutter inputs on clutter beyond the unambiguous range, the processor must gate out those pulses to remove the initial transient before passing inputs to the Doppler filter. The transient gating loss reflects the resulting loss of input energy relative to n_c pulses transmitted during the CPI:

$$L_{tg} = 1 - \frac{n_f}{n_c} \tag{10.42}$$

10.2.5.7 Straddling Losses

Whether electronic processing is carried out in analog or digital form, the four-dimensional radar space is sampled at discrete points rather than continuously. Unless these points are spaced within a fraction of the resolution cell, the SNR on targets that are displaced from the nearest sample point will be reduced at the processor output.

- Range straddling loss L_{er}. Range gates or strobes are usually spaced by approximately τ, but a signal having a peak that arrives other than at the strobe or the center of the gate is passed with reduced amplitude. The amount of straddling loss depends on the pulse shape and gate duration as well as on the spacing. For rectangular pulses passed through a rectangular IF filter, the loss is shown in Figure 10.13 as a function of the spacing of a narrow strobe.

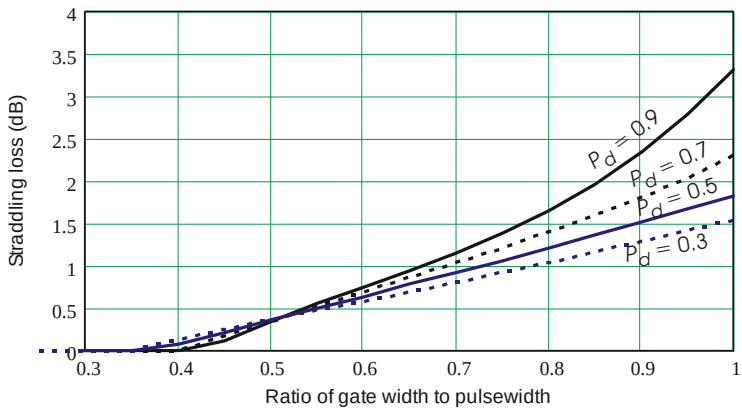

Figure 10.13 Range straddling loss versus sample spacing for rectangular pulse passed through a rectangular filter with $B\tau = 1.5$. From [1].

- Filter straddling loss L_{ef}. Signals may also be centered at frequencies between the Doppler filters, introducing a filter straddling loss. When heavily weighted filters are used, they overlap within the –3-dB points, making this loss insignificant, as shown in Figure 10.14.

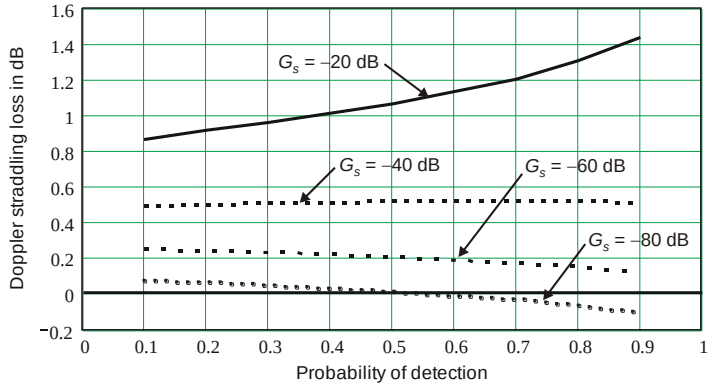

Figure 10.14 Filter straddling loss versus detection probability for bursts weighted to achieve sidelobe level G_s. From [1].

- Angle Straddling Loss L_{ea}. The beamshape loss accounts for the sampling in angle space by the scanning antenna beam. However, if the antenna scans continuously and integration or coherent processing is carried out in a single batch rather than continuously, the center of the batch may not coincide with the angle of the target. As a result, the peak of the echo envelope may straddle two processing intervals, introducing an angle straddling loss. This loss is absent if, for example, a moving-window integrator is used rather than a batch process or pulsed Doppler coherent process. Division of the observation time into two or more batch processing intervals reduces straddling loss to a negligible level, but reduces the integration gain unless the batch outputs are subsequently integrated in a moving-window process. Overlapping processing batches may also be used, but if the processing is coherent this precludes burst-to-burst PRF or RF agility.

10.2.6 Losses in Clutter Detectability Factor

In Chapter 3 it was shown that the interference spectral density C_0 contributed by clutter required adjustment before adding it to the density N_0 of white Gaussian noise to form the total interference density. The two factors discussed here are applied to calculate the clutter detectability factor D_{xc} used in that adjustment.

10.2.6.1 Clutter Correlation Loss L_{cc}

The input clutter is characterized by its correlation time t_c, given by (3.6), from which the number n_c of independent clutter samples available for integration can be calculated. The clutter correlation loss is then given by

$$L_{cc} = \frac{D_0(n_c)}{D_0(n)} \tag{10.43}$$

For example, if clutter remains correlated over the entire integration time, the upward adjustment in effective clutter spectral density is equal to the integration gain available on thermal noise.

10.2.6.2 Clutter Distribution Loss L_{cd}

Land clutter observed beyond the near region (see Figure 9.1) develops an amplitude distribution broader than the Rayleigh distribution, usually described by Weibull or lognormal models. The result is either an increase in false-alarm probability as the clutter peaks pass a threshold set for Rayleigh clutter with the same average value, or an increase in threshold that reduces detection probability on targets. Sea clutter also tends toward a Weibull or other spread distribution at low grazing angles in high-resolution radar.

A range-cell-averaging CFAR detector (Figure 10.9) is often used, based on the assumption of Rayleigh-distributed interference. With a large enough number of reference cells, it sets the threshold power, normalized to unity noise power, at a level given by (4.15):

$$p_{th} = \frac{E_t^2}{2} = \ln\frac{1}{P_{fa}} = \ln 10^y = 2.303y \tag{10.44}$$

where $y = \log(1/P_{fa})$.

The Weibull probability density function (9.23), normalized for a scale power $\alpha = 1$, becomes

$$P(x, a_w) = \frac{x^{1/a_w}}{a_w x}\exp\left(-x^{1/a_w}\right) \tag{10.45}$$

where x is power and a_w is the Weibull spread parameter, varying over $1 \le a_w \le 5$. The exponential power distribution (Rayleigh voltage) corresponds to $a_w = 1$. For

Weibull clutter with $a_w > 1$ the threshold rises relative to p_{th} given in (10.44) by the factor $\Gamma(1 + a_w) = a_w!$ that represents the ratio of average clutter power to the scale parameter α that was assumed unity in (10.45). However, when $a_w > 1$, the increase in p_{th} is insufficient to maintain the intended false-alarm probability P_{faw}, which becomes

$$P_{faw} = \int_{p_{th}}^{\infty} P\left[\Gamma\left(1+a_w\right)x, a_w\right]dx \tag{10.46}$$

The increase in false-alarm probability when the detection threshold is adjusted for a Rayleigh distribution ($a_w = 1$) based on the average clutter power measured in a cell-averaging CFAR detector is shown in Figure 10.15.

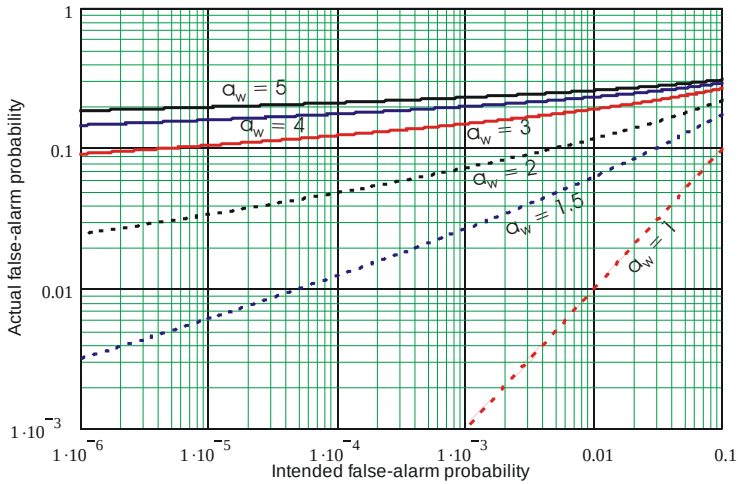

Figure 10.15 False-alarm probability achieved as a function of that intended, for different Weibull clutter spread parameters.

For example, if the intended $P_{fa} = 10^{-4}$, the achieved P_{faw} increases to 0.013 for clutter with $a_w = 1.5$, and to 0.05 for $a_w = 2$. In an overland search area containing 10^5 resolution cells, there would be 5,000 false alarms from land clutter in the latter case. While a human observer might be able to ignore these and detect targets in relatively clear regions of the display, effective measures to control false alarms are essential in any system using electronic detection.

An approach used with MTI in many radars is to precede the canceler with a limiter that is adjusted to restrict the input to a level above noise equal to the MTI improvement factor. The large peaks of Weibull or lognormal clutter are then

suppressed by the MTI, but at the expense of spectral spreading that significantly reduces the available improvement factor, typically to near 20 dB [20]. In addition, signals that overlap these peaks are suppressed by the limiting action. The false-alarm probability is controlled, but at the expense of reduced detection probability in regions of heavy clutter. The performance is acceptable in most cases, because targets moving between the clutter peaks become visible even with the reduced improvement factor, providing *interclutter visibility* [21].

A two-parameter CFAR has been proposed as another possible measure [22]. In this system, samples in reference cells are used to estimate both the mean and variance of the clutter, and the mean is multiplied by a constant times the variance to establish the threshold When a two-parameter CFAR detector is used to adjust the threshold for non-Rayleigh clutter, the clutter distribution loss given by (3.8) for Weibull-distributed clutter is as shown in Figure 10.16.

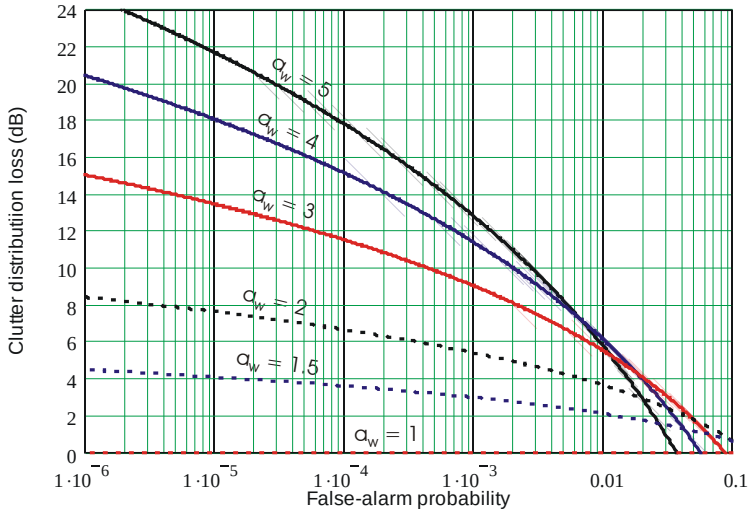

Figure 10.16 Clutter distribution loss L_{cd} for two-parameter CFAR as a function of false-alarm probability, for different Weibull clutter spread parameters.

For a lognormal clutter model, the loss can be approximated by using in (10.46) or Figure 10.16 an equivalent Weibull spread given by

$$a_w = \left(0.25\sigma_y\right)^{1.16} \tag{10.47}$$

where σ_y is the standard deviation in dB of the lognormal distribution. Both a_w and σ_y are modeled in Figure 9.4 as functions of the clutter propagation factor F_c.

Figure 10.16 shows the clutter distribution loss of the two-parameter CFAR detector. It is clear that use of this approach will introduce a large loss in regions where $a_w > 1$.

10.2.6.3 Clutter Map Loss L_{map}

The clutter map is an alternative to limiting or two-parameter CFAR to reduce false alarms from the clutter peaks discussed in Section 9.6.5. The clutter map sets a threshold based on a long-term average for each map resolution cell taken over several successive search scans. It is effective against discrete clutter sources to which the range-cell-averaging CFAR detector would be relatively insensitive.

The clutter map is characterized not by the loss in output SNR, such as imposed by a two-parameter CFAR detector over all resolution cells, but rather by a reduction in detection probability in those map cells containing significant clutter. Applying (3.2) and (3.10), the clutter improvement factor I_m provided by MTI or other Doppler processing reduces the average interference-to-noise ratio to

$$\frac{I_0}{N_0} = 1 + \frac{C_{0e}}{N_0} = 1 + \frac{C_0}{N_0}\frac{L_{cc}}{I_m} \approx 1 + \frac{C_0}{N_0 I_m} \tag{10.48}$$

where the approximation assumes that the output residue of the Doppler processor is uncorrelated ($L_{cd} \approx 1$).

The performance of an idealized clutter map, in which each map cell corresponds to a radar resolution cell, can be modeled by assuming that the gain applied to signals within a map cell varies inversely with I_0/N_0:

$$G(c) = \frac{1}{1+c} = \frac{1}{1 + C_0/N_0 I_m} \tag{10.49}$$

where c is the output clutter-to-noise ratio. Only the map cells with input clutter energy ratio C_0/N_0 approaching or exceeding I_m suffer reduction in detection performance, while other map cells preserve the detection performance achieved against thermal noise.

The average probability of detection over the map is then found, for the Case 1 target, as

$$P_{dav} = \int_0^\infty P(x) \exp\left[\frac{\ln(P_{fa})}{1 + sG(cx)}\right] dx \tag{10.50}$$

where s is the signal-to-noise ratio and $P(x)$ is the probability density of the Weibull-distributed clutter power given by (9.23). A root-finding procedure identifies the value of s required to obtain the required P_{dav}, and the clutter map loss L_{map} is the ratio of that value to D_1 required for that P_d in the absence of the variable gain G:

$$L_{\text{map}}\left(P_{dav}\right)=\frac{s\left(P_{dav}\right)}{D_1\left(P_{dav}\right)}=\frac{\text{root}_s\left\{P_{dav}=\int_0^{\infty}P(x)\exp\left[\frac{\ln\left(P_{fa}\right)}{1+sG(cx)}\right]dx\right\}}{\frac{\ln\left(P_{fa}\right)}{\ln\left(P_{dav}\right)}-1} \tag{10.51}$$

Figure 10.17 shows the clutter map loss as a function of required detection probability for a Case 1 target in several clutter environments. For example, assume that I_m = 40 dB, and that the average input clutter-to-noise energy ratio is C_0/N_0 = +30 dB, giving c –10 dB = 0.1. The dashed curves in Figure 10.17 show that P_{dav} = 80% can be achieved with a map loss of only 0.41 dB for Rayleigh clutter (a_w = 1), with the loss rising to 1.6 dB for a_w = 3 and to 3.8 dB for a_w = 5. A detection probability of 90% incurs only 0.42 dB of map loss for Rayleigh clutter, but 1.9 db for a_w = 3 and ≈ 7 dB for a_w = 5. These losses are much smaller than for other

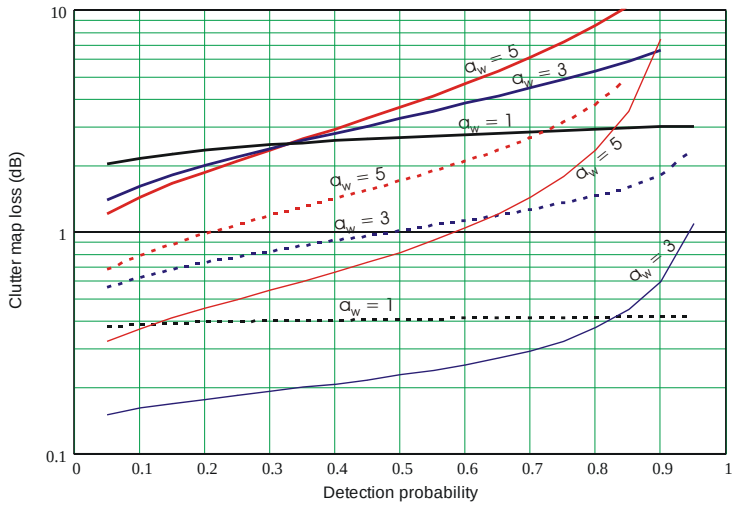

Figure 10.17 Clutter map loss as a function of average output clutter-to-noise ratio z for different Weibull clutter spread parameters and average output clutter-to-noise ratios of 1.0 (solid curves), 0.1 (dashed curves) and 0.01 (light solid curves).

methods of false-alarm control. The map also has two other advantages: it supports linear operation of all circuits preceding the MTI or Doppler filter, permitting those circuits to achieve their theoretical improvement factors (see Section 9.6, and when used to select MTI or normal video processing it permits detection of targets with zero radial velocity in cells without clutter, since it can select the processing path in response to the actual levels of clutter in each cell.

10.3 LOSSES IN VISUAL DETECTION

Operator detection based on a display is a purely analog process, although the information presented may be reconstituted digitally and passed at a high refresh rate to the display rather than relying on persistence of the phosphor to retain the displayed image. However the display is refreshed, the factors below apply when the detection threshold is human rather than electronic.

10.3.1 Losses in the Visibility Factor

The visibility factor $V_{0(50)}$ for a PPI display was discussed in Section 4.6 and plotted in Figure 4.13 for P_d = 50%, as a function of the number of pulses n exchanged with the target per beamwidth, under "optimum viewing conditions." The test signal used in developing V_0 was of constant amplitude.

If A comparison of $V_{0(50)}$ with the values of $D_{0(50)}$ for electronic detection, for n = 1 and n = 10 is shown in Table 10.5, with values for false-alarm probabilities of 10^{-4} and 10^{-6}, since the visual detection process might have provided performance within that range.

Table 10.5 Comparison of Visual and Electronic Detection for P_d= 0.5

n	P_{fa}	D_0 (dB)	V_0 (dB)	*Visual Loss* (dB)
1	10^{-4}	+9.4	+13.2	3.8
	10^{-6}	+11.2		2.0
10	10^{-4}	+2.2	+4.2	2.0
	10^{-6}	+3.7		0.5

Note: The false-alarm probability for visual detection was not measured.

The average visual detection loss is 2.1 dB over the four listed cases. It would be 2.9 dB if P_{fa} were 10^{-4} for the visual process, or 1.3 dB if P_{fa} were 10^{-6}. There appear to be no data to determine which estimate is more nearly correct.

10.3.2 Collapsing Loss on the Display

The typical PPI display for visual detection in a medium-range surveillance radar presents pulses of ≈ 3 μs width out to a range of 300 km, corresponding to 2,000 μs of delay. The radius of the display corresponds to 670 range cells. The PPI displays used in World War II had approximately 200 resolvable spots in the radius of the PPI, resulting in a collapsing ratio $\rho \approx 3$. While the beamwidth is normally wider than the angular resolution on the PPI at full range, there is also collapsing in angle for mid- and short-range targets. The collapsing ratio increases for shorter pulses, and the limited resolution of the human eye can add further collapsing. These losses explain at least part of the excess loss in the visibility factor.

10.3.3 Bandwidth Correction Factor C_b

The bandwidth correction factor, expressed by (1.17), adjusts for the loss in target visibility resulting from departure from the optimum IF bandwidth $B_n = 1.2/\tau$. The visibility factor, over a broad region near that value, remains close to the value for the optimum bandwidth, where it is ≈ 1.3–2.9 dB higher than the value for electronic threshold detection.

10.3.4 Operator Loss L_o

Discrepancies between expected and achieved detection ranges in operational systems have often been attributed to the ill-defined *operator loss*. Blake [9, p. 370] states that

> The operator loss tends in practice to become an arbitrary factor to account for observed discrepancies between computer and observed radar performance; and while in some cases it may be a valid explanation, in others it may be misused to conceal ignorance to why a radar's actual performance is less than that predicted by calculations. In any case it is too vague a concept to employ in a range calculation aimed at evaluating the merit of a particular radar design or for other engineering purposes.

The large number of losses listed in this chapter, many of which are uncertain even when the attempt is made to produce a complete loss budget, are a more likely explanation of the reduced performance actually observed in tests.

There are certainly physical and psychological problems that can reduce operator performance relative to the V_0 curves used to characterize what is expected under optimum conditions. Distractions from the observing task or absence of the operator from the display position reduce detection probability to zero over some periods. However, other than the few decibels excess in V_0 as compared to D_0, the use of an operator loss should be avoided in radar performance analysis.

10.4 SUMMARY OF LOSS FACTORS

This chapter has presented an inventory of the losses that must be included in some form in the radar equation to provide accurate performance predictions. Some of these are specifically called out in the equation, while others are embedded in other terms. Some are constant regardless of operating conditions and desired performance, while others depend on the environment and the target location in range and angles relative to the radar (and to the orientation of the face of an electronically scanned array). Still others are function of the detection probability desired, increasing steeply as $P_d \rightarrow 1$.

Procedures for calculation of most of these losses have been offered and curves provided showing typical values. In other cases, analysis of the specific design details of the radar and its signal processor, lying beyond the scope of this general discussion, are necessary. While the number of factors to be considered in loss assessment is large, it is hoped that the material presented will be useful in improving the accuracy and consistency of radar range performance analysis.

It is important in analysis, design, and operation of modern, software-controlled radar systems to account accurately for the variation of system loss with search and target acquisition strategy. For example, beamshape loss is reduced by close spacing of beam positions, at the expense of allocating more transmitter energy and radar time to search of a given sector. Scanning the volume repeatedly, with lower P_d per scan and increased beam spacing, may require less total energy and time than performing a single scan with high P_d, especially for fluctuating targets. The optimum strategy requires careful balance between the beamshape losses discussed in Chapter 5 and statistical losses discussed in this chapter. Signal processing losses can be reduced by more dense sampling of range-Doppler space to avoid straddling loss. Unlike beamshape loss from sampling in the two angle coordinates, this does not involve increasing transmitted energy or search time, requiring only greater processing throughput and memory. The cost (in hardware acquisition, size, weight, and power drain) of such oversampling decreases as Moore's law reduces the required digital hardware.

An area that has not been explored is the potential to oversample in angle space, without increasing energy and dwell time, by using multiple offset receiving beams surrounding the transmitting beam. In modern array radars this is possible with minimal added hardware by combining the monopulse sum and difference receiver outputs to form the offset beams. Parallel processors for the multiple beams are required for this mode of operation, but as the cost of the array and transmitter increase relative to receivers and processing, this may prove a more economical solution than scheduling closely spaced transmitting beams.

A careful study of losses is essential if the radar design is to permit efficient use of the increasingly expensive energy and time of these modern systems. If the

detailed loss analysis of this chapter provides the basis for such studies, one objective of this book will have been achieved.

References

[1] Barton, D. K., *Radar System Analysis and Modeling*, Norwood, MA: Artech House, 2005.

[2] Saad, T. S. and R. C. Hansen, (eds.), *Microwave Engineers' Handbook*, Dedham, MA: Artech House, 1971.

[3] Marcum, J. I., "A Statistical Theory of Target Detection by Pulsed Radar," *RAND Corp. Research Memo RM-754*, December 1, 1947. Reprinted: *IRE Trans. on Information Theory*, Vol. IT-6, No. 2, April 1960, pp. 59–144; *Detection and Estimation*, (S. S. Haykin, ed.), Stroudsberg, PA: Dowden, Hutchinson and Ross, 1976, pp. 57–121.

[4] Hansen, R. C., *Phased Array Antennas*, New York: John Wiley & Sons, 1998.

[5] Barton, D. K. and H. R. Ward, *Handbook of Radar Measurement*, Englewood Cliffs, NJ: Prentice-Hall, 1968; Dedham, MA: Artech House, 1984.

[6] Blevis, B. C., "Losses Due to Rain on Radomes and Antenna Reflecting Surfaces," *IEEE Trans. on Antennas and Propagation*, Vol. 13, No. 1, January 1965, pp. 175–176.

[7] Ruze, J., "More on Wet Radomes," *IEEE Trans. on Antennas and Propagation*, Vol. 13, No. 5, September 1965, pp. 823–824.

[8] Barton, D. K., "Simple Procedures for Radar Detection Calculations," *IEEE Trans. on Aerospace and Electronic Systems*, Vol. AES-5, No. 5, September 1969, pp. 837–846. Reprinted: *Radars*, Vol. 2, *The Radar Equation*, (D. K. Barton, ed.), Dedham, MA: Artech House, 1974, pp. 113–122.

[9] Blake, L. V., *Radar Range-Performance Analysis*, Lexington, MA: D. C. Heath, 1980; Dedham, MA: Artech House, 1986.

[10] Haeff, A. V., "Minimum Detectable Radar Signal and Its Dependence Upon Parameters of Radar Systems," *Proc. IRE*, Vol. 34, No. 11, November 1946, pp. 857–861.

[11] Schwartz, M., "A Coincidence Procedure for Signal Detection," *IRE Trans. on Information Theory*, Vol. 2, No. 4, December 1956, pp. 135–139.

[12] Gregers-Hansen, V., "Constant False-Alarm Rate Processing in Search Radars," *Radar–Present and Future*, IEE Conf. Publ. No. 105, October 1973, pp. 325–332.

[13] Blake, L. V., "The Effective Number of Pulses Per Beamwidth for a Scanning Radar," *Proc. IRE*, Vol. 41, No. 6, June 1953, pp. 770–774.

[14] Blake, L. V., "Addendum to Pulses Per Beamwidth for Radar,'" *Proc. IRE*, Vol. 41, No. 12, December 1953, p. 1785.

[15] Trunk, G. V., "Detection Results for Scanning Radars Employing Feedback Integration," *IEEE Trans. on Aerospace and Electronic Systems*, Vol. AES-6, No. 4, July 1970, pp. 522–527.

[16] Cantrell, B. H. and G. V Trunk, "Angular Accuracy of a Scanning Radar Employing a Two-Pole Filter, *IEEE Trans. on Aerospace and Electronic Systems*, Vol. AES-9, No. 5, September 1973, pp. 649–653 [with correction: November 1974, p. 878].

[17] IEEE Standard 100, *The Authoritative Dictionary of IEEE Standards Terms, 7th ed*., New York: IEEE Press, 2000.

[18] Trunk, G. V., "Comparison of the Collapsing Losses in Linear and Square-Law Detectors," *Proc IEEE*, Vol. 60, No. 6, June 1972, pp. 743–744. Reprinted in *Radars*, Vol. 2, *The Radar Equation*, (D. K. Barton, ed.), Dedham, MA: Artech House, 1974, pp. 125–126.

[19] Hall, W. M. and H. R. Ward, "Signal-to-Noise Loss in Moving Target Indicator," *Proc. IEEE*, Vol. 56, No. 2, February 1968, pp. 233–234.

[20] Ward, H. R. and W. W. Shrader, "MTI Performance Degradation Caused by Limiting," *IEEE Eascon-68 Record*, Washington, DC, September 9–12, 1968, pp. 168–174.

[21] Barton, D. K. and W. W. Shrader, "Interclutter Visibility in MTI Systems," *IEEE Eascon-69 Record*, Washington, DC, October 27–29, 1969, pp. 294–297.

[22] Sekine, M., et al., "Suppression of Weibull-Distributed Clutter Using a Cell-Averaging Log/CFAR Receiver," *IEEE Trans. on Aerospace and Electronic Systems*, Vol. 14, No. 5, September 1978, pp. 823–826.

List of Symbols

The following symbols are used in equations and text. The section numbers listed are the locations of their first use.

Symbol	*Meaning*	*Defined*
A	Physical aperture area	2.1
$A(f)$	Signal spectrum	7.5.5
$A_r(f)$	Received signal spectrum	7.5.5
A_b	Beam-axis azimuth	9.5.3
A_c	Area of surface clutter cell	3.3.1
A_{cs}	Area of surface in sidelobes	3.6.1
A_m	Azimuth search sector	2.1
A_r	Effective receiving aperture area	1.1.1
a	Factor in rain attenuation	7.3.1
a_e	Earth's radius	2.2.1
a_s	Fraction of antenna power radiated to surface	6.3.1
a_w	Spread parameter of Weibull distribution	3.2.3
B_n	Receiver noise bandwidth	1.3.1
b	Exponent of rainfall rate in attenuation equation	7.3.1
	Coefficient for vegetation factor	8.3.3
	Scale parameter of *K*-distribution	9.1.4
CA	Clutter attenuation	9.6.4
$C(v)$	Fresnel cosine integral	8.4.2
C_0	Clutter spectral density	3.1
C_{0e}	Effective clutter spectral density	3.1
C_i	Clutter energy in ambiguity i	3.2.1
	Input clutter energy	9.6
C_b	Bandwidth correction factor	1.3
C_o	Output clutter energy	9.6
C_x	Detector loss	4.4.2

C_{Ts}	Temperature correction factor for snow attenuation	7.3.4
c	Velocity of light	3.1
D	Detectability factor	1.1.2
	Divergence factor	8.3.4
	Diameter of water droplet	9.5.5
D_0	Steady-target detectability factor	1.3.2
D_{01}	Basic single-pulse detectability factor for steady target	2.1
$D_{1,2,3,4}$	Basic detectability factor for Case 1,2,3,4 targets	1.5.5
D_c	Detectability factor for coherent detector	4.4.1
D_{c1}	Detectability factor for coherent detector on single pulse	4.4.1
D_e	Detectability factor for general target	1.5.5
D_t, D_r	Directivity of transmitting, receiving antenna	2.6.1
D_x	Effective detectability factor	1.4.1
d	Diameter of rainstorm	7.3.3
dP_v	Probability increment of signal-plus-noise voltage	4.3.3
dP_p	Probability increment of signal-plus-noise power	4.3.3
d_1, d_2	Path segments to knife edge	8.4.2
E	Signal energy	1.1.1
	On-axis field strength	8.1.1
E_a	Energy density at receiving antenna	1.1.1
E_d	Direct field strength	8.1.1
E_n	Instantaneous noise voltage	4.2.4
E_p	Energy density	1.1.1
E_q	Quantizing noise voltage	6.5.3
E_r	Reflected field strength	8.1.1
E_s	Peak signal voltage	4.2.4
E_t	Energy of transmitted pulse	1.1.1
	Threshold voltage	4.2.4
e	Partial pressure of water vapor	7.1.1
	Electron charge	7.4.4
F	Pattern-propagation factor	1.4.1
$F(h)$	Factor in equation for total electron count	7.5.3
F_a	Fraction of velocities with acceptable response	9.6.4
F_c	Clutter pattern-propagation factor	3.3.3
F'_c	Clutter propagation factor	9.1.2
F_{d0}	First mode of smooth-sphere diffraction equation	8.4.1

F'_{d0}	Adjusted first mode of smooth-sphere diffraction equation	8.4.1
F_{dk}	Knife-edge diffraction factor	8.4.2
F_i	Pattern-propagation factor in interference region	8.1.1
F_n	Receiver noise figure	1.2
F_p	Polarization factor	1.4.4
F_t,F_r	Transmitting, receiving pattern-propagation factors	1.3
f	Frequency offset from carrier	7.5.5
$f(\theta)$	Antenna voltage pattern	3.3.4
f_0	Carrier frequency	1.6.3
f_c	Voltage pattern of antenna at clutter elevation	3.3.4
	Correlation frequency of target	4.5.2
$f_{cir}(\theta)$	Voltage pattern of circular aperture	5.2.2
$f_{cos}(\theta)$	Voltage pattern of cosine-illuminated rectangular aperture	5.2.2
$f_g(\theta)$	Gaussian voltage pattern	5.2.2
f_{Mc}	Radar frequency in megahertz	1.3.2
f_N	Oxygen resonance for rotational quantum number N	7.2.1
f_r	Pulse repetition frequency	1.1.2
f_t, f_r	Pattern component of pattern-propagation factor	5.
f_{tsf}, f_{rsf}	Voltage gains of far transmitting and receiving sidelobes	9.1.2
$f_u(\theta)$	Voltage pattern of uniformly illuminated aperture	5.2.2
G	Power gain	1.1.1
	Ground range	8.2.2
G_e	Electronic gain of repeater jammer	3.8.1
$G_e(\theta)$	Element gain	6.3.5
G_i	Integration gain	4.4.4
G_t, G_r	Transmitting and receiving antenna gains	1.1.1
G_{tsf}, G_{rsf}	Transmitting and receiving antenna far sidelobe gains	9.1.2
G_1	Gain of first receiver stage	6.5.1
	Ground range from radar to reflection point	8.2.4
G_2	Ground range from target to reflection point	8.2.5
H	Earth's magnetic field	7.5.1
	Natural unit of height	8.4.1
$H(\cdot)$	Filter response	6.1.1
$H'(\cdot)$	Normalized filter response	6.1.1
$H'_m(\cdot)$	Normalized filter response of m-delay canceler	9.6.1
H_m	Maximum target altitude	2.2.1

h	Aperture height (vertical dimension)	2.2.2
	Planck's constant	6.1.1
	Altitude	6.3.2
	Clearance from knife edge	8.4.2
h_0	Atmospheric scale height	7.1.4
h_c	Height of significant clutter above surface	9.1.2
h_m	Height at end of path	7.2.3
	Altitude of maximum electron density	7.5.1
$h_{\min}$	Minimum obstacle height for knife-edge diffraction	8.4.2
h_r	Antenna altitude above surface	3.1.1
h'_r	Antenna altitude above average surface	9.1.2
h_s	Surface altitude above sea level	7.1.4
h_{t1}	Target altitude above flat Earth	8.2.1
$I(x,n)$	Pearson's incomplete gamma function	4.2.2
I_0	Interference spectral density	3.1
I_{0e}	Effective interference energy	3.1
I_m	Clutter improvement factor	3.2.4
$I_{m1,\,2,\,3}$	MTI improvement factors of 1- 2- and 3-pulse cancelers	9.6.1
$I_{mn1,\,2,\,3}$	Noncoherent MTI improvement factors of 1- 2- and 3-pulse cancelers	9.6.2
$I_n(x)$	Modified Bessel function of first kind of order n	4.2.1
J_0	Jamming spectral density	3.1
J_{0e}	Effective jamming spectral density	3.1
K	Parameter in cloud attenuation $(\varepsilon_c - 1)/(\varepsilon_c + 2)$	7.3.5
K_B	Beaufort wind scale number	9.2.1
k	Boltzmann's constant	1.1.1
k_e	Effective Earth's radius factor	2.2.1
k_{sh}	Wind-shear constant	9.5.3
k_t	Threshold constant	4.2.2
k_{tn}	Threshold constant for n pulses	4.2.2
k_α	Atmospheric attenuation coefficient	6.3.2
$k_{\alpha 1}$	One-way atmospheric attenuation coefficient	6.3.2
$k_{\alpha c}$	Cloud attenuation coefficient	7.3.5
$k_{\alpha O}$	Oxygen attenuation coefficient	7.2.1
$k_{\alpha r}$	Rain attenuation coefficient	7.3.1
$k_{\alpha s}$	Snow attenuation coefficient	7.3.4

$k_{\alpha W}$	Water-vapor attenuation coefficient	6.2.1
L	System loss factor	1.3
	Natural unit of range	8.4.1
L_1	RF loss	1.1.1
L_a	Antenna loss	2.6.1
L_{as}	Antenna surface tolerance loss	10.1.5
L_c	Collapsing loss factor	1.4.1
L_{csc}	Cosecant factor loss	2.2.3
L_d	Scan distribution loss	2.6.2
L_{ecl}	Eclipsing loss = $1/F^2_{\text{ecl}}$	10.1.4
L_{Far}	Faraday rotation loss	7.5.4
L_f	Fluctuation loss	2.6.2
L_{fd}	Frequency-diversity loss = $1/F^2_{\text{fd}}$	2.6.3
L_i	Integration loss	2.6.2
L_{lens}	Atmospheric lens loss = $1/F^2_{\text{lens}}$	1.6.2
L_m	Matching loss factor	1.4.1
L_n	Pattern constant	2.1
L_o	Operator loss	1.4.1
L_p	Beamshape loss	1.3.1
L_{pe}	Elevation beamshape loss	2.2.2
L_{pn}	Net beamshape loss for search radar equation	2.3.2
L_{pT2}	Beamshape loss for 2-coordinate scan with triangular grid	5.5.1
L_{p0}	Beamshape loss in one coordinate with dense sampling	5.2.3
L_{p1}, L_{p2}	One-, two-coordinate beamshape loss	5.2.3
L_r	Receiving line loss	1.1.2
	Radial span of target	4.5.2
L_{rec}	Receiving noise loss	2.6.1
L_s	Search loss factor	2.1
L_{sc}	Scanning loss	10.2.1
L_{sector}	Scan sector loss	2.6.2
L_{stc}	Sensitivity time control loss = $1/F^2_{\text{ftc}}$	1.6.2
L_t	Transmitting line loss	1.2
L_{rdr}	Loss factor varying in range = $1/F^2_{\text{rdr}}$	2.6.1
L_x	Miscellaneous loss	1.3.1
	Target cross-range span	4.5.2
L_α	Atmospheric absorption loss	1.3.1

$L_{\alpha 1}$	One-way atmospheric attenuation	6.3.1
$L_{\alpha r}$, $L_{\alpha t}$	Transmitting and receiving atmospheric attenuation	1.4.1
$L_{\alpha t}$	Atmospheric attenuation through entire troposphere	7.2.3
L_{η}	Aperture efficiency loss = $1/\eta_a$	2.1
M	Matching factor	1.4.2
	Water density of cloud	7.3.5
m	Number of MFAR search sectors	2.4
	Electron mass	7.5.4
m_x	mean of integrated detector output	4.2.2
m_1	mean of single-pulse detector output	4.2.2
N	Noise power	1.1.1
	Refractivity of troposphere	7.1.1
N_0	Noise spectral density	1.1.1
	Refractivity of troposphere at sea level	7.1.3
N_{d0}	Refractivity of dry air at sea level	7.1.3
N_e	Electron density in ionosphere	7.5.2
N_i	Refractivity of ionosphere	7.5.5
N_m	Maximum electron density in ionosphere	7.5.2
N_t	Total electron count through ionosphere	7.5.3
N_{w0}	Refractivity of water vapor at sea level	7.1.3
n	Number of pulses integrated	1.1.2
$n(D)$	Distribution of droplets with diameter	9.5.5
n'	Number of samples noncoherently integration	1.4.2
n_{bt}	Number of transmitting beams in search sector	2.1
n_c	Number of independent clutter samples	3.2.3
	Number of pulses in CPI	9.6.4
n_e	Number of independent target samples	1.5.5
n_{ef}	Number of independent target samples in frequency	4.5.2
n_{ep}	Number of independent target samples in polarization	4.5.2
n_{es}	Number of independent target samples from spatial diversity	4.5.2
n_{et}	Number of independent target samples in time	4.5.2
n_f	Number of fill pulses in CPI	9.6.4
n_p	Number of pulses in Doppler processor	9.6.4
n_{sc}	Number of scans	2.5.1

P	Air pressure	6.3.2
	Total power	6.3.3
$P(x)$	Probability density function of clutter	9.1.4
$P_{a1,\ \ldots 4}$	Power components in noise temperature model	6.3.1
P_{av}	Average transmitter power	1.3.4
P_d	Probability of detection	1.3.2
$P_{d0,1,2,3,4}$	Probability of detection for steady target, Case 1,2,3,4	4.2.1
P_{da}	Partial pressure of dry air	7.1.1
P_{da0}	Partial pressure of dry air at sea level	7.1.3
P_{faf}	False-alarm probability	1.6.3
P_t	Transmitter peak power	1.1.1
$P_w^{-1}(p,a_w)$	Inverse integral of the Weibull distribution	3.2.3
$P_\chi(\chi^2,m)$	Integral of the chi-square distribution	4.3.2
$P_\chi^{-1}(p,m)$	Inverse of integral of the chi-square distribution	3.2.3
P_γ	Incomplete gamma function	4.2.2
P_γ^{-1}	Inverse of incomplete gamma function	4.2.2
p	Probability	3.2.3
	Instantaneous signal power	4.3.3
	Parameter in solution of cubic equation	8.2.5
R	Target range	1.1.1
	Circuit resistance	6.1.1
R'	Range with pattern-propagation factor	1.3.2
R_0	Free-space range	1.3.2
R_1	Range limit of near region for clutter	3.3.1
R_1, R_2	Segments of direct and reflected ranges	8.2.2
R_{50}	Range for 50% detection probability	1.3.2
R_c	Clutter range	3.2.1
	range for calculation of signal-to-noise ratio	8.6.3
R_d	Range corresponding to time delay t_d	7.1.5
R_h	Range to horizon	8.4.1
R_m	Maximum detection range	1.1
R_r	Target-to-receiver range	1.3.5
	Pathlength of reflected ray	8.1.1
R_t	Transmitter-to-target range	1.3.5
R_u	Unambiguous range	1.6.1
R_δ	Range limit of interference region, where $\delta = \lambda/6$	8.5

r	Range variable	6.3.2
	Ratio of DC to AC components of clutter spectrum	9.3.2
r_r	Rainfall rate	7.3.1
r_s	Snowfall rate in mm/h of water	7.3.4
S	Signal power	1.1.1
SS	Sea-state number	9.2.1
$S(v)$	Fresnel sine integral	8.4.2
s	Signal-to-noise power ratio at input to envelope detector	4.2.1
s_o	Output signal-to-noise ratio of detector	4.4.1
T	Temperature	1.2
T_0	Reference temperature = 290K	1.4.1
$T_{0.1}$	Galactic temperature at 100 MHz	6.3.2
T_a	Antenna temperature	1.3.2
T'_a	Sky noise	6.3.1
T_B	Brightness temperature of sun	6.3.2
T_c	Temperature of cosmos	6.3.1
T_e	Receiver temperature	1.3.2
T_{ext}	External noise temperature at antenna	6.3.5
T_F	Search time fraction	2.4.1
T_G	Surface temperature	6.3.1
T_p	Physical temperature	6.2
T_{pt}	Physical temperature of transmitter	6.3.5
T_q	Quantizing noise temperature	6.5.3
T_r	Receiving line loss	1.3.2
T_s	System noise temperature	1.1.1
T_α	Tropospheric noise temperature	6.3.2
t_c	Correlation time	3.2.3
t_d	Two-way time delay of signal	1.6.1
t_f	Coherent processing interval	1.3.4
t_o	Observation time	1.1.2
t_r	Pulse repetition interval	1.3.4
t_s	Search frame time	1.6.3
U	Height-gain factor	8.4.1
V	Visibility factor	1.1.2
$V(X)$	Attenuation (range) factor	8.4.1
$V_{0(50)}$	Visibility factor for P_d = 50% on steady target	1.1.2

V_c	Volume of clutter in resolution cell	3.4.1
v	Instantaneous signal-plus-noise voltage	4.3.3
	Knife-edge diffraction parameter	8.4.2
	Shape parameter of *K*-distribution	9.1.4
v_0	Mean wind speed	9.1.3
v_{0f}	Projection of fall rate normal to beam axis	9.5.3
v_{0w}	Projection of mean wind speed on beam axis	9.5.3
v_w	Wind speed	3.6.2
v_z	Vertical velocity of target	2.5.1
	Normalized mean clutter velocity	9.6.1
W	Weight of chaff	9.5.6
$W(\cdot)$	Power spectral density	9.1.3
W_0	Zero-frequency power spectral density	9.1.3
W_ρ	Water-vapor factor for attenuation	7.2.5
X	Range in natural units	8.4.1
x	Coordinate of raster scan	5.4.1
	Relative magnitude of reflected ray at receiver	8.1.1
	$2\pi f\tau$	8.3.1
	Weight factor in interpolation	8.6.1
x_{50}	Median value of x	9.1.4
x_{av}	Average value of x	9.1.4
y	Sum of detector output voltages for n pulses	4.2.1
	Weight factor in interpolation	8.6.1
y_b	Threshold normalized to rms noise at detector output	4.2.1
Z	Normalized altitude	7.5.1
	Terminal height in natural units	8.4.1
	Precipitation reflectivity factor	9.5.5
α	Phase angle of reflected ray	8.1.1
	Scale parameter of Weibull distribution	9.1.4
β	Exponent of cosine factor in element gain	6.3.5
	Slope of surface facet giving specular reflection	9.1.1
β_0	$\sqrt{2}$ times rms slope of surface	9.1.1
$\chi(t_d)$	Output waveform	7.5.5
Γ	Reflection coefficient of antenna	6.3.5
$\Gamma(n)$	Euler gamma function	4.2.2
Γ_0	Reflection coefficient of antenna at broadside	6.3.5

Γ_{cs}, Γ_{os}	Reflection coefficients of same- and opposite-sense CP	8.3.1
Γ_h, Γ_v	Fresnel reflection coefficients for H and V polarizations	8.3.1
γ	Surface clutter reflectivity factor	3.3.3
	Earth-center angle subtended by ground range	8.2.4
Δ	Angular sampling interval	5.1.2
Δf	Agile bandwidth	4.5.2
	Absorption-line broadening factor	7.2.1
$\Delta\lambda$	Term in equation for dielectric constants of water	7.3.5
$\Delta\theta$	Elevation width of fence	2.5.1
	Change in target aspect angle	4.5.2
Δ_t	Time delay in ionosphere	7.5.5
δ	Difference between reflected and direct paths	8.1.1
$\delta_1 \ldots \delta_6$	Approximations of pathlength difference	8.2
δ_1, δ_2	Factors in 1st and 2nd estimates of detection range	1.3.2
δ_h	Departure of surface from tangent plane	8.2.3
δ_t	Differential time delay in ionosphere	7.5.5
δ_ϕ	Phase shift from ionospheric dispersion	7.5.5
ε	Complex dielectric constant of surface	8.3.1
ε_0, ε_∞	Terms in equation for dielectric constants of water	7.3.5
ε_c	Complex dielectric constant of water	7.3.5
ε_i, ε_r	Imaginary an real components of dielectric constant	8.3.1
ε_s	Static dielectric constant of water	8.3.1
$\eta(P_d,P_{fa})$	Shnidman's parameter for detectability calculation	4.2.6
η_a	Aperture efficiency	2.1
η_i	Illumination efficiency of aperture	10.1.5
η_v	Volume clutter reflectivity	9.5.1
θ	Elevation angle	1.6.4
	Angle coordinate in plane of scan	5.2.1
	Angle between ray and Earth's magnetic field	7.5.4
	Angle in knife-edge geometry	8.4.2
θ'	Local ray elevation	7.5.4
θ_0	Lower limit of search elevation	2.1
	Angle of ray leaving surface	7.1.5
θ_1	Upper elevation of full-range coverage	2.2.1
θ_2	Upper elevation of $\csc^2$ coverage	2.2.1

θ_3	Half-power (–3 dB) beamwidth	5.2.1
θ_a	Azimuth beamwidth	3.2.1
θ_{at}	Transmitting azimuth beamwidth	2.1
θ_b	Beam axis angle	3.3.4
θ_c	Lobe width of target reflection pattern	4.5.2
$\theta_{c\max}$	Maximum elevation of clutter	3.4.1
$\theta_{c\min}$	Minimum elevation of clutter	3.4.1
θ_e	Elevation beamwidth	1.6.3
θ_{et}	Transmitting elevation beamwidth	2.1
θ_m	Upper limit of search elevation	2.1
$\theta_{\max}$	Elevation of upper edge of transmitting beam	2.1
$\theta_{\min}$	Elevation of lower edge of transmitting beam	2.1
θ_r	Elevation angle of reflected ray	8.1.1
θ'_{rd}	Elevation angle of diffuse reflection	8.3.2
θ_t	Target elevation angle	1.6.4
$\theta_{t\max,\ \min}$	Transmitting beam limits	2.1
θ_t	Target elevation angle	5.3.1
λ	Radar wavelength	1.1.1
μ_{dB}	Mean of lognormal distribution	9.1.4
ρ	Surface reflection coefficient	6.3.1
ρ_0	Fresnel reflection coefficient	6.3.3
ρ_s	Specular scattering factor	6.3.3
ρ_v	Vegetation factor	6.3.3
ρ_w	Density of water vapor	6.3.2
ρ_{w0}	Water vapor density at sea level	7.1.3
σ	Target cross section	1.1.1
	Rms noise voltage	6.1.2
σ^0	Surface clutter reflectivity	3.3.3
σ_1	Standard deviation of single-pulse detector output	4.2.2
	Radar cross section of single raindrop	9.5.5
σ_b	Bistatic target cross section	1.3.5
σ_c	Radar cross section of clutter	9.1.1
σ_{dB}	Standard deviation in dB of lognormal clutter	9.1.4
σ_e	Conductivity of surface	8.3.1

σ_f^0	Facet clutter reflectivity	9.1.1
σ_h	rms roughness of surface	3.3.3
σ_h'	Adjusted rms roughness of surface	8.3.2
σ_i	Ionic conductivity	8.3.1
σ_v	Standard deviation of total clutter velocity spread	9.1.3
σ_{v0}	Spread of fixed component of clutter	9.1.3
σ_{va}	Antenna scan component of clutter velocity spread	9.1.3
σ_{vc}	Standard deviation of clutter velocity	9.1.3
σ_{vf}	Standard deviation of fall velocity component	9.5.3
σ_{vs}	Wind-shear component of clutter velocity spread	9.5.3
$\sigma_{v\theta}$	Beamwidth component of clutter velocity spread	9.1.3
σ_x	Standard deviation of integrated detector output	4.2.2
σ_z	Normalized clutter velocity spread	9.6.1
τ	Transmitted pulsewidth	1.1.1
	Relaxation constant of water	8.3.1
τ_n	Processed pulsewidth	3.3.1
Φ	Parameter in solution of cubic equation	8.2.5
$\Phi(E)$	Integral of the normal distribution	4.2.2
$\Phi^{-1}(P)$	Inverse of integral of the normal distribution	4.2.2
ϕ	Angle coordinate orthogonal to θ	5.2.1
	Faraday rotation angle	7.4.4
ϕ_3	Half-power beamwidth in ϕ coordinate	5.2.1
χ	Probability in chi-squared distribution	4.3.2
ψ	Grazing angle	3.3.1
ψ_B	Brewster angle	8.3.1
ψ_c	Critical grazing angle	9.1.2
ψ_{bt}	Beam sector (solid angle)	2.1
ψ_s	Search sector (solid angle)	2.1
Ω_s	Solid angle of Sun as viewed from Earth	6.3.2
ω_a	Rate of change of target aspect angle	4.5.2
ω_e	Rate of change of target elevation	2.5.1
ω_s	Antenna scan rate	9.1.3

Appendix

Contents of DVD

The DVD in the back of this book contains Mathcad® worksheets that apply the equations from the text to problems commonly encountered in using the radar equation. Printouts of each worksheet are also included in PDF format to permit readers without the Mathcad® program to review the calculation procedures and generate worksheets in the language used by other mathematical programs.

The worksheets were written in Mathcad 11, and should run also on subsequent versions of that program. The filenames are listed here by the chapter to which they relate. Methods of calculation and results obtained are summarized.

Worksheets for Chapter 1

1-1 Revised Blake Chart.mcd

The Blake chart provides a convenient method for calculating radar detection range and recording the parameters used in the calculation. This worksheet implements Blake's procedure, as revised and shown in Figure 1.2 of the book. It requires separate calculations of the pattern-propagation factor, detectability factor and several loss terms that are inserted in the worksheet as user inputs. It includes subroutines for calculation of the sky temperature and atmospheric attenuation (including lens loss and the effect of any specified rain). The two-step iterative procedure for applying these attenuation terms is implemented automatically in the worksheet.

1-2 Range in Thermal Noise.mcd

This worksheet calculates the maximum detection range of a radar when thermal noise is the only source of interference. Propagation conditions may depart the simplified assumptions inherent in the Blake chart, and may include attenuation from rain. Detection range is calculated for either of two types of target trajectory: constant target elevation, or constant target altitude. In addition to the parameters entered in the Blake chart, the user enters data for other radar parameters such as the elevation beamwidth and local surface conditions, rain rate and extent. Effects of clutter are not included (see Worksheet 3-1).

1-3 Required Pd.mcd

This worksheet calculates the probabilities of track initiation and retention for a track-while-scan system, as functions of the scan number for different values of single-scan P_d. The criterion for track initiation is detection on two out of three scans following the initial detection. The criterion for dropping tracks is either two or three consecutive missed detections. The worksheet was used to generate Figures 1.7 and 1.8 of the book.

Worksheets for Chapter 2

2-1 Search Equation.mcd

This worksheet solves the search radar equation for detection range as a function of radar and target parameters. Supplementary relationships are given to guide in specification of certain radar parameters.

2-2 Power-Aperture Product.mcd

This worksheet solves the search radar equation for power-aperture product as a function of required detection range and target parameters. Supplementary relationships are given for derivation of radar parameters.

2-3 Air Surveillance Coverage.mcd

This worksheet plots coverage patterns for $\csc^x$ coverage with x = 1, 1.5, and 2, and for coverage matched to a constant-altitude profile. Coverage losses for each type of pattern are also calculated, as shown in Figure 2.2 of the book.

Worksheets for Chapter 3

3-1 Range in Interference.mcd

This worksheet calculates the maximum detection range of a radar, starting with benign conditions in which the propagation conditions may depart the simplified assumptions inherent in the Blake chart. Calculations are extended to environments with noise jamming and clutter, for which user inputs include propagation, clutter, jamming, and radar parameters that determine the effects of interference. Options are provided to permit skipping calculations for each jamming and clutter source to save computing time.

3-2 CW and HPRF PD Range.mcd

This worksheet calculates the clutter input energy and detection range of surface-based CW and HPRF PD radars, considering surface and volume clutter, as discussed in Sections 3.3.4 and 3.4.6 of the book. The equations generate Figures 3.3, 3.4, 3.5, 3.8, and 3.9 of the book.

3-3 Jamming.mcd

This worksheet calculates the effects of noise jamming on radar interference level, and the requirements on repeater jammers operating in both mainlobe and sidelobe regions.

Worksheets for Chapter 4

4-1 Detectability Factor.mcd

The detectability factor is defined as the input signal-to-noise energy ratio required to obtain specified probabilities of detection P_d and false alarm P_{fa} for a given number n of pulses integrated on a specified target type. This worksheet calculates the basic detectability factor (excluding matching, beamshape, and "miscellaneous signal processing losses" that are covered by Worksheet 10-1) as a function of P_d, P_{fa}, n, and target type, for single pulses and for video (noncoherent) integration, and the detection probability for specified input snr, P_{fa}, n and target type with and without integration. The target types include steady, Swerling Cases 1–4, and a generalized target providing n_e independent samples during the integration period. Curves of integration and fluctuation loss are also generated, as shown in Figures 4.9 and 4.10 of the book.

Worksheets for Chapter 5

5-1 Beamshape 1-D.mcd

This worksheet calculates the beamshape loss for one-dimensional scanning when the number of pulses per beamwidth is ≤ 1.5. The loss is defined as the increase in on-axis SNR required to maintain a given probability of detection. The reference for loss is the detectability factor for integration of the signal energy received during scan through one beamwidth with the on-axis antenna gain. Results are obtained here for both the case of constant energy per dwell is used (total energy for the scan increases as beams are overlapped) and of constant energy per scan, using either video integration or cumulative probability over the available samples. Two antenna tapers are considered: a Gaussian and a cosine illumination of a rectangular aperture. Steady and fluctuating targets are considered, and for the latter the signal can be correlated (Case 1) or uncorrelated (Case 2) from dwell to dwell.

5-2 Beamshape 2-D Steady.mcd

This worksheet calculates the beamshape loss on a steady target for one-dimensional scanning when the number of pulses per beamwidth is ≤ 1.5. The reference for loss is the detectability factor that would apply using the on-axis antenna gain over the time required to scan one beamwidth. Results are obtained for two cases: constant energy per dwell, in which the total energy for the scan increases as beams are overlapped, and constant energy per scan, in which the

energy per dwell is reduced as beams are overlapped. The beam pattern for cosine illumination is used.

5-3 Beamshape 2-D Case 1.mcd

This worksheet performs the same calculations as in 5-2 but for the Swerling Case 1 target.

5-4 Beamshape 2-D Case 2.mcd

This worksheet performs the same calculations as in 5-2 but for the Swerling Case 2 target.

5-5 Beamshape 2-D Diversity.mcd

This worksheet performs the same calculations as in 5-2 but for the a target that is correlated over each scan line but decorrelated from line to line.

5-6 Beamshape Triangle Steady.mcd

This worksheet performs the same calculations as in 5-2 but for the 2-D raster scan using a triangular grid of beam positions.

5-7 Beamshape Triangle Case 1.mcd

This worksheet performs the same calculations as in 5-3 but for the 2-D raster scan using a triangular grid of beam positions.

5-8 Beamshape Triangle Case 2.mcd

This worksheet performs the same calculations as in 5-4 but for the 2-D raster scan using a triangular grid of beam positions.

5-9 Beamshape Triangle Diversity.mcd

This worksheet performs the same calculations as in 5-5 but for the 2-D raster scan using a triangular grid of beam positions.

Worksheets for Chapter 6

6-1 Noise Temperature.mcd

This worksheet calculates the system input noise temperature of a radar with a narrow beam directed at a specified elevation angle. Effect of rain attenuation on sky temperature is not included, but a separate calculation for that is included in Worksheet 7-6.

6-2 Sky Temperature.mcd

This worksheet calculates the sky noise temperature for a narrow beam directed at a specified elevation angle, and plots results as a function of frequency for select-

ed beam angles, as in Figure 6.6 of the book. Effect of rain attenuation is not included. Sky temperature for specific conditions may be found by entering those conditions at the end of the worksheet.

6-3 Cascaded Receiver Stages.mcd

This worksheet calculates the receiver noise temperature T_e for a multistage receiver, with input parameters and output data as shown in Table 6.2 of the book.

Worksheets for Chapter 7

7-1 Standard Atmosphere.mcd

This worksheet stores the parameters of the 1976 U.S. Standard Atmosphere up to 30 km altitude for use in radar propagation worksheets. Analytical approximations are given for temperature, pressure, water-vapor density, and refractivity as functions of altitude. Parameters of the CRPL exponential reference atmospheres are listed, and the effective Earth's radius constant is derived for each of these models.

7-2 Attenuation and Noise.mcd

This worksheet generates a table of tropospheric attenuation coefficients and creates continuous functions by interpolation. The atmosphere model from worksheet 7-1 is used to calculate the refractive index profile for ray-tracing and to scale the attenuation coefficients to temperature and density of oxygen and water vapor as a function of altitude. These data are used to calculate the tropospheric attenuation as a function of range at specified elevation angles and radar frequencies, and to generate plots for Chapter 7.

7-3 Attenuation at Frequency F.mcd

This worksheet calculates the tropospheric attenuation as a function of range for a specified frequency F and beam elevation angle θ_b, using expressions from the worksheet 7-2 that are modified to run more rapidly for the specified frequency.

7-4 Weather Attenuation.mcd

This worksheet applies expressions for rain attenuation derived by Blake, and combines these with a temperature correction factor from referenced sources to obtain attenuation coefficients for arbitrary temperature. Attenuation coefficients for snow and clouds are also calculated.

7-5 Lens Factor.mcd

The lens factor F_{lens}^2 is the reciprocal of the two-way lens loss as defined by Weil, who provided plots of lens loss as a function of target range and elevation angle of the beam at the radar site. This worksheet calculates the lens loss and reproduces

Weil's plot. The method of solution is to use Blake's ray-tracing formula to find the pathlength of the ray that reaches a target at a given altitude above the Earth's surface. Two root-finding equations are then applied, the first finding the ray angle as a function of the target's range and true elevation, and second finding the true target elevation as a function of its range, as required to produce the plot for specific beam elevation angles. The two-way lens loss is given by the square of the ratio of a small increment of true target elevation to the corresponding change in beam angle at the radar. This ratio represents the spreading of energy in the beam as it travels through the refracting atmosphere. The lens factor $20\log(F_{\text{lens}})$ in dB is the negative of the lens loss in dB.

7-6 Total Loss at Frequency F.mcd

This worksheet calculates, for a specified frequency and elevation angle, the tropospheric absorption, lens loss, and weather attenuation as functions of range. The corresponding components of sky noise are also calculated.

7-7 Ionosphere.mcd

This worksheet performs calculations on ionospheric effects used in the radar equation: Faraday rotation loss and dispersion loss. The electron densities of the Chapman layers are modeled as in Figure 7.31 of the book. The total electron density as a function of a path to a specified altitude at specified elevation angle is calculated by integration to generate Figure 7.32. The corresponding Faraday rotation is calculated for f_0 = 100 MHz as a function of altitude (Figure 7.33), and for paths through the ionosphere as a function of frequency in daytime and nighttime at elevation angles of 0 and 90° (Figure 7.34). From these data, the Faraday rotation losses, both as the average over the total rotation angle and as a statistical loss in reaching a specified P_d, are found (Figures 7.35 and 10.5). The loss from dispersion over the signal spectrum (Figures 7.36–7.39) is also found.

Worksheets for Chapter 8

8-1 Propagation Factor.mcd

This worksheet calculates the propagation factor, including the reflected interference and diffraction factors, as a function of target range and height. In order to produce smooth plots in a minimum computation time, the range and target height are varied in logarithmic steps between specified minimum and maximum values. The factor for a specific target location is calculated.

8-2 Reflection Coefficient

This worksheet calculates and plots the reflection coefficient as a function of grazing angle, for a specified surface and wavelength, including its three components: (1) the Fresnel reflection coefficient for vertical and horizontal polarizations; (2)

the specular scattering factor; and (3) the vegetation factor. The Fresnel coefficient is calculated using the Saxton and Lane expressions for dielectric constant of sea water and user inputs for land surfaces. The specular scattering factor is given by (8.57) in the book. The vegetation factor is calculated using the empirical model developed by Barton for use in *Modern Radar System Analysis Software, Version 3*, and given by (8.61) in the book.

Worksheets for Chapter 9

9-1 Surface Clutter

This worksheet calculates the reflectivity, propagation factor, and spectral parameters of land and sea clutter, as described in Sections 9.1–9.4 of the book. Plots of the propagation factor (Figures 9.2 and 9.3 in the book) are generated, as well as the empirical relationship of Weibull and lognormal spread parameters to propagation factor (Figure 9.4) and the products $\sigma^0 F_c^4$ of Figures 9.5 and 9.8.

9-2 Volume Clutter

This worksheet calculates the reflectivity, propagation factor, and spectral parameters of rain and sea clutter, as described in Sections 9.5 of this book. Rain, snow, and cloud reflectivities are calculated using data from Battan's *Radar Observation of the Atmosphere* and Sauvageot's *Radar Meteorology*.

9-3 Clutter Improvement Factor

This worksheet calculates the clutter improvement factors of coherent and noncoherent MTI and pulsed Doppler processors. User inputs include the spectral parameters of the clutter, the radar waveform, and the parameters of the signal processor.

Worksheet for Chapter 10

10-1 Loss Factors.mcd

This worksheet calculates the losses that enter into the radar equation that are not specific subjects of other worksheets (e.g., atmospheric attenuation and beamshape loss). Losses are considered under five headings:

1. Those that reduce received signal energy: RF line loss and RF mismatch loss, polarization factor, and components of the range-dependent response factor (STC factor, beam-dwell factor, eclipsing factor), scan and scan-sector losses.
2. Losses in the search radar equation: elevation beamshape loss, beamwidth factor, aperture efficiency and illumination loss, scan distribution loss.

3. Losses in antenna gain: dimensional tolerances, phase-shifter quantization. feed and module phase and amplitude errors.
4. Filter matching loss, including receiver and pulse compression.
5. Signal processing losses: binary integration loss, CFAR loss, collapsing loss, MTI and PD processing losses, straddling losses in all coordinates, losses in the clutter detectability factor, and clutter map loss.

Supplemental Worksheets

For the convenience of users of *Modern Radar System Analysis Software, Version 3.0*, modified worksheets for several segments of that software are provided. These replace the corresponding worksheets that the user has already installed from Version 3.0, but the remainder of those worksheets are still required to perform the radar system analysis. The modifications include corrections and additions to worksheets that generate the radar, environment, and jammer models, and to the system analysis and search coverage worksheets.

About the Author

David K. Barton is a radar system consultant, with a home and office in Hanover, New Hampshire. He attended Harvard College from 1944 to 1949, with a two-year interruption for service in the U.S. Army at White Sands Proving Grounds. He returned to White Sands as a civilian engineer after receiving his A.B. in physics in 1949. In 1953, Mr. Barton transferred to the Signal Corps Laboratories at Fort Monmouth, New Jersey, to initiate development of the AN/FPS-16, the first monopulse instrumentation radar. In 1955, he joined the staff at RCA, where the radar development was carried out, and participated in the test and evaluation of the system. For this work RCA awarded him in 1958 the first David W. Sarnoff Medal for Outstanding Achievement in Engineering. Mr. Barton also scaled up that radar to create in 1960 the AN/FPS-49 radars for the Ballistic Missile Early Warning System, only recently replaced after 40 years of operation in Alaska and Great Britain.

From 1963 to 1984 he was a consulting scientist with Raytheon Company in Wayland and Bedford, Massachusetts, where he originated the radar concepts for the AN/TPS-19 radar-controlled landing system for the U.S. Air Force, and contributed to a number of other radar and guided missile studies and projects. He joined ANRO Engineering in 1984, engaging in radar and missile system studies until his retirement in 2004.

Mr. Barton was elected a Fellow of the IEEE in 1972 and to the National Academy of Engineering in 1997. In 2002, he received the IEEE Dennis J. Picard Medal for Radar Technologies and Applications. He has served on the scientific advisory boards of the U.S. Air Force, the Defense Intelligence Agency, and the Army Research Laboratories. Since 1975 he has been the editor of the Artech House Radar Series, of which this book is approximately the 165th volume.

Index